UNIVERSITY OF CALIFORNIA, SAN DIEGO

Numerical and Experimental Investigations of Nonlinear Behavior of RC Members and Slab-Column Assemblies in Bridges

A dissertation submitted in partial satisfaction of the requirements for the degree
Doctor of Philosophy

in

Structural Engineering

by

Vasileios Papadopoulos

Committee in charge:

Professor P. Benson Shing, Chair
Professor Yuri Bazilevs
Professor Juan C. Del Alamo
Professor Jose I. Restrepo
Professor Michael D. Todd

2015

The dissertation of Vasileios Papadopoulos is approved, and it is acceptable in quality and form for publication on microfilm and electronically:

Chair

University of California, San Diego

2015

DEDICATION

To my family,

EPIGRAPH

Η τρικυμία ποτέ δε θα σβηστεί

για μιαν ανεξιχνίαστη αιτία,

καρφώθηκα σε όμορφη εξορία,

το πέλαγο καρφί μου και σφυρί.

For a mysterious cause

the storm will never end,

I am stuck in a beautiful exile,

the ocean shall be my pin and hammer.

Vaggelis Liaros

TABLE OF CONTENTS

LIST OF ABBREVIATIONS

AASHTO: American Association of State Highway and Transportation Officials

ACI: American Concrete Institute

ASTM: American Society for Testing and Materials

BDS: Bridge Design Specifications

BDA: Bridge Design Aids

Caltrans: California Department of Transportation

CCT: Compression-Compression-Tension

CCD: Concrete Capacity Design

CIDH: Cast-In-Drilled-Hole

D-P: Damaged-Plasticity

FE: Finite Elements

FEA: Finite Element Analysis

HRC: Headed Reinforcement Corp.

LCF: Low Cycle Fatigue

LRFD: Load and Resistance Factor Design

MTD: Memo To Designers

PVC: Poly Vinyl Chloride

RC: Reinforced Concrete

SDC: Seismic Design Criteria

LIST OF SYMBOLS

Chapter 1

d_b : bar diameter

Chapter 2

Modeling of Steel Reinforcement

a_1 : constant for the transition of the stress-strain curve between the two asymptotes

a_2 : constant for the transition of the stress-strain curve between the two asymptotes

b : kinematic hardening parameter

c : low cycle fatigue coefficient

D : accumulated damage due to low cycle fatigue

D_i : low cycle fatigue damage due to the i-th strain reversal

d_b : bar diameter

E_0 : modulus of elasticity

E_1 : slope of the asymptote for kinematic hardening

f_y : yield stress of rebar in monotonic loading

$f_{y,m}$: stress parameter defining the asymptote for kinematic hardening

f_u : ultimate stress of steel

L : unsupported length of reinforcing bar

N_f : number of cycles to failure for a constant strain range $\Delta\varepsilon$

R : parameter controlling the transition of the stress-strain curve between the two asymptotes

R_{LCF} : ratio of minimum strain to maximum strain of the strain range in cyclic loading

R_0 : constant for the transition of the stress-strain curve between the two asymptotes

$\Delta\varepsilon$: strain range

ε : strain

ε^* : normalized strain

ε'_f : low cycle fatigue coefficient

$\varepsilon_{\max}$: maximum strain attained in previous cycles

$\varepsilon_{\text{mean}}$: mean strain in cyclic loading

$\varepsilon_{\min}$: minimum strain attained in previous cycles

ε_o : strain at which the asymptotes for elastic loading and kinematic hardening meet during reloading

ε_r : strain at reversal point

$\varepsilon_{y,m}$: strain parameter defining the asymptote of kinematic hardening

ξ : parameter for the transition of the stress-strain curve between the two asymptotes

σ : stress

σ^* : normalized stress

σ_{mean} : mean stress in cyclic loading

σ_o : stress at which the asymptotes meet during reloading

σ_r : stress at reversal point

Damaged-Plasticity model for Concrete

a : yield surface constant

d : damage parameter

d_c : damage parameter in compression

d_t : damage parameter in tension

$\mathbf{E}$: elastic stiffness tensor

$\mathbf{E_o}$: initial stiffness tensor

F : yield function

f_c : uniaxial compressive strength for concrete

f_{cc} : uniaxial compressive strength for confined concrete

G : plastic potential

I_1 : first stress invariant

J_2 : second deviatoric stress invariant

K_c : ratio of the deviatoric stress on the tensile meridian to that on the compressive meridian in the pi-plane at initial yield

w_c : compression recovery factor

w_t : tension recovery factor

β : yield surface parameter

γ : yield surface constant

ε : eccentricity for plastic potential

$\boldsymbol{\varepsilon}$: strain tensor

$\boldsymbol{\varepsilon}^{\mathbf{e}}$: elastic strain tensor

$\boldsymbol{\varepsilon}^{\mathbf{p}}$: plastic strain tensor

$\tilde{\varepsilon}_c^p$: equivalent plastic strain in compression

$\tilde{\varepsilon}_t^p$: equivalent plastic strain in tension

$\dot{\boldsymbol{\varepsilon}}^{\mathbf{p}}$: plastic strain rate tensor

$\dot{\varepsilon}_i^p$: principal plastic strain rates with $i = 1,\ 2,\ 3$

$\hat{\dot{\varepsilon}}_{\max}^p$: maximum principal plastic strain rate

$\hat{\dot{\varepsilon}}_{\min}^p$: minimum principal plastic strain rate

$\dot{\tilde{\varepsilon}}_c^{\ p}$: equivalent plastic strain rate in compression

$\dot{\tilde{\varepsilon}}_t^{\ p}$: equivalent plastic strain rate in tension

$\dot{\lambda}$: plastic multiplier

ρ_t : transverse reinforcement ratio

$\boldsymbol{\sigma}$: stress tensor

$\bar{\boldsymbol{\sigma}}$: effective stress tensor

$\hat{\bar{\boldsymbol{\sigma}}}$: principal effective stress tensor

σ_{b0} : initial equibiaxial compressive yield stress

σ_c : function of stress-strain curve in uniaxial compression

σ_{c0} : initial uniaxial compressive yield stress

σ_t : function of stress-strain curve in uniaxial tension

σ_{t0} : initial uniaxial tensile strength

$\bar{\sigma}_c$: effective compressive cohesion strength

$\bar{\sigma}_t$: effective tensile cohesion strength

$\hat{\sigma}_{\max}$: maximum principal stress

ψ : dilation angle

Microplane model for Concrete

a : volumetric boundary parameter

c_i : fixed parameters of microplane model with $i = 1,...,20$

E : elastic modulus for concrete in the microplane model

E_N : damaged normal elastic stiffness in the normal direction of the microplane

E_{N0} : undamaged elastic stiffness in the normal direction of the microplane

E_T : shear elastic stiffness in a direction parallel to the microplane

E_0 : reference elastic modulus for low-strength concrete

f_c' : compressive strength of concrete

f_{c0}' : reference compressive strength for low-strength concrete

k_i : free parameters of microplane model with $i = 1,...,5$

N_m : number of microplanes

$s_{ij}^{(\mu)}$: stress tensor contribution from each microplane

ν : Poisson's ratio

w_μ : weight for the integration of stresses over the microplanes

β_1 : normal stress boundary parameter

β_2 : deviatoric stress boundary parameter

β_3 : deviatoric stress boundary parameter

γ_0 : deviatoric stress boundary constant

γ_1 : deviatoric stress boundary parameter

$\Delta\varepsilon_D$: deviatoric strain increment at the microplane

$\Delta\varepsilon_L$: strain increment, parallel to the microplane, oriented in the direction of orthogonal unit $\mathbf{l}$

$\Delta\varepsilon_M$: strain increment, parallel to the microplane, oriented in the direction of orthogonal unit $\mathbf{m}$

$\Delta\varepsilon_N$: normal strain increment at the microplane

$\Delta\varepsilon_V$: volumetric strain increment

$\boldsymbol{\varepsilon}$: strain tensor

ε_D : deviatoric strain at the microplane

ε_e : strain parameter used in the calculation of the volumetric and damaged normal microplane elastic stiffness

ε_L : strain, parallel to the microplane, oriented in the direction of orthogonal unit $\mathbf{l}$

ε_M : strain, parallel to the microplane, oriented in the direction of orthogonal unit $\mathbf{m}$

ε_N : strain, normal to the microplane, oriented in the direction of orthogonal unit $\mathbf{n}$

ε_p : strain at peak compressive strength of concrete

ε_V : volumetric strain

ε_D^o : deviatoric strain at the microplane at previous step

ε_I^o : maximum principal strain at previous step

ε_{III}^o : minimum principal strain at previous step

ε_V^o : volumetric strain at previous step

ε_N^{0+} : maximum normal strain at the microplane, reached up to the current step

ε_N^{0-} : minimum normal strain at the microplane, reached up to the current step

ρ_t : transverse reinforcement ratio

$\boldsymbol{\sigma}$: stress tensor

σ_L : stress, parallel to the microplane, oriented in the direction of orthogonal unit $\mathbf{l}$

σ_M : stress, parallel to the microplane, oriented in the direction of orthogonal unit $\mathbf{m}$

σ_N : normal microplane stress, oriented in the direction of orthogonal unit $\mathbf{n}$

σ_V : volumetric stress

σ_D^b : deviatoric stress boundary

σ_N^b : normal stress boundary

σ_T^b : shear stress boundary

σ_V^b : volumetric stress boundary

σ_N^e : elastic normal microplane stress (trial stress)

σ_T^e : elastic shear microplane stress (trial stress)

σ_L^o : stress at the previous step, parallel to the microplane, oriented in the direction of orthogonal unit $\mathbf{l}$

σ_M^o : stress at the previous step, parallel to the microplane, oriented in the direction of orthogonal unit $\mathbf{m}$

σ_N^o : normal microplane stress at previous step

σ_V^o : volumetric stress at previous step

$\hat{\sigma}_N^o$: stress variable for the calculation of the shear stress boundary

Ω : surface of a unit hemisphere

Bond-Slip Interface Model

d_b : bar diameter

f_c' : compressive strength of concrete

$K_{pen,1}$: penalty stiffness coefficient in the normal direction

$K_{pen,3}$: penalty stiffness coefficient in the rotational direction

s_{peak} : slip at peak bond strength

s_R : clear spacing between the ribs of a deformed bar

s_1 : normal relative interface displacement

s_2 : tangential relative interface displacement

s_3 : relative interface rotation

θ : inclination angle of the bond forces with respect to the bar longitudinal axis

σ_1 : normal stress at the interface

$\tau_{\max}$: peak bond strength

τ_{rev} : resistance right after slip reversal

τ_2 : longitudinal tangential stress at the interface

τ_3 : rotational tangential stress at the interface

Chapter 3

A_g : area of pile cross section

D : pile diameter

D_c : diameter of confined core

d_b : bar diameter

F_y : lateral load at the yield of the equivalent elastic-perfectly plastic system

F_y' : lateral load at the first yield of longitudinal reinforcement

f_c' : compressive strength of concrete

s_l : lineal spacing of longitudinal reinforcement

s_t : spacing of transverse reinforcement

Δ : lateral displacement at the level of the actuator

Δ_y : lateral displacement at the yield of the equivalent elastic-perfectly plastic system

Δ_y' : lateral displacement at the first yield of longitudinal reinforcement

θ_l : angular spacing

μ : lateral displacement ductility

ρ_l : longitudinal reinforcement ratio

ρ_t : transverse reinforcement ratio

Chapter 4

A_g : area of pile cross section

c : low cycle fatigue coefficient

D : pile diameter

E : elastic modulus for concrete in microplane model

E_s : elastic stiffness of steel reinforcement

f_y : yield stress of steel reinforcement

f_c' : compressive strength of concrete

f_t' : tensile strength of concrete

K_c : ratio of the deviatoric stress on the tensile meridian to that on the compressive meridian in the pi-plane at initial yield in the damaged-plasticity model

k_i : free parameters of microplane model with $i = 1,...,5$

L : unsupported length of reinforcing bar

w_c : compression recovery factor in the damaged-plasticity model

w_t : tension recovery factor in the damaged-plasticity model

ε : eccentricity for plastic potential in the damaged-plasticity model

ε_f' : low cycle fatigue coefficient

ε_p : strain at peak stress of concrete in compression in the microplane model

$\varepsilon_{p,\mathrm{FEA}}$: normal plastic strain in concrete in the axial direction of the pile in the FEA

σ_{b0} : initial equibiaxial compressive yield stress in the damaged-plasticity model

σ_{c0} : initial uniaxial compressive yield stress in the damaged-plasticity model

ψ : dilation angle in the damaged-plasticity model

Chapter 5

A_b : bar area

A_n : total failure surface area

A_{cap}^{top} : area of top flexural reinforcement in the slab, in the longitudinal and transverse direction within the effective width

A_{cap}^{bot} : area of bottom flexural reinforcement in the slab, in the longitudinal and transverse direction within the effective width

A_{st} : area of main column reinforcement anchored in the slab-column joint

A_s^{j-bar} : area of J-bars inside the core region of the slab-column joint

A_s^{jv} : total area of vertical stirrups in the joint region of the slab-column joint

A_s^{jvp} : total area of vertical stirrups the joint perimeter of the slab-column joint

A_s^{jh} : total area of horizontal ties in the joint region along the longitudinal direction

A_s^{sf} : total area of bent cap side face reinforcement

$A_{v,joint}$: transverse column reinforcement in the joint region

B_{eff} : effective width in the slab for the longitudinal and transverse directions

C_1 : minimum edge distance from anchored headed bar

D_c : column diameter

D_s : slab thickness

d_b : bar diameter

F : lateral load capacity

F_y : lateral load at the yield of the equivalent elastic-perfectly plastic system

F_y' : lateral load at the first yield of longitudinal reinforcement

f_c' : compressive strength of concrete

f_y : yield stress for steel

h_d : embedment length for headed bar by De Vries et al. (1999)

l_{dt} : minimum development length for headed bar in tension by ACI 318-11

P_n : anchor capacity of headed bar

Δ : lateral displacement at the level of the actuator

Δ_{C4} : average displacement amplitude at Cycle 4 during the test

Δ_y : lateral displacement at the yield of the equivalent elastic-perfectly plastic system

Δ_y' : lateral displacement at the first yield of longitudinal reinforcement

ε_u : strain at ultimate stress of steel

ε_y : yield strain of steel

μ : lateral displacement ductility

ρ_l : longitudinal reinforcement ratio

Ψ : reduction factor of anchor capacity due to edge placement

ψ_e : parameter for different types of reinforcement

Chapter 6

c : low cycle fatigue coefficient

E : elastic modulus for concrete in microplane model

E_s : elastic stiffness of steel reinforcement

d_b : bar diameter

f_c' : compressive strength of concrete

f_t' : tensile strength of concrete

f_u : ultimate stress of steel

f_y : yield stress of steel

G_f^I : fracture energy in the damaged-plasticity model

k_i : free parameters of microplane model with $i = 1,...,5$

l_e : embedment length of headed bar

P_{FEA} : anchor capacity of headed bar in the FEA

P_{test} : anchor capacity of headed bar in the test

s_t : spacing of transverse reinforcement

w_c : compression recovery factor in the damaged-plasticity model

w_t : tension recovery factor in the damaged-plasticity model

ε : eccentricity for plastic potential in the damaged-plasticity model

ε_f' : low cycle fatigue coefficient

ε_p : strain at peak stress of concrete in compression in the microplane model

ε_y : yield strain of steel

σ_{b0} : initial equibiaxial compressive yield stress in the damaged-plasticity model

σ_{c0} : initial uniaxial compressive yield stress in the damaged-plasticity model

ψ : dilation angle in the damaged-plasticity model

LIST OF FIGURES

LIST OF TABLES

ACKNOWLEDGEMENTS

The research presented in this dissertation was conducted under the supervision of Professor P. Benson Shing at the University of California at San Diego. The core of this research was related to the projects "Influence of the Spacing of Longitudinal Reinforcement on the Performance of Laterally Loaded CIDH Piles" and "Development Length for Headed Bars in Slab-Column Joints of RC Slab Bridges", supported by the California Department of Transportation (Caltrans).

I would like to express my deepest gratitude and appreciation to my advisor, Professor P. Benson Shing. His wise guidance, encouragement and courteousness have been a great support during my doctoral studies at UC San Diego. I want to thank him for giving me the opportunity to work with an individual of his expertise and high moral standards.

I would like to thank my Ph.D. Committee, Professor Yuri Bazilevs, Professor Jose I. Restrepo, Professor Michael D. Todd and associate Professor Juan Carlos Del Alamo for their inspiring courses, which were invaluable for my research, and for providing useful suggestions for my dissertation.

I am also grateful to Caltrans for financially supporting my graduate studies for the past 5 years. I would also like to express my honor and gratitude to Fulbright, for awarding me a scholarship and for the partial financial support of the 1st year of my graduate studies.

The experiments presented in this dissertation were conducted in the Powell Structural Engineering Laboratories at UC San Diego. I would like to express my sincere gratitude to the laboratory staff for their professionalism, technical support and guidance. Special thanks to Dr. Christopher Latham, Mr. Paul Greco, Mr. Noah Aldrich and Mr. Darren McKay for having the honor and pleasure to work with, and for building an environment of cooperation and accountability.

I would like to acknowledge the contributions of Professor Ioannis Koutromanos and Dr. Juan Murcia-Delso to this dissertation. Professor Ioannis Koutromanos contributed as a post-doctoral researcher in the implementation of the microplane model for concrete in finite-element analyses. I want to thank Dr. Juan Murcia-Delso for his valuable contributions in the finite-element modeling, and his participation in the design and testing of the 1st slab-column specimen presented in Chapter 5. I am grateful for their precious support and advice.

I would like to thank all the people in the Department of Structural Engineering, my colleagues, the faculty and staff members, who I have had the pleasure to work and interact with, and especially Mr./Ms. Alexandra Kottari, Marios Mavros and Andreas Koutras. I am also grateful to my old and new friends with whom I have lived and shared so many beautiful moments to remember. I greatly value their friendship and I deeply appreciate our mutual support and care for each other.

I feel the need to express my gratitude to poet and sailor Nikos Kavvadias, who has been one of my greatest sources of inspiration. His work has been the wind filling my sails, helping me to start and enjoy this long journey.

Finally, I would like to thank my family, my parents, Evaggelos and Georgia, and my sisters, Konstantina and Penny, for their unconditional love and support through every step of my life. They have always been by my side, in the bright but most importantly the dark times, throughout all these years. It is to them that I dedicate this dissertation.

Chapter 2, in full, is a reprint of the material as it appears in the report submitted to the California Department of Transportation in 2015, Papadopoulos, V., Shing, P. B., under the title "Influence of the Spacing of Longitudinal Reinforcement on the Performance of Laterally Loaded CIDH Piles – Analytical Investigation". The dissertation author was the primary investigator and author of this report.

Chapter 3, in full, is a reprint of the material as it appears in the report submitted to the California Department of Transportation in 2014, Papadopoulos, V., Shing, P. B., under the title "Influence of the Spacing of Longitudinal Reinforcement on the Performance of Laterally Loaded CIDH Piles – Experimental Investigation". The dissertation author was the primary investigator and author of this report.

Chapter 4, , in full, is a reprint of the material as it appears in the report submitted to the California Department of Transportation in 2015, Papadopoulos, V., Shing, P. B., under the title "Influence of the Spacing of Longitudinal Reinforcement on the Performance of Laterally Loaded CIDH Piles – Analytical Investigation". The dissertation author was the primary investigator and author of this report.

Chapters 5 and 6, in full, are a reprint of the material as it appears in the report submitted to the California Department of Transportation in 2015, Papadopoulos, V., Murcia-Delso, J., Shing, P. B., under the title "Development Length for Headed Bars in Slab-Column Joints of RC Slab Bridges". The dissertation author was the primary investigator and author of this report.

VITA

2010 Diploma in Civil Engineering, National Technical University of Athens

2012 Master of Science in Structural Engineering, University of California, San Diego

2015 Doctor of Philosophy in Structural Engineering, University of California, San Diego

ABSTRACT OF THE DISSERTATION

Numerical and Experimental Investigations of Nonlinear Behavior of RC Members and Slab-Column Assemblies in Bridges

by

Vasileios Papadopoulos

Doctor of Philosophy in Structural Engineering

University of California, San Diego 2015

Professor P. Benson, Shing, Chair

Reinforced concrete (RC) bridges constitute a significant part of the infrastructure inventory around the world. The understanding of the different failure mechanisms of their components and the development of accurate analysis tools for their simulation are important to assess their nonlinear behavior during earthquake events.

This dissertation presents two studies investigating the nonlinear behavior of RC bridge components and assemblies using large-scale experimental testing and nonlinear finite-element (FE) modeling. For these studies, suitable constitutive models for concrete and the bond-slip behavior of reinforcing bars embedded in concrete have been identified and calibrated, and a constitutive model that accounts for the low-cycle fatigue behavior of steel has been developed and implemented in a finite element analysis program.

In the first study, the impact of the spacing of longitudinal bars on the performance of circular RC piles under lateral loading was investigated. Two full-scale RC pile specimens were tested under lateral loading.

The second study was aimed to determine the minimum development length required for headed bars in slab-column joints of RC bridges, so that the thickness of the slab does not have to be larger than that required for normal traffic loads. Three full-scale RC slab-column specimens, with embedment lengths of the headed bars smaller than the minimum allowed in current design provisions, were tested.

In both studies, nonlinear FE models were developed to evaluate the performance of the test specimens, and to conduct numerical parametric investigations examining the influence of different design details. The capability of the constitutive models in simulating the nonlinear behavior of RC members is established through the FE analyses. Finally, based on the experimental and numerical findings of these studies, recommendations and possible changes for the design of RC piles in terms of the spacing of the longitudinal reinforcement and of slab-column joints with headed bars are provided.

CHAPTER 1

INTRODUCTION

The performance of reinforced concrete (RC) bridge members depends on the combined action of concrete and reinforcing steel. When subjected to earthquake loads, they may experience significant ductility demands, reaching or exceeding their deformation capacities. The strength and ductility of RC members depend on the nonlinear behavior of the concrete and reinforcing steel as well as the bond and interaction between the two. The ability to predict different possible failure mechanisms in RC members is important for the evaluation of their structural performance, and the development of improved design details. The finite element analysis method can be used for such purpose.

This dissertation presents two studies investigating the nonlinear behavior of RC bridge components and assemblies using large-scale experimental testing and nonlinear finite-element (FE) modeling. For these studies, suitable constitutive models for concrete and the bond-slip behavior of reinforcing bars embedded in concrete have been identified and calibrated, and a constitutive model that accounts for the low-cycle fatigue behavior of steel has been developed and implemented in a finite element analysis program. The first study investigated the effect of the lineal spacing of longitudinal bars on the performance of circular RC piles under lateral loading. The second study was aimed to determine the minimum development length required for headed bars in RC slab-column joints.

1.1 Finite-Element Modeling of RC Bridge Members

For this study, a phenomenological stress-strain law is developed to simulate the behavior of steel reinforcement under cyclic loading, including the low-cycle fatigue induced by bar

buckling. For modeling the nonlinear behavior of concrete, a damaged-plasticity model implemented in Abaqus has been calibrated and validated. Its limitations have been identified and remedies have been developed to circumvent them. In addition, a microplane model for concrete, developed by Caner and Bazant (2013) has been implemented, and validated with experimental data. The microplane model does not have the limitations of the damaged-plasticity model, and it can simulate the nonlinear behavior of concrete in tension and compression more accurately. Finally, a phenomenological bond-slip model, developed by Murcia-Delso and Shing (2015), has been used to simulate the bond behavior between the steel reinforcement and concrete.

1.2 Studies of Nonlinear Behavior of Bridge Components and Assemblies

Two studies were conducted to evaluate the structural performance of RC bridge components and assemblies. The studies consisted of large-scale experimental testing and nonlinear FE modeling. In the first study, the effect of the lineal spacing of longitudinal bars on the performance of circular RC piles under lateral loading was investigated. Two full-scale RC pile specimens with different lineal spacings of the longitudinal bars were tested, and a numerical parametric investigation has been conducted to extrapolate the test results. The second study was aimed to determine the minimum development length required for headed bars in RC slab-column joints. To this end, three full-scale RC slab-column specimens with different embedment lengths for the headed bars were tested. The test results have been used to validate nonlinear FE models, which have been subsequently used to evaluate the influence of additional design parameters on the anchorage capacity of headed bars.

1.2.1 Effect of Spacing of Longitudinal Bars on the Structural Performance of Bridge RC piles

In the presence of ground water, the slurry displacement method is used for the placement of concrete during the construction of cast-in-drilled-hole (CIDH) piles to ensure the stability of the drilled hole before concrete placement. When concrete is placed under water without compaction, defects or cavities may occur, affecting the structural integrity of the pile. Hence, the construction of CIDH piles larger than 2 ft. in diameter under wet conditions requires the installation of inspection (PVC) tubes for non-destructive detection of potential anomalies in the concrete using methods such as gamma-gamma testing, as shown in Figure 1.1. Normally, one inspection tube is required per foot of pile diameter. The inspection tubes are placed in contact with the outermost hoops, along the same circumference as that of the longitudinal bars, as shown in the figure. Since the clear spacing between a tube and an adjacent bar needs to be 3 in. to permit a good flow of the concrete paste, the clear spacing between the longitudinal reinforcing bars immediately adjacent to a tube has to be 8.5 in. Hence, the placement of inspection tubes will result in the violation of the maximum allowable center-to-center spacing of 8 in. for longitudinal bars, as specified in the Caltrans Bridge Design Specifications (Caltrans 2004) and the AASHTO LRFD Bridge Design Specifications (AASHTO 2014). While this can be understood for members with rectangular sections, in which the spacing of the cross-ties is normally related to the spacing of the longitudinal bars, it is less so for circular members, where there is no compelling justification for the limit of 8 in. suggested by Caltrans and AASHTO.

In order to investigate the impact of the lineal spacing of longitudinal bars on the structural performance of circular RC piles and columns subjected under lateral loading, two full-scale RC piles were tested under lateral loading. One specimen was designed according to the Caltrans Bridge Design Specifications (Caltrans 2004) and the AASHTO LRFD Bridge Design Specifications (AASHTO 2014). The other had the same design except that its longitudinal

reinforcement had spacing much greater than 8 in., violating the current design requirements. Nonlinear FE models of the pile specimens were used for pre-test analyses and in a parametric study to further verify the experimental findings.

1.2.2 Development Length for Headed Bars in Slab-Column Joints of RC Slab Bridges

Slab bridges are economical to construct. For seismic resistance, Caltrans requires that these bridges, like other bridge types, be so designed that plastic hinges will be formed in substructure elements in the event of a major earthquake. The substructure elements can be RC pile extensions, columns, or pier walls. This requirement is stated in Memo to Designer (MTD) 20-7 (Caltrans, October 2014), and the Seismic Design Criteria (SDC) (Caltrans, April 2013). The pile extensions must behave in a ductile manner and meet the ductility requirements for column elements specified in Section 4.1 of SDC. In order for this to happen, a substructure element can be pin-connected to the deck slab, or the longitudinal reinforcement extending from a substructure element must have a sufficient embedment length in the slab to develop the full tension capacity of the longitudinal bars. Nevertheless, slab thickness determined in accordance with Bridge Design Aids (BDA) 4-10 – Design of Standard Slab Bridge (Caltrans 2009), which complies with the AASHTO LRFD Bridge Design Specifications (AASHTO 2014), often may not provide a sufficient embedment length to develop the longitudinal reinforcement even when standard hooks are provided. The use of headed deformed bars can significantly reduce the required embedment length and also avoid the congestion that could be introduced by hooked bars. For example, with 4,000 psi concrete, a Grade 60 No. 9 bar with a standard hook requires a development length of $19d_b$ according to Section 5.11.2.4 of the AASHTO LRFD Specifications (2014). If a headed bar is used, the development length can be reduced to $15d_b$ according to Section 12.6.2 of ACI 318-11 (ACI 2011). Considering that the expected compressive strength of concrete is at least 5,000 psi, MTD 20-7 (Caltrans 2014) and MTD 20-19 (Caltrans 2013) have an

interim requirement that for a bar with a full-size head, which has a net bearing area 9 times the bar cross-sectional area, the development length inside the slab be at least $14d_b$.

In spite of the aforementioned benefits, the use of headed bars in slab bridges had two major concerns. First, it was not clear as to whether the ACI 318-11 specification was intended for developing the full tensile strength of a bar or just the expected yield strength. Second, a development length of $14d_b$, as recommended in Caltrans MTD 20-19, might still be too long to be accommodated in a deck slab designed according to Caltrans BDA 4-10 and the AASHTO LRFD Specifications. For example, for No. 9 bars, $14d_b$ is 15.8 inches, while a multi-span slab bridge that has a maximum span length of 30 ft. can have a 16-in. thick slab, which can provide no more than 11.25 in. of embedment, as shown in Figure 1.2. Hence, there was a need to investigate if the development length for headed bars could be reduced to $10d_b$ not to have an unnecessarily thick slab.

Laboratory tests were conducted on three full-scale slab-column assemblies in an upside down position. Each of the slab-column assemblies had a 2-ft. diameter, 12-ft. tall, cast-in-place column, with the column height measured from the top surface of the slab to the elevation at which the lateral load was applied. The reinforcement details for the slabs and slab-column joints conform to Caltrans BDA 4-10 and MTD 20-7. With the tests, the performance of the slab-column joints for different embedment lengths was evaluated. For Specimen #1, eight No. 9 headed bars were used for the longitudinal reinforcement of the column. The thickness of the slab was 16 in. The embedment length was 11 in., which is $9.8d_b$ for No. 9 bars. For Specimen #2, the column longitudinal reinforcement consisted of six No. 10 headed bars. It had the same thickness and same embedment length as Specimen #1. For No. 10 bars, an 11 in. embedment length corresponds to $8.7d_b$. For Specimen #3, six No. 10 headed bars were used for the column longitudinal reinforcement. A 3-in. drop cap was added to the 16-in. thick slab, providing an

embedment length of $11d_b$ for No. 10 bars. Nonlinear FEA of the slab-column assemblies were used to evaluate the performance of the tests specimens before and after the tests, and a numerical parametric study to evaluate additional design variables.

Based on the experimental and numerical findings, the minimum desired development length has been determined and possible changes to MTD 20-7 for the design of slab-column joints have been suggested.

1.3 Outline of the Dissertation

Chapter 2 presents the constitutive models and modeling techniques developed and implemented to simulate the behavior of RC components. Constitutive models for concrete, steel reinforcement and bond between the two are presented.

Chapter 3 presents the experimental investigation on the effect of the lineal spacing of longitudinal bars on the structural performance of circular RC members. First, the past research is presented, followed by the tests of two full-scale circular pile specimens under lateral loading with different lineal spacings for the longitudinal reinforcement. The test program and design of the pile specimens are documented, followed by the test results and observations.

Chapter 4 presents the three-dimensional FE models developed to simulate the pile specimens. The correlation of the numerical and experimental data is presented. The FE model is then used for a parametric study, considering piles of different diameters and varying the lineal spacing of the longitudinal bars and the level of the axial load. Finally, the microplane model is successfully implemented to simulate concrete in the FEA of the pile specimens.

Chapter 5 presents the experimental investigation on the minimum embedment length for headed bars anchored in slab-column joints. First, it discusses the anchorage mechanism and capacity of headed reinforcing bars embedded in concrete and presents a concise literature review of experimental studies conducted on this topic. The tests of three full-scale slab-column

assemblies, conducted to determine the minimum development length for headed bars in slab-column joint are then presented. The test program and design followed by the test results and findings are presented. Design recommendations for the minimum embedment length in slab-column joint and reinforcing details of the slab are presented.

Chapter 6 presents nonlinear FE models for bar pull-out tests and the slab-column tests, and their numerical results. With the FE model for slab-column assemblies, the capabilities of the constitutive models in reproducing failure mechanisms such as bond deterioration between steel reinforcement and concrete, and punching damage in the top face of the slab, are demonstrated. A parametric study is conducted with the FE model, to evaluate additional design variables. Finally, Chapter 7 presents the summary and conclusions of the studies.

Figure 1.1 – Typical drilled shaft reinforcing cage with PVC inspection tubes (Alter 2011)

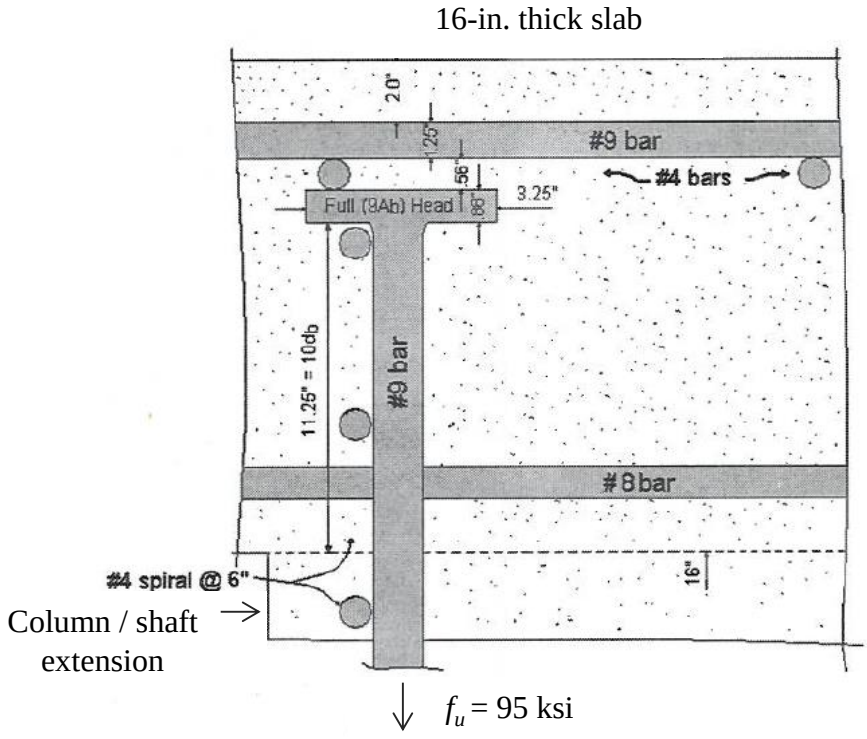

Figure 1.2 – Available development length for a 16-in.-thick slab (MTD 20-19, Caltrans 2013)

CHAPTER 2

CONSTITUTIVE MODELS

This chapter presents the constitutive models employed to describe the nonlinear behavior of RC components. Suitable constitutive models for concrete and the bond-slip behavior of reinforcing bars embedded in concrete have been identified and calibrated, and a constitutive model that accounts for the low-cycle fatigue behavior of steel has been developed and implemented in a finite element analysis program.

2.1 Modeling of Steel Reinforcement

For the purpose of this study, the stress-strain relation for steel reinforcing bars under cyclic loading has to be accurately described and efficient to calculate. However, Abaqus (Simulia 2014) only provides an elasto-plastic constitutive law with linear kinematic hardening. For this reason, a more realistic uniaxial stress-strain model has been implemented in Abaqus. In this model, the stress-strain relation for cyclic loading is based on the Menegotto-Pinto model (1973), and the low-cycle fatigue (LCF) law proposed by Manson (1953) and Coffin (1954) is incorporated. This steel model has been used in beam and truss elements.

A number of phenomenological steel models have been proposed in various studies to simulate the behavior of steel reinforcement under cyclic loading. Filippou et al. (1983) have adopted the Menegotto-Pinto model (1973), and added isotropic hardening to it. Dodd and Restrepo (1995) have proposed an analytical model that differentiates tensile behavior from compressive behavior by formulating the basic stress-strain relation in terms of the natural strain and true stress, and then converting it to a relation in terms of the engineering stress and strain based on an assumption that the volume of the reinforcing bar remains constant. Monti and Nutti

(1992) have proposed a phenomenological stress-strain law that indirectly accounts for the drop of compressive resistance due to bar buckling. Kunnath et al. (2009a) have proposed a phenomenological steel model accounting for the LCF of a reinforcing bar based on the law developed by Manson (1953) and Coffin (1954). The model has been calibrated with experimental data from LCF tests of bar specimens with specific slenderness ratios and a range of bar diameters. For the basic uniaxial stress-strain relation, Kunnath et al. (2009a) have adopted the Menegotto-Pinto model (1973) with modifications. They have also adopted the work of Dhakal and Maekawa (2002) to describe the drop of compressive strength due to bar buckling in the material model.

In this study, the Menegotto-Pinto model (1973) has been adopted, due to its simple formulation, and improved to better capture the stress-strain behavior of reinforcing bars when they are subjected to partial unloading and reloading, for which the original formulation has an issue. Similar to Kunnath et al.'s model (2009a), the LCF law proposed by Manson (1953) and Coffin (1954) has been incorporated. This law has been calibrated with experimental data obtained from LCF tests conducted on reinforcing bars. To account for bar buckling occurring in these tests, a calibration method is proposed here to extract the LCF properties of steel at the material level.

2.1.1 Cyclic Stress-Strain Relation

The model adopted here is formulated in terms of the engineering stress and strain. For a reinforcing bar made of mild steel and subjected to monotonically increasing strain, the model represents the stress-strain relation in tension or compression with four segments: (a) a linearly elastic segment, (b) a plateau at the yield stress, f_y, (c) a strain hardening segment described by the Menegotto-Pinto relation, and (d) a plateau at the ultimate stress, f_u. As shown in Figure 2.1, the aforementioned idealized stress-strain relation matches the tensile test result for a No. 11 well.

The ultimate strain at which bar fracture occurs is determined by a LCF law, which will be described later.

Upon strain reversal after the yield strain, ε_y, has been reached in tension or compression, the Menegotto-Pinto model (1973) is used to describe the cyclic stress-strain relation, as shown in Figure 2.2. The Menegotto-Pinto model (1973) has the following formulation:

$$\sigma^* = b\varepsilon^* + \frac{(1-b)\varepsilon^*}{\left(1+\varepsilon^{*R}\right)^{\frac{1}{R}}} \tag{2.1}$$

where

$$\varepsilon^* = \frac{\varepsilon - \varepsilon_r}{\varepsilon_o - \varepsilon_r} \tag{2.2}$$

$$\sigma^* = \frac{\sigma - \sigma_r}{\sigma_o - \sigma_r} \tag{2.3}$$

Eq. (2.1) relates the normalized stress, σ^*, to the normalized strain, ε^*, representing the stress-strain curve for unloading from the strain reversal point $\left(\varepsilon_r, \sigma_r\right)$ and reloading in the other direction. This curve has two asymptotes. One has a slope corresponding to the modulus of elasticity of steel and the other has a slope governing kinematic hardening. Figure 2.2 shows the stress-strain relation without normalization. In this figure, σ_o and ε_o are the stress and strain at which the two asymptotes meet. The second asymptote intersects with the straight line representing the linearly elastic behavior of steel under monotonic loading at $\left(\varepsilon_{y,m}, f_{y,m}\right)$ or $\left(-\varepsilon_{y,m}, -f_{y,m}\right)$ depending on whether it is on the tension or the compression side. Parameters $\varepsilon_{y,m}$ and $f_{y,m}$ assume positive values that are determined by calibration. Parameter b in Eq. (2.1) governs kinematic hardening in that $b = E_1 / E_0$, where E_0 is the modulus of elasticity and

E_1 is the slope of the second asymptote, as shown in Figure 2.2, and R is a parameter which controls the stress-strain curvature of the curve simulating the Bauschinger effect. A smaller value of R corresponds to a larger radius of curvature. The values of $(\varepsilon_o, \sigma_o)$, and $(\varepsilon_r, \sigma_r)$ are updated after each strain reversal. In the original Menegotto-Pinto model, R is calculated with the following equation:

$$R = R_0 - \frac{a_1 \xi}{a_2 + \xi} \tag{2.4}$$

where the variable ξ is defined as:

$$\xi = \begin{cases} \dfrac{|\varepsilon_{\max} - \varepsilon_o|}{\varepsilon_{y,m}} & \text{for reloading from compression to tension} \\ \dfrac{|\varepsilon_{\min} - \varepsilon_o|}{\varepsilon_{y,m}} & \text{for reloading from tension to compression} \end{cases} \tag{2.5}$$

in which $\varepsilon_{\max}$ and $\varepsilon_{\min}$ are the maximum and minimum strains attained in previous cycles. The constants, R_0, a_1, and a_2, are determined by calibration.

One issue with the original Menegotto-Pinto model is that it is not able to accurately reproduce the stress-strain response during reloading right after partial unloading, showing stress overshoot, as noted by Filippou et al. (1983) and Kunnath et al. (2009a). This is illustrated in Figure 2.3, in which the curve with the original *R*, calculated with Eq. (2.4), shows a significant stress overshoot during reloading on the compression side. Besides the inaccuracy, this can also cause convergence problems in finite element analysis. In this study, this problem is corrected by introducing a modification to the expression for R in Eq. (2.24) so that the value of R also depends on the stress difference between the intersection point of the asymptotes, $(\varepsilon_o, \sigma_o)$, and the previous load reversal point, $(\varepsilon_r, \sigma_r)$, as shown in the following equation.

$$R = \left(R_o - \frac{a_1 \xi}{a_2 + \xi} \right) \left| \frac{\sigma_o - \sigma_r}{2 f_{y,m}} \right|^{\left(1 - \left| \frac{\sigma}{2\sigma_o} \right| \right)} \tag{2.6}$$

in which σ is the stress at the previous step. The curve with the modified *R* in Figure 2.3 shows that this change corrects the stress overshoot problem.

The steel model has been validated with experimental data. Figure 2.4 through Figure 2.6 compare stress-strain curves from the steel model and the tests conducted by Dodd and Restrepo (1995), Aktan et al. (1973), and Kent and Park (2973). The values of the model parameters used in the analyses are summarized in Table 2.1.

2.1.2 Low-Cycle Fatigue

Under severe earthquake loading, flexural reinforcement in plastic-hinge regions of RC members can be subjected to large-amplitude cyclic plastic strain reversals, due to direct tension and bending once the reinforcing bars have buckled. This can result in bar fracture due to low-cycle fatigue (LCF).

The LCF of steel under cyclic loading with constant strain amplitude can be described with the following expression by Manson (1953) and Coffin (1954), as adopted in this study:

$$N_f = \left(\frac{\Delta\varepsilon}{2\varepsilon_f'} \right)^{-\frac{1}{c}} \tag{2.7}$$

in which N_f is the number of half cycles to failure and $\Delta\varepsilon$ is the strain range, defined as $\Delta\varepsilon = \varepsilon_{\max} - \varepsilon_{\min}$, attained in the cyclic loading, as shown in Figure 2.7; and ε_f' and c are coefficients representing the LCF properties of the material. Parameters ε_f' and c have to be calibrated with experimental data.

To account for the random strain history during an earthquake event, the range counting method is adopted, and damage due to LCF is linearly accumulated according to Miner's rule

(1945). During any strain reversal i, the strain range $\Delta\varepsilon_i = \varepsilon_{\max,i} - \varepsilon_{\min,i}$ is computed in terms of the maximum and minimum strains attained in that half cycle no matter it is completed or not, as shown in Figure 2.8, and damage in that half cycle is defined as:

$$D_i = \frac{1}{\left(N_f\right)_i} \tag{2.8}$$

in which $\left(N_f\right)_i$ is the number of half cycles to failure if the strain range were constant at $\Delta\varepsilon_i$ according to Eq. (2.7). Total damage due to LCF during or right after the completion of the n^{th} half cycle is then calculated as follows:

$$D = \sum_{i=1}^{n} D_i \tag{2.9}$$

When the damage accumulated reaches or exceeds one, it is assumed that the steel will fracture and the stress will drop to zero following a steep descending curve in the stress-strain relation. However, in order to ensure the robustness of the finite element analyses (FEA), fracture is not sudden and the stress drop follows a descending curve that has a slope equal to $-0.034E_0$ till it reaches a residual stress of $0.1f_y$.

The effects of the mean strain, $\varepsilon_{\text{mean}}$, and mean stress, σ_{mean}, which are defined in Figure 2.9 and Figure 2.10, are not taken into consideration in the LCF law adopted here. The strain amplitudes, defined as $\Delta\varepsilon/2$, of interest in this study are above 0.01. According to Koh and Stephens (1991), the effects of the mean strain and mean stress on the LCF of steel can be neglected for strain amplitudes above that level, as shown in Figure 2.11.

Pfister and Hognestad (1964) and Helgason et al. (1976) have shown that the lug geometry of a bar can have a significant effect on the LCF life. Rolled-on deformations lead to regions of stress concentration in which fatigue cracks initiate. Fei and Darwin (1999) have shown that the LCF life decreases when the base radius-to-height ratio (*r*/*h*) of a lug decreases.

Furthermore, it has been shown that larger-diameter and higher-strength bars have smaller LCF life (MacGregor et al., 1971). Hence, the calibration of the proposed LCF law is bar specific.

2.1.3 Calibration of Low-cycle Fatigue Law

In LCF tests, reinforcing bars were normally subjected to severe tensile and compressive load cycles, and would eventually buckle. Bar buckling exacerbated LCF because of large localized strains introduced by bar bending. In RC columns, flexural reinforcement in the plastic-hinge region may buckle after the cover concrete spalls, accelerating the LCF of these bars. The tendency of a bar to buckle depends on its slenderness ratio, which depends on the bar diameter and its unsupported length as determined by the spacing of the lateral reinforcement in the RC member. Therefore, LCF laws directly calibrated with tests conducted on bars with specific slenderness ratios may not reflect the true material behavior and introduce an issue in modeling. If the computational model explicitly captures bar buckling, the model so calibrated will double count the effect of bar buckling on LCF. If the model does not explicitly consider bar buckling, then the calibrated model, in the strict sense, will only be appropriate for bars that have a similar slenderness ratio as the specimens that provided the data. To address this issue, a calibration strategy is proposed here.

The proposed strategy uses a nonlinear beam element model that captures bar buckling to extract the LCF properties of the steel material from the LCF tests of the bars. The bar is modeled with beam elements in Abaqus considering material and geometric nonlinearities. For material nonlinearity, the Menegotto-Pinto model with the LCF law of Manson and Coffin [Eq. (2.8)] as presented in the previous sections is used. To calibrate the material model, the LCF tests conducted by Brown and Kunnath (2004) and Kunnath et al. (2009b) are considered. Figure 2.12a shows the test apparatus used by Kunnath et al. (2009b) including a buckled bar specimen, while Figure 2.12b shows the FE model for the bar specimen. The bar is modeled with 2-node beam

elements with one integration point at their middle length. The bending moment and axial force at the sampled section of a beam element are calculated with the trapezoidal rule based on stresses determined at the cross-sectional sampling points shown in Figure 2.13. The axial strains of the bars reported for these tests are the average values based on the axial deformation measured over the entire unsupported length of the bar specimen. The bar is modeled with 10 beam elements with an initial imperfection (initial offset at mid-span) of $L/1000$. The FE model is subjected to the same average-axial strain history (or more exactly the relative end displacement) experienced by the bar during the test. The values of ε_f' and c for the LCF law are so determined that the model exhibits bar fracture in the same cycle as in the test of the bar specimen. The stress-average axial strain curves obtained by the FE model and the tests by Kunnath et al. (2009b) are compared in Figure 2.14. The decrease of the compressive resistance due to the buckling of the bars is adequately described by the FE model. The element size has been determined with a mesh sensitivity analysis. Figure 2.15 shows the stress-strain curves for FE models with different element sizes.

The LCF law has been calibrated with tests conducted on No. 9, 11, and 14 bars obtained by Brown and Kunnath (2004) and Kunnath et al. (2009b). The values of ε_f' and c have been determined to be 0.382 and 0.455, respectively. Table 2.2 compares the number of cycles to failure, $\left(N_f/2\right)$, obtained by the FE analyses with this calibration and the tests. Figure 2.16 compares the LCF law calibrated here for the steel material to the LCF law calibrated by Brown and Kunnath (2004) directly with the average strain data for a No. 9 bar that had clear length of 6 times the bar diameter. As expected, the LCF law calibrated for the material gives a much larger number of cycles to failure for a given strain amplitude.

The use of nonlinear beam elements to model the buckling and LCF of reinforcing bars in RC members requires very refined FE meshes, at least for the plastic-hinge regions, and thus

significant computational resources. Very often, geometric nonlinearity is ignored in the modeling of reinforcing bars and a mesh that is coarser than what is needed to simulate bar buckling is used to improve computational efficiency. It is even more common to represent reinforcing bars with truss elements, which only simulate the uniaxial stress-strain behavior of bars. With these simplified models, the LCF law calibrated for steel material will not be appropriate because the effect of bar buckling is not accounted for. On the other hand, a LCF law calibrated directly with bar test data may not be appropriate for bars that have a slenderness ratio different from that of the bar specimen that provided the data. The slenderness ratio will affect the tendency of the bar to buckle and the resulting bending deformation. In an RC member, the slenderness of a longitudinal reinforcing bar after the cover concrete spalls is governed by the spacing of the lateral reinforcement.

To address the aforementioned issue, the following procedure is used to calibrate the steel model when bar buckling is not explicitly accounted for in the FE analysis of an RC member or structure. First, a single bar is modeled with a refined mesh using nonlinear beam elements which account for bar buckling. The LCF law calibrated for the steel material is used. The clear length of the bar is set to be equal to the center-to-center spacing of the lateral reinforcement in the member. Finite element analyses are conducted with the model to simulate LCF tests with varying average-strain ranges. For each strain range, $\Delta\varepsilon$, the number of cycles to fracture is obtained. A plot of N_f versus $\Delta\varepsilon$ is then generated with the numerical data. From this plot, the values of ε_f' and c are determined to obtain a LCF law that accounts for the effect of bar buckling and can therefore be used for simplified bar models used in the structural analysis. This has to be repeated for every bar size and every lateral steel spacing. Figure 2.17 shows results obtained for No. 9 bars with different slenderness.

2.2 Damaged-Plasticity Model for Concrete

Models combining plasticity and damage mechanics theories are attractive for simulating the behavior of concrete in that they can account for both plastic deformation and stiffness degradation in concrete under severe multi-axial stress reversals. The concrete damaged-plasticity model available in Abaqus is based on the formulations proposed by Lubliner et al. (1989) and Lee and Fenves (1998). This section summarizes the basic formulation for this model, and describes how the model has been calibrated and validated in this study with the experimental data of Hurblut (1985) and Mander et al. (1988b).

2.2.1 Damaged-Plasticity Model Formulation

The model complies with the classical theory of plasticity in that the strain tensor is decomposed into an elastic part and a plastic part, and the stress tensor is obtained as the double contraction of the elastic stiffness tensor and the elastic strain tensor.

$$\boldsymbol{\varepsilon} = \boldsymbol{\varepsilon}^{\mathbf{e}} + \boldsymbol{\varepsilon}^{\mathbf{p}} \tag{2.10}$$

$$\boldsymbol{\sigma} = \mathbf{E} : \boldsymbol{\varepsilon}^{\mathbf{e}} = \mathbf{E} : \left(\boldsymbol{\varepsilon} - \boldsymbol{\varepsilon}^{\mathbf{p}} \right) \tag{2.11}$$

To account for stiffness degradation using the damage mechanics theory, the elastic stiffness tensor is related to the initial stiffness tensor as:

$$\mathbf{E} = (1-d)\mathbf{E}_{\mathbf{o}} \tag{2.12}$$

where d is a scalar damage parameter that assumes a value between 0 and 1, with 0 representing the state of no damage. For a uniaxial stress state, d can be interpreted as the ratio of the damaged cross-sectional area, which cannot carry any load, to the total cross-sectional area under consideration. The actual stress developed in the undamaged material is called the effective stress and is defined as:

$$\bar{\boldsymbol{\sigma}} = \mathbf{E}_{\mathbf{o}} : \boldsymbol{\varepsilon}^{\mathbf{e}} = \mathbf{E}_{\mathbf{o}} : \left(\boldsymbol{\varepsilon} - \boldsymbol{\varepsilon}^{\mathbf{p}} \right) \tag{2.13}$$

The damage parameter d is a function of the damage parameter in tension, $d_t\left(\tilde{\varepsilon}_t^{\,p}\right)$, and the damage parameter in compression, $d_c\left(\tilde{\varepsilon}_c^{\,p}\right)$, as follows:

$$(1-d)=\left(1-s_t d_c\right)\left(1-s_c d_t\right) \tag{2.14}$$

The damage parameters, $d_t = d_t\left(\tilde{\varepsilon}_t^{\,p}\right)$ and $d_c = d_c\left(\tilde{\varepsilon}_c^{\,p}\right)$, are calibrated from cyclic uniaxial tension and compression tests and are functions of the plastic tensile and compressive strain, respectively.

Variables s_t and s_c are defined as:

$$s_t = 1 - w_t r\left(\hat{\bar{\boldsymbol{\sigma}}}\right) \tag{2.15}$$

$$s_c = 1 - w_c\left(1 - r\left(\hat{\bar{\boldsymbol{\sigma}}}\right)\right) \tag{2.16}$$

In Eq. (2.15) and (2.16), w_t and w_c are constants that control the recovery of stiffness upon stress reversal from compression to tension and from tension to compression, respectively. The values of w_t and w_c can be between 0, where no stiffness recovery is assigned, and 1, where total stiffness recovery is assigned. $r\left(\hat{\bar{\boldsymbol{\sigma}}}\right)$ is a weight factor, with a value between 0 and 1, defined as:

$$r\left(\hat{\bar{\boldsymbol{\sigma}}}\right) = \begin{cases} 0 & \text{if } \hat{\bar{\boldsymbol{\sigma}}} = \mathbf{0} \\ \dfrac{\sum_{i=1}^{3}\left\langle \hat{\bar{\sigma}}_i \right\rangle}{\sum_{i=1}^{3}\left|\hat{\bar{\sigma}}_i\right|} & \text{otherwise} \end{cases} \qquad ; 0 \le r\left(\hat{\bar{\boldsymbol{\sigma}}}\right) \le 1 \tag{2.17}$$

where $\hat{\bar{\sigma}}_i$'s are the principal effective stresses.

The solid line in Figure 2.18 shows the stress-strain response of the concrete model under uniaxial loading, with total stiffness recovery ($w_c = 1$) upon stress reversal from tension to

compression, and no stiffness recovery ($w_t = 0$) from compression to tension. The equivalent plastic strains, $\tilde{\varepsilon}_c^{\,p}$ and $\tilde{\varepsilon}_t^{\,p}$, are calculated from the equivalent plastic strain rates, $\dot{\tilde{\varepsilon}}_c^{\,p}$ and $\dot{\tilde{\varepsilon}}_t^{\,p}$, as follows:

$$\tilde{\varepsilon}_t^{\,p} = \int_0^t \dot{\tilde{\varepsilon}}_t^{\,p} dt \tag{2.18}$$

$$\tilde{\varepsilon}_c^{\,p} = \int_0^t \dot{\tilde{\varepsilon}}_c^{\,p} dt \tag{2.19}$$

The equivalent plastic strain rates, $\dot{\tilde{\varepsilon}}_c^{\,p}$ and $\dot{\tilde{\varepsilon}}_t^{\,p}$, are evaluated with the following expressions:

$$\dot{\tilde{\varepsilon}}_t^{\,p} = r\left(\hat{\bar{\boldsymbol{\sigma}}}\right)\hat{\dot{\varepsilon}}_{\max}^{p} \tag{2.20}$$

$$\dot{\tilde{\varepsilon}}_c^{\,p} = \left(1 - r\left(\hat{\bar{\boldsymbol{\sigma}}}\right)\right)\hat{\dot{\varepsilon}}_{\min}^{p} \tag{2.21}$$

in which $\hat{\dot{\varepsilon}}_{\max}^{p}$ and $\hat{\dot{\varepsilon}}_{\min}^{p}$ are obtained from the principal plastic strain rates ($\dot{\varepsilon}_1^p, \dot{\varepsilon}_2^p, \dot{\varepsilon}_3^p$) in that $\hat{\dot{\varepsilon}}_{\max}^{p} = \dot{\varepsilon}_1^p$ and $\hat{\dot{\varepsilon}}_{\min}^{p} = \dot{\varepsilon}_3^p$ with $\dot{\varepsilon}_1^p > \dot{\varepsilon}_2^p > \dot{\varepsilon}_3^p$.

The yield surface of the damaged-plasticity model is based on that proposed by Lubliner et al. (1989) with the modifications introduced by Lee and Fenves (1998) to account for the different behaviors of concrete in tension and compression. The initial shape of the yield surface in the principal stress plane for the plane-stress condition is shown in Figure 2.19. The yield function is defined in terms of the first stress invariant I_1, the second deviatoric stress invariant J_2, and the maximum principal stress as $\hat{\sigma}_{\max}$:

$$F = \frac{1}{1-a}\left(aI_1 + \sqrt{3J_2} + \beta\left(\tilde{\varepsilon}_c^{\,p}, \tilde{\varepsilon}_t^{\,p}\right)\left\langle\hat{\sigma}_{\max}\right\rangle - \gamma\left\langle-\hat{\sigma}_{\max}\right\rangle\right) - \bar{\sigma}_c\left(\tilde{\varepsilon}_c^{\,p}\right) \tag{2.22}$$

in which < - > denotes the Macauley brackets. Variable $\bar{\sigma}_c$, along with $\bar{\sigma}_t$, which is used to calculate variable β, defined in Eq. (2.28), are the effective compressive and tensile cohesion strengths, and are defined as:

$$\bar{\sigma}_c = \frac{\sigma_c}{(1-d_c)} \tag{2.23}$$

$$\bar{\sigma}_t = \frac{\sigma_t}{(1-d_t)} \tag{2.24}$$

in which the functions $\sigma_t\left(\tilde{\varepsilon}_t^{\,p}\right)$ and $\sigma_c\left(\tilde{\varepsilon}_c^{\,p}\right)$ represent the stress-vs.-plastic strain curves for uniaxial tension and compression, and are calibrated from uniaxial tension and compression test data. Constant a in Eq. (2.22) is defined as:

$$a = \frac{(\sigma_{b0}/\sigma_{c0})-1}{2(\sigma_{b0}/\sigma_{c0})-1} \tag{2.25}$$

in which $(\sigma_{b0}/\sigma_{c0})$ is the ratio of the initial equibiaxial compressive yield stress to the initial uniaxial compressive yield stress. In this study, the default value of 1.16 is used for $(\sigma_{b0}/\sigma_{c0})$. Constant γ is defined as:

$$\gamma = \frac{3(1-K_c)}{2K_c-1} \tag{2.26}$$

in which K_c, as defined in Eq. (2.27), is the ratio of the second deviatoric stress invariant for a stress state on the tensile meridian to that on the compressive meridian at the initial yield, for any given value of the pressure invariant such that the maximum principal stress is negative, $\hat{\sigma}_{\max} < 0$.

$$K_c = \frac{(J_2)_{TM}}{(J_2)_{CM}} \tag{2.27}$$

The value of K_c must satisfy the condition that $0.5 < K_c \leq 1.0$. As shown in Figure 2.20, the shape of the deviatoric plane depends on the value of K_c. The value of K_c also affects the slopes of the tensile and compressive meridians in the meridian plane as it is shown in Figure 2.21. For low hydrostatic pressure states, $K_c = 2/3$ provides a good fit of experimental data, while a higher value of K_c is more appropriate for high hydrostatic pressure states, as pointed out by Ottosen (1977).

The variable β is defined as:

$$\beta = \frac{\bar{\sigma}_c\left(\tilde{\varepsilon}_c^{\,p}\right)}{\bar{\sigma}_t\left(\tilde{\varepsilon}_t^{\,p}\right)}(1-a)-(1+a) \tag{2.28}$$

For the yield surface originally proposed by Lubliner et al. (1989), β is a constant, dependent only on the initial ratio of $\bar{\sigma}_c / \bar{\sigma}_t$. According to Lee and Fenves (1998), this gives good results for monotonic loading, but to model the cyclic behavior of concrete, β has to be dependent on the evolution of the compressive strength and tensile strength.

A non-associated flow rule has been adopted with the plastic strain rate is defined as $\dot{\boldsymbol{\varepsilon}}^{\mathbf{p}} = \dot{\lambda}\dfrac{\partial G}{\partial \boldsymbol{\sigma}}$, where $\dot{\lambda}$ is the plastic multiplier. The plastic potential G is defined as:

$$G = \sqrt{\left(\varepsilon\sigma_{t0}\tan\psi\right)^2 + 3J_2} + \frac{I_1}{3}\tan\psi \tag{2.29}$$

where σ_{t0} is the uniaxial tensile strength, which can be obtained from uniaxial tension test data, ψ is the dilation angle and ε is a parameter, referred to as the eccentricity that defines the rate at which the function approaches the asymptote. Figure 2.22 shows the shape of the plastic potential for different values of ε. The plastic potential tends to a straight line as ε approaches zero as shown in the figure. For $\varepsilon = 0$, the plastic potential takes the form of the Drucker-Prager (1952) criterion. The default value for ε is 0.1.

2.2.2 Validation and Calibration of the Damaged-Plasticity Model

Lee and Fenves (1998) validated the model for monotonic uniaxial and biaxial compression and tension loading. The model available in Abaqus (Simulia 2014) has been calibrated and further validated here for cyclic uniaxial compression-tension behavior and compression under lateral confinement. The calibration of the model in Abaqus requires the specification of the uniaxial compressive stress- inelastic strain curve and the uniaxial tensile stress-cracking displacement curve. Given the value of the compressive strength of concrete, the uniaxial compressive stress-plastic strain curve has been defined in this study based on the model proposed by Karthik and Mander (2011) for unconfined concrete. For tension, the tensile strength is assumed to decay linearly with the cracking displacement, reflecting the fracture energy released.

In cyclic loading, the damaged-plasticity model has stiffness degradation during unloading and reloading in tension to simulate the closing and opening of a crack. However, when the inelastic tensile strain is large, the complete closure of a crack would require a very large stiffness degradation (with the value of the damage parameter, d_t, very close to one), which leads to numerical problems. Hence, the model cannot be appropriately calibrated to simulate the complete closure of a crack with a small residual crack opening upon unloading. To circumvent this problem, contact conditions in Abaqus are used in this study to represent major flexural cracks in a discrete manner. Figure 2.23 shows a simple assembly of a finite element (FE) model which demonstrates how contact conditions can improve the behavior of concrete in simulation under uniaxial cyclic loading. In Figure 2.24, the dashed curve is the result from the model without contact conditions, and the solid curve is the result when contact conditions are introduced as shown in Figure 2.23.

The parameters affecting the yield surface have been calibrated with experimental data obtained by Hurblut (1985) and Mander et al. (1988b) to capture the behavior of confined

concrete in compression. The values of the parameters determined for the damaged-plasticity model are shown in Table 2.3

Figure 2.25 shows a FE model to simulate the compressive behavior of concrete under equal bilateral compressive stresses. The assembly, whose mesh has 100 elements is simply supported at its base, and hydrostatic pressure is applied first. Then, additional compression is applied in one direction by controlling the displacement of the top face. As shown in Figure 2.26, the model is capable of reproducing the effect of the lateral confining stress on the compressive strength and lateral expansion of concrete observed in the tests of Hurblut (1985). However, the increase of ductility in compression (i.e., a less steep declining slope in the stress-strain curve) due to increasing confining pressure is not captured by the model. This is due to the fact that the softening rule used in this damaged-plasticity model is defined only in terms of the uniaxial compressive stress-strain curve, which is embedded in the term $\bar{c}_c\left(\tilde{\varepsilon}_c^{\,p}\right)$, as shown in the expression for the yield surface in Eq. (2.22), without taking into account the effect of the confining pressure. For the model to match the experimental results, the slope of the decaying branch of the input uniaxial compressive stress-strain curve has to be modified a priori based on the level of the confining pressure or the amount of the confining steel, as shown in Figure 2.27. In this figure, f_c is the uniaxial compressive strength of unconfined concrete, while f_{cc} is the uniaxial compressive strength of confined concrete. In this study, the post-peak slope of the input uniaxial compressive stress-strain curve is determined according to the confinement level based on the work of Karthik and Mander (2011). With this modification, the model is capable of capturing the increase of ductility with the increase of the confining pressure, which was observed in the tests of Hurblut (1985) as shown in Figure 2.28.

The damaged-plasticity model was further validated by replicating the experimental results of Mander et al. (1988b) on the compression tests of circular-sectioned RC columns with

different amounts of confining steel. Figure 2.29 shows a FE model of one of the RC columns tested by Mander et al. (1988b). The longitudinal bars are modeled with beam elements and the hoops are modeled with truss elements. An elasto-plastic constitutive law with linear kinematic hardening is assigned to the steel reinforcement.

As shown in Figure 2.30, the FE model can adequately describe the effect of the lateral confining stress on the compressive strength and ductility of the RC columns, as shown in the experimental tests of Mander et al. (1988b).

2.3 Microplane Model for Concrete

An improved version of the microplane model (M7) for concrete proposed by Caner and Bazant (2013a) has been implemented in a user-defined subroutine in Abaqus (Simulia 2014). The model can more accurately simulate the opening and closing of cracks and the confinement effect in concrete than the damaged-plasticity constitutive model provided in Abaqus. The limitations of the damaged-plasticity model in simulating the aforementioned phenomena were discussed in Section 2.1.2, along with the ad hoc remedies proposed in this study. In this section, the key features of the microplane model implemented in Abaqus and its calibration are described. In this study, the microplane model has been calibrated and validated with the experimental data of Hurblut (1985) and Mander et al. (1988).

2.3.1 Microplane Model formulation

The microplane model is formulated in terms of a constitutive relation between the stress and strain components defined on a plane, called a microplane, of any orientation in the material (Brocca and Bazant 2000). It is based on the hypothesis that the free energy density of the material is a sum of the free energy densities associated with microplanes of various orientations. The free energy density for each microplane is defined as a function of the corresponding strain

components, which are derived from the strain tensor based on a kinematic constraint. The stresses at the micro and macro levels satisfy equilibrium in an approximate sense by virtue of the principle of virtual work.

As shown in Figure 2.31, the direction of a microplane is identified by a unit normal vector $\mathbf{n}$, defined in the global Cartesian coordinates, x_1, x_2, and x_3. Each microplane has an associated normal strain component ε_N and two shear strain components, ε_M and ε_L, in directions defined by two orthogonal unit vectors, $\mathbf{m}$ and $\mathbf{l}$, respectively, oriented parallel to the microplane. These strain components are derived from the strain tensor $\boldsymbol{\varepsilon}$ by projections on $\mathbf{n}$, $\mathbf{m}$ and $\mathbf{l}$ as follows.

$$\varepsilon_N = N_{ij}\varepsilon_{ij},\ \varepsilon_L = L_{ij}\varepsilon_{ij},\ \varepsilon_M = M_{ij}\varepsilon_{ij} \tag{2.30}$$

where

$$N_{ij} = n_i n_j,\ L_{ij} = \left(l_i n_j + l_j n_i\right)/2,\ M_{ij} = \left(m_i n_j + m_j n_i\right)/2 \tag{2.31}$$

in which the subscripts $i, j = 1,2,3$, representing the directions along x_1, x_2, and x_3, respectively, ε_{ij} denotes the strain tensor, and n_i, m_i, and l_i are projections of unit vectors $\mathbf{n}$, $\mathbf{m}$, and $\mathbf{l}$ on x_i. Repeated indices in the above equations denote summation over $i, j = 1,2,3$, e.g., $a_i b_i = a_1 b_1 + a_2 b_2 + a_3 b_3$.

It is impossible for both the stress and strain components on the microplanes to be projections of the stress and strain tensors. Therefore, the static equivalence, or equilibrium, between the stress components, σ_N, σ_L, and σ_M, over all the microplanes and the stress tensor $\boldsymbol{\sigma}$ are enforced in an approximate manner using the principle of virtual work (Bazant, 1984) as follows:

$$\frac{2\pi}{3}\sigma_{ij}\delta\varepsilon_{ij} = \int_\Omega \left(\sigma_N \delta\varepsilon_N + \sigma_L \delta\varepsilon_L + \sigma_M \delta\varepsilon_M\right) d\Omega \tag{2.32}$$

in which Ω is the surface of a unit hemisphere centered at the material point, and $2\pi/3$ is its volume. The above equation implies that the volume bounded by the microplanes, as shown in Figure 2.31(a), can be represented by a unit sphere, and that the virtual work of continuum stresses within a unit sphere is equal to the virtual work of the stress components on the surface (microplanes) of the unit sphere. By substituting $\delta\varepsilon_N = N_{ij}\delta\varepsilon_{ij}$, $\delta\varepsilon_L = L_{ij}\delta\varepsilon_{ij}$, and $\delta\varepsilon_M = M_{ij}\delta\varepsilon_{ij}$ into the above equation, and noting that the equation must hold for any virtue strain $\delta\varepsilon_{ij}$, the following basic equilibrium relation is obtained:

$$\sigma_{ij} = \frac{3}{2\pi}\int_{\Omega} s_{ij}\, d\Omega \approx 6\sum_{\mu=1}^{N_m} w_\mu s_{ij}^{(\mu)} \tag{2.33}$$

where

$$s_{ij} = \sigma_N N_{ij} + \sigma_L L_{ij} + \sigma_M M_{ij} \tag{2.34}$$

As shown in Eq. (2.33), the integral is approximated by an optimal Gaussian integration over a spherical surface (Stroud 1971, Bazant and Oh 1985), which is a weighted sum over N_m microplanes of orientations $\mathbf{n}_\mu$, with the weights w_μ normalized so that $\sum_{\mu=1}^{N_m} w_\mu = 1/2$. The implemented microplane model has 37 microplanes.

The model has four strain-dependent strength (or yield) limits, enforced at the microplane level, called the stress-strain boundaries. These are the volumetric boundary, σ_V^b, the deviatoric boundary, σ_D^b, the normal boundary, σ_N^b, and the shear boundary, σ_T^b, which are presented in Figure 2.32. When the stresses are within the boundaries, the response is elastic. If, during a strain increment, the boundary is exceeded, the stress is reduced to the boundary keeping the strain constant, as illustrated for the normal stress, σ_N, in Figure 2.33.

The volumetric boundary, σ_V^b, is calculated by the following equation:

$$\sigma_V^b = -Ek_1k_3e^{-\varepsilon_V/k_1a} \tag{2.35}$$

in which *E* is the elastic modulus of the concrete, and k_1 and k_3 are parameters that need to be calibrated. The physical meaning and suggested values of these parameters are presented in Table 2.4. The volumetric strain, ε_v, for each microplane is calculated from the strain tensor in an incremental manner as follows:

$$\varepsilon_V = \varepsilon_V^o + \Delta\varepsilon_V \tag{2.36}$$

where

$$\varepsilon_V^o = \varepsilon_{kk}^o / 3 \text{ and } \Delta\varepsilon_V = \Delta\varepsilon_{kk} / 3 \tag{2.37}$$

The superscript o in the above variables denotes the values attained in the previous step. The variable a in Eq. (2.35) is defined as follows:

$$a = \frac{k_5}{1+\varepsilon_e}\left(\frac{\varepsilon_I^o - \varepsilon_{III}^o}{k_1}\right)^{c_{20}} + k_4 \tag{2.38}$$

in which k_4 and k_5 are parameters whose physical meaning and suggested values are presented in Table 2.4. ε_e is defined as:

$$\varepsilon_e = \left\langle -\sigma_V^o / E_{N0} \right\rangle \tag{2.39}$$

where $\langle x \rangle = \max(x, 0)$ (the Macauley brackets), σ_v^o is the volumetric stress attained in the previous step, defined in Eq.(2.52), and E_{N0} is the undamaged elastic stiffness in the normal direction of the microplane and is calculated as:

$$E_{N0} = \frac{E}{1-2v} \tag{2.40}$$

with *v* being the Poisson's ratio, which is set to 0.18. The variables ε_I^o and ε_{III}^o denote the maximum and the minimum principal strains attained at the previous step. The difference of the principal strains helps to distinguish the compressive behavior of weakly confined concrete,

which can have significant strain softening, from that of highly confined concrete, which has milder strain softening.

The deviatoric boundary, σ_D^b, is specified as:

$$\sigma_D^b = -\frac{Ek_1\beta_3}{1+\left[\langle -\varepsilon_D \rangle / (k_1\beta_2)\right]^2} \tag{2.41}$$

where

$$\beta_2 = c_5\gamma_1 + c_7, \quad \beta_3 = c_6\gamma_1 + c_8, \quad \gamma_1 = e^{\gamma_0}\tanh\left(c_9\langle -\varepsilon_V \rangle / k_1\right) \tag{2.42}$$

$$\gamma_0 = f'_{c0} / E_0 - f'_c / E \tag{2.43}$$

in which c_i (i = 5, 6, 7, 8, 9) are parameters that need to be calibrated. The physical meaning and suggested values of these parameters, along with those others used in the calculation of the rest of the stress boundaries, are presented in Table 2.5. The values of parameters f'_{c0} and E_0 are given in Table 2.5, while f'_c and E are the compressive strength and elastic modulus for the concrete being modeled. The deviatoric strain, ε_D, is calculated from the normal and volumetric strains as follows:

$$\Delta\varepsilon_D = \Delta\varepsilon_N - \Delta\varepsilon_V, \quad \varepsilon_D^o = \varepsilon_N^o - \varepsilon_V^o, \quad \varepsilon_D = \varepsilon_D^o + \Delta\varepsilon_D \tag{2.44}$$

The normal boundary, σ_N^b, is specified as:

$$\sigma_N^b = Ek_1\beta_1 e^{-\langle \varepsilon_N - \beta_1 c_2 k_1 \rangle / \left[-c_4\varepsilon_e \operatorname{sgn}(\varepsilon_e) + k_1 c_3\right]} \tag{2.45}$$

in which

$$\beta_1 = -c_1 + c_{17}e^{-c_{19}\langle \varepsilon_e - c_{18} \rangle} \tag{2.46}$$

The elastic normal microplane stress (trial elastic stress) is calculated as:

$$\sigma_N^e = \sigma_N^o + E_N\Delta\varepsilon_N \tag{2.47}$$

in which E_N is the damaged value of the normal microplane elastic stiffness:

$$E_N = E_{N0}e^{-c_{13}\varepsilon_N^{0+}} f(\zeta) \quad \text{for} \quad \sigma_N^o \geq 0 \tag{2.48}$$

but

$$E_N = E_{N0} \quad \text{if} \quad \sigma_N^o \geq E_{N0}\varepsilon_N \quad \text{and} \quad \sigma_N^o \Delta\varepsilon_N < 0 \tag{2.49}$$

$$E_N = E_{N0}\left(e^{-c_{14}\left|\varepsilon_N^{0-}\right|/\left(1+c_{15}\varepsilon_e\right)} + c_{16}\varepsilon_e\right) \quad \text{for} \quad \sigma_N^o < 0 \tag{2.50}$$

in which ε_N^{0+} and ε_N^{0-} are the maximum and minimum normal strains reached so far. In Eq. (2.48), $f(\zeta) = \left(1 + a\zeta^2\right)^{-1}$, with $\zeta = \int \langle d\varepsilon_v \rangle$ and $a = 0.1$, which has been specified to avoid negative dissipation during load cycles. Accurate simulation of the closing of opened cracks during tensile unloading is attained with the stiffness degradation calculated with Eq. (2.48). Parameter c_{13} controls the unloading slope from tension, with a suggested value of 4,500 (see Table 2.5). Only those microplanes whose normal forms a sufficiently small angle with the maximum principal strain direction can reach the post-peak regime. Other microplanes will remain elastic.

Having calculated the elastic normal stress and the volumetric, deviatoric and normal stress boundaries, the vertical drop of stress at constant strain to the stress-strain boundary for the normal stress, as shown in Figure 2.33, is enforced:

$$\sigma_N = \max\left[\min\left(\sigma_N^e, \sigma_N^b\right), \sigma_V^b + \sigma_D^b\right] \tag{2.51}$$

The volumetric stress is calculated as the average value of the normal stress at every microplane:

$$\sigma_V \approx \frac{1}{2\pi}\sum_{\mu=1}^{N_m} w_\mu \sigma_N \tag{2.52}$$

The shear boundary, σ_T^b, is calculated as:

$$\sigma_T^b = \left[\left(c_{10}\left\langle \hat{\sigma}_N^o - \sigma_N \right\rangle\right)^{-1} + \left(E_T k_1 k_2\right)^{-1}\right]^{-1} \quad \text{for} \quad \sigma_N \leq 0 \tag{2.53}$$

$$\sigma_T^b = \left[\left(c_{10}\hat{\sigma}_N^o\right)^{-1} + \left(E_T k_1 k_2\right)^{-1}\right]^{-1} \quad \text{for} \quad \sigma_N > 0 \tag{2.54}$$

in which

$$E_T = E_{N0}\frac{1-4\nu}{1+\nu} \tag{2.55}$$

$$\hat{\sigma}_N^o = \left\langle E_T k_1 c_{11} - c_{12}\left\langle \varepsilon_V \right\rangle \right\rangle \tag{2.56}$$

The elastic shear microplane stress (trial stress) is:

$$\sigma_T^e = \sqrt{\left(\sigma_L^o + E_T\Delta\varepsilon_L\right)^2 + \left(\sigma_M^o + E_T\Delta\varepsilon_M\right)^2} \tag{2.57}$$

in which σ_L^o and σ_M^o are the shear stresses in the L and M directions of the microplane in the previous step, and $\Delta\varepsilon_L$, $\Delta\varepsilon_M$ the equivalent strain increments.

The shear stress return to the boundary is calculated by the following equations:

$$\sigma_T = \min\left(\sigma_T^b, \left|\sigma_T^e\right|\right) \tag{2.58}$$

$$\sigma_L = \left(\sigma_L^o + E_T\Delta\varepsilon_L\right)\sigma_T / \sigma_T^e \tag{2.59}$$

$$\sigma_M = \left(\sigma_M^o + E_T\Delta\varepsilon_M\right)\sigma_T / \sigma_T^e \tag{2.60}$$

Having calculated the normal stress , σ_N , and the shear-stress components, σ_L and σ_M , at every microplane, the stress tensor, σ_{ij} , at every integration point is obtained through Eq. (2.33) and (2.34).

The fact that the stress-strain boundaries are reached at different microplanes at different moments of loading is what causes both the pre-peak and post-peak macro-level stress-strain curves to vary their slope gradually. Similarly during macroscopic unloading, different microplanes have the stresses returning into the elastic domain at different moments, which again causes the unloading curves to change the unloading slope gradually.

The calibration of the microplane model involves the determination of the parameters E , k_i and c_j , which govern the stress-strain boundaries at every microplane. The values shown in Table 2.4 and Table 2.5 are suggested by Caner and Bazant (2013b), and will result in a uniaxial compressive strength of 46.7 MPa and the compressive strain at the peak stress equal to 0.0033,

which can be confirmed numerically. To have a different concrete strength, strain at the peak stress, and post-peak behavior under uniaxial compression, the values of E and k_i have to be changed, while those of c_j can remain the same.

In fact, with the set of parameters that determine the reference concrete properties, the desired uniaxial compressive strength, f_c', and compressive strain at the peak stress, ε_p, can be obtained solely with the values of k_1 and E calculated with the following equations:

$$k_1 = \tilde{k}_1 \frac{\varepsilon_p}{\tilde{\varepsilon}_p} \quad \text{and} \quad E = \tilde{E} \frac{f_c'}{\tilde{f}_c'} \frac{\tilde{\varepsilon}_p}{\varepsilon_p} \tag{2.61}$$

in which $\tilde{k}_1$ and $\tilde{E}$ are the values of the parameters that result in the reference properties $\tilde{f}_c'$, and $\tilde{\varepsilon}_p$. For the parameters shown in Table 2.4 and Table 2.5, we have $\tilde{k}_1 = 1.1 \cdot 10^{-4}$, $\tilde{E} = 25{,}000$ MPa, $\tilde{f}_c' = 46.7$ MPa, and $\tilde{\varepsilon}_p = 0.0033$. Changing the value of E results in a vertical scaling transformation of the stress-strain curve, such that all the stresses are scaled by the ratio $E / \tilde{E}$ with no change of strains. Changing the value of k_1 results in a radial scaling of the stress-strain curve, in which all the distances from the origin are scaled by the ratio $k_1 / \tilde{k}_1$.

2.3.2 Validation and Calibration of the Microplane model

The microplane model has been calibrated and verified by Caner and Bazant (2013b) for a range of strain histories. In this study, the performance of the model in capturing the compressive behavior of confined concrete has been further examined. For this purpose, the tests of Hurblut (1985) on the compressive behavior of concrete under different lateral confining stresses, the test by van Mier (1986) on the uniaxial compressive behavior of unconfined concrete, and the tests of Mander et al. (1988b) on the compressive behavior of circular columns

with different amounts of lateral steel confinement are considered. For these analyses, the default values of some of the modeling parameters have been changed as shown in Table 2.6.

The finite element (FE) model used to simulate the tests of Hurblut (1985) is presented in Figure 2.25. The default values of k_i $\left(\text{for } i = 2,...,5\right)$ and c_j $\left(\text{for } j = 1,...,20\right)$, which are presented in Table 2.4 and Table 2.5, are first used, while $E = 26,030 \text{ MPa}$ and $k_1 = 0.5 \cdot 10^{-4}$ (see Table 2.6), which have been selected to capture the compressive behavior of the concrete. As shown in Figure 2.34, the microplane model is capable of reproducing the effect of the lateral confining stress on the compressive strength and the post-peak slope of the stress-strain curve. However, for the case of uniaxial compression with no confining stress, the microplane model shows a relatively ductile behavior, with the stress-strain curve similar to that for the 100-psi confining stress. To examine this further, the uniaxial compression test of van Mier (1986) is considered. As shown in Figure 2.35, the microplane model demonstrates a more ductile post-peak behavior than the test. To have a more brittle behavior under uniaxial compression, the model has been re-calibrated with the values of k_2 and k_3 changed to one. With $k_2 = k_3 = 1$, $E = 27,865 \text{ MPa}$, and $k_1 = 1.65 \cdot 10^{-4}$, the model gives $f_c' = 21.4 \text{ MPa}$ and $\varepsilon_p = 0.0015$. As shown in Figure 2.35, this results in a much better match of the test data. This value of k_2 and k_3 is used for unconfined concrete in all subsequent analyses, as shown in Table 2.6.

With the aforementioned recalibration, the microplane model was further evaluated with the experimental results of Mander et al. (1988b) on the compressive behavior of circular-sectioned RC columns with different amounts of lateral confining steel. The calibration of the model to yield the concrete properties of the tests is summarized in Table 2.6. The same FE model as that presented in Figure 2.12 is used. However, in contrast to the damaged-plasticity model, which requires different input uniaxial compressive stress-strain relations for different amounts of confining steel, as discussed in Section 2.1.2, the microplane model uses the same

calibration for different confinement levels. As shown in Figure 2.36, the FE model satisfactorily captures the effect of the lateral confining steel on the compressive strength and the ductility of the RC columns.

Unlike the damaged-plasticity model provided in Abaqus, the microplane model is able to simulate the tensile unloading and reloading behavior of concrete in an accurate manner. To demonstrate this, a single solid element, as shown in Figure 2.37, is subjected to uniaxial cyclic tension and compression. Both the damaged-plasticity model and the microplane model are considered. Figure 2.38 shows the stress-strain curves obtained with the two different constitutive models. It can be seen that the damaged-plasticity model shows early crack closing with an unrealistically large residual tensile strain due to its inability to represent severe degradation of the tensile stiffness during unloading, as pointed out in Section 2.1.2, while the microplane model shows a satisfactory performance.

2.4 Modeling of Bond-Slip

The bond-slip behavior between the longitudinal bars and the concrete in an RC member is simulated in the finite element analyses (FEA) with a bond-slip model developed by Murcia-Delso and Shing (2015). The model adopts a semi-empirical law, based on concepts originally proposed by Eligehausen et al. (1983) and further extended by others (Pochanart and Harmon 1989; Yankelevsky et al. 1992 and Lowes et al. 2004), accounting for bond deterioration caused by cyclic slip reversals, the tensile yielding of the bars, and the opening of radial splitting cracks in concrete. The bond-slip model has been implemented in interface elements in Abaqus, which can be used to connect steel to concrete in the three-dimensional FEA of RC members.

2.4.1 Bond-Slip Interface Model

The relative displacements and stresses in the normal and tangential directions of the interface between a reinforcing bar and the surrounding concrete are defined in Figure 2.39. The bar slip and bond stress are denoted by s_2 and τ_2, respectively.

2.4.2 Bond Stress-Slip Law

In the bond-slip law of Murcia-Delso and Shing (2015), the total bond resistance consists of the bearing resistance and the friction resistance. Figure 2.40(a) shows the monotonic bond stress-slip curves with the contributions of these two mechanisms. The model has three parameters, namely, the peak bond strength for an elastic bar, $\tau_{\max}$, the slip at which the peak strength is attained, s_{peak}, and the clear spacing between the ribs, s_R, to calibrate. s_R is a known geometric property of the bar and is usually between 40% and 60% of the bar diameter. $\tau_{\max}$ and s_{peak} depend on many factors and no theoretical formulas are available to accurately predict their values. Thus, they should be determined experimentally for each case, if possible. When no experimental data are available, the following empirical formulas can be used to estimate the values as suggested by Murcia-Delso and Shing (2015).

$$\tau_{\max} = 0.72 f_c'^{3/4} \text{ (in ksi)} \tag{2.62}$$

$$s_{peak} = 0.07 d_b \tag{2.63}$$

in which f_c' is the compressive strength of concrete and d_b is the bar diameter.

The bond-slip model accounts for the deterioration of both the bearing and the friction resistances as a function of the maximum and cumulative slips, the yielding of the bar in tension, and the opening of the steel-concrete interface with respect to the rib height. Figure 2.40(b) shows the bond stress-vs.-slip relations for cyclic loading. As shown in the figure, when the bar slips

between previously attained slip levels, the bond stress is bounded by the friction resistance, τ_{rev}. This is because part of the concrete in contact with the ribs of the bar on the bearing side has been crushed, and a gap has been created on the other side of the ribs. This gap needs to be closed before the bearing resistance of the ribs in the opposite direction can be activated. Once contact is resumed, the bond resistance increases, but up to a lower peak due to the deterioration of the bearing resistance.

2.4.3 Normal and Transverse Tangential Stresses

To simulate the wedging action of the bar ribs, the resultant force exerted by the bar on the surrounding concrete is assumed to have a fixed angle of inclination, θ, with respect to the longitudinal axis of the bar. The normal component of the interface stress, as shown in Eq.(2.64), is proportional to the bond stress with the proportionality constant determined by the angle, θ, while a penalty stiffness $K_{pen,1}$ is added, which is active only in compression to minimize the interpenetration of the steel and concrete.

$$\sigma_1 = -\left|\tau_2\right| \tan\theta + K_{pen,1} \min\left(s_1, 0\right) \tag{2.64}$$

The rotation of the bar around its longitudinal axis is restrained by a penalty stiffness $K_{pen,3}$, as presented in the following equation.

$$\tau_3 = K_{pen,3} s_3 \tag{2.65}$$

2.4.4 Interface Element Implementation

The bond-slip law serves as a constitutive model for the interface element that connects truss or beam elements representing reinforcing bars to the surrounding concrete, as shown in Figure 2.41. To evaluate the stress for a given relative displacement, the value of the axial strain in the bar may be calculated inside the interface element from the displacements parallel to the

bar axis at the nodes connected to the bar (nodes A and B in Figure 2.41) and the length of the element L_e, as

$$\varepsilon_s = \frac{u_{2B} - u_{2A}}{L_e} \tag{2.66}$$

An interface element that allows the computation of ε_s with Eq. (2.66) has been implemented in Abaqus in a user-defined subroutine. The interface element has four nodes (with two nodes connected to the bar and two connected to the concrete), linear shape functions, and two integration points at its ends, as shown in Figure 2.41.

2.5 Final Remarks

The constitutive models presented in this chapter for steel reinforcement, concrete and the bond between the two can be used to simulate the behavior of RC bridge components, such as piles, columns and slab-column joints, in an accurate manner. They have been validated with experimental data. The phenomenological model for steel can adequately simulate the response of flexural reinforcement during cyclic loading and its low-cycle fatigue behavior.

A damaged-plasticity model and a microplane model have been calibrated and evaluated for their ability to simulate concrete. However, the damaged-plasticity model cannot capture the increase in the ductility of concrete in compression due to an increase in the confining pressure. Furthermore, it cannot represent large stiffness degradation during unloading and reloading in tension, resulting in a large residual tensile strain upon unloading when a large crack opening has occurred. Calibration and modeling remedies have been developed to circumvent these limitations. The microplane model, which has been implemented in Abaqus, does not have these deficiencies.

2.6 Acknowledgement of Publication

This chapter, in full, is a reprint of the material as it appears in the report submitted to the California Department of Transportation in 2015, Papadopoulos, V., Shing, P. B., under the title "Influence of the Spacing of Longitudinal Reinforcement on the Performance of Laterally Loaded CIDH Piles – Analytical Investigation". The dissertation author was the primary investigator and author of this report.

Table 2.1 – Calibration of the Menegotto-Pinto Model

$f_{y,m}$	1.25 f_y
$\varepsilon_{y,m}$	1.25 ε_y
f_u	1.45 f_y
b	0.01
R_o	0.03
a_1	0.15
a_2	0.02

Table 2.2 – Comparison of number of cycles to failure in the FEA and tests

Bar size	Strain amplitude, $\varepsilon_a = \Delta\varepsilon / 2$	$N_f/2$	
		FEA	Test
#9	0.015	54	63-67
#9	0.02	25	27-31
#9	0.03	9	7-9
#11	0.02/0.04	8/3	8/3
#11	0.05	4	3
#14	0.01	53	41-45
#14	0.02	17	14-16
#14	0.04	2	4

Table 2.3 – Damaged-plasticity model calibration

Parameter	Description	Value
σ_{b0}/σ_{c0}	Controls biaxial compressive strength	0.12
ψ	Dilation angle	20^o
ε	eccentricity	0
K_c	Controls shape of yield surface	2/3
w_c	Compression recovery factor	0
w_t	Tension recovery factor	1

Table 2.4 – Free parameters of microplane model by Caner and Bazant (2013b)

Parameter	Value	Description
v	0.18	Poisson's ratio
E	25,000 MPa	Elastic modulus
k_1	$1.1 \cdot 10^{-4}$	Radial scaling parameter
k_2	110	Controls the horizontal asymptote value in the shear boundary
k_3	30	Controls the shape of the volumetric boundary
k_4	100	Controls the shape of the volumetric boundary
k_5	0.0001	Controls the volumetric-deviatoric coupling at low pressures

Table 2.5 – Fixed parameters of microplane model by Caner and Bazant (2013b)

Parameter	value	meaning
f'_{c0}	15.1 MPa	Reference compressive strength for low-strength concrete
E_0	20,000 MPa	Reference elastic modulus for low-strength concrete
c_1	0.089	Controls the uniaxial tensile strength
c_2	0.176	Controls the roundness of the peak in uniaxial tension
c_3	4	Controls the slope of the post-peak tail in uniaxial tension
c_4	50	Controls the slope of the post-peak tail in uniaxial compression
c_5	3,500	Controls the volumetric expansion under compression
c_6	20	Controls the roundness of the peak in volumetric expansion under compression
c_7	1	Controls the slope of the initial post-peak curve in uniaxial compression
c_8	8	Controls the peak strength in uniaxial compression
c_9	0.012	Controls the peak roundness in uniaxial compression
c_{10}	0.33	Controls the effective friction coefficient
c_{11}	0.5	Initial cohesion in frictional response
c_{12}	2.36	Controls the change of cohesion with tensile volumetric strains
c_{13}	4,500	Controls the unloading slope in tension
c_{14}	300	Controls the unloading slope at low hydrostatic compression
c_{15}	4,000	Controls the transition from unloading slope at high confinement to that at low confinement
c_{16}	60	Controls the unloading slope at high hydrostatic compression
c_{17}	1.4	Controls the tensile strength
c_{18}	0.0016	Controls the tensile cracking under compression
c_{19}	1,000	Controls the tensile softening rate under compression
c_{20}	1.8	Controls the volumetric-deviatoric coupling at high pressures

Table 2.6 – Calibration of microplane model

Test	Concrete	k_2, k_3	E (MPa)	k_1 (x10^{-4})	f_c' (MPa), ε_p
Hurblut (1985)	Confined	default	26,030	0.5	22.1, 0.0015
van Mier (1986)	Unconfined	default	25,200	0.5	21.4, 0.0015
	Unconfined	1, 1	27,865	1.65	21.4, 0.0015
Mander et al. (1988b)	Confined	default	34,035	0.5	28.9, 0.0015
	Unconfined	1, 1	37,630	1.65	28.9, 0.0015

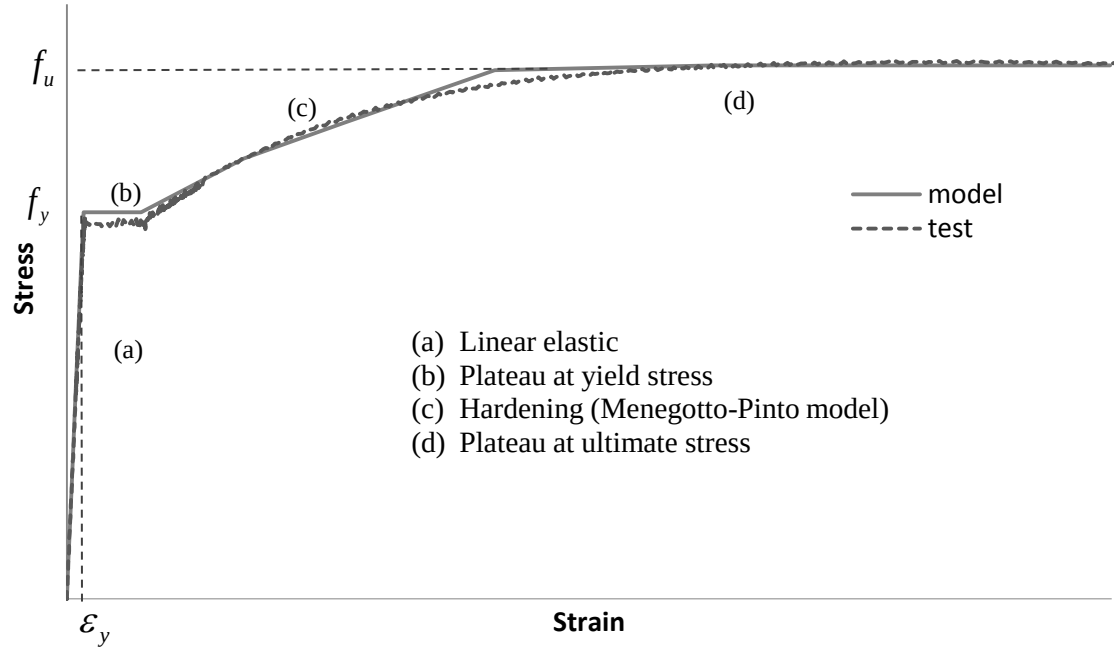

Figure 2.1 – Steel Model for monotonic loading

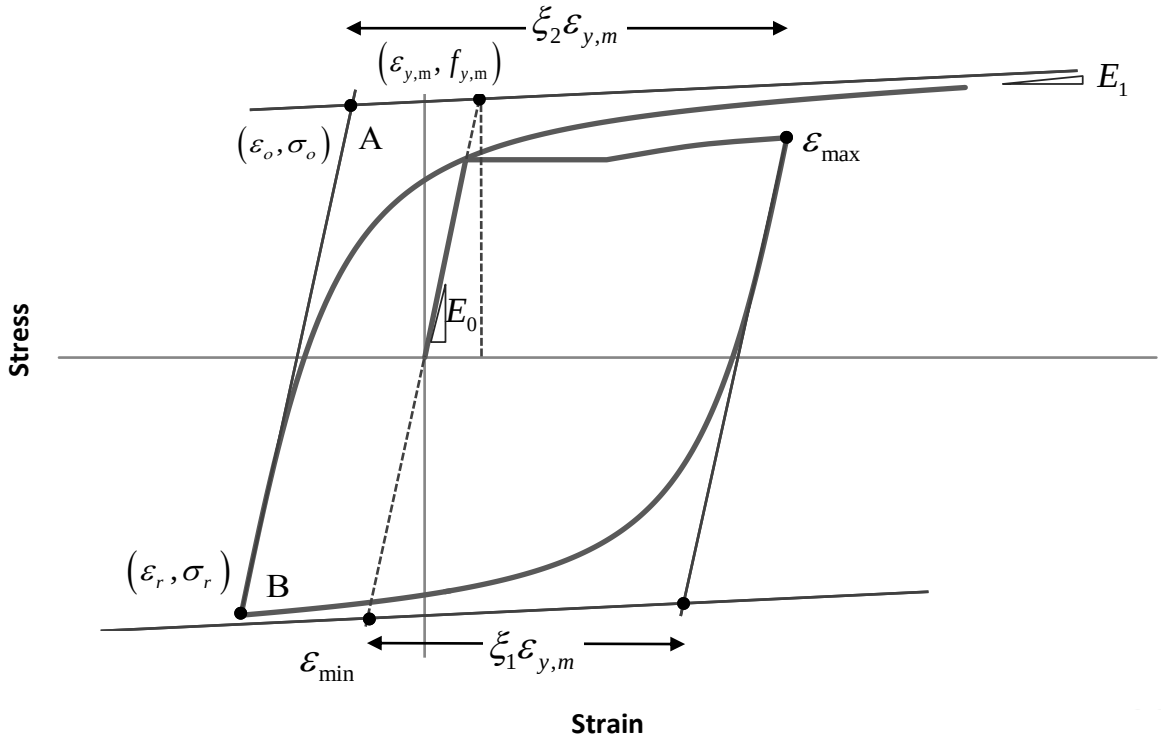

Figure 2.2 –Menegotto-Pinto model for cyclic stress-stain relation

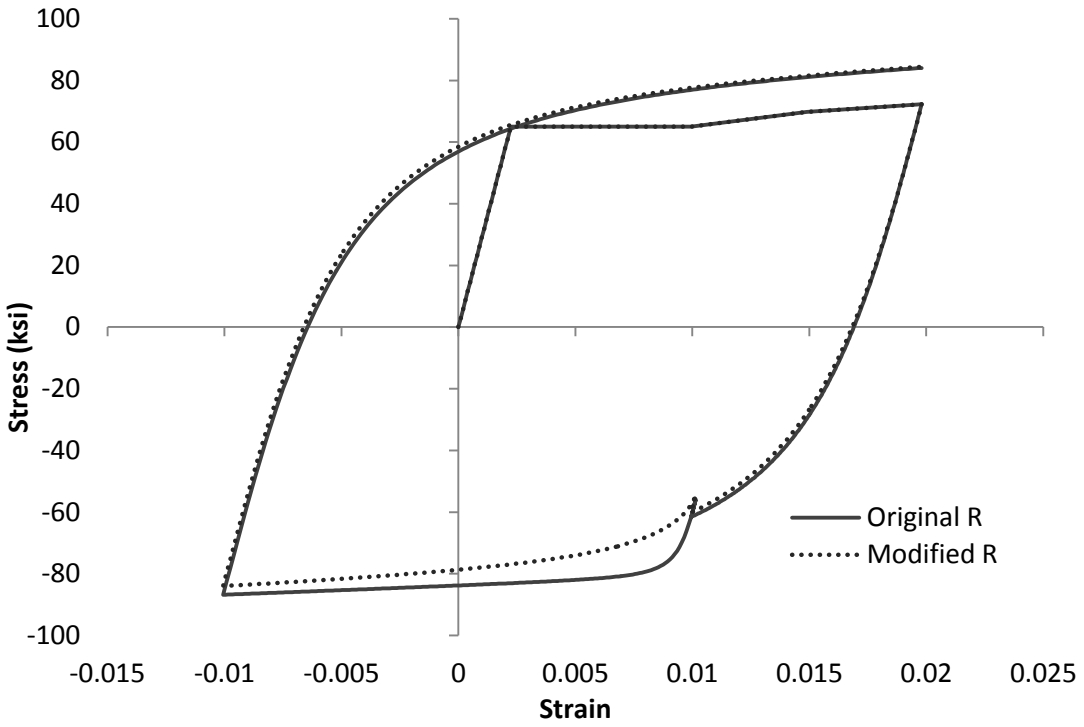

Figure 2.3– Hysteretic curves by Menegotto-Pinto model with partial unloading and reloading

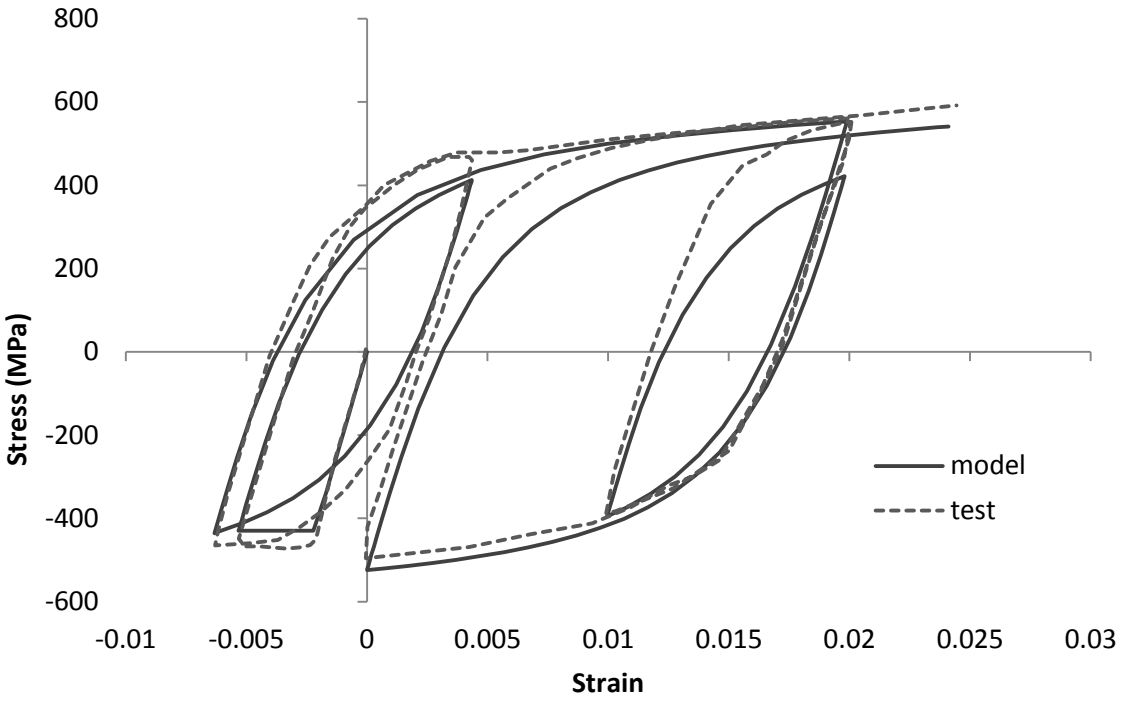

(a)

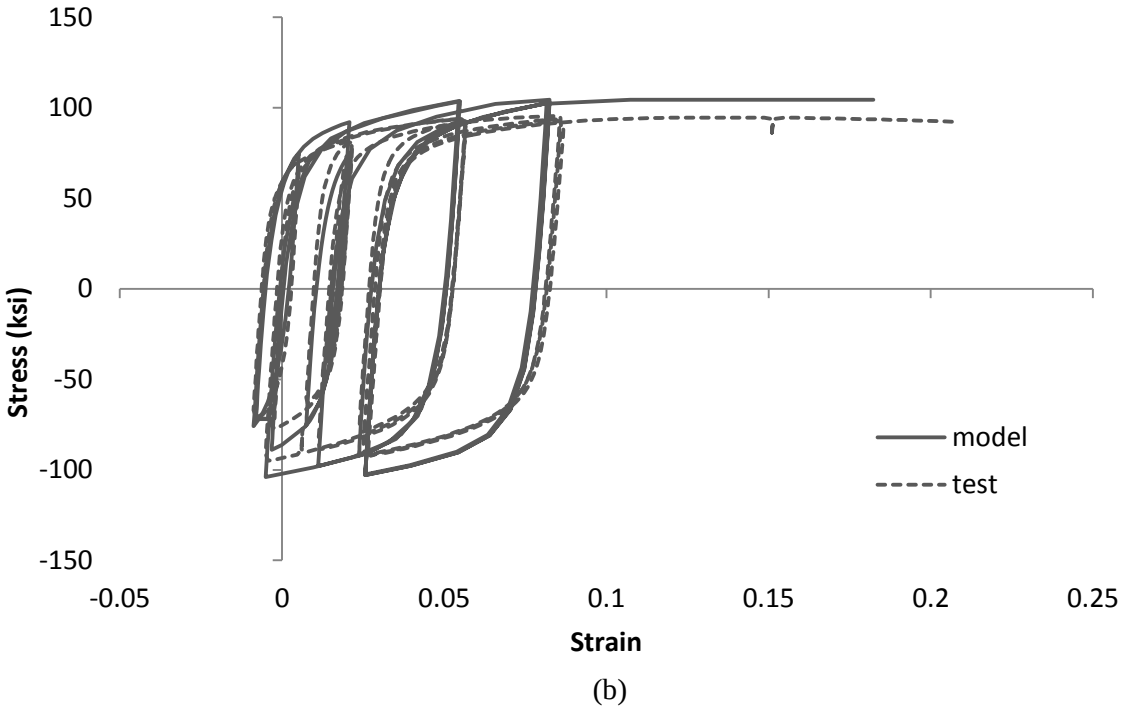

(b)

Figure 2.4 – Cyclic tests of steel reinforcing bars by Dodd and Restrepo (1995)

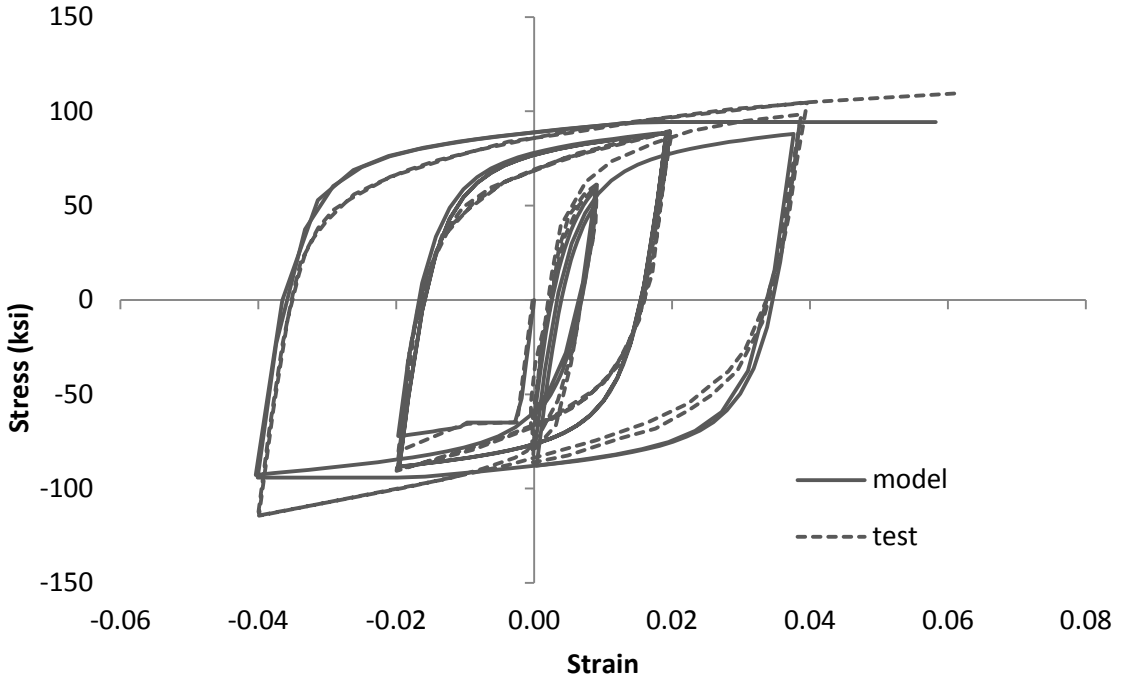

(a)

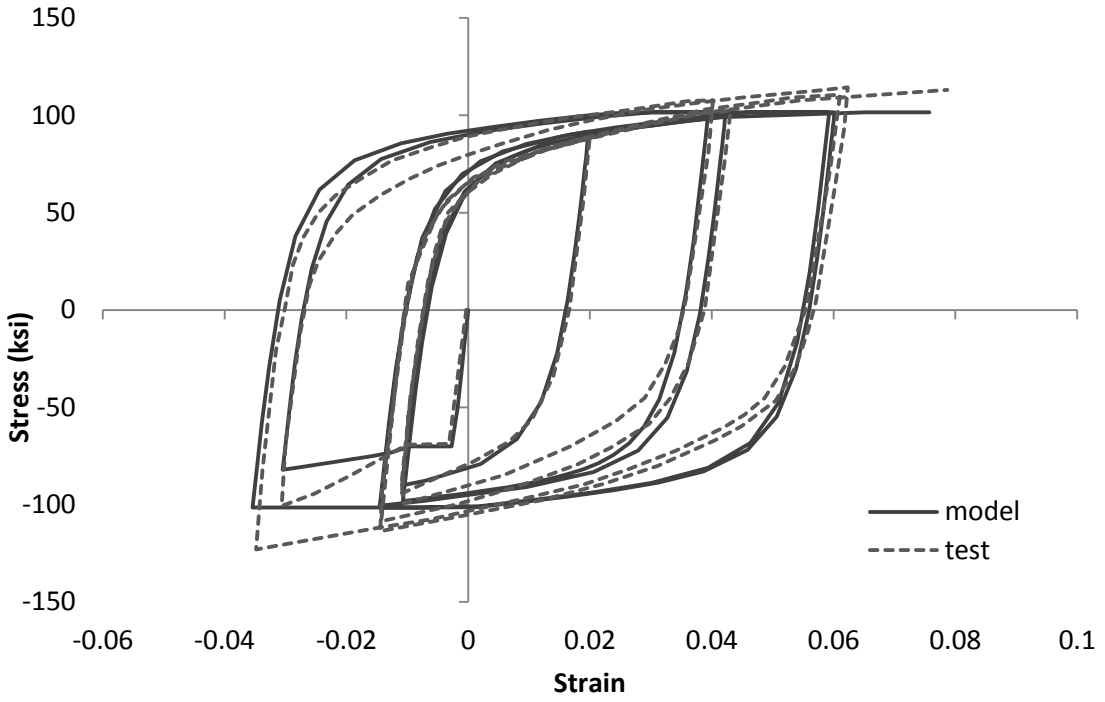

(b)

Figure 2.5 – Cyclic tests of steel reinforcing bars by Aktan et al. (1973)

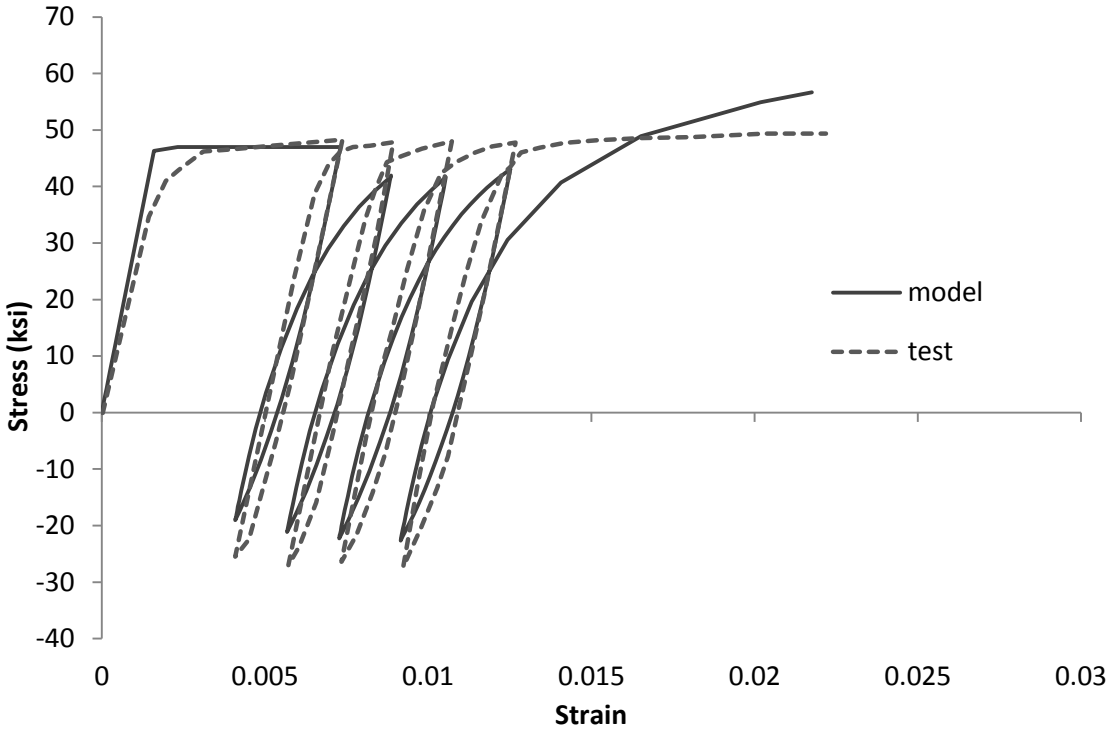

Figure 2.6 – Cyclic test of steel reinforcing bar by Kent and Park (1973)

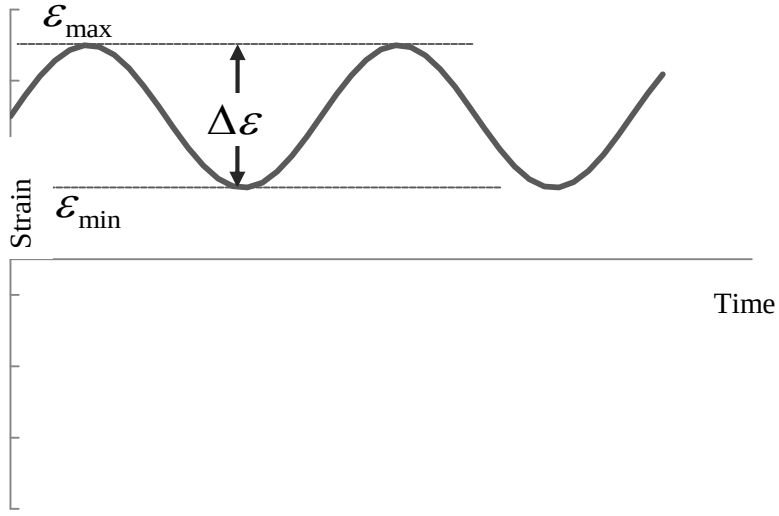

Figure 2.7 – Cycles with constant strain amplitudes

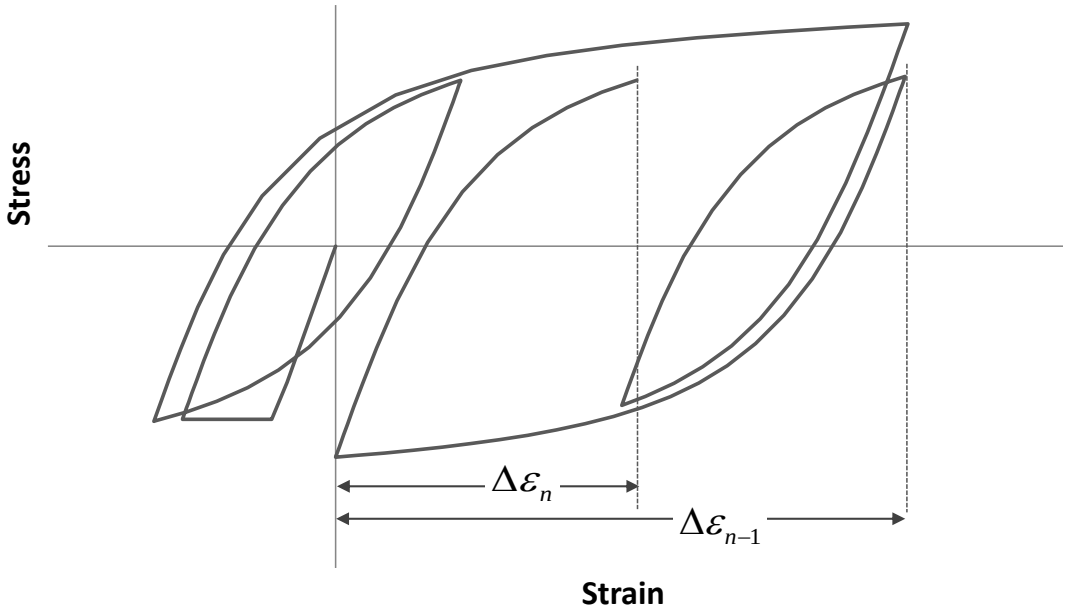

Figure 2.8 – Strain ranges, $\Delta\varepsilon$, with random strain reversals

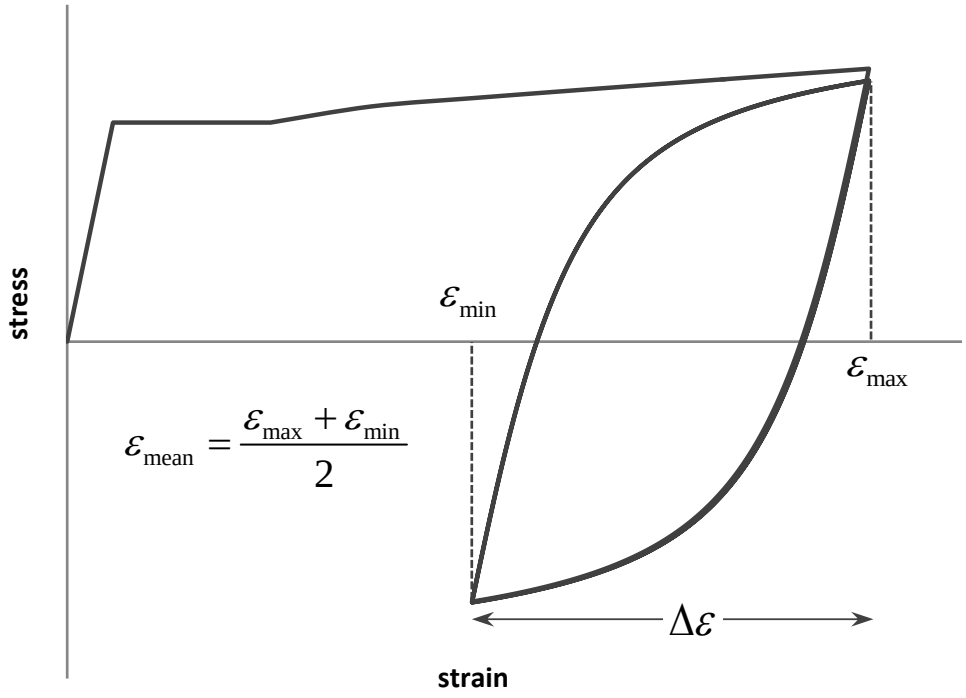

Figure 2.9 – Strain reversals with mean strain, $\varepsilon_{\text{mean}}$

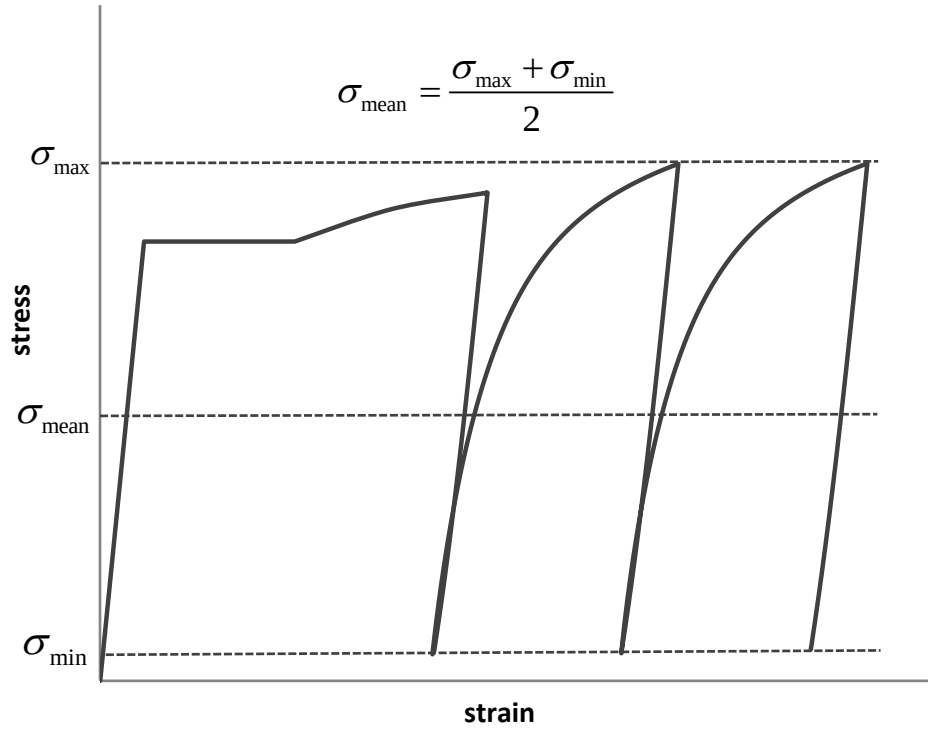

Figure 2.10 – Strain reversals with mean stress, σ_{mean}

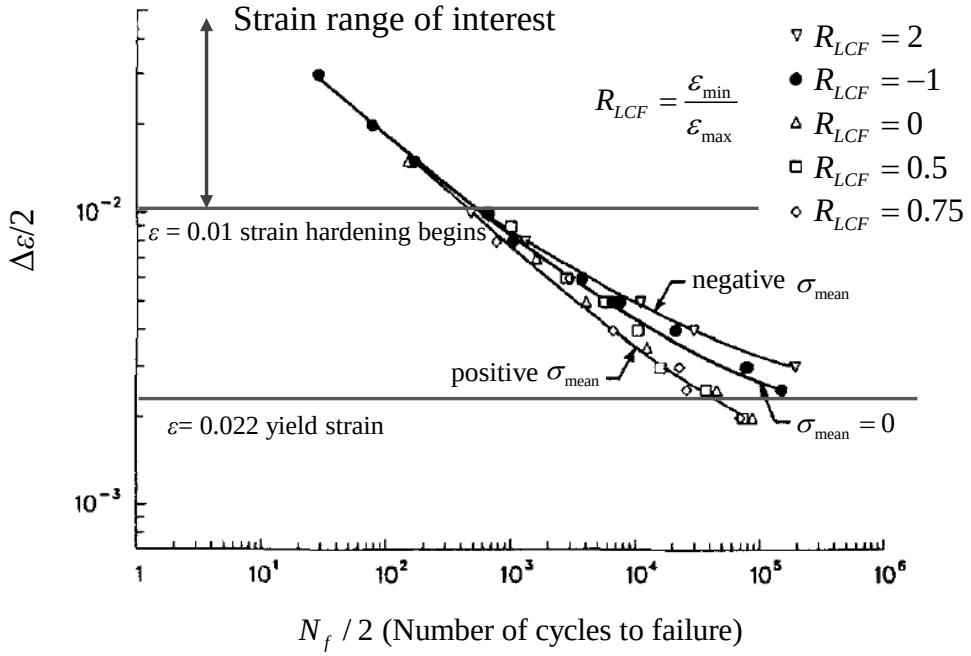

Figure 2.11 – Effect of mean strain and stress on LCF (Koh and Stephens, 1991)

(a) Test apparatus with a buckled bar

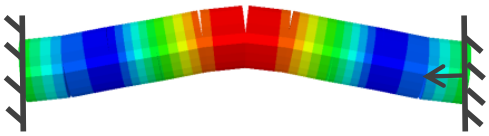

(b) FE model of a single bar

Figure 2.12 – LCF test by Kunnath et al. (2009b)

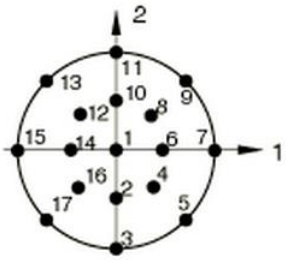

Figure 2.13 – Integration points in the circular section of a beam element in Abaqus

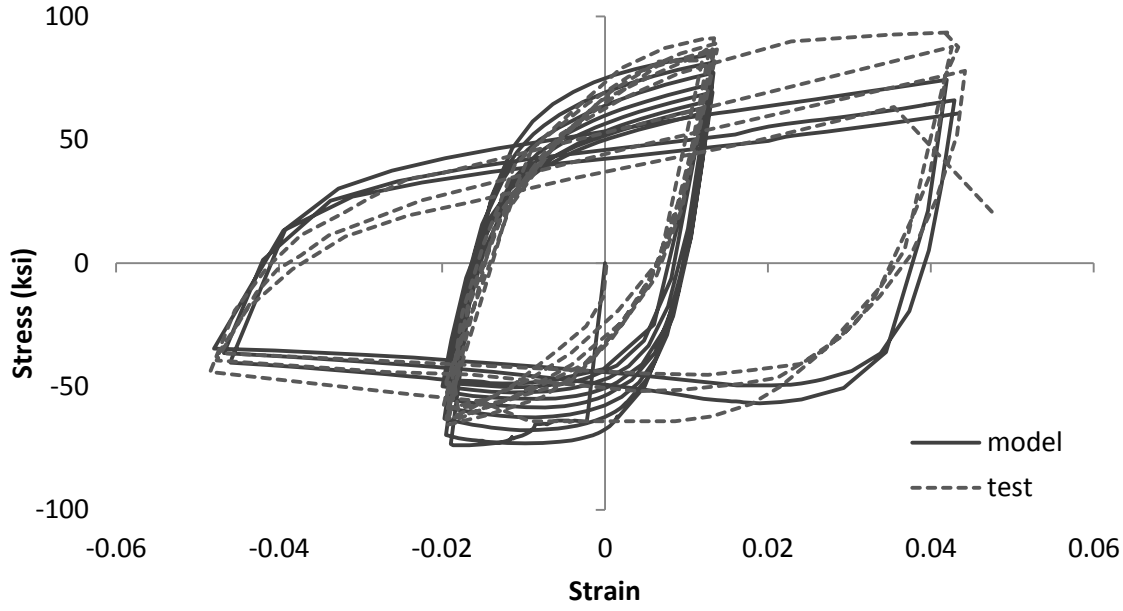

(a) Specimen N11Y4

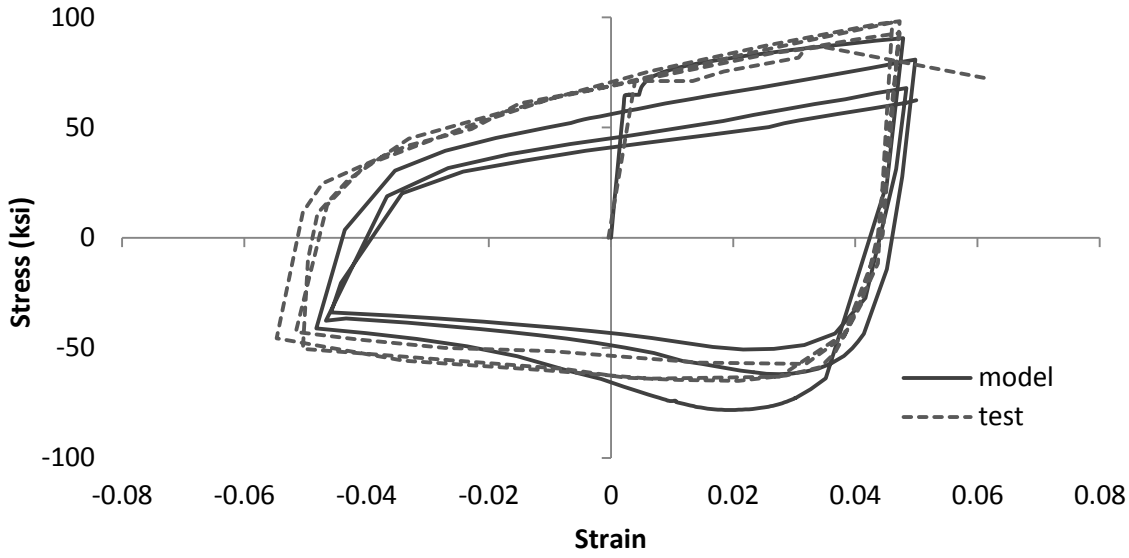

(b) Specimen N11Y8

Figure 2.14 – Cyclic tests of No. 11 bar specimens by Kunnath et al. (2009b)

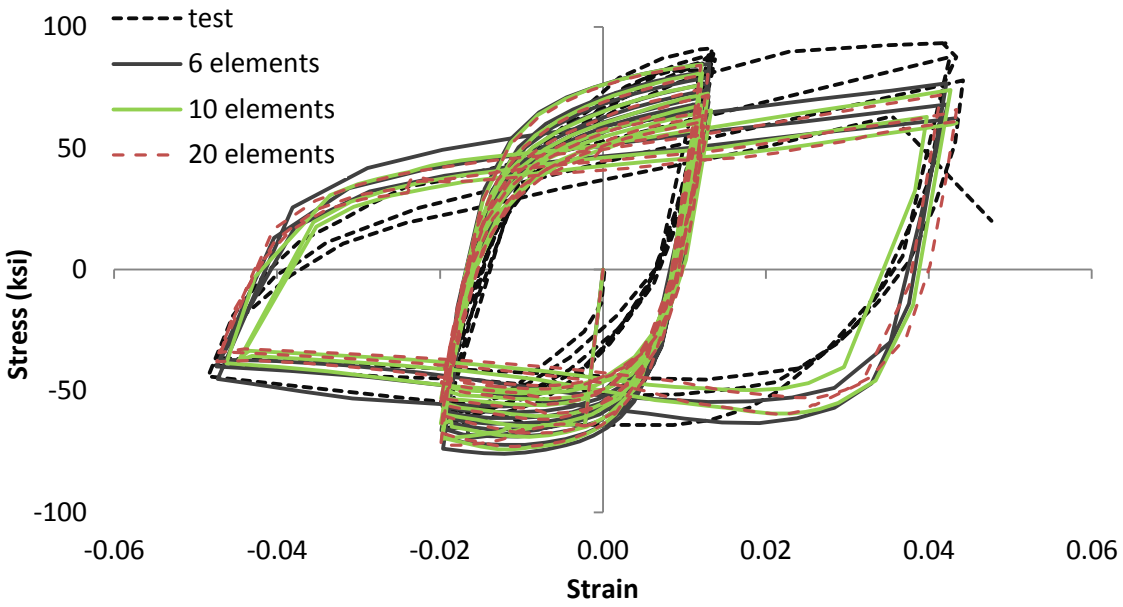

Figure 2.15 – Mesh-size sensitivity study with No. 11 bar (Specimen N11Y4) tested by Kunnath et al. (2009b)

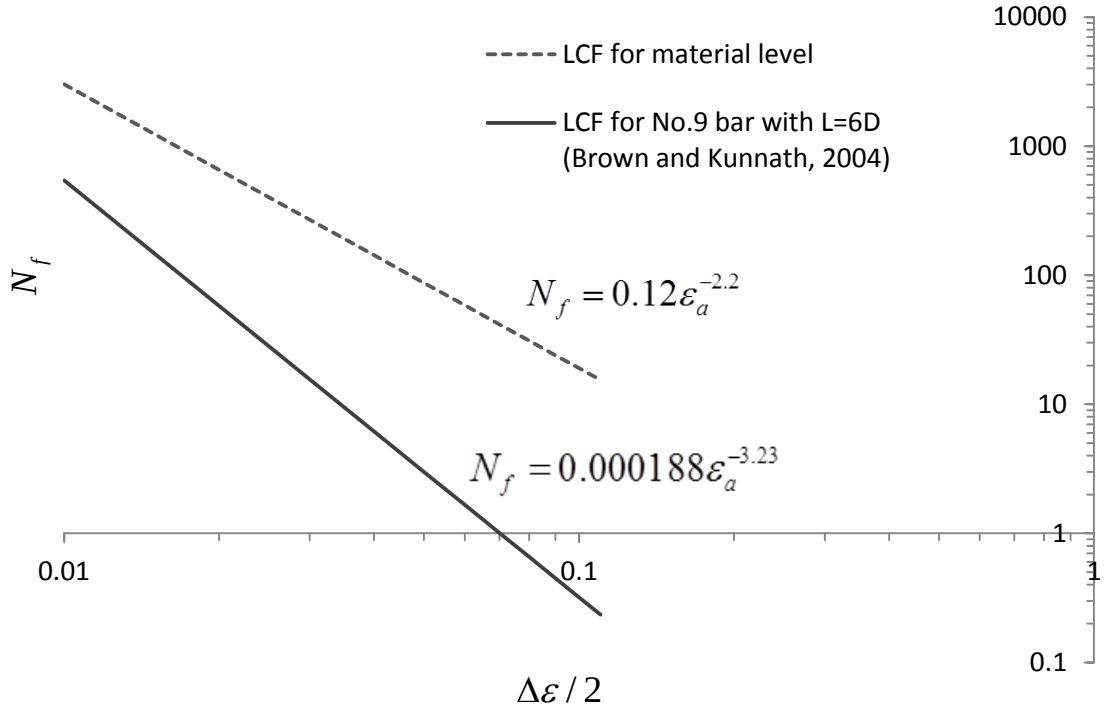

Figure 2.16 – Comparison of LCF laws for material level and bar level

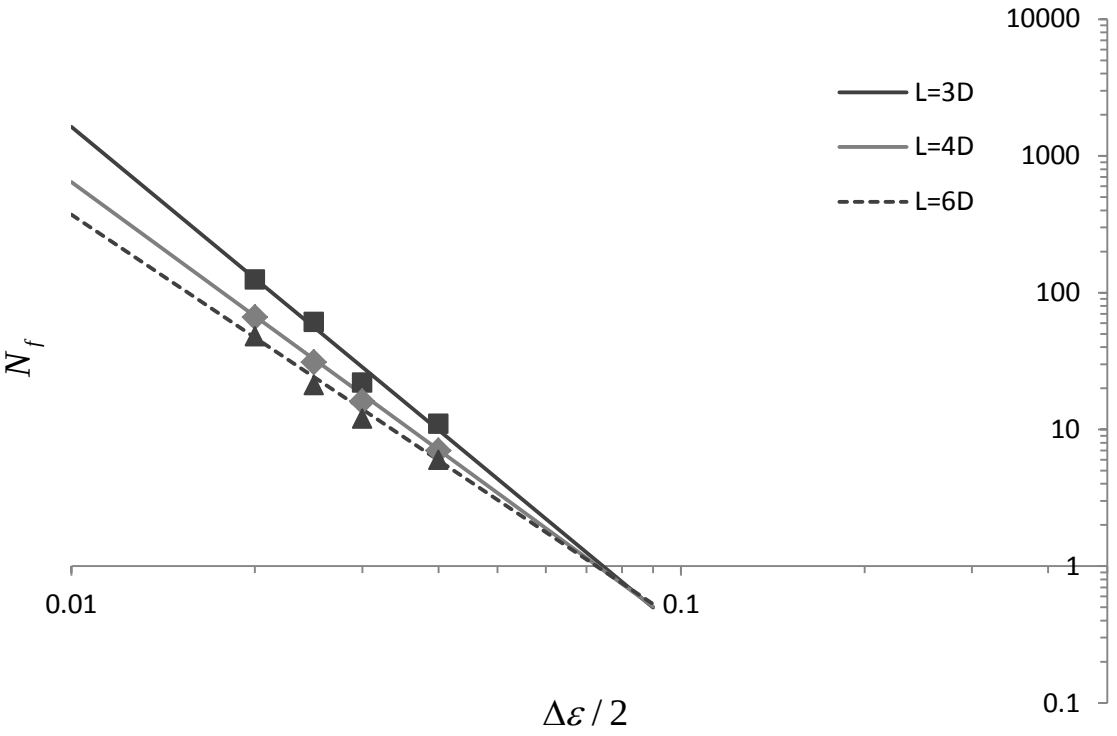

Figure 2.17 – LCF law for No. 9 bars with different slenderness

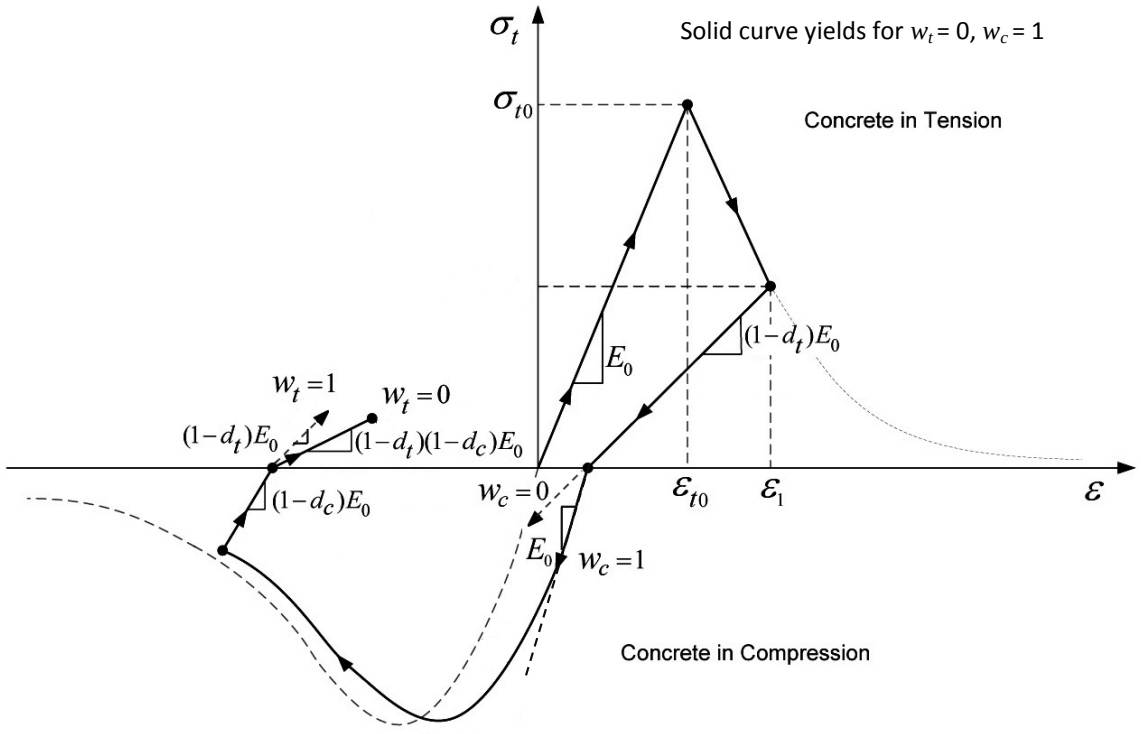

Figure 2.18 – Stiffness recovery under uniaxial load cycle for damaged-plasticity model

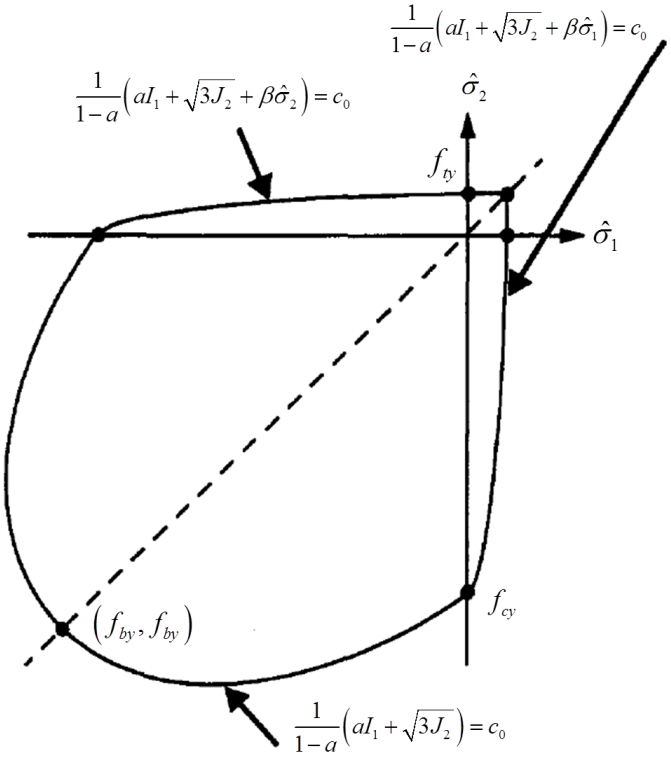

Figure 2.19 – Initial yield function in principal stress space under plane-stress condition (Lee and Fenves 1998)

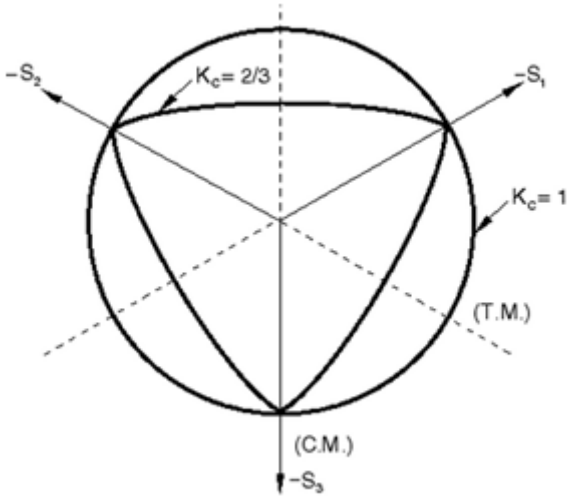

Figure 2.20 – Deviatoric plane for different values of K_c

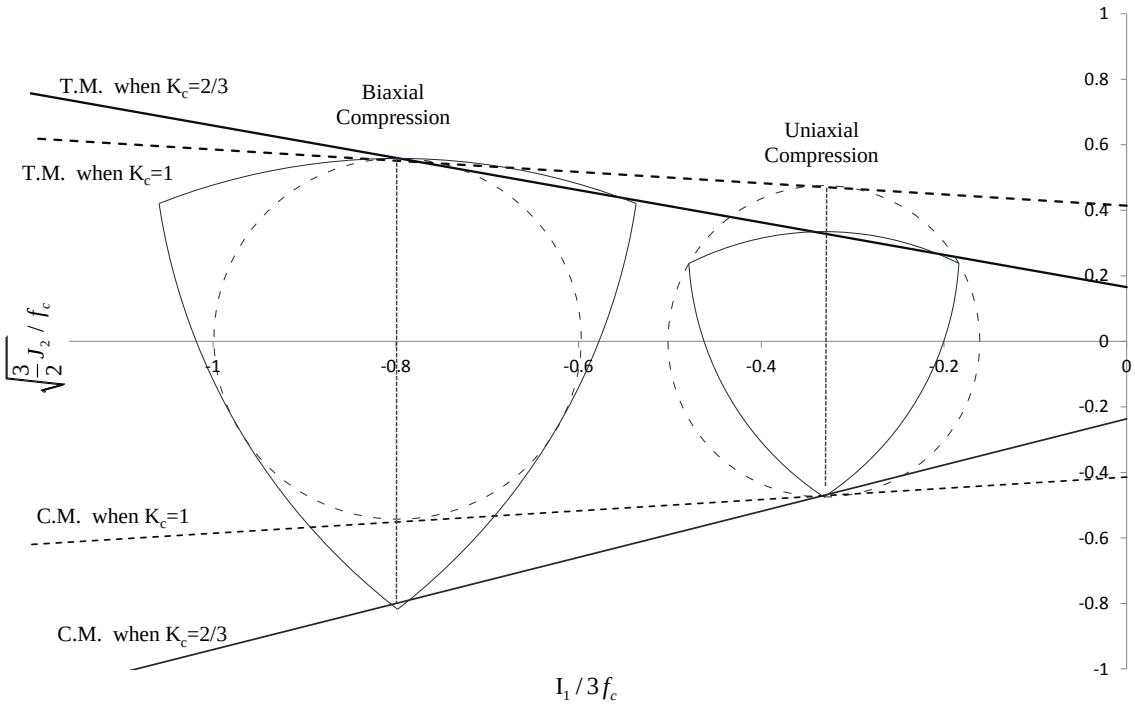

Figure 2.21 – Meridian plane of yield surface for different values of K_c

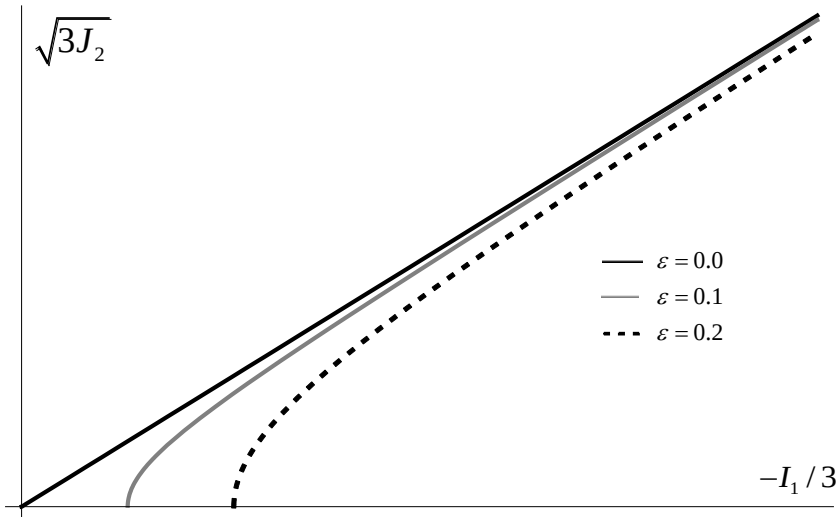

Figure 2.22 – Plastic potential for different values of ε

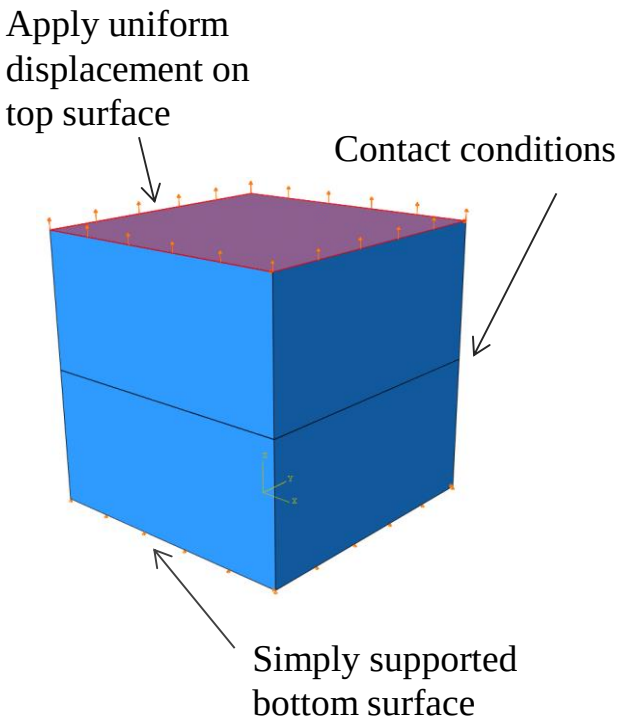

Figure 2.23 – Model for uniaxial loading with contact conditions

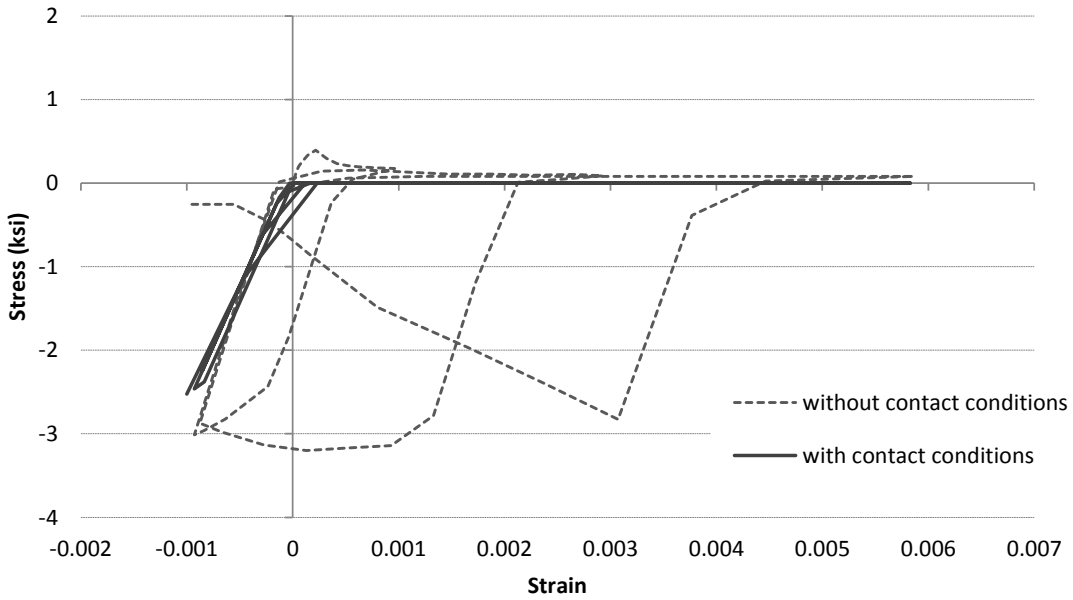

Figure 2.24 – Uniaxial loading test of models with and without contact conditions

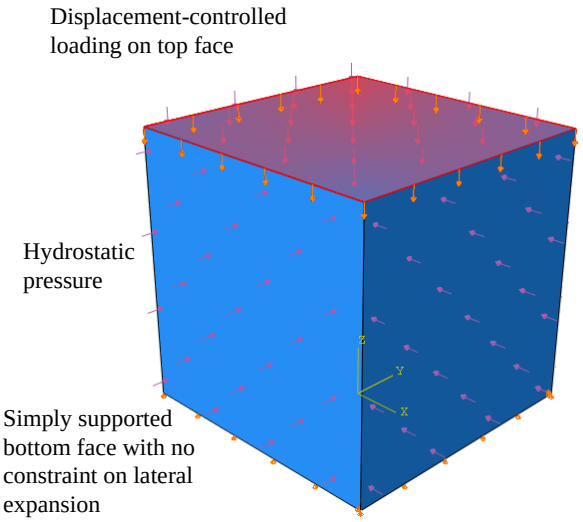

Figure 2.25 – FE model of hydrostatic pressure tests by Hurblut (1985)

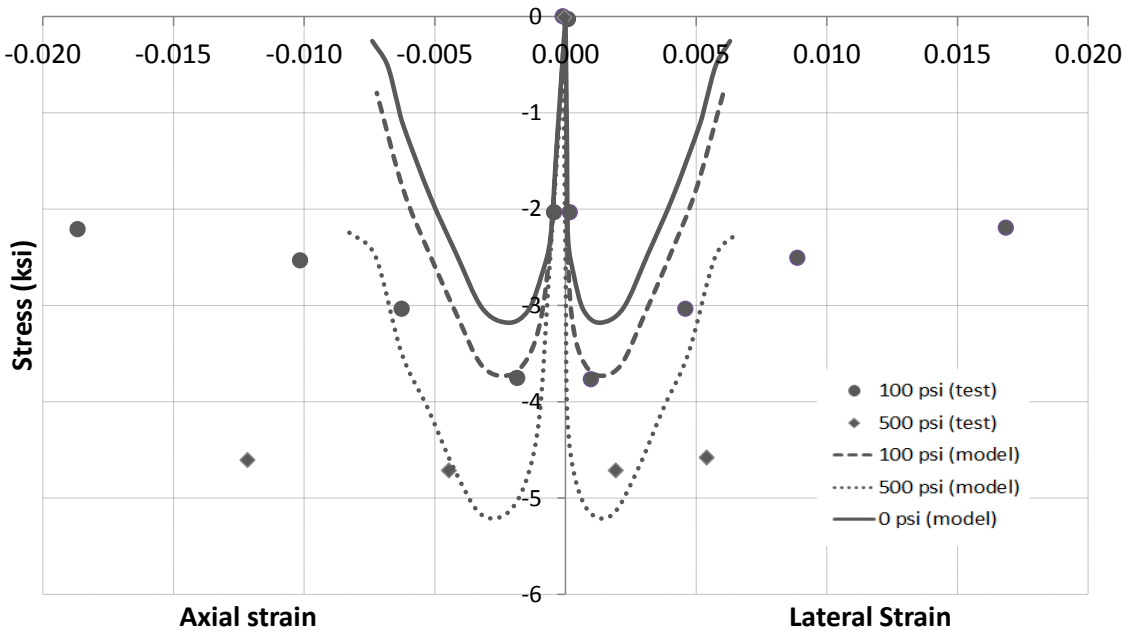

Figure 2.26 – Confined compression tests by Hurblut (1985)

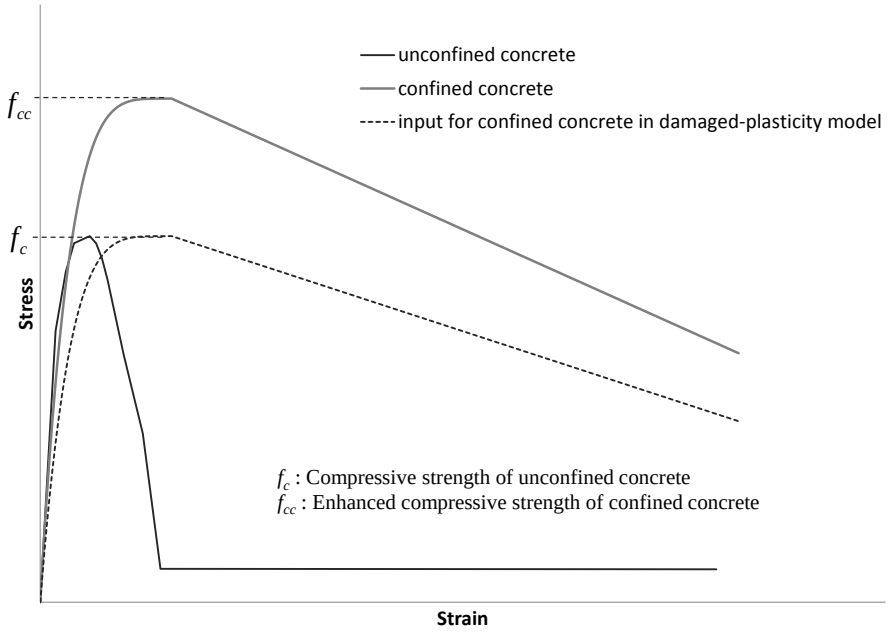

Figure 2.27 – Calibration of input uniaxial compressive stress-strain curve in damaged-plasticity model accounting for confinement effect

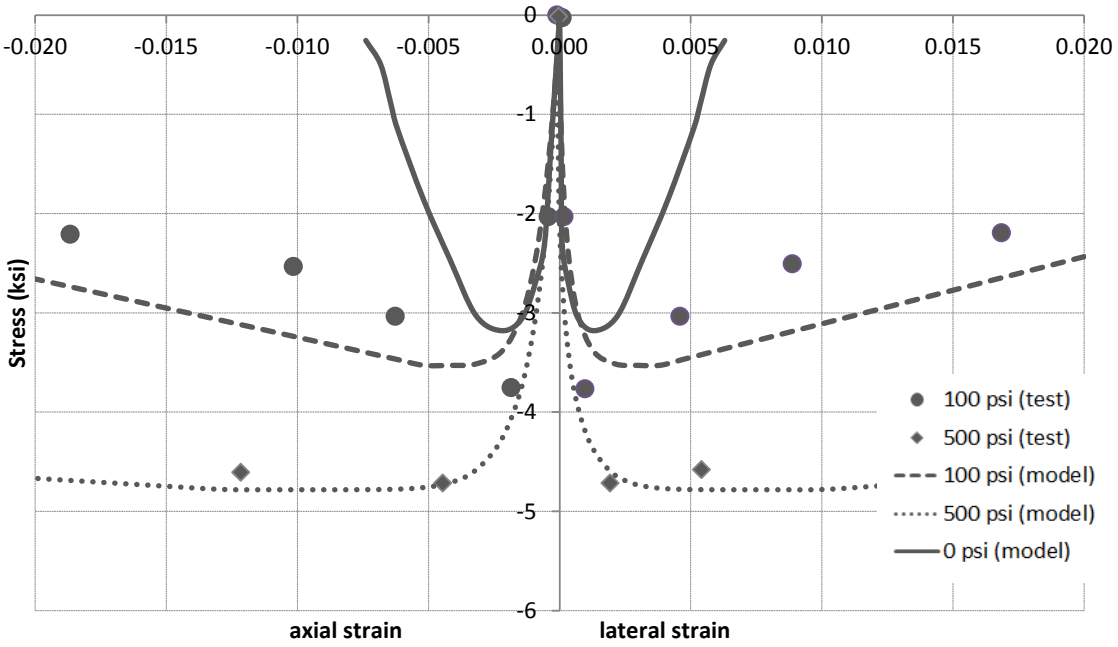

Figure 2.28 – Comparison of model with modified post-peak behavior to experimental results by Hurblut (1985)

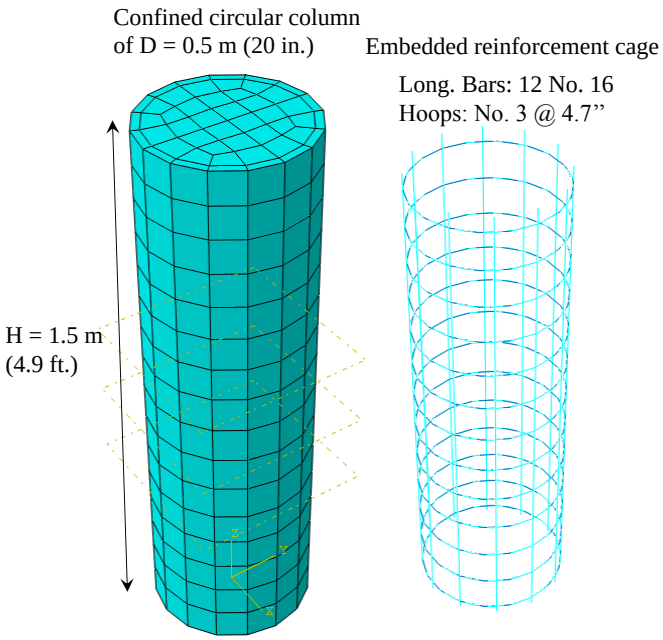

Figure 2.29 – FE model of compression tests on confined circular-sectioned RC columns by Mander et al. (1988b)

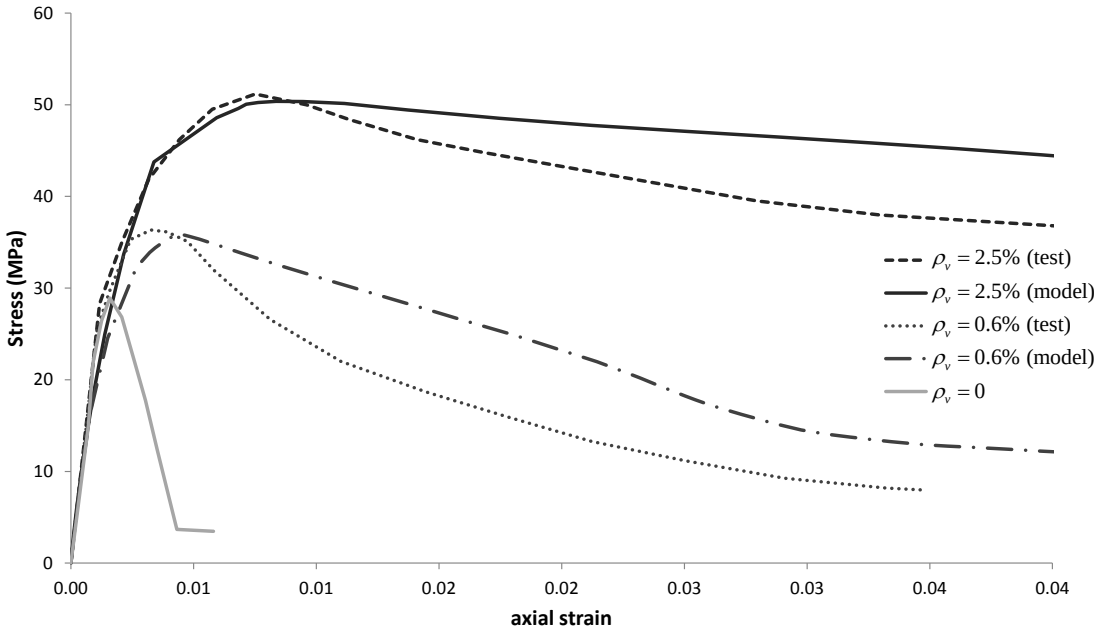

Figure 2.30 – Comparison of model with modified post-peak behavior to experimental results by Mander et al. (1988b)

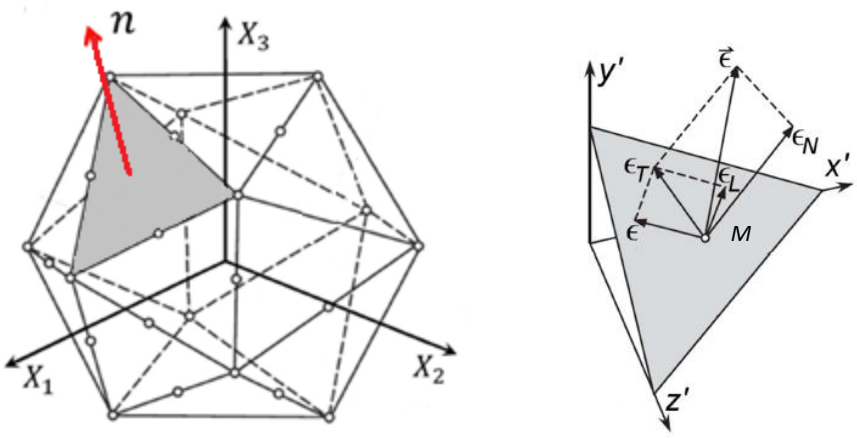

(a) (b)

Figure 2.31 – (a) System of discrete microplanes, (b) Microplane strain vector and its components (Caner and Bazant, 2013a)

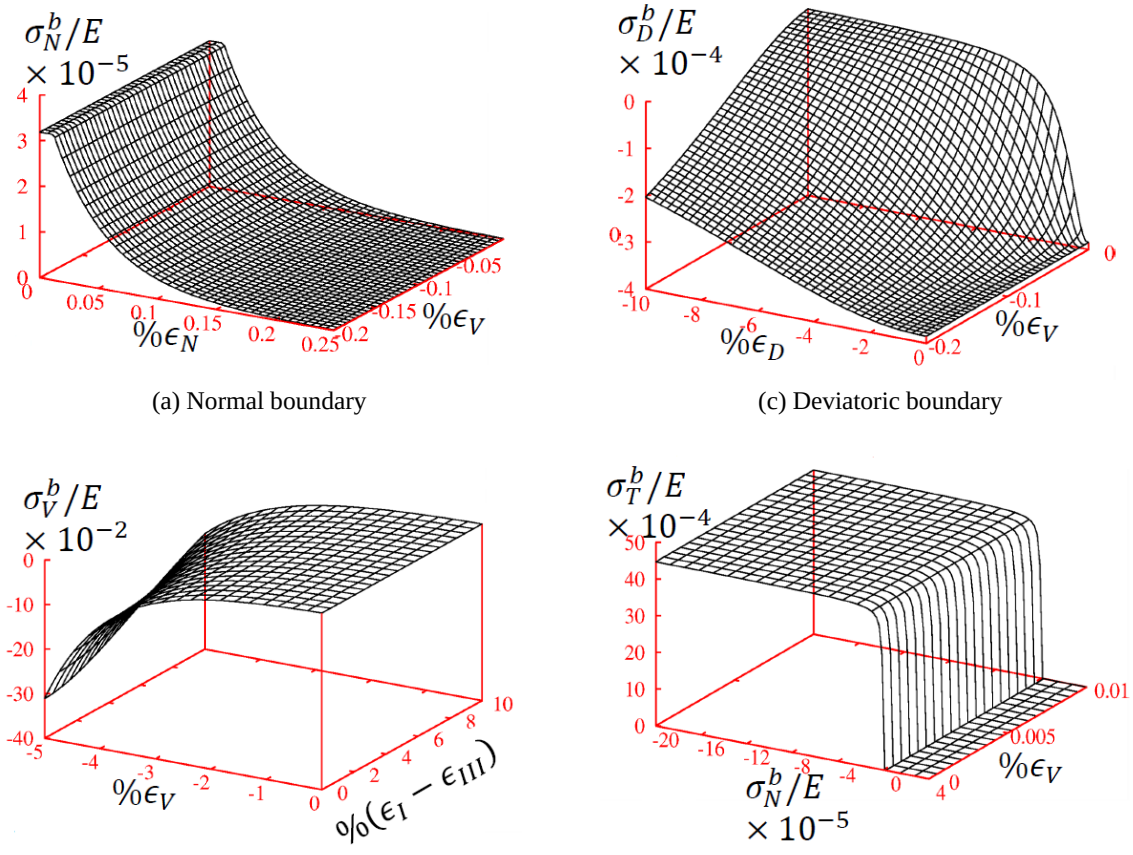

(a) Normal boundary

(c) Deviatoric boundary

(b) Volumetric boundary

(d) Shear boundary

Figure 2.32 – Stress-strain boundaries of the microplane model (Caner and Bazant, 2013a)

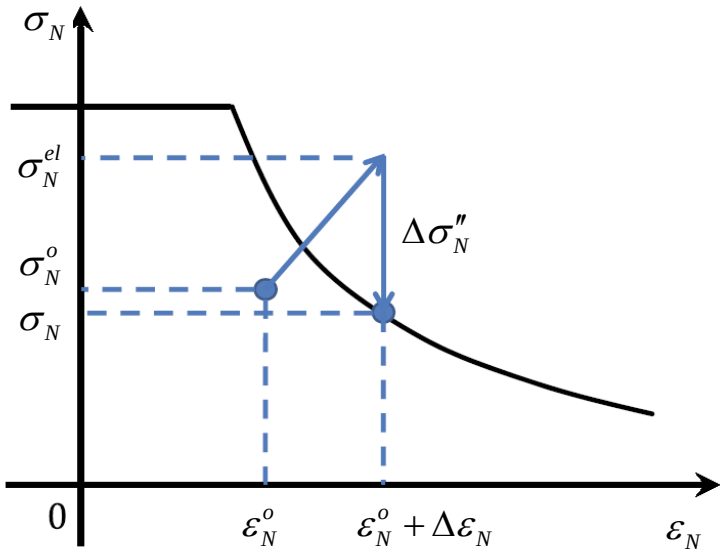

Figure 2.33 – Vertical return to normal boundary when the boundary is exceeded by an elastic trial stress in a finite load step (Caner and Bazant, 2013a)

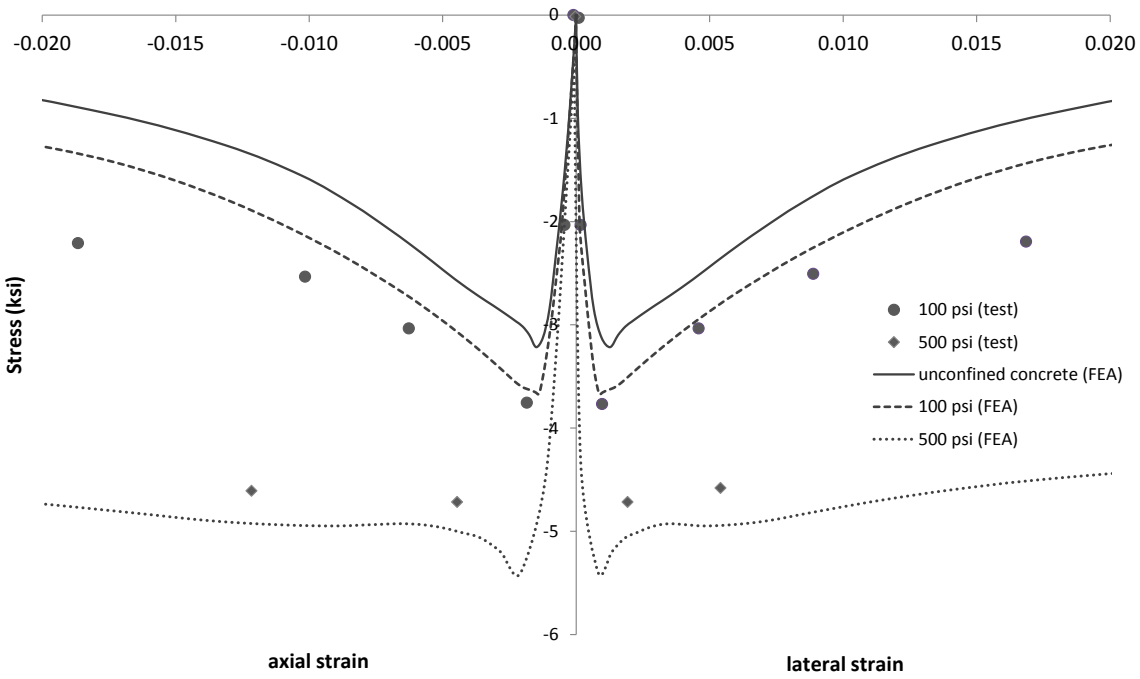

Figure 2.34 – Comparison of microplane model with default parameters to experimental results by Hurblut (1985)

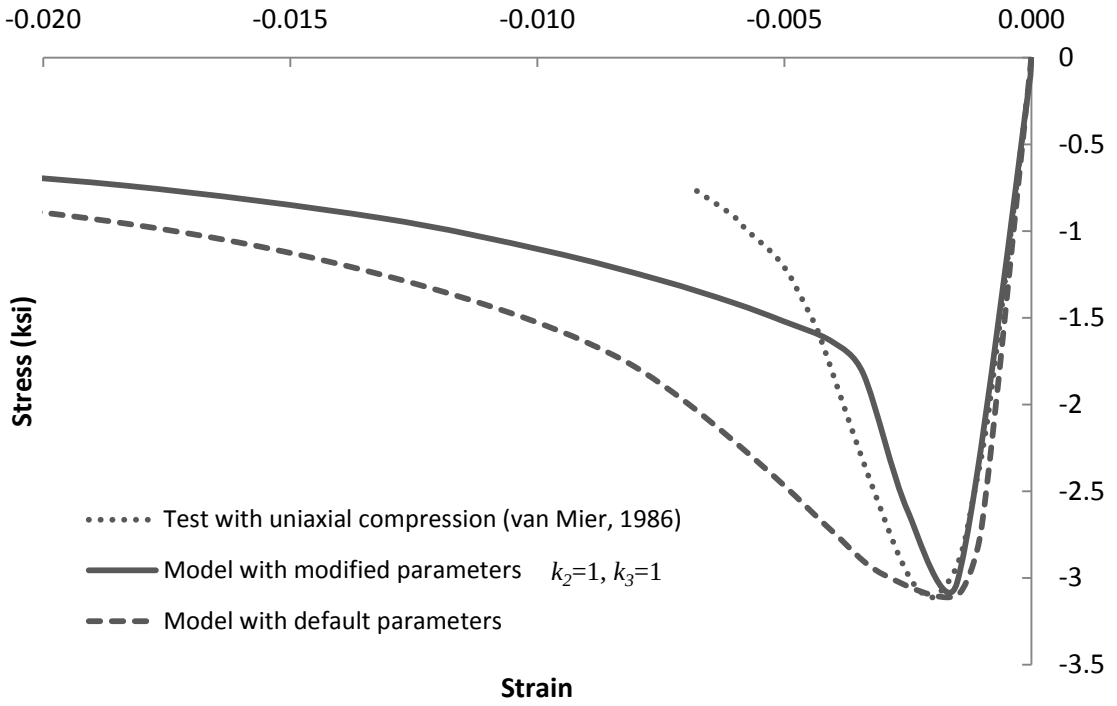

Figure 2.35 – Comparison of microplane model to uniaxial compression test by van Mier (1986)

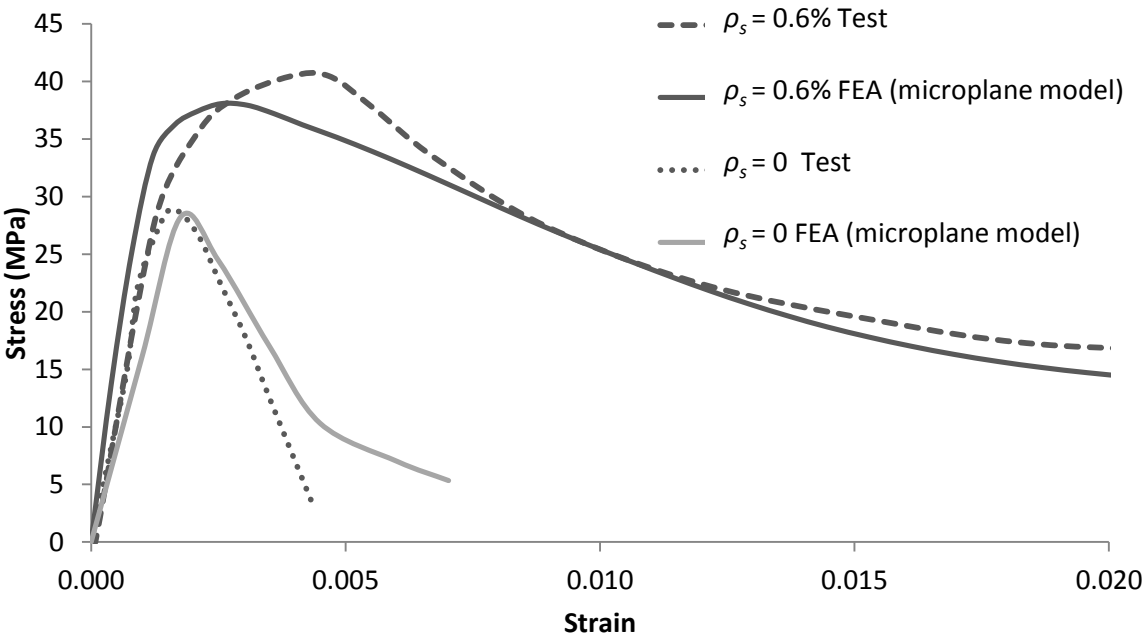

(a) ρ_s=0.6%

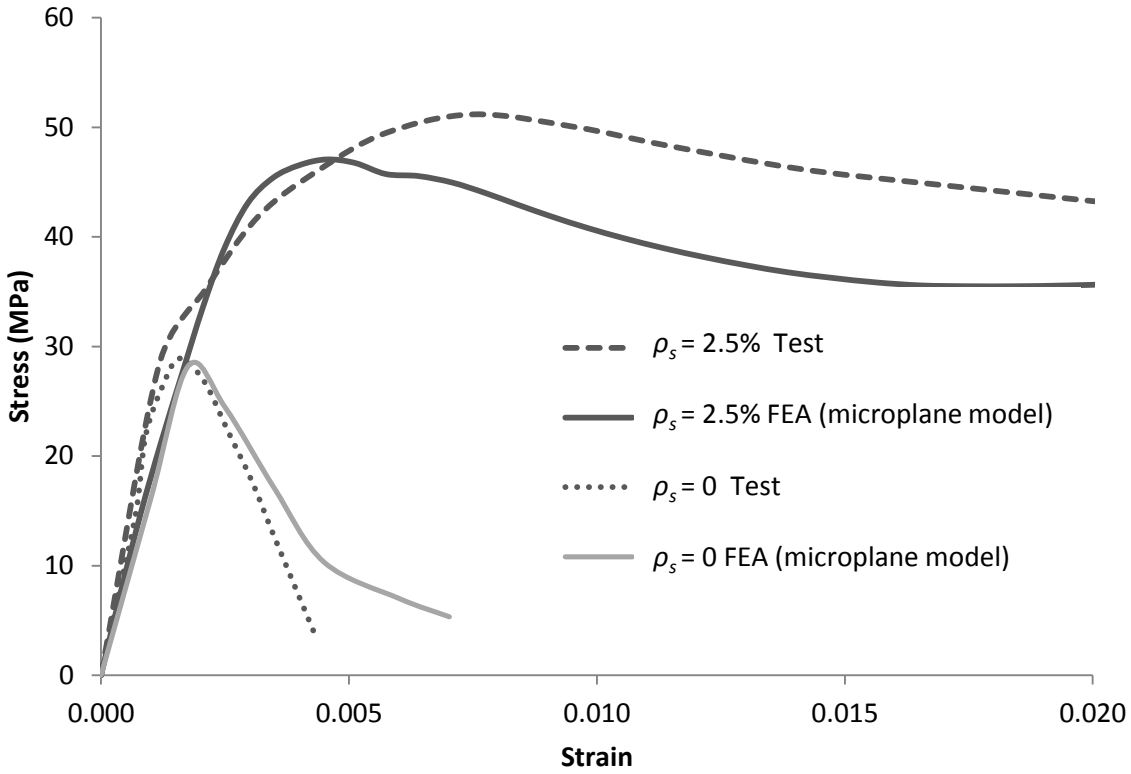

(b) ρ_s=2.5%

Figure 2.36 – Comparison of microplane model to experimental results by Mander et al. (1988b)

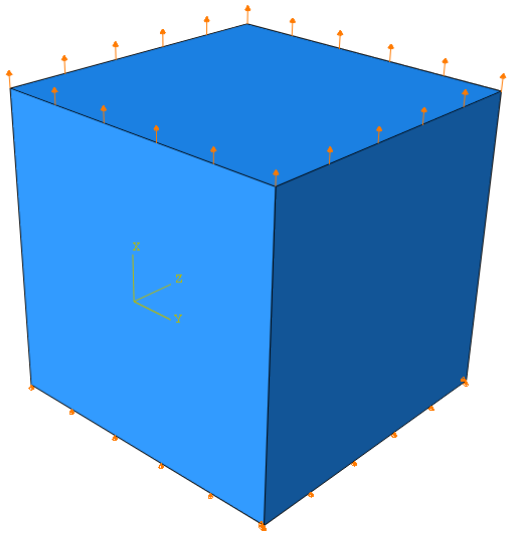

Figure 2.37 – Model for cyclic loading in tension

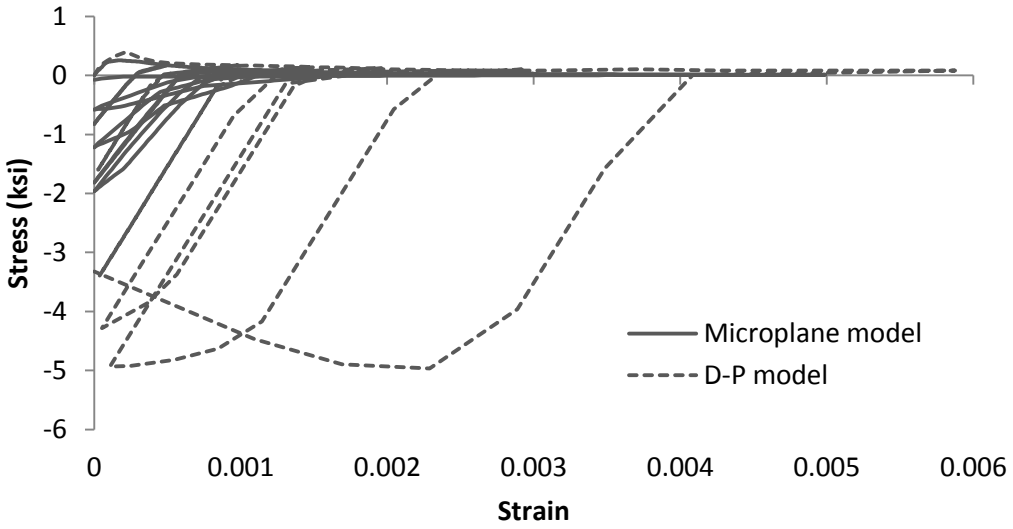

Figure 2.38 – Comparison of microplane model and D-P model under cyclic loading in tension

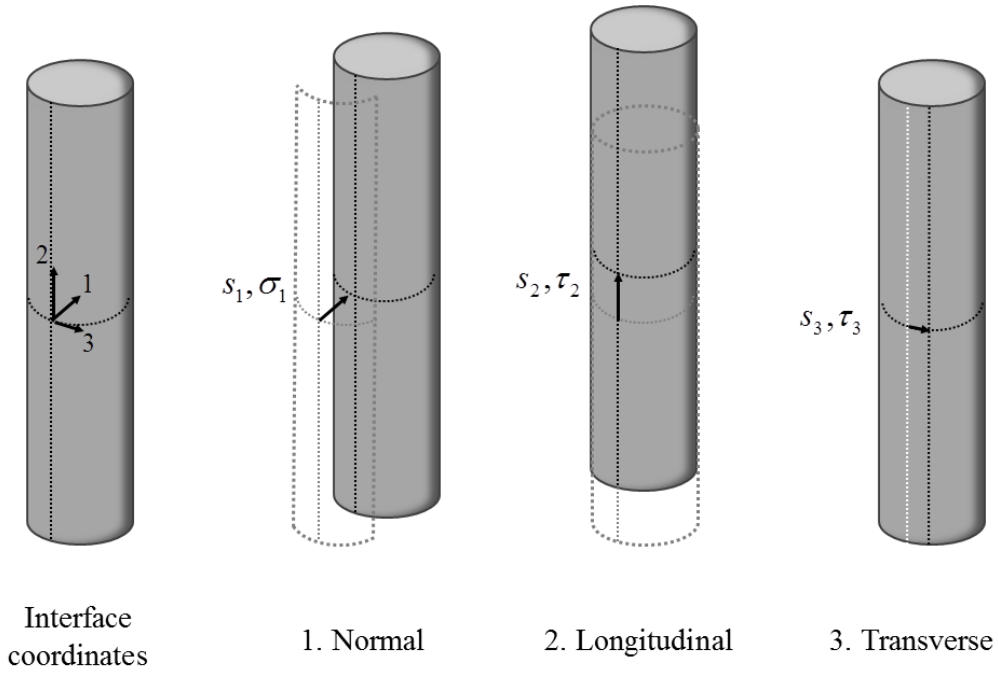

Figure 2.39 – Stresses and relative displacements at the bar-concrete interface

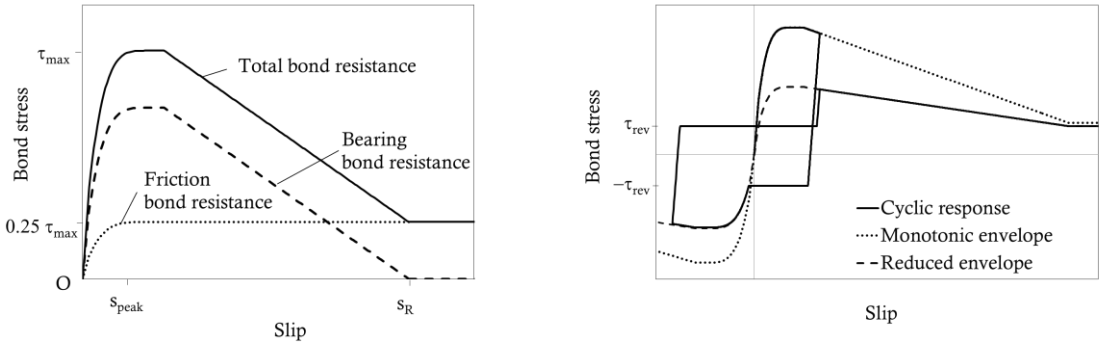

(a) monotonic response (b) cyclic response

Figure 2.40 – Analytical bond stress-slip model by Murcia-Delso and Shing (2015)

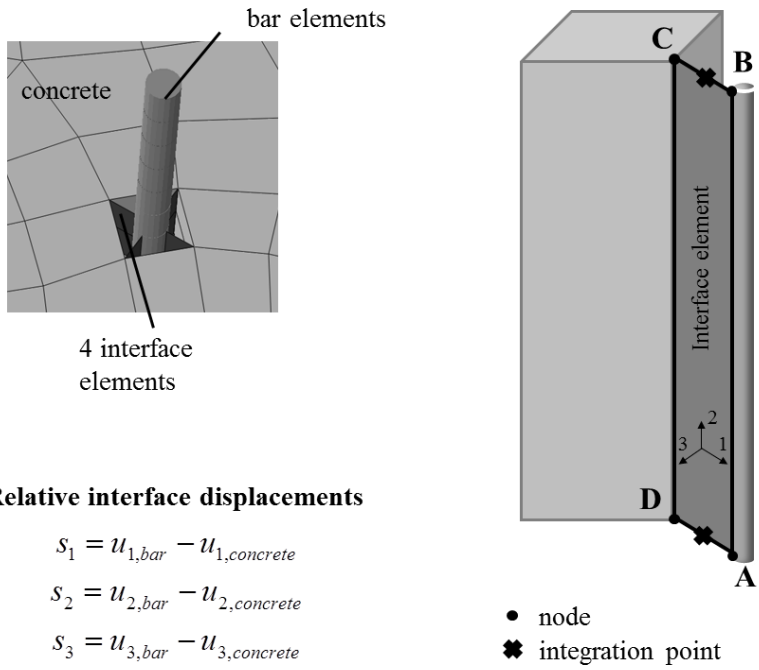

Relative interface displacements

$$s_1 = u_{1,bar} - u_{1,concrete}$$

$$s_2 = u_{2,bar} - u_{2,concrete}$$

$$s_3 = u_{3,bar} - u_{3,concrete}$$

Figure 2.41 – Interface element by Murcia-Delso and Shing (2015)

CHAPTER 3

EXPERIMENTAL INVESTIGATION OF EFFECTS OF SPACING OF LONGITUDINAL REINFORCEMENT ON PILE BEHAVIOR

The aim of this study was to investigate the influence of the lineal spacing of longitudinal reinforcing bars on the structural performance of circular RC piles; and in particular, to examine the impact of having the bar spacing greater than 8 in., which is the maximum permitted by the Caltrans Bridge Design Specifications (BDS) (Caltrans 2004) and the AASHTO LRFD Bridge Design Specifications (AASHTO 2014) for longitudinal bars in compression members. The need for a lineal spacing of longitudinal bars in CIDH piles, greater than the 8 in., comes from the requirement of the installation of inspection (PVC) tubes for non-destructive detection of potential anomalies in the concrete. These tubes are placed in contact with the outermost hoops, along the same circumference as that of the longitudinal bars, resulting the violation of the maximum spacing of 8 in.

3.1 Past Research

The influence of the quantity and spacing of transverse reinforcement on the ductility and structural performance of RC members subjected to axial and flexural loads has been well studied and understood. However, there is only limited information on the influence of the spacing of longitudinal reinforcement on the structural performance of an RC member. It has been perceived that the spacing of longitudinal bars has a certain influence on the effectiveness of the confinement provided by transverse reinforcement. While this can be understood for members with rectangular sections, in which the spacing of the cross-ties is normally related to the spacing

of the longitudinal bars, it is less so for circular members. Pauley and Priestley (1992) have recommended that this spacing be no greater than 8 in. for both rectangular and circular columns. They have stated that this could lead to better confined concrete, but they have also pointed out that there is no compelling justification for this recommendation. Both Caltrans (2004) and AASHTO (2014) have specified the spacing limit of 8 in. for compression members. Nevertheless, from the structural performance stand point, the spacing limit for the longitudinal bars in a circular member should depend on the diameter of the member, and it is reasonable to expect that a member with a larger diameter can have a larger circumferential spacing of the longitudinal bars without affecting its structural performance. However, before the study reported here, there was no experimental data available to support or discourage the use of longitudinal bar spacing greater than 8 in.

Parameters that may influence the confinement effect in a circular RC member include: (a) the longitudinal reinforcement ratio, ρ_l, (b) the transverse reinforcement ratio, ρ_t, (c) the angular spacing, θ_l, and the lineal spacing, s_l, of the longitudinal bars, (d) the spacing, s_t, of the transverse reinforcement, (e) the yield strength of the steel, and (f) the compressive strength of the concrete. This report focuses on the impact of the circumferential spacing of the longitudinal bars. The influence of the transverse reinforcement has been well studied and will not be considered here.

The impact of the spacing of longitudinal bars on the seismic performance of a bridge column or pile was not well understood. It has been perceived that larger spacing may negatively affect the efficiency of the confinement on concrete and, thereby, reduce the flexural ductility of the member (Pauley and Priestley 1992). However, limited experimental data obtained by Mander et al. (1988b) has shown that the influence of the spacing of longitudinal bars on the behavior of circular RC columns under compression is almost negligible as shown in Figure 3.1. Nevertheless, the maximum center-to-center spacing of longitudinal bars considered in their study

was less than 6.5 in. For rectangular columns, a closer spacing of longitudinal bars has a clear benefit of enhancing the compressive strength and ductility, as shown in Figure 3.2. However, for rectangular columns, a closer spacing of longitudinal bars also means a closer spacing of cross-ties, which results in a better arching action and a more effectively confined concrete as illustrated in Figure 3.3.

3.2 Test program

Two full-scale RC pile shafts were tested under cyclic lateral loading to investigate the impact of having the spacing of longitudinal bars greater than 8 in. on the structural performance of piles. One specimen was designed according to the Caltrans Bridge Design Specifications (Caltrans 2004) and the AASHTO LRFD Bridge Design Specifications (AASHTO 2014). The other had the same design except that its longitudinal reinforcement had spacing much greater than 8 in., violating the current design requirements. The design of the specimens, the test program and its findings are presented in this chapter.

3.2.1 Test Specimens

The specimens were tested as cantilever piles with a constant axial load. They had the same dimensions. The height of each pile was 10 ft. (from the base to the mid-height of the cap) and the diameter was 28 in.

The design and reinforcing details of the specimens are shown in Figure 3.4 through Figure 3.9 and summarized in Table 3.1. As shown in Figure 3.4 and the table, the two specimens had the same design with more or less the same amount of longitudinal reinforcement. The only difference between the two was the size and the spacing of the longitudinal bars. As shown in Figure 3.5, the longitudinal reinforcement of Specimen #1 consisted of 6 No. 11bars, which corresponds to a steel ratio of 1.52%. The center-to-center spacing of the bars was 11 in.,

violating the maximum limit of 8 in. permitted by the Caltrans and AASHTO LRFD specifications. In Specimen #2, the longitudinal reinforcement consisted of 10 No. 9 bars spaced at 6.75 in. on center, which corresponds to a steel ratio of 1.62%. The transverse reinforcement in both specimens consisted of No. 6 hoops spaced at 5.75 in. on center, which met the minimum clear spacing of 5 in. for reinforcing steel in piles according to Caltrans (2004) and AASHTO (2014). The volumetric ratio of the transverse steel is 1.28%, which is only slightly less than the minimum (1.35%) required by Caltrans (2004) for compression members.

The concrete used for the pile specimens had a specified slump of 7 in. and a specified compressive strength of 4,500 psi with the maximum aggregate size of 3/8 in., conforming to concrete mixes typically used for cast-in-place drilled hole (CIDH) piles. Table 3.2 summarizes the mix design specified for the concrete. The expected compressive strength of the concrete at 28 days was 5,000 psi. The reinforcement used for the test program was Grade 60 steel conforming to ASTM A706/A706M-09b standards (ASTM 2009).

3.2.2 Test Setup and Procedure

The two pile specimens had the same test setup, which is shown in Figure 3.10 and Figure 3.11. They were tested as cantilever columns. The footing of each specimen was fixed onto the strong floor of the laboratory with 6 steel bars, each of which was post-tensioned to 200 kips. A constant axial load of 280 kips was applied on each specimen with a steel cross beam set on top of the pile cap, corresponding to 9% of the actual compressive strength of the specimens $\left(A_g f_c'\right)$. The steel beam was loaded by two steel rods that were post-tensioned with center-hole jacks located underneath the strong floor. Each specimen was loaded by one horizontal actuator with a load capacity of 220 kips and a total stroke of 48 in. One end of the actuator was attached to the reaction wall, while the other end was attached to the pile cap. The line of the horizontal

load was 10 ft. above the base of the pile specimen. The specimens were subjected to cyclic lateral loading. A picture of the test setup is shown in Figure 3.12.

The loading history used in the tests is shown in the second column of Table 3.3. The lateral load-vs.-displacement curves for the two specimens were expected to be very similar, but Specimen #2 was expected to have a slightly higher lateral resistance not only because of the higher reinforcement ratio but also a higher proportion of the longitudinal bars in tension when the section was subjected to bending. To facilitate the comparison of the behaviors of the two specimens, it was decided that the same loading history be used in the two tests. The loading history was first determined for Specimen #1 with the help of a pre-test finite element analysis conducted on the specimen. In the first 4 cycles, the actuator was under force control, with the load increased in each cycle up to the level that corresponded to the first yield of the longitudinal reinforcement in Specimen #1 as predicted in the pre-test analysis. The specimen was then subjected to fully-reversed displacement-controlled load cycles with increasing ductility demands until the lateral load resistance dropped significantly due to the fracture of the longitudinal reinforcement.

The ductility demand on the pile specimens is defined as $\mu = \Delta / \Delta_y$, in which Δ is the lateral displacement at the level of the actuator, and Δ_y is the yield displacement of an equivalent elastic-perfectly plastic system as defined in Figure 3.13. As shown in the figure, Δ_y is the displacement at the intersection of the secant line passing through the original and the point $\left(\Delta_y', F_y'\right)$ with the horizontal line passing through the ultimate load F_y, i.e.,

$$\Delta_y = \frac{F_y}{F_y'}\Delta_y' \tag{3.1}$$

In the above expression, F_y' is the lateral load at which the first yield of the longitudinal bars occurs and Δ_y' is the corresponding displacement. The displacement amplitudes shown in the

second column of Table 3.3 were determined as an integer multiple of Δ_y that was calculated to be 1.2 in. with Eq. (3.1) using the forces F_y' and F_y determined in the pre-test analysis and Δ_y' measured in the test, all for Specimen #1. However, the actual ductility demands and the values of Δ_y shown in the third and fourth columns of Table 3.3 are based on the actual values of F_y' and F_y obtained from the tests of the respective specimens. The maximum displacement applied in each test was 12 in., corresponding to 10% drift. The tests were stopped after a significant load drop had occurred due to the fracture of the longitudinal bars in the plastic-hinge zone near the base of the piles.

3.2.3 Instrumentation Schemes

As shown in Figure 3.14 and Figure 3.15, each pile specimen was instrumented with displacement transducers along its height, an inclinometer at the mid-height of its cap, and strain gages on the longitudinal and lateral reinforcement. Transducers L48, L49, L50 and L51 were string potentiometers used to monitor the lateral deflection of each pile specimen at different elevations. Vertical linear potentiometers were mounted on the east and west faces of each pile specimen to measure the bending curvature developed along the height of the pile. Horizontal and diagonal linear potentiometers were mounted on the east face to measure shear deformation. Pictures of the west and east faces of the specimens are shown on Figure 3.16 and Figure 3.17, respectively.

Strain gages were attached onto the longitudinal reinforcement in positions close to the base of the pile specimens, as shown in Figure 3.18, to measure strains in the plastic-hinge zone, and in the footings to measure strain penetration. At elevations adjacent to the base of a pile, two strain gages were attached at each location on opposite sides of a reinforcing bar so that bending strains (due to bar buckling for example) could be identified and separated from the axial strain.

The transverse reinforcement near the base of a pile also had strain gages, as shown in Figure 3.19. A picture of strain gages attached to the reinforcement of Specimen #1 is shown in Figure 3.20.

3.2.4 Specimen Construction and Material Properties

The two pile specimens were constructed at the same time by an outside contractor. Each specimen was cast in two phases. First, the reinforcement cages were assembled and the forms for the footings were fabricated. The footings were cast first. Thirty days later, the piles and the caps were cast. The time separation between these two concrete placements was decided according to the test dates scheduled for the two specimens in order that the age of the concrete in the piles would not significantly exceed 28 days and the compressive strength would be close to 5,000 psi. The forms for the footings and the piles were removed about one week after the casting of the piles. The steel cages of the pile specimens before casting are shown in Figure 3.21 and Figure 3.22. During the concrete placements, six-inch-diameter concrete cylinders were prepared for compression and split-cylinder tests. Compression tests were conducted during the curing of the pile specimens to determine whether the targeted concrete strength of 5,000 psi had been reached. Compression and split-cylinder tests were conducted on the day of each pile test. Table 3.4 shows the average uniaxial compressive strengths and split-cylinder strengths of the concrete in the pile specimens on the day of structural testing. The stress-strain curves for the reinforcing bars were obtained by tension tests. Three bars were tested for each bar size. The average yield and ultimate strengths of the bars are shown in Table 3.5, while the stress-strain curves are shown in Figure 3.23 through Figure 3.25. The material samples for the hoops were cut and straightened prior to the test. As a result of the plastic deformation they experienced from bending, the stress-strain curves from the samples did not show a distinct yield plateau but a gradual transition from the

elastic regime to the inelastic regime (see Figure 3.23). Hence, the yield strength for the hoops is defined with the 0.2% offset strain method.

3.3 Test Results

3.3.1 Overall Behavior of Specimen #1

The lateral load-vs.-lateral drift ratio for Specimen #1 is shown in Figure 3.26. The lateral displacement is obtained by transducer L51 as shown in Figure 3.14. The dashed curve shows the total lateral force applied by the actuator, while the solid curve shows the corrected lateral force, which takes into account the large displacement effect of the post-tensioned rods that exerted the vertical load. The corrected force is obtained by subtracting the horizontal component of the total force exerted by the post-tensioned rods from the actuator force. Figure 3.27 shows the variation of the total force exerted by the rods as the drift of the pile increased. It can be seen that the force varied between 270 and 300 kips while the target value was 280 kips. As shown in Figure 3.26, Specimen #1 had a lateral load capacity of 69 kips, which was reached at a drift ratio of 1.7%. After the maximum lateral resistance had been reached, the peak resistance attained in the subsequent cycle shows a significant decrease as compared to that in the previous. This was caused by the compressive failure of the concrete cover at the compression toe of the pile specimen. The corrected lateral load-vs.-drift curve shows a mild gradual decrease of the lateral resistance with increasing drift due to the *P-Δ* effect. Buckling of Bar 1, which was near the south face of the pile as shown in Figure 3.26, was observed in the 2nd cycle at -8% drift, corresponding to a ductility demand of 9.8. During the 1st cycle at +10%, Bar 4, which was near the north face, buckled. In the 2nd cycle at +10% drift, Bar 1 fractured in tension, resulting a sharp drop in the resistance of the pile. In the subsequent unloading and reloading to the other direction, Bar 4 fractured. Figure 3.28 shows a plot of the moment resistance of the cross-section at an elevation

of 0.5 ft. from the base against the average curvature measured over a distance of 1 ft. from the base of the pile specimen. The calculation of the applied moment includes the lateral load and the *P-Δ* effect of the vertical load. The moment-curvature relation shows a very ductile behavior with little decrease in the moment resistance as the curvature increased till bar fracture occurred.

Flexural cracking in concrete initiated in the 1st force-controlled cycle. The horizontal cracks around the circumference of the pile propagated from cycle to cycle quite rapidly. At 1% drift, corresponding to a ductility demand of 1.22, flexural cracks developed over a height of 5 ft. with more or less uniform spacing of 9 to 12 in. as shown in Figure 3.29. At a drift of 2%, concrete cover near the base of the pile started to show compressive damage with visible vertical cracks, as shown in Figure 3.30. At this drift level, widely opened flexural cracks were observed. Figure 3.31 shows the spalling of the concrete cover near the base of the pile specimen at 3% drift. In this cycle, a peak load of 10 kips was reached, which is lower than that in the previous cycle of 2% drift as shown in Figure 3.26. This was probably caused by the spalling of the concrete as noted above. At this drift level, the width of the flexural cracks was more than ¼ in. as shown in Figure 3.31.

As shown in Figure 3.32, at 6% drift, concrete spalling was deeper into the pile and extended from the base of the pile up to a height of 1.5 ft. Moreover, a longitudinal reinforcing bar and part of the horizontal hoops were exposed due to the concrete spalling. In the 2nd cycle of -8% drift, corresponding to a ductility demand of 9.8, Bar 1 at the south face buckled, as shown in Figure 3.33. During the 1st cycle of -10% drift, the buckling of Bar 1 became quite severe, as shown in Figure 3.34a. Figure 3.34b shows the bending deformation observed in Bar 4 at the north face during the 1st cycle of +10% drift. Both bars bent outward between two adjacent hoops. Concrete spalling extended up to a height of 2 ft. from the base of the specimen exposing the longitudinal bars and the hoops. Parts of the confined core were crushed as shown in Figure 3.34.

During the 2nd cycle of +10% drift, buckled Bar 1 at the south face fractured in tension (Figure 3.35a), while Bar 4 at the north face had severe buckling (Figure 3.35b). During the load reversal, buckled Bar 4 at the north face also fractured in tension as shown in Figure 3.36. At that point, the test was terminated and the top of the specimen was brought back to zero lateral displacement. A drift of 10% corresponds to a lateral displacement of 12 in. Figure 3.37 shows pictures of Specimen #1 at the end of the test, zooming-in on the two bars that fractured, with one at each face of the pile, and the severe crushing of the concrete. The section at 10 in. above the base of the pile had the most severe damage.

3.3.2 Overall Behavior of Specimen #2

Figure 3.38 shows the lateral load-vs.-drift curves of Specimen #2, which had 10 No. 9 longitudinal bars. The corrected lateral load-vs.-drift ratio curve is derived in the same way as that for Specimen #1. Figure 3.39 shows the variation of the total force exerted by the post-tensioned rods with drift. Pile Specimen #2 had a maximum load capacity of 78 kips, which was reached at a drift of 1.6%. The drop of the load resistance of Specimen #2 due to the *P-Δ* effect is clearly shown.

During the 1st cycle of +8% drift, corresponding to a ductility demand of 9.9, Bar 4 placed at the north face started to buckle. During the load reversal at -8% drift, Bar 1 at the south face buckled. In the 2nd cycle of +8% drift, Bar 4 at the north face had severe buckling. During the reversal to -8% drift, Bar 2 at the south face also buckled, while the bending deformation of Bar 1 was quite large. During the 1st cycle of +10% drift, Bar 1 fractured in tension, while Bars 3, 4 and 5, which were in compression, buckled. In the following displacement reversal, Bars 4 and 5 at the north face fractured in tension, resulting in sharp drops in the lateral load resistance as shown in Figure 3.38. Figure 3.40 shows the moment resistance plotted against the average curvature measured over a distance of 1 ft. from the base of the pile specimen. Similar to that for

Specimen #1, the moment-curvature relation shows a very ductile behavior till bar fracture occurred.

For Specimen #2, flexural cracking in concrete initiated in the 2nd force-controlled cycle, one cycle later as compared to Specimen #1. At 1% drift, corresponding to a ductility demand of 1.24, flexural cracks spaced at 6 to 9 in. developed over a height of 6 ft., as shown in Figure 3.41. Figure 3.42 shows the bottom portion of Specimen #2 at the drift of 2% where the concrete cover had multiple vertical cracks indicating the initiation of toe crushing. The flexural cracks in Specimen #2 were more closely spaced than those in Specimen #1, and their spreading from cycle to cycle was slower.

As shown in Figure 3.43, at 3% drift, the spalling of the concrete cover extended up to 2.5 ft. from the base. In this cycle, the peak load had a significant drop as compared to that in the previous cycle, as Figure 3.38 shows. The flexural cracks developed in the pile were quite wide with a width of about 0.25 in. At 4% drift, the extent of the spalling of the concrete cover remained at 2.5 ft. as shown in Figure 3.44. As shown in Figure 3.45, at 6% drift, the spalling of the concrete cover near the base was severe, exposing parts of the transverse and longitudinal reinforcement on the south and north faces. The spalling of the concrete cover extended up to a height of about 3 ft. from the base of the pile, which is more extensive than that in Specimen #1 at the same drift level.

During the 1st cycle of +8% drift, Bar 4 at the north face had some bending deformation, as shown in Figure 3.46b. During the subsequent displacement reversal at -8% drift, Bar 1 at the south face buckled, as shown in Figure 3.46a. Figure 3.47a shows buckled Bars 1 and 6 at the south face of Specimen #2 during the 2nd cycle of -8% drift. Figure 3.47b shows the north face of Specimen #2 where Bar 4 bent in a plane that was tangential to the circumference of the pile. Crushing of the concrete core was also observed around the region where the longitudinal bars buckled.

At the beginning of the 1st cycle of +10% drift, buckled Bar 1 at the south face fractured in tension, while Bars 4 and 5 at the north face, which were in compression, had severe buckling, as shown in Figure 3.48. In the following displacement reversal at -10% drift, buckled Bars 4 and 5 at the north face fractured in tension as shown in Figure 3.49. At that point, with the fracture of Bars 1, 4, 5, and the buckling of Bars 2 and 6, the test was terminated. The maximum drift of 8% reached before the fracture of the longitudinal bars corresponds to a lateral displacement of 9.3 in. Figure 3.50 shows pictures of Specimen #2 at the end of the test. The section at 12 in. above the base of Specimen #2 had the most severe crushing of the concrete core.

3.3.3 Comparison of Specimens

3.3.3.1 Load-vs.-Displacement Response

The lateral load-vs.-drift behaviors of the two specimens are very similar. The two specimens had the same dimensions, almost the same quantities of reinforcement, and similar material properties. The lateral load capacity of Specimen #2 was 78 kips, which is 9 kips higher than that of Specimen #1. The higher load capacity of Specimen #2 can be attributed to the slightly higher quantity of the longitudinal reinforcement and also to a higher proportion of the longitudinal bars in tension when the section was subjected to bending.

The normalized lateral force-vs.-drift curves for Specimens #1 and #2 are compared in Figure 3.51. It can be seen that Specimens #1 and #2 had similar responses up to 8% drift. After that, Specimen #2 had load degradation started earlier than Specimen #1 due to the fracture of longitudinal bars. For Specimen #2, the fracture of longitudinal bars occurred during the 1st cycle of 10% drift, while for Specimen #1, bar fracture occurred in the 2nd cycle of 10% drift. This is because bar fracture was largely caused by the severe bending strain induced by buckling and

Specimen #1 had No. 11 bars, which had a better resistance against buckling than the No. 9 bars in Specimen #2 given the same hoop spacing in the two specimens.

For both specimens, the gradual decrease of the lateral load resistance with increasing drift was mainly caused by the *P-Δ* effect. The above conclusion is supported by the fact that this gradual drop in resistance is not observed in the moment-curvature relations measured near the base of the two specimens, as shown in Figure 3.52. As shown, the moment resistances were more or less maintained with very mild decrease as the curvatures increased until the buckled bars fractured in tension. Specimens #1 and #2 had the same quantities of confinement steel, which were No. 6 hoops spaced at 5.75 in. on center, complying with the Caltrans BDS (Caltrans 2004) and the AASHTO LRFD BDS (AASHTO 2014). With this confinement level, the pile sections showed a very ductile behavior.

Moreover, Figure 3.52 shows that Specimen #1 developed a larger curvature near the base than Specimen #2, while the drift levels reached in the two specimens are not so different. This is consistent with the observation that the plastic deformation (i.e., the bar yielding and concrete crushing) observed in Specimen #1 was more localized at the bottom of the pile than that in Specimen #2, resulting in a higher curvature demand in Specimen #1.

3.3.3.2 Flexural Crack Pattern

The tests have shown a clear influence of the spacing and the size of the longitudinal reinforcement on the spacing and the width of the horizontal flexural cracks, which is a well-known fact. As shown in Figure 3.29 and Figure 3.41, flexural cracks were more widely spaced in Specimen #1 than in Specimen #2. Distances of flexural cracks in Specimen #1 were 6 to 9 in., while those in Specimen #2 were 9 to 12 in. Moreover, the width of the flexural cracks in Specimen #1 was also larger as shown in Figure 3.31 and Figure 3.43.

3.3.3.3 Curvature Distribution

Curvature distributions along the height of Specimens #1 and #2 are shown in Figure 3.53 and Figure 3.54, respectively. The curvature was calculated with the readings from the vertical transducers mounted on the pile specimens, namely, L01 to L12 on the east face and L29 to L40 on the west face of each pile specimen, as shown in Figure 3.14 and Figure 3.15. As shown, the curvature distributions are consistent with the extent of concrete spalling observed in the two specimens (see Figure 3.37 and Figure 3.50). Specimen #1 had both the concrete spalling and plastic curvature more localized near the base, while those of Specimen #2 were distributed along a greater distance. As noted before, Specimen #1 had also the horizontal flexural cracks spaced farther apart due to the larger spacing and larger diameter of the longitudinal bars. Whether the difference in curvature distributions in the two specimens is related to the size and spacing of the bars or crack spacing requires further studies. However, this could be related to the higher tensile stresses developed in the longitudinal bars in Specimen #2 as discussed below.

3.3.3.4 Strains in Longitudinal Reinforcement

Figure 3.55 through Figure 3.60 show the strains in the longitudinal bars of Specimens #1 and #2 at different drift levels. At large drifts, some of the bars buckled at an elevation of 12 in. from the base. Within this region, two gages were mounted at each location on the diagonally opposite sides of a bar. To take out the influence of bar bending, values obtained from these pairs of gages are averaged.

Figure 3.55 shows that at a drift of 1%, the maximum tensile strain in the longitudinal bars at the base of Specimen #1 slightly exceeded the yield strain of 0.0023, while Figure 3.56 shows that for Specimen #2, the maximum tensile strain in the bars slightly exceeded 0.01 at +1% drift. Figure 3.57 and Figure 3.58 show the strains in the bars in Specimens #1 and #2 at a drift of 4%. The maximum tensile strains measured were between 0.02 and 0.04. For drift ratios between

6% and 8%, many of the gages were damaged and the maximum tensile strains measured were between 0.04 and 0.05. The higher tensile strains attained in Specimen #2 can be attributed to the smaller diameter of the longitudinal bars, which had less bond demand and therefore less slip and more concentrated plastic deformation in the vicinity of a crack. The higher tensile strains resulted in higher tensile stresses in the longitudinal bars, which could have led to more a more uniform curvature distribution in Specimen #2 as noted in the previous section. Furthermore, the No. 9 bars in Specimen #2 had higher yield and tensile strengths that the No. 11 bars in Specimen #1 (see Table 3.5).

3.3.3.5 Extent of Plastic Zone

The plastic zone is defined as the region in which the tensile strains in the longitudinal bars reached or exceeded the yield strain of 0.0023. Figure 3.57 shows that at a drift of 4%, the plastic zone of Specimen #1 covered a distance of 3 ft. from the base of the pile. This is about 1.3 times the pile diameter. Figure 3.58 shows that at 4% drift, the tensile strains measured at 3 ft. from the base of Specimen #2 exceeded the yield strain. In fact, the tensile strain in the bar closest to the north face (Bar 4) at this height reached 0.007. By extrapolating the strain in this bar, it can be estimated that the plastic zone of Specimen #2 was about 3.5 ft., which is 1.5 times the pile diameter. As shown in Figure 3.59 and Figure 3.60, the lengths of the plastic zones of both specimens did not have significant changes at 8% drift.

Specimen #1 had its concrete cover spalling occurring over a distance of 2 ft. from the base as shown in Figure 3.37, while Specimen #2 had the concrete spalling occurring over a distance of 3 ft. as shown in Figure 3.50. These distances are comparable to the extent of plastic deformation in the longitudinal reinforcement.

3.3.3.6 Plastic Strain Penetration

Figure 3.55 through Figure 3.60 also show the tensile strains in the longitudinal bars inside the footings of the pile specimens up to a depth of 2.25 ft. Figure 3.55 shows that at 1% drift, the tensile strains in the No. 11 longitudinal bars in Specimen #1 at a distance of 1.25 ft. (11 times the bar diameter, d_b) below the top face of the footing were lower than the yield strain of 0.0023. As shown in Figure 3.57b, at -4% drift, one bar (Bar 5) in Specimen #1 yielded reaching a tensile strain of 0.0042 at the distance of 1.25 ft. below the top face of the footing. Figure 3.59 shows that the plastic strain penetration in the No. 11 bars exceeded 1.25 ft. ($11\,d_b$) but was less than 2.25 ft. ($19\,d_b$) at 8% drift.

Figure 3.58 shows that the tensile strains in the No. 9 longitudinal bars in Specimen #2 were below the yield strain at 4% drift. At -8% drift, the tensile strain in one bar (Bar 5) at a depth of 1.25 ft. exceeded the yield strain, as shown in Figure 3.60b. Hence, the plastic strain penetration was deeper than 1.25 ft. ($13\,d_b$). The generally lower plastic strain penetration observed in this specimen as compared to that in Specimen #1 is consistent with the higher tensile strains observed at the base of this pile specimen. As discussed before, this was because of the lower demand on the bond stress for the smaller diameter bars in Specimen #2.

3.3.3.7 Strains in Lateral Reinforcement

Figure 3.61 and Figure 3.62 show the tensile strains in the hoops in Specimens #1 and #2, respectively. The positions of the strain gages are shown in Figure 3.19. As shown, the hoop strains remained small for both specimens, with some gages measuring tensile strains higher than the yield value when the drift exceeded 6%. Figure 3.61 shows that one hoop in Specimen #2 had a tensile strain of 0.006 at 8% drift. The strain level measured is consistent with the fact that no hoop fracture was observed in the tests.

3.4 Summary and Conclusions

3.4.1 Ductility under Lateral Loading

The test results have shown that the large spacing of the longitudinal reinforcement exceeding 8 in. in Specimen #1 had no detrimental effect on the ductility and the lateral load-vs.-lateral displacement behavior of the pile. The lateral load-vs.-lateral displacement curves of Specimens #1 and #2 are almost identical up to the drift level of 8%. Nevertheless, Specimen #2 exhibited significant load degradation in the 1st cycle of 10% drift, caused by the fracture of the longitudinal bars, while that for Specimen #1 occurred in the 2nd cycle of 10% drift. Hence, Specimen #1 was slightly more ductile than Specimen #2 even though its longitudinal bars were spaced farther apart. This difference is largely attributed to the fact that the longitudinal bars of Specimen #1 had a larger diameter and were therefore more resistant to buckling after the spalling of the cover concrete. Bar buckling was responsible for the fracture of the longitudinal bars. The lateral load resistance of the two pile specimens exhibited a mild degradation after passing a drift ratio of 1% due to the P-Δ effect of the vertical load. However, both specimens showed very ductile behavior with no noticeable strength degradation in the moment-vs.-curvature relations till the fracture of longitudinal bars occurred.

Both specimens had severe crushing in the concrete core adjacent to the steel cage prior to bar buckling. Crushing was most severe at the section 10 in. above the base for both pile specimens. Specimen #1 had plastic deformation more concentrated near the base as compared to Specimen #2. This led to a higher curvature measured near the base of Specimen #1 at comparable drift levels. Specimen #1 also had a slightly shorter plastic zone, which is defined as the region in which the tensile strains in the longitudinal bars reached or exceeded the yield strain, and had smaller plastic strains in the longitudinal bars. The cover concrete in Specimen #1

spalled over a distance of 2 ft. from the base, while that in Specimen #2 spalled over a distance of 3 ft.

3.4.2 Flexural Crack Pattern

Specimen #1 had flexural cracks spaced farther apart and larger crack widths than Specimen #2. The distances of flexural cracks in Specimen #1 were 6 to 9 in., while those in Specimen #2 were 9 to 12 in. At 1% drift, at which the longitudinal bars in the piles started to yield, the flexural cracks in Specimen #1 had propagated around half of the circumference of the pile, while those in Specimen #2 did not propagate as far. However, for both specimens, the crack widths remained small at this drift level.

3.4.3 Conclusions

The spacing of longitudinal bars in circular RC members can be larger than 8 in. without jeopardizing the structural performance of the member. This spacing does not seem to affect the effectiveness of the confinement on the concrete core. However, the diameter of longitudinal bars can affect the ductility of a laterally loaded member. Larger-diameter bars are more resistant to bucking for the same spacing of the transverse reinforcement, and can therefore lead to more ductile flexural behavior. The limited experimental data also show that the spacing and the size of longitudinal bars may affect the extent of the plastic zone of a laterally loaded member, in which flexural cracking, concrete spalling, and the yielding of the longitudinal bars occur. The specimen with larger-diameter longitudinal bars and larger bar spacing had more concentrated plastic deformation near the base. The underlying reason for this needs to be further studied. However, one possible explanation is that smaller-diameter bars have a lower bond stress demand and therefore less bond slip. This leads to higher strains and therefore higher stresses in the bars in the vicinity of flexural cracks. The higher bar stresses can lead to a more uniform distribution of pile

curvature. Finally, the spacing and the size of longitudinal bars have a clear influence on the spacing and the width of flexural cracks, which is a well-known fact.

3.5 Acknowledgement of Publication

This chapter, in full, is a reprint of the material as it appears in the report submitted to the California Department of Transportation in 2014, Papadopoulos, V., Shing, P. B., under the title "Influence of the Spacing of Longitudinal Reinforcement on the Performance of Laterally Loaded CIDH Piles – Experimental Investigation". The dissertation author was the primary investigator and author of this report.

Table 3.1 - Reinforcement details of Specimens #1 and #2

Spec.	Pile Diameter D (in.)	Diameter of Confined Core* D_c (in.)	Long. Steel Ratio ρ_l	Long. Bars	Transverse Steel Ratio ρ_t	Angular Spacing of Long. Bars θ_l (deg.)	Lineal Spacing of Long. Bars s_l (in.)
1	28	24	0.0152	6 No. 11	0.0128	60	11.04
2	28	24	0.0162	10 No. 9	0.0128	36	6.75

*Out-to-out diameter of hoops

Table 3.2 – Concrete Mix Design

Specified compressive strength = 4.5 ksi		
Material	Quantity (lbs/yd^3)	Proportion of Aggregate (%)
Cement	572.00	-
Flyash	143.00	-
Course aggregate	1455.00	51.88
Sand	1386.00	48.12
Water (w/c)	38.50 (0.45)	-
WRDA-64 (admixture)	18.00	-
ADVAHRWR (admixture)	43.00	-
Air content (%)	2.00	-

Table 3.3 - Loading protocol for pile specimens

Cycle No.	Load/Displ. Amplitude (Same for both specimens)	Specimen #1 (Δ_y=0.98") Actual Ductility Demand	Specimen #2 (Δ_y=0.97") Actual Ductility Demand	Comment
1	±15 kips	-	-	25% of theoretical first yield
2	±30 kips	-	-	50% of theoretical first yield
3	±45 kips	-	-	75% of theoretical first yield
4	±60 kips	-	-	100% of theoretical first yield
5a, 5b	±1.2"	1.22	1.24	1% drift
6a, 6b	±2.4"	2.45	2.47	2% drift
7a, 7b	±3.6"	3.67	3.71	3% drift
8a, 8b	±4.8"	4.90	4.95	4% drift
9a, 9b	±7.2"	7.35	7.42	6% drift
10a, 10b	±9.6"	9.80	9.90	8% drift
11a, 11b	±12.0"	12.2	12.4	10% drift

Table 3.4 - Uniaxial compressive strengths of concrete

Concrete	Date cast	Date tested	Days after casting	f_c' (ksi)	f_t' (ksi)[1]
Spec #1 pile	June 12, 2012	July 12, 2012	30	4.9	0.40
Spec #1 footing	March 8, 2012	July 12, 2012	157	7.4	-
Spec #2 pile	June 12, 2012	July 17, 2012	35	5.2	0.37
Spec #2 footing	March 8, 2012	July 17, 2012	162	7.5	-

[1]Split-cylinder strength

Table 3.5 – Reinforcement properties

	No. 6 (hoops)	No. 9 (long.)	No. 11 (long.)
Yield stress(ksi)	69.7[1]	67	64
Ultimate stress (ksi)	95	96	90

[1]Stress at 0.002 plastic strain.

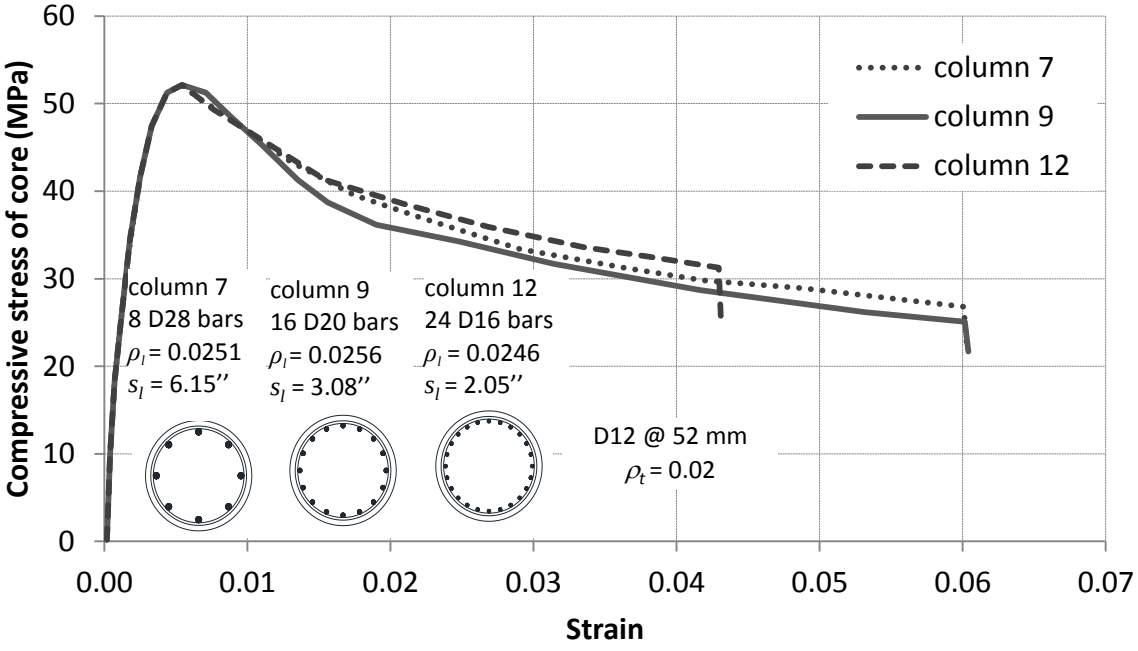

Figure 3.1 – Effect of spacing of longitudinal bars on circular columns (Mander et al. 1988b)

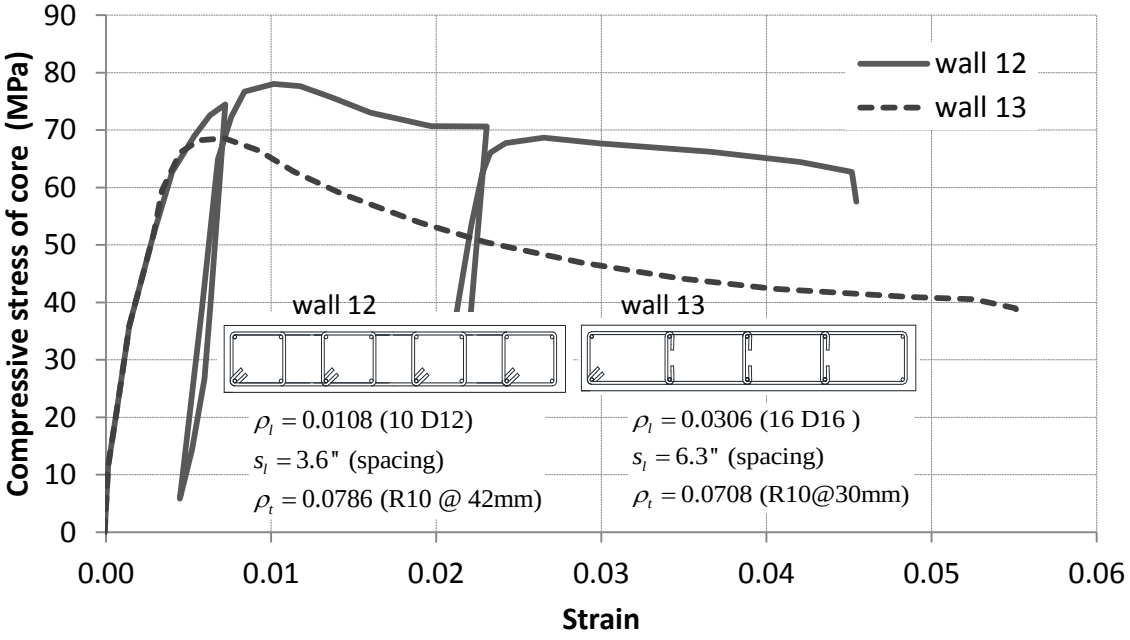

Figure 3.2 - Effect of spacing of longitudinal bars on rectangular sections (Mander et al. 1988b)

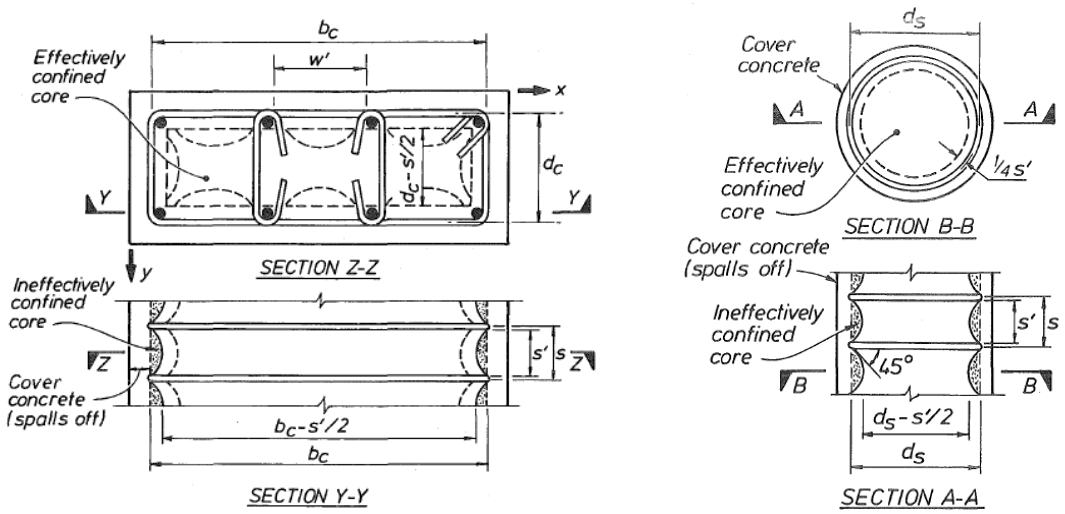

(a) Rectangular column (b) Circular column

Figure 3.3 – Arching action of confining reinforcement (Mander et al. 1988a)

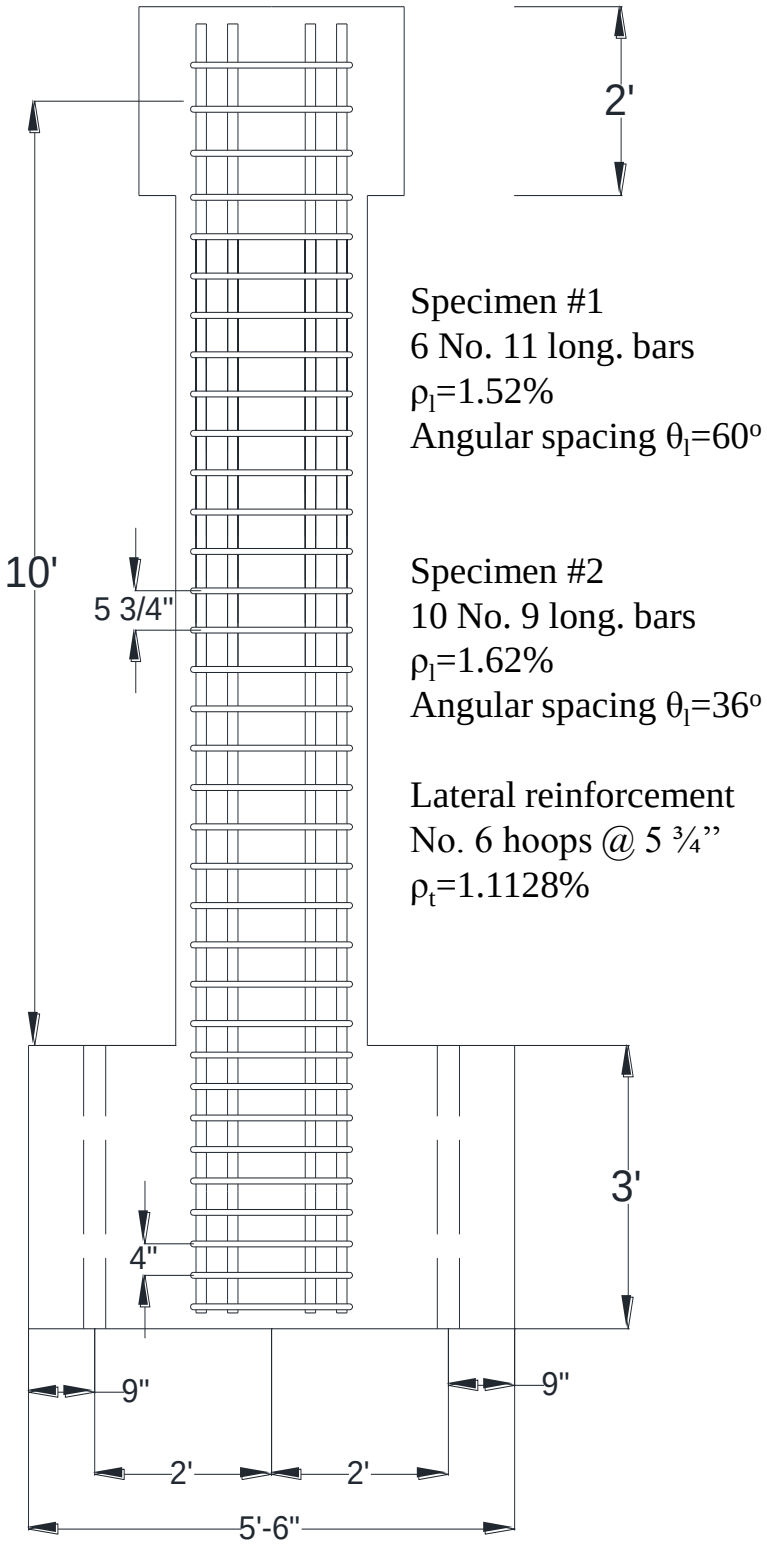

Figure 3.4 - Elevation view of Specimens #1 and #2

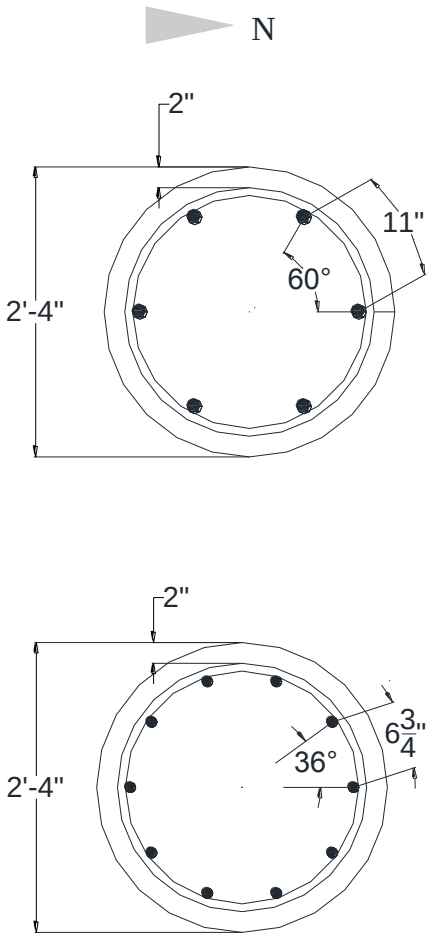

Figure 3.5 – Cross-sections of Specimens #1 and #2

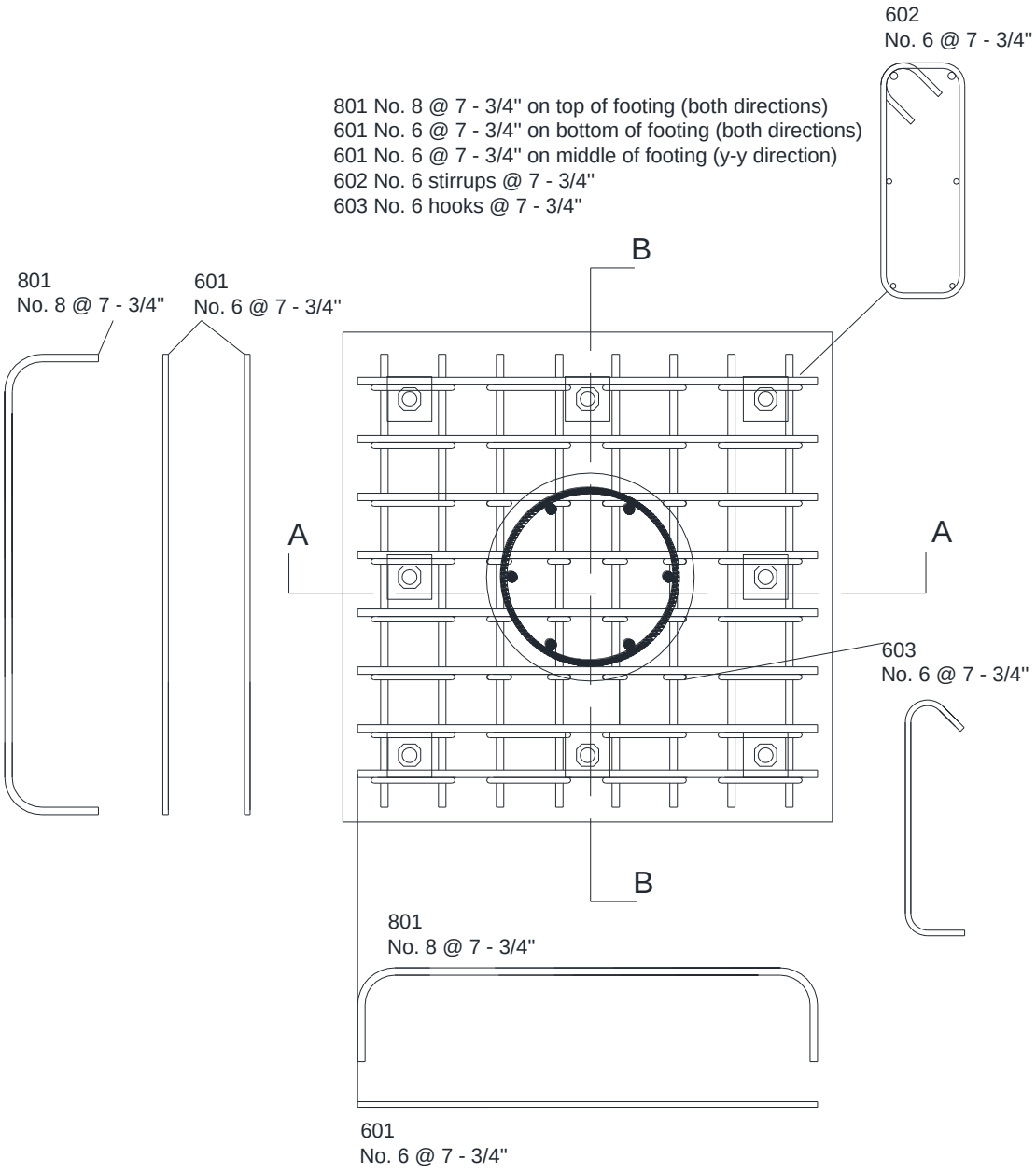

Figure 3.6- Plan view of footing details

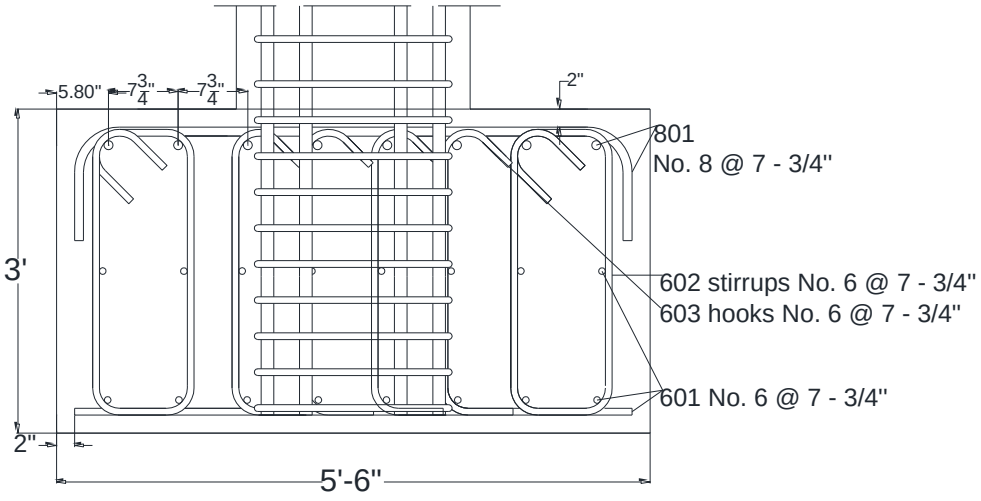

Section A-A

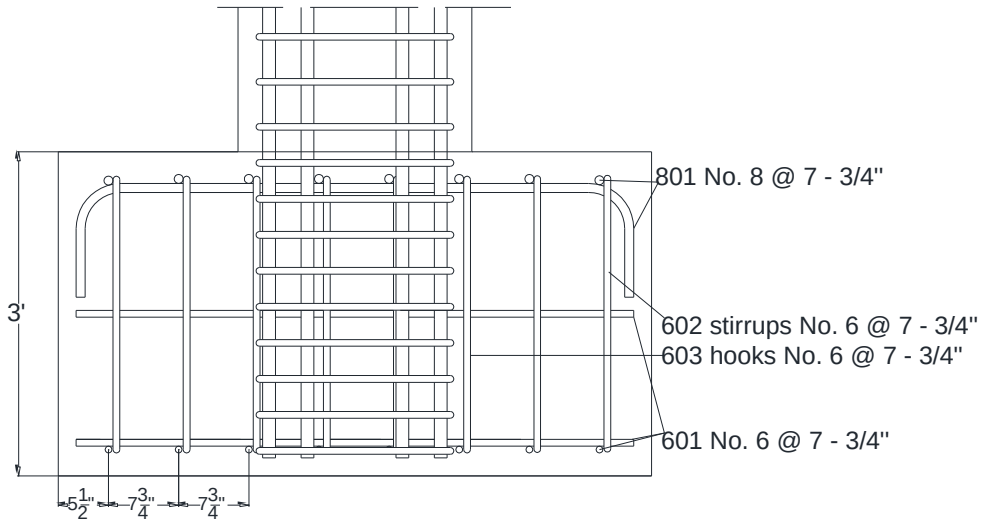

Section B-B

Figure 3.7 – Elevation view of footing details (see Figure 3.6 for section locations)

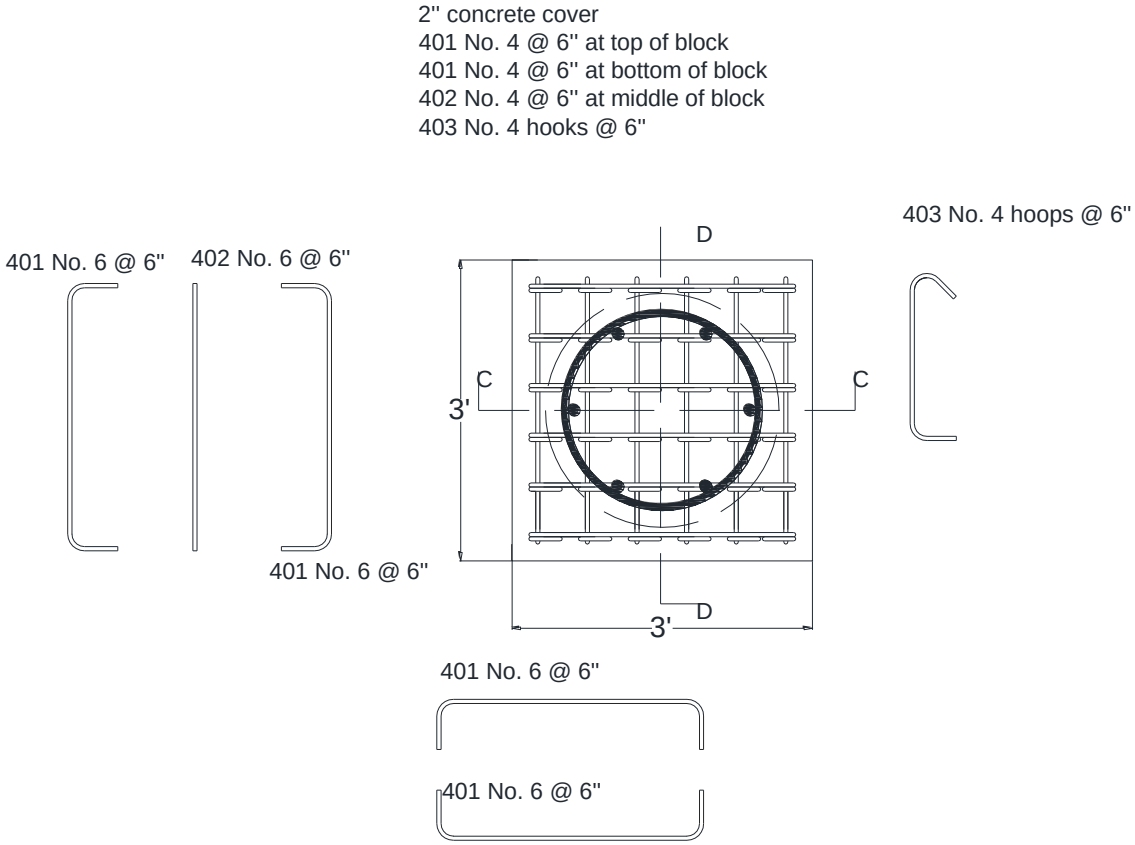

Figure 3.8 – Plan View of cap details

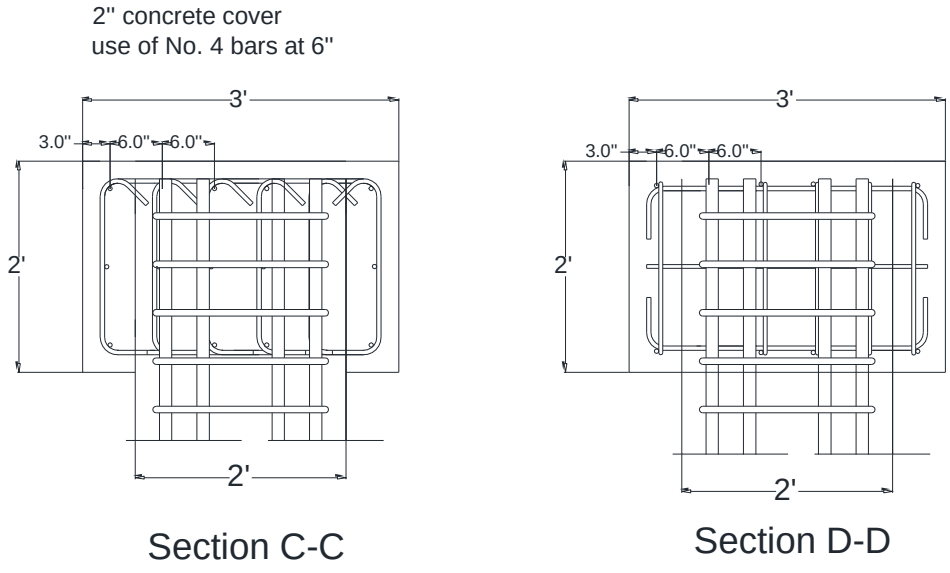

Figure 3.9 – Elevation view of cap details (see Figure 3.8 for section locations)

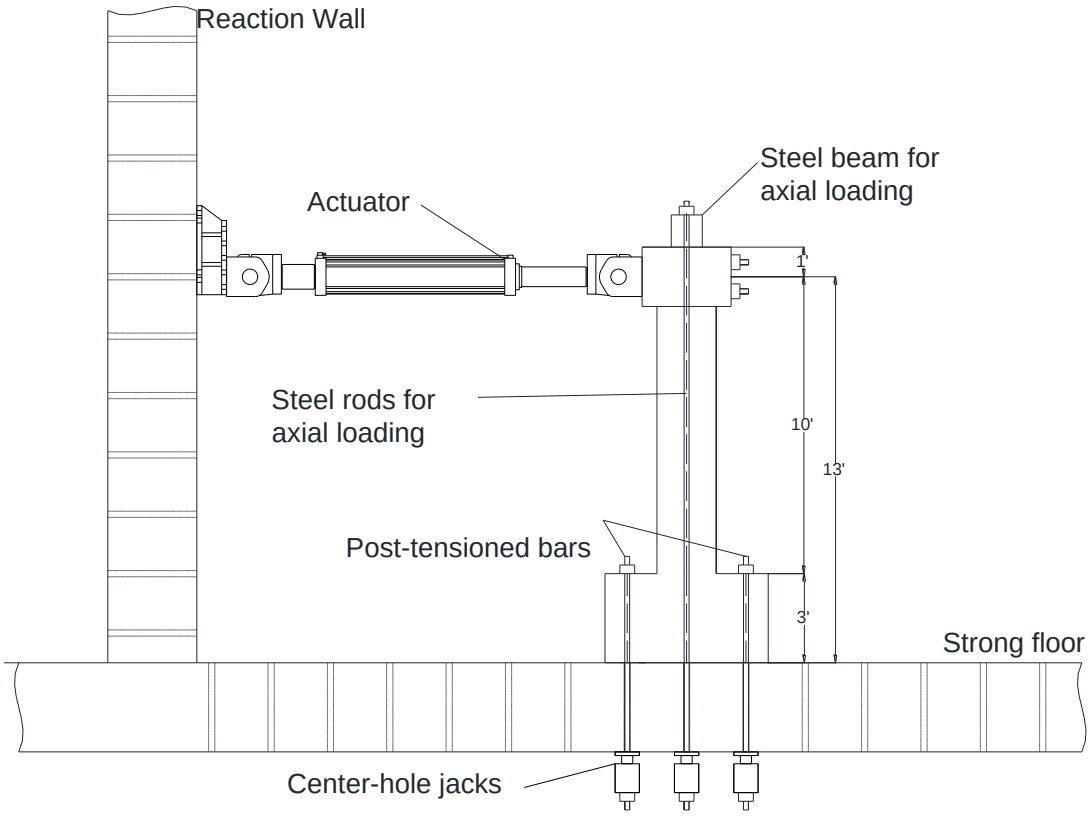

Figure 3.10 - Elevation view of test setup

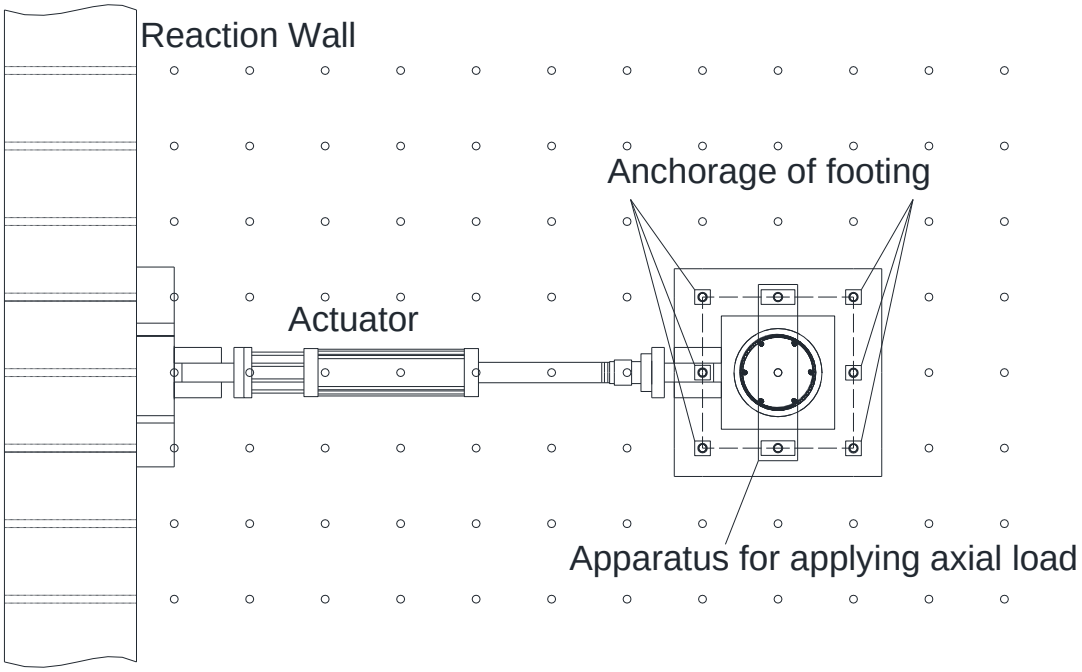

Figure 3.11 - Plan view of test setup

Figure 3.12 Picture of Specimen #1 test setup

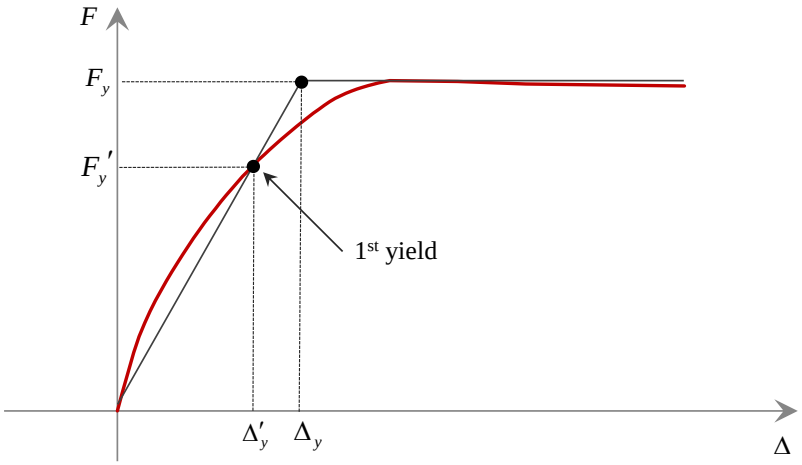

Figure 3.13 – Equivalent elastic-perfectly plastic system

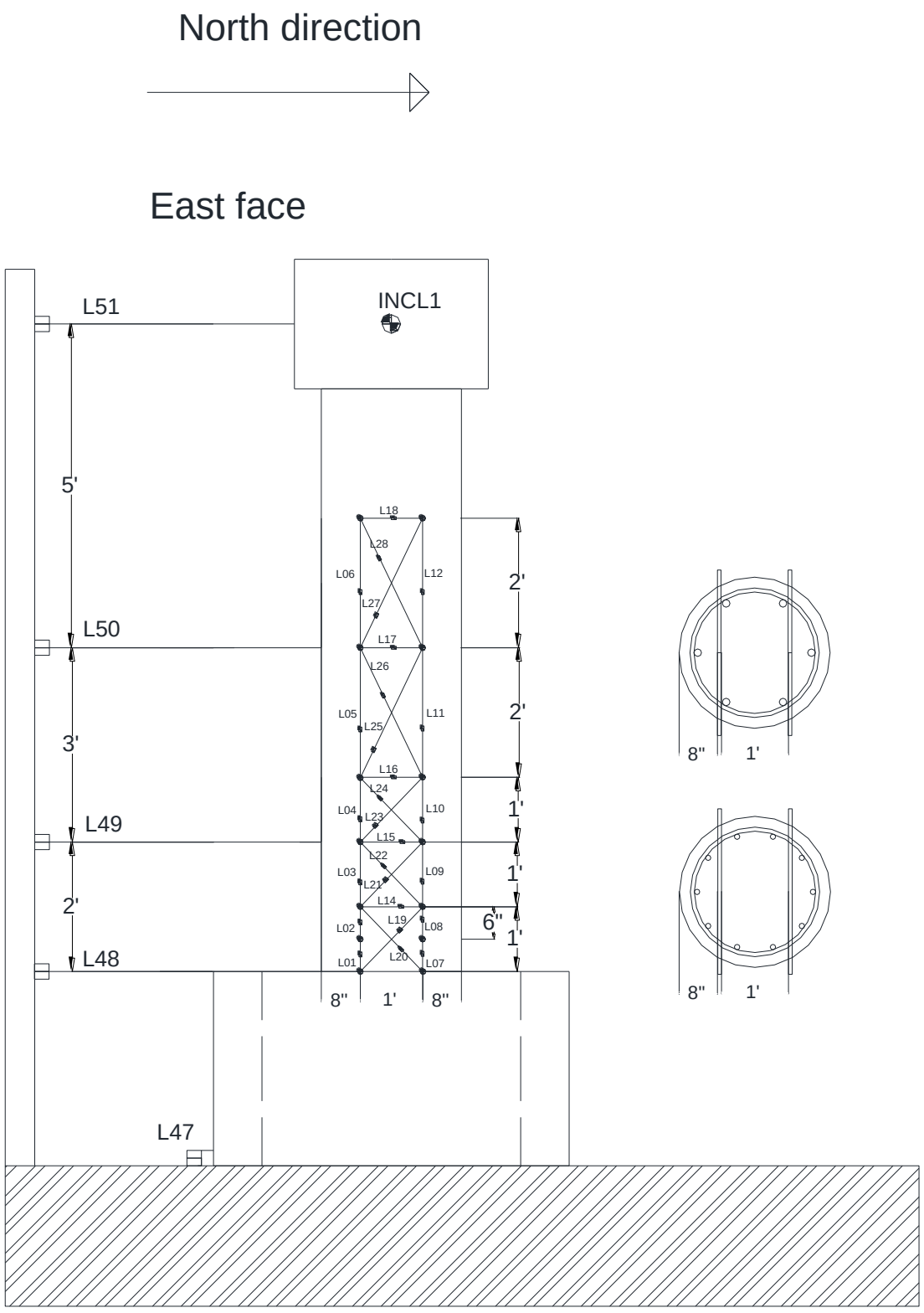

Figure 3.14 - Elevation view of displacement transducers (East face)

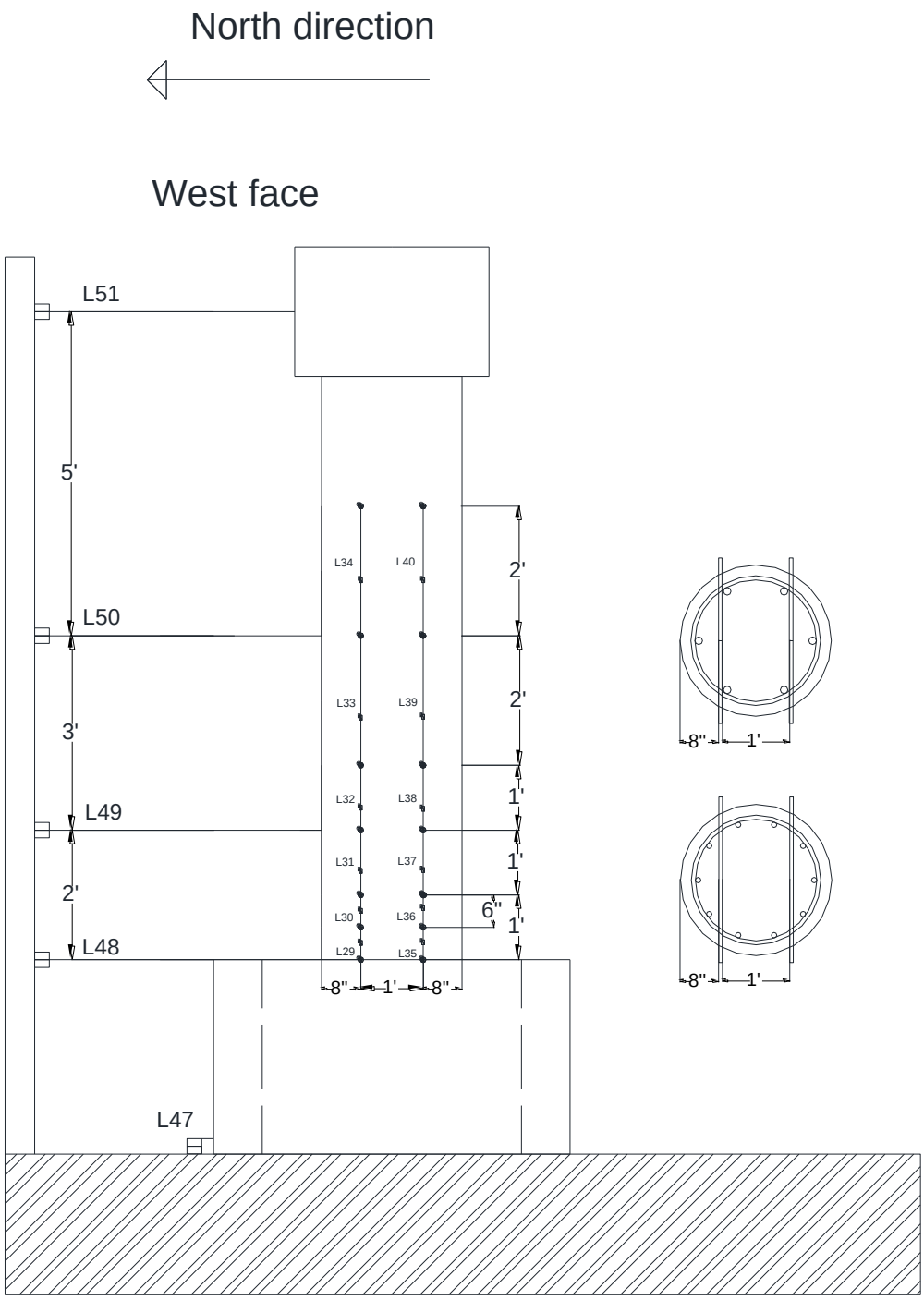

Figure 3.15 - Elevation view of displacement transducers (West face)

Figure 3.16 - Picture of displacement transducers mounted on west face of Specimen #1

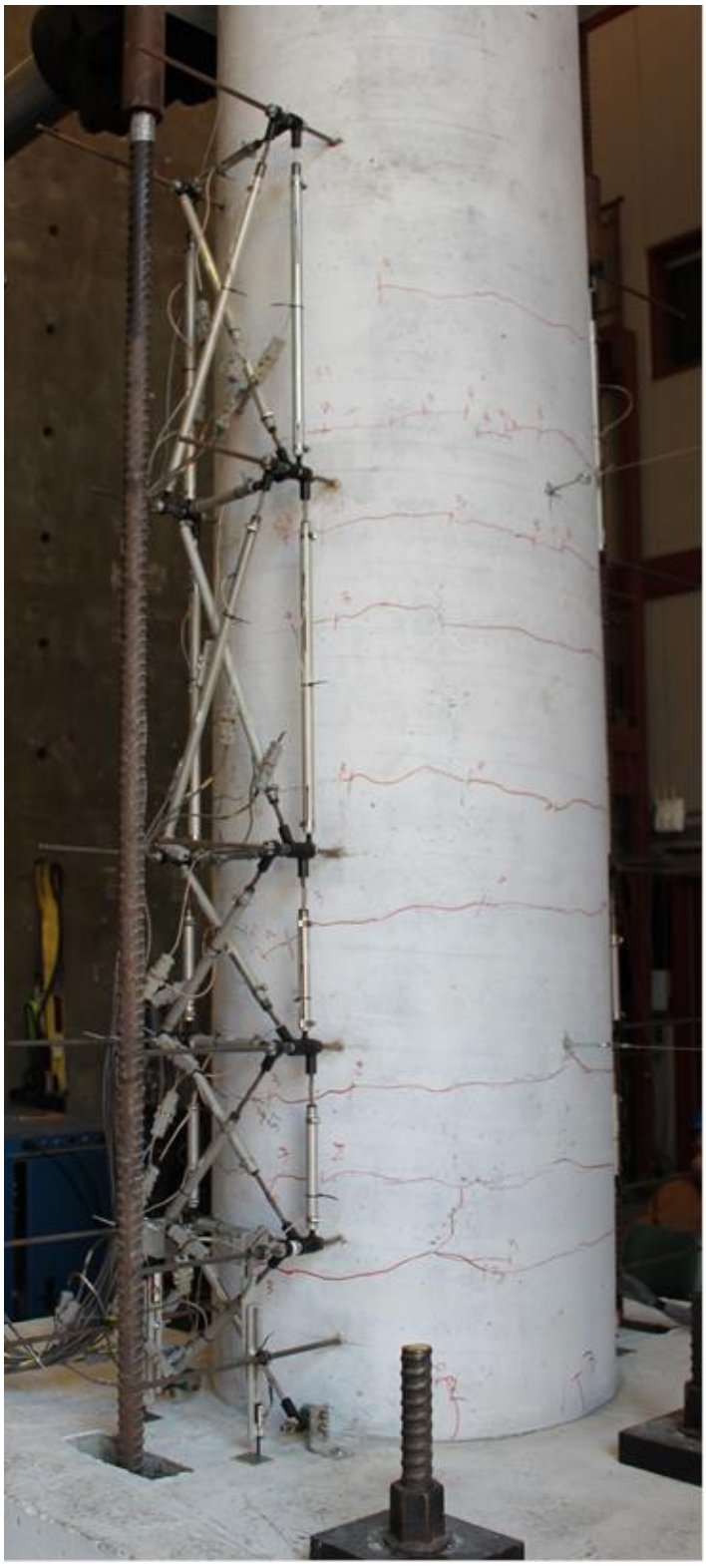

Figure 3.17 – Picture of displacement transducers mounted on east face of Specimen #2

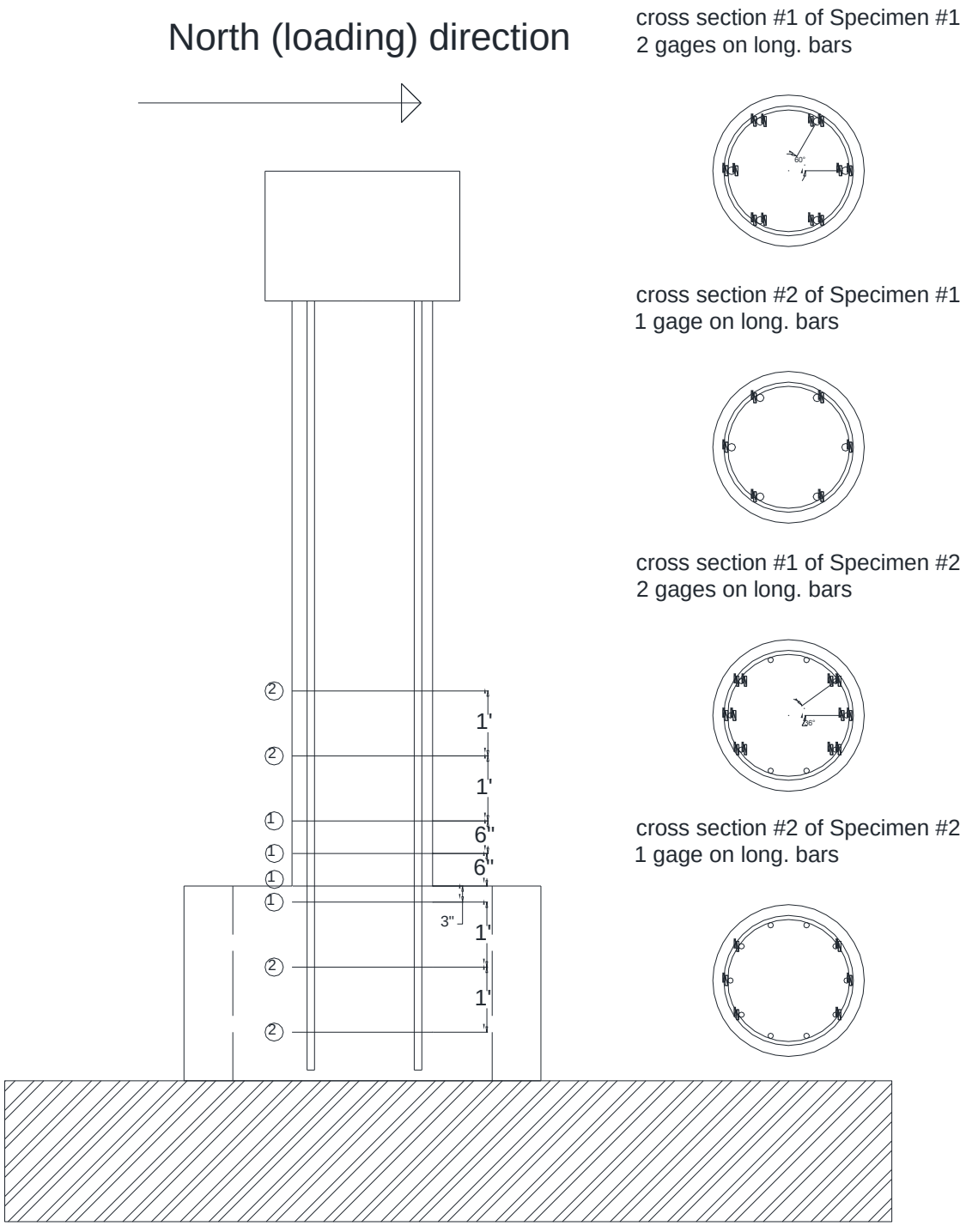

Figure 3.18 - Strain gages on longitudinal bars of Specimens #1 and #2

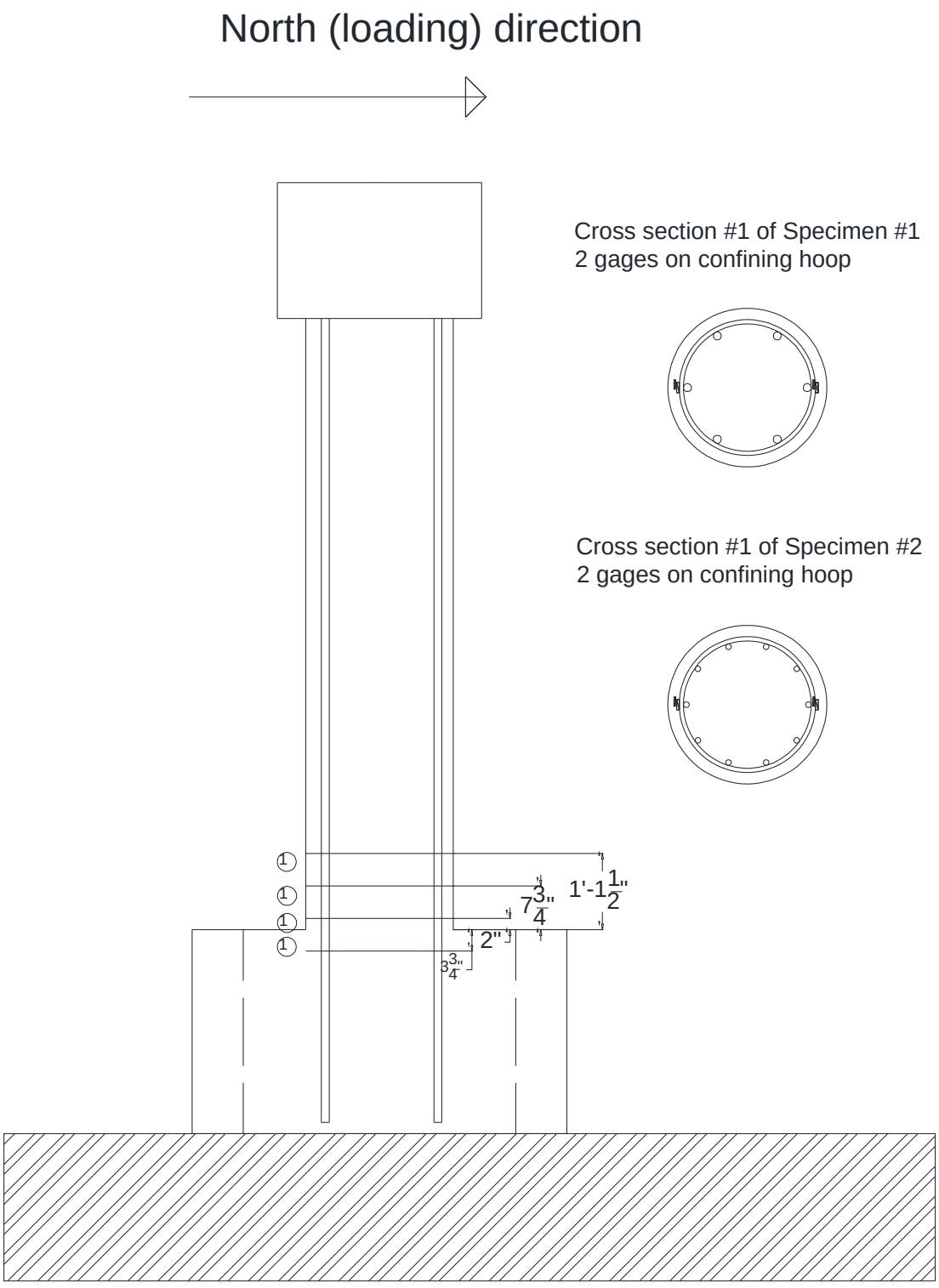

Figure 3.19 - Strain gages on steel hoops of Specimens #1 and #2

Figure 3.20 – Picture of strain gages on reinforcing bars of Specimen #1

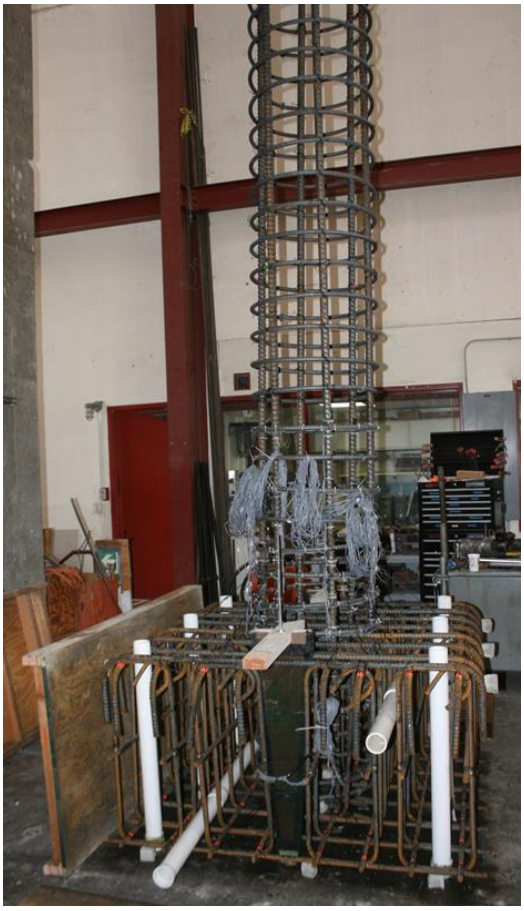

Figure 3.21 - Reinforcement cage for Specimen #1

Figure 3.22 – Assembled forms for casting of footings

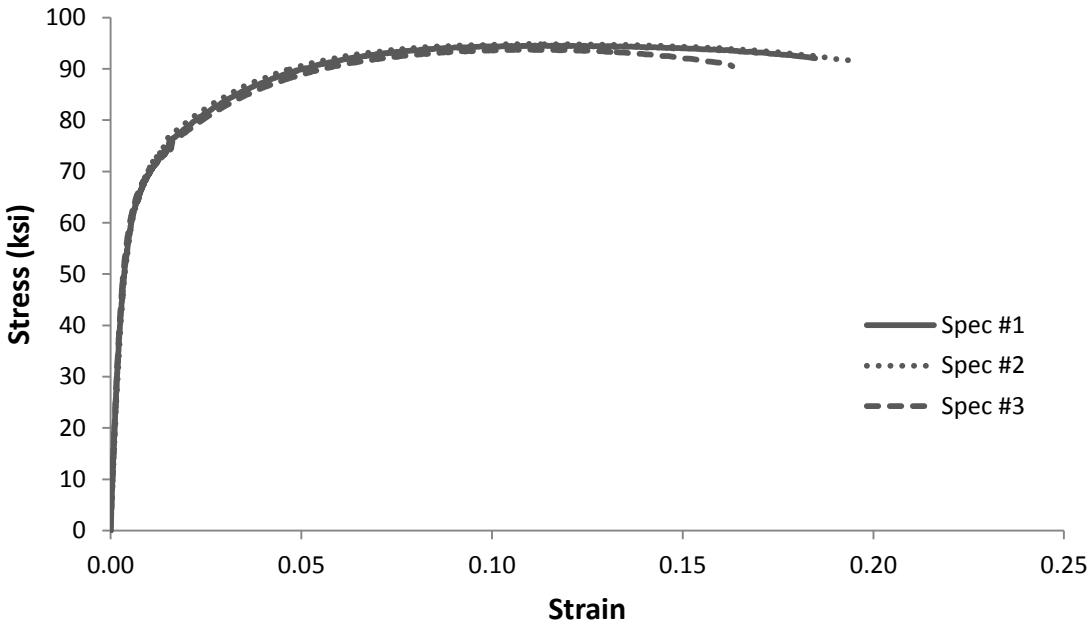

Figure 3.23 – Stress – strain curves for No. 6 hoop reinforcement

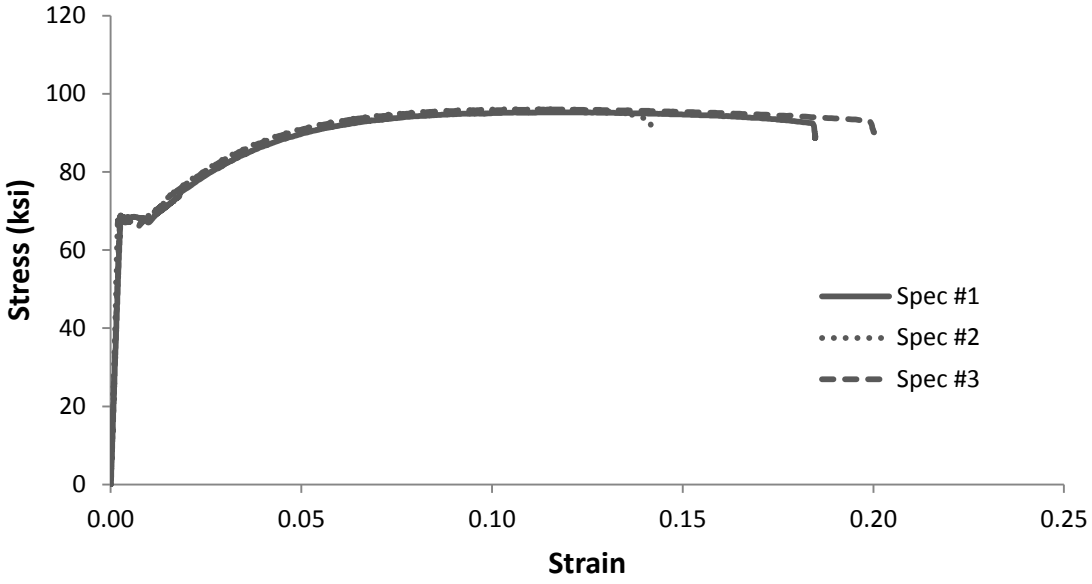

Figure 3.24 - Stress – strain curves for No. 9 longitudinal reinforcement

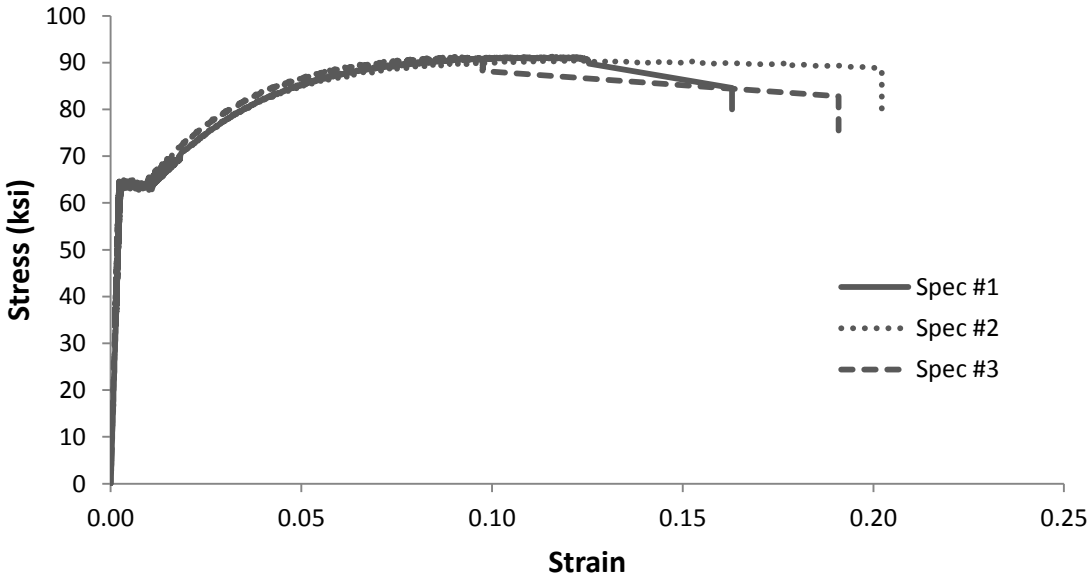

Figure 3.25 – Stress - strain curves for No. 11 longitudinal reinforcement

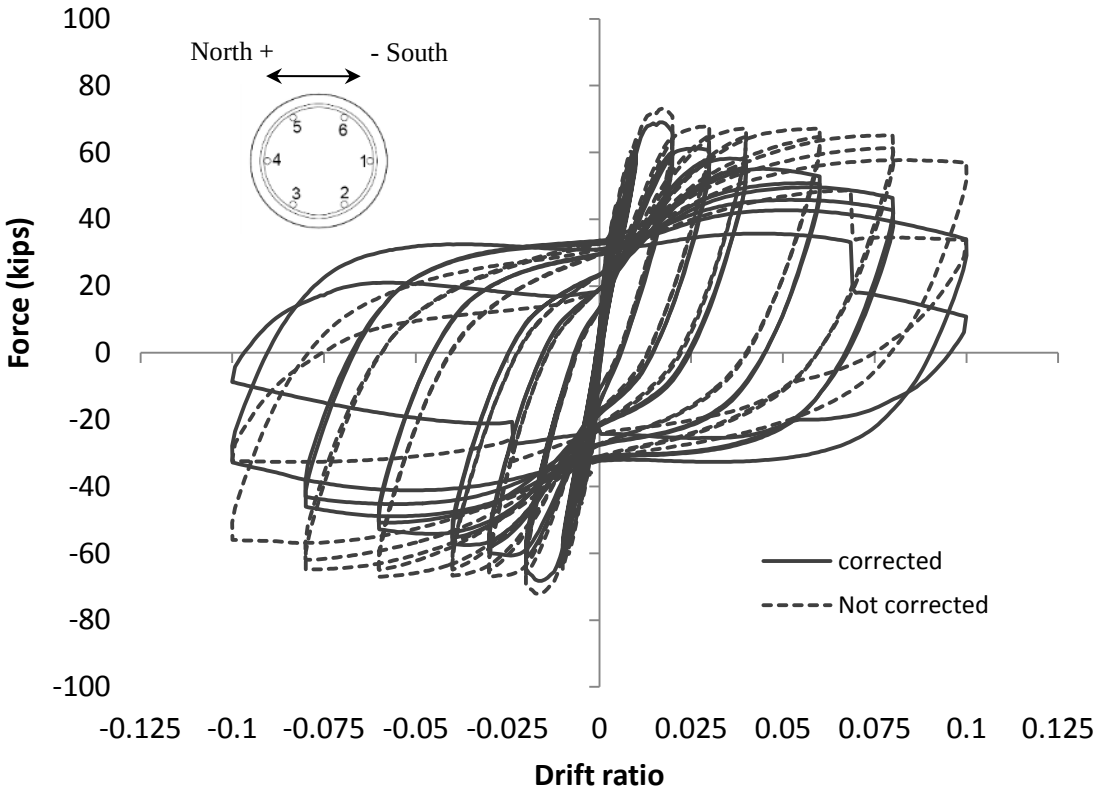

Figure 3.26 – Lateral load-vs.-drift ratio plots for Specimen #1

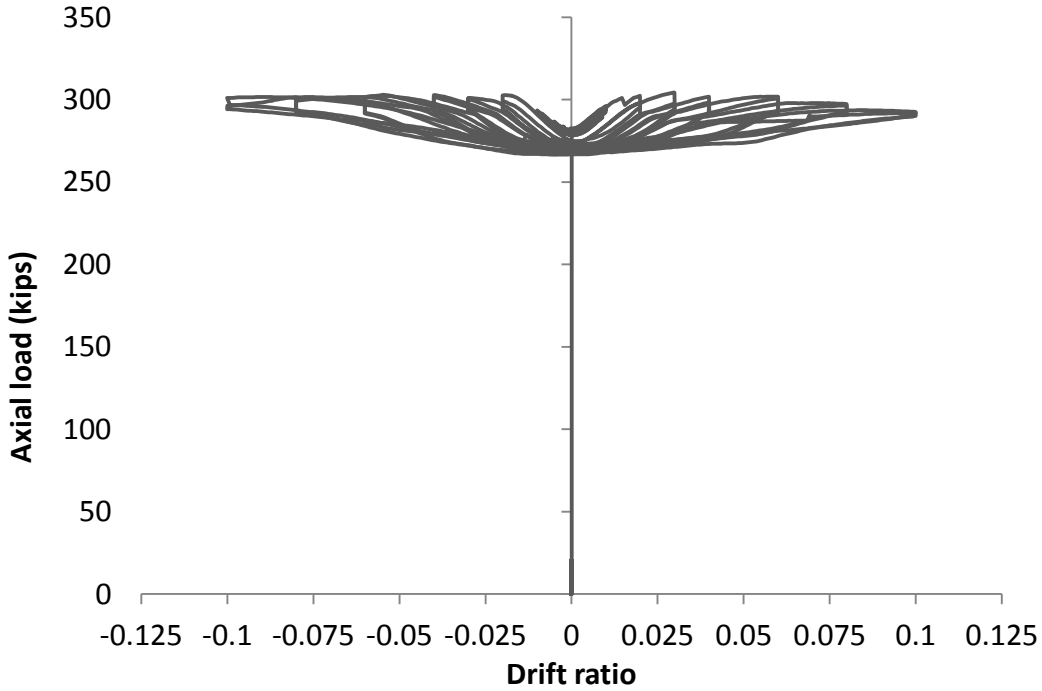

Figure 3.27 – Axial load-vs.-drift ratio plot for Specimen #1

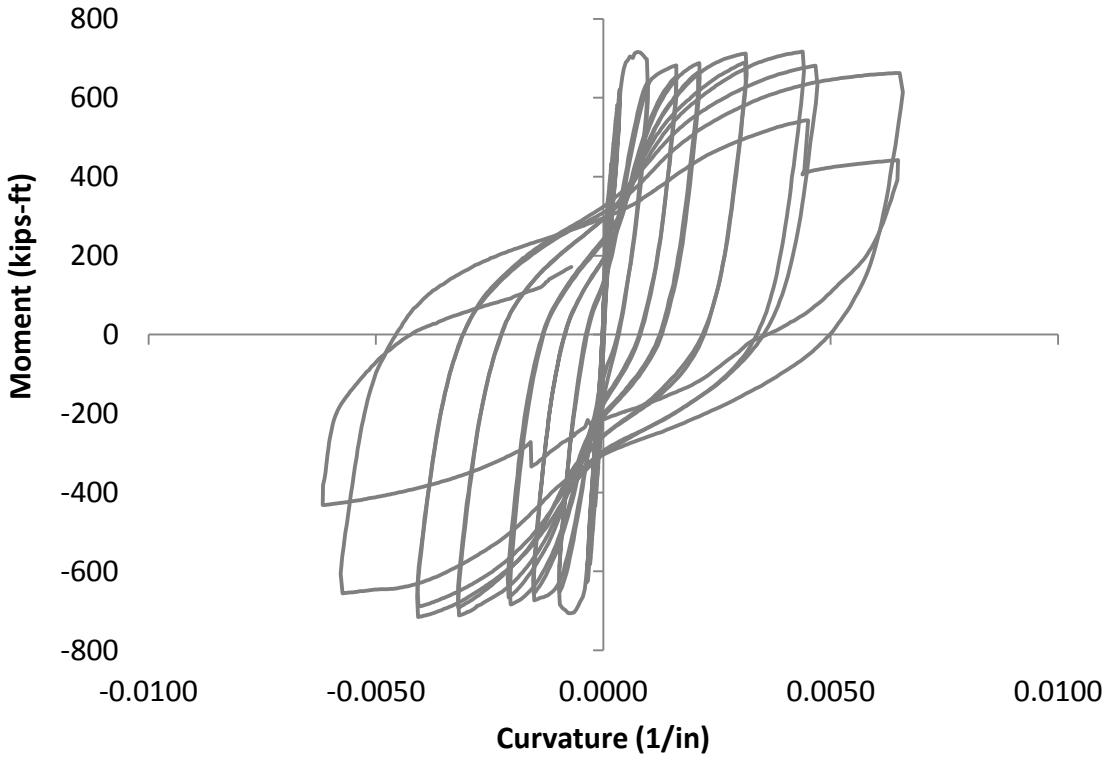

Figure 3.28 – Moment-vs.-curvature plot for Specimen #1 (average curvature over 1 ft. height from base)

(a) South face (b) North face

Figure 3.29 – Specimen #1 at 1% drift

Figure 3.30 – Specimen #1 at 2% drift

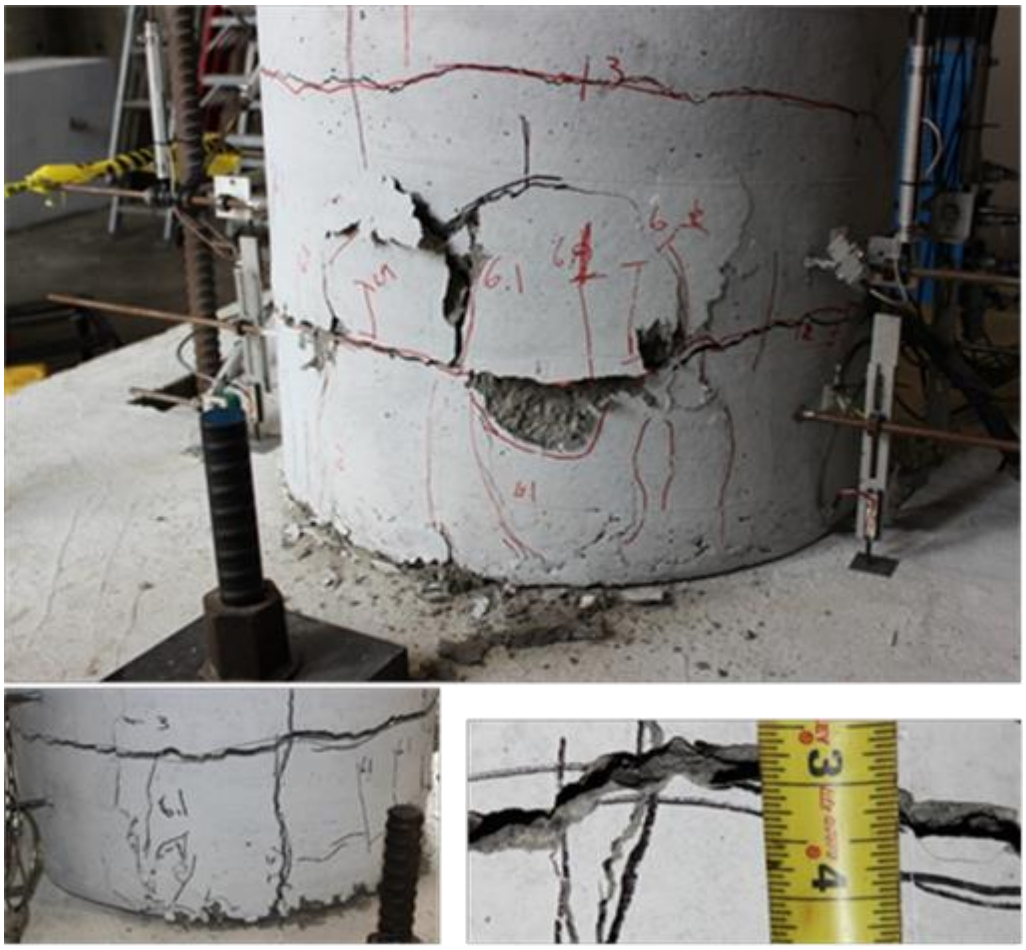

Figure 3.31 - Specimen #1 at 3% drift

Figure 3.32 – Specimen #1 at 6% drift

Figure 3.33 – Buckled Bar 1 at south face of Specimen #1 during 2nd cycle of -8% drift

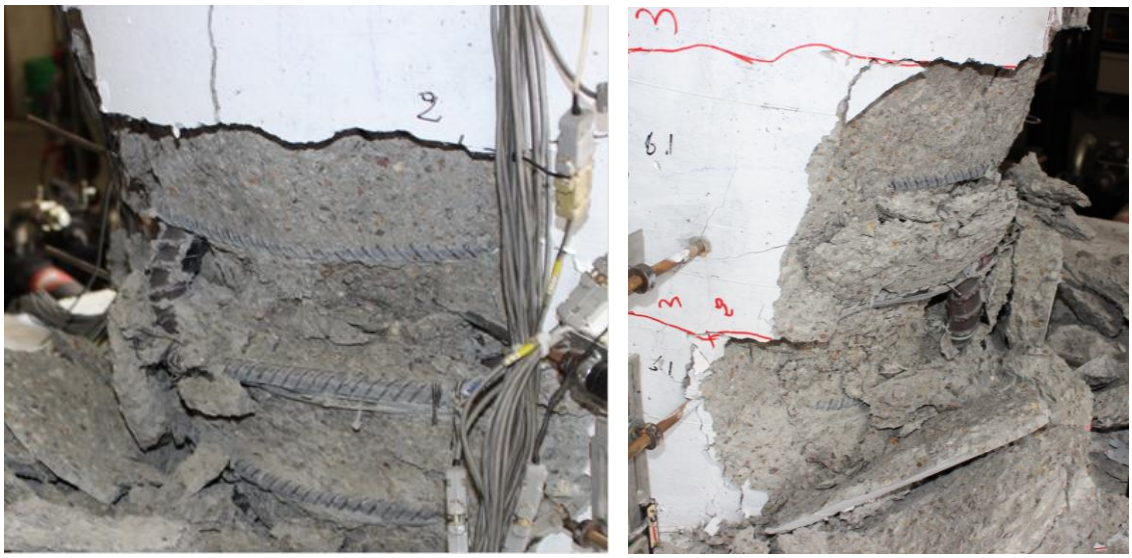

(a) South face (b) North face

Figure 3.34 – Crushing in Specimen #1 during 1st cycle of 10% drift

(a) South face (b) North face

Figure 3.35 – Crushing in Specimen #1 during 2nd cycle of +10% drift

Figure 3.36 – Fractured bar 4 at north face of Specimen #1 during 2nd cycle of -10% drift

Figure 3.37 – Specimen #1 at the end of testing

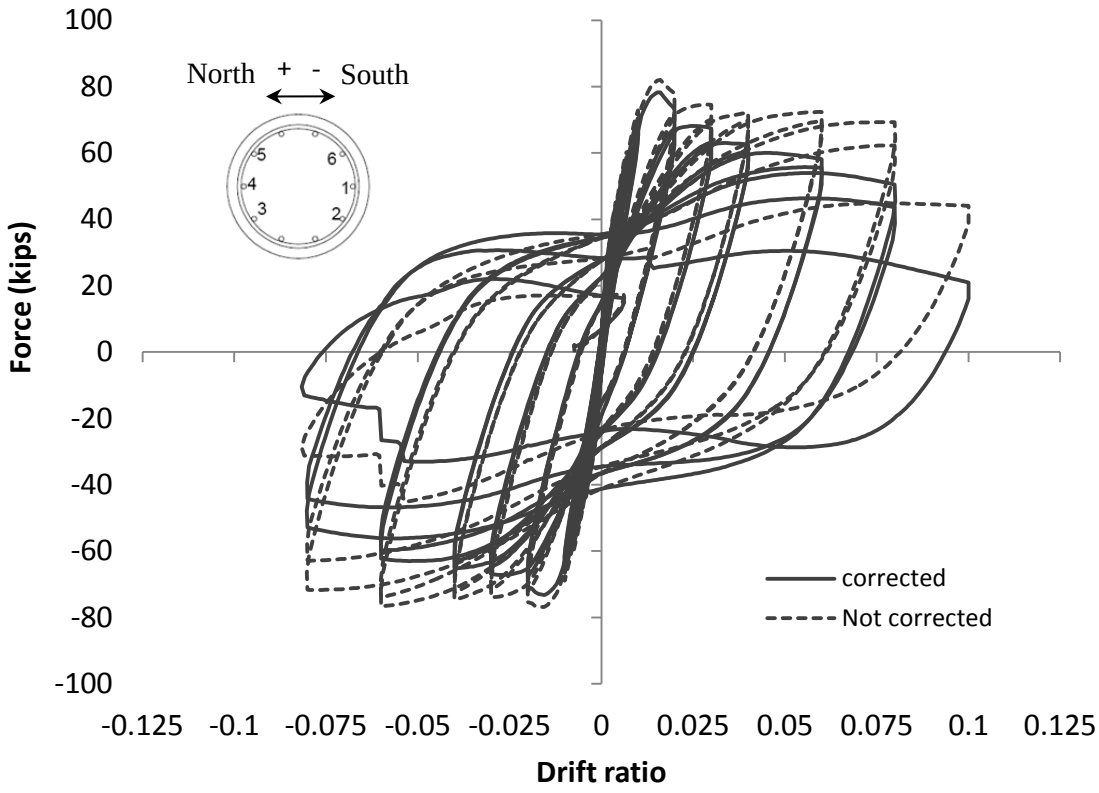

Figure 3.38 - Lateral load-vs.-drift ratio plots for Specimen #2

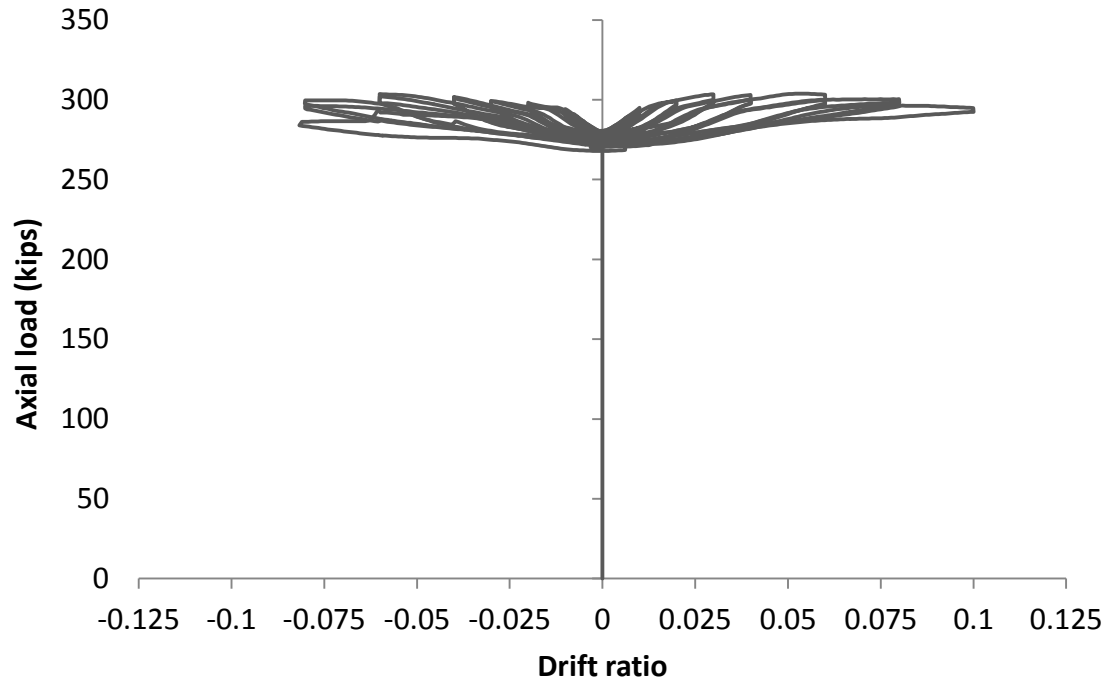

Figure 3.39 – Axial load-vs.-drift ratio plot for Specimen #2

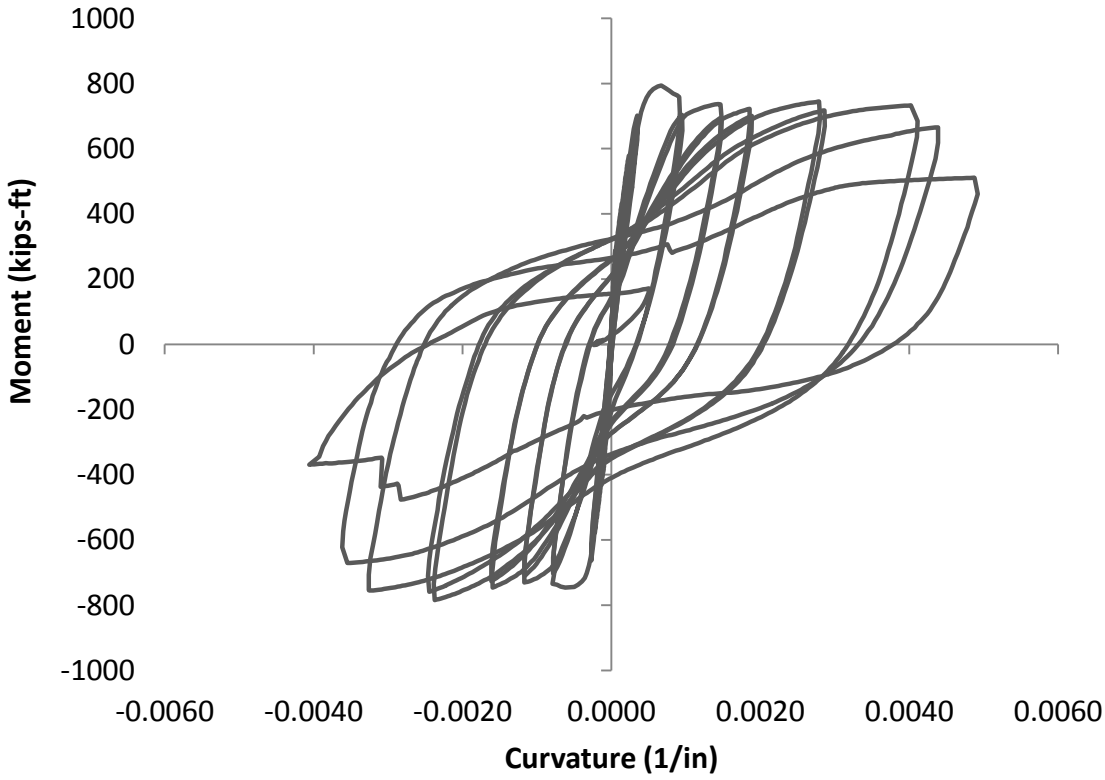

Figure 3.40 - Moment-vs.-curvature plot for Specimen #2 (average curvature over 1 ft. height from base)

(a) South face (b) North face

Figure 3.41 – Specimen #2 at 1% drift

(a) North face (b) South face

Figure 3.42 - Specimen #2 at 2% drift

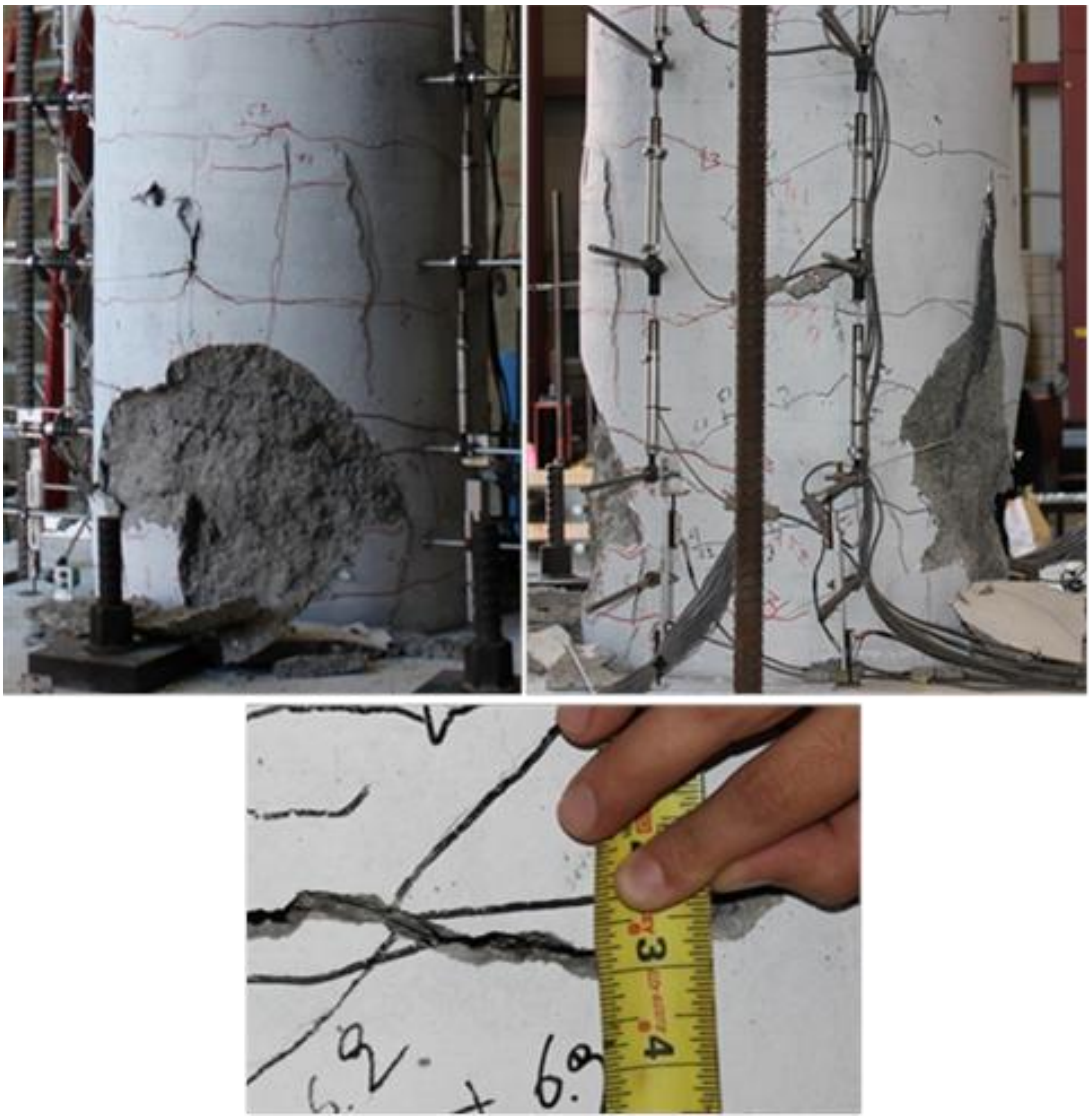

Figure 3.43 – Specimen #2 at 3% drift

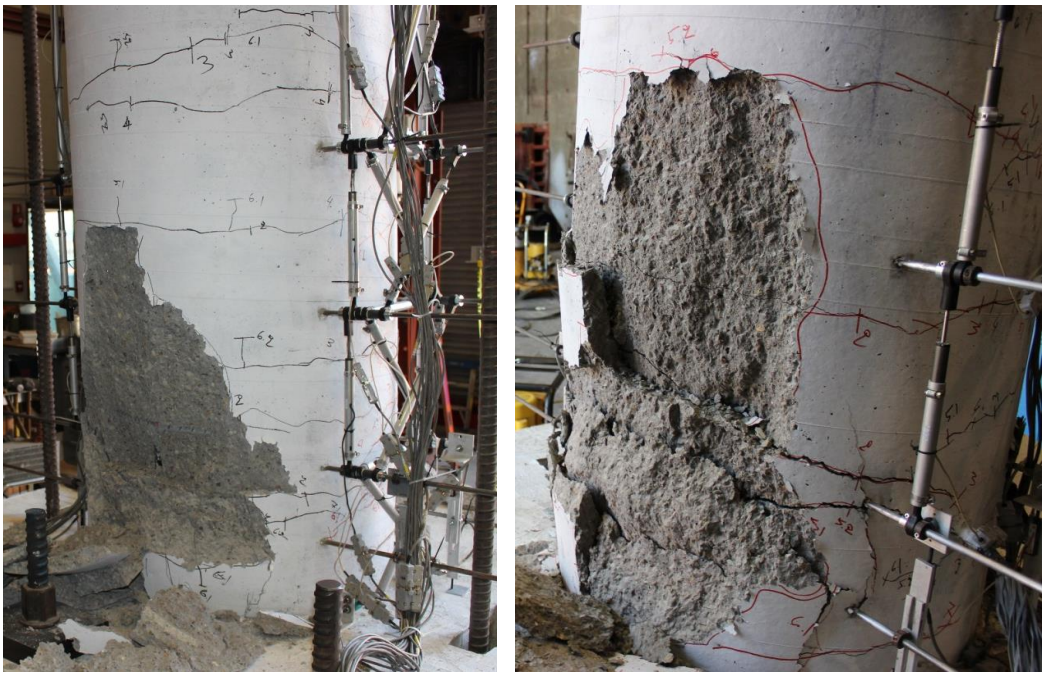

(a) South face (b) North face

Figure 3.44 –Specimen #2 at 4% drift

Figure 3.45 - Specimen #2 at 6% drift

(a) South face (b) North face

Figure 3.46 – Crushing in Specimen #2 at 1st cycle of 8% drift

(a) South face (b) North face

Figure 3.47 – Crushing in Specimen #2 at 2nd cycle of 8% drift

(a) South face (b) North face

Figure 3.48 – Fracture of bar 1 in Specimen #2 during 1st cycle of +10% drift

(a) South face (b) North face

Figure 3.49 – Fractured bars in Specimen #2 during 1st cycle of -10% drift

Figure 3.50 – Specimen #2 at the end of testing

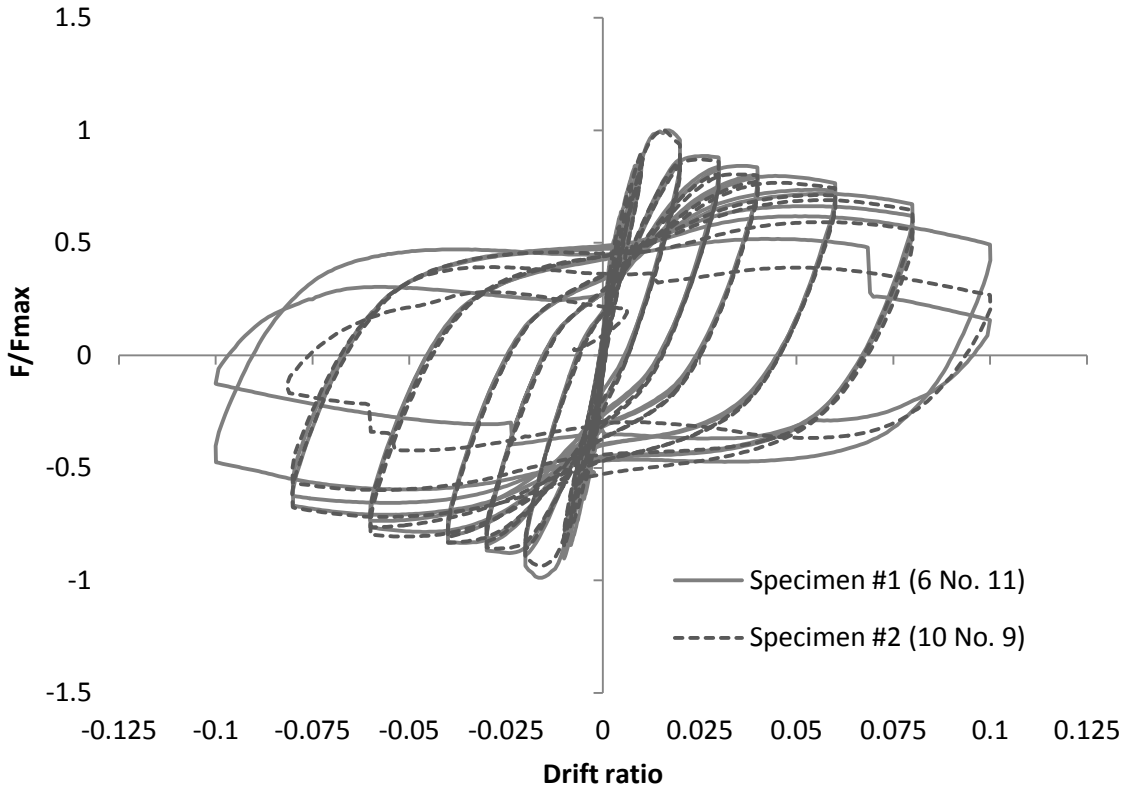

Figure 3.51 – Normalized lateral force-vs.-drift ratio curves for Specimens #1and #2

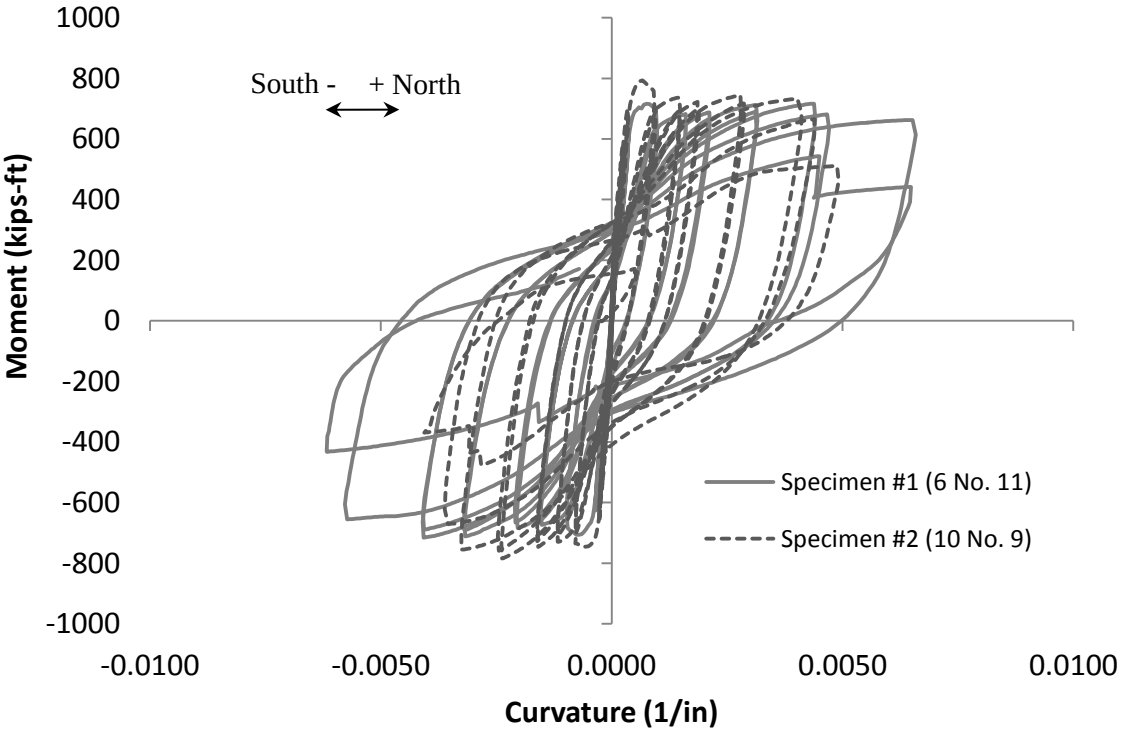

Figure 3.52 – Moment-vs.-curvature curves for Specimens #1 and #2

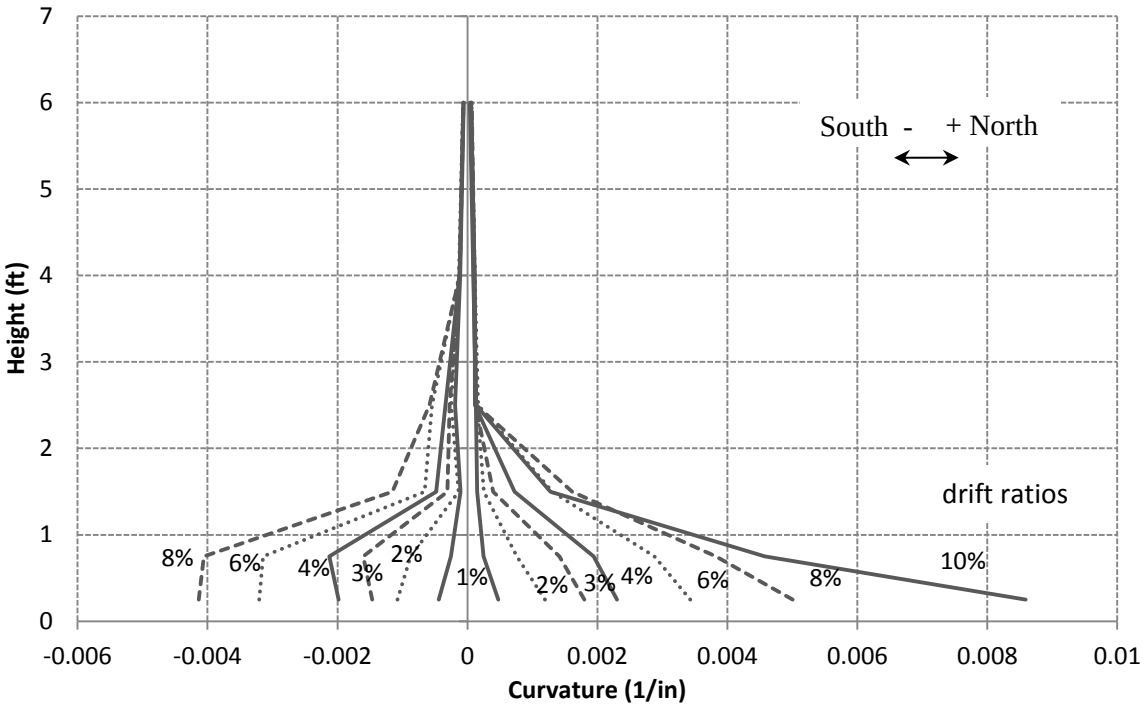

Figure 3.53 – Curvature along the height of Specimen #1

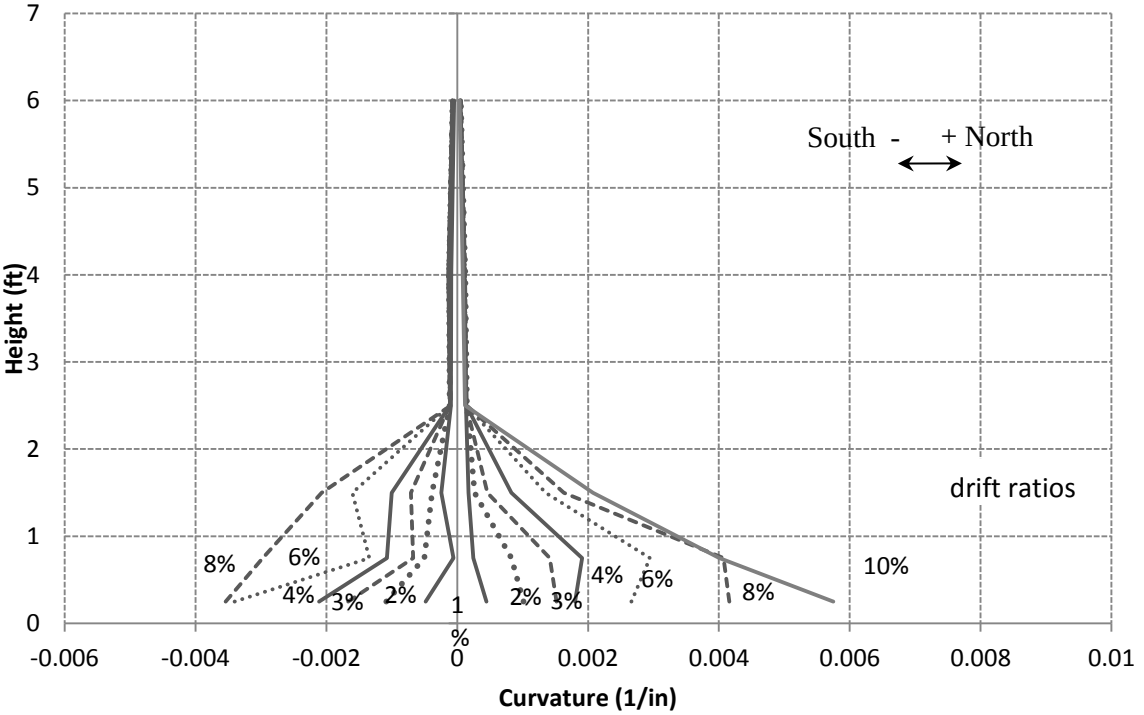

Figure 3.54 – Curvature along the height of Specimen #2

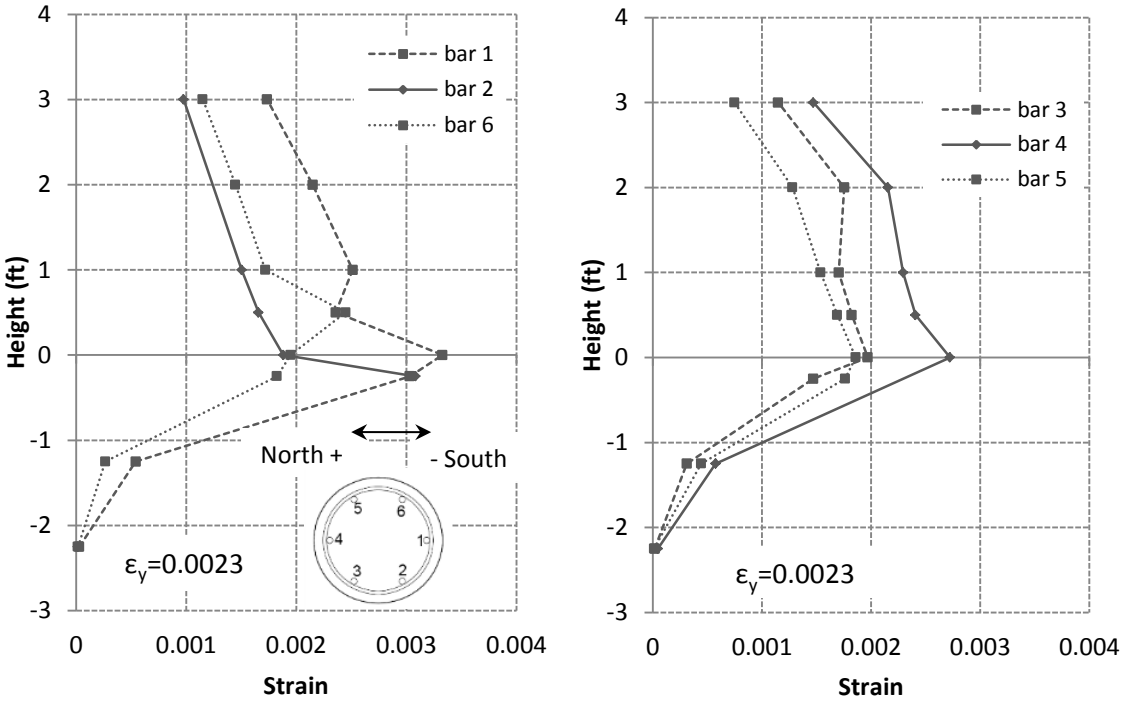

(a) +1% drift (b) -1% drift

Figure 3.55 - Tensile strains in longitudinal bars of Specimen #1 at 1% drift

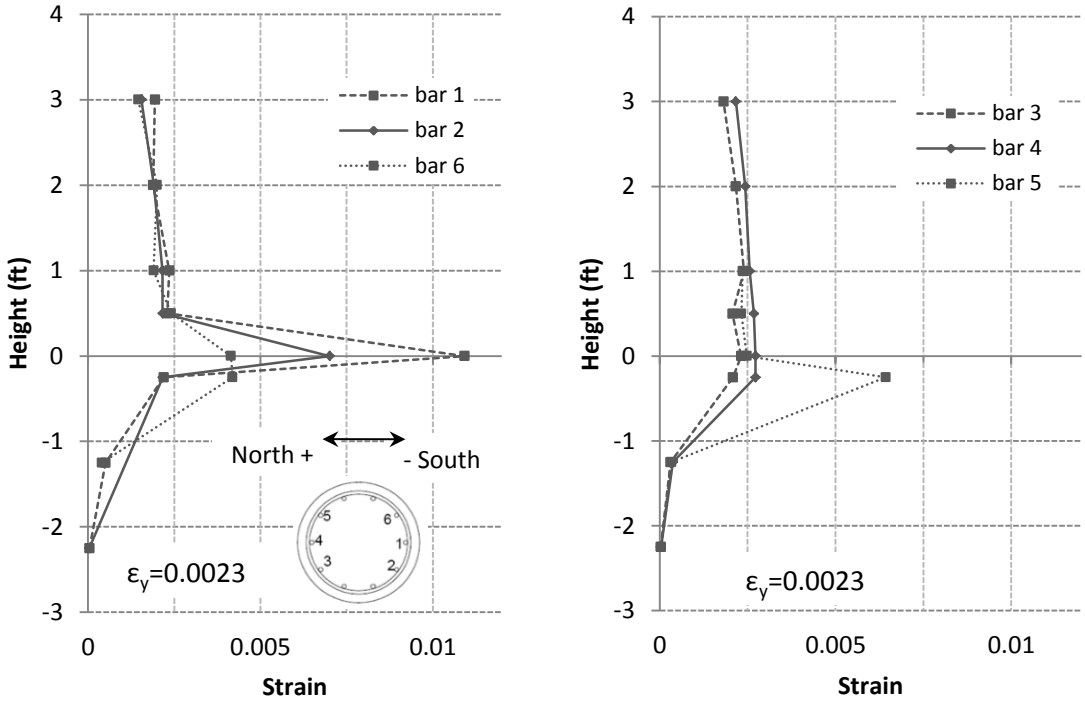

(a) +1% drift (b) -1% drift

Figure 3.56 - Tensile strains in longitudinal bars of Specimen #2 at 1% drift

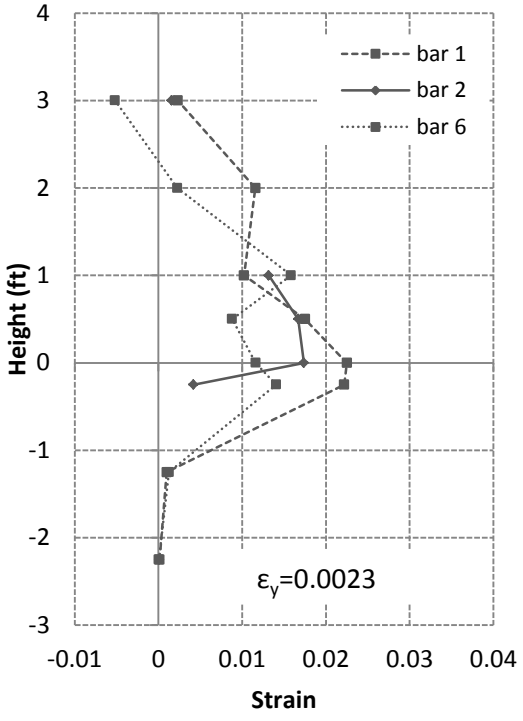

(a) +4% drift

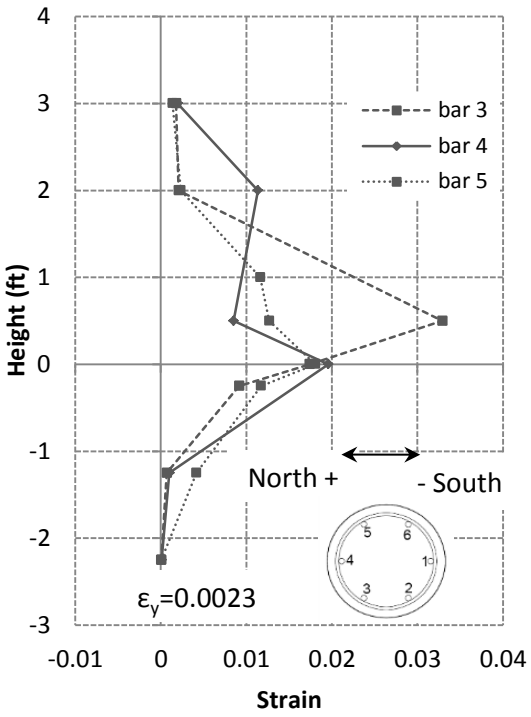

(b) -4% drift

Figure 3.57 - Tensile strains in longitudinal bars of Specimen #1 at 4% drift

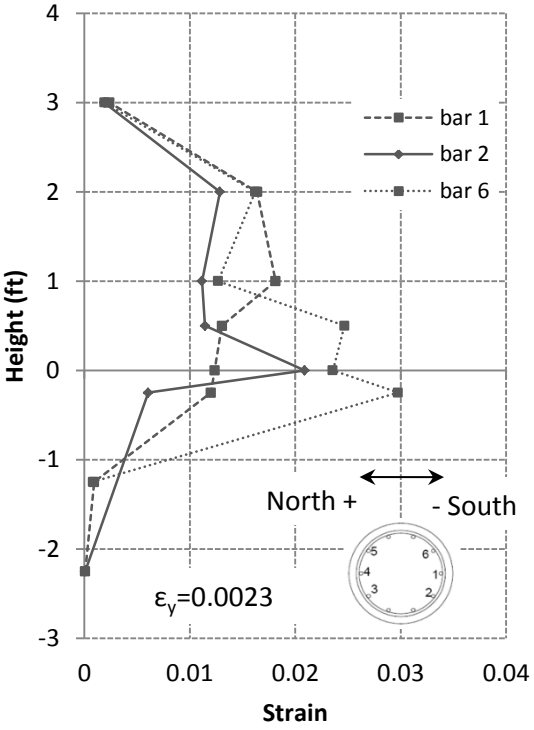

(a) +4% drift

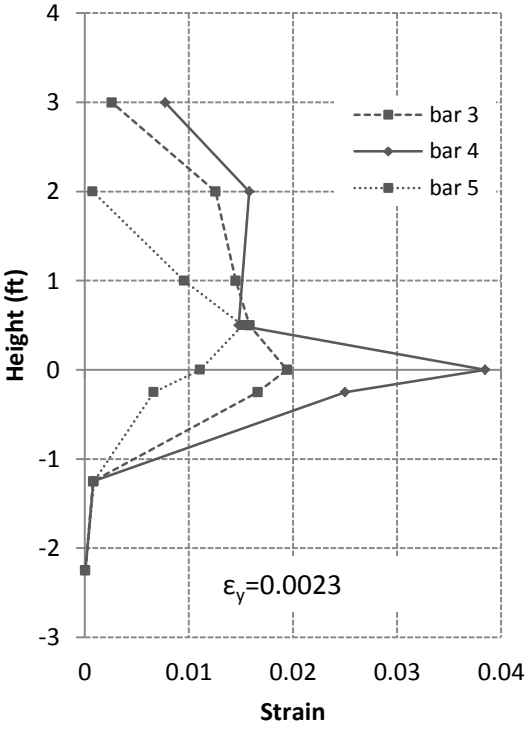

(b) -4% drift

Figure 3.58 - Tensile strains in longitudinal bars of Specimen #2 at 4% drift

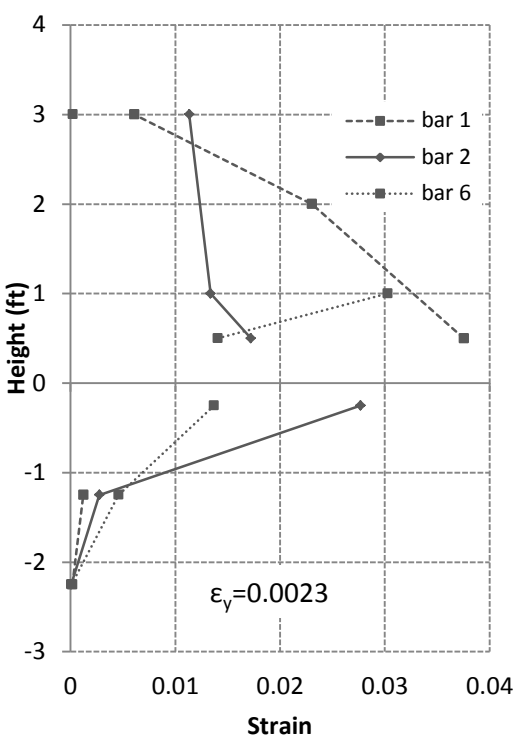

(a) +8%

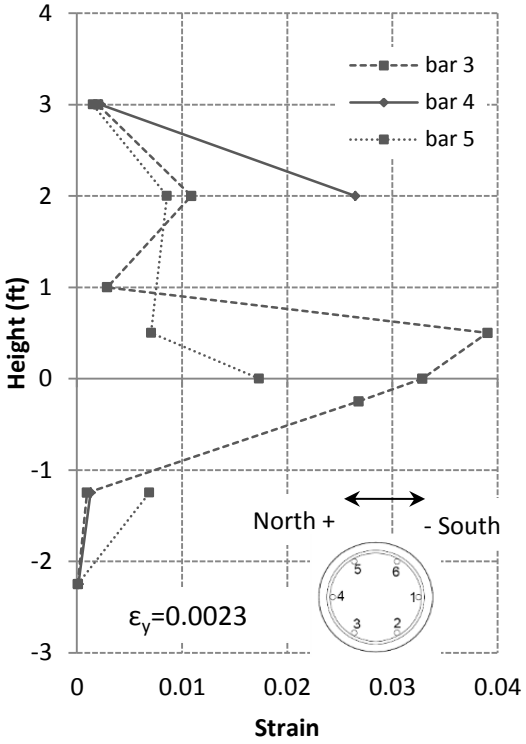

(b) -8%

Figure 3.59 - Tensile strains in longitudinal bars of Specimen #1 at 8% drift

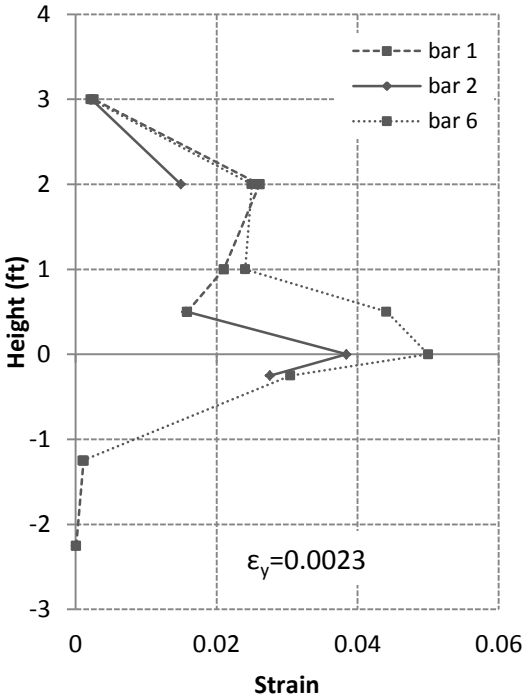

(a) +8% drift

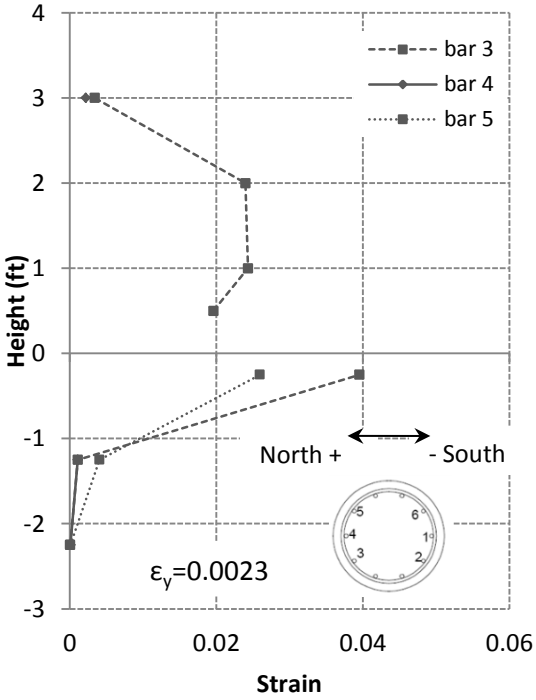

(b) -8% drift

Figure 3.60 - Tensile strains in longitudinal bars of Specimen #2 at 8% drift

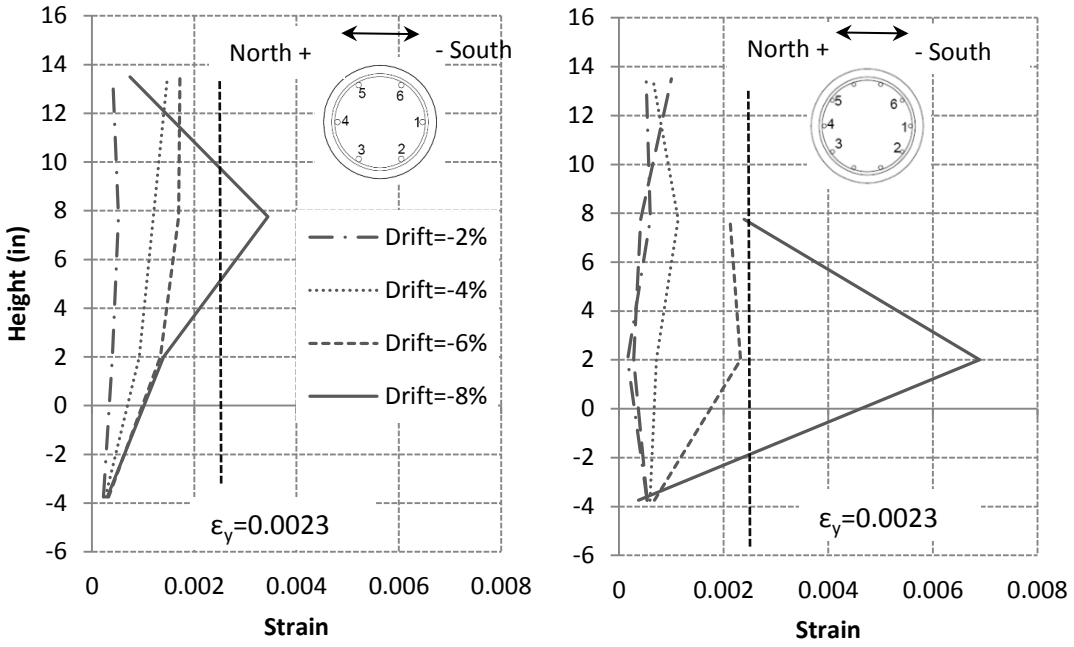

(a) Specimen #1 (b) Specimen #2

Figure 3.61 – Tensile strains in hoops near south face at different drift levels

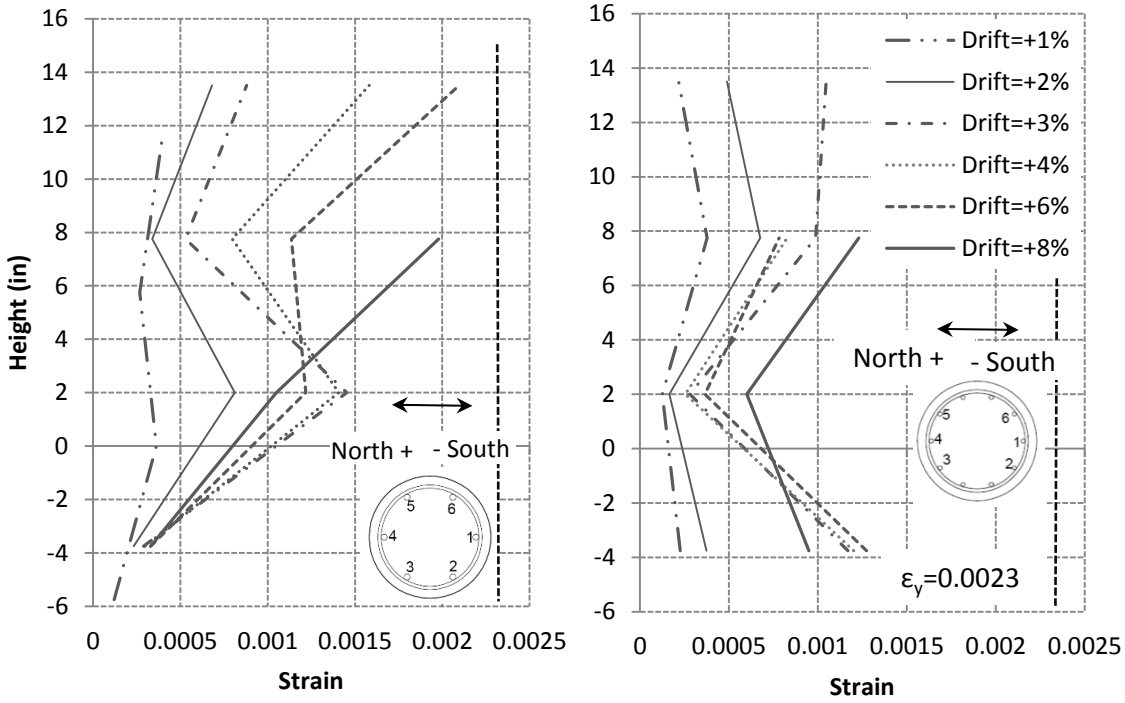

(a) Specimen #1 (b) Specimen #2

Figure 3.62 – Tensile strains in hoops near north face at different drift levels

CHAPTER 4

NUMERICAL INVESTIGATION OF EFFECTS OF SPACING OF LONGITUDINAL REINFORCEMENT ON PILE BEHAVIOR

Finite element analyses (FEA) have been conducted to simulate the structural behavior of the two pile specimens tested under cyclic lateral loading in this study. The finite element (FE) models were first used for the pre-test assessment of the performance of the pile specimens and to assist the development of the loading protocols for the tests. After being validated by the test results and further refined, the FE models have been used in a parametric study to examine the influence of the lineal and angular spacing of the longitudinal bars and the level of axial load on the structural performance of piles of different diameters. Furthermore, the microplane model is also employed to simulate concrete in the FEA of the RC pile specimens.

4.1 Finite Element model

Figure 4.1 shows the FE model of Specimen #1. Specimen #2 was modeled in the same way. The only difference between Specimens #1 and #2 was in the longitudinal reinforcement. Specimen #1 consisted of 6 No. 11 bars, while Specimen #2 consisted of 10 No. 9 bars, resulting in almost the same longitudinal steel ratio but different bar spacing. Only half of the specimen is represented in the FE model by taking advantage of the symmetry of the specimen about the applied lateral load. Geometric nonlinearity is considered in the FEA.

The damaged-plasticity model presented in Section 2.1 is used to model the unconfined and confined concrete in the piles, while the footings and the pile caps are assumed to remain

elastic. The calibration of the damaged-plasticity model has been discussed in Chapter 2. While the compressive properties of the concrete are specified in terms of the stress-strain relation, the tensile properties are defined in terms of the stress-displacement relation. The latter is to avoid the sensitivity of the tensile behavior of concrete to the element size. For 3-D concrete models whose failure surfaces account for the effect of the hydrostatic stress, the compressive behavior of concrete will not be as sensitive to the element size, as will be demonstrated by the numerical study presented here. The properties of the concrete in the piles, based on the material test data for the two specimens, are summarized in Table 4.1. Parameter K_c, which controls the shape of the yield surface in the deviatoric plane as well as the slopes of the tensile and compressive meridians, is assigned the value of 1. This is appropriate for the maximum hydrostatic pressure expected for the concrete elements near the toe regions of the pile, and the resulting model can accurately simulate the spalling of the concrete cover.

Contact conditions are imposed at the interface between the pile and the footing. This is to improve the simulation of the opening and closing of large flexural cracks at the base, which cannot be well represented by the damaged-plasticity concrete model, as explained in Section 2.1. The longitudinal bars are modeled with beam elements using the phenomenological steel law presented in Section 2.3. The material properties for the longitudinal reinforcement are summarized in Table 4.2. The calibration of the stress-strain relation has been discussed in Section 2.3.1. For the calibration of the low cycle fatigue (LCF) parameters, the procedure described in Section 2.3.3 has been followed. For Specimen #1, the LCF law has been calibrated for No. 11 bars with an unsupported length L = 5.75 in., while for Specimen #2, the LCF law has been calibrated for No. 9 bars with an unsupported length L = 5.75 in. The slip of the longitudinal bars in concrete is also considered by using the phenomenological bond-slip model of Murcia-Delso and Shing (2015), which has been calibrated with the procedure discussed in Section 2.4. Perfect bond is considered for the transverse reinforcement, which is modeled with truss

elements, assigned an elasto-plastic law for steel, with a yield stress of 65 ksi and an ultimate stress of 95 ksi.

To investigate whether the height of the elements along the length of the pile will affect the numerical results, an element-size sensitivity analysis has been conducted. Figure 4.2 shows the lateral load-vs.-drift ratio curves from the FEA of Specimen #1 with different element heights. As shown in the figure, the numerical results are not sensitive to the element size. For the analysis of the pile specimens, an element height of 2 in. has been selected.

4.2 Validation of Finite Element Models with Experimental Results

4.2.1 Load – vs. – Displacement Response

The FE models are subjected to the same vertical and lateral displacement demands as the tested pile specimens. The lateral load-vs.- drift ratio curves obtained for Specimens #1 and #2 by the tests and the FEA are shown in Figure 4.3 and Figure 4.4, respectively. The curves from the FEA provide a good match with the test results. The lateral load capacities obtained from the tests and the FEA are compared in Table 4.3. The FEA underestimate the lateral load capacity by 2% (south direction for Specimen #2) to 11% (north direction for Specimens #1 and #2). The load capacities obtained in the FEA are in general smaller with the crushing of the cover concrete occurring one cycle earlier than that observed in the tests. The gradual drop of the lateral load resistance caused by the P-Δ effect of the vertical load and the crushing of concrete at the toes of the piles is well reproduced in the FEA.

The unloading and reloading curves are well reproduced. The pinching due to the closing of flexural cracks is accurately simulated in the FEA because of the contact conditions introduced at the pile-footing interface.

The large drop of the lateral load resistance due to the fracture of longitudinal bars during the last cycles of the tests is simulated by the low-cycle fatigue (LCF) law used in the FE model. The predictions for bar fracture in the FEA are close to the experimental results for both specimens. Bar fracture due to LCF occurs in bar elements very close to the footing-pile interface. Table 4.4 and Table 4.5 show the cycle numbers in which longitudinal bars in Specimens #1 and #2 fractured in the tests and in the FEA. The numbering of the longitudinal bars in the pile specimens is shown in Figure 4.5. Since only half of the pile is modeled in the FEA, it is assumed that the longitudinal bars on the west side and the east side exhibit the same behavior. When the fracture of the steel occurs, the stress-strain law assumes a gradual drop of stress to enhance the robustness of the numerical solution. Thus, the very steep load drops exhibited by the lateral load-vs.-drift ratio curves from the tests due to bar fracture are not observed in the numerical results.

The FEA verify that the spacing of the longitudinal bars does not have a significant effect on the structural performance of the RC pile specimens. Up to 8% drift, the two specimens exhibit the same lateral load-vs.-drift ratio response. However, the ductility can be affected by the diameter of the longitudinal bars. Larger-diameter bars are more resistant to buckling for the same spacing of the transverse reinforcement. This will delay bar fracture and lead to a more ductile behavior.

4.2.2 Flexural Crack Spacing

In the experimental study, it was observed that the spacing of longitudinal bars had an influence on the spacing of the flexural cracks in the pile specimens. While the amounts of longitudinal reinforcement in the two specimens were almost the same, the longitudinal bars in Specimen #1 had a larger spacing. Figure 4.6 and Figure 4.7 show that flexural cracks were more widely spaced in Specimen #1 than in Specimen #2. Most of the flexural cracks in Specimen #1

had a spacing between 10 and 12 in. Some had a spacing as small as 6 in. or as large as 18 in. Most of the flexural cracks in Specimen #2 had a spacing between 6 and 12 in., with some at less than 6 in. Moreover, the width of the flexural cracks in Specimen #1 was larger than that in Specimen #2, as observed in later cycles during the tests.

The damaged-plasticity concrete model, used in the FEA, does not represent cracks in a discrete fashion. Rather cracks are represented in a distributed fashion by plastic tensile strains. The normal plastic strains developed in concrete in the axial direction of the pile in the FEA of the two pile specimens at a drift ratio of 1% are presented in Figure 4.8. In this figure, flexural cracks can be identified as localized plastic tensile strains. As shown in Figure 4.8(a), the spacing of the flexural cracks in Specimen #1 from the FEA is 6 to 8 in. with the maximum normal plastic strain $\varepsilon_{p,\mathrm{FEA}} = 0.0039$. As shown in Figure 4.8(b), the flexural cracks in Specimen #2 are more closely spaced at about 6 in. with $\varepsilon_{p,\mathrm{FEA}} = 0.0036$. The concrete elements close to the base of the pile specimens do not develop plastic tensile strains. This is because the opening of the pile-footing contact interface and the slip of the longitudinal bars in tension reduce the tensile stresses in the concrete elements in the vicinity.

Figure 4.8 also shows the extent of flexural cracking in Specimens #1 and #2 from the FEA. For Specimen #1, flexural cracks occur over a height of 5.6 ft. from the base of the pile, while those for Specimen #2 over a height of 5.9 ft. In the tests, flexural cracks in Specimen #1 extended over a height of 5.1 ft. from the base at the south face and 6 ft. at the north face, as shown in Figure 4.6, while those in Specimen #2 extended over a height of 5.5 ft. at the south face and 6 ft. at the north face, as shown in Figure 4.7. The larger extent of flexural cracking in Specimen #2 can be explained by its slightly higher moment capacity, as compared to Specimen #1, as illustrated in Figure 4.9.

4.2.3 Strains in Longitudinal Bars

Figure 4.11 through Figure 4.16 compare the strains in the longitudinal bars of Specimen #1 from the tests and the FEA at drift ratios of 1, 4 and 8%. Overall, the numerical results match the test data reasonably well. For Specimen #1, the tensile strains in Bars 1 and 4 are significantly overestimated at the base of the pile by the FE model at drift ratios of 1 and 4%. It should be noted that the tensile strains in the bars are highly influenced by the integrity of the bond and the surrounding concrete. It is likely that the damage of the concrete and the bond at the base of the pile at these drift levels can be slightly under-estimated by the FE model. At larger drift ratios, many strain gages were damaged, resulting in no strain measurements. Attributed to the bond-slip model, the plastic strain penetration of the longitudinal bars in footing is well captured by the FE model.

Figure 4.17 through Figure 4.22 compare the strains in the longitudinal bars of Specimen #2 from the tests and the FEA at drift ratios of 1, 4 and 8%. The same observations as above have been obtained. In general, it can be observed that Specimen #2 has more severe bar strains developed at the base of the pile than Specimen #1. This can be attributed to the fact that the longitudinal bars in Specimen #2 had a smaller diameter and therefore less bond stress demand and less slip in the vicinity of the flexural crack at the base.

4.2.4 Plastic Deformation in the Piles

The experimental study showed that Specimen #1, which had larger-diameter longitudinal bars and larger bar spacing, had more plastic deformation concentrated near the base as compared to Specimen #2. The FE models provide the same observation, as shown in Figure 4.10, which compares the strain distributions along the longitudinal bars placed at the south face of Specimens #1 and #2 at a drift ratio of 4% from the tests and the FEA. This difference can be explained by the fact that the longitudinal bars in Specimen #2 had a smaller diameter and

therefore less bond stress demand and less slip in the vicinity of a flexural crack. This will lead to higher tensile strains in the bars.

4.2.5 Stresses in Concrete

Figure 4.23 show the normal stress-vs.-normal strain curves of concrete elements at the cover and the core of the pile section. In the FEA, the maximum compressive stress in the cover concrete is 5.1 ksi, being very close to the prescribed value of 4.9 ksi for unconfined concrete from material test data. The stress developed in the concrete core element is higher, due to the confining effect of the lateral reinforcement. Moreover, the cover concrete shows a more brittle behavior, compared to the core concrete, as shown in Figure 4.23.

4.2.6 Stresses in the Longitudinal Bars

Figure 4.24 shows the axial stress – strain response in the elements of longitudinal bars #1 and #4 at the base of the pile of Specimen #1. As shown, fracture due to LCF is described with a gentle descending curve in the stress-strain relation till it reaches a residual stress of 10 ksi. As mentioned in Section 4.2.1, the FE models adequately predict the cycles at which the longitudinal bars fractured in the tests.

4.3 Parametric Study with Finite Element Models

By using the FE modeling method validated in the previous section, a numerical parametric study has been conducted to further evaluate the influence of the spacing of longitudinal bars on the structural performance and crack spacing of circular RC piles, and for piles with larger diameters and higher axial load levels. Table 4.6 summarizes the properties of the piles considered in the parametric study. Models D28S1 and D28S2 in the table have the same properties as the two specimens tested. As shown in Table 4.7, these two models are also

subjected to higher axial loads in the parametric study. All the pile models considered have the same volumetric ratio of transverse reinforcement, and more or less the same ratio of the cross-sectional area of the longitudinal reinforcement to the cross-sectional area of the pile.

4.3.1 Impact of Lineal Spacing of Bars on Ductility

The lateral load-vs.-drift ratio curves for Models D28S1 through D28S4 are presented in Figure 4.25. All four specimens have similar lateral load capacities since they are designed with similar longitudinal reinforcement ratios. The spacing of longitudinal bars does not have an effect on the ductility of the piles.

However, similarly to what was observed in the experimental study, the size of the longitudinal bars has a small influence on pile ductility, as it can be seen in Figure 4.25. The fracture of larger-diameter longitudinal bars occurs slightly later because they are more resistant to buckling for the same spacing of transverse reinforcement. Figure 4.26 shows the cycle numbers at which the longitudinal bars in the piles with diameter equal to 28 in. fractured.

4.3.2 Impact of Lineal Spacing of Bars on Flexural Crack Spacing

Flexural cracks are simulated in the form of plastic tensile strains in the FEA. Figure 4.27 shows the normal plastic strains in concrete in the axial direction of the pile at 1% drift for piles D28S1through D28S4. It can be observed, as in the experimental study, that flexural cracks are more closely spaced and have smaller widths as the spacing of the longitudinal bars decreases.

4.3.3 Piles with Larger Diameters

Piles D56S1, D56S2, and D56S3 have a diameter of 56 in., a height of 20 ft. and the same angular spacings of longitudinal bars as piles D28S1, D28S2 and D28S3, respectively, as shown in Table 4.6. However, the lineal spacing of the longitudinal bars in these piles is more than doubled, with the concrete cover in the two set of piles remaining the same. The length of

the elements along the height of the piles is twice as large as that for the piles with a diameter of 28 in. so that the total number of element layers remains the same. As mentioned in Section 4.1, load-vs.-drift ratio curves from FE models are not sensitive to the size of the elements.

The lateral load-vs.-drift ratio curves for piles D56S1 through D56S3 are shown in Figure 4.28. It can be observed that the lineal spacing of longitudinal bars does not have an impact on the ductility of the piles of larger diameter. Figure 4.29 shows the normalized lateral load-vs.-drift ratio curves for piles D28S2 and D56S2, which have the same angular spacing, but different lineal spacings because of the larger diameter of the latter. For these curves, the loads are normalized by the respective peak load reached in each test. As it can be seen, there is no major difference in the hysteresis curves except that D28S2 shows a more rapid load degradation in later cycles because it has smaller diameter longitudinal bars, which are more vulnerable to buckling and fracture caused by LCF. Figure 4.30 shows the cycle numbers at which the longitudinal bars in piles D56S1 through D56S3 fractured.

As shown in Figure 4.31, the lineal spacing of the longitudinal bars has a small impact on the width and spacing of flexural cracks, similar to that observed for the smaller diameter piles. A larger bar spacing leads to a wider spacing of flexural cracks and wider crack widths.

Figure 4.32 compares the normal plastic strains in the axial direction of piles D28S2 and D56S2. The diameter of pile D56S2 is twice as that of D28S2, but both piles have a concrete cover of 2 in. Since the longitudinal bars in both piles have the same angular spacing, those in D56S2 have a larger lineal spacing. It can be seen that the flexural cracks in pile D56S2 are more widely spaced than those in pile D28S2. The maximum plastic tensile strain in D56S2 is slightly smaller than that in D28S2. This means that the flexural cracks in D56S2 are wider than those in D28S2 because the element height for the former is twice as large. This conclusion is supported by the results of an element-size sensitivity study conducted on D56S1. Figure 4.33 compares the plastic strains obtained for this pile with element heights of 4 in. and 2 in., respectively. It can be

seen that the maximum plastic tensile strain obtained with an element height of 4 in. is slightly less than half of that with a height of 2 in. This confirms the fact that the width of a flexural crack is represented by the plastic elongation of the element, which is proportional to the plastic strain and the element size.

4.3.4 Piles Subjected to Higher Axial Loads

Figure 4.34 and Figure 4.35 show the lateral load-vs.-drift ratio curves for piles D28S1 and D28S2 when they are subjected to higher axial loads that are 15% and 20% of the compressive strength ($A_g f_c'$) of the piles, respectively. As the plots show, increasing the axial load increases the lateral load capacity, but it leads to a steeper negative slope in the load-displacement curves because of the *P-Δ* effect of the axial load. Even for these cases, the lineal spacing of the longitudinal bars has no impact on the ductility of the piles.

4.4 Finite Element Analysis with the Microplane Model

The microplane model, presented in Section 2.2, is used in the finite element analysis of the RC pile specimens tested in this study. As shown in Figure 4.36, the FE model for the pile specimens is similar to the one presented in Section 4.1, except that the contact conditions at the pile-footing interface have been eliminated. This is because the microplane model can adequately simulate the opening and closing of flexural cracks. Table 4.8 summarizes the values of E and k_1 selected to match the properties of the concrete in the piles. The longitudinal bars and the confining hoops are modeled in the same way as that presented in Section 4.1. Bond-slip between the concrete and the longitudinal bars is also modeled in the same manner.

4.4.1 Specimen #1

Figure 4.37 shows the lateral load-vs.-top drift curves obtained for Specimen #1 by the test and the FE model. The curve form the FEA matches the test result well in terms of the lateral-load capacity, the post-peak behavior, and the pinching due to the opening and closing of flexural cracks. The drop of the lateral-load resistance at the 2nd cycle of 10% drift, due to the fracture of the longitudinal bars, is also reproduced by the FEA with the use of the phenomenological LCF law for steel presented in Section 2.3.2. Figure 4.38 shows the deformed shape of Specimen #1 at the end of the 2nd cycle of 10% drift. With the elimination of the contact conditions at the pile-footing interface, flexural cracking tends to largely concentrate in the first layer of the concrete elements at the base of the pile. The opening and closing of flexural cracks is accurately simulated. Figure 4.39 and Figure 4.40 show the axial stress-strain responses of concrete cover and core elements at the toe of the pile in Specimen #1. The microplane model is capable of accurately simulating the opening and closing of flexural cracks.

As shown in Figure 4.39, an element in the concrete cover experiences large tensile strains, which goes back to almost zero before developing a maximum compressive stress of 6 ksi, which is slightly larger than the prescribed unconfined compressive strength of 5 ksi. This slight increase in strength can be attributed to the confinement effect provided by the footing. Similar observations can be made for an element in the concrete core, which develops a high compressive stress of 9 ksi due to the confinement provided by the transverse reinforcement.

Table 4.9 summarizes the cycles in which the longitudinal bars of Specimen #1 fractured in the test and in the FEA, showing a close correlation of the experimental and numerical results. The positions of Bars 1 and 4, along with the cycles in which they fracture in the FEA, are shown in Figure 4.41.

The strains in the longitudinal bars on the south side of the pile at different drift levels are plotted in Figure 4.44 through Figure 4.46. The strains predicted in the FEA are compared to the

test results in these plots. In general, the numerical results match the test data well. However, at locations close to the pile-footing interface, the tensile strain in Bar 1, which is at the extreme position on the south side, at pile drift ratios of 1% and 4% is significantly over-estimated in the FEA. As discussed in Sec. 3.2.3, one possible explanation is that the damage of the concrete and the bond at the base of the pile at these drift levels can be slightly under-estimated by the FE model and the tensile strain in a bar is highly sensitive to the damage. It is interesting to note that the FEA accurately captures the strains in the longitudinal bars embedded inside the footing.

4.4.2 Specimen #2

Specimen #2, which consisted of 10 No. 9 longitudinal bars, is also modeled with the microplane model. Figure 4.42 shows the good match of the lateral load-vs.-top drift curves obtained from the test and the FEA. The numerical results for Specimen #2 are similar to those for Specimen #1. Table 4.10 summarizes the cycles in which the bars fractured in the test and in the FEA. The FE model is able to accurately predict the LCF of the longitudinal bars. Figure 4.43 shows the positions of the longitudinal bars, along with the cycles in which the bars fractured.

Similar to the analyses with the damaged-plasticity model, presented in this chapter, the results here show that the difference in the lineal spacing of longitudinal bars for the two specimens does not have any effect on the ductility of the lateral load-vs.-drift ratio response. The size of the longitudinal bars, however, can have an effect to the ductility of the pile. The No. 9 longitudinal bars of Specimen #2, fractured earlier than the No. 11 longitudinal bars of Specimen #1. Smaller-diameter bars are less resistant to buckling for the same spacing of the transverse reinforcement, and can therefore lead to a less ductile behavior of a laterally loaded RC member.

The strains in the longitudinal bars placed on the south side of the pile at different drift levels are shown in Figure 4.47 through Figure 4.49. Expect for some discrepancies observed at

the pile-footing interface, like those observed for Specimen 1, the strains in the longitudinal bars obtained from the FE model satisfactorily match the experimental data.

4.4.3 Flexural Crack Pattern

Figure 4.50 shows the normal strains developed in concrete, in the axial direction of the pile, at a drift ratio of 1% in the FEA of the two pile specimens. In this figure, flexural cracks can be identified as localized tensile strains. The maximum tensile strains developed in Specimen #1 are larger than those in Specimen #2, consistent with the experimental observations. Moreover, the flexural cracks in Specimen #2 spread over a larger distance than those in Specimen #1. However, the spacings of the flexural cracks are more or less the same for the two cases, with Specimen #2 showing a slightly smaller spacing between the first two cracks near the base.

4.5 Conclusions

The FE models developed for the circular RC pile shafts can adequately reproduce the tests. It has been used to further investigate the effect of the lineal spacing of longitudinal bars on the structural performance of the piles.

Both the numerical and experimental observations indicate that the lineal spacing of longitudinal bars does not have any effect on the ductility of the circular piles and the lateral load-vs.-drift ratio response. However, the ductility of a pile can be affected by the size of the longitudinal bars. Larger-diameter bars are more resistant to buckling for the same spacing of the transverse reinforcement, and can therefore lead to a more ductile behavior of a laterally loaded RC member. A numerical parametric study has confirmed that these observations are valid for pile with larger diameters and subjected to higher axial loads.

The numerical study has also confirmed the fact that the lineal spacing and the size of the longitudinal bars have a small influence on the spacing and the width of flexural cracks. A closer

bar spacing with a larger number of smaller-size longitudinal bars leads to smaller crack widths and more closely spaced flexural cracks. Moreover, as observed both in the tests and the FEA, a pile with larger-diameter longitudinal bars and larger bar spacing has more concentrated plastic deformation near the base. Bars of smaller diameter have a lower bond stress demand and therefore less bond slip. This leads to higher tensile strains in the bars in the vicinity of flexural cracks.

The new microplane model developed by Caner and Bazant (2013a) was also employed to simulate the behavior of concrete in the pile specimens. It was first implemented in a user-defined subroutine in Abaqus (Simulia 2014) and was calibrated and verified with the tests of Hurblut (1985), van Mier (1986) and Mander et al. (1988b). One superior feature of the microplane model, compared to the damaged-plasticity model provided in Abaqus, is its ability to accurately simulate the tensile unloading and reloading behavior of concrete. Furthermore, the microplane model can accurately reproduce both the enhanced compressive strength and the more ductile post-peak behavior of confined concrete. The damaged-plasticity model can only reproduce the enhanced compressive strength and not the enhanced ductility when the concrete is confined.

4.6 Acknowledgement of Publication

This chapter, in full, is a reprint of the material as it appears in the report submitted to the California Department of Transportation in 2015, Papadopoulos, V., Shing, P. B., under the title "Influence of the Spacing of Longitudinal Reinforcement on the Performance of Laterally Loaded CIDH Piles – Analytical Investigation". The dissertation author was the primary investigator and author of this report.

Table 4.1 – Damaged-plasticity model calibration for concrete in the pile

Parameter	Description	Specimen #1	Specimen #2
f_c' (ksi)	Compressive strength	4.9	5.2
f_t' (ksi)	Tensile strength	$f_t' = 8\sqrt{f_c'}$	
$\sigma_{b0/}\,\sigma_{c0}$	Controls biaxial compressive strength	0.12	
ψ	Dilation angle	20^o	
ε	eccentricity	0	
K_c	Controls shape of yield surface	1	
w_c	Compression recovery factor	0	
w_t	Tension recovery factor	1	

Table 4.2 – Steel material parameters for longitudinal reinforcement

Parameter	Description	Specimen #1	Specimen #2
f_y (ksi)	Yield stress	64	67
E_s (ksi)	Elastic Stiffness	29000	
ε_f'	1st LCF coefficient	0.0966	0.0936
c	2nd LCF coefficient	0.4000	0.4077

Table 4.3 – Lateral load capacity of pile specimens

Specimen no.	Test (kips)	FEA (kips)	FE prediction error
#1 (north)	73	65	0.11
#1 (south)	72	66	0.08
#2 (north)	78	69	0.11
#2 (south)	73	71.5	0.02

Table 4.4 – Cycles at which bars fractured in Specimen #1

Bar no.	Bar fracture in test	Bar fracture in FEA
1	2nd cycle at +10%	1st cycle at -10%
4	2nd cycle at -10%	2nd cycle at +10%

Table 4.5 – Cycles at which bars fractured in Specimen #2

Bar no.	Bar fracture in test	Prediction of bar fracture in FEA
1	1st cycle at +10%	2nd cycle at -8%
4	1st cycle at -10%	1st cycle at +10%
3, 5	1st cycle at -10%	1st cycle at -10%
2, 6	no fracture-	2nd cycle at +10%

Table 4.6 –Piles properties for parametric study

Pile Model	Diameter (in.)	Height (ft.)	Number of bars	Angular spacing (degree)	Lineal spacing (in.)	Longitudinal reinf. ratio (%)	Transverse reinf. (ratio)
D28S1	28	10	6 No. 11	60	11.0	1.52	No. 6 @5.75'' (1.28%)
D28S2			10 No. 9	36	6.75	1.62	
D28S3			16 No. 7	22.5	4.25	1.56	
D28S4			8 No. 10	45	8.80	1.65	
D56S1	56	20	6 No. 18 & 6 No. 14	60	24.7	1.52	No. 9 @6.0'' (1.28)
D56S2			10 No.18	36	15.0	1.62	
D56S3			16 No. 14	22.5	9.50	1.46	

Table 4.7 – Pile models with varying level of axial load

Pile Model	Lineal Spacing (in.)	Axial load (% of $A_g f_c'$)
D28S1	11	10 (tested)
		15
		20
D28S2	6.75	10 (tested)
		15
		20

Table 4.8 – Calibration of microplane model for concrete in pile specimens

Concrete	k_2, k_3	E (MPa)	k_1 (x10^{-4})	f_c' (MPa), ε_p
Confined	default	5,890	0.5	5.0, 0.0015
Unconfined	1, 1	6,520	1.65	5.0, 0.0015

Table 4.9 – Cycles at which bars fractured in Specimen #1

Bar no.	Bar fracture in test	Bar fracture in FEA
1	2nd cycle at +10%	1st cycle at -10%
4	2nd cycle at -10%	2nd cycle at +10%

Table 4.10 – Cycles at which bars fractured in Specimen #2

Bar no.	Bar fracture in test	Bar fracture in FEA
1	1st cycle at +10%	2nd cycle at +8%
4	1st cycle at -10%	2nd cycle at -8%
3, 5	1st cycle at -10%	1st cycle at -10%
2, 6	no fracture	2nd cycle at +10%

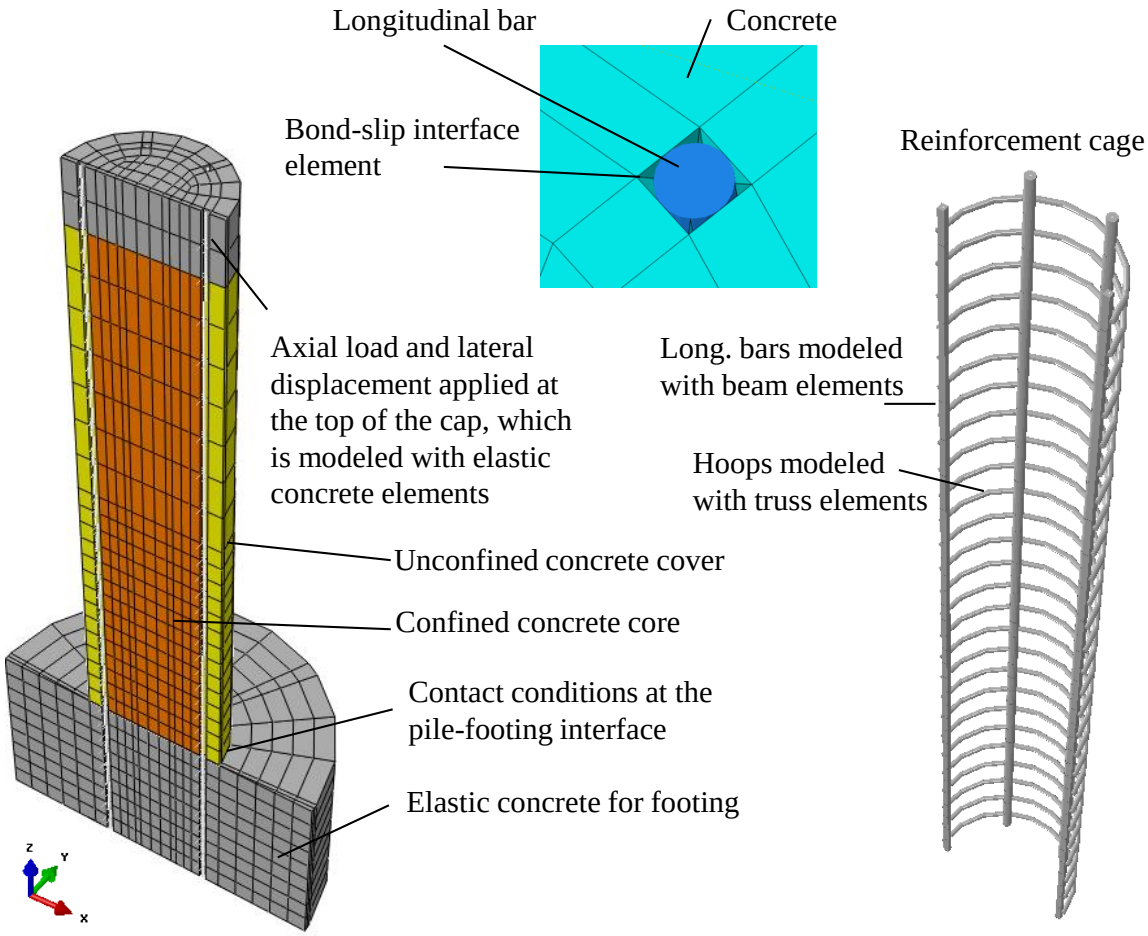

Figure 4.1 – FE model of Specimen #1

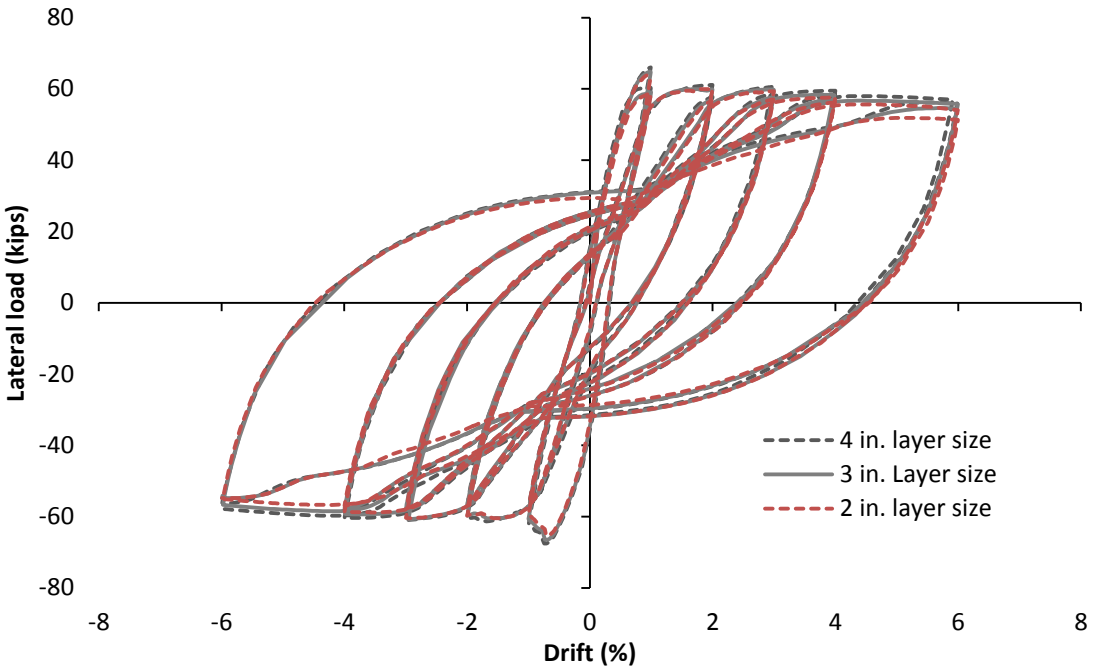

Figure 4.2 – Mesh-size sensitivity study with the FE model of Specimen #1

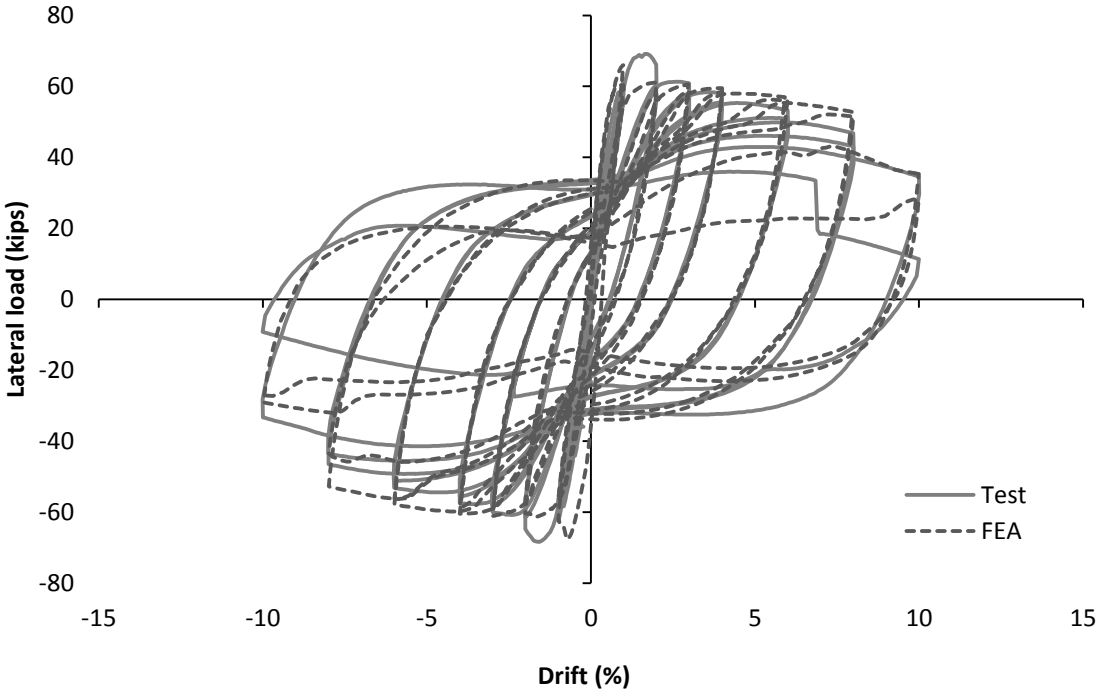

Figure 4.3 - Lateral load-vs.- drift ratio curves for Specimen #1

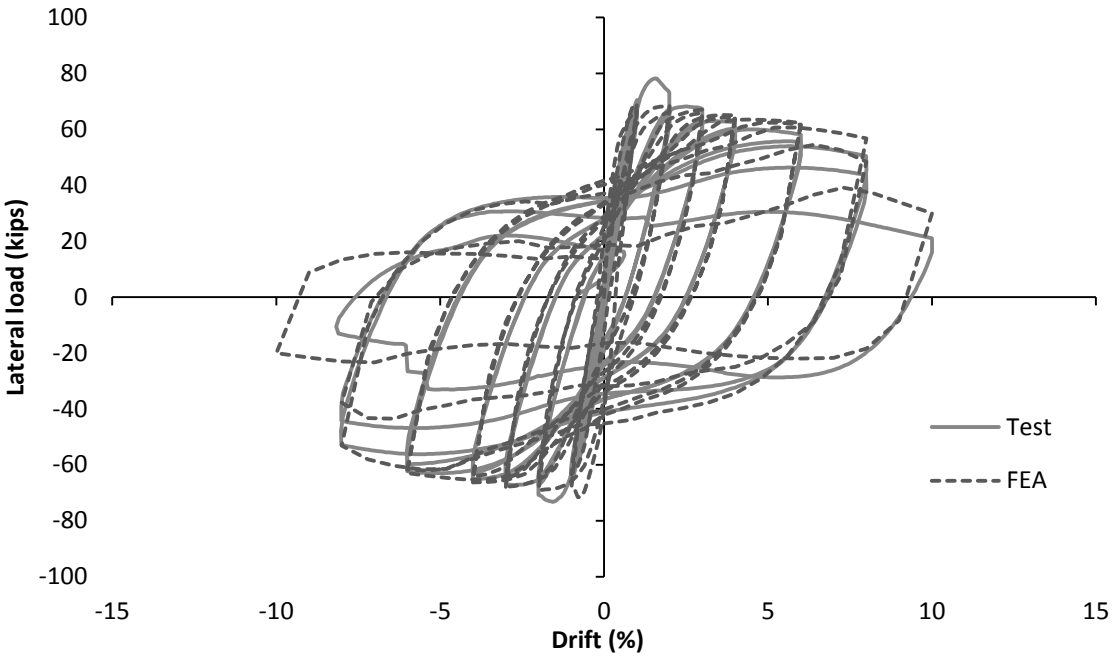

Figure 4.4 – Lateral load-vs.- drift ratio curves for Specimen #2

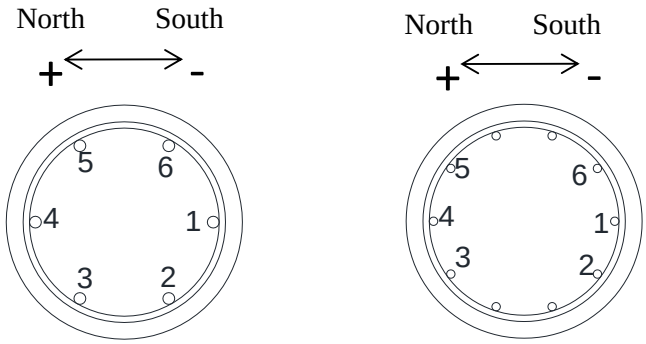

(a) Specimen #1 (b) Specimen #2

Figure 4.5 – Numbering of longitudinal bars in Specimens #1 and #2

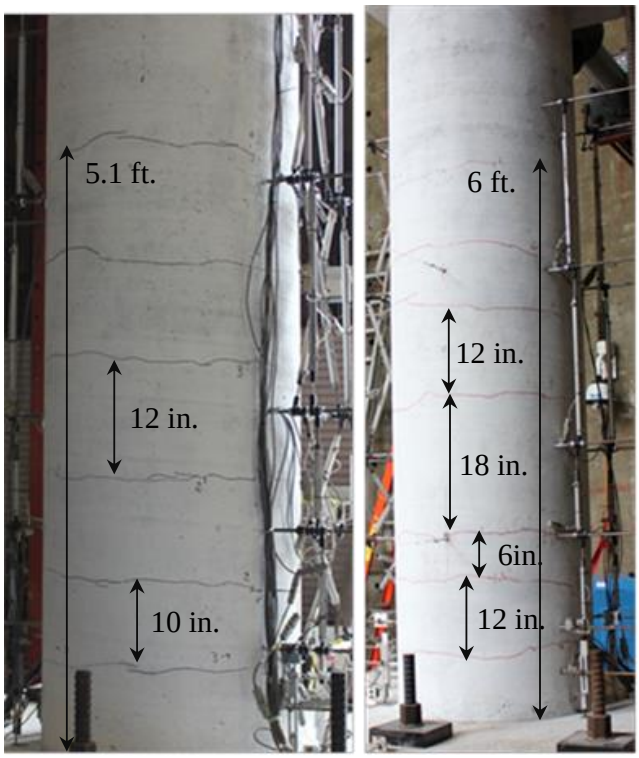

(a) South face (b) North face

Figure 4.6 – Flexural cracking in Specimen #1 at 1% drift

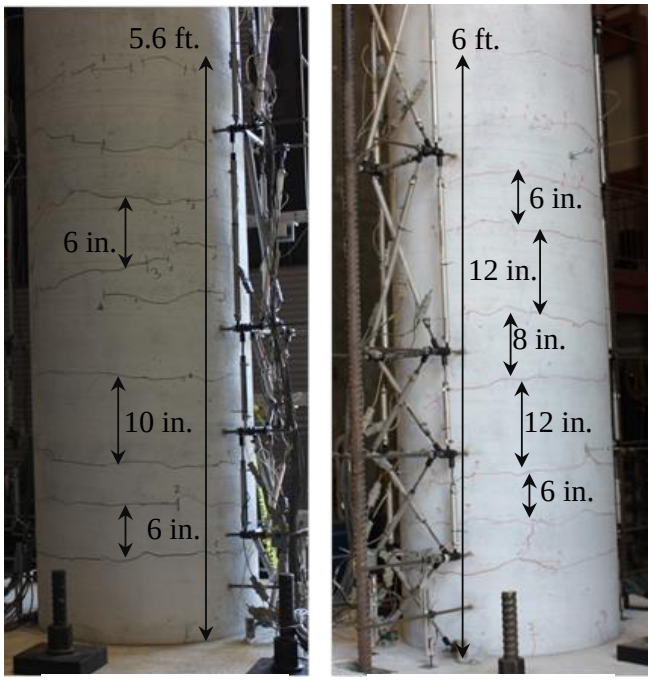

(a) South face (b) North face

Figure 4.7 – Flexural cracking in Specimen #2 at 1% drift

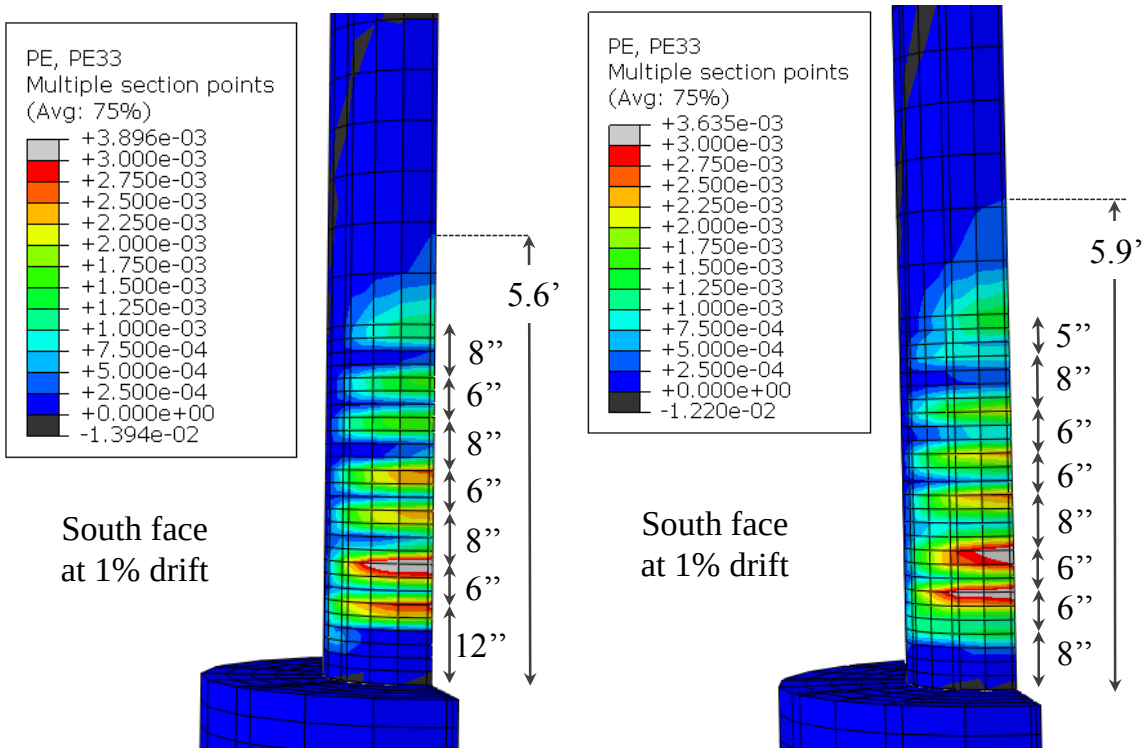

(a) Specimen #1 (b) Specimen #2

Figure 4.8 – Normal plastic strains in concrete

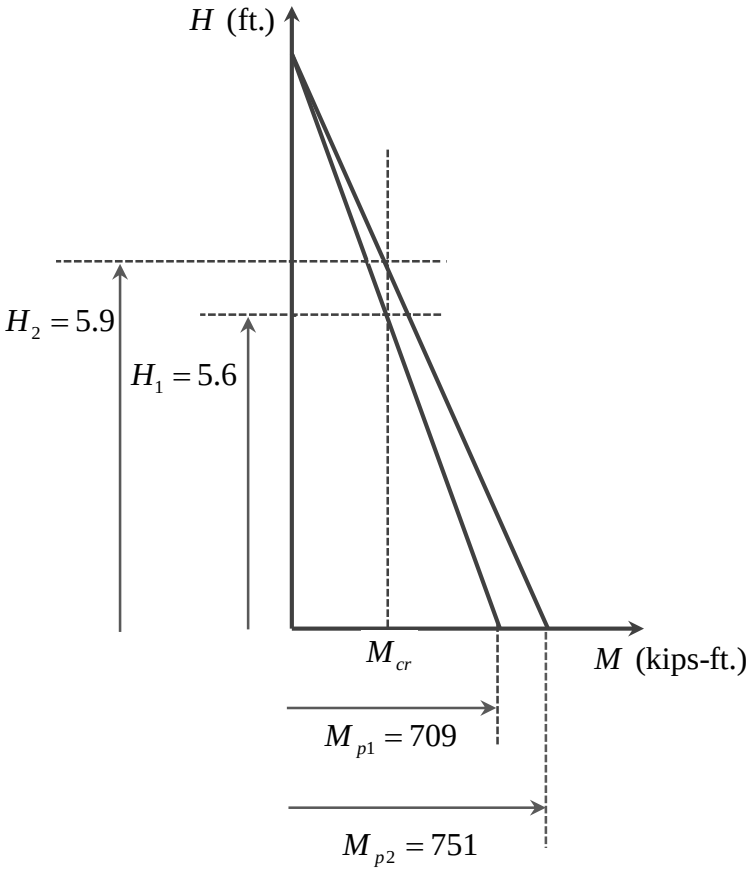

Figure 4.9 – Extent of flexural cracking for moment capacities M_{p1} (Specimen #1) and M_{p2} (Specimen #2)

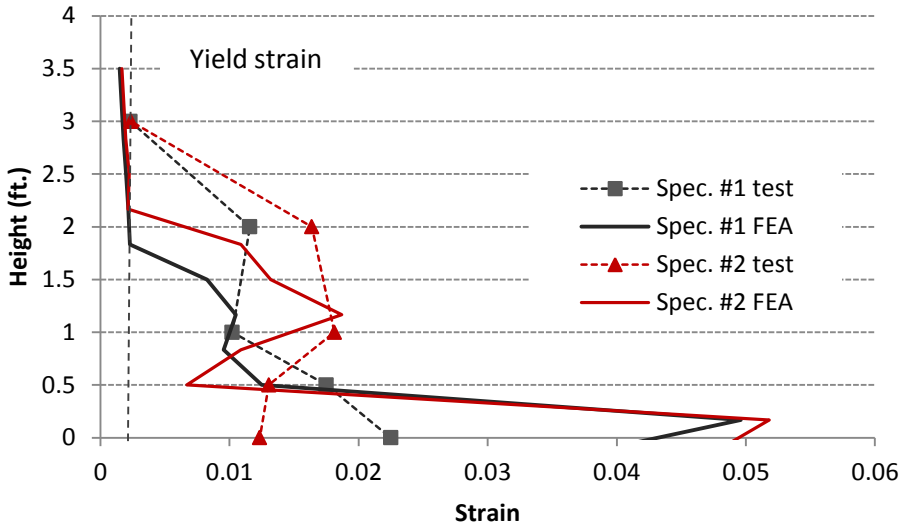

Figure 4.10 – Strains along the longitudinal bar 1 at the south face at +4% drift

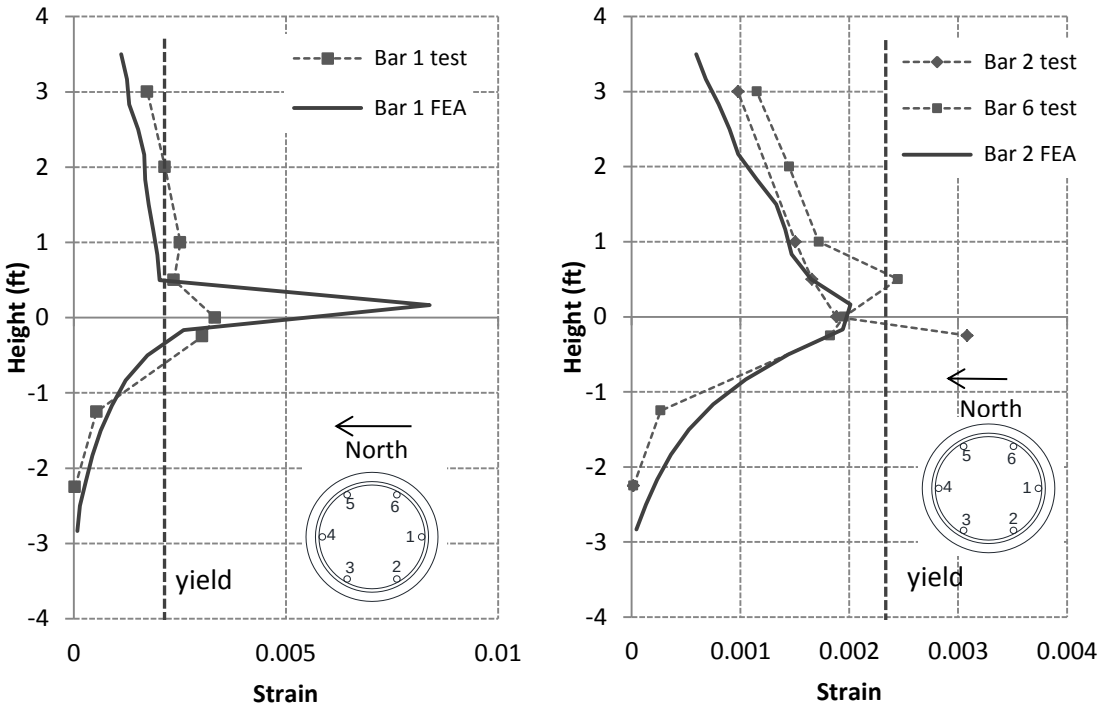

(a) Bar 1 (b) Bars 2 & 6

Figure 4.11 – Strains in bars at the south face of Specimen #1 at +1% drift

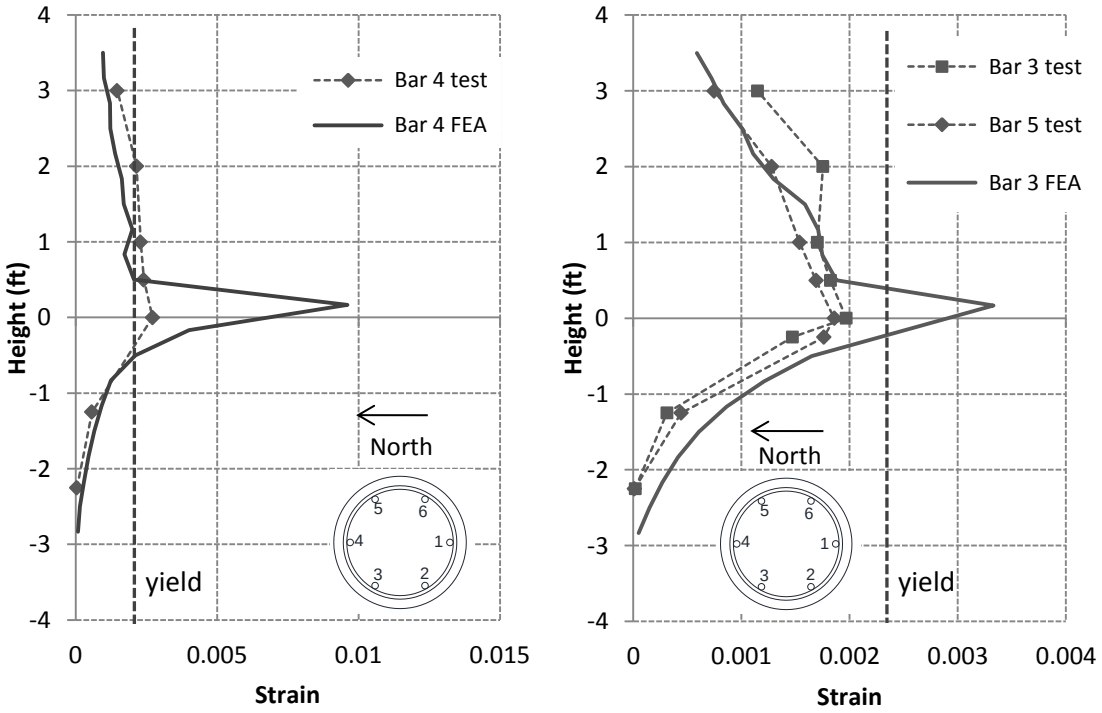

(a) Bar 4 (b) Bars 3 & 5

Figure 4.12 – Strains in bars at the north face of Specimen #1 at -1% drift

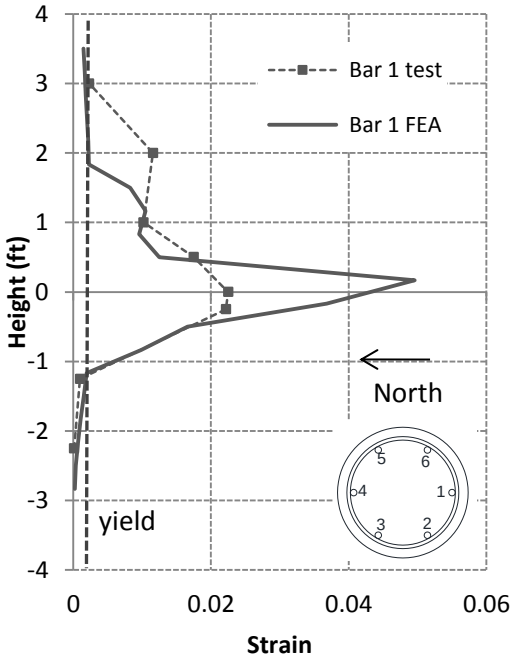

(a) Bar 1

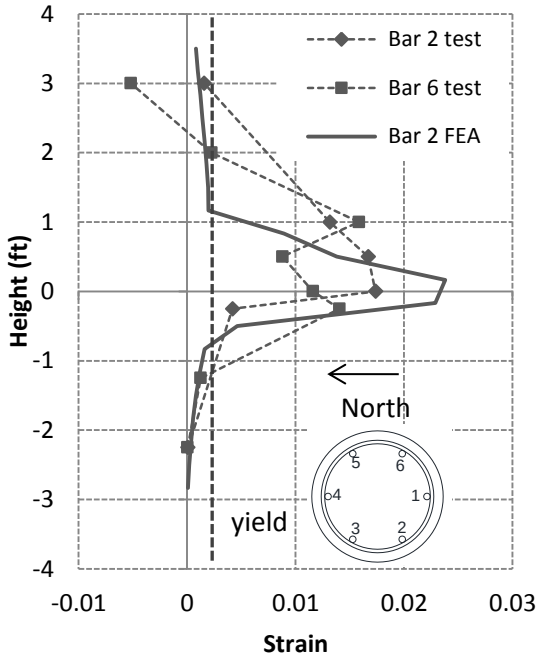

(b) Bars 2 & 6

Figure 4.13 – Strains in bars at the south face of Specimen #1 at +4% drift

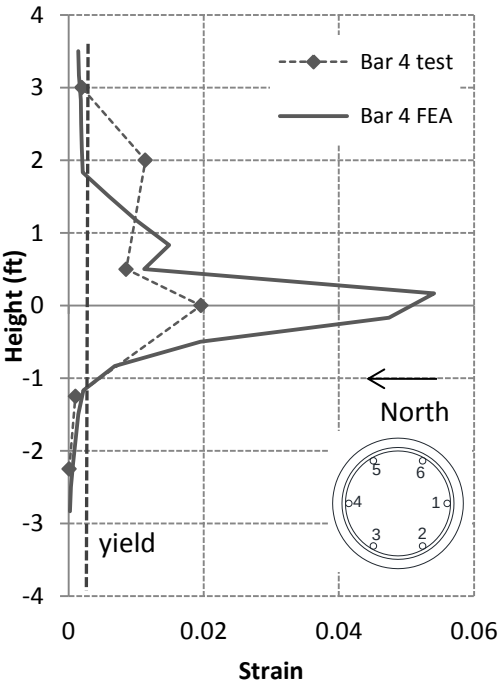

(a) Bar 4

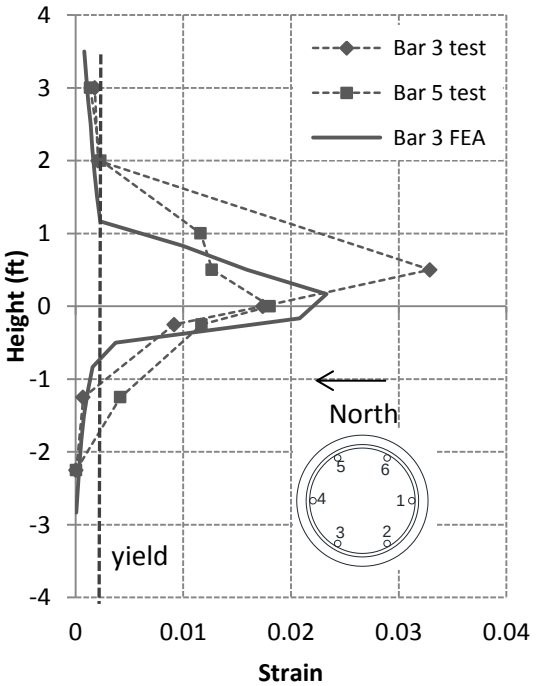

(b) Bars 3 & 5

Figure 4.14 – Strains in bars at the north face of Specimen #1 at -4% drift

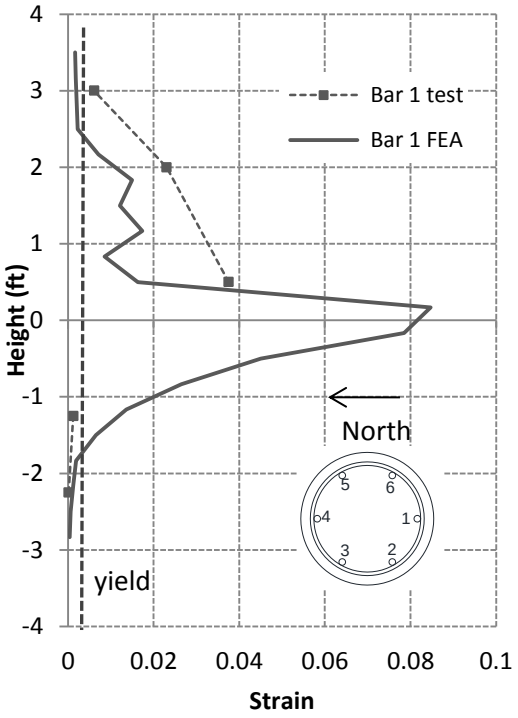

(a) Bar 1

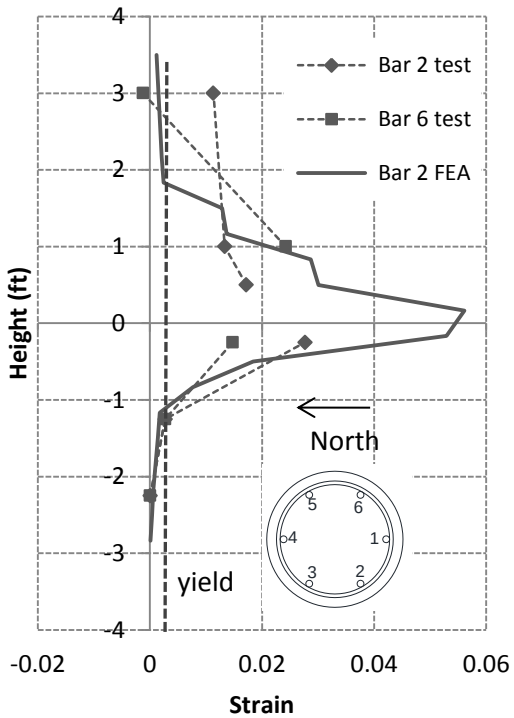

(b) Bars 2 & 6

Figure 4.15 – Strains in bars at the south face of Specimen #1 at +8% drift

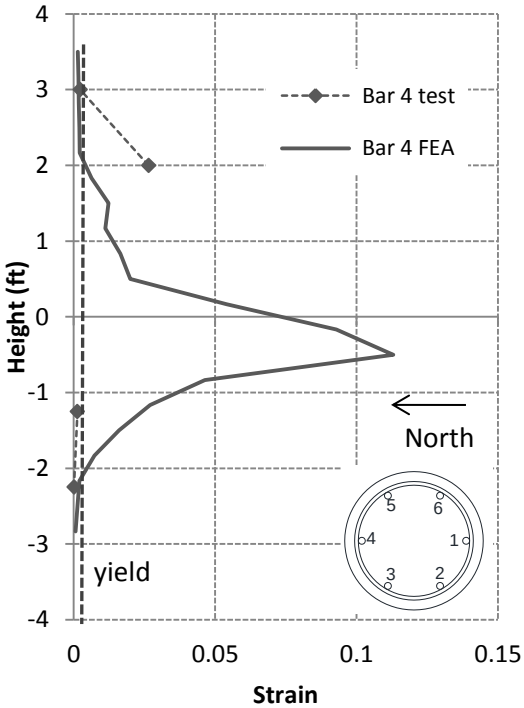

(a) Bar 4

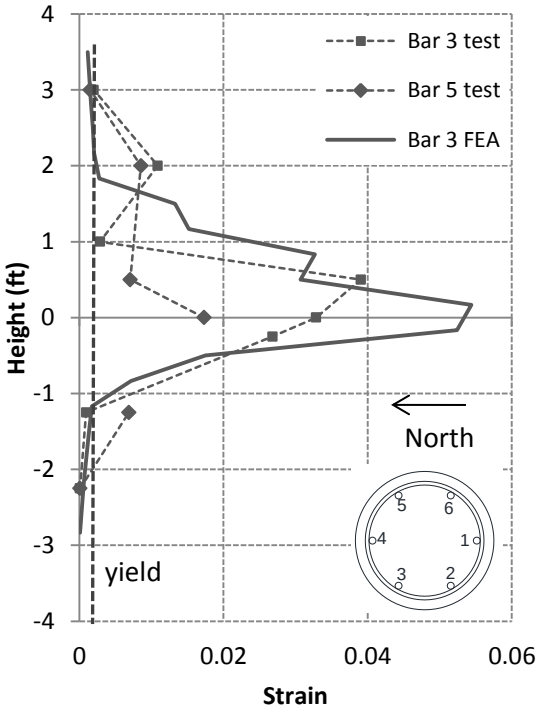

(b) Bars 3 &5

Figure 4.16 – Strains in bars at the north face of Specimen #1 at -8% drift

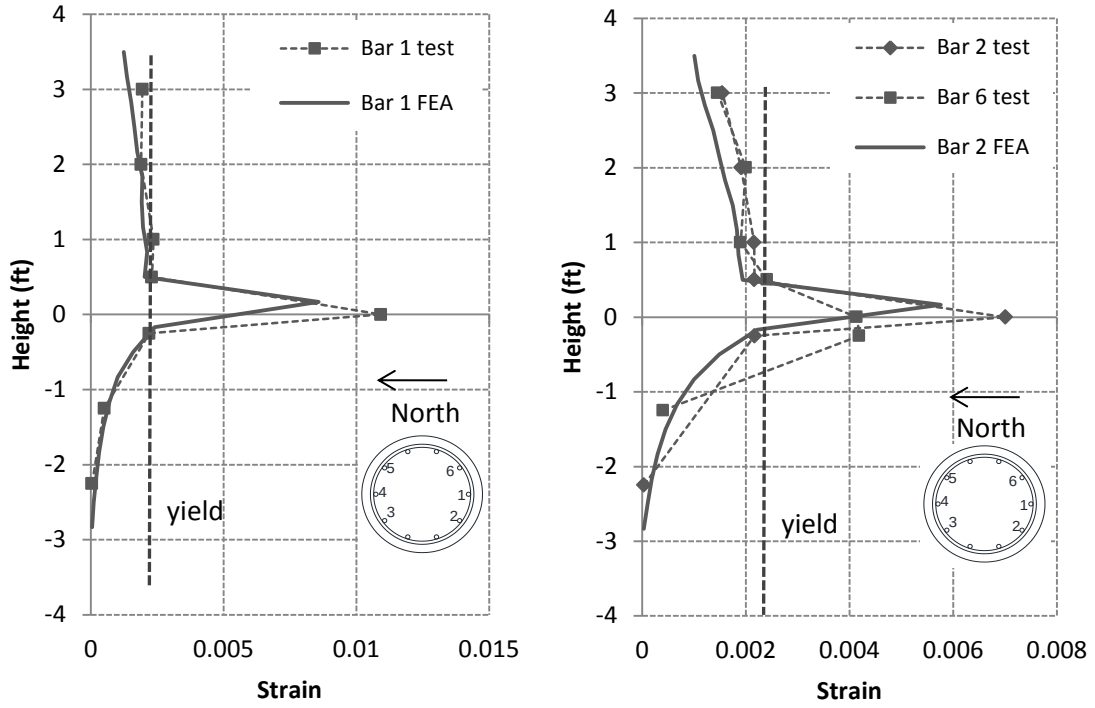

(a) Bar 1 (b) Bars 2 & 6

Figure 4.17 - Strains in bars at the south face of Specimen #2 at +1% drift

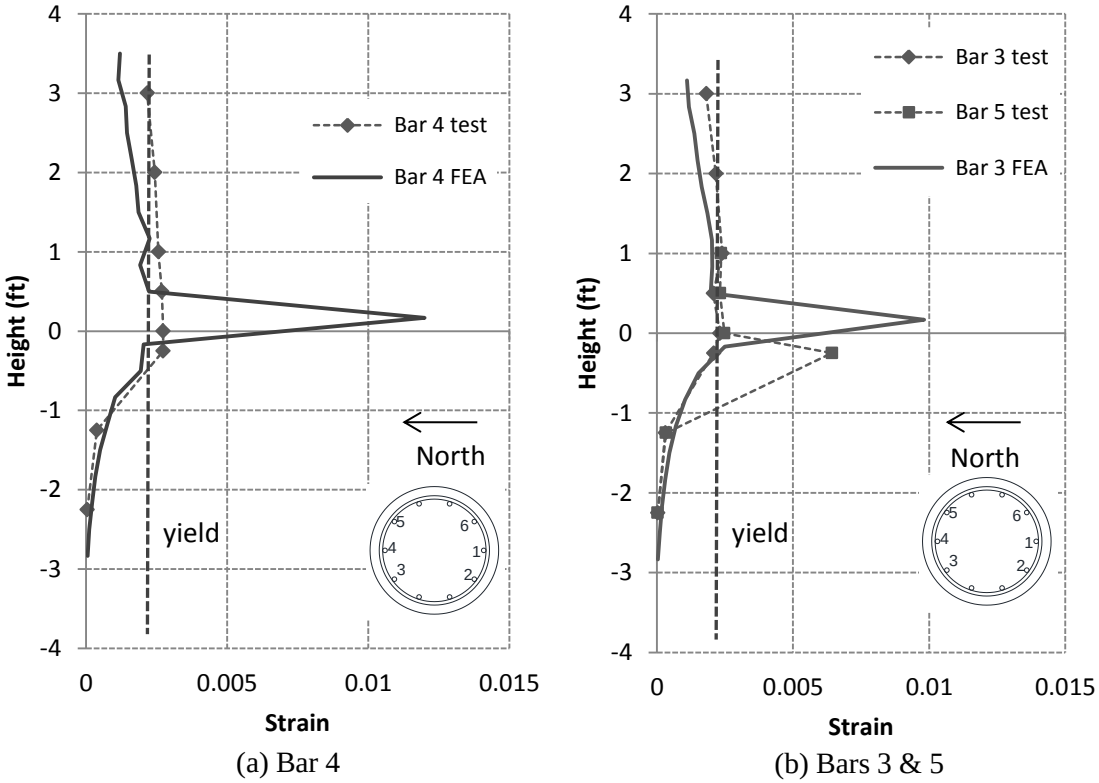

(a) Bar 4 (b) Bars 3 & 5

Figure 4.18 – Strains in bars at north face of Specimen #2 at -1% drift

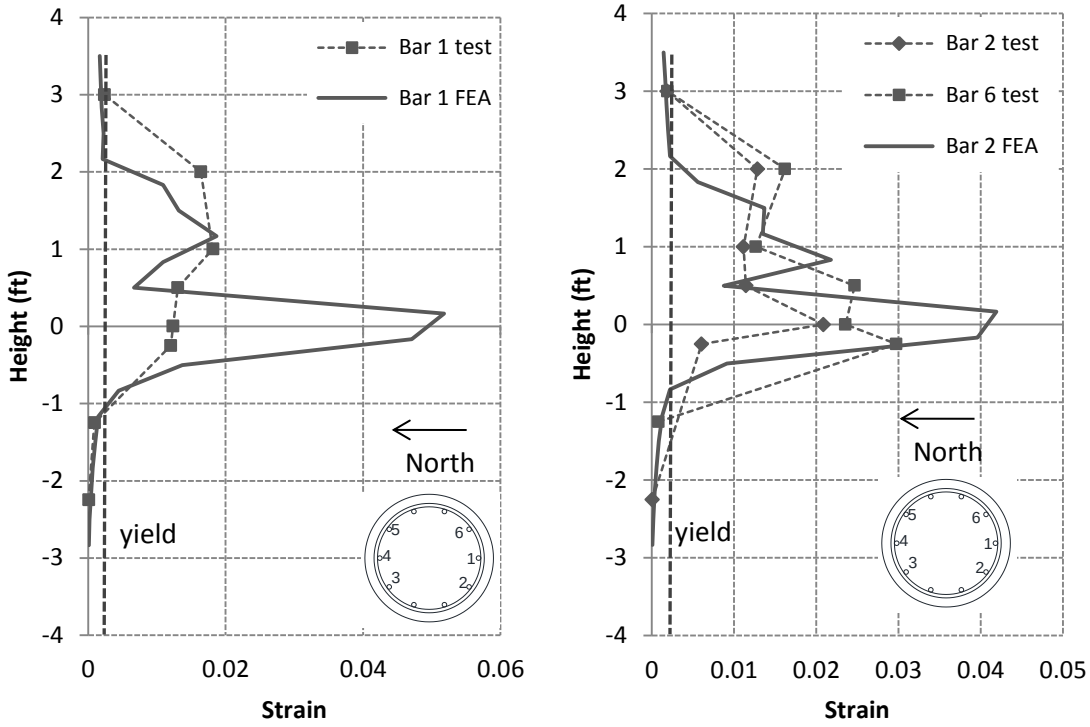

(a) Bar 1 (b) Bars 2 & 6

Figure 4.19 – Strains in bars at south face of Specimen #2 at +4% drift

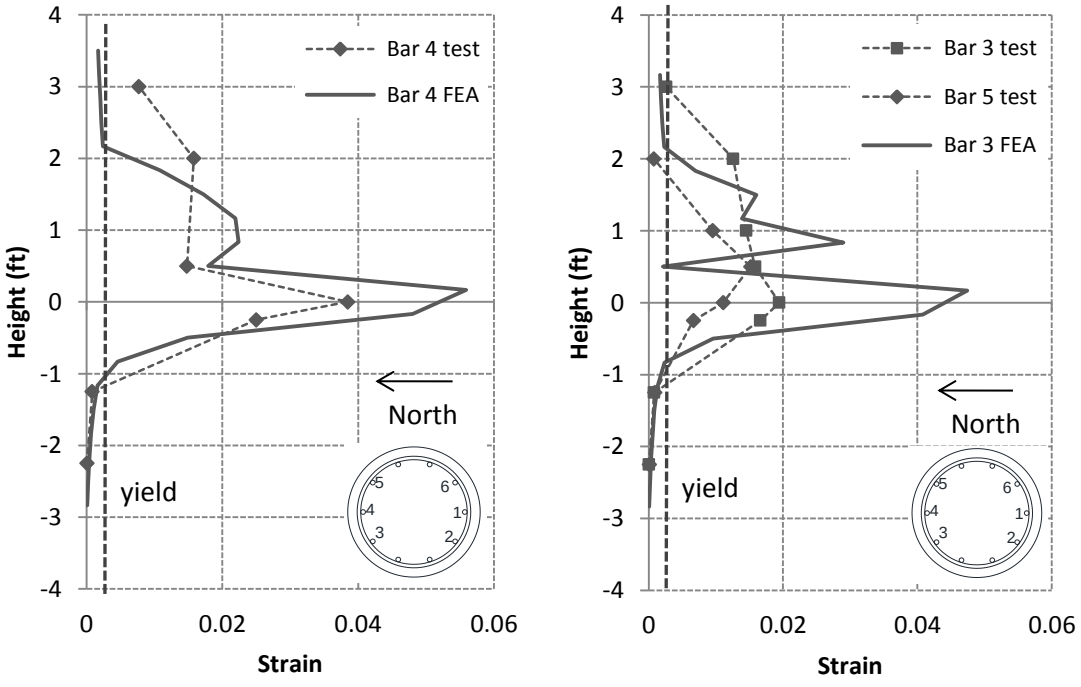

(a) Bar 4 (b) Bars 3 & 5

Figure 4.20 – Strains in bars at north face of Specimen #2 at -4% drift

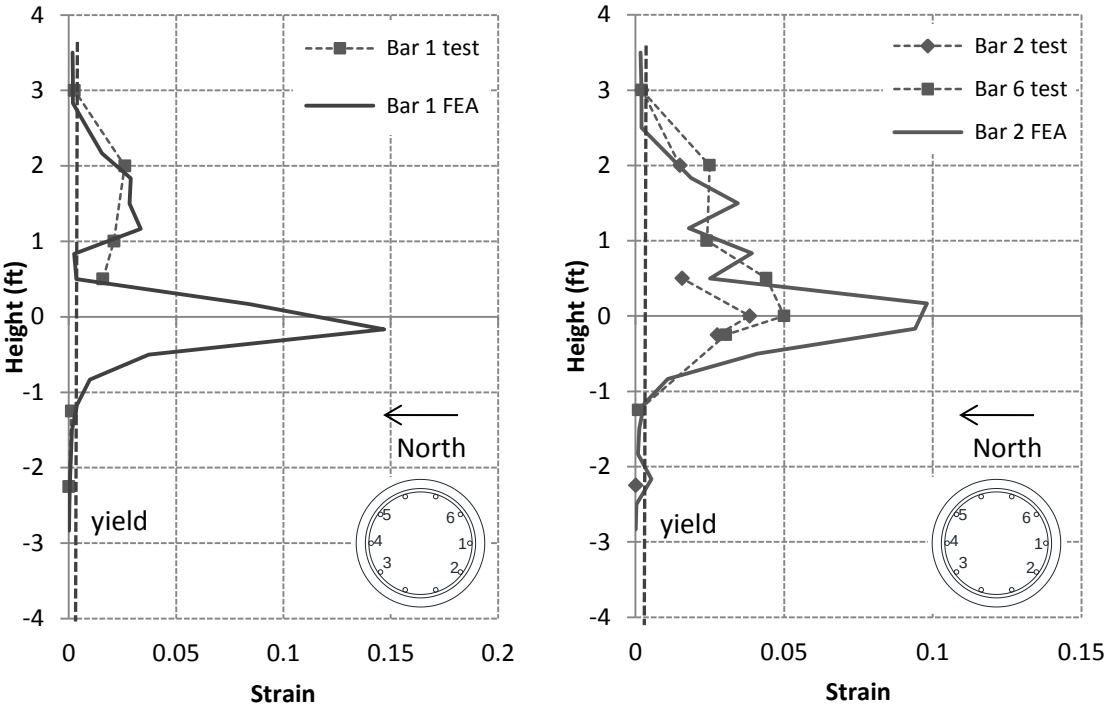

(a) Bar 1 (b) Bars 2 & 6

Figure 4.21 – Strains in bars at south face of Specimen #2 at +8% drift

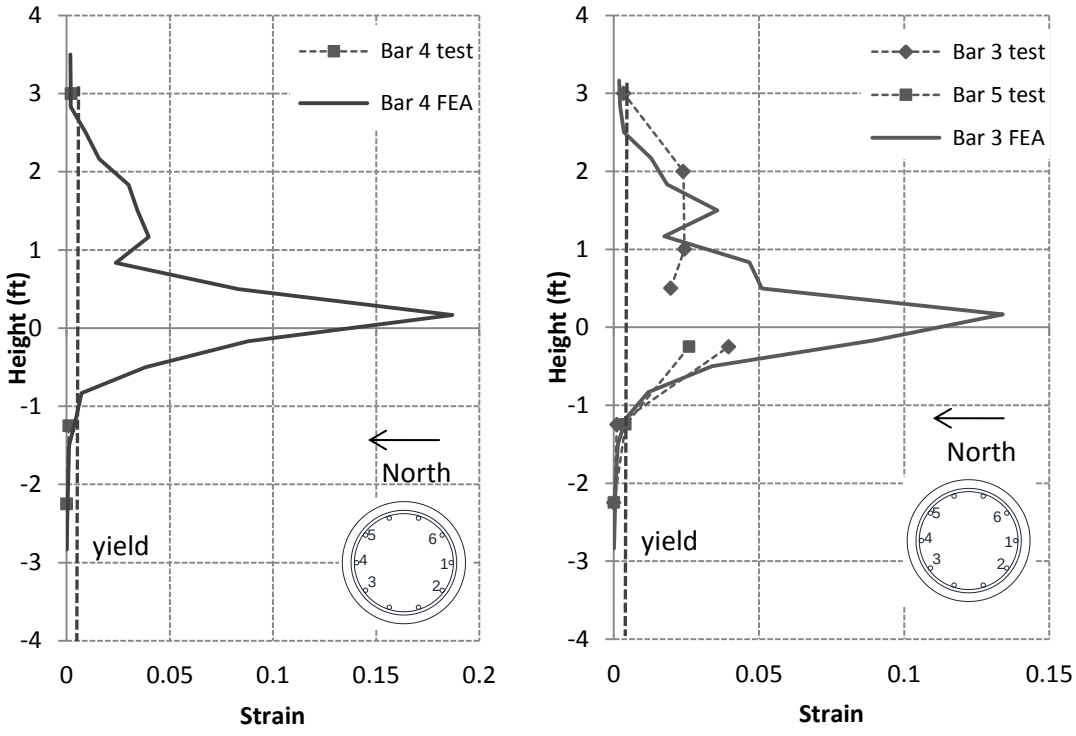

(a) Bar 4 (b) Bars 3 & 5

Figure 4.22 – Strains in bars at north face of Specimen #2 at -8% drift

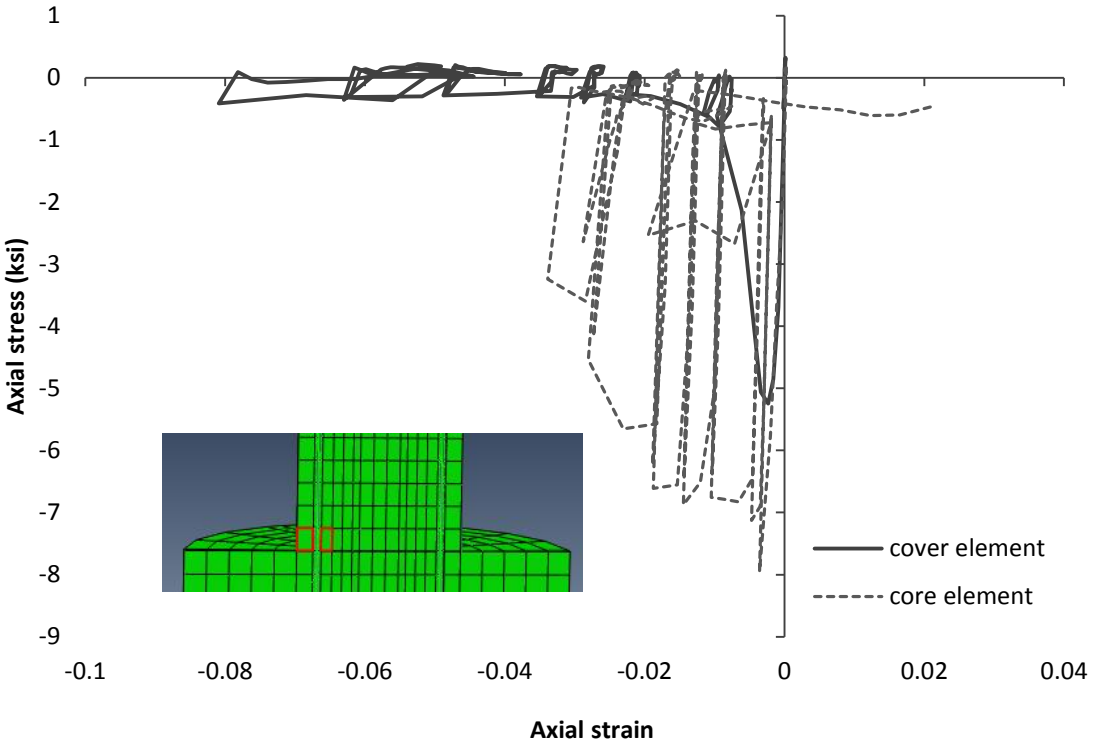

Figure 4.23 – Axial stress-strain curves from cover concrete and core concrete for Specimen #1

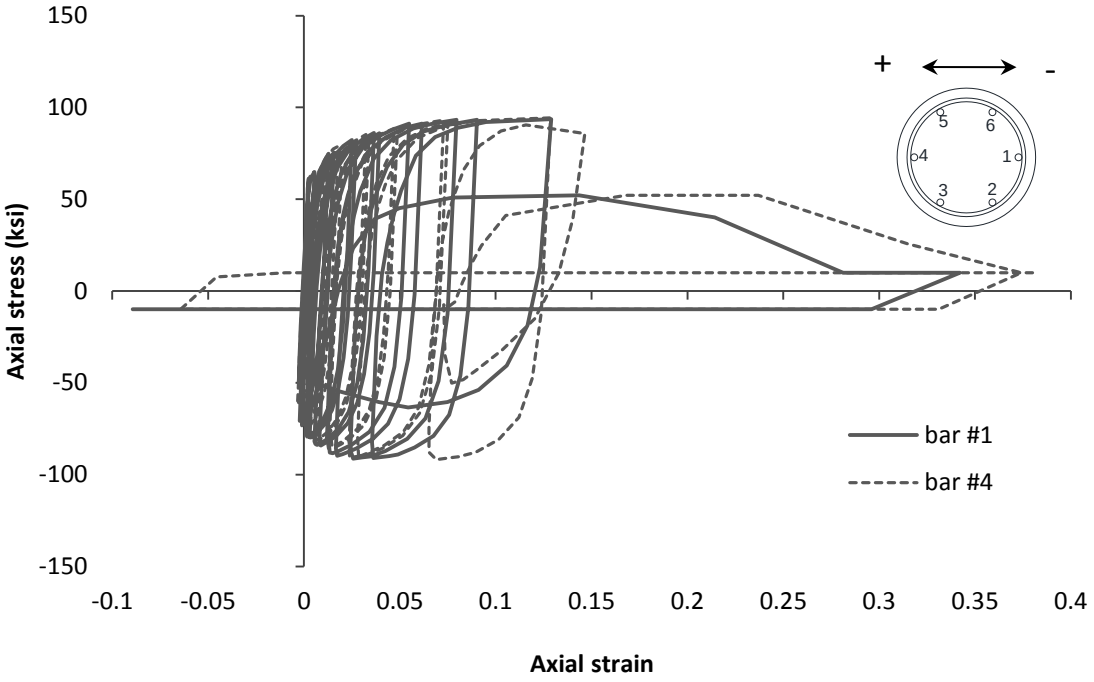

Figure 4.24 –Stress-strain curves for longitudinal bars at the base of the pile of Specimen #1

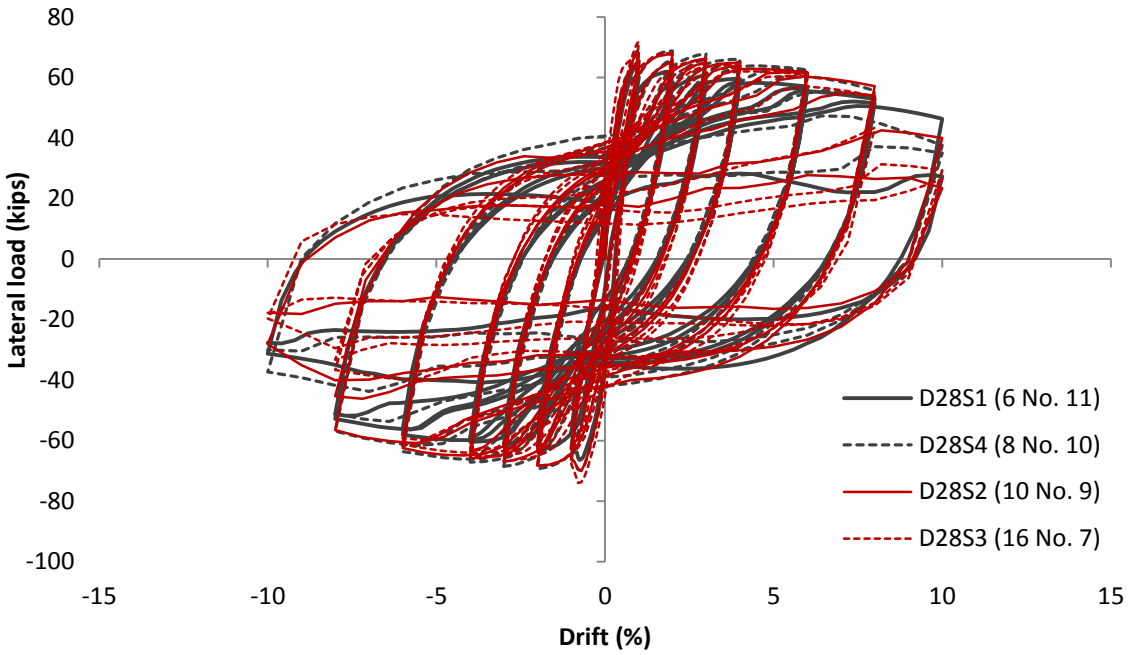

Figure 4.25 – Lateral load-vs.-drift ratio curves for models with *D*=28 in.

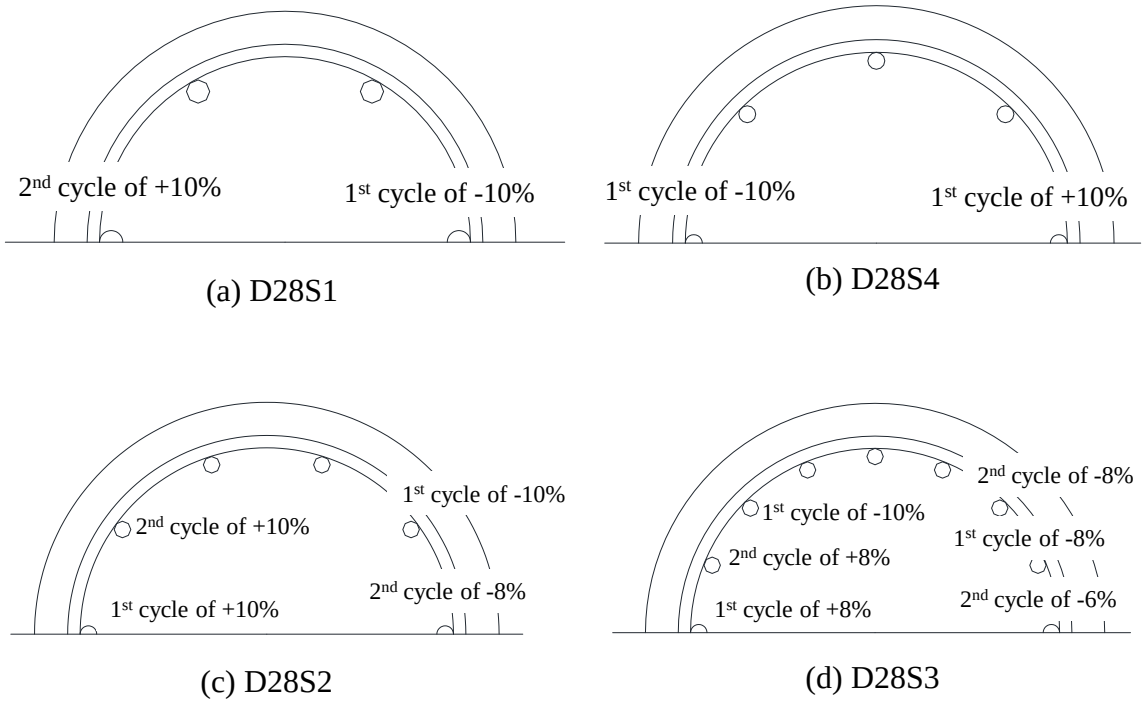

Figure 4.26 – Cycles at which the longitudinal bars fractured for models with *D*=28 in.

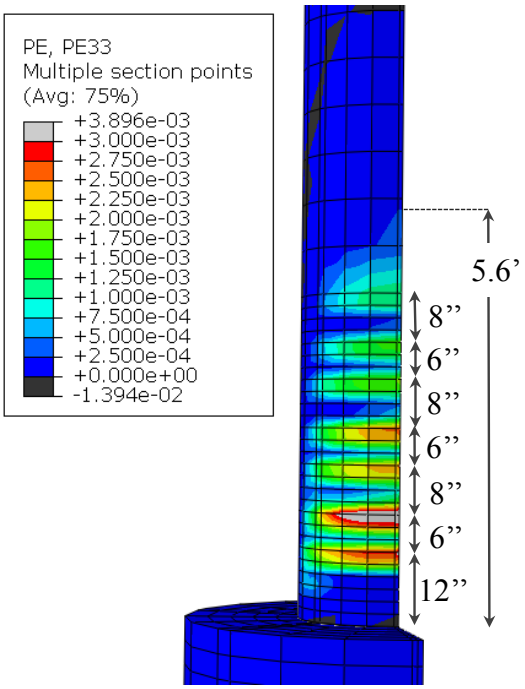

(a) D28S1

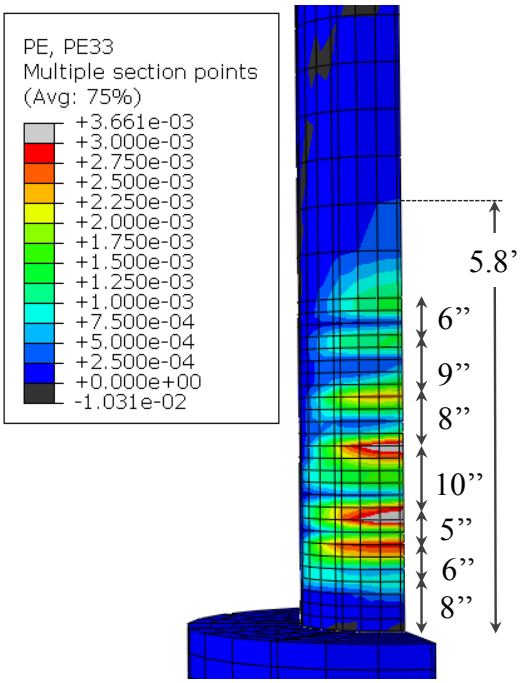

(b) D28S4

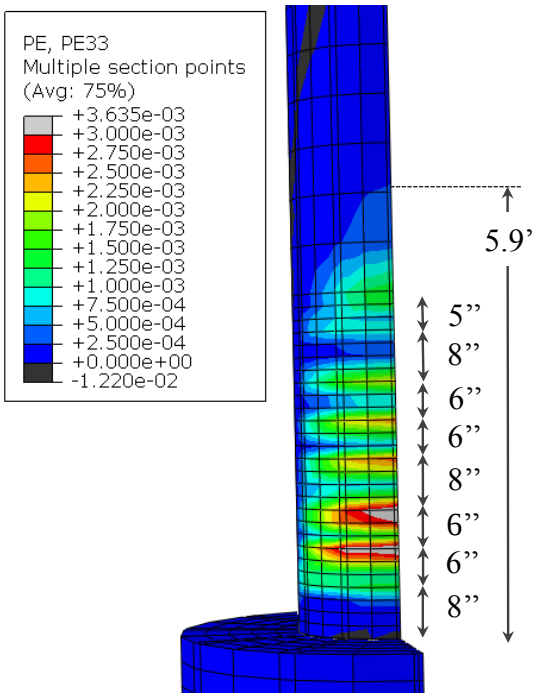

(c) D28S2

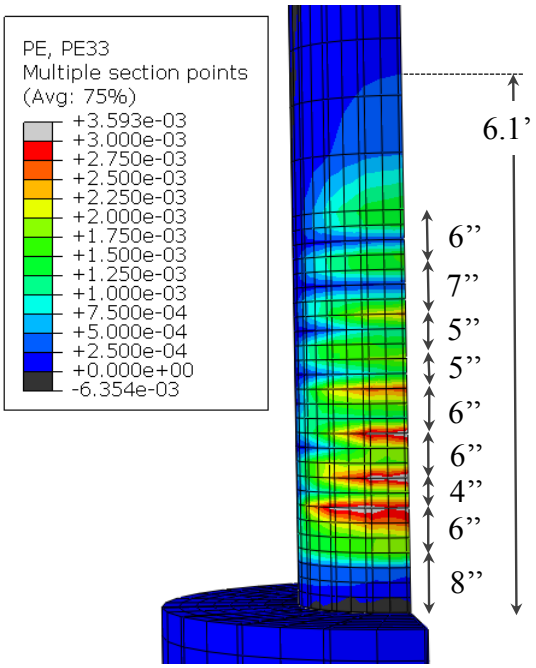

(d) D28S3

Figure 4.27 – Normal plastic strains in the axial direction at 1% drift for models with *D*=28 in.

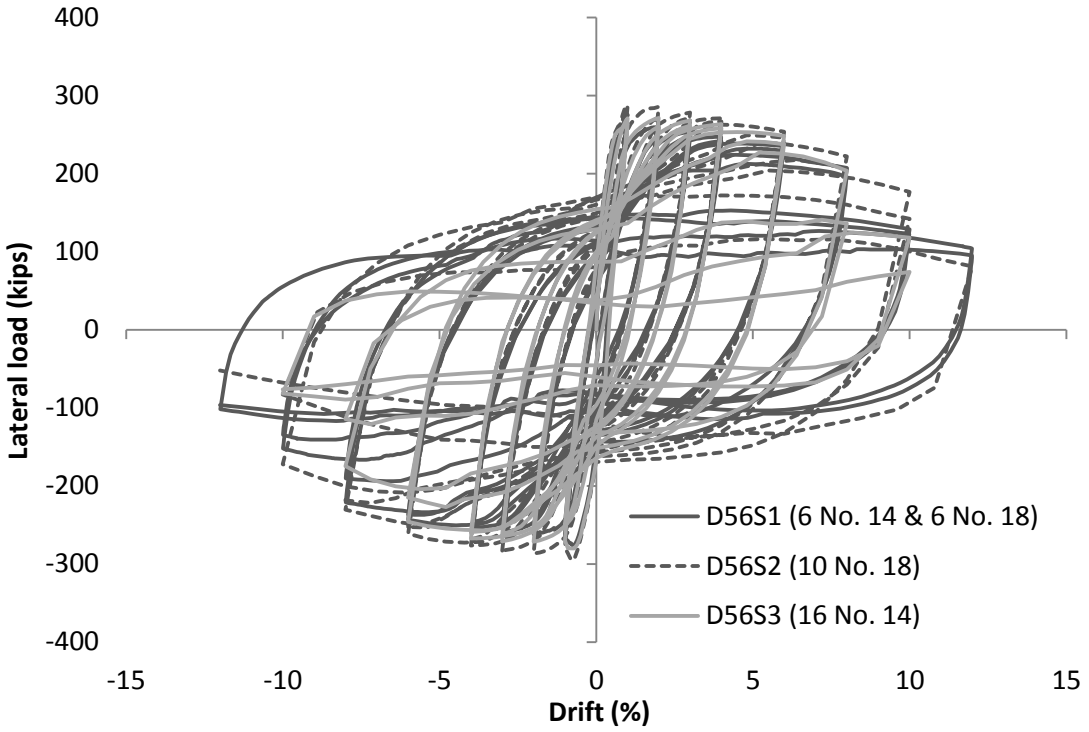

Figure 4.28 – Lateral load-vs.-drift ratio curves for models with *D*=56 in.

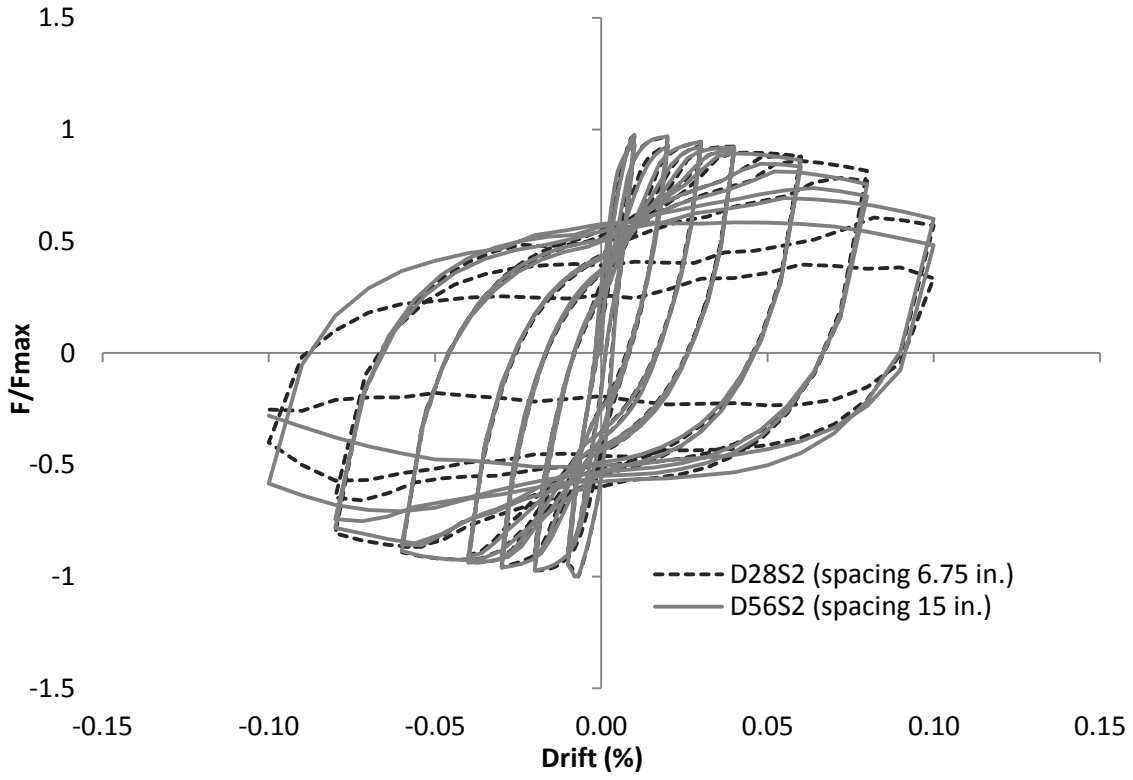

Figure 4.29 – Normalized lateral load-vs.-drift ratio curves of pile models with different diameter

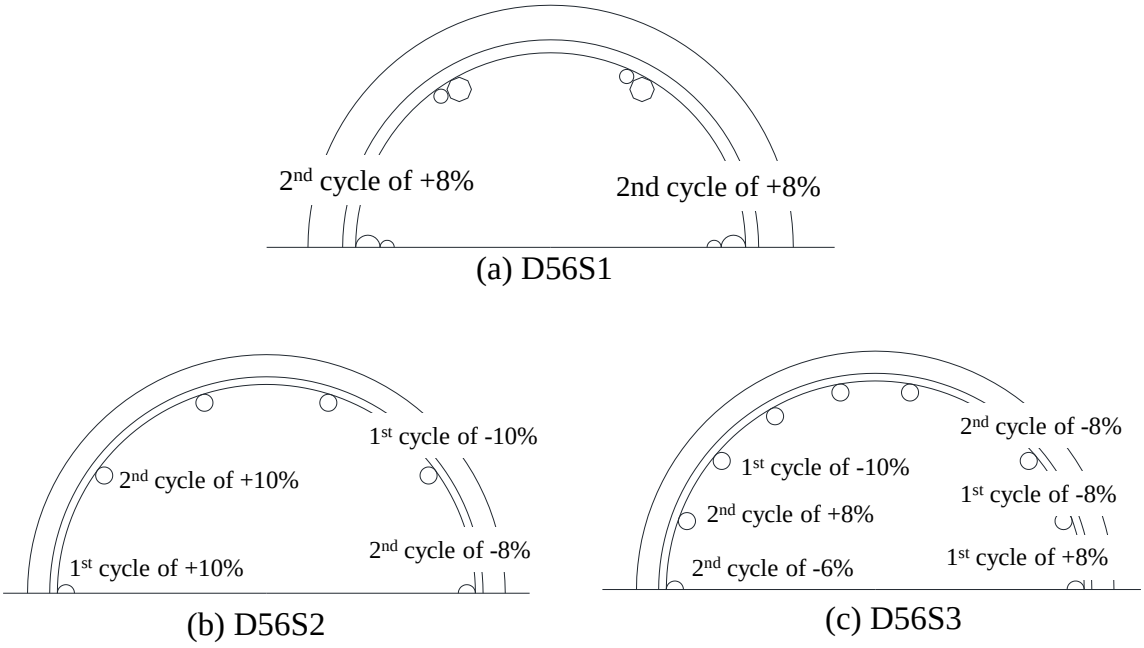

Figure 4.30 – Cycles at which the longitudinal bars fractured for models with *D*=56 in.

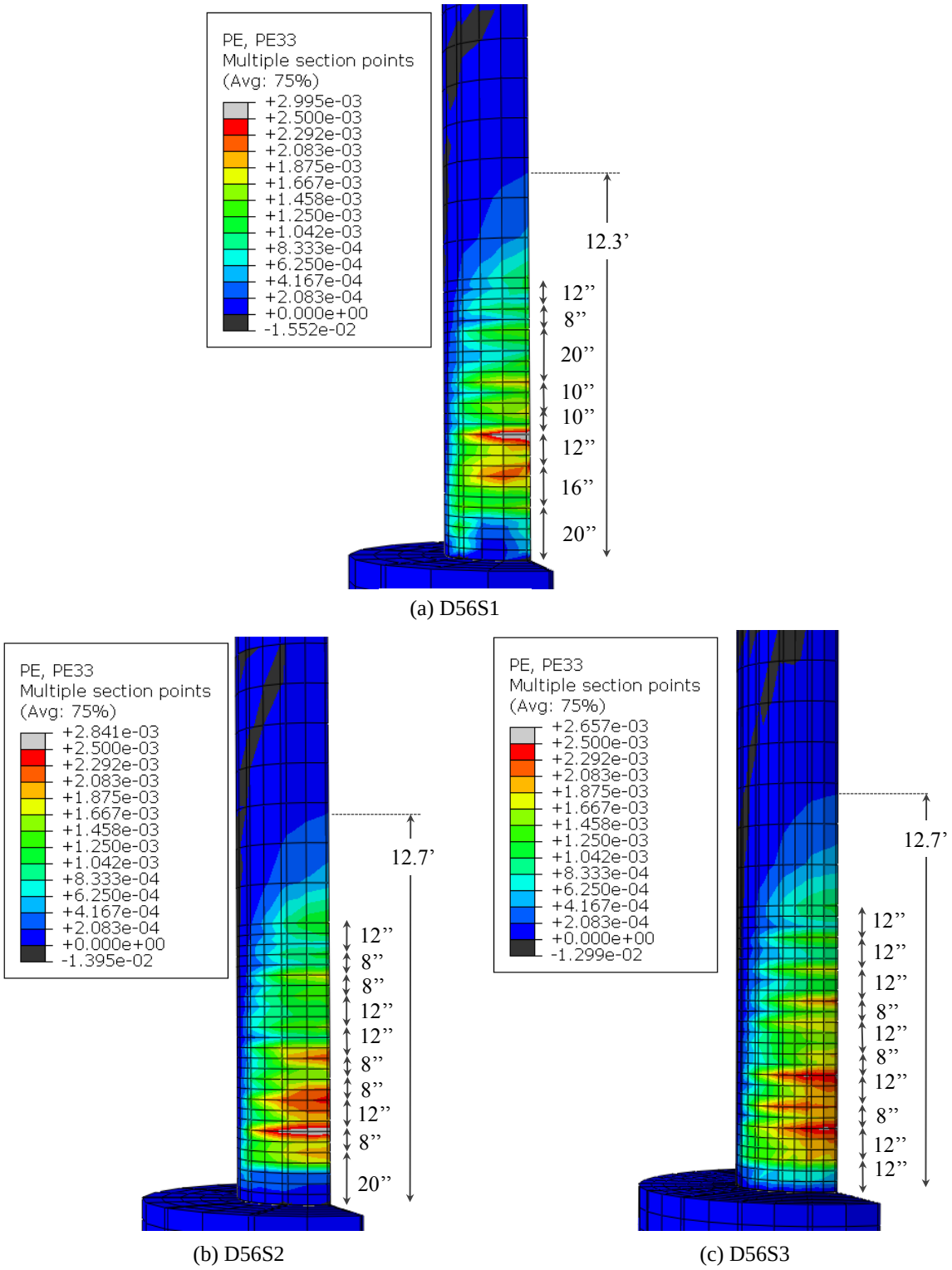

(a) D56S1

(b) D56S2

(c) D56S3

Figure 4.31 – Normal plastic strains in the axial direction at 1% drift for models with *D*=56 in.

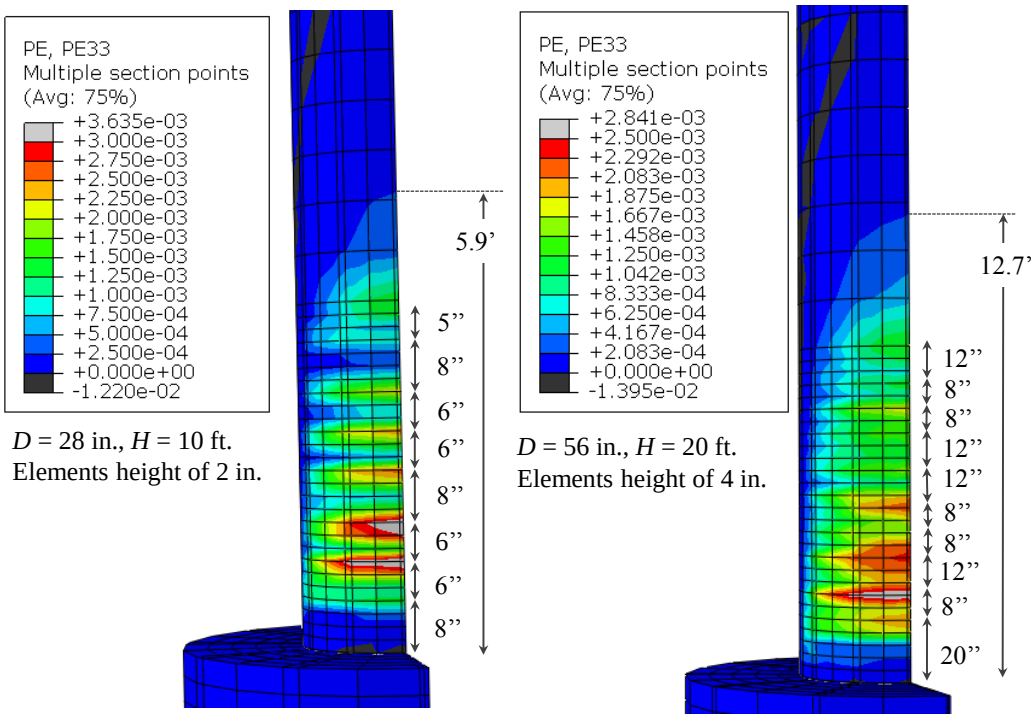

Figure 4.32 – Normal plastic strains in the axial direction at 1% drift for piles D28S2 and D56S2

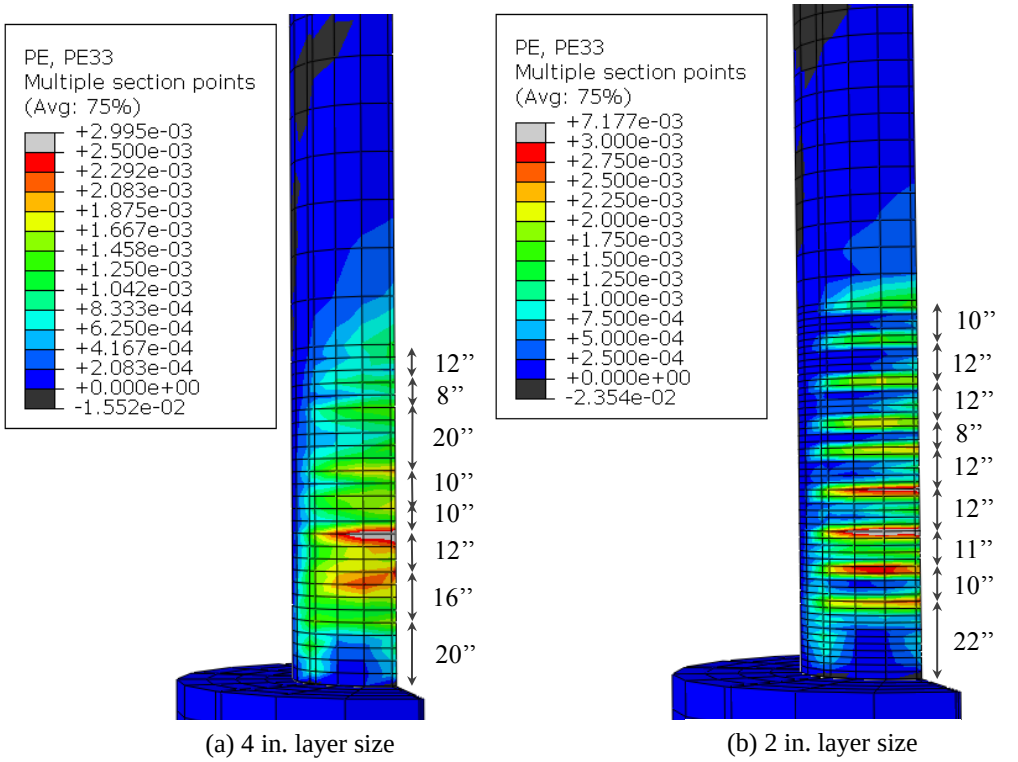

Figure 4.33 – Mesh sensitivity study for the normal plastic strains in pile D56S1

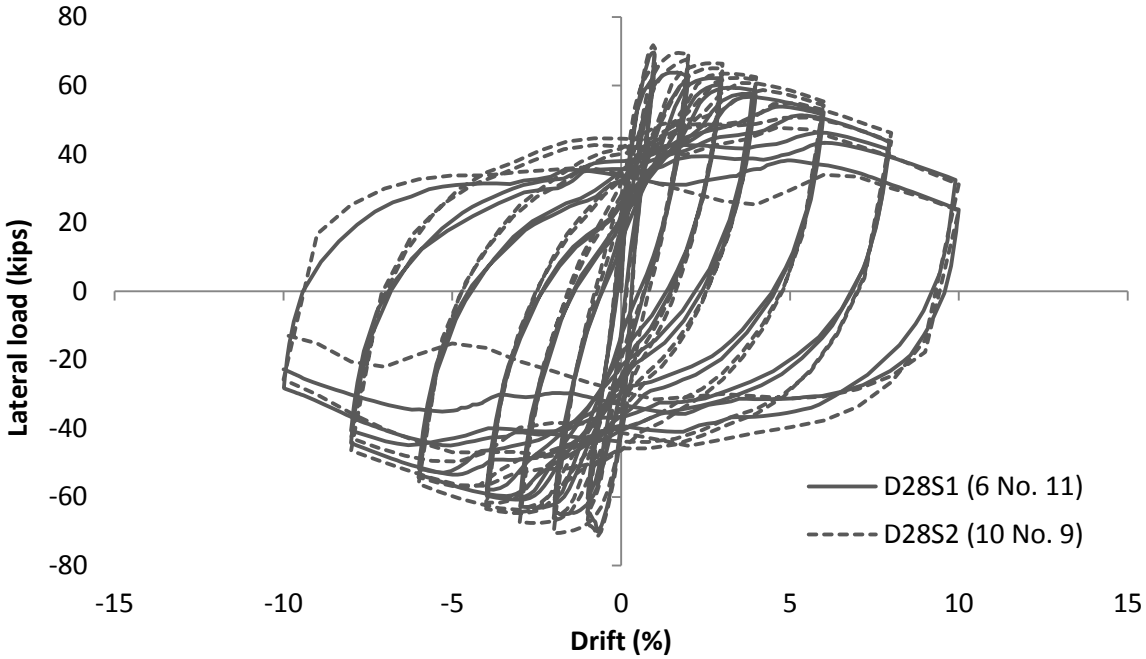

Figure 4.34 – Lateral load-vs.-drift ratio curves for models with axial load equal to 0.15 $A_g f_c'$

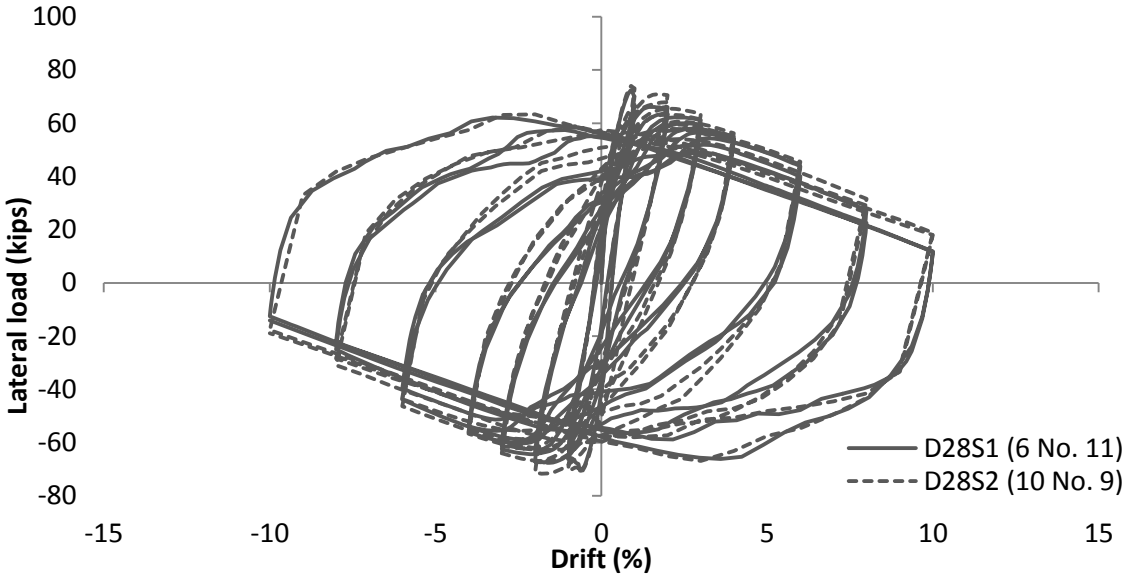

Figure 4.35 – Lateral load-vs.-drift ratio curves for models with axial load equal to 0.20 $A_g f_c'$

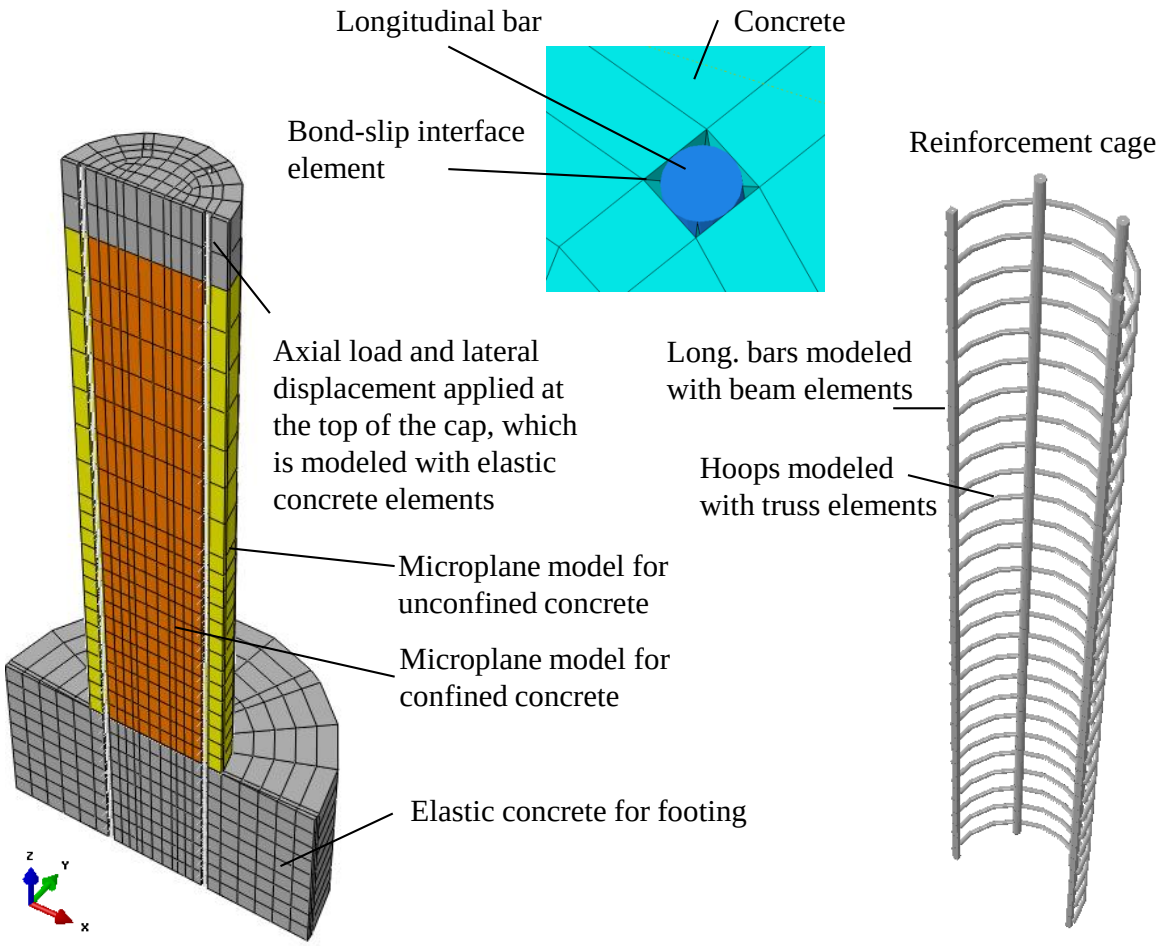

Figure 4.36 – FE model of Specimen #1 assembly with microplane model for concrete

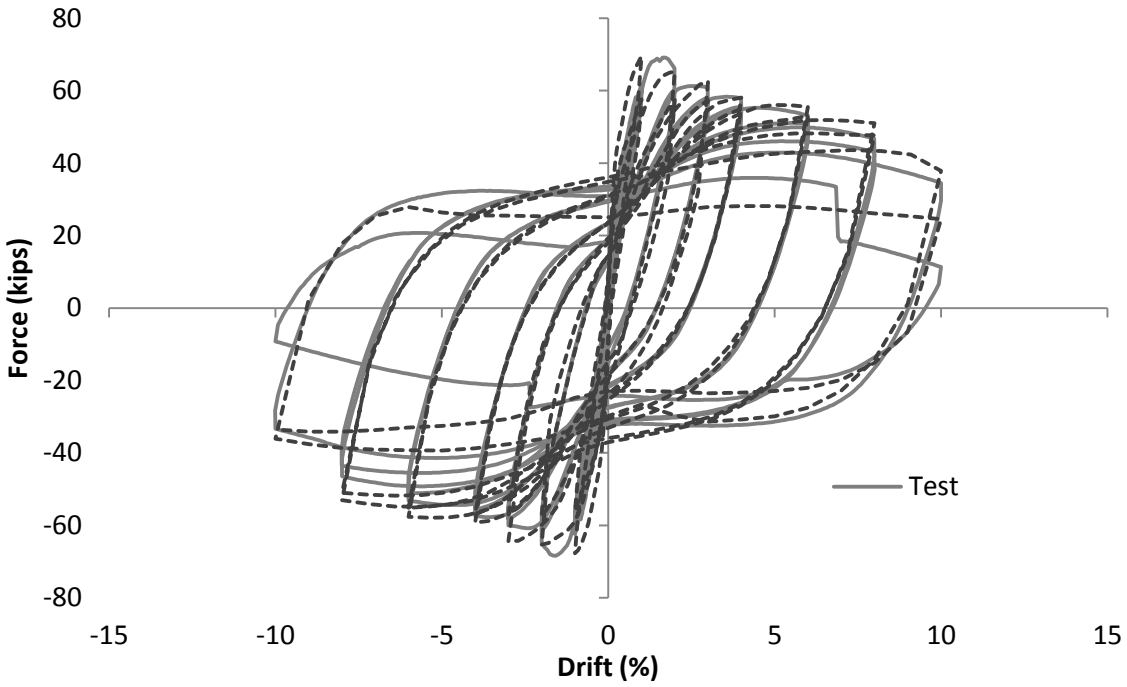

Figure 4.37 – Lateral load-vs.-top drift ratio curves for Specimen #1

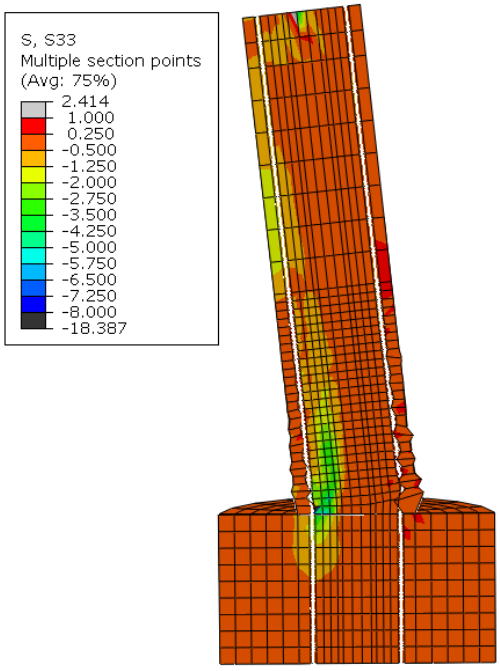

Figure 4.38 – Deformed shape of FE model of Specimen #1 at 10% drift

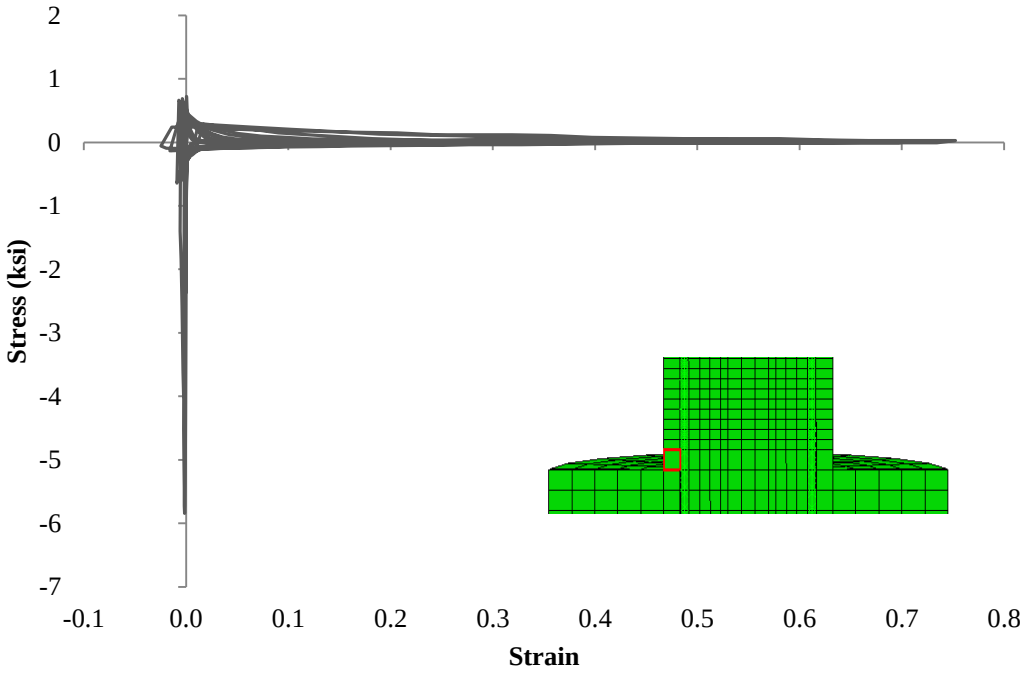

Figure 4.39 – Axial stress-strain curve for cover concrete at the base of Specimen #1

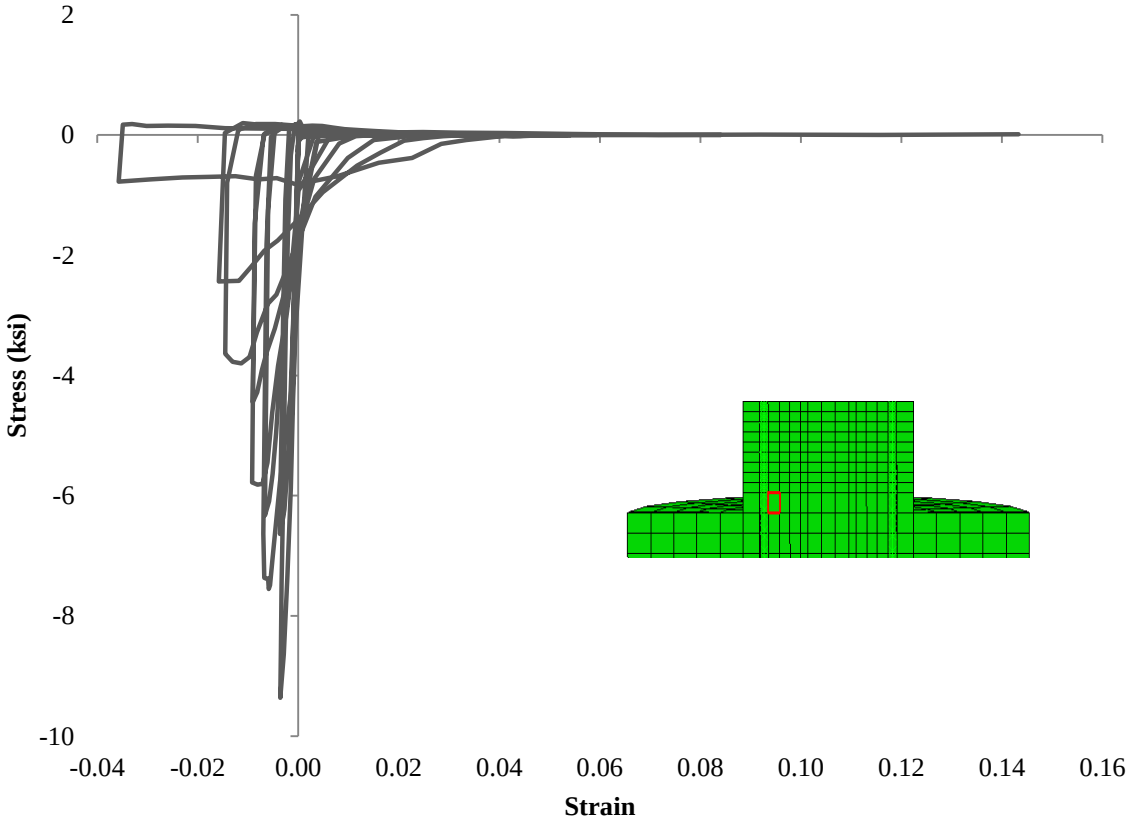

Figure 4.40 – Axial stress-strain curve for core concrete at the base of Specimen #1

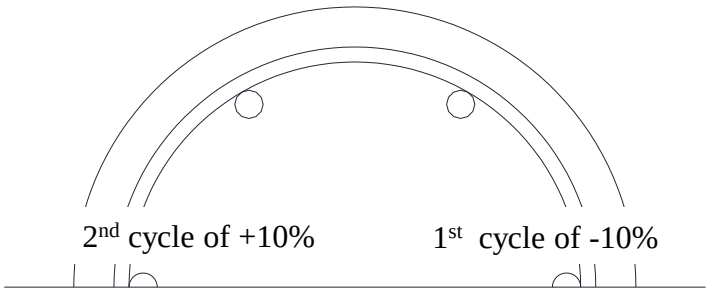

Figure 4.41 – Cycles at which bars fracture in the FEA of Specimen #1

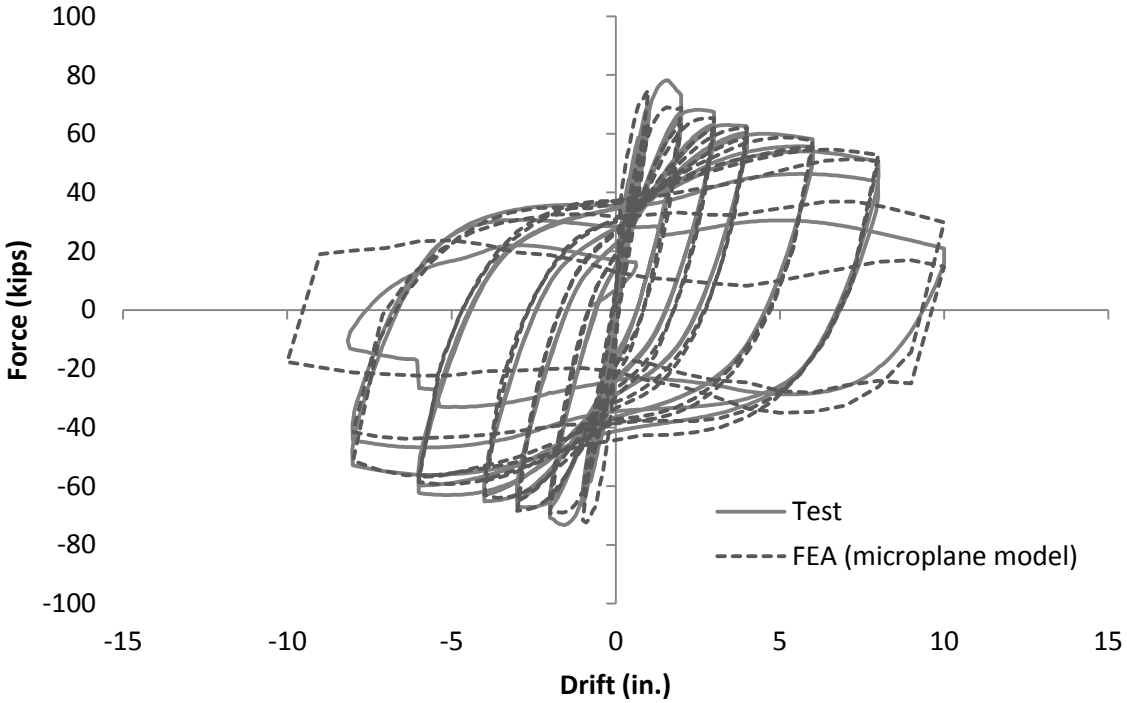

Figure 4.42 – Lateral load-vs.-top drift ratio curves for Specimen #2

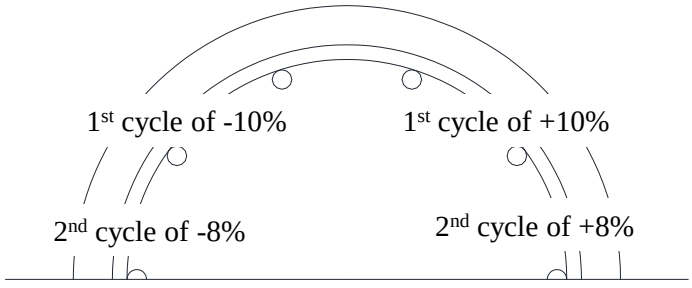

Figure 4.43 – Cycles at which bars fracture in the FEA of Specimen #2

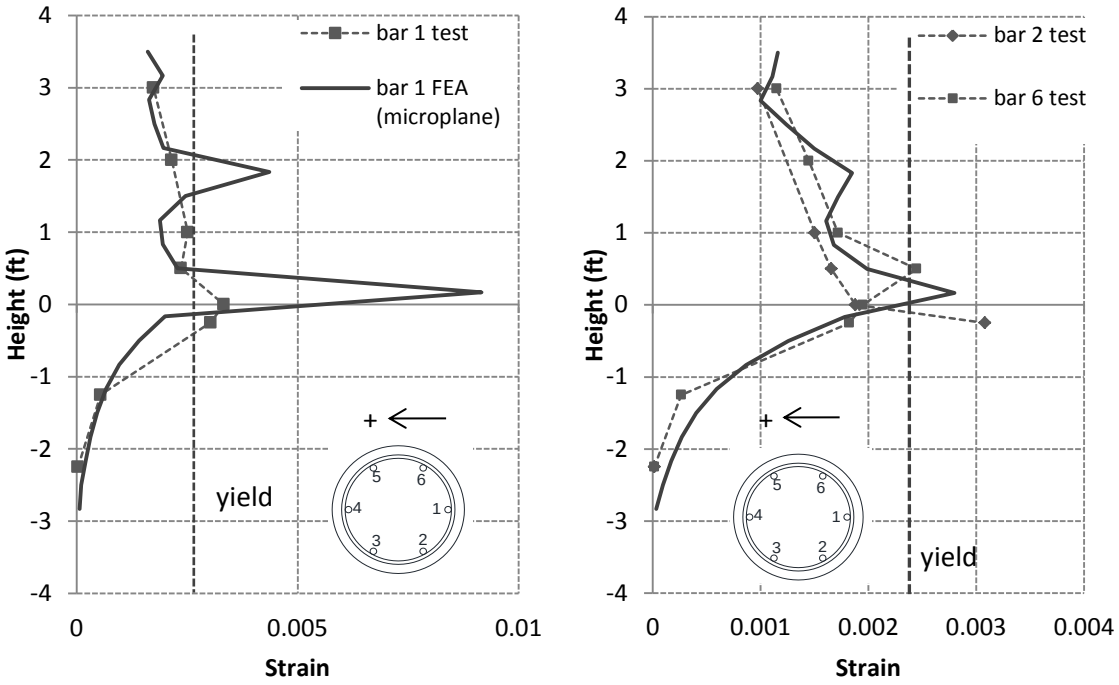

(b) Bar 1 (a) Bar 2 & 6

Figure 4.44 – Strains in bars at south face of Specimen #1 at +1% drift

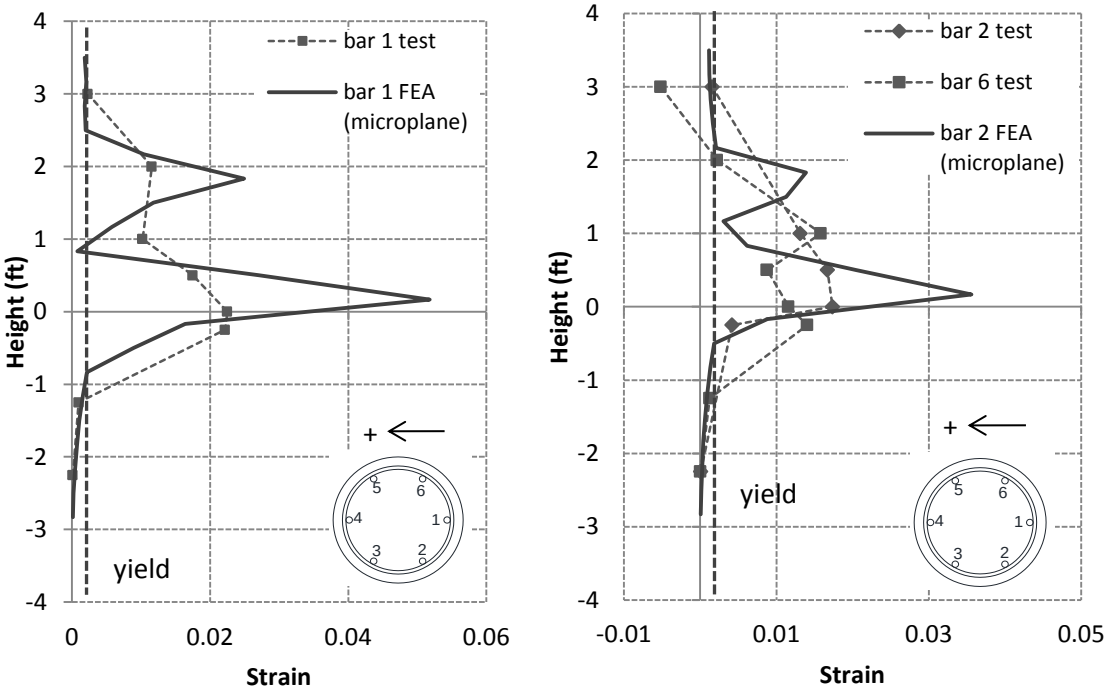

(a) Bar 1 (b) Bars 2 & 6

Figure 4.45 – Strains in bars at south face of Specimen #1 at +4% drift

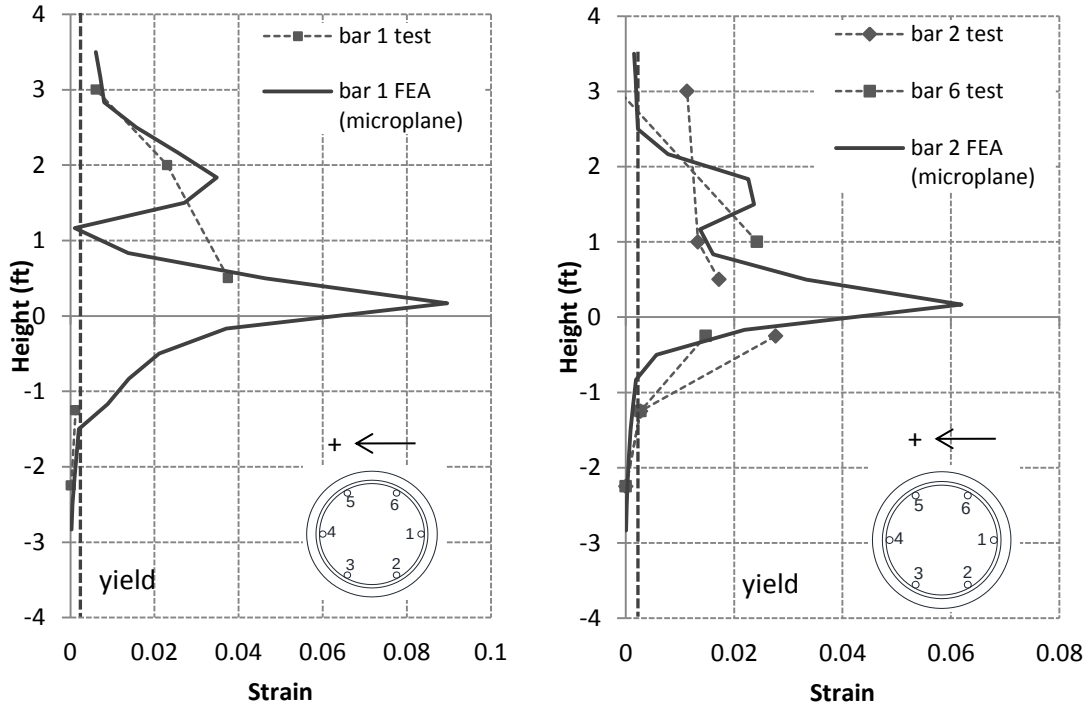

(a) Bar 1 (b) Bars 2 & 6

Figure 4.46 – Strains in bars at the south face of Specimen #1 at +8% drift

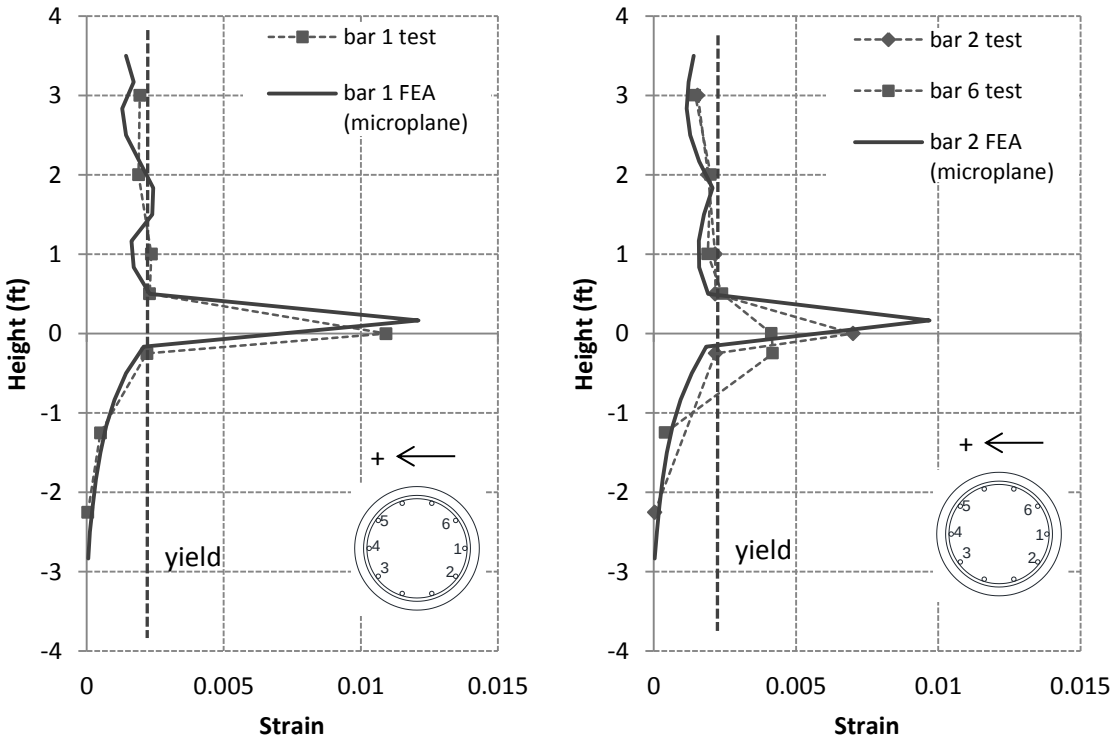

(a) Bar 1 (b) Bars 2 & 6

Figure 4.47 – Strains in bars at south face of Specimen #2 at +1% drift

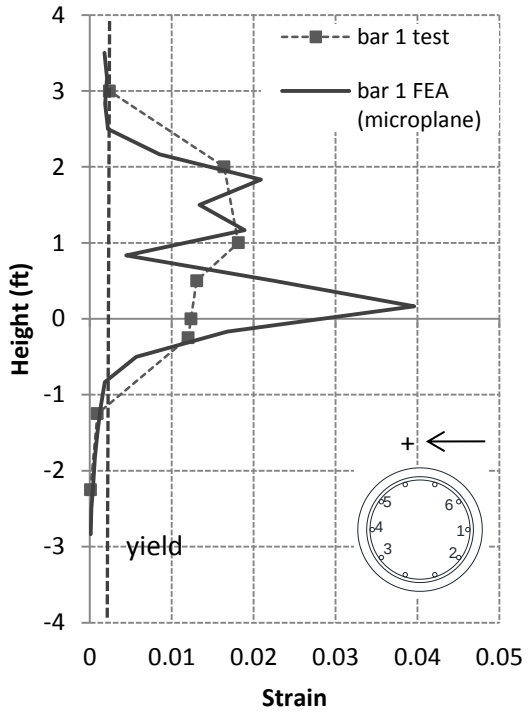

(a) Bar 1

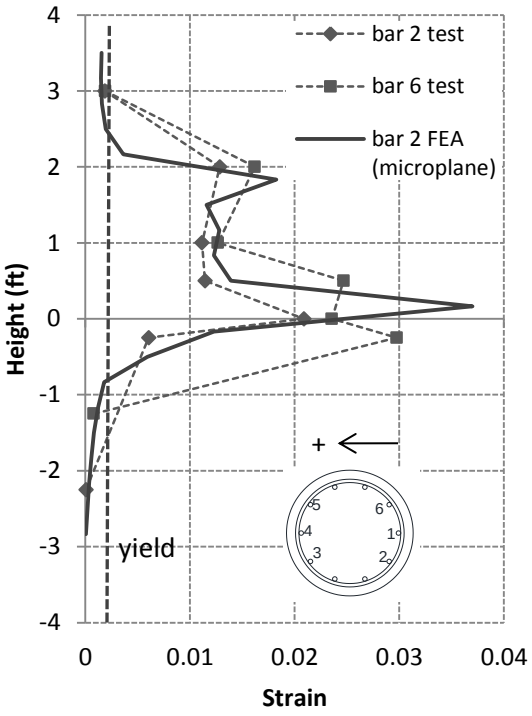

(b) Bars 2 & 6

Figure 4.48 – Strains in bars at south face of Specimen #2 at +4% drift

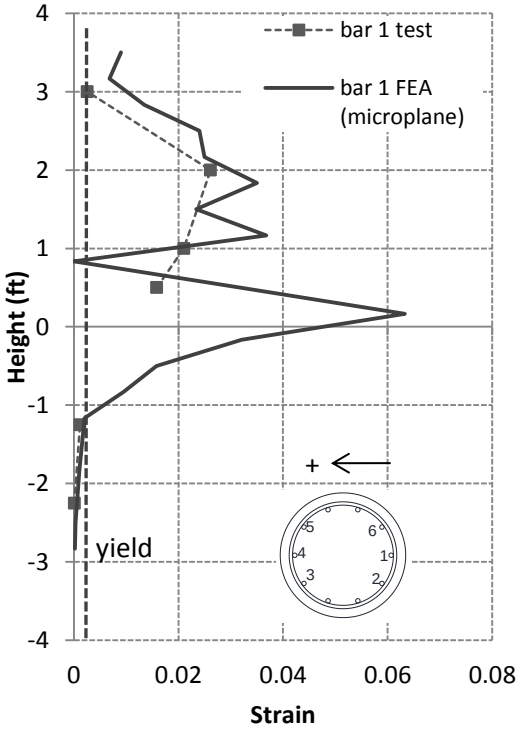

(a) Bar 1

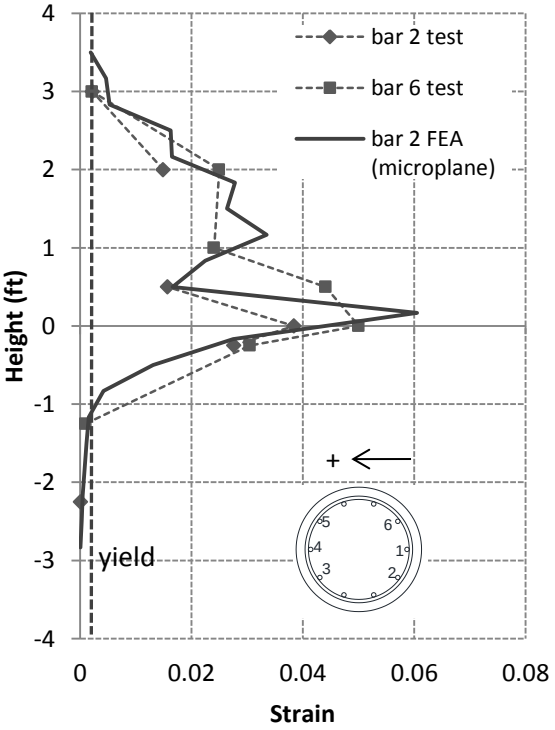

(b) Bars 2 & 6

Figure 4.49 – Strains in bars at south face of Specimen #2 at +8% drift

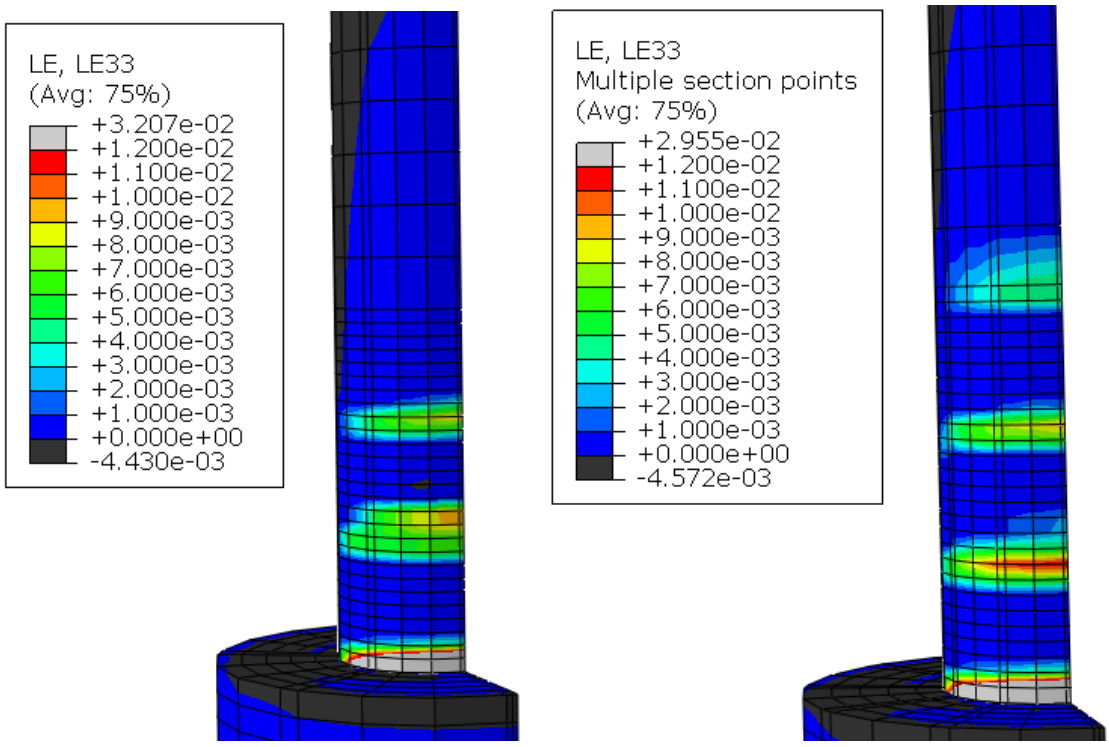

(a) Specimen #1 (b) Specimen #2

Figure 4.50 – Normal strains in concrete at 1% drift

CHAPTER 5

EXPERIMENTAL INVESTIGATION OF EMBEDMENT LENGTH OF HEADED BARS IN SLAB-COLUMN JOINTS

This study was aimed to determine the minimum development length required for headed bars in RC slab-column joints. Reinforcing bars with headed ends (headed bars) are being increasingly used in reinforced concrete structures because they require less development length as compared to straight bars, and can reduce reinforcement congestion as compared to hooked bars. The development of tensile or compressive stress in a headed bar rely on the bearing action of the head as well as the bond stress along the embedment length of the bar. Headed bars have been extensively used in offshore platforms and nuclear power plant structures, which often have a large amount of large-diameter bars and do not have sufficient room to accommodate hooked bars. Headed bars are also desirable for joints in bridge and building structures, e.g., column-bent cap joints in bridges, and beam-column joints in buildings.

To assess the minimum development length required for headed longitudinal bars extending from a bridge column into the superstructure of a slab bridge, three full-scale slab-column assemblies were tested. The slab-column joint is reinforced according to the requirements of Memo To Designer (MTD) 20-7 (Caltrans, October 2014).

This chapter first discusses the anchorage mechanism of headed reinforcing bars in concrete, and presents a concise literature review of experimental studies conducted to investigate the anchorage mechanism and capacity, and formulas and design equations available to determine the anchorage capacity and development length required of headed bars. A comprehensive literature review and summary of some of the early studies can be found in Thompson et al. (2002).

The test program and the design of the specimens are then presented. The findings of the experimental investigation, and in particular the lateral load-vs.-displacement curves for the specimens, the main test observations, the deformations of the columns and slabs, and strains in the reinforcing bars are presented and compared.

5.1 Past research

5.1.1 Anchorage Behavior of Headed Bars

The anchorage capacity of a headed bar is contributed by the bearing of the head against the concrete and the bond between the bar and the surrounding concrete, as shown in Figure 5.1. Past research has shown that the anchorage failure of a headed bar is governed by three main mechanisms: (1) side-face blowout failure of concrete when the bar is close to the edge of a concrete slab or block; (2) concrete breakout failure when the embedment length is shallow; and (3) bearing failure at the anchor head. A side-blowout failure is characterized by the spalling of the concrete cover on the surface parallel and adjacent to the bar, as shown in Figure 5.2(a). This type of failure can occur in beams and columns, and has been observed in tests on bars with deep embedment lengths (as compared to the side cover) and in beam-column joint tests. Breakout failures are characterized by the formation of a pullout cone failure on the concrete surface perpendicular to the bar, as shown in Figure 5.2(b). A bar with a short embedment length, compared to the lateral concrete cover, such as a bar embedded in the central portion of a slab, may experience this type of failure. Bearing failure at the anchor head can be characterized by the lateral splitting and/or crushing of the concrete in front of the head, as shown in Figure 5.2(c). This type of failure has been observed in the anchorage region of longitudinal bars at the end of a beam.

5.1.2 Experimental Studies on the Development of Headed Bars

Stoker et al. (1974) conducted 18 pullout tests on No. 11, 14, and 18 Grade 60 headed bars, and one test on a straight No. 18 bar for comparison. The variables considered in their study included the embedment length, the concrete cover, and the concrete strength. The embedment length considered for the headed bars ranged from $11d_b$ to $37d_b$. The concrete specimens had reinforcement details representative of those in the cap beams of a box-girder bridge designed according to the specifications used in that time period. Four of the specimens had 4 No. 11 bars in a group, while the rest had single bars. In eight of these tests, loading was terminated before any failure occurred. Six of the specimens developed concrete failure in the anchorage region, and three had bar failure. The shortest embedment length that resulted in bar failure was $17d_b$, with the concrete strength equal to 4,840 psi. Their results also showed that bar groups had a weaker anchorage than single bars.

De Vries et al. (1996 and 1999) conducted over 140 pullout tests to evaluate the anchorage behavior and capacities of headed bars with variables including the embedment length (distance from the bearing surface of the bar head to the concrete surface), bonded length (less than or equal to the embedment length), concrete strength, transverse reinforcement, head geometry, and edge distance of bars. Eighteen of these tests (De Vries et al. 1999) were conducted with shallow embedment lengths varying from $1.8d_b$ to $11.5d_b$. Some of the bars had a small edge distance of 2 in. Some of the concrete specimens had transverse reinforcement perpendicular to the bars. Of the 18 specimens, 3 had bar fracture while the rest had anchorage failure. Two of the specimens with bar fracture had an embedment length of $5.7d_b$ and a concrete compressive strength of 12,000 psi, while the third had twice as much embedment length and a concrete strength of 4,000 psi. These three specimens had the bar located at least 18 in. from the edges. Furthermore, the bars did not have bonding with the concrete. Therefore, the anchorage capacity was entirely

provided by the bearing of the bar head against the concrete. For the other specimens, the failure mechanism was concrete breakout (with cone-shaped fracture) as shown in Figure 5.3. Their results showed that an embedment length as short as $11.5d_b$ could be sufficient to develop the full tensile capacity of headed bars embedded in 4,000-psi concrete without breakout failure. Furthermore, they observed that the bond force between a bar and the surrounding concrete slightly increased the anchorage capacity, and that the transverse reinforcement did not affect the anchorage capacity.

Bashandy (1996) conducted 32 pullout tests to study the anchorage behavior of headed bars in exterior beam-to-column joints. Each specimen had two headed reinforcing bars (mimicking the longitudinal bars extending from the beam) anchored in the column. The variables included the bar size (No. 8 and No. 11), the embedment length ($6d_b$ to $13d_b$), the ratio of the head area to the bar area (3 to 8.1), and the presence or absence of confining reinforcement in the joint. The compressive strength of concrete in the specimens was between 3,000 psi and 5,800 psi. The yield strength of the headed bars was approximately 80 ksi. During the tests, the bars did not yield and the load capacity was governed by anchorage failure in these tests. Eighteen specimens had side-blowout failure, as shown in Figure 5.4. The remaining fourteen had shear failure in the joint region. His study showed that the concrete cover, embedment length, and confining reinforcement were the primary factors affecting the anchorage capacity, while the size of a head had little influence on the anchorage capacity.

Wright and McCabe (1997) conducted "beam-end" tests to examine the anchorage capacities of headed bars. The bars in their beam-end specimens had limited concrete cover. They considered only Grade 75 No. 8 bars with an embedment length of 12 in. ($12d_b$), and a concrete strength of 4,500 to 5,000 psi. The variables investigated were the concrete cover ($2d_b$ and $3d_b$), the bonded length of the bars, and the quantity and spacing of transverse reinforcement. The

bars yielded in some of the tests, but none of the specimens was loaded to bar fracture. They observed that for a concrete cover of $2d_b$, the presence of transverse reinforcement enhanced the anchorage capacity of a bar. However, for a cover of $3d_b$, the effect of transverse reinforcement is not noticeable. Interestingly, they also showed that the addition of a PVC tube to avoid the bonding of the bar with the surrounding concrete reduced concrete cracking and increased the anchorage capacity. However, this seems to be related to the fact that the specimens had side-blowout failure.

The anchorage capacity of headed bars in compression-compression-tension (CCT) nodes of an idealized strut-&-tie model was studied by Thompson et al. (2005 and 2006a). In their tests, they observed that the anchorage failure in CCT nodes is characterized by the crushing of concrete in front of the bar ribs and lateral splitting. They postulated that the anchorage capacity of a headed bar in a CCT node was contributed by the bearing capacity of the concrete at the bar head and the bond force between the bar and the concrete. However, because the bond force would have passed the peak value before the peak bearing capacity would develop, a reduced bond strength should be considered in calculating the anchorage capacity. They also studied experimentally the behavior of lap splices using headed bars (Thompson et al. 2006b). Based on their experimental data, they proposed formulas to calculate the reduced bond strength and the bearing capacity of concrete against a bar head in CCT nodes and lap splices (Thompson et al. 2006c). They further concluded that the formulas were also applicable to headed bars with deep embedment and beam-column joints. However, it seems that their model is valid only when the breakout failure of concrete is prohibited.

Choi et al. (2002) conducted pullout tests of headed bars to study the pullout capacity of a beam longitudinal bar terminated in a column-beam joint. They studied the effect of the column longitudinal and transverse reinforcement on the anchorage of single as well as multiple headed

bars. No. 5, No. 6, and No. 7 bars were tested with concrete compressive strengths of 3.9 and 5.7 ksi. The bars had embedment lengths between $6d_b$ and $10d_b$. The column sections and reinforcement were different depending on the size and number of bars. The smallest section was 11.8 in. x 5.8 in., and the largest was 15.7 in. x 19.6 in. The column reinforcement consisted of No. 5 or No. 6 longitudinal bars and No. 3 or No. 4 stirrups. Only the bars which had an embedment length of $10d_b$ yielded. The tests revealed that reducing the spacing of the stirrups increased the pullout strengths of the bars. The amount of longitudinal reinforcement in the column did not affect the pullout strengths.

Kang et al. (2010) studied the behavior of bars with small heads ($2.7A_b$) in exterior beam-column joints. Pullout tests were conducted on No. 6 bars with a specified yield strength of 58 ksi. The bars were embedded $10d_b$ in 5,000-psi concrete blocks. Different types of heads and loading conditions (monotonic and cyclic) were tested. They were subjected to monotonic and cyclic loads. All the bars yielded and experienced strain hardening. The specimens failed by the splitting of the concrete and the local concrete crushing in front of the head. The anchorage strength was not significantly affected by the difference in the heads and the cyclic loading. Two beam-column assemblies were also tested under cyclic loading. One assembly had headed bars as the beam longitudinal reinforcement, and the other had hooked bars. Both had a development length of $15d_b$ in the beam-column joint. While the specimen with headed bars performed adequately, the anchorage failure of the hooked bars triggered an early failure of the joint.

5.1.3 Predictive Equations for the Anchorage Capacity of Headed Bars

De Vries et al. (1999) proposed the concrete capacity design (CCD) method, which was originally developed by Fuchs et al. (1995) and Eligehausen and Balogh (1995) for anchor bolts in concrete, for calculating the anchorage capacity of a headed bar in plain concrete. They

validated this method with their test data from shallow-embedment pullout tests. For single headed bars with sufficient edge distance to allow a full cone-shaped failure, the following formula has been proposed:

$$P_n = 21.2 h_d^{1.5} \sqrt{f_c'} \tag{5.1}$$

in which P_n is the anchor capacity, h_d is the embedment length and f_c' is the specified concrete strength, with all units in pounds and inches. This formula was derived for a failure surface with a pyramidal shape and a $3h_d$ x $3h_d$ square base. For a group of bars, the failure surfaces of individual anchors may intersect, resulting in a total capacity less than the sum of the capacities of the individual anchors. To account for the group effects, as well as the reduction of the failure surface area due to edge placements, they have proposed a more general equation:

$$P_n = \Psi \frac{A_n}{9h_d^2} 21.2 h_d^{1.5} \sqrt{f_c'} \tag{5.2}$$

in which P_n is the pullout capacity of the entire group of bars, A_n is the total failure surface area available, $9h_d^2$ is the failure surface for one bar, and Ψ is a factor to account for the reduction due to edge placement and is calculated as:

$$\Psi = 0.7 + 0.3 \frac{C_1}{1.5 h_d} \leq 1 \tag{5.3}$$

where C_1 is the minimum edge distance. The equations proposed by De Vries et al. (1999) do not consider the effect of the slab reinforcement on the capacity of the anchors.

5.1.4 Design Equations for the Development Length of Headed Bars

Based on the work of Thompson et al. (2005 and 2006a), Section 12.6.2 of ACI 318-11 (2011) has the minimum development length for headed bars in tension calculated with the following formula:

$$l_{dt} = \frac{0.016\psi_e f_y}{\sqrt{f_c'}} d_b \tag{5.4}$$

in which, ψ_e shall be taken as 1.2 for epoxy-coated reinforcement and 1.0 for other cases, f_y is the specified yield stress of the reinforcing bar, d_b is the bar diameter, and f_c' is the specified compressive strength for concrete, which shall not exceed 6,000 psi. All units are in pounds and inches. The commentary in ACI 318-11 states that this formula considers the different possible failure modes of an anchorage, such as concrete breakout, side-face blowout, and pullout failures. By referring to the work of Thompson et al. (2005 and 2006a), it implies that bearing failure is also considered. Transverse reinforcement is perceived to be largely ineffective in improving the anchorage of headed bars. Therefore, it is not considered. Evidently, a formula that accounts for all these vastly different mechanisms must be empirical. However, it is not clear as to whether the formula is intended to develop the full tensile capacity of a bar or just the yield strength. For Grade 60 No. 9 bars and concrete with a specified compressive strength of 4,500 psi, Eq. (5.4) yields a minimum embedment length of 16 in., which cannot be accommodated in a typical slab bridge whose deck slab can have a thickness as small as 16 in. Furthermore, it is not clear as to whether the above formula applies to multiple headed bars in a slab-column joint, which may lead to intersecting failure surfaces and thereby reduce the anchorage capacity.

5.1.5 Final Remarks

In spite of the fact that a number of experimental studies have been conducted to evaluate the anchorage behavior and capacities of headed bars in concrete, there is no conclusive data available to determine the minimum embedment length required for headed bars embedded in concrete. Most of the tests conducted so far had either long development lengths or very short development lengths that resulted in anchorage failure. Some of the tests were terminated before reaching bar fracture or anchor failure. However, limited data have shown that an embedment length of $11d_b$ is a borderline condition to develop the full tension capacity of a single headed bar. The development length required is likely to be longer for groups of bars.

For slab bridges, if a column or pile extension is sufficiently far away from the edge of the deck slab, the anchorage failure of a headed bar will likely be caused by concrete breakout failure or the bearing failure at the anchor head. Studies have shown that the anchorage capacity of a headed bar group like that in a column or pile extension is weaker than that of a single bar. As to reinforcing details, there is limited data that indicates that stirrups placed parallel to an anchored bar contribute to the anchorage capacity, while stirrups placed transversely to the bar have small or no effect. However, the concrete specimens tested had reinforcing details very different from those in a typical column-slab joint of a slab bridge.

5.2 Test Program

5.2.1 Test Specimens and Test Setup

The configuration of a test specimen and the test setup are shown in Figure 5.5. The slab-column assemblies were tested in an upside-down position with two edges of the slab hinge-supported. Each specimen was subjected to quasi-static cyclic lateral displacements in the north-south direction using a 220-kip load capacity, 48-in. stroke, actuator attached to the hammerhead

of the column on the south side of the specimen. The other end of the actuator was attached to a strong wall. The test setup mimicked the loading condition for a slab bridge when it is subjected to a lateral seismic force in the transverse direction. As shown in Figure 5.5, the test assembly represented a portion of the bridge. The hinge supports for the slab were based on the assumption that inflection points developed during the bending of the cap beam were located midway between two adjacent columns when the superstructure was subjected to the lateral seismic force. The point of horizontal application represented the inflection point of column bending. Figure 5.6 shows a picture of the test setup. The total axial compressive stress applied to the base section of the column was 3.5% of the targeted compression strength of the concrete. It was applied by two post-tensioning rods. This was to simulate the expected gravity load on the column from the superstructure. The forces in the post-tensioning rods were controlled by center-hole hydraulic jacks placed on top of the steel beam sitting on the hammer head. These rods passed through holes in the steel beam and the slab, and were anchored to the bottom of the slab with a hinge mechanism.

The specimens were designed according to the AASHTO LRFD Bridge Design Specifications (AASHTO 2014), and the Caltrans Seismic Design Criteria (SDC) (2013), MTD 20-7 (October 2014) and Bridge Design Aids (BDA) 4-10 (2009). Each of the slab-column assemblies had a 2-ft. diameter cast-in-place column with a height of 12 ft., measured from the bottom surface of the slab (top surface in the specimen) to the elevation at which the lateral load was applied. The main differences among the test specimens were the size of the longitudinal reinforcing bars in the columns and the thickness of the slab at the slab-column joint. Table 5.1 summarizes the design details of Specimens #1, #2 and #3. The specimens were tested in sequence, and the reinforcement details of the second and third specimens were based on the test results obtained from the first specimen.

For Specimen #1, eight No. 9 headed bars were used for the longitudinal reinforcement of the column. The thickness of the slab was 16 in. The embedment length for the headed bars was $9.8d_b$, measured from the bottom surface of the head to bottom surface of the slab considering the upright position of an actual bridge. This was the maximum embedment length practically possible for the 16-in. thick slab with the condition that the head of a bar had to be below the top mat of reinforcement in the slab. A pre-test finite element analysis using a model similar to that presented in Chapter 6 indicated that this length would be sufficient to develop the tensile strength of the headed bars.

Specimen #2 had six No. 10 headed bars for the longitudinal reinforcement of the column. The total cross-sectional area of the longitudinal reinforcement was almost the same as that for Specimen #1. The thickness of the slab was kept at 16 in. The embedment length provided for the headed bars was the same as that in Specimen #1 and is $8.7d_b$ for the No. 10 bars. This specimen was intended to establish the lower limit of the required development length.

Specimen #3 also had six No. 10 headed bars for the longitudinal reinforcement of the column. However, as shown in Figure 5.7, a 3-in. deep drop cap was added to the 16-in. thick slab, providing an embedment length of $11d_b$ for the headed bars. This specimen was intended to check if structural performance could be improved, in terms of the severity of punching cracks in the slab, with the increase of the development length.

5.2.2 Design Details and Materials

5.2.2.1 Specimen #1

The steel reinforcement for the column of Specimen #1 is shown in Figure 5.8. The column longitudinal reinforcement consisted of 8 No. 9 bars (with a reinforcement ratio of 1.77 %), and the transverse reinforcement consisted of No. 5 hoops spaced at 3.5 in. on center (with a

volumetric reinforcement ratio of 1.77%). The concrete clear cover in the column was 2 in., measured from the outer perimeter of the transverse hoops. The column was connected to a 10 x 8 ft. slab with a thickness of 16 in. The embedment length of the column longitudinal bars in the slab was 11 in., which is $9.8d_b$, measured to the bottom face of the head considering the upright position of the assembly. This length is shorter than the $14d_b$ currently required in Caltrans MTD 20-7 and MTD 20-19 for concrete with a compressive strength of 5,000 psi.

The reinforcement details for the slab are shown in Figure 5.9. The clear concrete cover in the slab was 2 in., measured from the top and bottom most longitudinal bars in the slab. Detailed design drawings for the specimen are provided in Appendix A. The longitudinal slab reinforcement was determined according to BDA 4-10 for a 3-span bridge, with the length of each span equal to 30 ft. and a slab thickness of 16 in. The shear reinforcement was determined according to Section 5.13.3.6 of the AASHTO LRFD Bridge Design Specifications. The slab reinforcement within the effective bending width at a slab-column joint also complied with Caltrans SDC Section 4.3, which requires that the moment and shear capacities of the slab over the effective bending width be greater than the demands caused by the over strength moment capacity of the column. In addition to the longitudinal reinforcement required to carry the over strength of the column, extra longitudinal reinforcement was added within the effective bending width region of the slab according to the requirements of MTD 20-7, which are shown in Table 5.2. Different regions at a slab-column joint, as referred to in the table, are defined in Figure 5.10. As shown, MTD 20-7 requires J-bars in the core region of a joint, stirrups in the outer joint region and the joint perimeter region, horizontal side reinforcement, and a minimum amount of column hoops inside the slab. These reinforcement requirements are to ensure the structural integrity of a joint that is subjected the moment and shear exerted by the column, and are based on the recommendations of Ayoub and Sanders (2010) derived from a strut-and-tie model. However, the

original recommendations have been modified to improve the implementation and to prevent breakout failure that could be induced by headed column bars with a reduced development length. Even though not specified in MTD 20-7, all the vertical stirrups and J-bars were hooked around the outermost longitudinal bars in the slab. The effectiveness of these requirements for the latter purpose is the subject of this investigation. These details can be seen in Figure 5.11, where a picture of the slab and column reinforcement during the construction of Specimen #1 is shown. The placement of the heads of the bars above the mat of the longitudinal and transverse reinforcement at the bottom face the slab specimen (top face in the bridge deck) can also be seen in the figure. Finally, the figure clearly shows the concrete cover of 2 in. measured from the longitudinal bars of the top face of the slab (bottom face in the specimen). The same detailing in the reinforcement was followed for Specimens #2 and #3. Figure 5.12 shows the slab and column reinforcement of Specimen #1 before the concrete cast.

The concrete for the slab had a specified compressive strength of 4,000 psi at 28 days, a slump of 4 in., and a maximum aggregate size of 1 in. The mix design for the slab concrete is shown in Table 5.3. The concrete in the column had a specified compressive strength of 4,500 psi at 28 days, and the same slump and maximum aggregate size as those for the slab concrete. Table 5.4 summarizes the mix design for the column concrete. The concrete in the slab was poured first, and the concrete in the column was poured one week later. The specimens were to be tested when the strength of the concrete in the slab was close to but did not exceed 5,000 psi. It was intended that the strength of the column concrete would be equal to or higher than that of the slab concrete when the specimens were tested. The actual strengths of the concrete measured on the day of each test are presented in Table 5.5. All the reinforcement was Grade 60 complying with the ASTM A706 specifications. The column longitudinal reinforcement (HRC 150) had a full-size head (with a net bearing area of $9A_b$), complying with the ASTM A970 specifications. Results from material tests on the steel reinforcement for Specimen #1 are presented in Table 5.6. The material

samples for the column hoops were cut and straightened prior to the test. As a result of the plastic deformation they experienced from bending, the stress-strain curves from the samples did not show a distinct yield plateau but a gradual transition from the elastic regime to the inelastic regime. Hence, the yield strength for the hoops is defined with the 0.2% offset strain method as shown in Figure 5.13.

As shown in Table 5.1, the concrete strength for the column was much lower than the expected. On the day of the test, the compressive strength was only 3,200 psi. This decrease of the concrete strength could compromise the ductility of the column and might also slightly reduce its moment capacity, thus reducing the load demand on the slab-column joint. To circumvent this problem, external rings of steel straps were added in the lower 4-ft. region of the column as exterior confinement, as shown in Figure 5.6. The straps were of Grade 50 steel, and were 1-in. wide with a thickness of 3/16 in. They were spaced at 4 in. on center. The rings were fabricated in halves and welded together at the site. Their inner diameter was 0.5 in. larger than the diameter of the column. A fluid high-strength grout was injected into the gaps between the column and the rings. The testing of three coupon samples from the steel straps showed a yield strength of 54 ksi and a tensile strength70 ksi.

5.2.2.2 Specimen #2

The steel reinforcement for the column of Specimen #2 is shown in Figure 5.14. Specimen #2 differed from Specimen #1 only in the longitudinal reinforcement in the column. Its longitudinal reinforcement consisted of 6 No. 10 bars (with a reinforcement ratio of 1.68 %). Figure 5.15 shows the plan view of the slab reinforcement for Specimen #2, while detailed design drawings are provided in Appendix A. The slab of Specimen #2 had the same thickness (16 in.) and the same reinforcement as that of Specimen #1, except that it had four additional vertical stirrups at positions next to the column cage, as shown in Figure 5.15. These four vertical stirrups

were not required according to MTD 20-7 but were deemed useful as observed from the test of Specimen #1. The embedment length of the column longitudinal bars was 11 in., which is $8.7d_b$ for the No. 10 bars.

The concrete mix designs for Specimen #2 were the same as those for Specimen #1. The actual strengths of the concrete on the day of the test are presented in Table 5.5. For this specimen, both the slab and column concrete reached the desired strength even though the column concrete was a little weaker. All the reinforcement was Grade 60 complying with the ASTM A706 specifications. The strengths of the steel reinforcement from material tests are presented in Table 5.6.

5.2.2.3 Specimen #3

Specimen #3 had the same column design as Specimen #2 but differed in the slab design. It had a 16-in.-thick slab with a 3-in. deep drop cap. With the addition of the drop cap, the embedment length was 14 in., which is $11d_b$ for the No. 10 bars. The plan view of Specimen #3, along with the south and east elevation views are shown in Figure 5.16. The reinforcement for the drop-cap region was determined according to MTD 20-7. Figure 5.17 shows a plan view of the steel reinforcement for the slab. Detailed design drawings are provided in Appendix A. Figure 5.18 shows a picture of the slab and column reinforcement of Specimen #3 before the concrete cast.

The concrete mix designs specified for this specimen were the same as those for the other two specimens. The actual strengths of the concrete measured on the day of the test are provided Table 5.5. It should be noted that the slab concrete reached a compressive strength of 4,500 psi, which was a little lower than the targeted. All the reinforcement was Grade 60 complying with the ASTM A706 specifications. The strengths of the steel reinforcement from material tests are presented in Table 5.6.

5.2.3 Instrumentation

Electrical resistance strain gages were attached to selected column and slab reinforcement of the specimens. Strain gages were placed at different elevations in selected column longitudinal bars near the north and south faces of the specimen (which were loaded in the north-south direction as shown in Figure 5.5) to monitor the strain distributions along these bars, including the strains along their embedment length in the joint region. The strain gages were placed on the longitudinal ribs of the bars to avoid disturbing the transverse ribs, which could affect the bond characteristics.

Displacement and rotation transducers were used to measure the lateral displacement of the column and the rotations of the slab. Vertical displacement transducers were mounted near the base of the column to measure the rotation of the column base with respect to the slab caused by bar slip.

For Specimens #2 and #3, two vertical transducers were placed underneath the slab to measure the vertical displacements of the top surface of the slab (bottom surface face in the specimen) at the positions of the two extreme longitudinal bars at the north and south faces of the column. These displacements were caused by the punching force of the headed bars as the rotation of the slab was extremely small. Detailed instrumentation plans for the specimens are provided in Appendix A.

5.2.4 Loading protocol

The test setup is shown in Figure 5.5 and Figure 5.6. In each test, the column was subjected to a constant vertical load of 70 kips using the two post-tensioned rods. Together with the self-weight of the column and the hammer head, this load subjected the base section of the column to an axial stress equal to 3.5% of the targeted compressive strength of the column concrete (which was 5,000 psi).

With the slab hinge-supported, the top of the column of each specimen was subjected to fully reverse lateral displacement cycles. The loading protocol is shown in Figure 5.19(a). Initially, the specimen was subjected to four fully-reversed force-controlled load cycles, with load amplitudes of 25, 50, 75, and 100% of the lateral load, F_y', that corresponds to the theoretical first yield of the longitudinal reinforcement at the base of the column. The specimen was then subjected to fully-reversed displacement-controlled load cycles with increasing ductility demands of 1, 2, 3, 4, and so forth, until the lateral load resistance dropped significantly. There were two cycles at each ductility level. The ductility demand is defined as $\mu = \Delta / \Delta_y$, in which Δ is the lateral displacement of the specimen at the level of the centerline of the horizontal actuators, and Δ_y is the effective yield displacement. As shown in Figure 5.19(b), Δ_y is defined as the displacement at the intersection of the secant line passing through the origin and the point $\left(\Delta_y', F_y'\right)$, which corresponds to the theoretical first yield of the column longitudinal bars, with the horizontal line passing through the theoretical ultimate load (F_y). Hence, it can be calculated as

$$\Delta_y = \frac{F_y}{F_y'}\Delta_y' \tag{5.5}$$

To determine the loading protocol, F_y' and F_y were estimated from finite element analyses using models that will be described in Chapter 6, and Δ_y' was taken as the average of the absolute maximum displacements measured in both loading directions in Cycle 4 of the test, in which the theoretical first yield was reached.

5.3 Test Results

5.3.1 General Observations and Lateral Load-vs.-Displacement Response

The lateral load-vs.-drift ratio curves for Specimens #1 and #2 are presented and compared in Figure 5.20. The horizontal component of the force exerted by the post-tensioning rods has been corrected for in these curves. The drift ratio is defined as the lateral displacement of the column measured at the point of lateral load application divided by the height of the column (12 ft.) measured from the top surface of the slab to the point of load application in the test configuration. Hence, the drift ratio also includes the slab deformation. The positive direction of loading and displacement is defined to be towards the north.

The lateral load capacity attained by Specimen #1 was 36 kips, while that of Specimen #2 was 35 kips. Specimen #1 had a longitudinal reinforcement ratio $\rho_l = 1.77\%$, while Specimen #2 had $\rho_l = 1.68\%$. As shown in Figure 5.20, Specimen #2 exhibited more rapid load degradation than Specimen #1. This can be attributed to the external confinement applied to the column of Specimen #1, which helped to alleviate the crushing of concrete at the compression toes.

The maximum displacement and ductility demand reached in each loading cycle are summarized in Table 5.7 and Table 5.8. The ductility values presented here are calculated with the effective yield displacement, Δ_y, defined in Eq. (5.5). However, instead of using the theoretical values, the actual displacement and force at the first yield and the actual maximum lateral force measured in the test are used to calculate the effective yield displacement for each specimen. The effective yield displacement calculated for Specimen #1 is $\Delta_y = 2.5$ in. The test of Specimen #1 was stopped after the ductility demand had reached 6 to avoid possible damage to the vertical post-tensioning rods. Due to the high drift level, these rods were slightly bent near their anchorage on the slab. A hinge mechanism was thus introduced to the rod anchorages in the

subsequent tests. Figure 5.21 shows the lateral deformation of Specimen #1 at ductility 6. This corresponds to a drift ratio of 10.4%.

For Specimen #2, the effective yield displacement calculated is $\Delta_y = 2.0$ in. During the 2nd cycle of positive drift at ductility 6, concrete spalling was observed at the top surface of the slab (bottom surface in the specimen), with big concrete pieces coming off. The spalling was limited to the cover concrete and was caused by the punching action of the headed bars when they were in compression. The test was stopped at that point, due to the significant drop of the lateral load resistance in the following load reversal, as it can be seen in Figure 5.20. The maximum drift ratio attained was 8.3 %. The smaller embedment length ($8.7d_b$) of the headed bars in Specimen #2, as compared to $9.8d_b$ in Specimen #1, resulted in more severe deterioration of the bar anchorage and the more significant load drop in the later cycles due to bar slip. It can also be noted from Figure 5.20 that the hysteresis curves for Specimen #2 are more pinched because of the more significant slip of the headed bars within the slab.

Figure 5.22 compares the lateral load-vs.-drift ratio curves for Specimens #2 and #3. The columns in Specimens #2 and #3 had the same longitudinal and transverse reinforcement, which resulted in the same lateral load capacities. However, Specimen #3 had a 3-in. drop cap, which with the 16-in. slab, provided an embedment length of $11d_b$, which is the largest among the three specimens. The effective yield displacement calculated for Specimen #3 is $\Delta_y = 2.0$ in., which is the same as that for Specimen #2. As shown in Figure 5.20and Figure 5.22, the higher embedment length in Specimen #3 resulted in less pinched hysteresis curves. However, the rate of degradation of the peak load in each cycle for Specimen #3 appears to be the same as that for Specimen #2 till the ductility demand of 6 was reached. This load degradation was caused by the crushing of concrete in the compression toes of the column. Compared to Specimen #2, Specimen #3 was subjected to two additional displacement cycles at ductility 7. At that point, the test was

ended to avoid possible damage to the vertical post-tensioning rods. The damage at the top surface of the slab (bottom surface in the specimen) of Specimen #3 was very mild, compared to that observed in Specimen #2.

5.3.2 Detailed Test Observations

For all three specimens, flexural cracks started to be visible in the lower half of the columns during Cycle 2, at a lateral load that was about 50% of the force predicted by analysis to cause the first yield of the longitudinal bars. At Cycle 4, when the load approached the theoretical first yield, flexural cracks were formed almost along the whole height of the columns, as shown in Figure 5.23 for Specimens #1 and #2. The same observations also stand for Specimen #3. Up to Cycle 4, no cracks were observed in the slabs. Observations obtained in latter cycles are presented below. For all three specimens, plastic hinges eventually developed at the bottom of columns.

5.3.2.1 Specimen #1

Figure 5.24 shows the evolution of damage near the bottom of the column in Specimen #1. Crushing of the concrete cover started in Cycle 6(a), which was the 1st cycle of ductility 2, as shown in Figure 5.24(a) and Figure 5.24(b). Concrete cover spalling and large flexural cracks were observed in the 1st cycle of ductility 5, as shown in Figure 5.24(c) and Figure 5.24(d). However, the spalling of concrete was not severe because of the external steel confinement. This is reflected in the small load degradation exhibited by the lateral load-vs.-drift ratio curve presented in Figure 5.20. Figure 5.25 shows the hoop strains in the two steel straps closest to the base of the column. The straps were located 4 in. and 8 in. away from the column base. As shown, the straps yielded in tension, with the lowest one experiencing larger strains. This shows that they were fully engaged in the confinement action.

Figure 5.26 shows the evolution of damage in the slab of Specimen #1. Flexural cracks were observed at the bottom face of the slab (top face in the specimen) in the 1st cycle of ductility 1. In Cycle 7a, corresponding to a ductility demand of 3, additional cracks, radiating from the column, appeared at the bottom face of the slab (top face in the specimen). These cracks extended towards the east and west edges of the slab, as the displacement applied to the column increased. The crack pattern at the bottom face of the slab (top face in the specimen), at the end of the test, is shown in Figure 5.27. At the top face of the slab (bottom face in the specimen), punching cracks could be observed in the 2nd cycle of ductility 3, as shown in Figure 5.26(c). The punching cracks were formed as the heads of the bars under compression pushed against concrete. The punching cracks were marked and measured after the end of the test. Relative vertical displacements were observed across punching cracks. After the end of the test, the residual punching crack displacements in the north and south region were 0.12 in. and 0.2 in., respectively. The punching crack displacement is defined as the differential vertical displacement of the slab surface across a punching crack measured with a micrometer. Figure 5.28 shows the crack pattern at the end of the test, with the locations of the column and the heads of the longitudinal bars marked. As shown in the figure, two large punching cracks were formed outside the column perimeter, at a maximum distance of 10 in. Cracks crossing the footprints of the column and the bar heads were also observed. After the test, concrete pieces between large punching cracks were removed with the use of mechanical tools, and some fracture surface was exposed, as shown in Figure 5.29. The average inclination of the fracture surface radiating from a bar head varies between 20^o and 40^o.

5.3.2.2 Specimen #2

Crushing of concrete started near the base of the column of Specimen #2 in the 2nd cycle of ductility 2, as shown in Figure 5.30(a). This was followed by a noticeable drop of the lateral resistance of the column as shown in the lateral load-vs.-drift ratio curve in Figure 5.20. Figure

5.30(b) through Figure 5.30(d) show the evolution of damage near the base of the column, where severe concrete cover spalling was observed. In the last cycle at ductility 6, the transverse reinforcement was exposed due to the cover spalling, as shown in Figure 5.30(d).

The evolution of damage at the bottom face of the slab (top face in the specimen) is shown in Figure 5.31. In the 2nd cycle of ductility 1, cracks, radiating from the column, started to form at the bottom face of the slab (top face in the specimen). These cracks propagated in the following cycles, extending towards the west and east sides of the slab, as shown in Figure 5.31(a) and Figure 5.31(b). At Cycles 8a and 8b, corresponding to ductility 4, column pullout cracks were observed at the bottom face of the slab (top face in the specimen), 2 to 4 in. away from the column. Figure 5.31(c) and Figure 5.31(d) show these pullout cracks during the 1st cycle of ductility 5.

Figure 5.32 shows the evolution of damage at the top face of the slab (bottom face in the specimen). Punching cracks started to form during the 2nd cycle of ductility 1. In every subsequent cycle, existing cracks propagated and new cracks were formed. Figure 5.32(a) shows the punching cracks at the top face of the slab (bottom face in the specimen) in the 2nd cycle of ductility 3. In that cycle, the maximum punching crack displacement measured was 0.012 in. Figure 5.32(b) shows severe punching cracks on the north side of the slab in the 2nd cycle of ductility 5. In that cycle, the maximum punching crack displacement of the cracked slab surface measured was 0.26 in. In the 1st cycle of ductility 6, the punching crack displacement increased even more and concrete spalling was observed, as shown in Figure 5.32(c). In the 2nd cycle of ductility 6, concrete pieces came off, as shown in Figure 5.32(d). At that point, the test was ended.

Figure 5.33 shows the extensive damage at the top face of the slab (bottom face in the specimen) at the end of the test. Part of the concrete cover on the north side came off, while another part with an area larger than the footprint of the column was detached. Figure 5.34 shows

the top face of the slab before and after removing the loose concrete pieces. The loose concrete pieces were removed with no effort and a clear fracture surface was exposed. Some vertical stirrups and longitudinal bars in the slab were exposed as shown in Figure 5.34(b). The average inclination of the fracture surface was between 10^o and 15^o.

5.3.2.3 Specimen #3

Similar to Specimen #2, crushing of concrete near the base of the column of Specimen #3 was observed during the 2nd cycle of ductility 2, as shown in Figure 5.35(a). This was responsible for the subsequent drop of the lateral resistance of the column as shown in Figure 5.22. Figure 5.35(b) shows the damage near the base of the column during the 1st cycle of ductility 4. The column of Specimen #3 experienced more severe cover spalling near the base as compared to Specimen #2 (see Figure 5.30(b)). This can be attributed to the less slip of the headed longitudinal bars within the joint region of the slab of Specimen #3, which resulted in more severe bar deformation in the plastic-hinge region. Figure 5.35(c) and Figure 5.35(d) show the evolution of damage in the column up to the 2nd cycle of ductility 7. The transverse hoops and the longitudinal bars in the column were exposed due to the cover spalling, which extended to a height of 15 in. from the column base.

The evolution of damage at the bottom face of the slab (top face in the specimen) is shown in Figure 5.36. In the 1st cycle of ductility 2, cracks radiating from the column towards the west and east sides of the slab were observed, as shown in Figure 5.36(a). During the 2nd cycle of ductility 4, severe column pullout cracks were observed at the bottom face of the slab (top face in the specimen) around the column, as shown in Figure 5.36(b). In the following cycle of ductility 5, the pullout cracks became wider, as shown in Figure 5.36(c). During the last cycle at ductility 7, the pullout cracks had some interior fracture surface exposed as shown in Figure 5.36(d).

Figure 5.37 shows the exposed fracture surface around the column after pieces of concrete had been removed.

Figure 5.38 shows the evolution of damage at the top face of the slab (bottom face in the specimen). Some minor punching cracks were formed during the 1st cycle of ductility 4, as shown in Figure 5.38(a). For later cycles, existing cracks propagated and new ones were formed, as shown in Figure 5.38(b) and (c). The maximum punching crack displacement (relative displacement across a crack) measured was 0.021 in., and it was reached during the 2nd cycle of ductility 6, with no further increase in the subsequent cycles of ductility 7. The punching crack pattern at the top face of the slab (bottom face in the specimen) after the test is shown in Figure 5.38(d). The damage due to the punching of the headed bars was very minor.

The vertical displacements of the top surface of the slab (bottom surface in the specimen) of Specimens #2 and #3, measured by displacement transducers at the positions of the headed bars on the extreme north and south sides of the column, are plotted against the column displacement, expressed in terms of the ductility level, in Figure 5.39 and Figure 5.40. It can be observed that Specimen #2 had much larger displacements than Specimen #3. During the cycles of ductility 6, the vertical displacements in Specimen #2 increased significantly, which is consistent with the severe punching cracks observed.

5.3.3 Global Lateral Deformations

The lateral displacement of the column had contributions from (1) the rotation of the slab due to bending, (2) the rotation of the column at its base caused by the strain penetration of the column longitudinal bars into the anchorage region in the slab, as well as the pullout and punching mechanisms of the column longitudinal bars in the slab-column joint, (3) the flexural deformation of the column, and (4) the shear deformation of the column. Figure 5.41 through Figure 5.43 show the lateral displacements along the columns at the peaks of different cycles for

Specimens #1, #2 and #3. During the tests, the slab rotation and base rotation of the columns were monitored. The flexural and shear deformations of the columns were not measured, but the summed displacement due to these two mechanisms has been calculated by subtracting the displacements contributed by the slab deformation and the base rotation of the columns from the total displacement measured at the top. For the aspect ratio of the columns, the contribution of the shear deformation is expected to be negligible. Table 5.10 through Table 5.12 show the contributions of the aforementioned mechanisms to the lateral displacements at the top of the columns of Specimens #1, #2 and #3. The contribution of the slab rotation was negligible for all three specimens. Figure 5.44 through Figure 5.46 show the lateral load-vs.-slab rotation curves for Specimens #1, #2 and #3. The rotations were measured at the midspan of the slab. It can be seen that the slab rotation was more or less linearly proportional to the load. However, some minor change in stiffness can be observed for Specimens #1 and #2. This can be attributed to cracking in the slabs.

In the 5^{th} cycle with ductility 1, column deformation was the major contributor of the lateral displacement, accounting for 77% of the total displacement for Specimen #1, 72% for Specimen #2, and 82% for Specimen #3, while the remaining displacement was contributed by the rotation at the column base. The contribution of the base rotation increases in the subsequent cycles reaching 42% for Specimens #1, 50% for Specimen #2, and 34% for Specimen #3. Specimen #3 had the least column base rotation because of the adequate embedment length for the headed bars.

5.3.4 Strains in Column Longitudinal Bars

The strain variations along the longitudinal bars close to the north and south faces of the columns were measured by strain gages. Figure 5.47 and Figure 5.48 show the strain variations in Bars 1 and 5 (placed at the extreme locations) for Specimen #1, along the lower part of the

column and inside the slab. In these plots, a solid line corresponds to the bar in tension, and a dashed line to the bar in compression. Figure 5.49 and Figure 5.50 plot the strains at the gage locations within the embedment length of Bars 1 and 5,against the ductility demand. A number of strain gages were damaged in later cycles, as indicated by the missing data points in the figures. The measurements taken at 10 in. below the top face of the slab in the test configuration show that the yield strain penetrated the entire embedment length during the 1st cycle of ductility 5 as the top face of the bar heads (in the inverted T orientation) was located at a depth of 11 in. below the slab-column interface. Bars 1 and 5 reached a maximum tensile strain of about 0.03 before the strain gages failed. This indicates that an embedment length of $9.8d_b$ was sufficient to develop not only the yield strength of the headed bars, but also strain hardening. The large strain reversals shown in the plots indicate that the bars also developed large compressive stresses.

The strains along the Bars 1 and 4 in Specimen #2 are presented in Figure 5.51 through Figure 5.54. The observations for the strains in Specimen #2 are very similar to those for Specimen #1. Even with an embedment length as small as $8.7d_b$, the headed bars were able to develop the tensile yield strain and strain levels larger than 0.01, beyond which strain hardening is expected to occur. The measurement taken from Bar 1 at 10 in. below the top face of the slab shows that yielding penetrated the entire embedment length at the 1st cycle of ductility 4. The similar reading from Bar 4 shows that the yield strain was exceeded at the 2nd cycle of ductility 4. Specimen #2 had bar yielding penetrated to the heads one to two cycles earlier than Specimen #1.

Figure 5.55 through Figure 5.58 show the strains in Bars 1 and 4, for Specimen #3. The bars yielded in tension and developed large tensile strains in the strain-hardening regime. As shown in Figure 5.58, up to ductility 5, Bar 4 had not reached the tensile yield strain at the gage location that was 13 in. below the top face of the slab (1 in. above the head surface) in the test configuration. The gage was damaged after this ductility level. For this bar, the gage reading that was taken 9 in. below top face of the slab barely reached the yield strain at ductility 5. However,

at the depth of 9 in., Bar 1 reached a tensile strain much larger than the yield strain, as shown in Figure 5.57.

In all three specimens, the bars developed their yield strength and reached strain hardening. Specimens #1 and #2, which had development lengths of $9.8d_b$ and $8.7d_b$, respectively, had tensile yielding penetrating all the way to the heads of the longitudinal bars close to the north and south faces of the columns. Specimen #3, which had an embedment length of $11d_b$, had much smaller tensile strains developed near the heads, indicating that the headed bars were better developed compared to those in Specimens #1 and #2.

5.3.5 Strains in J-bars

Figure 5.59 shows the strains developed in the J-bars placed in the core region of the slab-column joint of Specimen #1. The strain measurements were taken at the mid-height of the J-bars (as shown in Figure A.23). It can be seen that the J-bars developed tensile strains close to the yield level. These bars were always subjected to tension with comparable strain levels when the column was pushed towards the north or the south (i.e., regardless of the fact that the longitudinal headed bars next to the J-bars were subjected to tension or compression). This indicates that the J-bars were engaged to resist both the pullout and punching forces exerted by the headed bars after diagonal breakout cracks developed in the joint region of the slab. Similar tensile strains were measured in the J-bars of Specimen #2, as shown in Figure 5.60. However, the strain level was a little lower than that for Specimen #1.

The strains in the J-bars of Specimen #3 are shown in Figure 5.61. The strains in the J-bars, except for J4 (placed at the center), barely reached half of the yield strain. This indicates that the J-bars in Specimen #3 were not engaged as much as those in Specimens #1 and #2, in which the deterioration of the anchorage of the headed bars in the slabs was much more severe.

5.3.6 Strains in Vertical Stirrups

Figure 5.62 shows the strains in the 1st row of vertical stirrups next to the column steel cage for Specimen #1. The strain measurement was taken at the mid-height of the stirrups. These stirrups exhibited a similar behavior as the J-bars, developing tensile strains when the adjacent column longitudinal bars were subjected to tension or compression. They developed strains up to 0.0015 (less than 75% of the yield strain). Figure 5.63 shows the strains in the 1st row of vertical stirrups next to the column steel cage for Specimen #2. Both Specimens #2 and #3 had four additional vertical stirrups, V4, V7, V10, and V13, placed in the first rows, which were not required according to MTD 20-7 (October 2014). Stirrup V4 developed a strain level close the yield strain, while V7, V10 and V13 reached a maximum strain around 0.0015. The rest of the vertical stirrups in the 1st row developed strains up to 0.001, which was a little less than those in Specimen #1. This indicates that V4, V7, V10, and V13 can take a large share of the pullout and punching forces exerted by the headed bars when the column is displaced in the respective directions.

Figure 5.64 shows the strains in the 1st row of vertical stirrups in Specimen #3. The strains measured are much smaller than those in Specimens #1 and #2. This can be attributed to the better development of the headed bars in Specimen #3.

Figure 5.65 through Figure 5.67 show the strains in the 2nd row of vertical stirrups for Specimens #1, #2 and #3. In all three specimens, the strains developed were very small, reaching values of about 25% of the yield strain. This indicates that the vertical stirrups farther away from the slab-column joint will not be as actively engaged as those adjacent to the headed longitudinal bars.

5.3.7 Strains in Longitudinal Bars in Slabs

Figure 5.68 through Figure 5.70 plot the strains in the longitudinal bars at the bottom face of the slab (top face in the specimen), against the ductility demand, at a section close to the north face of the columns, for Specimens #1, #2 and #3. For all three specimens, the strains in the longitudinal bars remained within the elastic regime, not exceeding 0.001. It is interesting to note that the bars did not experience the expected compressive strains for a section subjected to positive and negative bending moments. However, the tensile strains do appear to be smaller when the columns were displaced towards north (the positive direction), especially for Specimen #3. This behavior can be attributed to the proximity of the measurement locations to the column-joint region, which is subjected to a complex distribution of forces.

Figure 5.71 through Figure 5.73 plot the strains in the longitudinal bars at the top face of the slabs (bottom face in the specimen) against the ductility demand, at a section close to the north face of the columns, for Specimens #1, #2 and #3. For Specimen #1, in which moderate punching cracks were observed at the top face of the slab (bottom face in the specimen), the strains in the longitudinal bars remained within the elastic regime with a maximum of 0.0012. For Specimen #2, where the top face of the slab experienced significant damage due to the punching action of the headed bars, Bar B3 experienced a maximum compressive strain of -0.012 during the last cycle of ductility 6. Up to ductility 5, the strain in Bar B3 remained within the elastic regime. Only during the last two cycles at ductility 6, the bar yielded in compression. This is probably due to the fact that it experienced significant bending deformation caused by the punching action of the headed bars. For Specimen #3, in which very limited damage was observed at the top face of the slab (bottom face of the specimen), the strains developed in the longitudinal bars were small, as shown in Figure 5.73.

5.4 Conclusions

The test results have shown that an embedment length of $8.7d_b$ (Specimen #2) was able to develop the tensile yield strength of the headed bars and the plastic moment capacity of the column. However, the severe anchorage deterioration of the headed bars led to more pinched hysteretic load-displacement curves, as compared to the other two cases with higher embedment lengths. Furthermore, the top face of the slab (bottom face in the specimen) was severely damaged by the punching action of the headed bars. Specimen #1, which had an embedment length of $10d_b$, had moderate punching cracks and a better hysteretic load-displacement behavior. Specimen #3, which had an embedment length of $11d_b$, exhibited the most satisfactory behavior with very minor punching cracks.

The J-bars adjacent to the headed bars within the column cage, and the vertical stirrups right outside the column cage played a significant role in restraining breakout cracks and punching cracks when the headed bars were subjected to tension and compression. The vertical stirrups in the 2nd row and farther away from the column cage did not develop any significant stress during the tests. The specifications for J-bars and vertical stirrups in MTD 20-7 appear to be adequate to restrain breakout and punching cracks in the slab for an embedment length of $10d_b$. Nevertheless, it is recommended that MTD 20-7 be revised to include four additional stirrups adjacent to the column cage, as for Specimens #2 and #3. When probably restrained by the J-bars and vertical stirrups, the mat of longitudinal and transverse bars at the top face of the slab (bottom face in the specimen) can resist the punching action of the headed bars. Therefore, the bar heads should be below the top mat of reinforcement in the bridge slab.

5.5 Acknowledgement of Publication

This chapter, in full, is a reprint of the material as it appears in the report submitted to the California Department of Transportation in 2015, Papadopoulos, V., Murcia-Delso, J., Shing, P. B., under the title “Development Length for Headed Bars in Slab-Column Joints of RC Slab Bridges”. The dissertation author was the primary investigator and author of this report.

Table 5.1 – Design details of slab-column specimens

	Specimen #1	Specimen #2	Specimen #3
Column diameter		24 in.	
Confined core diameter		20 in.	
Column height		12 ft.	
Column longitudinal bars	8 No. 9	6 No. 10	6 No. 10
Long. steel ratio	1.77 %	1.68 %	1.68 %
Column hoops		No. 5 @ 3.5 in.	
Transverse steel ratio		1.77 %	
Slab thickness at slab-column joint	16 in.	16 in.	19 in.
Embedment length of long. bars	11 in. ($9.8d_b$)	11 in. ($8.7d_b$)	14 in. ($11d_b$)

Table 5.2 – Slab reinforcement in the slab-column joint region per MTD 20-7 (October 2014)

Description	Requirement	Specimen #1	Specimen #2	Specimen #3
Area of flexural reinforcement in the longitudinal and the transverse directions within effective width	$A_{cap}^{top}, A_{cap}^{bot}$ = [Flexural reinf. required + additional reinf.] Addit. reinf. = $0.25\times A_{st}$ for drop cap Addit. reinf. = $0.35\times A_{st}$ for flat slab	No. 8 @ 6 in. (longitudinal) No. 8 @ 6 in. (transverse)	No. 8 @ 6 in. (longitudinal) No. 8 @ 6 in. (transverse)	No. 8 @ 6 in. (longitudinal) No. 7 @ 6 in. (transverse)
J-bars in the core zone of joint region	$A_s^{j-bar} = 0.35\times A_{st}$		9 No. 5	
Total area of vertical stirrups in Joint region	$A_s^{jv} = 1.15\times A_{st}$	36 No. 5	40 No. 5*	40 No. 5*
Total area of vertical stirrups in Joint Perimeter	$A_s^{jvp} = 1.15\times A_{st}$		32 No. 5	
Horizontal ties	$A_s^{jh} = 0.1\times A_{st}$		8 No. 3	
Horizontal side reinforcement	$A_s^{sf} \geq \begin{cases} 0.1\times A_{cap}^{top} \\ or \\ 0.1\times A_{cap}^{bot} \end{cases}$		4 No. 4	
Transverse column reinf. extended into slab	$A_{v,\,joint} \geq 0.18\times A_{st}$		3 No. 5 hoops	

*Slightly more than that required by MTD 20-7.

Table 5.3 – Concrete mix design for the slab of slab-column specimens

Specified compressive strength = 4,000 psi		
Material	Quantity	Proportion of Aggregate (%)
Cement	560 lbs./yd^3	-
Flyash	118 lbs./yd^3	-
1'' x #4 Agg.	1344 lbs./yd^3	44
3/8'' x #8 Agg.	351 lbs./yd^3	11
Fine Agg.	1286 lbs./yd^3	45
Water (w/c)	38.1 gl./yd^3 (0.471)	-
WRDA-64 (admixture)	25 oz./yd^3	-
Air content	2 %	-

Table 5.4 – Concrete mix design for the column of slab-column specimens

Specified compressive strength = 4,500 psi		
Material	Quantity	Proportion of aggregate (%)
Cement	560 lbs./yd^3	-
Flyash	118 lbs./yd^3	-
1'' x #4 Agg.	1223 lbs./yd^3	42
3/8'' x #8 Agg.	445 lbs./yd^3	15
Fine Agg.	1240 lbs./yd^3	43
Water (w/c)	39 gl./yd^3 (0.448)	-
WRDA-64 (admixture)	21 oz./yd^3	-
Air content	2 %	-

Table 5.5 – Compressive and tensile strengths of concrete on the day of test

Specimen	Region	Compressive strength of concrete (ksi)	Splitting tensile strength of concrete (ksi)
#1	Column	3.2	0.46
	Slab	5.0	0.35
#2	Column	4.8	0.41
	Slab	4.9	0.45
#3	Column	5.0	0.43
	Slab	4.5	0.43

Table 5.6 – Yield and tensile strengths of steel reinforcement

Specimen	Reinforcement	Bar size	Yield strength, ksi	Tensile strength, ksi
#1	Column longitudinal bars	No. 9	69.0	99.5
	Column hoops	No. 5	67.5 [1]	91.2
	Slab longitudinal bars	No. 8	66.5	91.5
	Vertical ties in slab	No. 5	67.5	96.0
#2	Column longitudinal bars	No. 10	64.5	94.2
	Column hoops	No. 5	69.6 [1]	92.2
	Slab longitudinal bars	No. 8	68.2	98.2
	Vertical ties in slab	No. 5	61.0	85.0
#3	Column longitudinal bars	No. 10	71.1	90.1
	Column hoops	No. 5	64.0 [1]	97.9
	Slab longitudinal bars	No. 7	64.5	96.5
	Slab longitudinal bars	No. 8	67.6	97.5
	Vertical ties in slab	No. 5	63.2	90.1

[1]Stress at 0.002 plastic strain.

Table 5.7 – Loading Protocol for Specimen #1

Cycle no.	Drift (in.)	Ductility demand
1	0.2	0.1
2	0.6	0.2
3	1.1	0.4
4	1.8	0.7
5a, 5b	2.5	1
6a, 6b	5.0	2
7a, 7b	7.5	3
8a, 8b	10.0	4
9a, 9b	12.5	5
10a, 10b	15.0	6

Table 5.8 – Loading Protocol for Specimen #2

Cycle no.	Drift (in.)	Ductility demand
1	0.1	0.05
2	0.5	0.25
3	1.0	0.5
4	1.5	0.75
5a, 5b	2.0	1
6a, 6b	4.0	2
7a, 7b	6.0	3
8a, 8b	8.0	4
9a, 9b	10.0	5
10a, 10b	12.0	6

Table 5.9 – Loading Protocol for Specimen #3

Cycle no.	Drift (in.)	Ductility demand
1	0.1	0.05
2	0.5	0.25
3	1.0	0.5
4	1.5	0.75
5a, 5b	2.0	1
6a, 6b	4.0	2
7a, 7b	6.0	3
8a, 8b	8.0	4
9a, 9b	10.0	5
10a, 10b	12.0	6
11a, 11b	14.0	7

Table 5.10 – Contributions of different deformation sources to the column drift in Specimen #1

Cycle no. (drift)	Rotation of the slab (%)	Column base rotation (%)	Flexural and shear deformations of column (%)
5a (+ 2.5 in.)	2	24	74
5a (- 2.5 in.)	0	26	74
6a (+ 5.0 in.)	2	27	71
6a (- 5.0 in.)	0	27	73
8a (+ 10.0 in.)	2	30	68
8a (- 10.0 in.)	0	33	68
9a (+ 12.5 in.)	2	33	65
9a (- 12.5 in.)	0	35	65
10a (+ 15.0 in.)	2	38	60
10a (- 15.0 in.)	0	40	60
10b (+ 15.0 in.)	1	40	58
10b (- 15.0 in.)	0	42	58

Table 5.11 – Contributions of different deformation sources to the column drift in Specimen #2

Cycle no. (drift)	Rotation of the slab (%)	Column base rotation (%)	Flexural and shear deformations of column (%)
5a (+ 2.0 in.)	1	27	72
5a (- 2.0 in.)	0	29	71
6a (+ 4.0 in.)	1	35	64
6a (- 4.0 in.)	0	40	60
8a (+ 8.0 in.)	0	42	58
8a (- 8.0 in.)	0	40	60
9a (+ 10.0 in.)	0	45	55
9a (- 10.0 in.)	0	41	59
10a (+ 12.0 in.)	1	48	51
10a (- 12.0 in.)	0	44	56
10b (+ 12.0 in.)	1	50	49
10b (- 12.0 in.)	-	-	-

Table 5.12 – Contributions of different deformation sources to the column drift in Specimen #3

Cycle no. (drift)	Rotation of the slab (%)	Column base rotation (%)	Flexural and shear deformations of column (%)
5a (+ 2.0 in.)	0	19	81
5a (- 2.0 in.)	0	18	82
6a (+ 4.0 in.)	0	24	77
6a (- 4.0 in.)	1	25	74
8a (+ 8.0 in.)	0	22	78
8a (- 8.0 in.)	1	27	72
9a (+ 10.0 in.)	0	21	79
9a (- 10.0 in.)	0	30	70
10a (+ 12.0 in.)	0	16	84
10a (- 12.0 in.)	1	33	66
11a (+ 14.0 in.)	0	15	85
11a (- 14.0 in.)	1	34	65

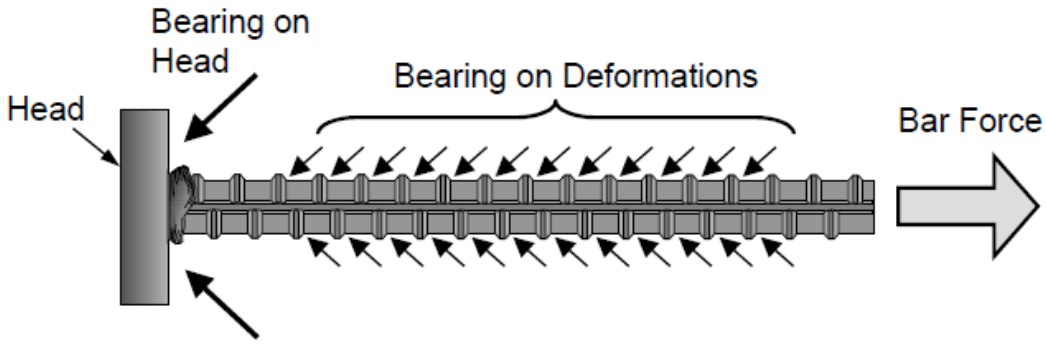

Figure 5.1 – Anchorage of a headed bar (Thompson et al. 2002)

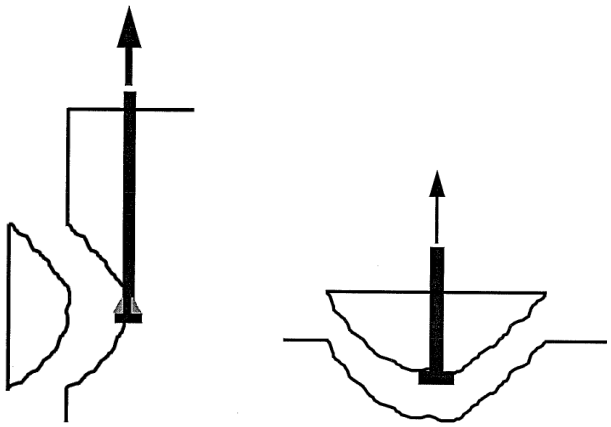

(a) Side-blowout failure (b) Concrete breakout failure

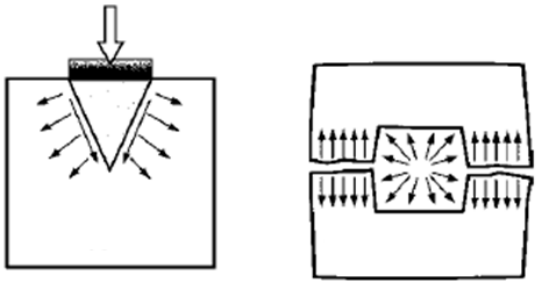

Side view Top view

(c) Bearing failure

Figure 5.2 – Anchorage failure mechanisms for headed bars

Figure 5.3 – Concrete Breakout failure in a shallow embedment test (DeVries et al. 1999)

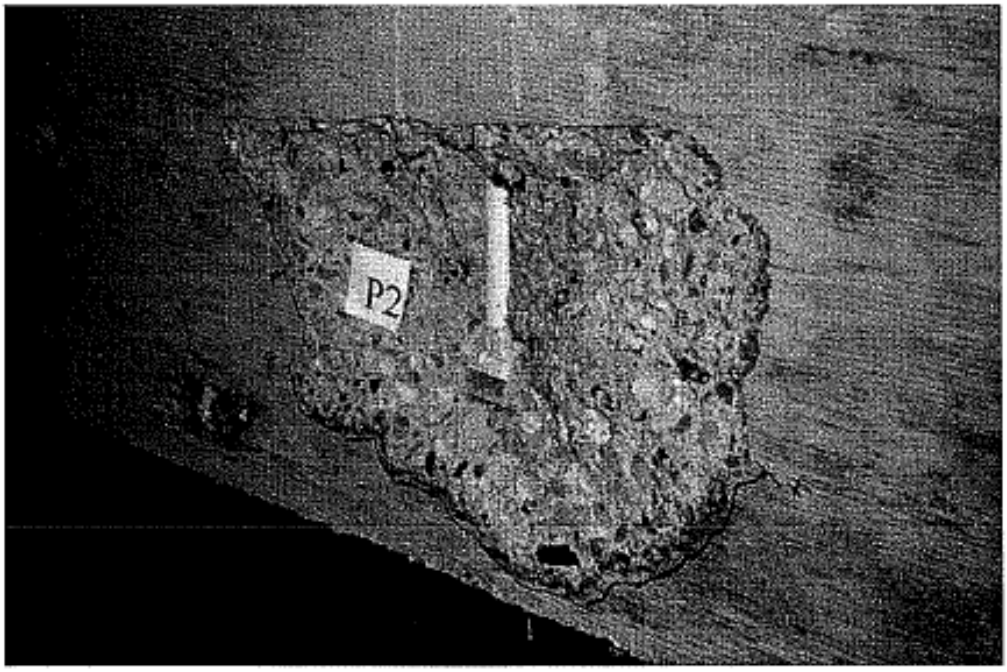

Figure 5.4 – Side-blowout failure in a beam-column joint test (Bashandy 1996)

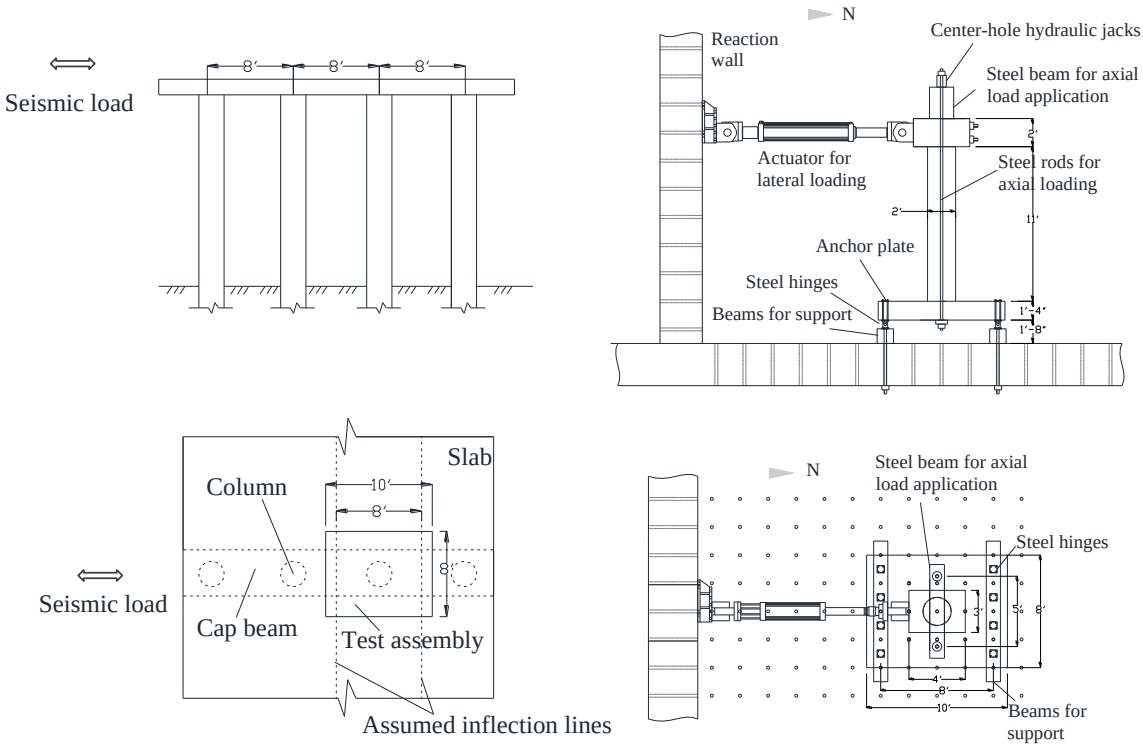

(a) Slab bridge (b) Slab-column assembly

Figure 5.5 – Slab-column assembly test setup

Figure 5.6 – Picture of test setup (Specimen #1)

Figure 5.7 – Slab with drop cap in Specimen #3

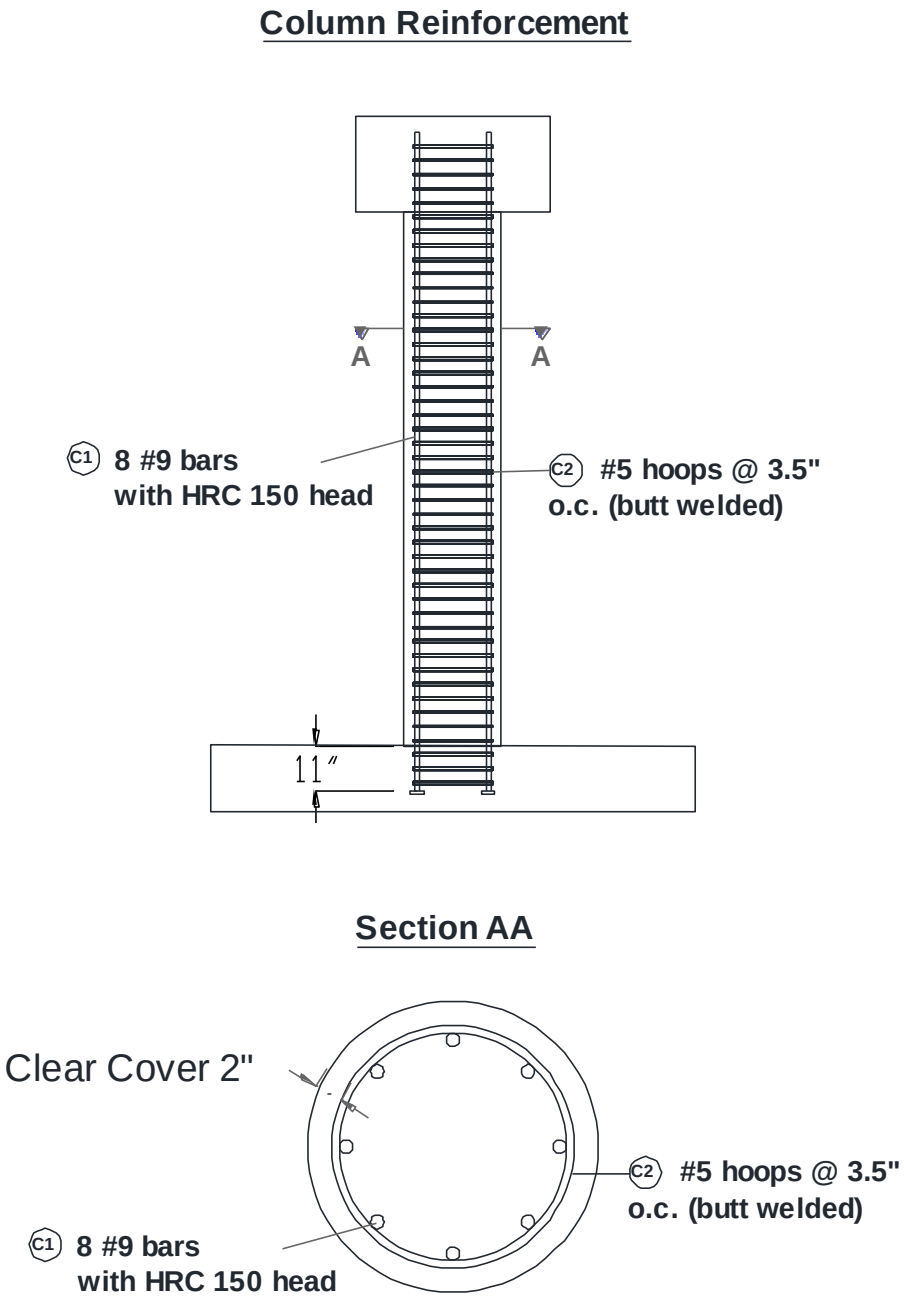

Figure 5.8 – Column reinforcement for Specimen #1

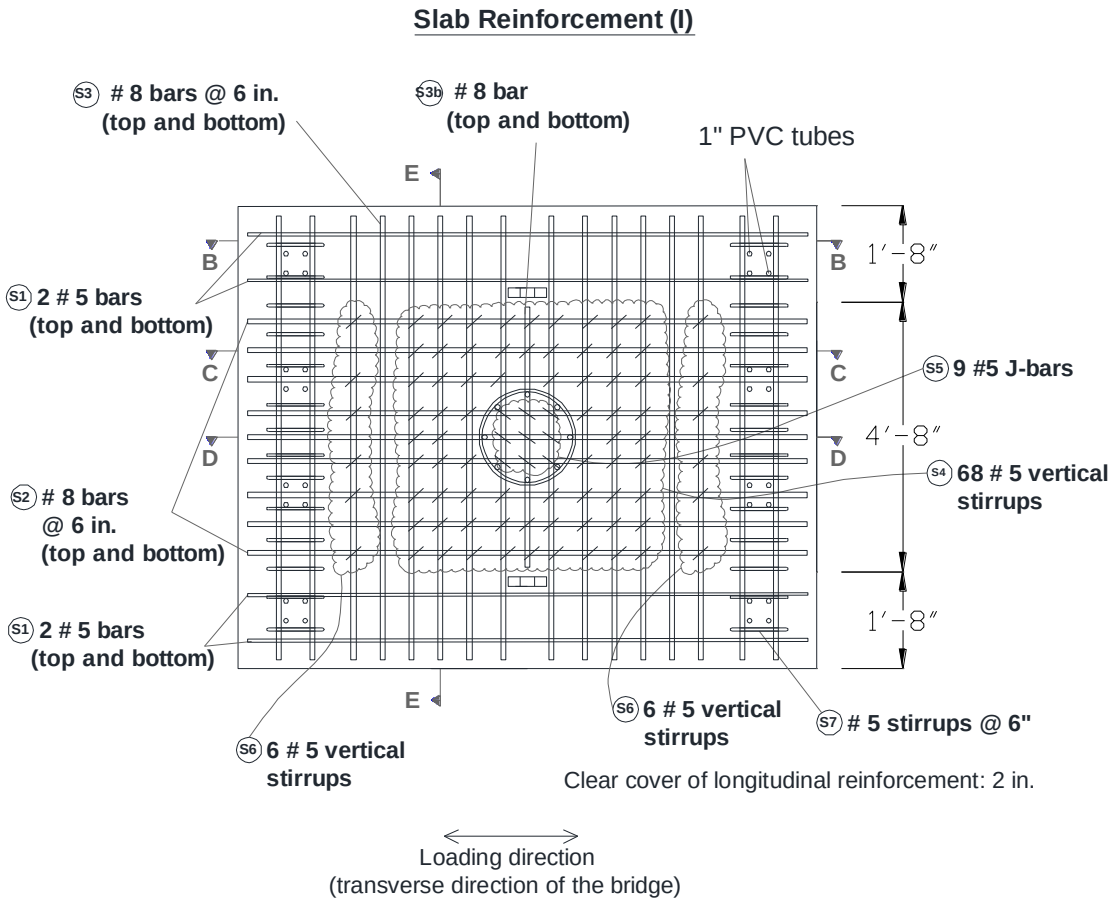

Figure 5.9 – Plan view of slab reinforcement for Specimen #1

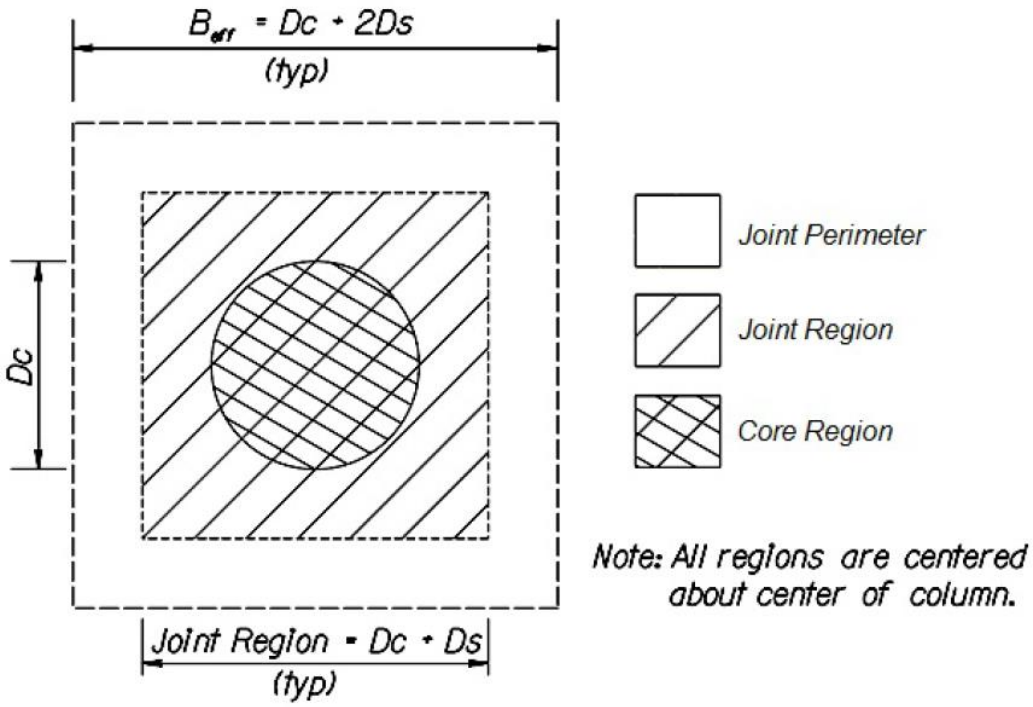

Figure 5.10 –Regions in a slab-column joint defined in MTD 20-7(October 2014)

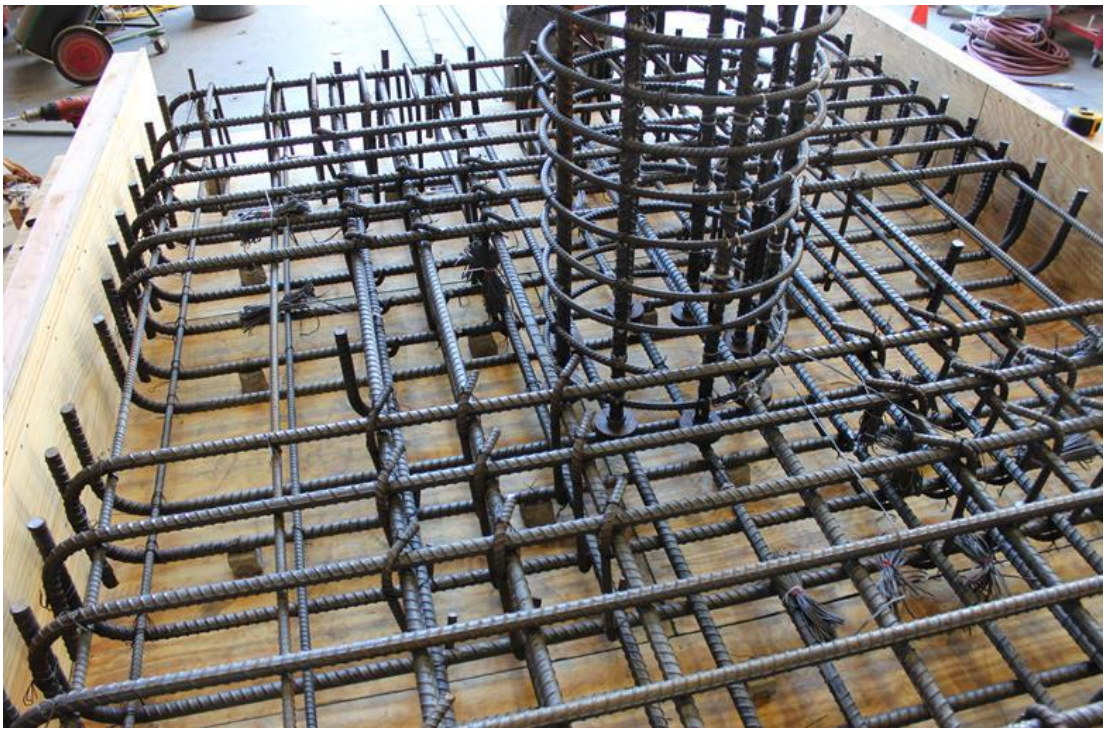

Figure 5.11 – Picture of the slab and column reinforcement of Specimen #1 during construction

Figure 5.12 – Picture of the slab and column reinforcement of Specimen #1 prior to cast

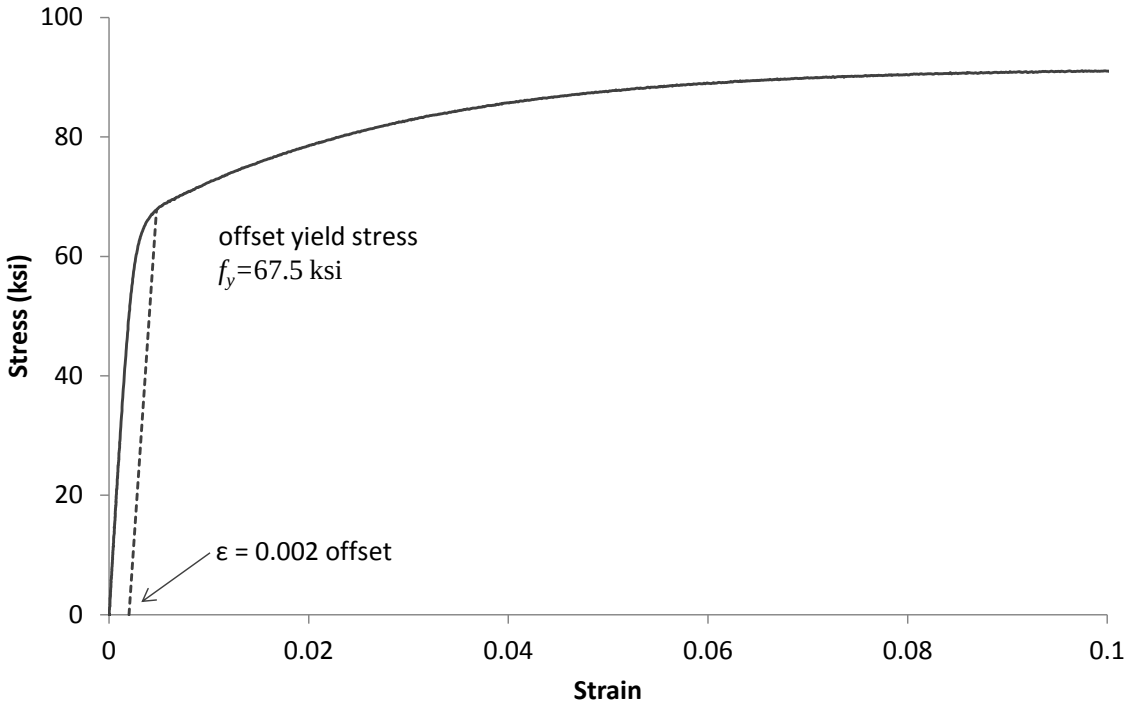

Figure 5.13 – Stress-strain curve for material sample of column hoops in Specimen #1

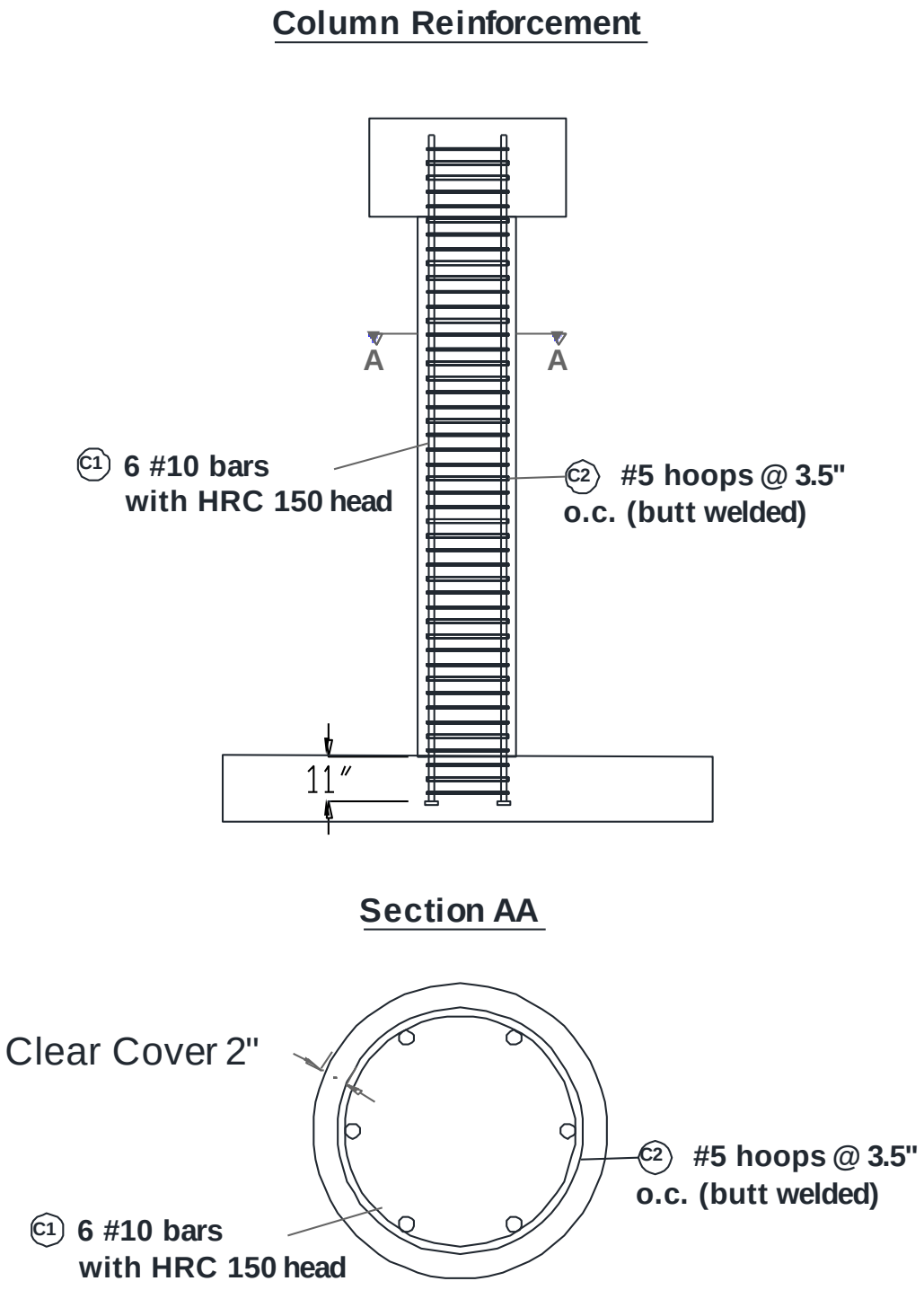

Figure 5.14 – Column reinforcement for Specimen #2

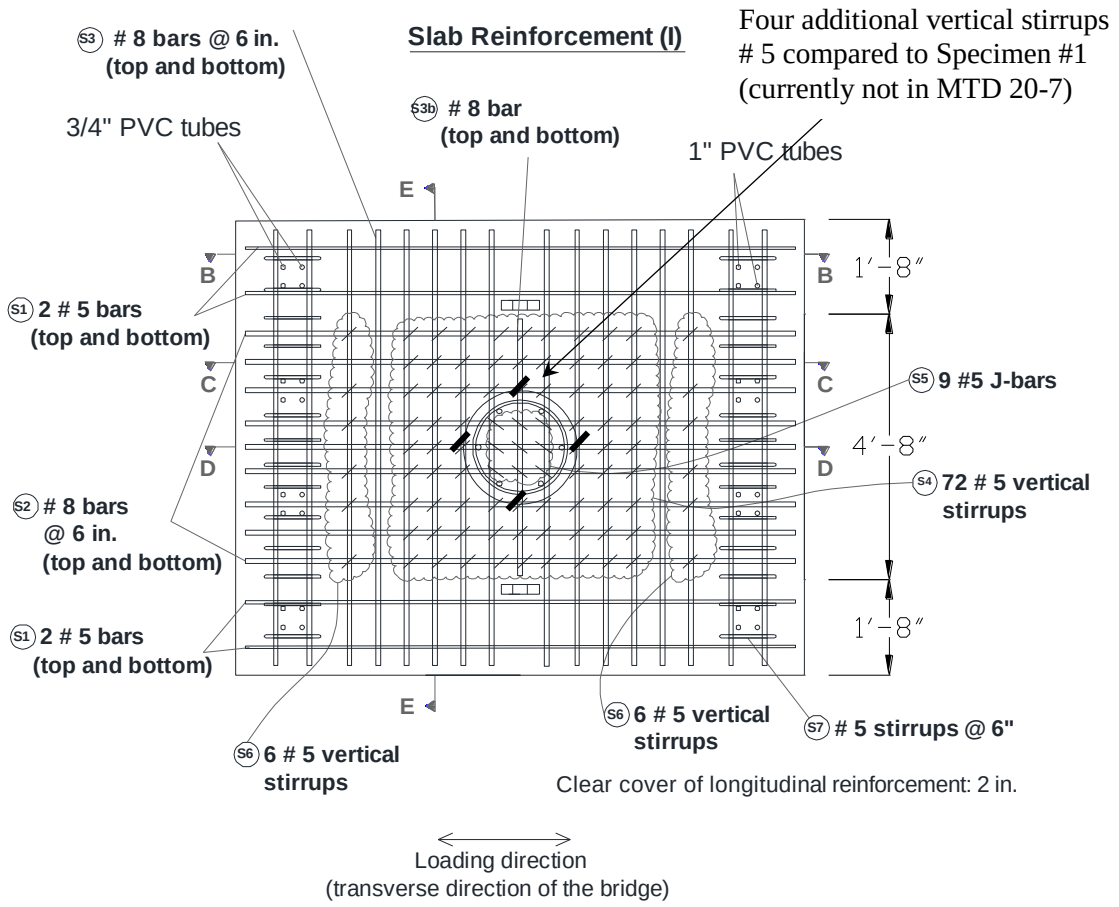

Figure 5.15 – Plan view of slab reinforcement for Specimen #2

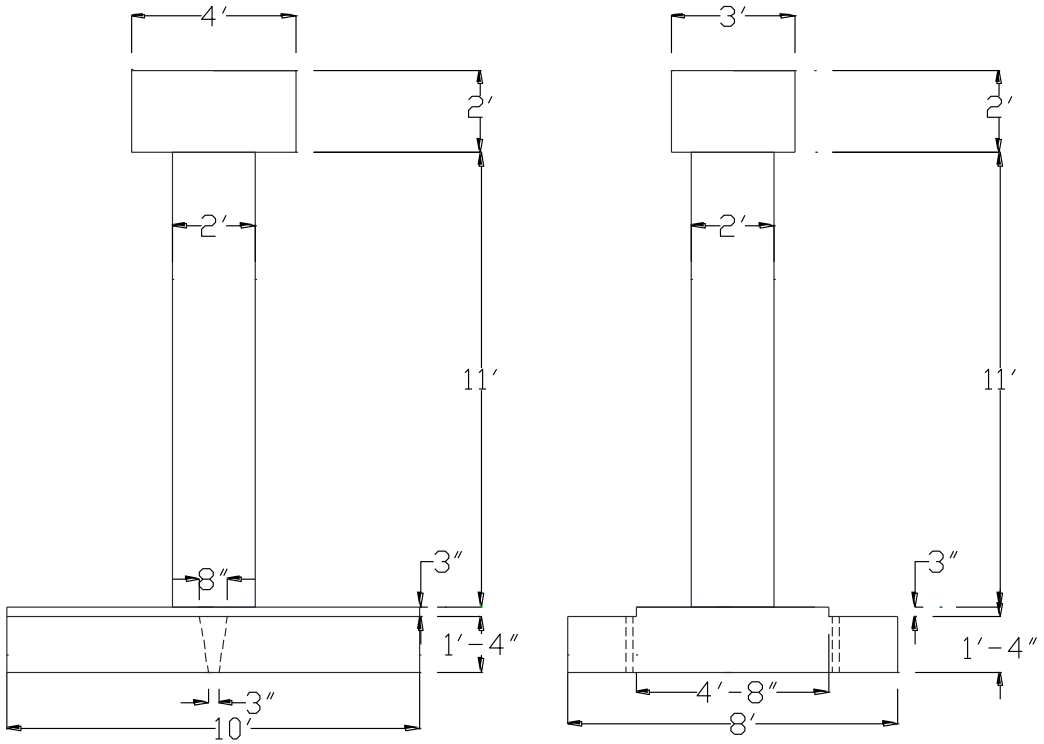

(a) Elevation view AA (east) (b) Elevation view BB (south)

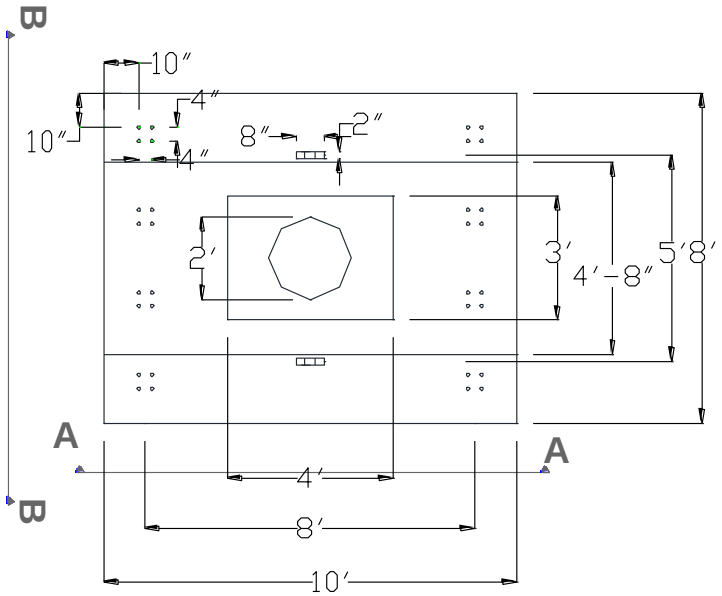

(c) Plan view

Figure 5.16 – Plan and elevation views for Specimen #3

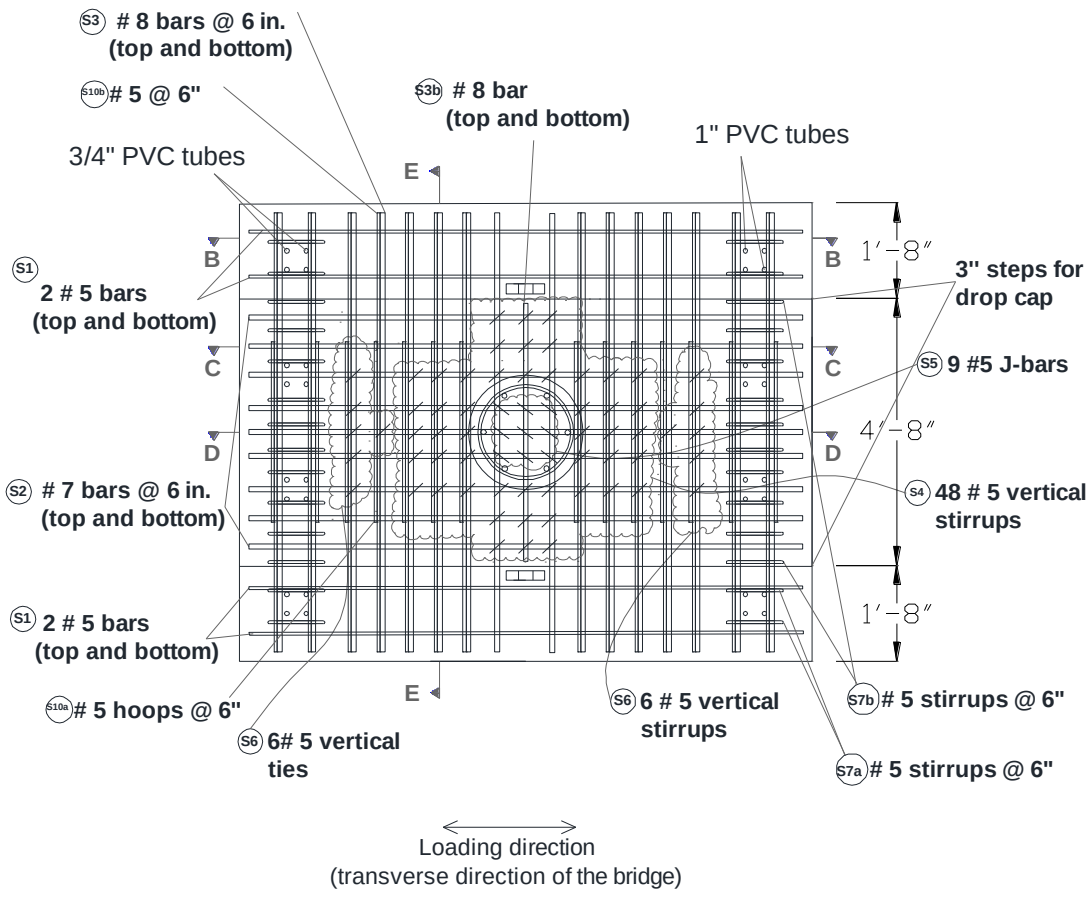

Figure 5.17 – Plan view of slab reinforcement for Specimen #3

Figure 5.18 – Picture of slab and column reinforcement of Specimen #3 prior to cast

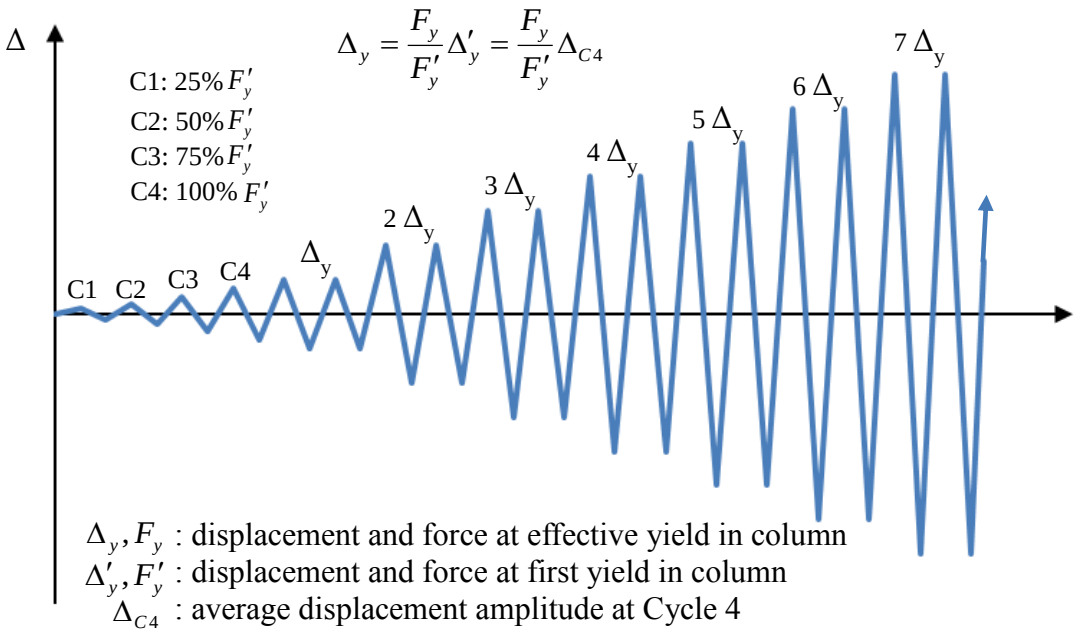

(a) loading history

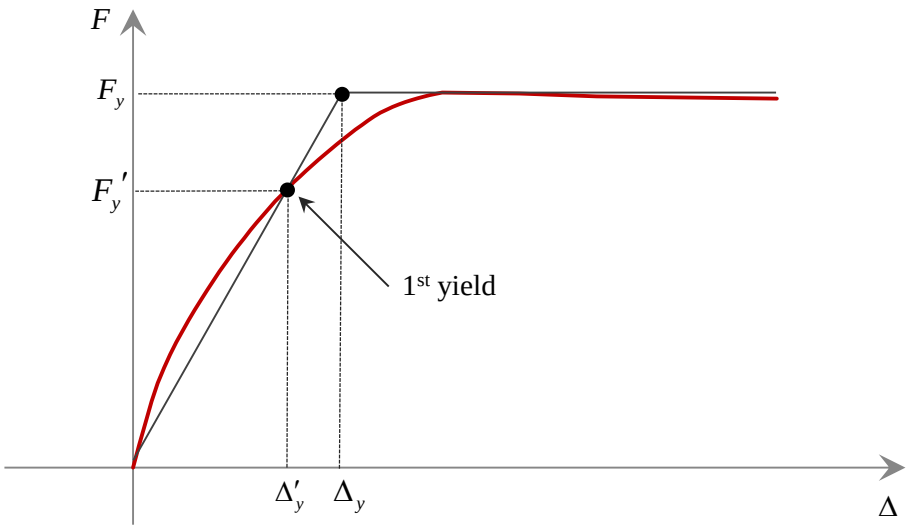

(b) first yield and effective yield

Figure 5.19 – Loading protocol

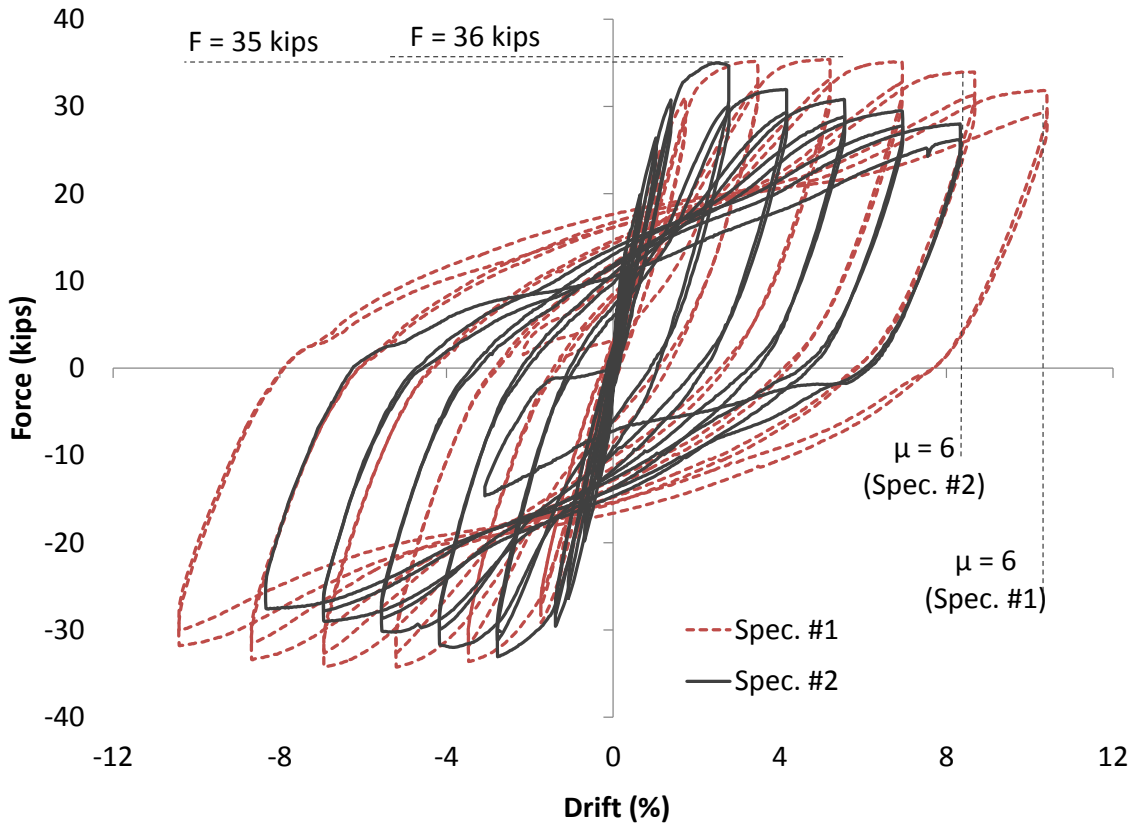

Figure 5.20 – Lateral force-vs.-drift ratio for Specimens #1 and #2

Figure 5.21 – Deflected shape of Specimen #1 at ductility 6

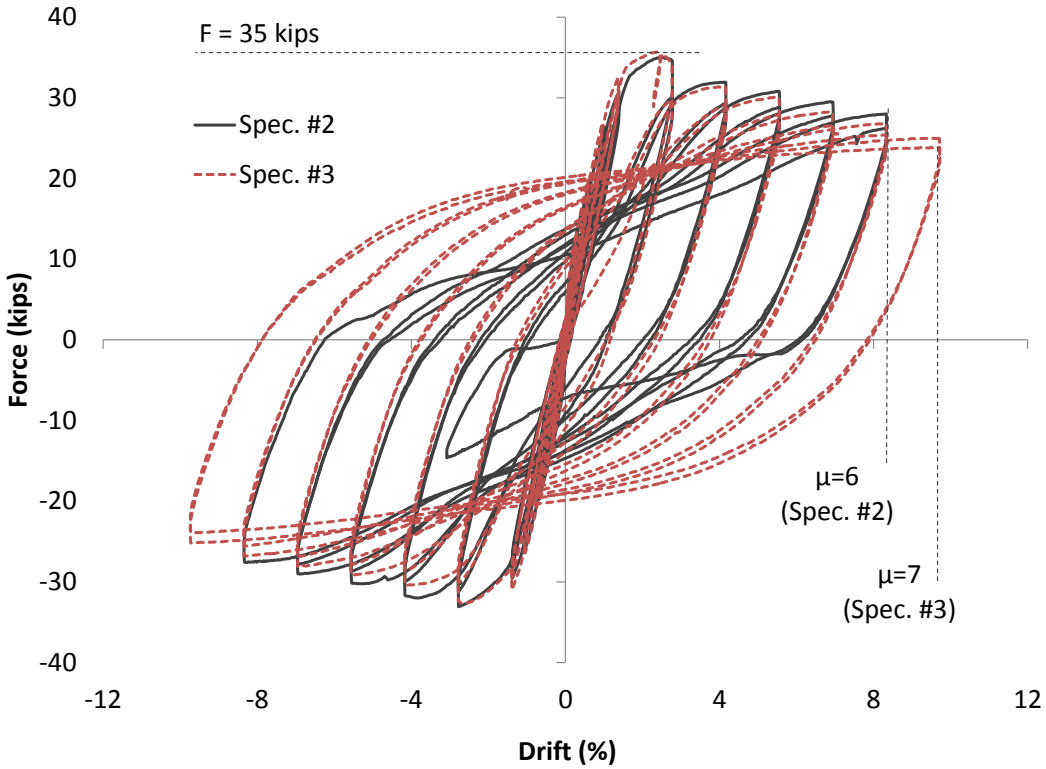

Figure 5.22 – Lateral force-vs.-drift ratio for Specimens #2 and #3

(a) Specimen #1 (b) Specimen #2

Figure 5.23 – Flexural cracks at the south face of the columns of Specimens #1 and #2 at Cycle 4 (1st yield)

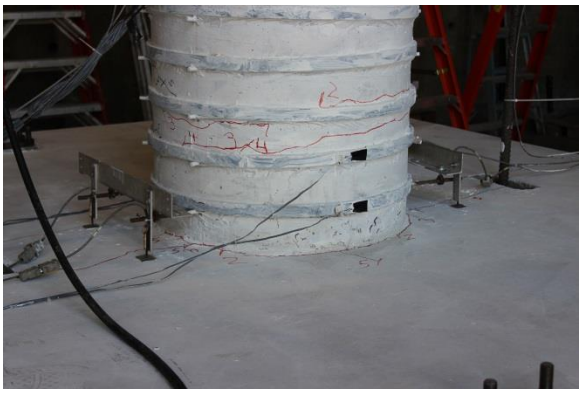

(a) north face at Cycle 6a (μ = 2)

(b) south face at Cycle 6a (μ = 2)

(c) north face at Cycle 9a (μ = 5)

(d) south face at Cycle 9a (μ = 5)

Figure 5.24 – Evolution of damage at the bottom of the column of Specimen #1

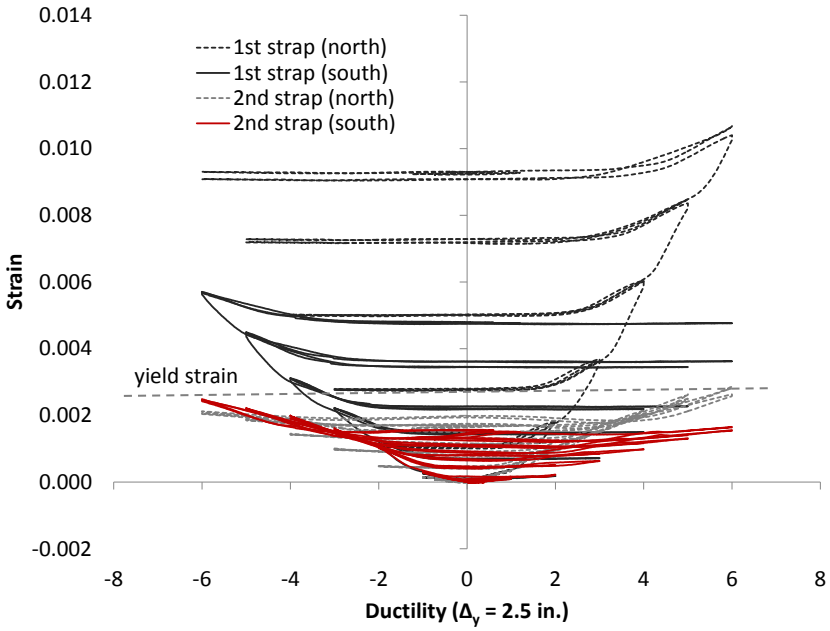

Figure 5.25 – Strains in confining steel straps around the column of Specimen #1

(a) Cycle 5a (μ = 1)

(b) Cycle 7a (μ = 3)

(c) Cycle 7b (μ = 3)

(d) Cycle 10a (μ = 6)

Figure 5.26 – Evolution of damage in the slab of Specimen #1

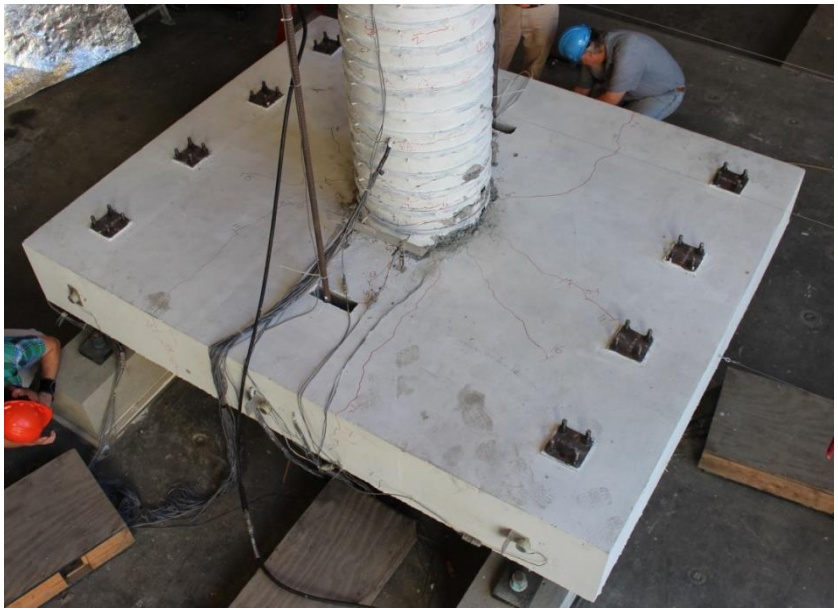

Figure 5.27 – Damage at the bottom face of the slab (top face in the specimen) of Specimen #1 at the end of testing

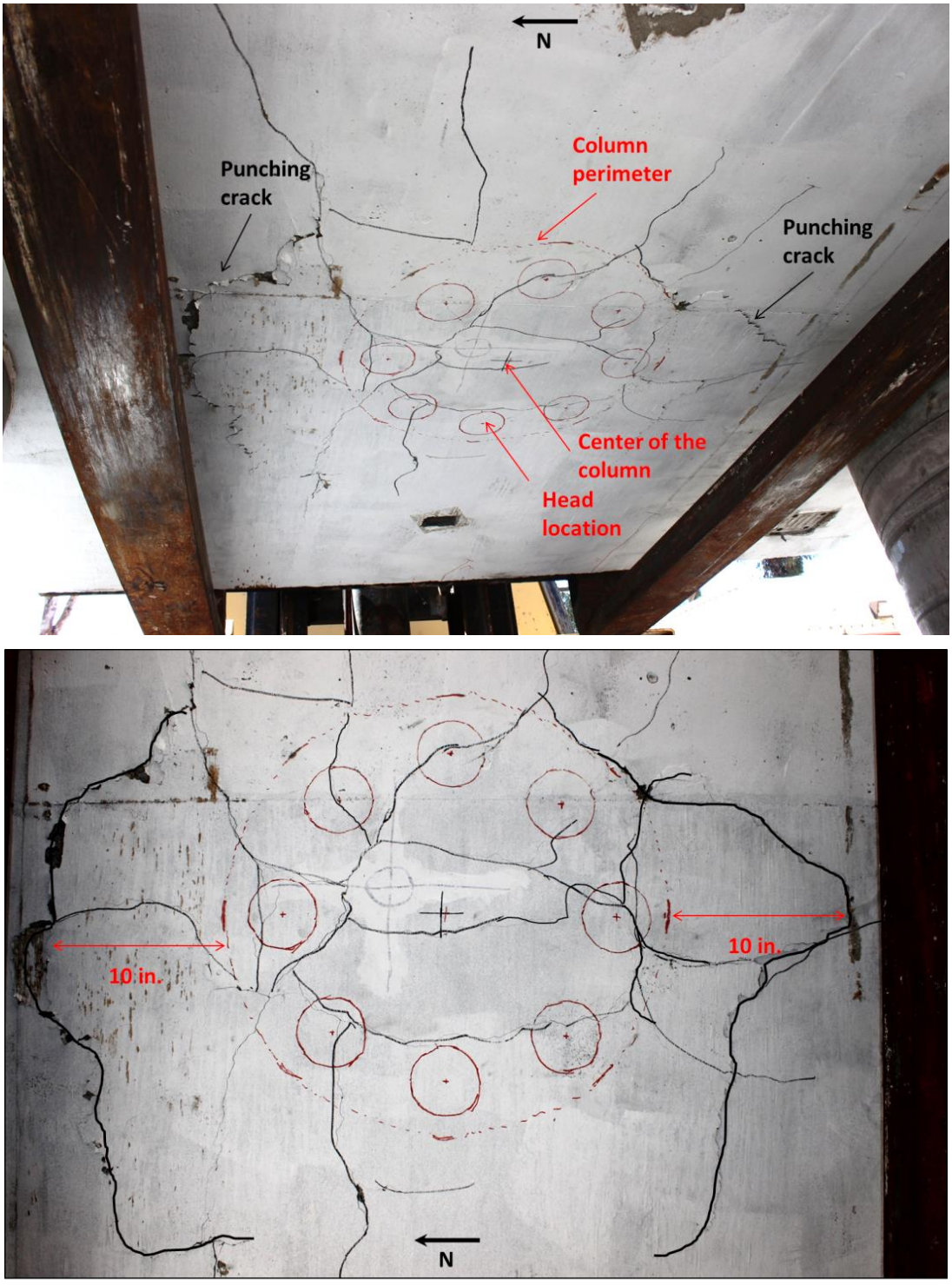

Figure 5.28 – Crack pattern at the top face of the slab (bottom face in the specimen) after the testing of Specimen #1

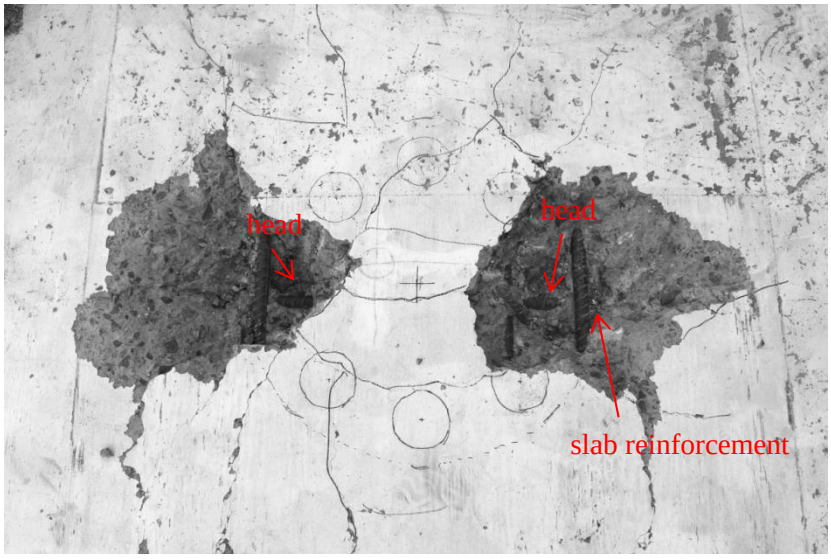

Figure 5.29 – Exposure of fracture surface at the top face of the slab (bottom face in the specimen) of Specimen #1

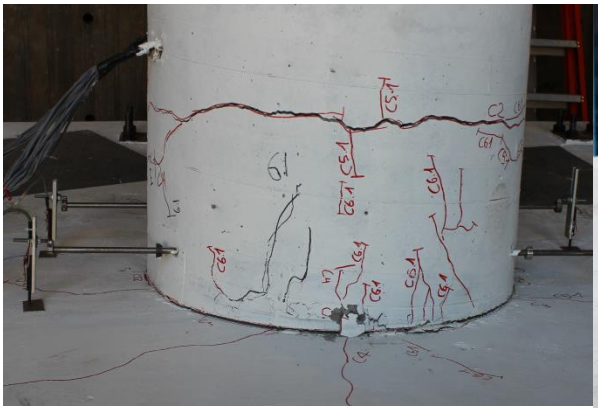

(a) north face at Cycle 6b (μ = 2)

(b) west face at Cycle 8a (μ = 4)

(c) east face at Cycle 10a (μ = 6)

(d) north face at Cycle 10a (μ = 6)

Figure 5.30 – Evolution of damage at the bottom of the column of Specimen #2

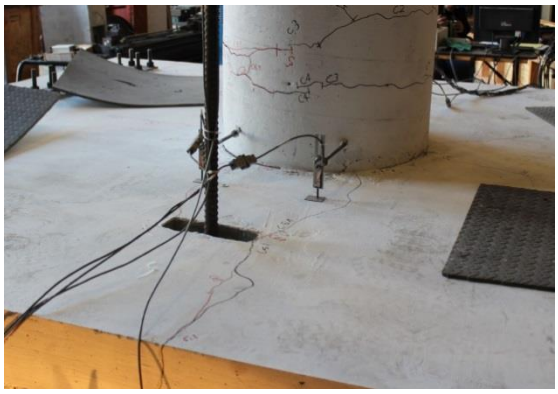

(a) west face at Cycle 6a (μ = 2)

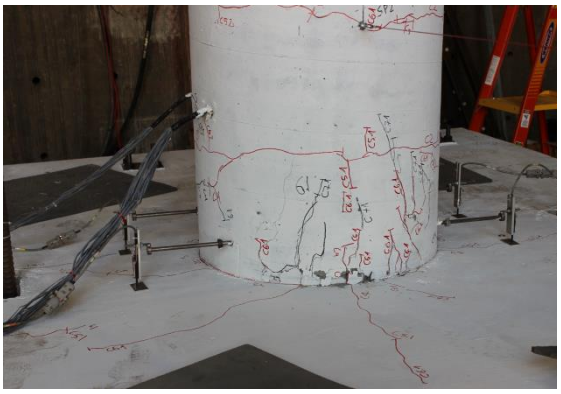

(b) north face at Cycle 7a (μ = 3)

(c) east face at Cycle 9a (μ = 5)

(d) north face at Cycle 9a (μ = 5)

Figure 5.31 – Evolution of damage at the bottom face of the slab (top face in the specimen) of Specimen #2

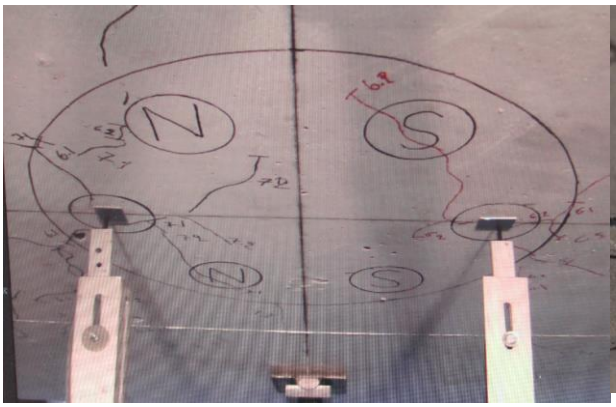

(a) Cycle 7b (μ = 3)

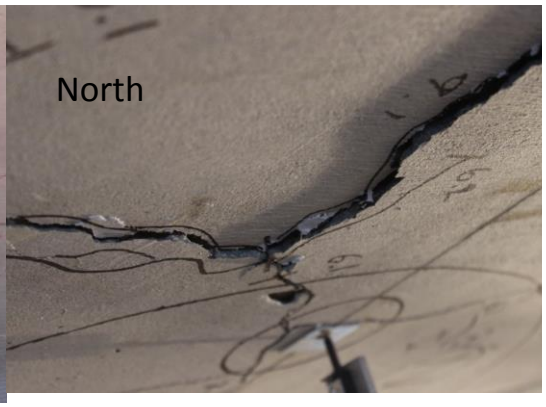

(b) Cycle 9b (μ = 5)

(c) Cycle 10a (μ = 6)

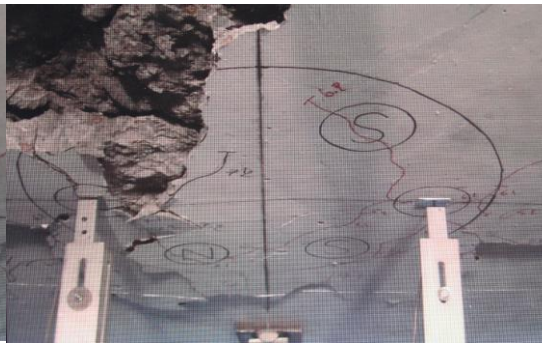

(d) Cycle 10b (μ = 6)

Figure 5.32 – Evolution of damage at the top face of the slab (bottom face in the specimen) of Specimen #2

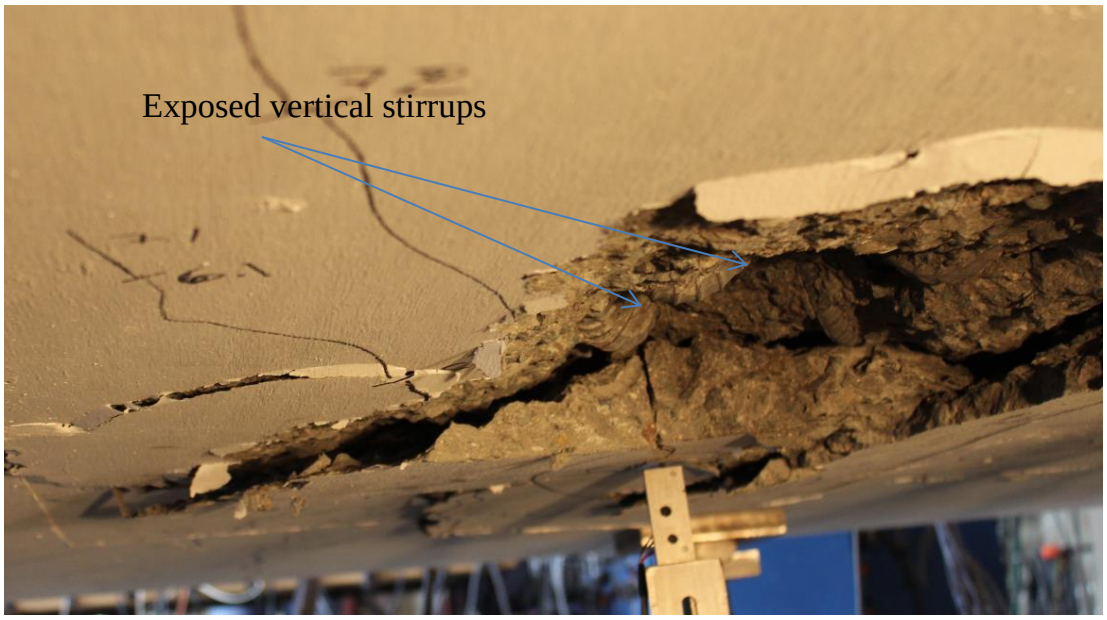

(a) North region

(b) South region

Figure 5.33 – Damage at the top face of the slab (bottom face in the specimen) of Specimen #2 at the end of testing

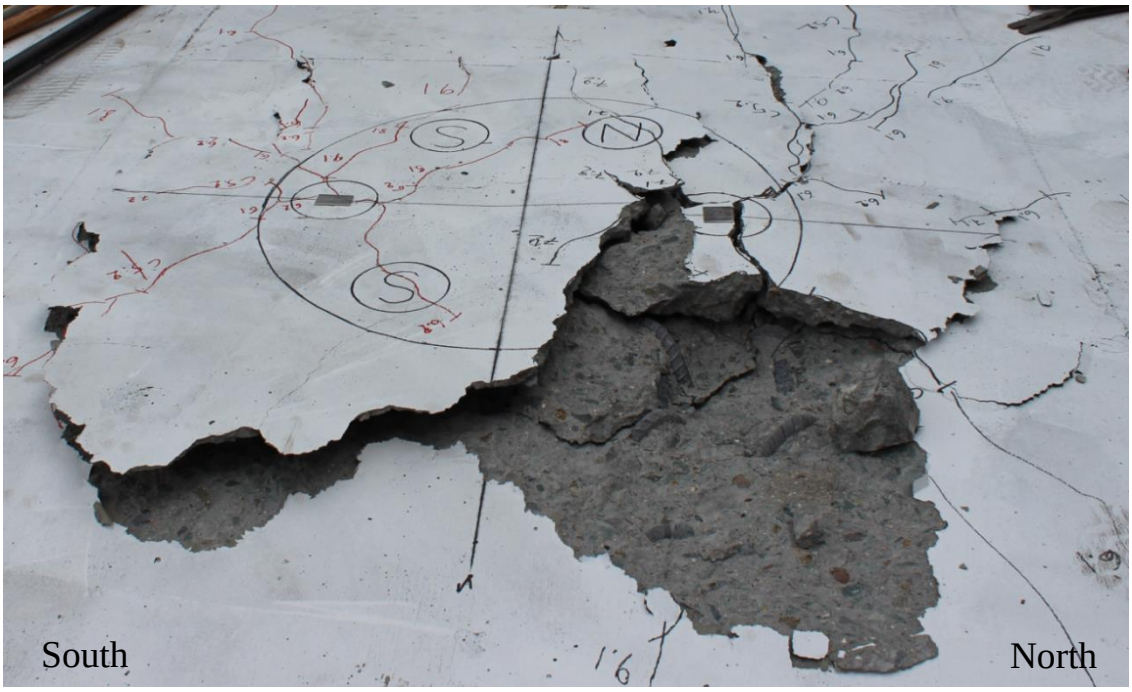

(a) Before removing loose concrete pieces

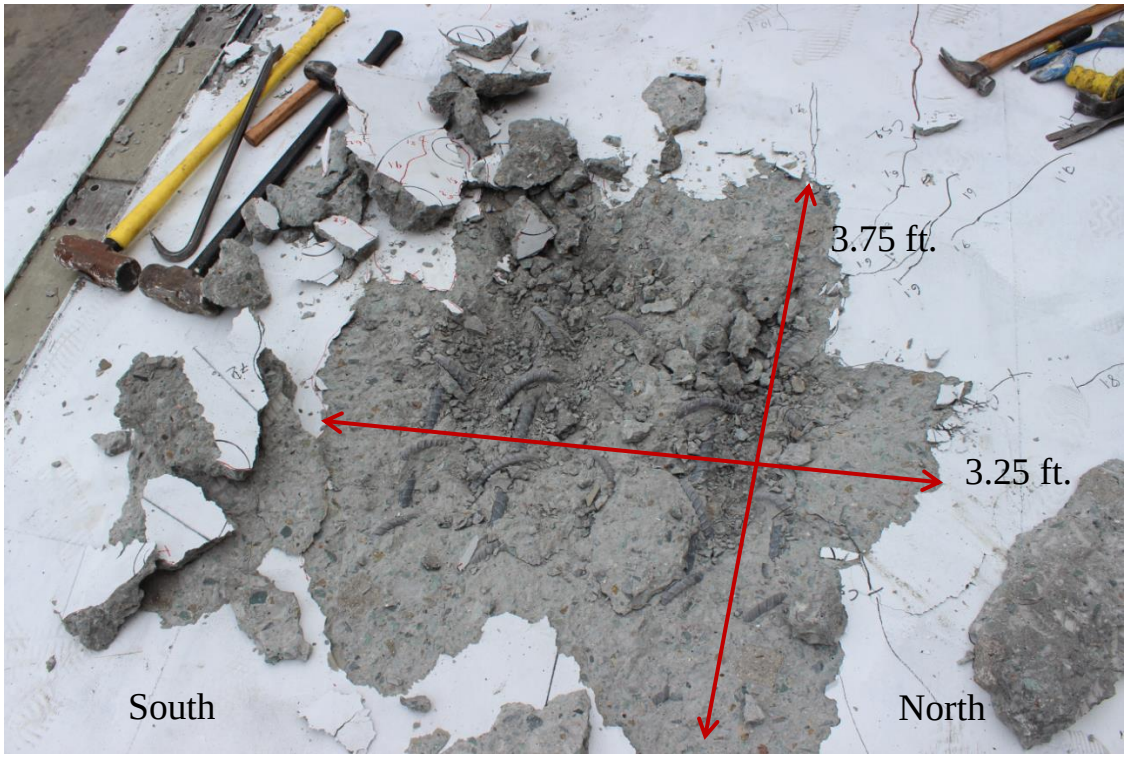

(b) After removing loose concrete pieces

Figure 5.34 – Exposure of fracture surface at the top face of the slab (bottom face in the specimen) of Specimen #2

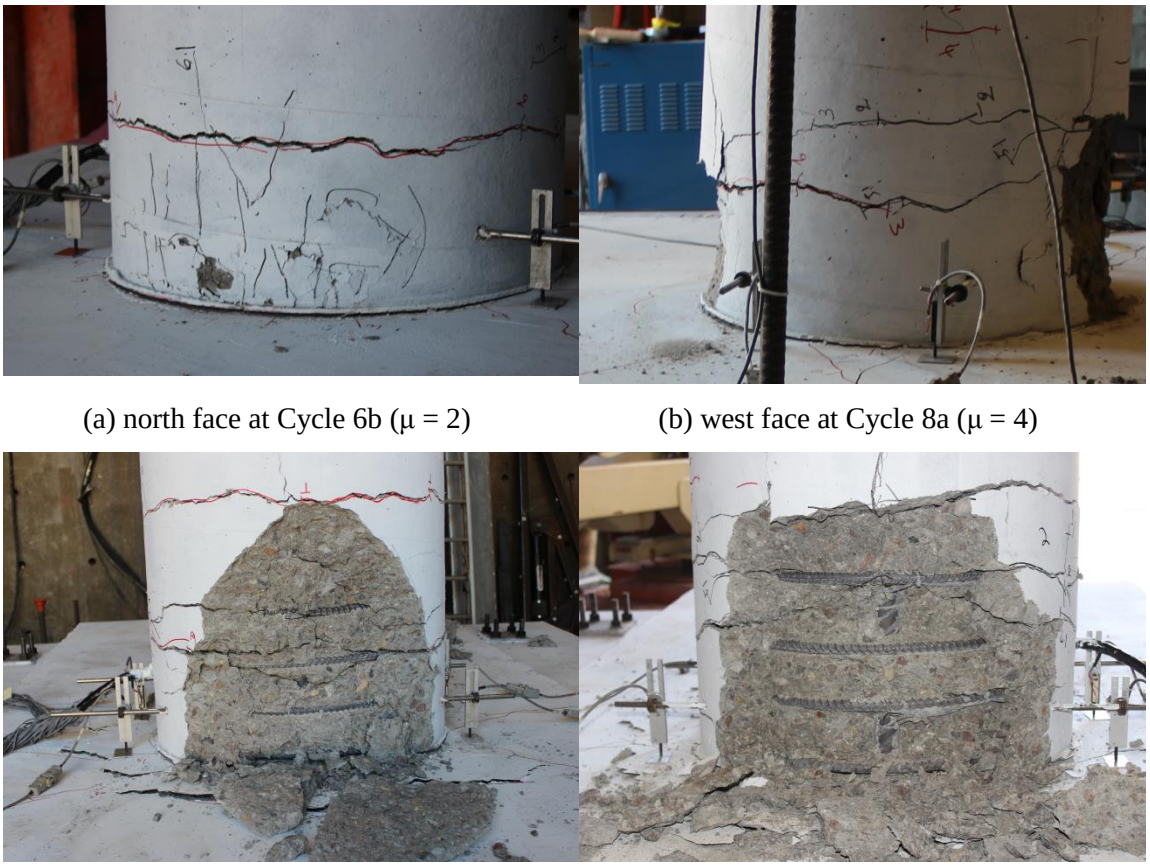

(a) north face at Cycle 6b (μ = 2)

(b) west face at Cycle 8a (μ = 4)

(c) north face at Cycle 10b (μ = 6)

(d) south face at Cycle 11b (μ = 7)

Figure 5.35 – Evolution of damage at the base of the column of Specimen #3

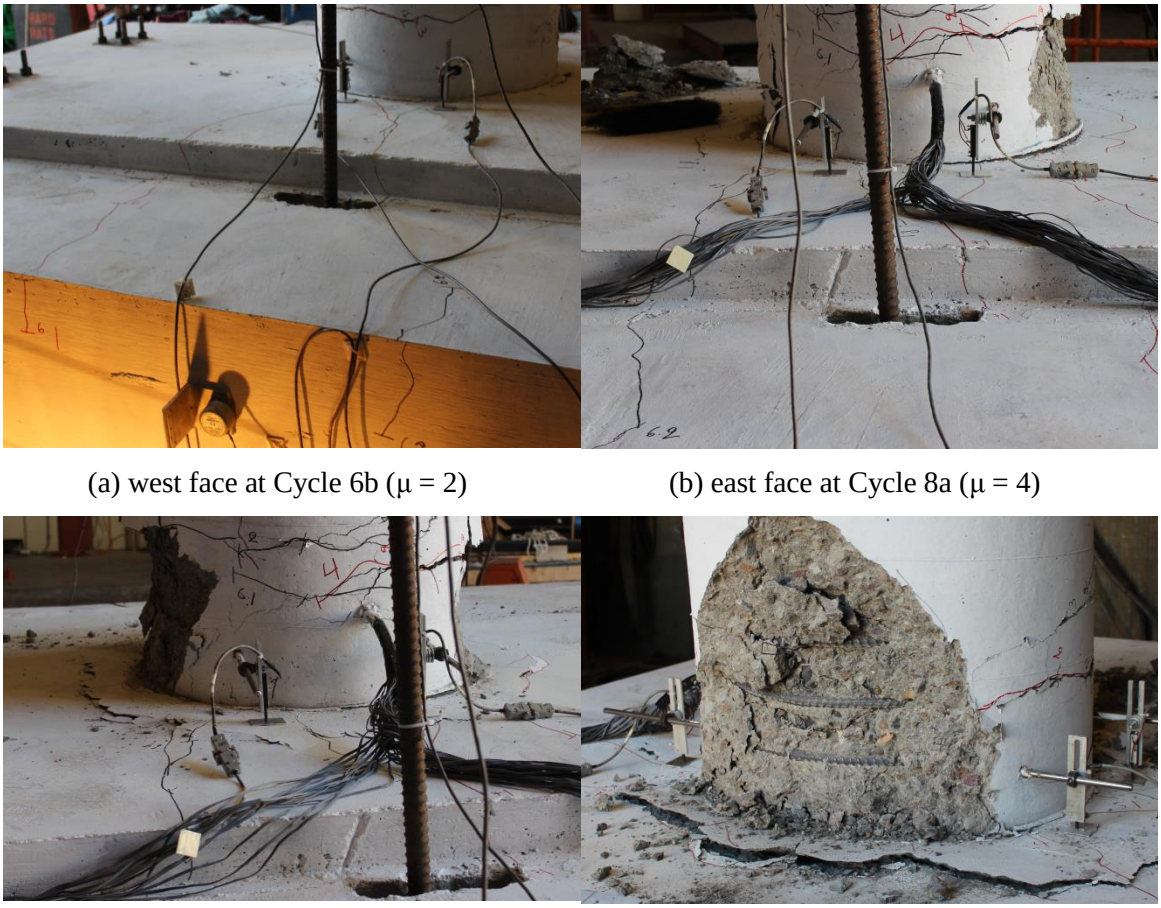

(a) west face at Cycle 6b (μ = 2)

(b) east face at Cycle 8a (μ = 4)

(c) east face at Cycle 9a (μ = 5)

(d) north face at Cycle 11b (μ = 7)

Figure 5.36 – Evolution of damage at the bottom face of the slab (top face in the specimen) of Specimen #3

Figure 5.37 – Damage at the slab-column interface after the testing of Specimen #3

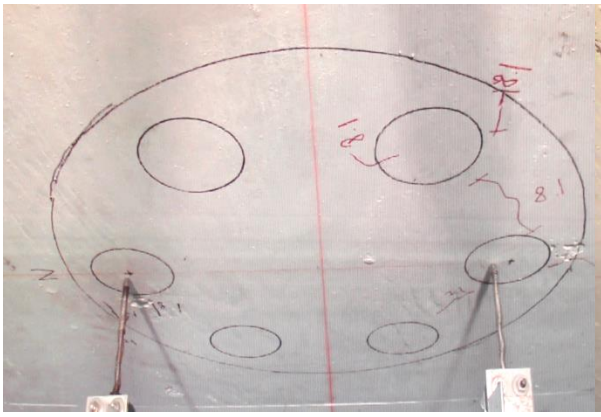

(a) Cycle 8a (μ = 4)

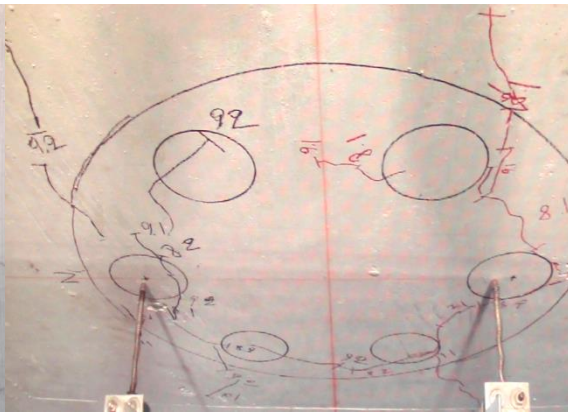

(b) Cycle 10b (μ = 6)

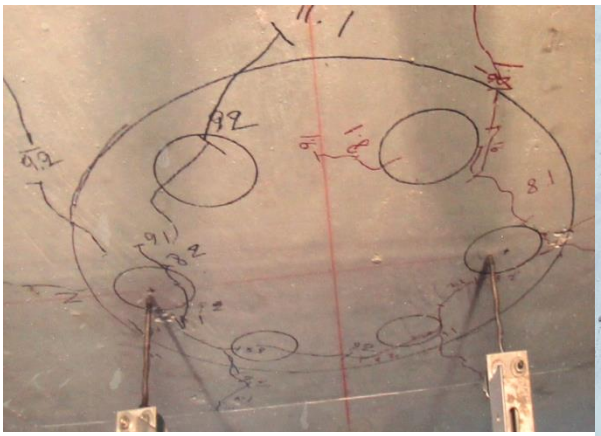

(c) Cycle 11b (μ = 7)

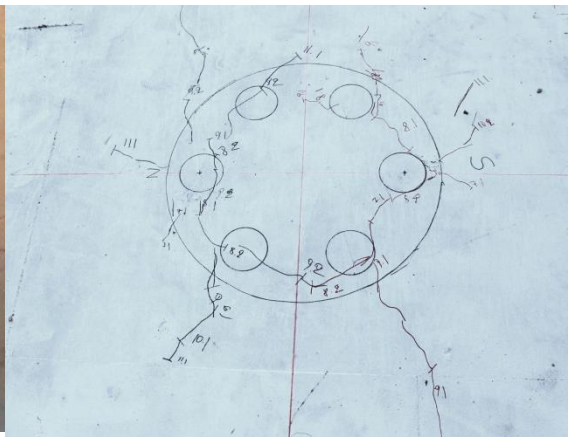

(d) After the end of the test

Figure 5.38 – Evolution of damage at the top face of the slab (bottom face in the specimen) of Specimen #3

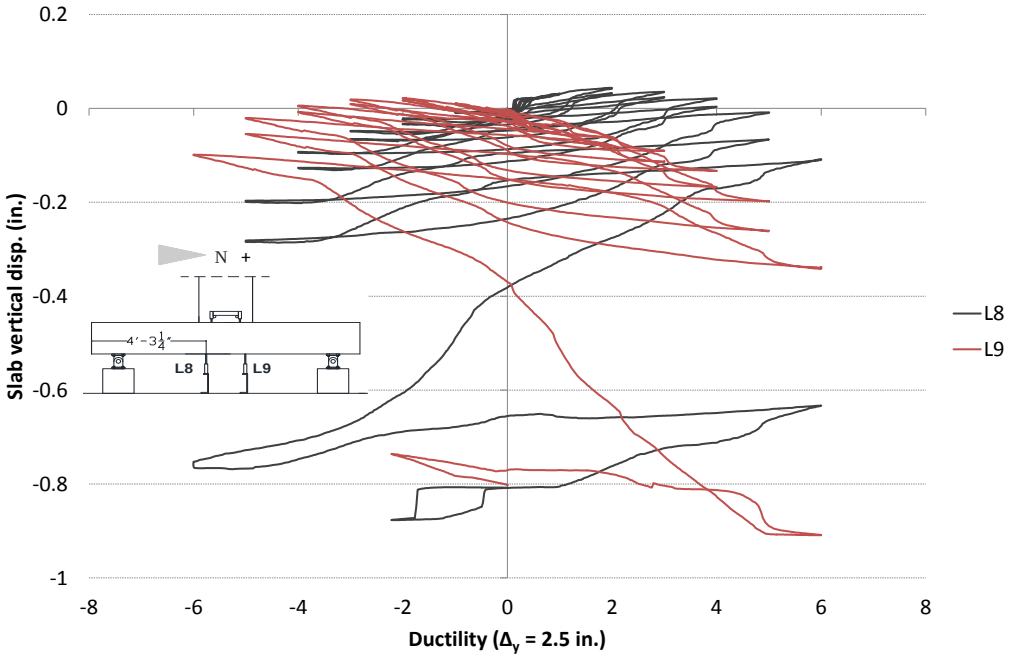

Figure 5.39 – Vertical displacement of the top face of the slab (bottom face in the specimen) of Specimen #2

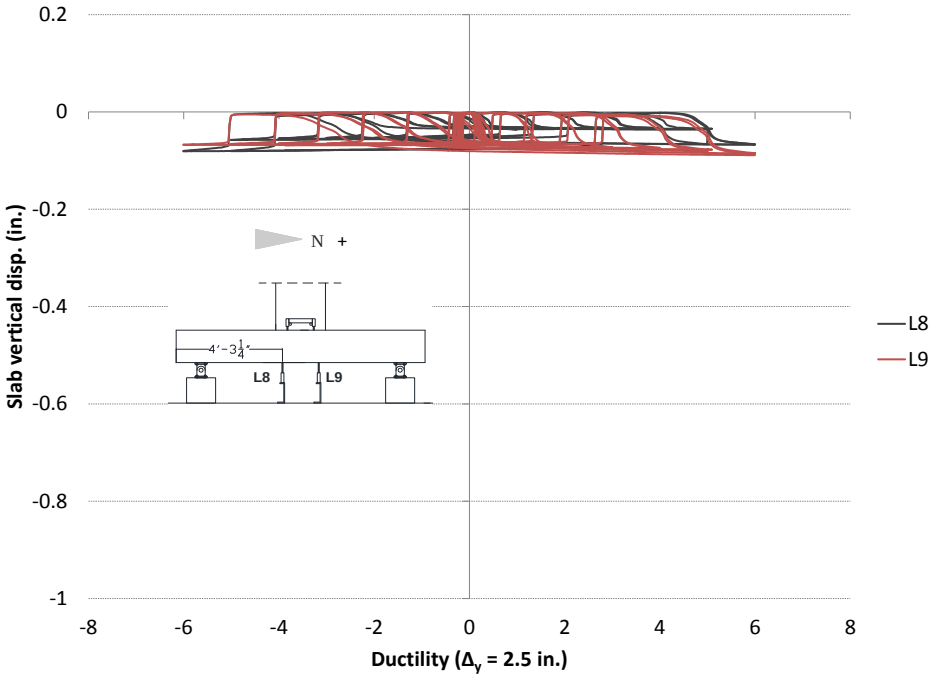

Figure 5.40 – Vertical displacement of the top face of the slab (bottom face in the specimen) of Specimen #3

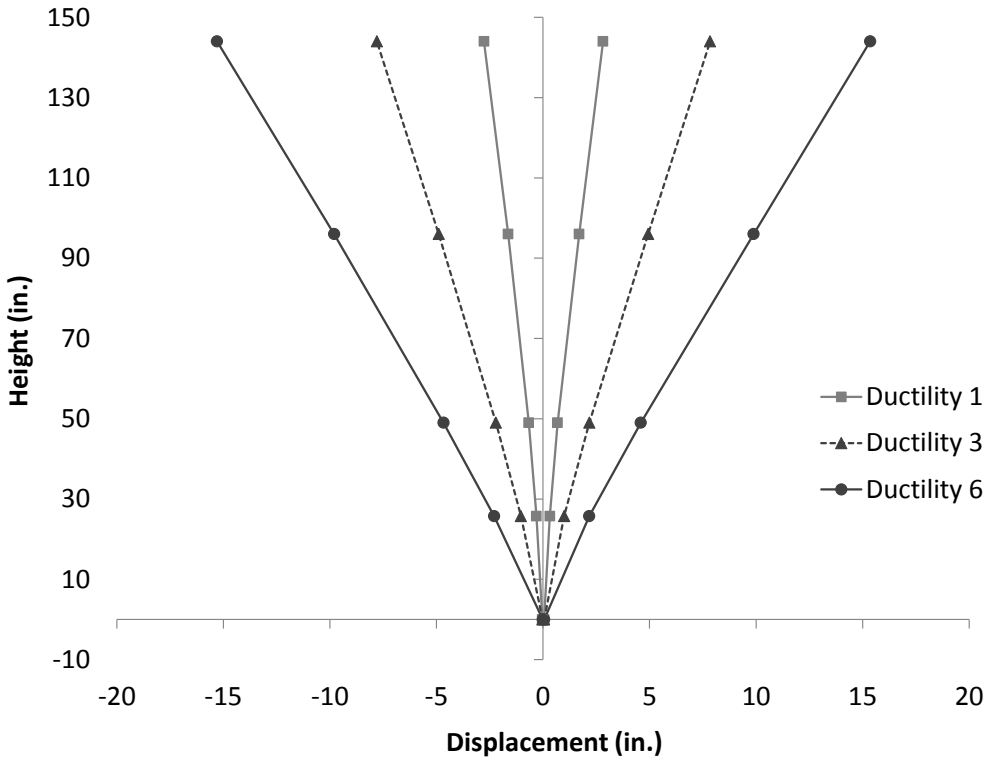

Figure 5.41 – Lateral displacement of the column of Specimen #1

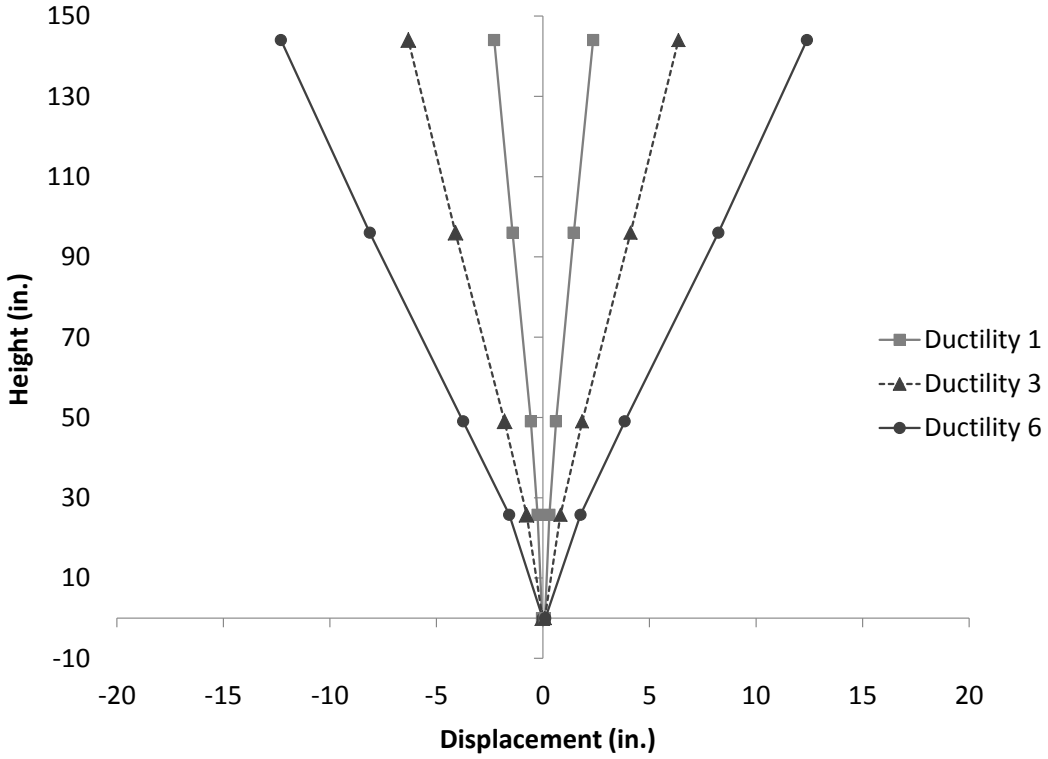

Figure 5.42 – Lateral displacement of the column of Specimen #2

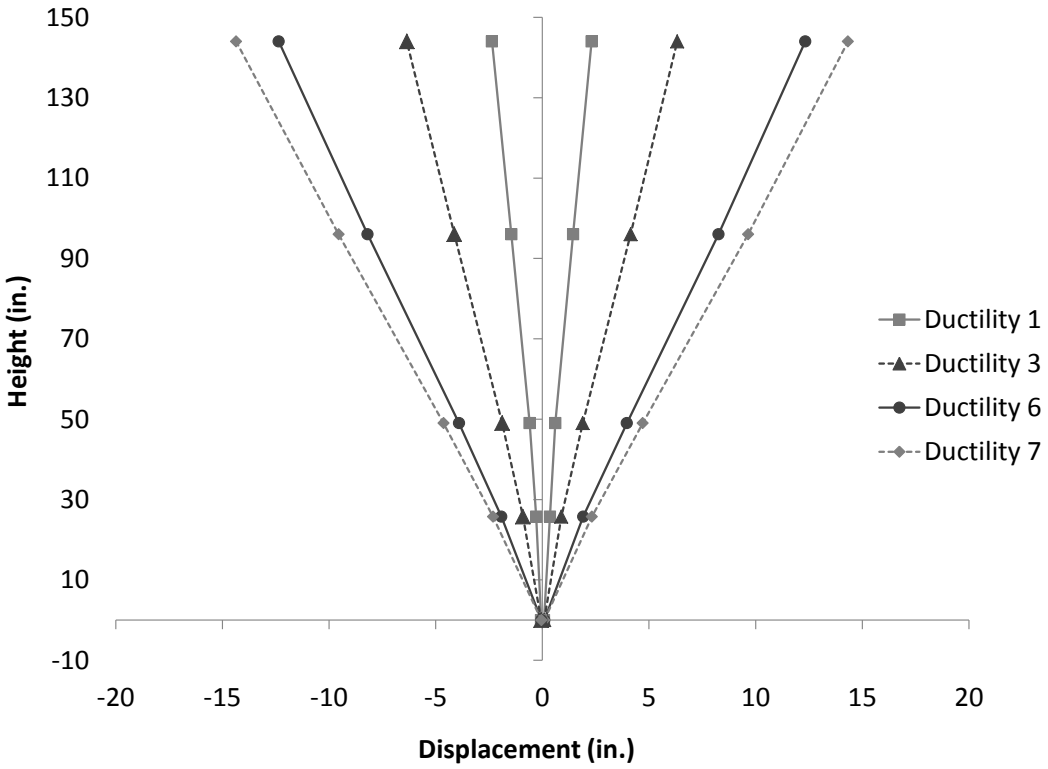

Figure 5.43 – Lateral displacement of the column of Specimen #3

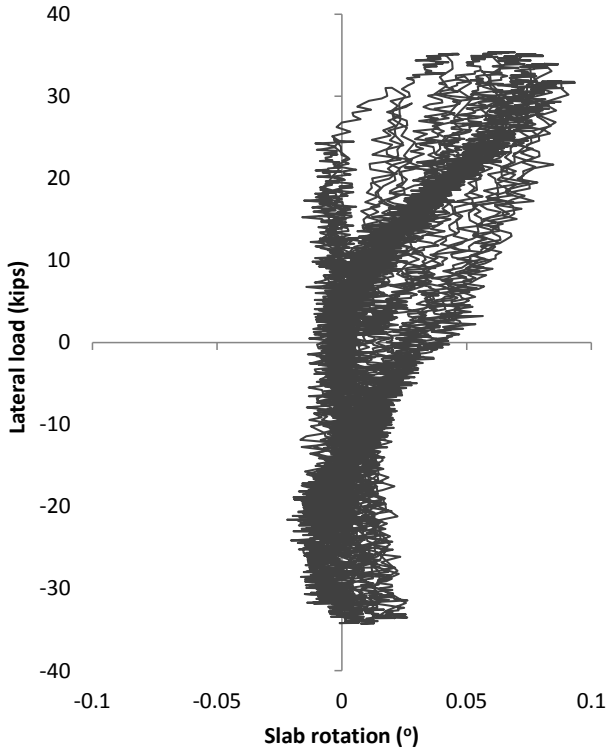

Figure 5.44 – Lateral load-vs.-slab rotation (at center) curves for Specimen #1

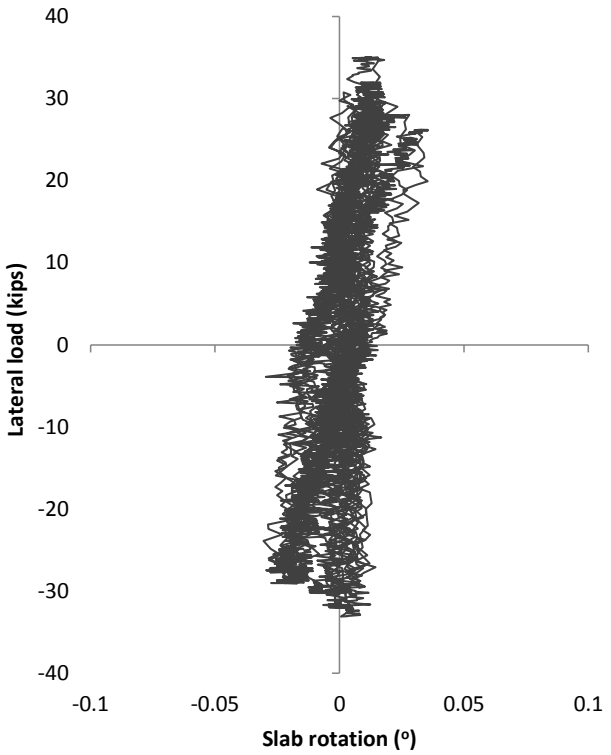

Figure 5.45 – Lateral load-vs.-slab rotation (at center) curves for Specimen #2

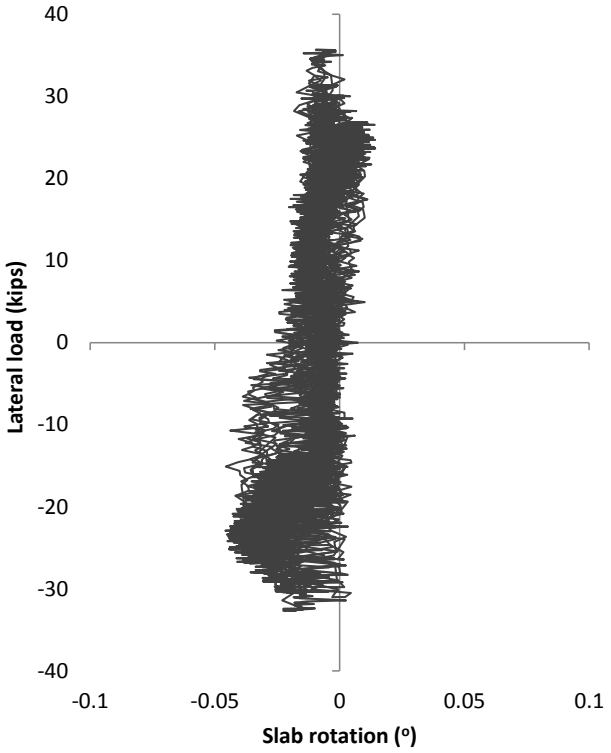

Figure 5.46 – Lateral load-vs.-slab rotation (at center) curves for Specimen #3

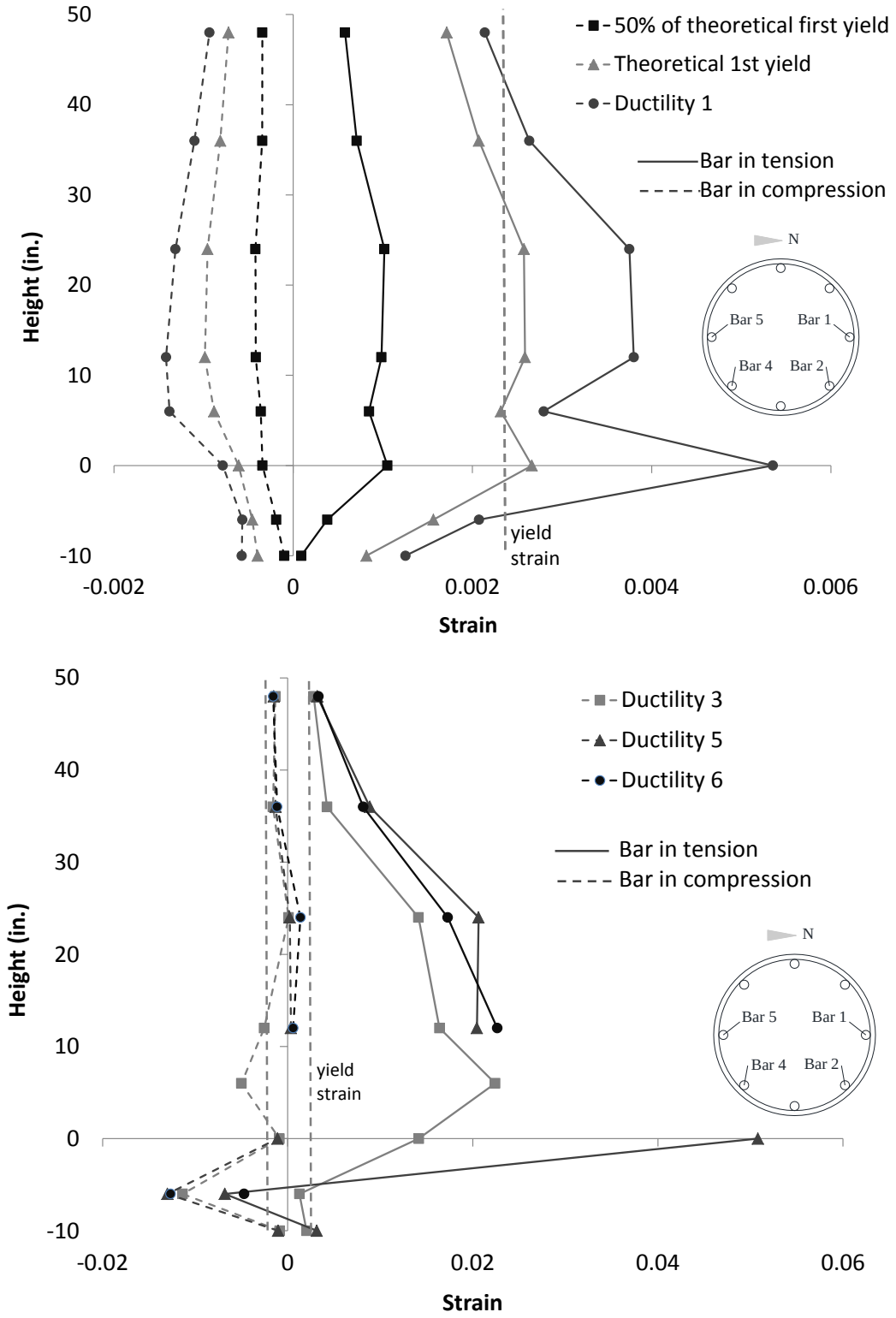

Figure 5.47 – Strains along Bar 1 in Specimen #1

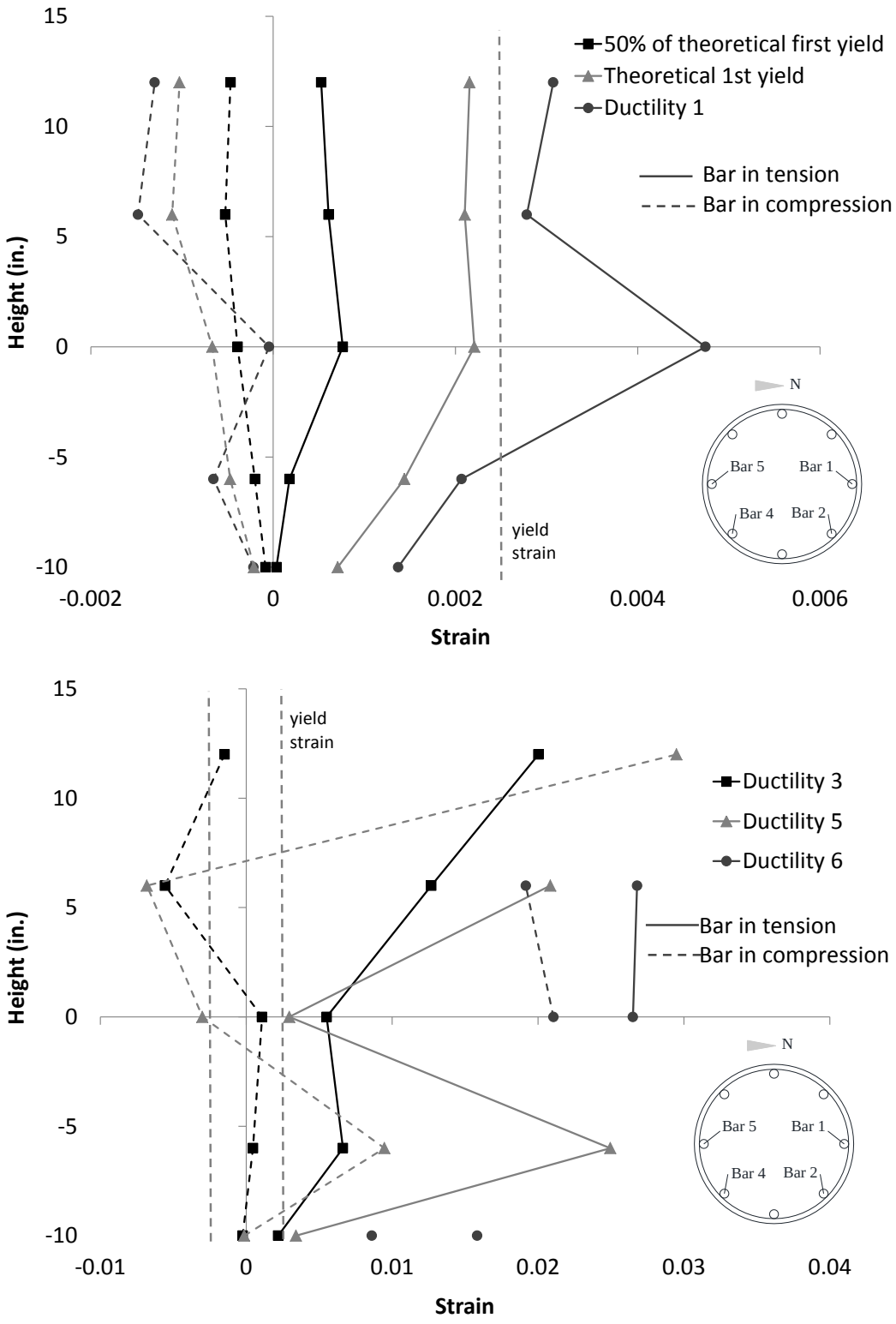

Figure 5.48 – Stains along Bar 5 in Specimen #1

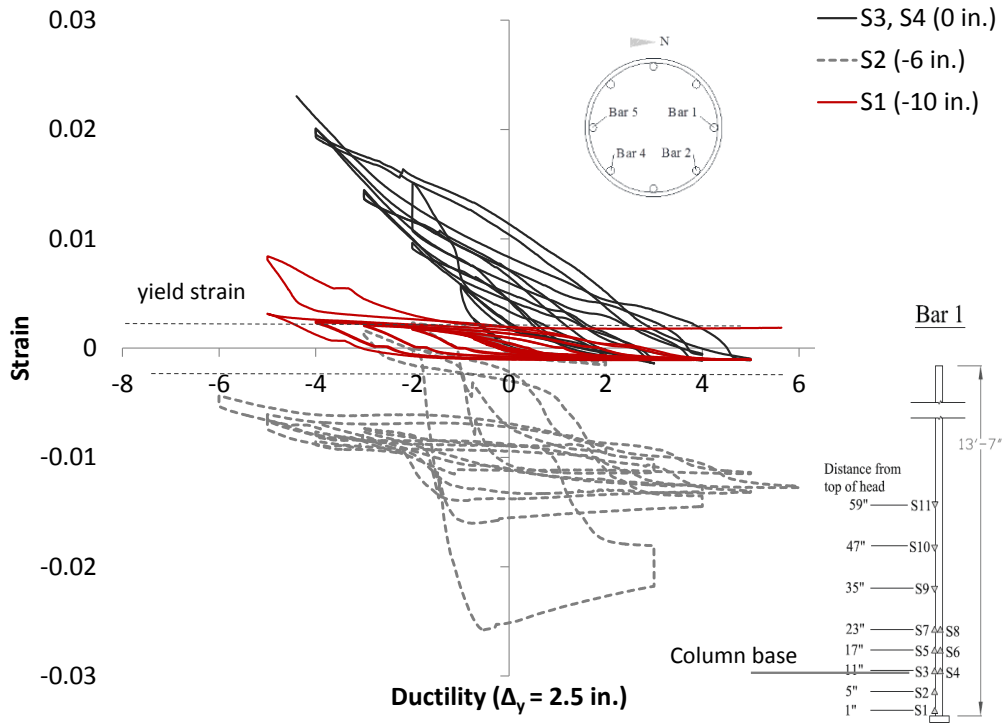

Figure 5.49 – Strain-vs.-ductility curves for Bar 1 in the slab-column joint of Specimen #1

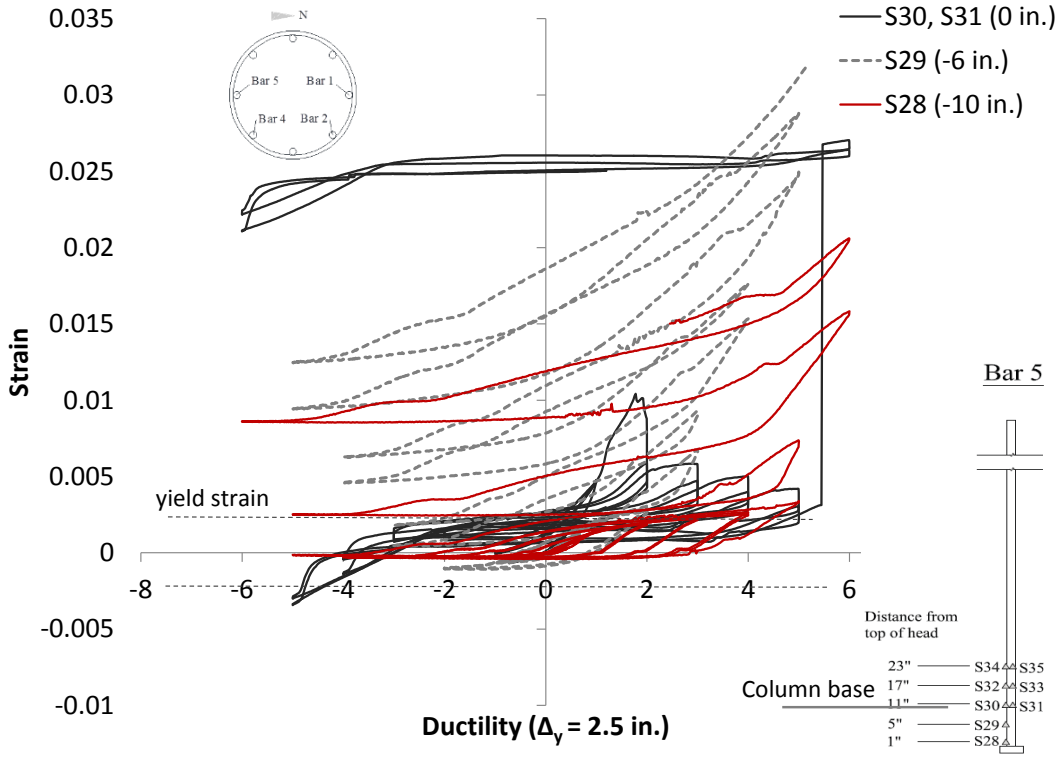

Figure 5.50 – Strain-vs.-ductility curves for Bar 5 in the slab-column joint of Specimen #1

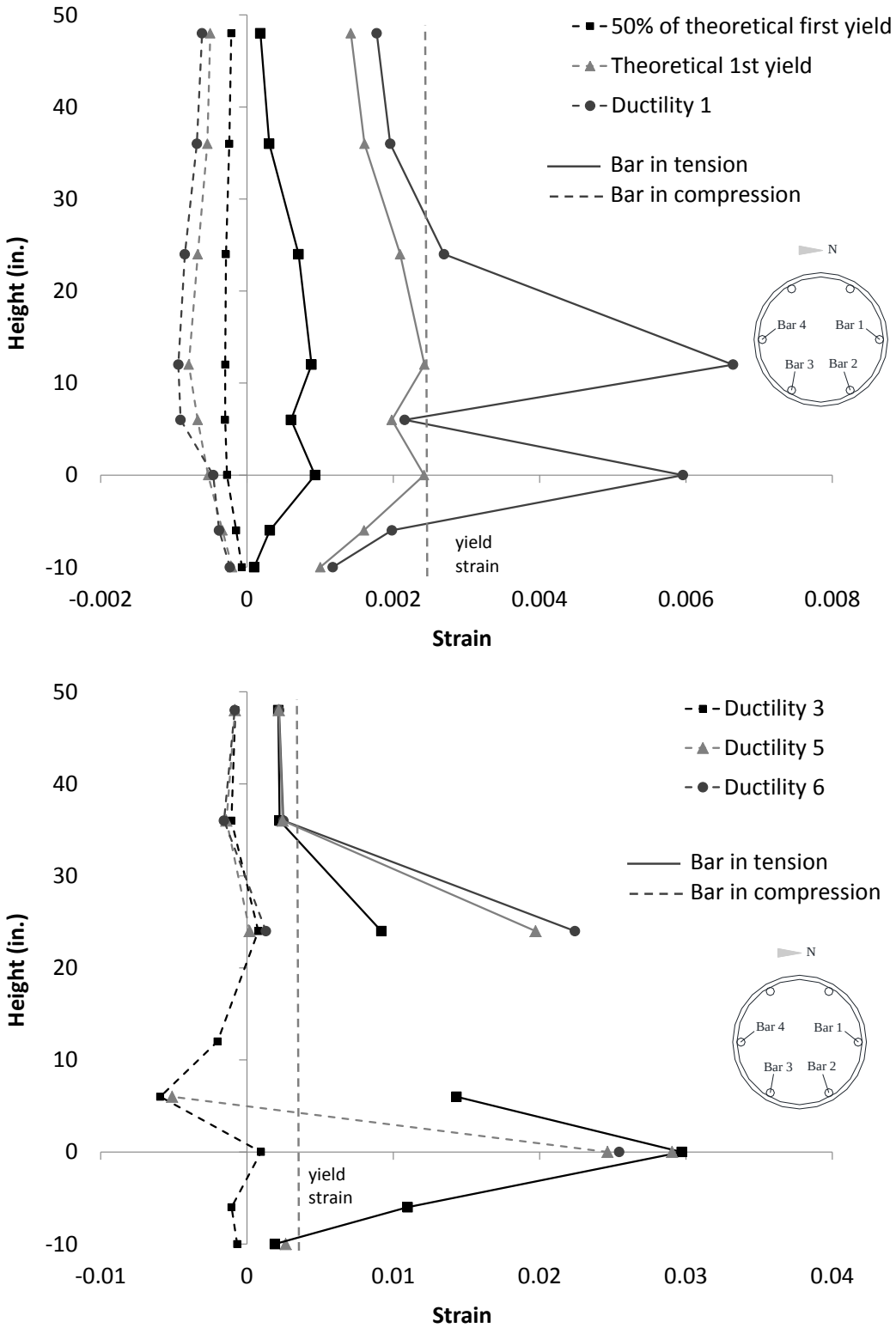

Figure 5.51 – Strains along Bar 1 in Specimen #2

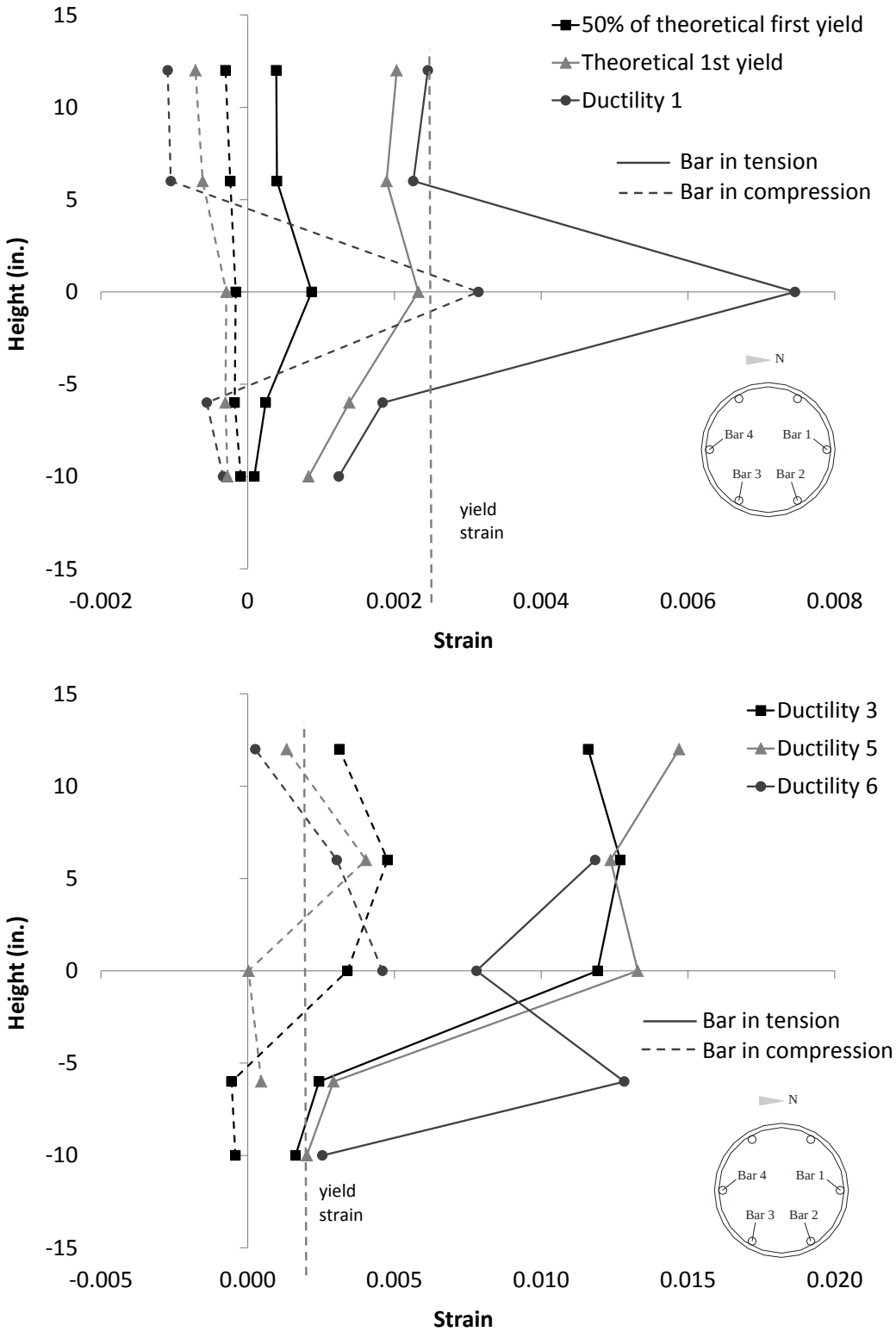

Figure 5.52 – Strains along Bar 4 in Specimen #2

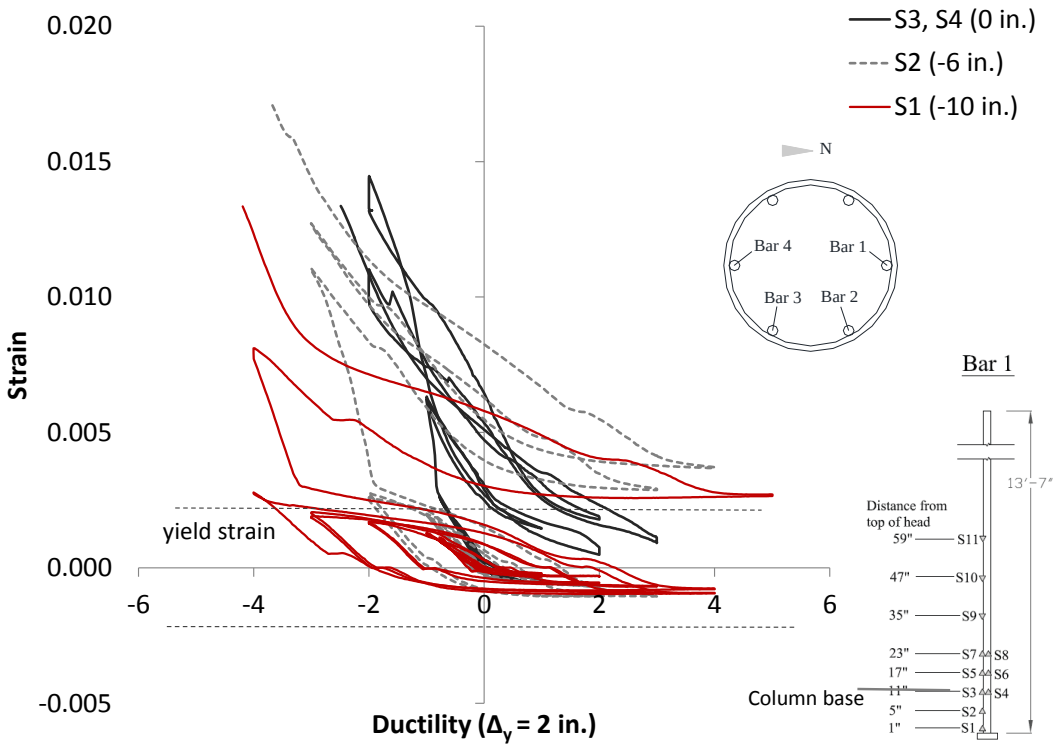

Figure 5.53 – Strain-vs.-ductility curves for Bar 1 in the slab-column joint of Specimen #2

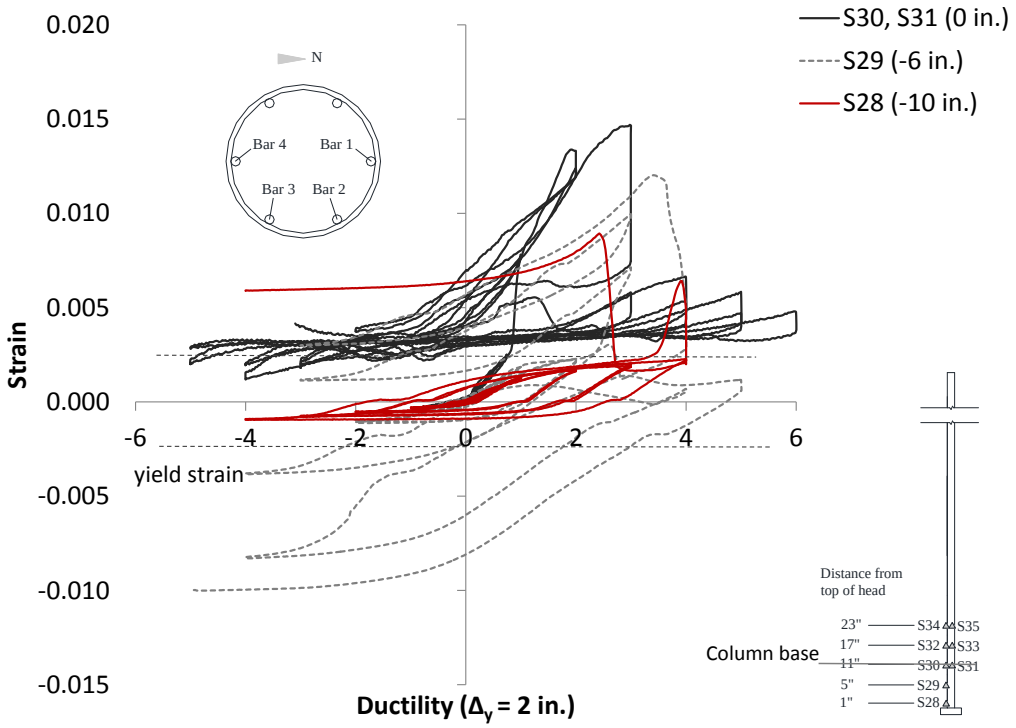

Figure 5.54 – Strain-vs.-ductility curves for Bar 4 in the slab-column joint of Specimen #2

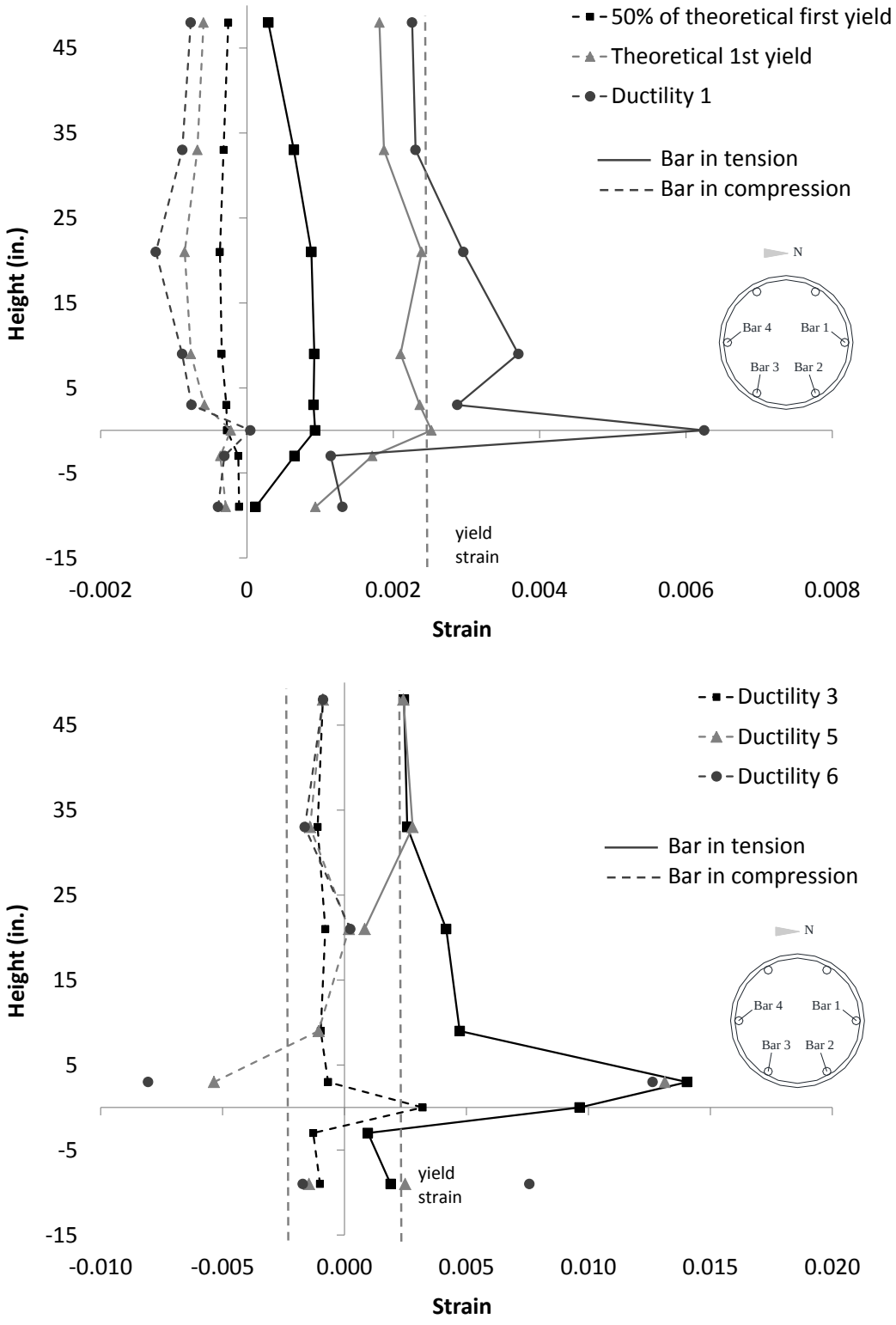

Figure 5.55 – Strains along Bar 1 in Specimen #3

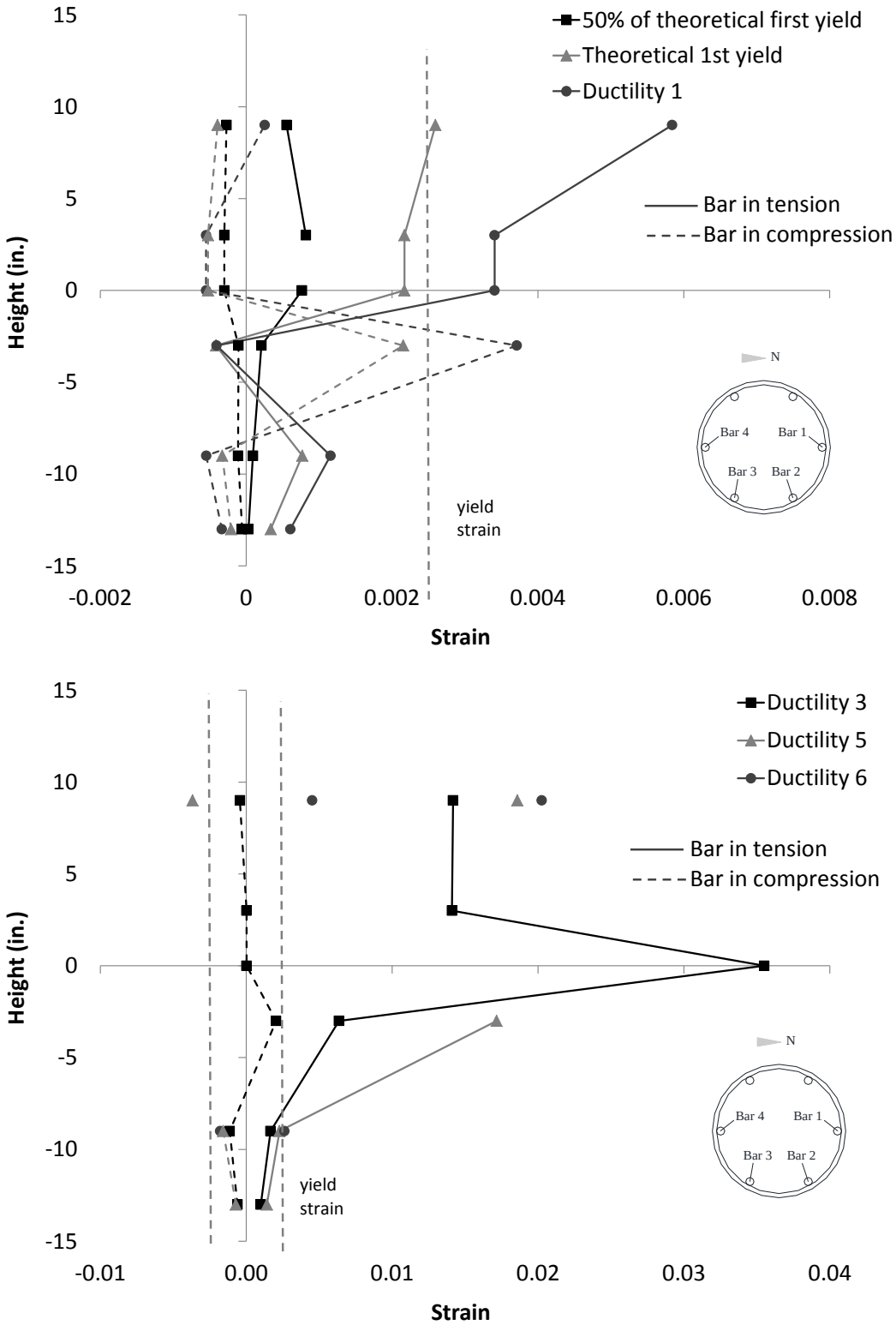

Figure 5.56 – Strains along Bar 4 in Specimen #3

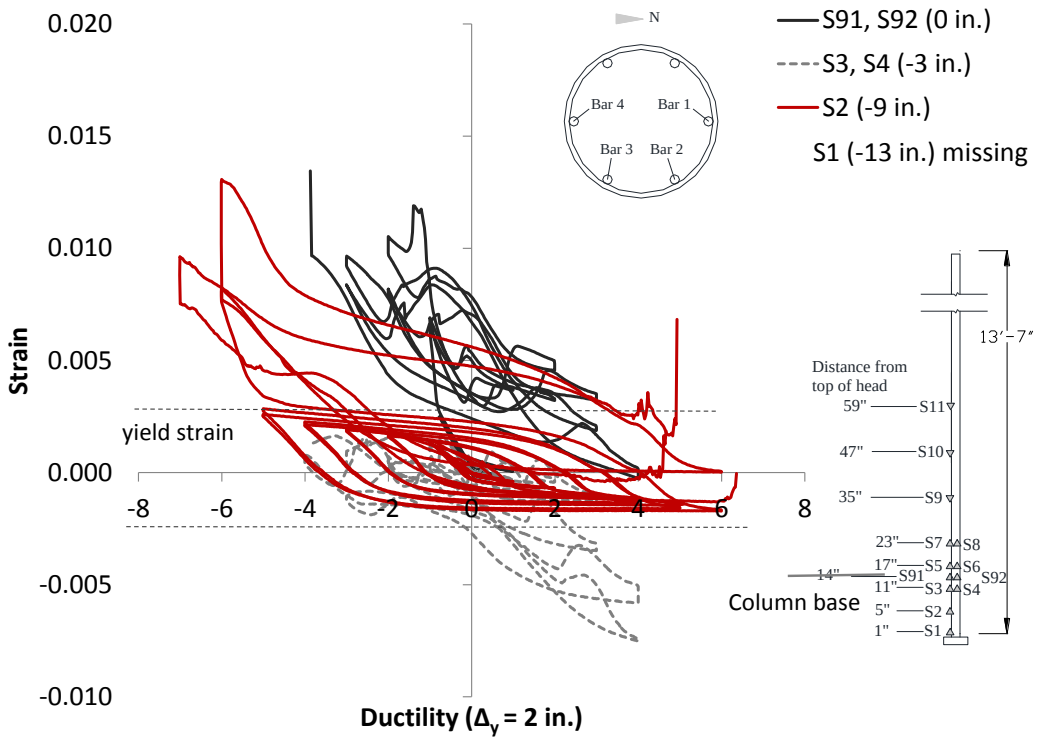

Figure 5.57 – Strain-vs.-ductility curves for Bar 1 in the slab-column joint of Specimen #3

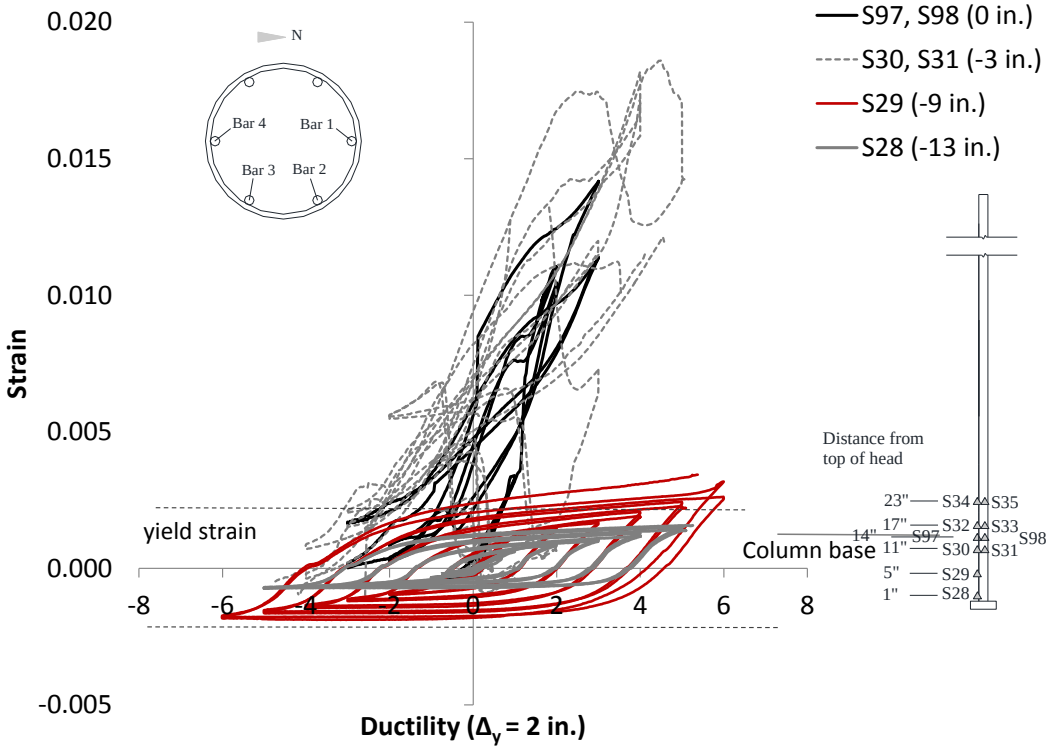

Figure 5.58 – Strain-vs.-ductility curves for Bar 4 in the slab-column joint of Specimen #3

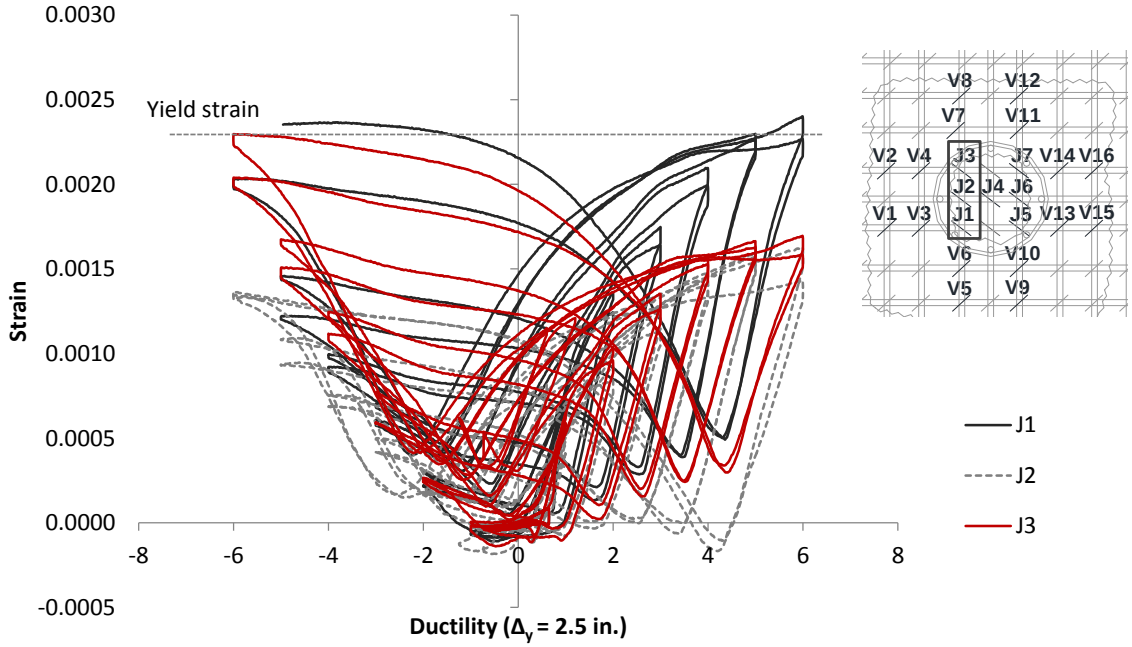

(a) J-bars on the south side

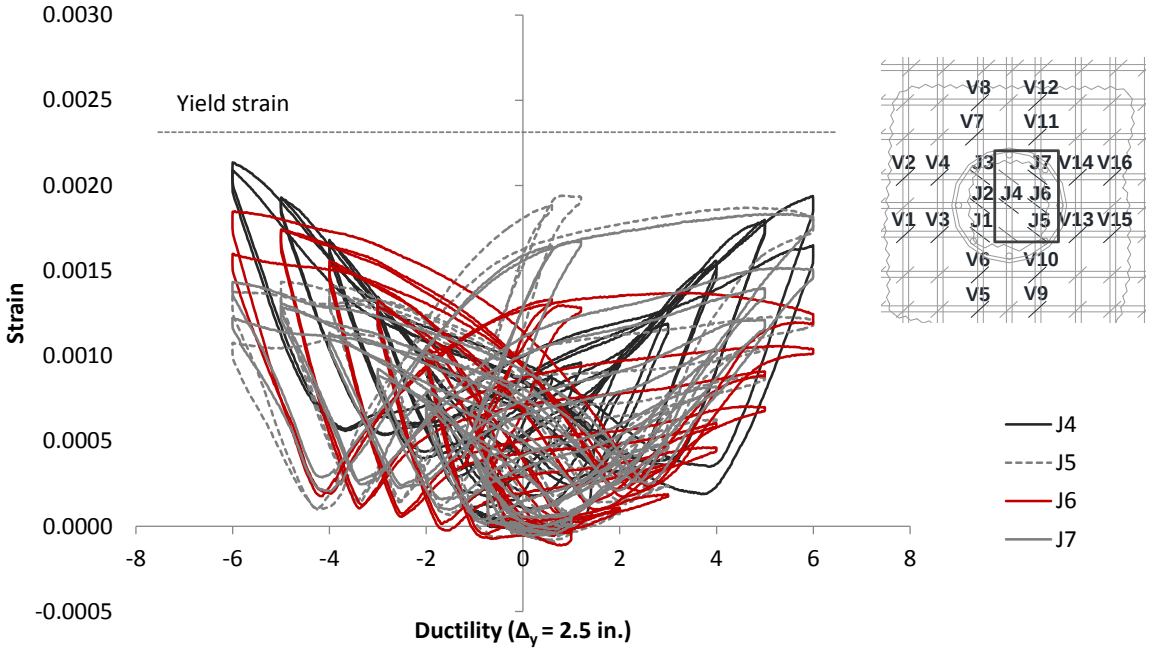

(b) J-bars at the center and on the north side

Figure 5.59 – Strains in J-bars of Specimen #1

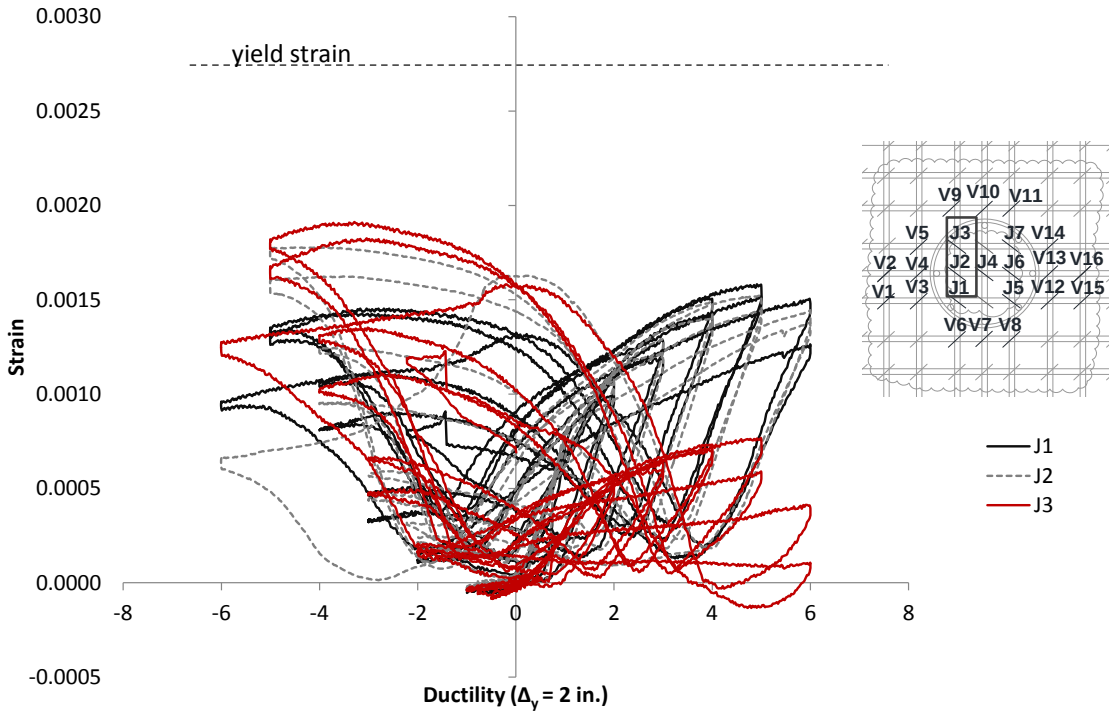

(a) J-bars on the south side

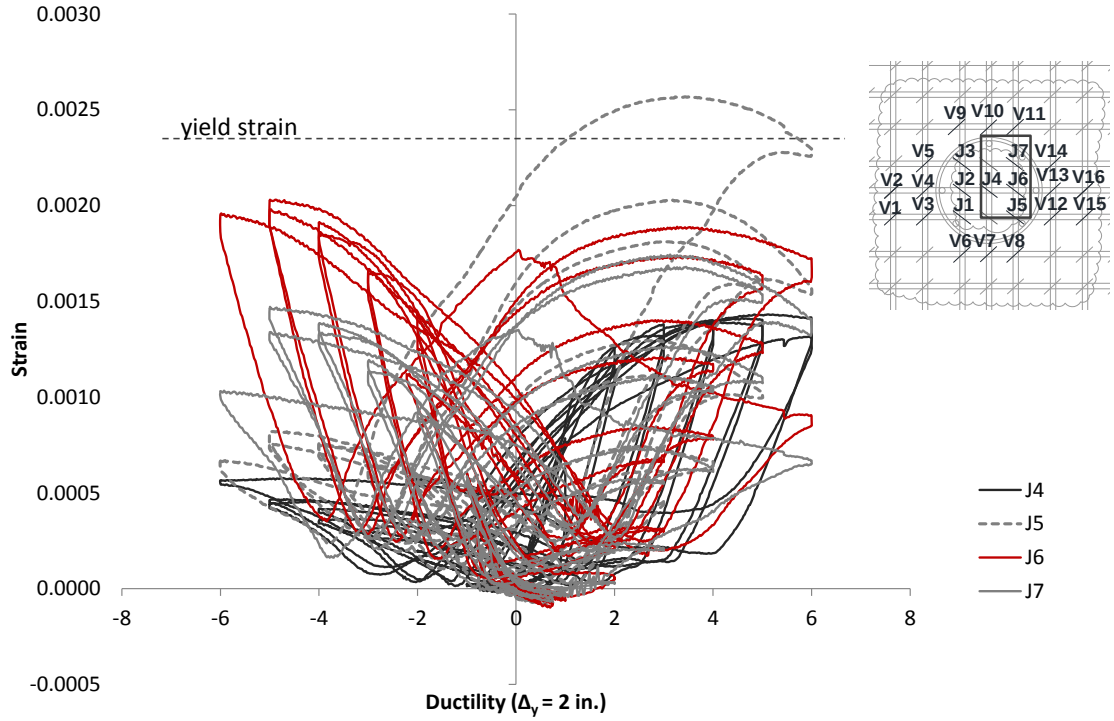

(b) J-bars at the center and on the north side

Figure 5.60 – Strains in J-bars of Specimen #2

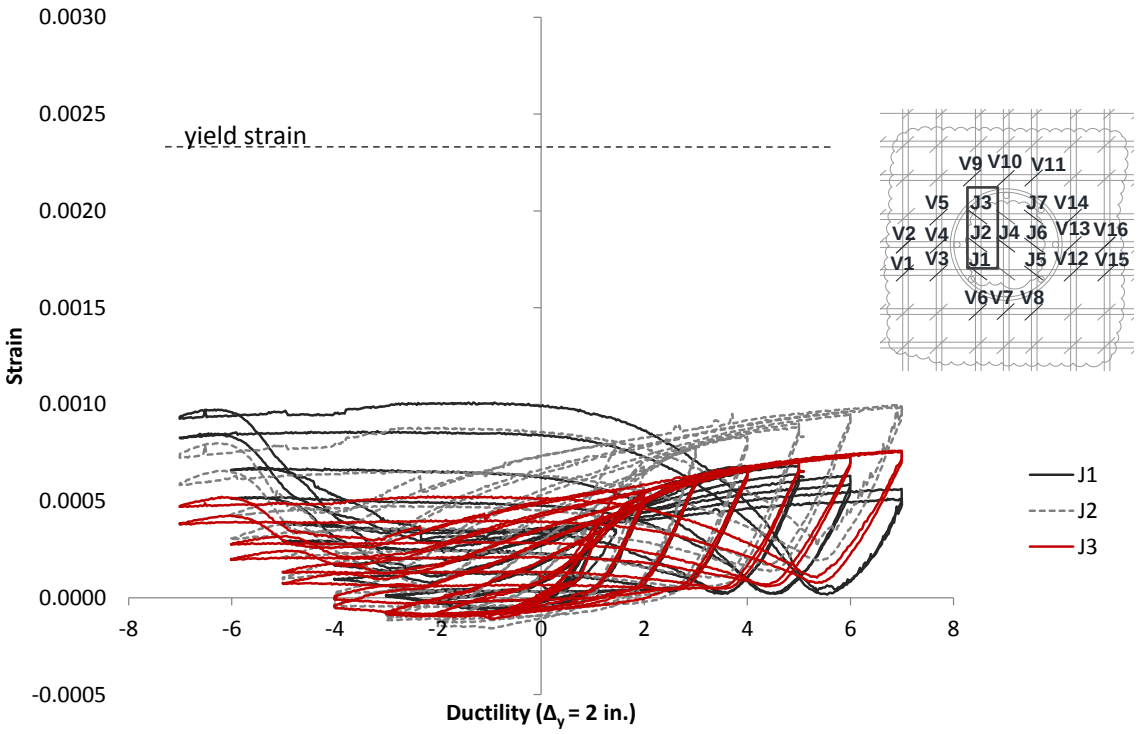

(a) J-bars on the south side

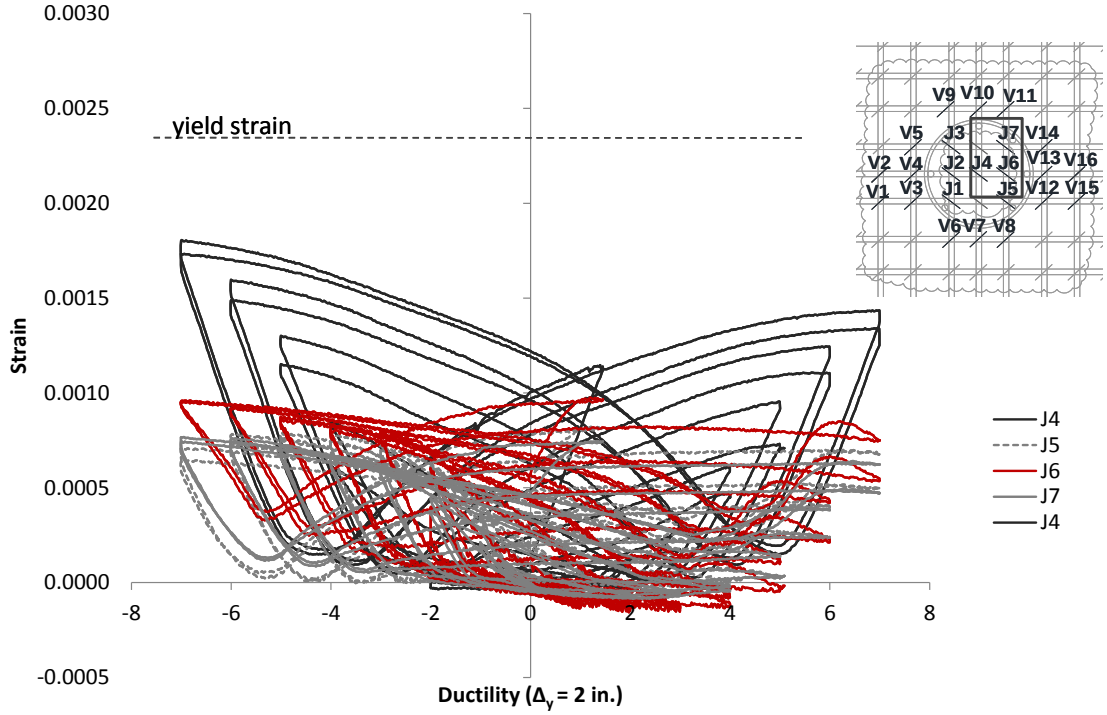

(b) J-bars at the central and on the north side

Figure 5.61 – Strains in J-bars of Specimen #3

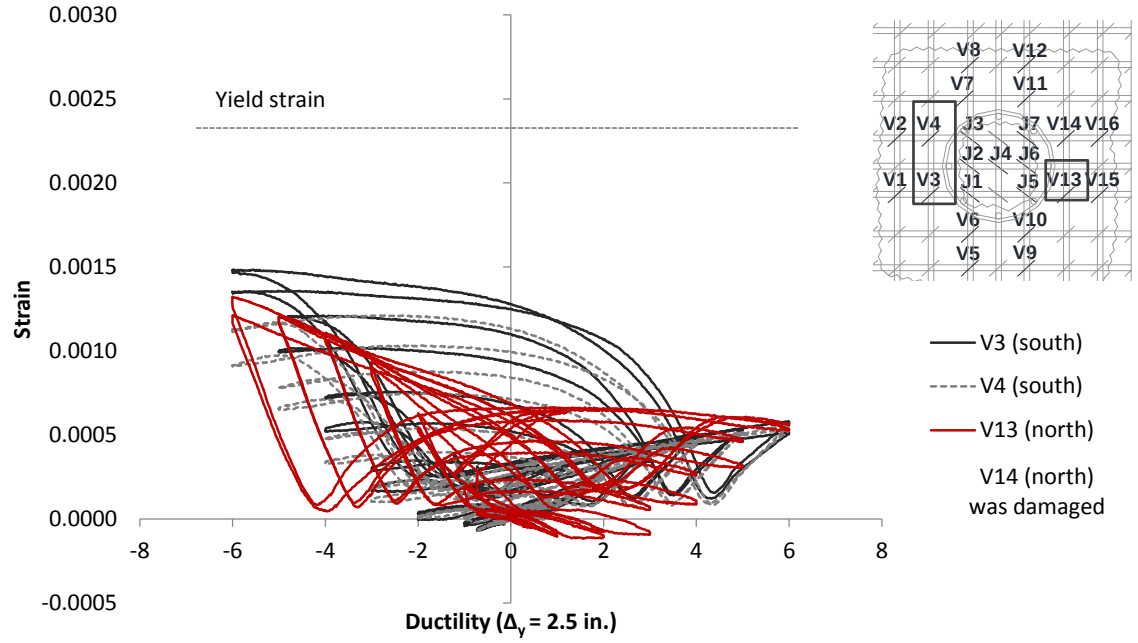

(a) south and north faces

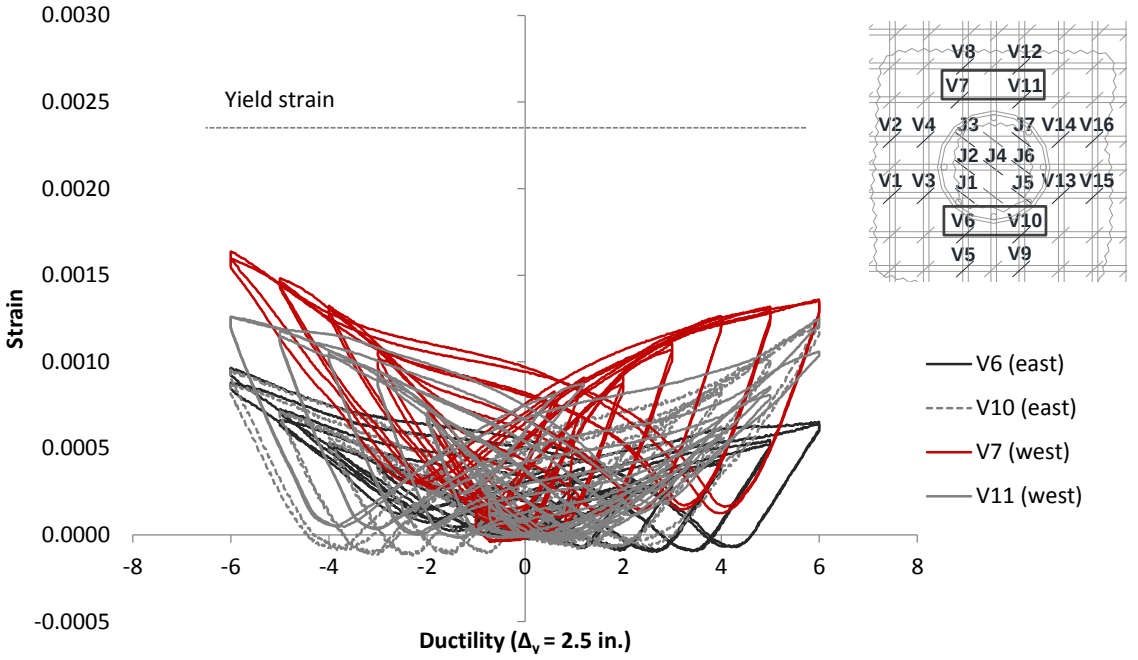

(b) east and west faces

Figure 5.62 – Strains in the 1st row of vertical stirrups of Specimen #1

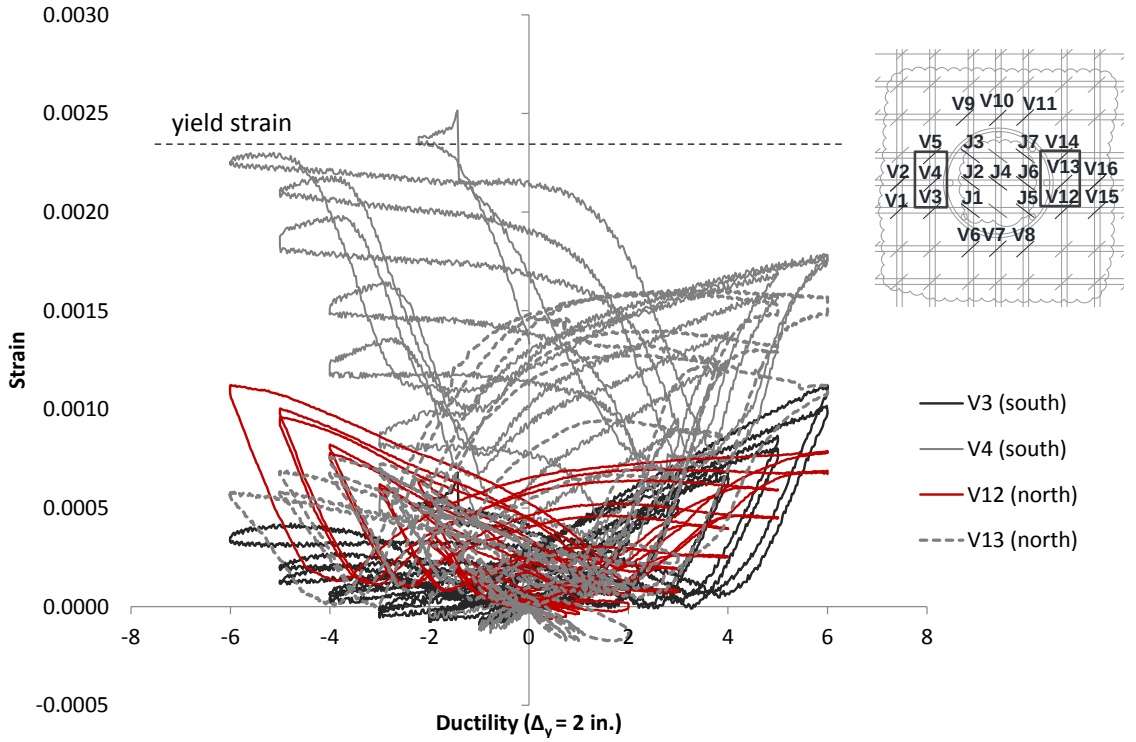

(a) south and north faces

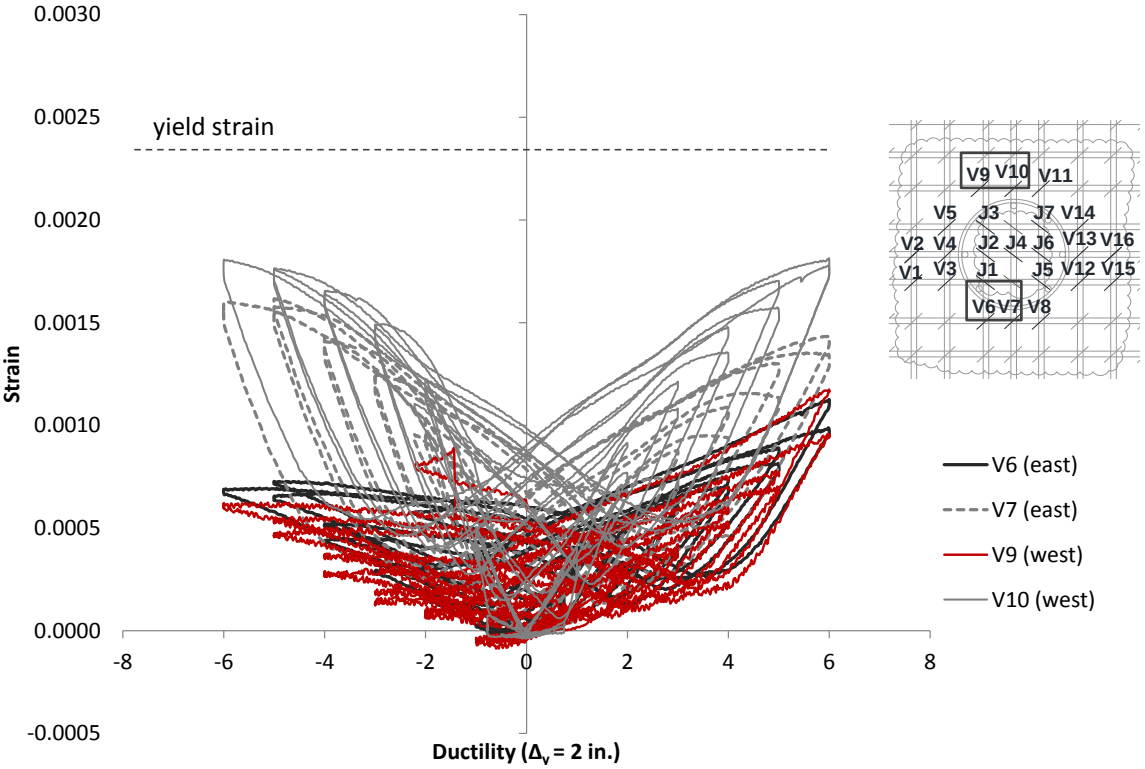

(b) east and west faces

Figure 5.63 – Strains in the 1st row of vertical stirrups of Specimen #2

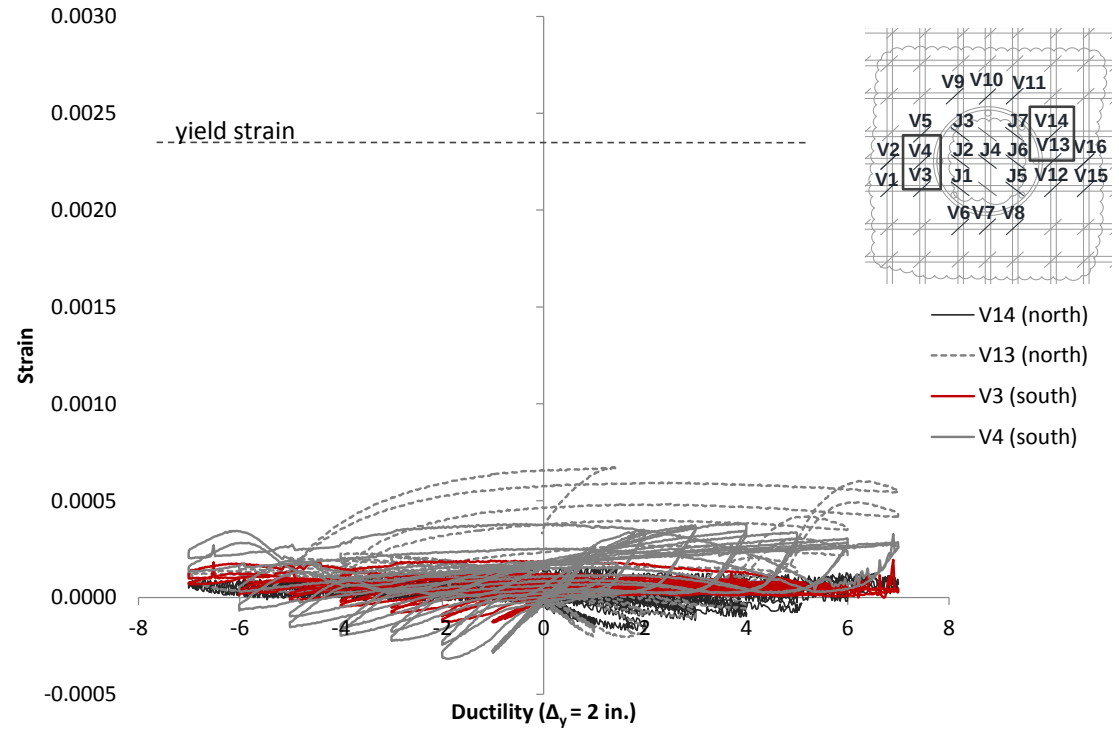

(a) south and north faces

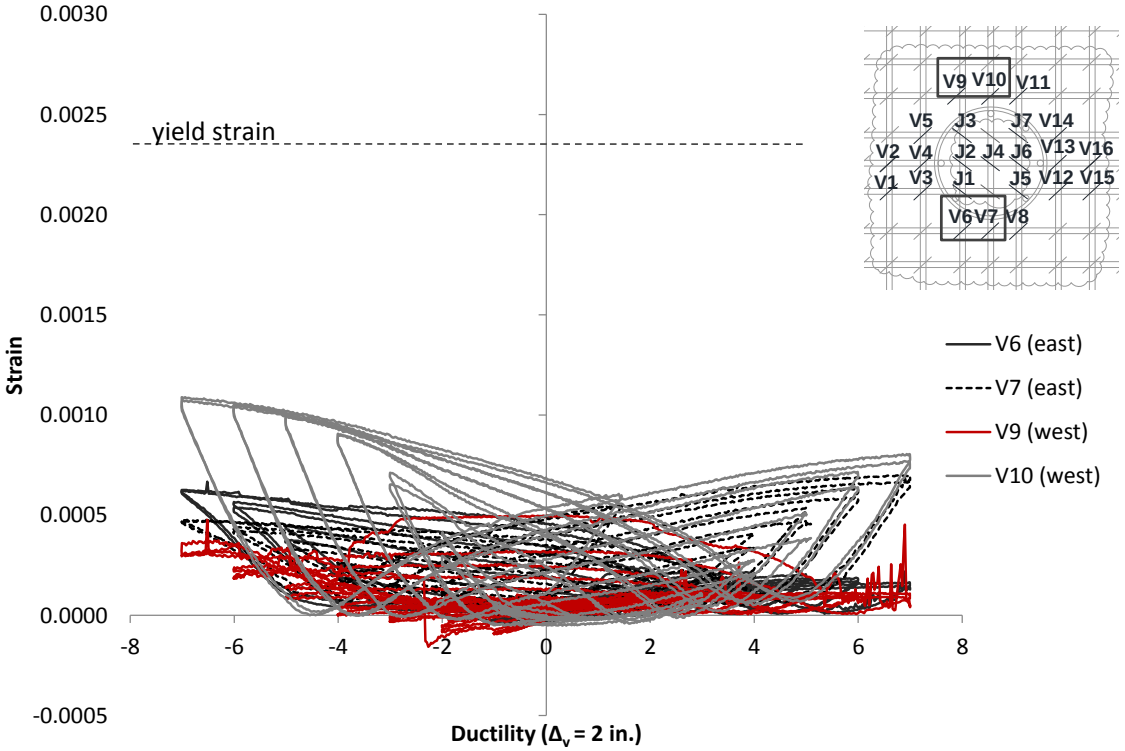

(b) east and west faces

Figure 5.64 – Strains in the 1st row of vertical stirrups of Specimen #3

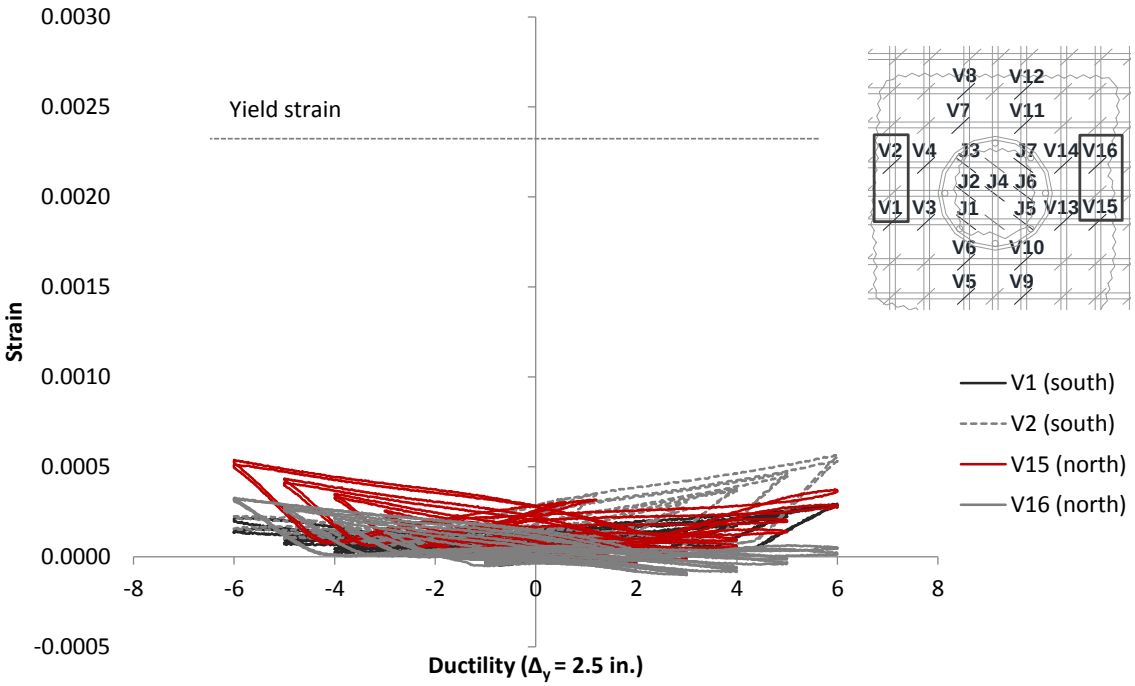

(a) south and north faces

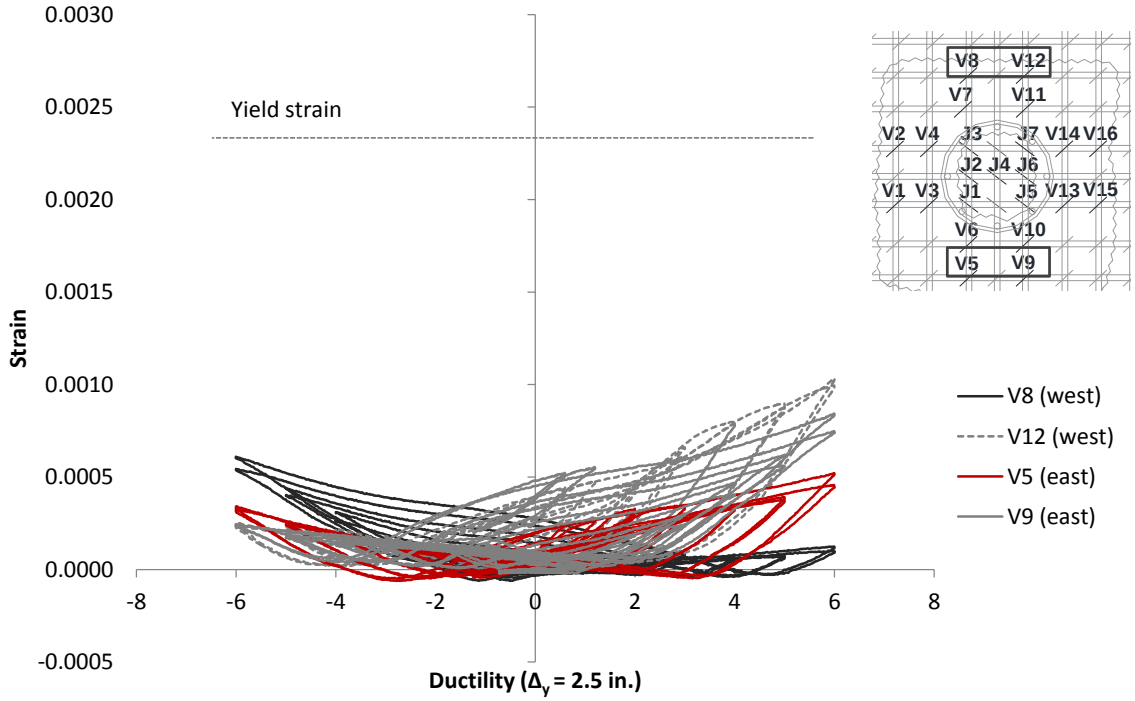

(b) east and west faces

Figure 5.65 – Strains in the 2nd row of vertical stirrups of Specimen #1

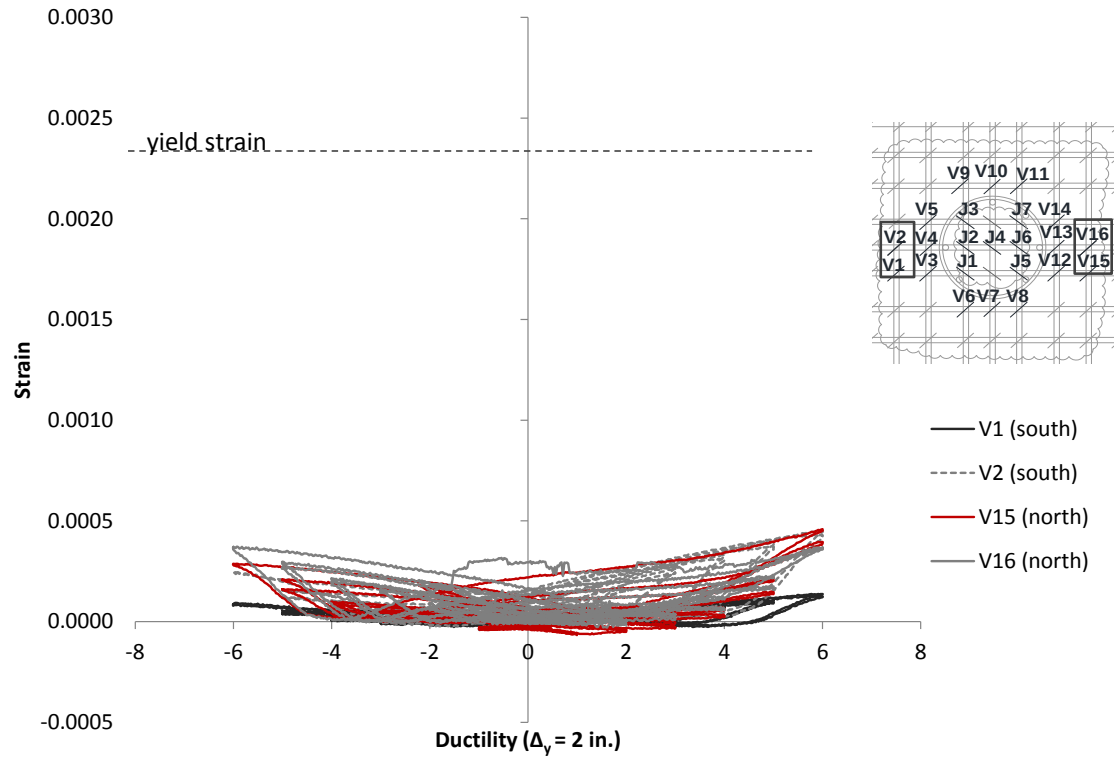

Figure 5.66 – Strains in the 2nd row of vertical stirrups of Specimen #2

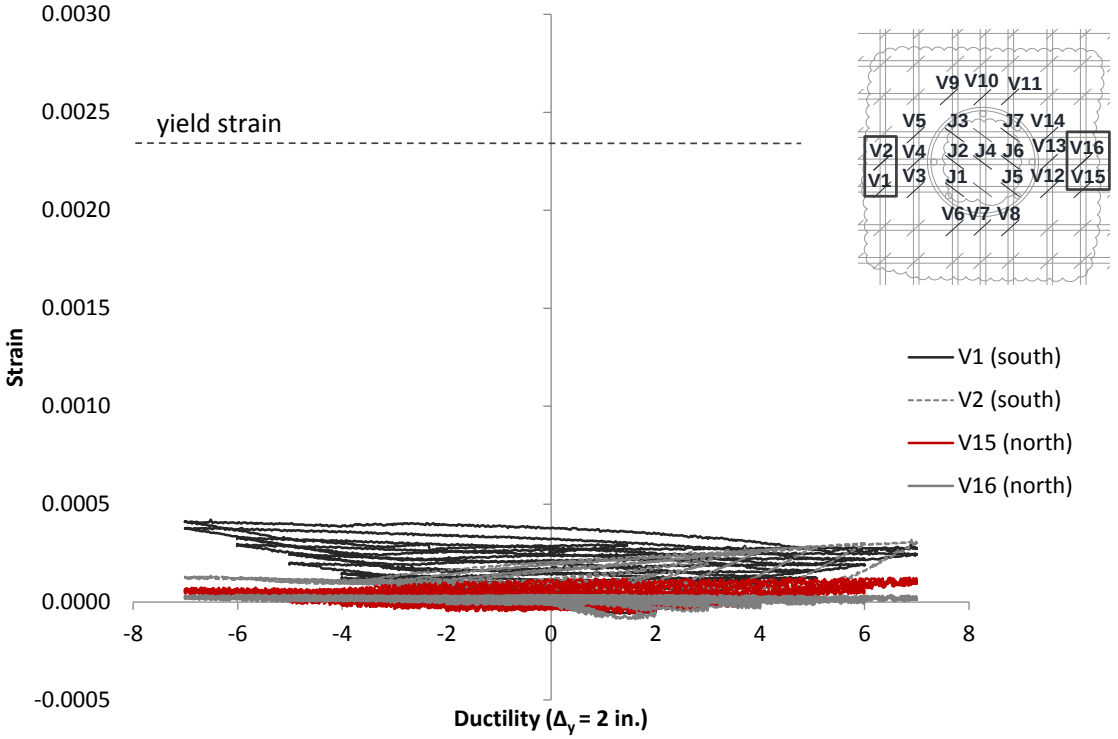

Figure 5.67 – Strains in the 2nd row of vertical stirrups of Specimen #3

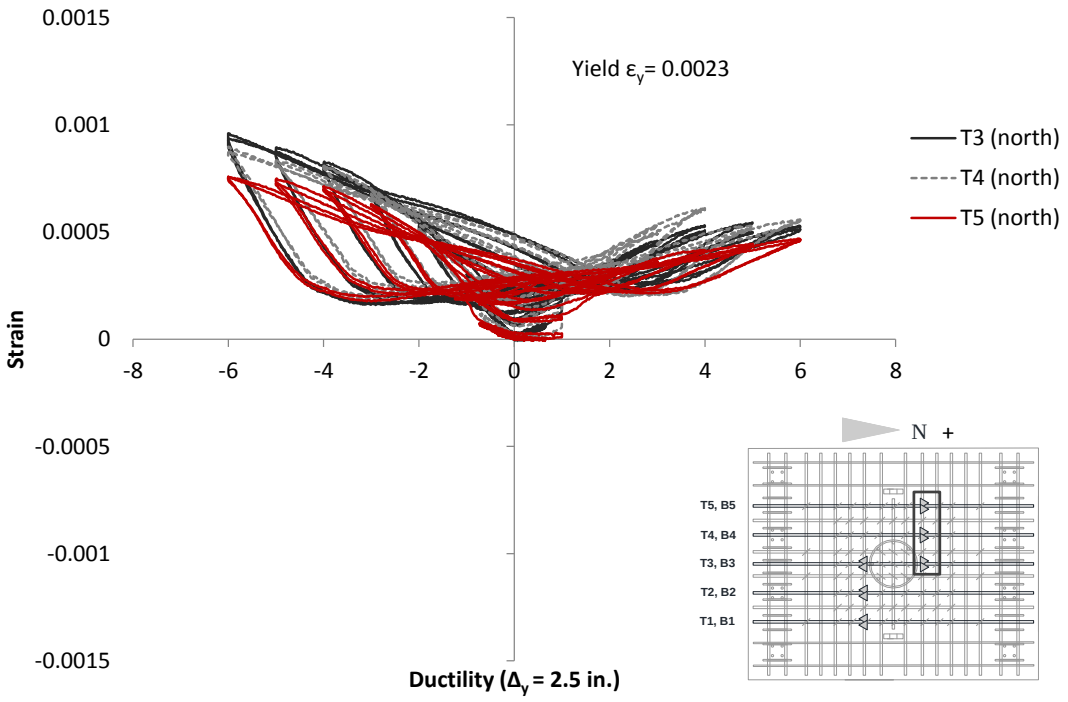

Figure 5.68 – Strains in longitudinal bars at the bottom face of the slab (top face in the specimen) of Specimen #1

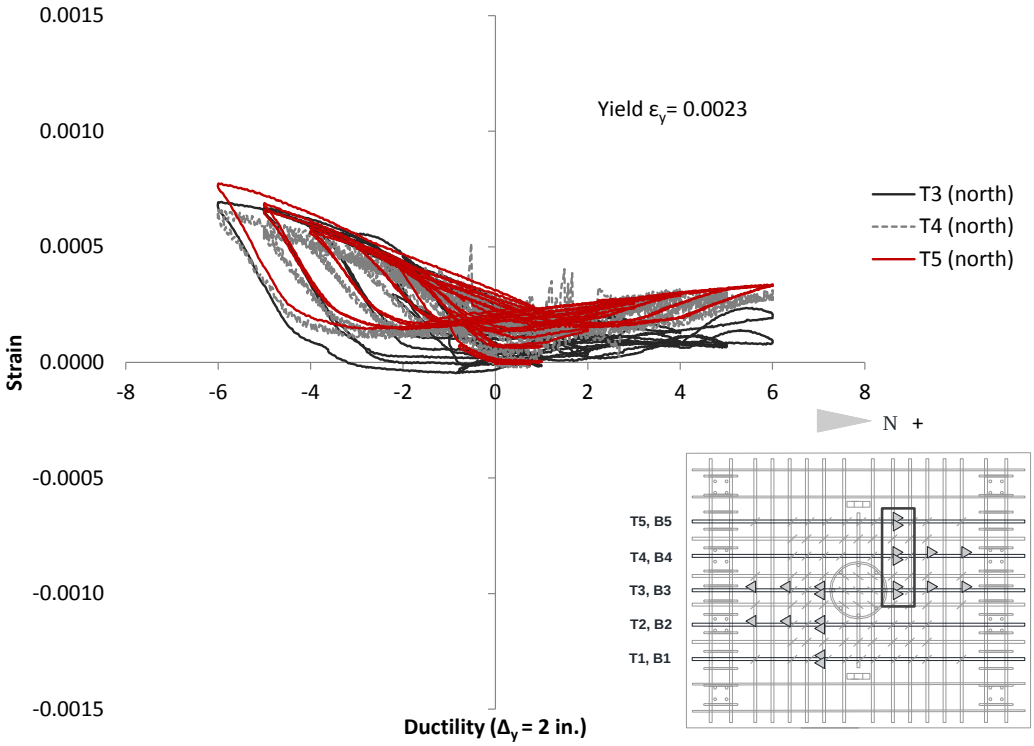

Figure 5.69 – Strains in longitudinal bars at the bottom face of the slab (top face in the specimen) of Specimen #2

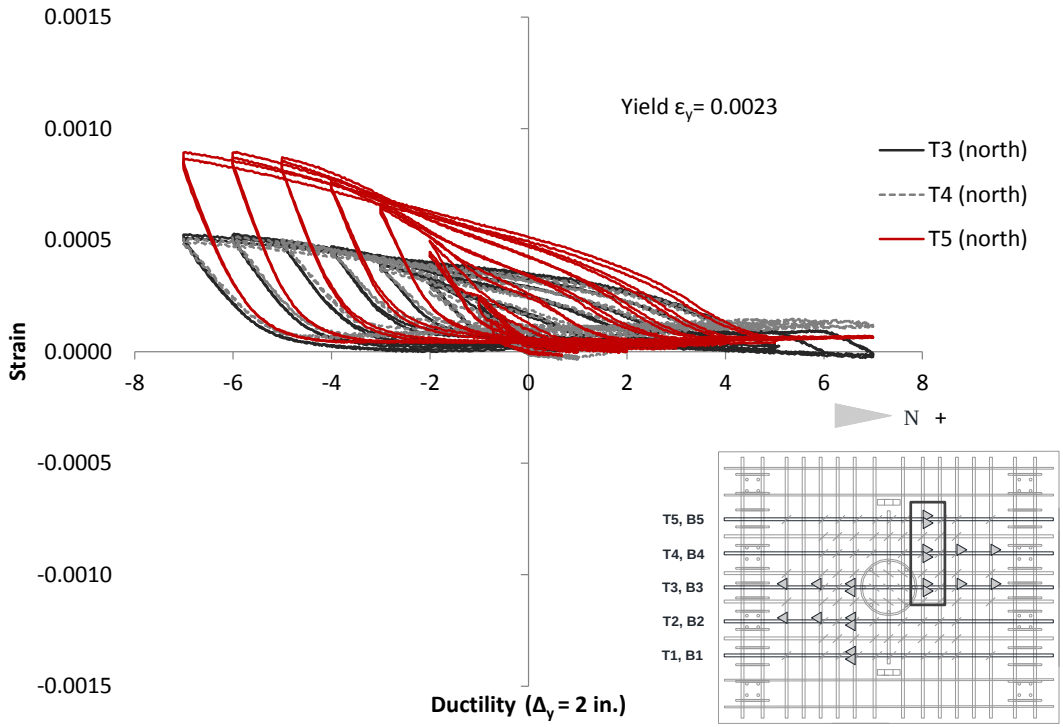

Figure 5.70 – Strains in longitudinal bars at the bottom face of the slab (top face in the specimen) of Specimen #3

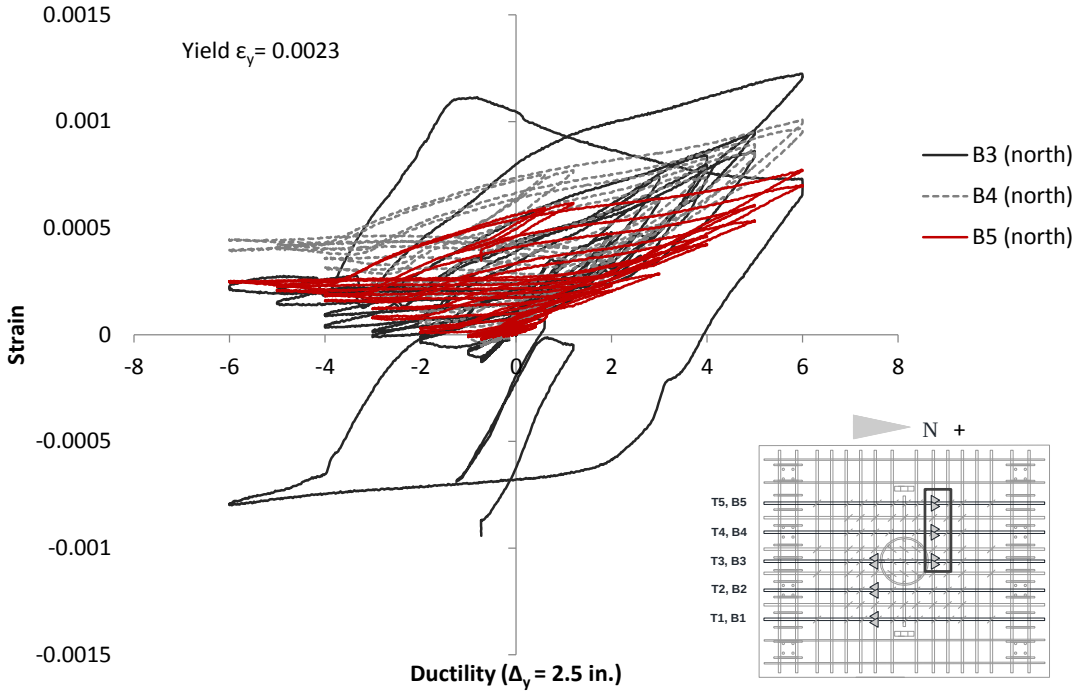

Figure 5.71 – Strains in longitudinal bars at the top face of the slab (bottom face in the specimen) of Specimen #1

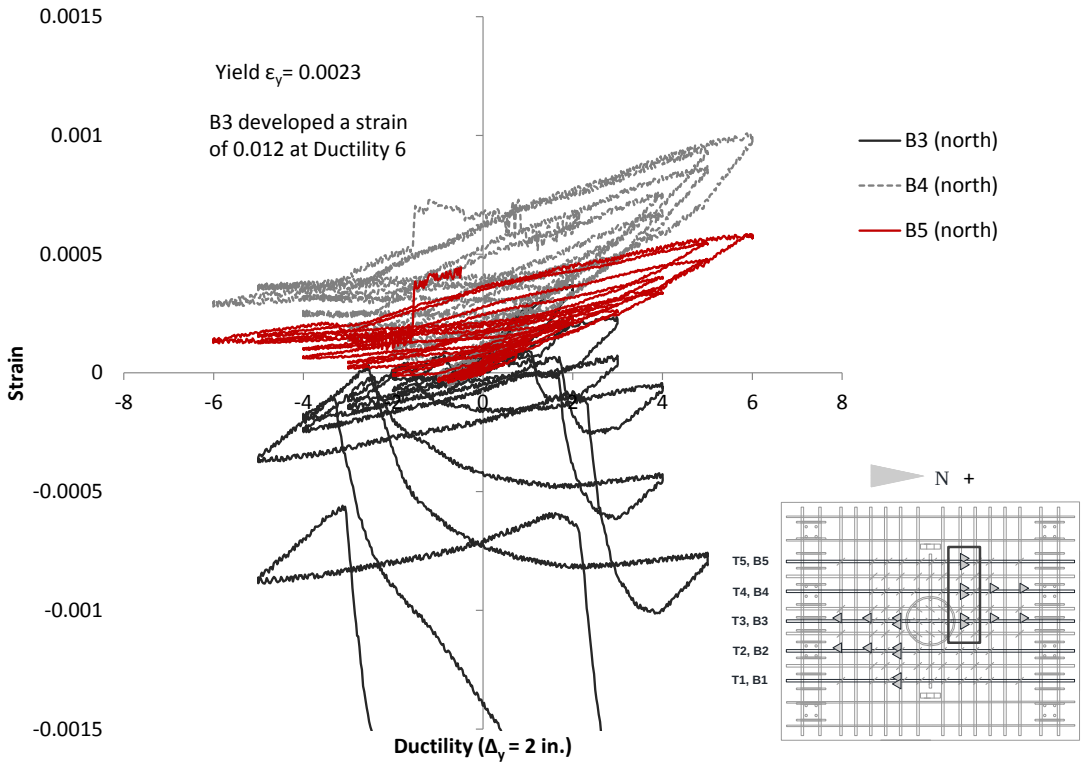

Figure 5.72 – Strains in longitudinal bars at the top face of the slab (bottom face in the specimen) of Specimen #2

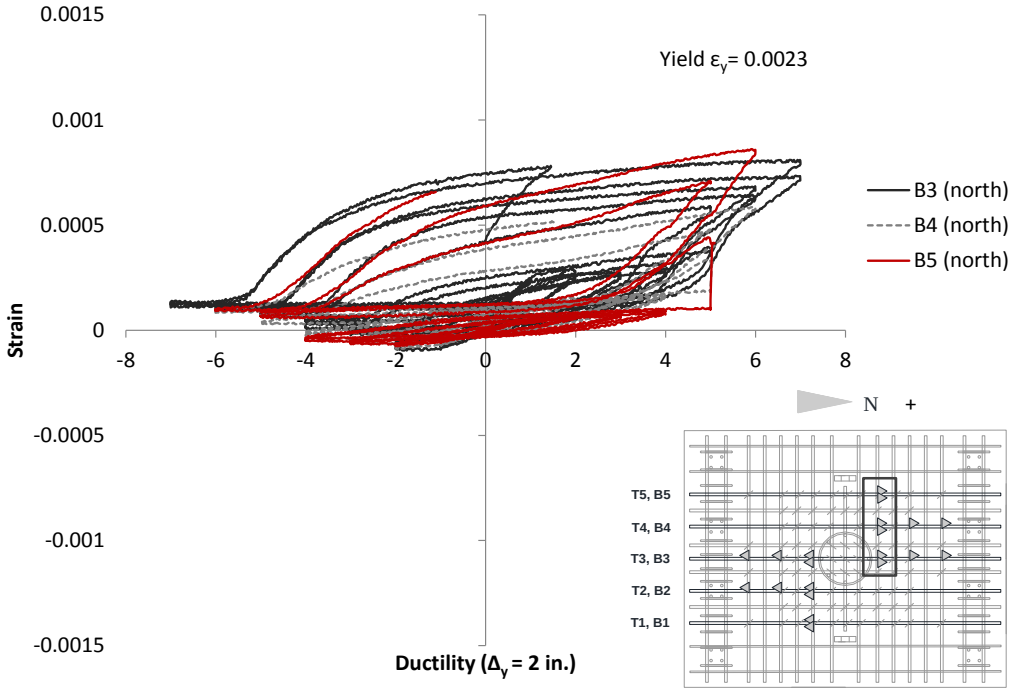

Figure 5.73 – Strains in longitudinal bars at the top face of the slab (bottom face in the specimen) of Specimen #3

CHAPTER 6

NUMERICAL INVESTIGATION OF EMBEDMENT LENGTH OF HEADED BARS IN SLAB-COLUMN JOINTS

Finite element (FE) models have been developed to study the anchorage of headed bars in concrete, and have been verified with experimental data from pullout tests. The column-slab assemblies that were tested in this study have been modeled with FE. The FE models were used in pre-test analyses and in a parametric study to investigate additional design variables. In this chapter, the FE models are presented, and the numerical results are compared with the experimental data. Finally, the findings of the parametric study are presented.

6.1 Finite Element Analysis of Pullout Tests on Headed Bars

A three-dimensional FE model developed to evaluate the anchorage capacity of headed bars is presented in Figure 6.1. It is used to simulate the tests of De Vries et al. (1996) and Choi et al. (2002). The concrete blocks in the former tests were unreinforced, while those in the latter had horizontal and vertical bars as shown in Figure 6.1. The finite element analyses (FEA) are performed with the program Abaqus (Simulia 2014).

For the modeling of concrete, the two different constitutive models, have been employed, the damaged-plasticity (D-P) model, available in Abaqus, and the microplane model developed by Caner and Bazant (2013a). They have been described, calibrated, and validated in Chapter 2. The microplane model can adequately simulate the opening and closing of cracks in concrete, while the D-P model cannot. The microplane model is also able to capture the influence of confinement on the post-peak behavior of concrete in a more accurate manner.

For model calibration, the compressive strength of concrete is obtained from material test data in the respective experimental studies. Table 6.1 shows the values selected for the key material parameters in the D-P model for all the analyses presented in this chapter. For different levels of confinement, the D-P requires different uniaxial stress-strain relations as input, as explained in Section 2.1. The key material parameters for the microplane model for the simulation of the pullout tests are shown in Table 6.2. Both the D-P model and the microplane model are calibrated to have the same uniaxial compressive strength and tensile strength for the given test.

The headed bar is modeled with beam elements and an elasto-plastic law with linear kinematic hardening. The tri-linear stress-strain curve for the steel model with a yield stress of 80 ksi and an ultimate stress of 95 ksi is plotted in Figure 6.2. The yield strength and ultimate strength are based on the respective tensile test data. The bar head is modeled with solid elements and elastic steel properties. A contact condition is imposed between the head and the concrete. The interaction between the bar and the surrounding concrete is modeled with a bond-slip interface element, developed and implemented in Abaqus by Murcia-Delso and Shing (2015). This model accounts for bond deterioration caused by bar yielding in tension and by cyclic loading. The bond-slip model is calibrated based on the compressive strength of the concrete (f_c') and the diameter of the bars (d_b) as discussed in Murcia-Delso and Shing (2015).

The ability of the FE model to predict the anchorage capacity and failure mode for headed bars has been verified with bar pullout tests conducted by De Vries et al. (1996), and Choi et al. (2002). The main characteristics of the test specimens, and the results of the tests and the FEA, with the D-P model and the microplane model for concrete, are given in Table 6.3.

De Vries et al. (1996) conducted pullout tests of bars with shallow embedment lengths. The concrete is unreinforced. Three of their test specimens have been analyzed with a FE model. A picture of a specimen and the corresponding FE model are shown in Figure 6.3. Only one

quarter of the specimen is modeled, given the double symmetry in the tests. Specimens T1B1 and T1B3 had an unbonded bar of diameter 0.79 in., embedded $1.8d_b$ and $5.7d_b$, respectively, in a concrete slab with a compressive strength of 12,000 psi, while Specimen T1B7 had an unbonded bar of diameter 1.38 in., embedded $6d_b$ in a concrete slab of the same compressive strength. The FEA can satisfactorily differiantiate the anchorage load capacities for the different specimens.

Choi et al. (2002) conducted pullout tests of bars embedded in concrete blocks with horizontal bars and vertical ties, which contributed to the increase of the anchorage load capacity. The test specimens modeled here had a No. 5 bar embedded in an RC beam with an 11.8 in. x 5.7 in. cross-section and No. 3 horizontal bars and vertical stirrups, which are modeled by truss elements, assigned an elasto-plastic material law with a yield stress of 61 ksi. The specimens had different spacings of the vertical stirrups. Only one quarter of the test specimen has been modeled, given the double symmetry of the tests. Figure 6.4 shows the maximum principal strains developed in the FE model of specimen C16-6DB-1A, which had vertical stirrups spaced at $3d_b$, while Figure 6.5 shows the maximum principal strains of specimen C16-6DB-1D, which had vertical stirrups spaced at $9d_b$. The FEA with the D-P model and the microplane model satisfactorily reproduce the breakout failure, with the development of splitting cracks and a cone-shaped failure surface, as shown in the figures. The anchorage load capacities from the FEA and the tests are summarized in Table 6.3.

6.2 Finite Element Analysis of Column-Slab Assemblies

The column-slab assemblies, tested in this study and presented in Chapter 5, have also been modeled with FE. Three-dimensional FE models were developed to simulate the structural behavior of the column-slab assemblies. Initially, the FE models were used for the pre-test assessment of the performance of the slab-column assemblies and to assist the development of the loading protocols for the tests presented in Chapter 5. Once the FE models were validated by the

test results and were further refined, they were used to obtain detailed information, such as strains in the column and slab reinforcement, bond stresses between concrete and steel, and punching crack displacements at the top face of the slab (bottom face in the specimen).

6.2.1 Finite Element Model

Figure 6.6 shows the FE model of Specimen #1. Specimens #2 and #3 have been modeled in the same way. Geometric nonlinearity is considered in the FEA. Only half of the specimen is represented in the model by taking advantage of the symmetry of the specimen about the applied lateral load.

Figure 6.7 shows the FE model of the reinforcement cage of Specimen #1. The column longitudinal bars are modeled with beam elements and are assigned the phenomenological stress-strain law presented in Section 2.3, which is based on the Menegotto-Pinto model and accounts for low-cycle fatigue (LCF) of reinforcing bars. The values of the material parameters for the longitudinal reinforcement are summarized in Table 6.4. Bond slip between the longitudinal bars and concrete is considered, using the bond-slip model of Murcia-Delso and Shing (2015). The heads of the bars are modeled with solid elements and elastic steel properties are assigned to them. They are connected to the bars.

The lateral reinforcement in the column is modeled with truss elements and is assigned an elasto-plastic constitutive law with linear kinematic hardening. The slab longitudinal bars are modeled with beam elements, while the vertical bars are modeled with truss elements. Both of them are assigned the elasto-plastic law for steel with linear kinematic hardening. A yield stress of 65 ksi and an ultimate stress of 95 ksi at strain 0.1 are assigned, based on average values of the material test data. A perfect bond with concrete is considered for the slab reinforcement and the lateral reinforcement in the column.

Concrete is modeled with solid elements and both the damaged-plasticity (D-P) and microplane constitutive models have been employed to model the concrete in the column-slab assembly. With the D-P model, contact conditions are introduced to at the column-to-slab interface as well as between the bar heads and concrete to better simulate the opening and closing of cracks during cycling loading, as shown in Figure 6.8. The compressive strengths of concrete, as shown in Table 6.5, are based on the material test data. The other material parameters for the D-P model are the same as those summarized in Table 6.1. With the microplane model, there is no need to introduce contact conditions as it can accurately capture the tensile unloading and reloading stiffness of cracked concrete. The microplane model has been calibrated to have the compressive strengths shown in Table 6.5. It also has the same tensile strengths as the D-P model. Table 6.6 presents the values of the model parameters that will result in the desired strengths.

Both models adequately simulate the behavior of the slab-column assemblies under lateral loading. However, the microplane model provides more accurate results than the D-P model. For this reason, this report presents detailed results for the microplane model only.

For Specimen #1, the steel straps, installed on the outer perimeter of the column to compensate for the lower-than-expected compressive strength of concrete, are also modeled, as shown in Figure 6.8. They are modeled with solid elements and are assigned the elasto-plastic steel law, with a yield stress of 55 ksi and an ultimate stress of 70 ksi at strain 0.1, based on material test data. Figure 6.9 shows the FE model of Specimen #3, whose slab geometry is slightly different from that of Specimens #1 and #2, with a 3-in. drop cap in the slab.

6.2.2 Lateral Load-vs.-Displacement Response

6.2.2.1 Specimen #1

Figure 6.10 shows the lateral load-vs.-drift ratio curves for Specimen #1 from the FEA with the D-P model and the microplane model, along with the experimental result. The numerical result with the D-P model matches the test result sufficiently well. The hysteresis curves from the FEA show a slightly higher strength and a better energy-dissipation capability than the test data. The relatively ductile behavior of Specimen #1, due to the confining steel straps placed at the bottom of the column, is well reproduced in the FEA.

The hysteresis curves obtained with the microplane model closely match the experimental result, in terms of the lateral load capacity, the strength degradation, and the pinching of the hysteresis loops. The microplane model is able to better capture the pinching of the hysteresis loops as compared to the D-P model.

6.2.2.2 Specimen #2

Figure 6.11 shows the lateral load-vs.-drift ratio curves for Specimen #2 from the FEA with the D-P model and the microplane model, along with the experimental result. Both models are able to capture the experimental result well. The D-P model appears to over-estimate the strength but better capture the pinching phenomenon probably related to the deterioration of the anchorage of the headed bars.

6.2.2.3 Specimen #3

Figure 6.12 shows the lateral load-vs.-drift ratio curves for Specimen #3 from the FEA with the D-P model and the microplane model, along with the experimental result. Both models are able to capture the shape of the hysteresis curves well with the D-P again slightly over-estimates the strength.

6.2.3 Vertical Displacement underneath the Test Slabs

6.2.3.1 Specimen #1

During the test of Specimen #1 $\left(l_e = 9.8d_b\right)$, the vertical displacement at the bottom face of the slab was not monitored by displacement transducers. However, it was clearly observed that it experienced some damage caused by the punching of the headed bars, as discussed in Chapter 5. At the end of the test, the vertical displacement of the top face of the slab (bottom face of the specimen), at the position of the headed bar placed at the extreme south side was measured to be between 0.3 and 0.4 in. Figure 6.13 shows the vertical displacement of the top face of the slab (bottom face in the specimen) at the same position, as obtained from the FEA with the microplane model.. The analysis predicts a maximum vertical displacement of 0.3 in.

The deformed shapes of the FE models with the D-P model and the microplane model, at the 2nd cycle of ductility 6, are shown in Figure 6.14. The vertical deformation of the slab surface due to the punching of the headed longitudinal bars is not too noticeable, which is consistent with the experimental observations.

6.2.3.2 Specimen #2

During the test of Specimen #2 $\left(l_e = 8.7d_b\right)$, the damage at the top face of the slab (bottom face in the specimen) due to the pinching of the headed bars was significant, resulting in the severe spalling of the concrete during the second cycle of ductility 6. Figure 6.15 plots the vertical displacement of the top face of the slab (the bottom face of the specimen), at the position of the headed bar placed at the extreme south side, against the column displacement (in terms of the ductility level) for the test and the analysis with the microplane model. The numerical result matches the test well. Figure 6.16 shows the deformed shapes of the FE models of Specimen #2. The punching deformations are well captured by the FE models.

6.2.3.3 Specimen #3

Figure 6.17 shows the vertical displacement of the top face of the slab for Specimen #3 $\left(l_e = 11d_b\right)$. The numerical result matches the experimental result well. The vertical displacement due to the punching of the headed bars is extremely limited, indicating the benefit of the increased embedment length for the headed bars. The deformed shapes of the FE models for Specimen #3, at ductility 7, are presented in Figure 6.18. The numerical result is consistent with the very limited damage at the top face of the slab (bottom face in the specimen) observed in the test.

6.2.4 Strains in Column Longitudinal Bars

Figure 6.19 shows the strain variations along the headed bar on the extreme north side of the column of Specimen #1. The numerical results (with the microplane model) are compared to those measured in the test. Some of the strain gages were damaged as the ductility demand on the column increases, resulting in missing strain data in the plots. Near the slab-column interface, the analysis overestimates the strains in the bar. Away from there, the analysis results satisfactorily match the strains measured in the test.

The strains along the embedment length of the headed bar inside the slab are predicted by the FEA sufficiently well up to a ductility demand of 1. As the ductility demand increases, the strains are overestimated in the FEA. The yield strain penetrated all the way to the head of the bar in the test of Specimen #1, which has also been captured in the analysis.

Figure 6.20 and Figure 6.21 plot the strains in the headed bar on the extreme north side obtained from the analysis and the test of Specimens #2 and #3. The numerical results match the test results sufficiently well with similar observations as those for Specimen #1.

The analyses show that the strain developed close to the head of the bar in Specimen #3 at high ductility demands of 3, 5, and 6 is much smaller than that in Specimen #2, as shown in

Figure 6.20 and Figure 6.21 . This indicates that the headed bars in Specimen #3 are better developed than those in Specimen #2.

The better development of the headed bars and the less severe anchorage deterioration in Specimen #3, as compared to Specimen #2, can also be seen in Figure 6.22 and Figure 6.23. Each figure presents the axial forces in the longitudinal bar at the elevation of the slab-column interface and at its head, as well as the total bond force along the embedment length, obtained in the analyses of Specimens #2 and #3. The total bond force is calculated as the difference in the bar forces at the aforementioned locations. When the headed bar is in tension, the bond force is maintained in Specimen #3 $\left(l_e = 11 d_b\right)$ as the ductility demand increases, while it drops significantly in Specimen #2 $\left(l_e = 8.7 d_b\right)$. Moreover, at higher ductility demand levels (4, 5, and 6), when the bar in Specimen #2 is reloaded in tension, the force-displacement curves show some pinching and then a sudden increase in resistance, as shown in Figure 6.22, which can be attributed to the punching failure of the concrete next to the bar head causing the disengagement and reengagement of bearing action of the bar head as the bar slips back and forth. This is not observed for Specimen #3.

When the bar is in compression, the bond force in Specimen #3 is maintained up to ductility 5, while it drops significantly in Specimen #2. For both specimens, a maximum compressive force of about 82 kips is developed at the head of the bar. This indicates that 82 kips is the borderline punching force that can induce the punching failure of the concrete layer below the bar head in the specimen. The ability of Specimen #3 to maintain the bond force up to a large ductility demand, due to the larger bar embedment length, can avert the punching failure.

For Specimen #3, bar elements, presenting the headed bars in the column above the slab-column interface, experience significant bending deformations due to buckling when the ductility demand exceeds 5. Due to this, the forces in the headed bars embedded in the slab drop; so is the

bond force. However, during the test of Specimen #3, no evidence of bar buckling was observed, even though the concrete spalling at the base of the column was more severe in Specimen #3 than that in Specimen #2.

6.2.5 Strains in J-Bars

Figure 6.24 shows the strains in J-bars, J5 and J7, placed in the core region of the slab-column joint in Specimen #1 $\left(l_e = 9.8d_b\right)$. The strains from the analysis (with the microplane model) and the test are plotted together. The J-bars are modeled with truss elements and are embedded in concrete with perfect bond (i.e., without bond-slip elements). Since only half of the slab-column assembly is modeled assuming a perfect symmetry, J7 and J5 should have the same behavior. As shown in the figure, the numerical data match the experimental findings sufficiently well. The strains developed in the J-bars reach values close to the yield strain.

It should be mentioned that the test data were obtained from strain gages attached at the middle height of the J-bars. The strains from the FEA, as shown in Figure 6.24, are obtained from the middle truss element (out of three) representing the modeled J-bar. The element near the top face of the slab (bottom face in the specimen) develops a maximum tensile strain of 0.008, exceeding the yield strain (which is 0.0023).

For Specimen #2 $\left(l_e = 8.7d_b\right)$, the strains in the same J-bars are shown in Figure 6.25. The numerical data are in accordance with the test measurements. The strains developed in Specimen #2 $\left(l_e = 8.7d_b\right)$ slightly exceed the yield strain, larger than those in Specimen #1. This more significant engagement of the J-bars is attributed to the more severe anchorage deterioration of the headed bars in Specimen #2, as compared to Specimen #1.

The strains in the J-bars of Specimen #3 $\left(l_e = 11d_b\right)$, which had the largest embedment length for the headed bars and experienced the least severe anchorage deterioration among the

three specimens, are shown in Figure 6.26. The analysis matches the test well. The strains in Specimen #3 $\left(l_e = 11d_b\right)$ are quite smaller than those in Specimen #2.

6.2.6 Strains in Vertical Stirrups

Figure 6.27 shows the strains in V13, a vertical stirrup in the 1st row next to the column cage, obtained from the FEA (microplane) and the test of Specimen #1. The vertical stirrups are modeled in the same way as the J-bars. The numerical results match the experimental measurements well. The 1st row of vertical stirrups develops significant tensile strains, resisting the punching and bearing actions of the headed bars.

Figure 6.28 shows the strains in vertical stirrup V13, obtained from the FEA and the test of Specimen #2. The numerical results match the test sufficiently well, with the maximum strain slightly exceeding 0.0015. Figure 6.29 shows the strains in V13 from the FEA and the test of Specimen #3. The maximum strain developed in V13 in Specimen #3 is 0.0006, significantly smaller than that in Specimen #2 (Figure 6.28). This indicates that the 1st row of vertical stirrups in Specimen #3 is not engaged as much as that in Specimen #2, consistent with the better anchorage and less slip of the headed bars in Specimen #3.

Figure 6.30 through Figure 6.32 show the strains developed in the stirrups in the 2nd row away from the column cage for Specimens #1, #2, and #3, obtained from the FEA and the tests. For all three specimens, the strains developed are significantly smaller than the yield strain. The numerical results match the measurements in the tests very well.

6.2.7 Strains in Longitudinal Bars in Slabs

Figure 6.33 through Figure 6.35 show the strains (average strain over the section of the beam element) in the longitudinal bar, T3, at the top face of the slab of Specimens #1, #2 and #3 (bottom face in a real bridge), obtained from the FEA and the tests. The numerical results (with

microplane model) match the tests well, with strains way below the yield level. In the negative displacement direction, the numerical results adequately match the experimental measurements, reaching a maximum strain of about 0.001. For the positive direction, the FEA results show a more linear behavior of the bar. However, both the test and the numerical results show that the bar tends to be in tension most of the time when the column was displaced towards the positive direction. This contradicts the direction of the bending moment induced on the slab, and can be attributed to the strut action developed in the short-span slab.

Figure 6.36 shows the strains developed in the longitudinal bar, B3, placed at the bottom face of the slab of Specimen #2, from the test and the FEA. Only the reading from one of the two gages is plotted, because the other gage was damaged. For the numerical result, the strain is taken at a point that can be subjected to the most severe compression in the cross-section of the beam element due to bending. The comparison shows that the longitudinal bar was subjected to significant bending caused by the punching of the headed bars in the test.

Figure 6.37 shows the strain (averaged strain from two gages) developed in longitudinal bar B3 near the column cage obtained in the test of Specimen #3, and the average strain obtained from the FEA at a similar location. The longitudinal bar develops only elastic strains, since no significant punching force from the headed bars was observed. Figure 6.38 shows how the longitudinal bars at the bottom face of the specimen are deformed in the FEA of Specimens #2 and #3. It can be seen that the mat of longitudinal and transverse bars in the slab, the J-bars, and the vertical stirrups are engaged to resist the punching action of the headed bars. This is much more significant in Specimen #2 than in Specimen #3.

6.2.8 Effectiveness of Slab Vertical Reinforcement to the Development of Headed Bars

Two additional FEA of Specimen #3 have been conducted with variations in the amount of the vertical stirrups and J-bars in the slab. In one case, identified as Specimen #3B, all the J-

bars and vertical stirrups have been removed, and in the second, identified as Specimen #3C, only the J-bars and the 1st row of vertical stirrups closest to the column cage have been retained, while all the other vertical stirrups have been removed.

Figure 6.39 compares the lateral load-vs.-top drift curves for Specimens #3 and #3B. It can be seen that while the lateral load capacity of the column can be developed in Specimen #3B, the hysteresis loops are more pinched, indicating some significant deterioration of the anchorage capacity of the headed bars. Furthermore, the drop of the lateral load resistance with increasing drift amplitude is slightly larger in Specimen #3B than in Specimen #3. Figure 6.40 shows the deformed meshes for Specimens #3 and #3B. The damage at the bottom face of the slab in Specimen #3B is obvious while Specimen #3 does not show noticeable damage.

Figure 6.41 compares the lateral load-vs.-top drift curves for Specimens #3 and #3C. It can be seen that the two specimens have almost the same behavior. Figure 6.42 shows the deformed meshes of Specimens #3 and #3C. Again, the difference between the two cases is not noticeable. This comparison shows that the vertical stirrups in the 2nd row and farther away the column cage have little influence on the behavior of a slab-column joint provided the headed bars are adequately developed with a minimum development length of $11d_b$.

6.2.9 Influence of Concrete Cover Thickness

An additional FEA of Specimen #2 has been conducted by changing the embedment length of the headed bars. Specimen #2, which had $8.7d_b$ embedment length, experienced severe punching damage at the top face of the slab (bottom face in the specimen). To investigate the influence of the concrete cover above the bar head, the headed bars in Specimen #2 are moved away from the bottom face of the specimen (top face in the bridge slab) by $2d_b$ reducing the embedment length to $6.7d_b$, while increasing the distance of the bar heads from the nearest slab surface by $2d_b$. This is referred to as Specimen #2B.

Figure 6.43 compares the lateral load-vs.-top drift curve for Specimens #2B with that for Specimen #2. The two specimens exhibit a very similar behavior. Even with a development length of $6.7d_b$, the lateral load capacity of the column is developed. The hysteresis curves for Specimen #2B are less pinched than those for Specimen #2. This can be attributed to the increased concrete cover, which provides more resistance to the punching forces of the bars and thereby reduces the punching damage. Figure 6.44 shows the deformed meshes for Specimens #2 and #2B. It is clearly observed that the punching damage at the bottom of the slab is much less severe in Specimen #2B.

Figure 6.45 plots the strains developed in vertical stirrup V13, placed in the 1st row next to the column cage, for Specimens #2 and #2B. By reducing the embedment length for the headed bars, V13 develops larger strains when the adjacent headed bar is in tension (in the negative displacement direction), indicating its more active engagement to resist the tension in the bar. When the adjacent bar is loaded in compression (in the positive displacement direction), V13 develops smaller strains. This can be attributed to the additional concrete cover, which helps to resist punching forces. However, further experimental investigation is required to verify the numerical findings.

6.3 Conclusions

The FE models produce results consistent with the experimental data and observations. For the slab reinforcing details and thickness considered in this study, the FEA have shown that the slab can sustain a punching force of 82 kips from a bar head without punching failure. Furthermore, the analyses have confirmed the experimental observation that the vertical stirrups in the slab farther away from the first row next to the column cage have little contribution to the resistance of the punching and bearing forces of the headed bars. Finally, the analyses have

indicated that if there is not enough room to provide an adequate embedment length of $11d_b$, it may be advantageous to reduce the embedment length and increase the distance of the bar head from the slab surface to reduce or avoid punching damage.

6.4 Acknowledgement of Publication

This chapter, in full, is a reprint of the material as it appears in the report submitted to the California Department of Transportation in 2015, Papadopoulos, V., Murcia-Delso, J., Shing, P. B., under the title "Development Length for Headed Bars in Slab-Column Joints of RC Slab Bridges". The dissertation author was the primary investigator and author of this report.

Table 6.1 – Key parameters of the D-P model for concrete

Parameter	Description	
f_c' (ksi)	Compressive strength	From material test data
f_t' (ksi)	Tensile strength	$f_t' = 8\sqrt{f_c'}$
G_f^I (lb/in)	Fracture energy	2.9
$\sigma_{b0/}\,\sigma_{c0}$	Controls biaxial compressive strength	0.12
ψ	Dilation angle	20^o
ε	Eccentricity	0
K_c	Controls shape of yield surface	1
w_c	Compression recovery factor	0
w_t	Tension recovery factor	1

Table 6.2 – Key parameters of the microplane model for pullout tests

Test	k_2, k_3	E (ksi)	k_1 (x10^{-4})	f_c' (ksi), ε_p
De Vries et al.	1, 1	15,700	1.65	12, 0.0015
Choi et al.	1, 1	7,380	1.65	5.7, 0.0015

Table 6.3 – Numerical results for pullout tests

Test	Specimen	d_b (in.)	f_y (ksi)	f_u [1] (ksi)	l_e (d_b)	Vertical ties	f_c' (ksi)	P_{test} (kips) & failure mode	P_{FEA} D-P (kips)	P_{FEA} microplane (kips)
De Vries et al.	T1B1	0.79	80	95	1.8	-	12.0	17.0 Concrete breakout	10.0	18.5
	T1B3	0.79	80	95	5.7	-	12.0	46.0 Bar fracture	43.0[2]	46.0
	T1B7	1.38	78	95	6.0	-	12.0	110.0 Concrete breakout	108.0	140.0[3]
Choi et al.	C16-6DB-1A	0.63	61	85[4]	6.0	No. 3 stirrups, $s_t = 3d_b$	5.7	18.9 Concrete breakout	14.7	18.9
	C16-6DB-1C	0.63	61	85[4]	6.0	No. 3 stirrups, $s_t = 6d_b$	5.7	18.0 Concrete breakout	13.3	18.4
	C16-6DB-1D	0.63	61	85[4]	6.0	No. 3 stirrups, $s_t = 9d_b$	5.7	17.5 Concrete breakout	13.0	18.0
	Specimen without ties	0.63	61	61[3]	6.0	-	5.7	-	8.3	9.4

[1]The strain at ultimate stress of steel was assumed as $\varepsilon_u = 0.12$
[2]FEA with D-P failed by concrete breakout
[3]FEA with microplane model failed by bar fracture
[4]The ultimate stress of rebars is not documented in the study of Choi et al.

Table 6.4 – Steel material parameters for column longitudinal reinforcement

Parameter	Description	Specimen #1	Specimen #2	Specimen #3
f_y (ksi)	Yield stress	69	65	65
E_s (ksi)	Elastic Stiffness		29000	
ε_f'	LCF coefficient	0.0645	0.0656	0.0656
c	LCF coefficient	0.2534	0.2518	0.2518

Table 6.5 – Compressive strengths of concrete (in ksi) for slab-column specimens

	Specimen #1	Specimen #2	Specimen #3
Slab	5.0	4.9	4.5
Column	3.2	4.8	5.0

Table 6.6 – Calibration of the microplane model for the slab-column assemblies

Specimen		Concrete	k_2, k_3	E (MPa)	k_1 (x10^{-4})	f_c' (ksi), ε_p
#1	Slab	Confined	Default	40,620	0.5	5.0, 0.0015
		Unconfined	1, 1	44,800	1.65	5.0, 0.0015
	Column	Confined	Default	26,000	0.5	3.2, 0.0015
		Unconfined	1, 1	28,670	1.65	3.2, 0.0015
#2	Slab	Confined	Default	39,810	0.5	4.9, 0.0015
		Unconfined	1,1	43,910	1.65	4.9, 0.0015
	Column	Confined	Default	39,900	0.5	4.8, 0.0015
		Unconfined	1, 1	43,010	1.65	4.8, 0.0015
#3	Slab	Confined	Default	36,560	0.5	4.5, 0.0015
		Unconfined	1, 1	40,320	1.65	4.5, 0.0015
	Column	Confined	Default	40,625	0.5	5.0, 0.0015
		Unconfined	1, 1	44,800	1.65	5.0, 0.0015

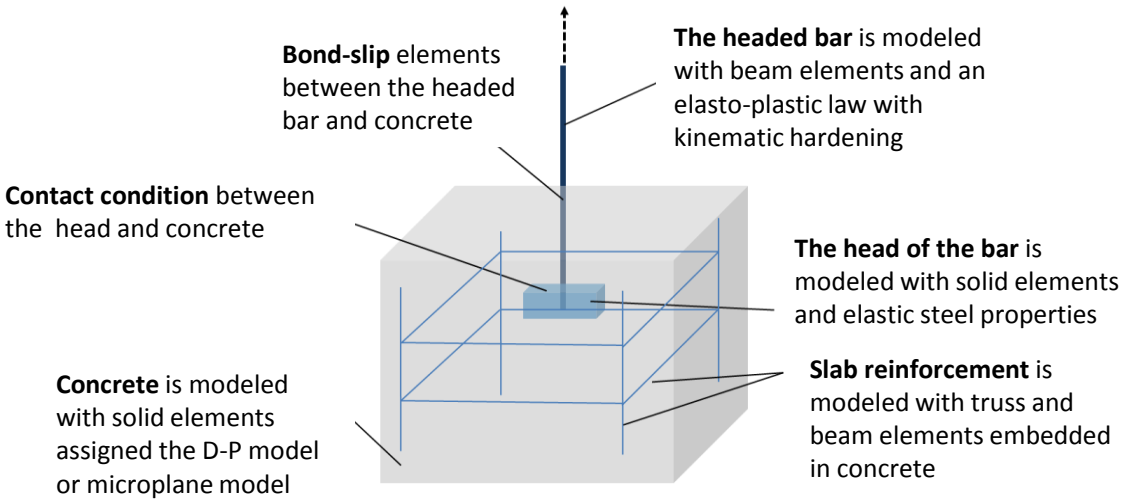

Figure 6.1 – FE model for pullout tests

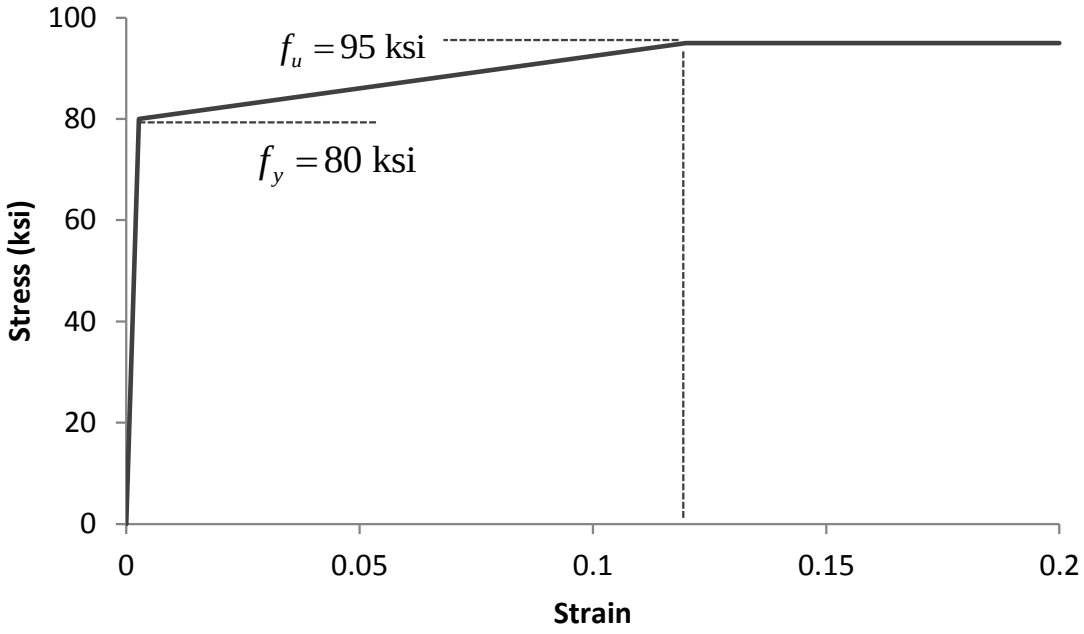

Figure 6.2 – Stress-strain curve for steel model

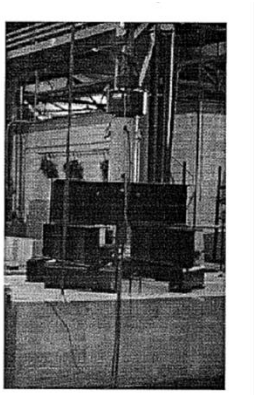

(a) Test specimen and setup

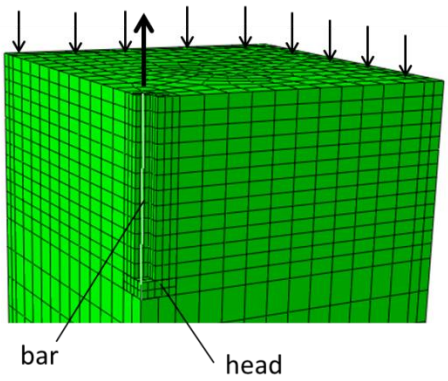

(b) FE model of ¼ of a test specimen

Figure 6.3 – Tests by De Vries et al. (1996)

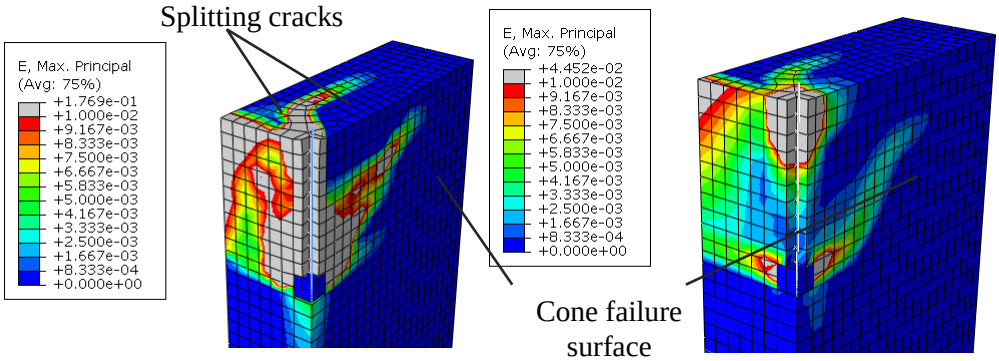

(b) D-P model (a) Microplane model

Figure 6.4 – Maximum principal strains in FE model of Specimen C16-6DB-1A by Choi et al. (2002)

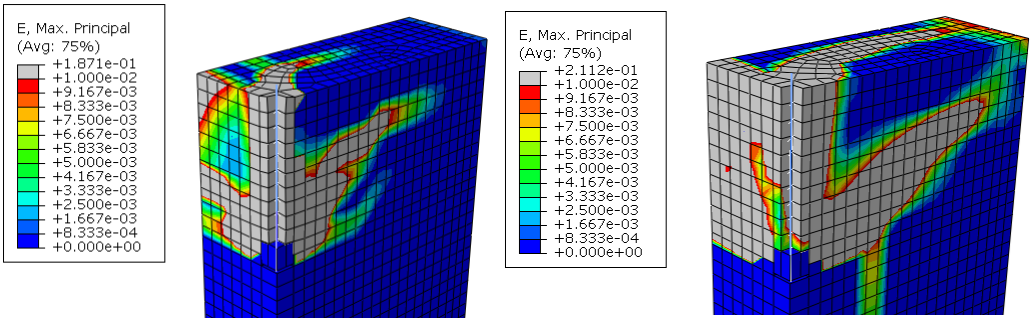

(a) D-P model (b) Microplane model

Figure 6.5 – Maximum principal strains in FE model of Specimen C16-6DB-1D by Choi et al. (2002)

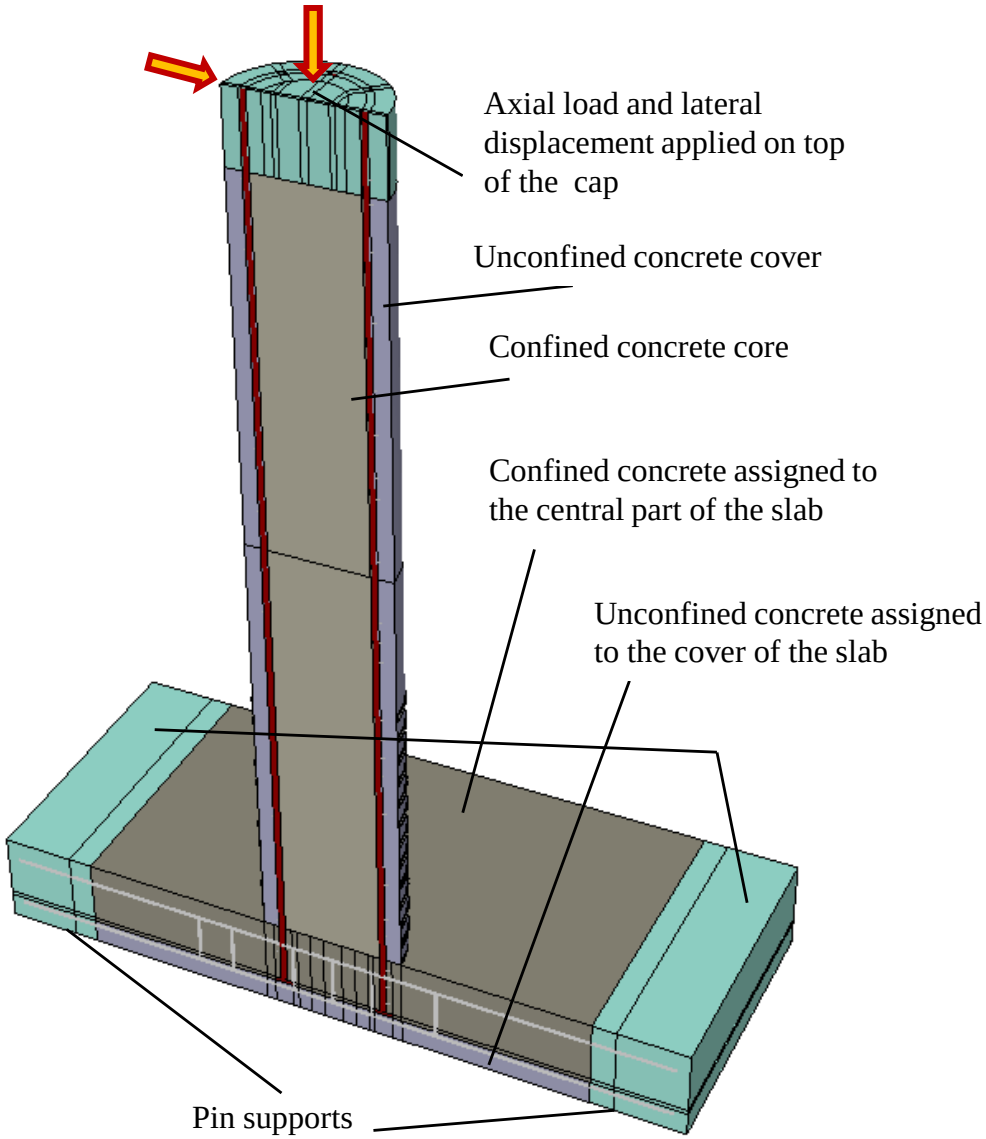

Figure 6.6 – FE model of slab-column Specimen #1

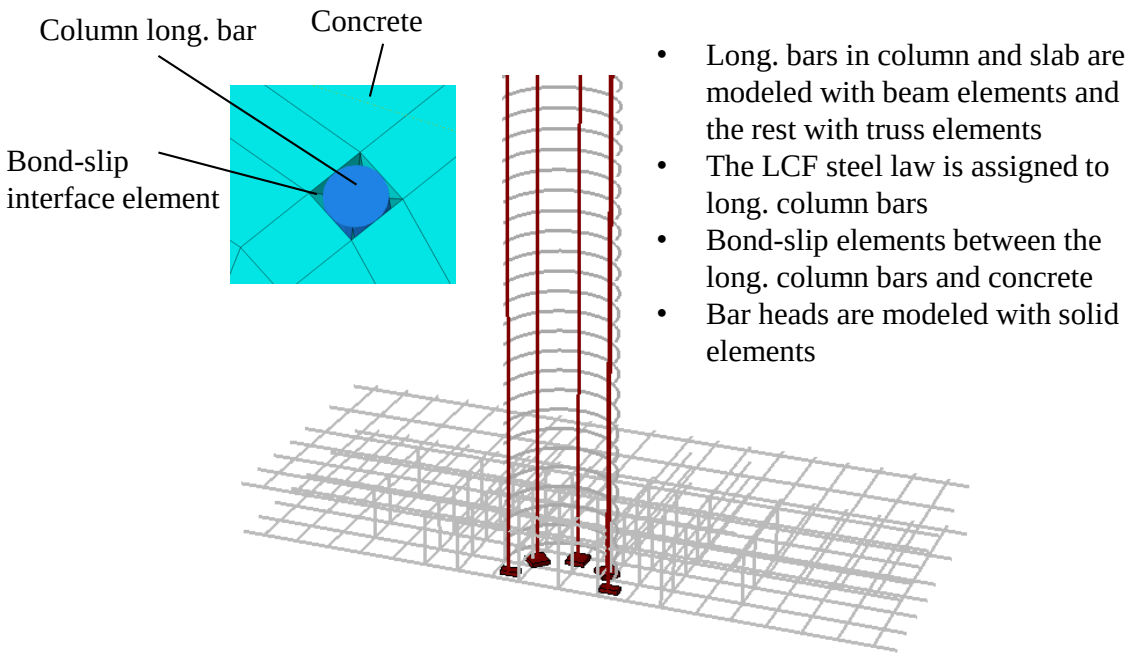

Figure 6.7 – FE assembly for reinforcement cage of Specimen #1

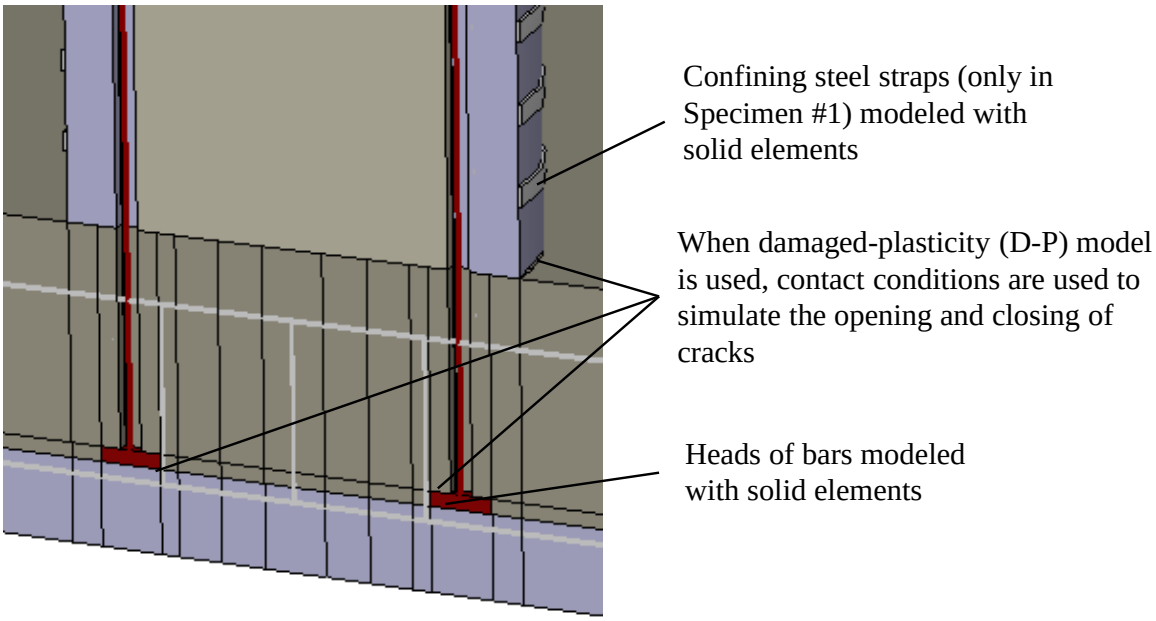

Figure 6.8 – Close-up details for the FE model of Specimen #1

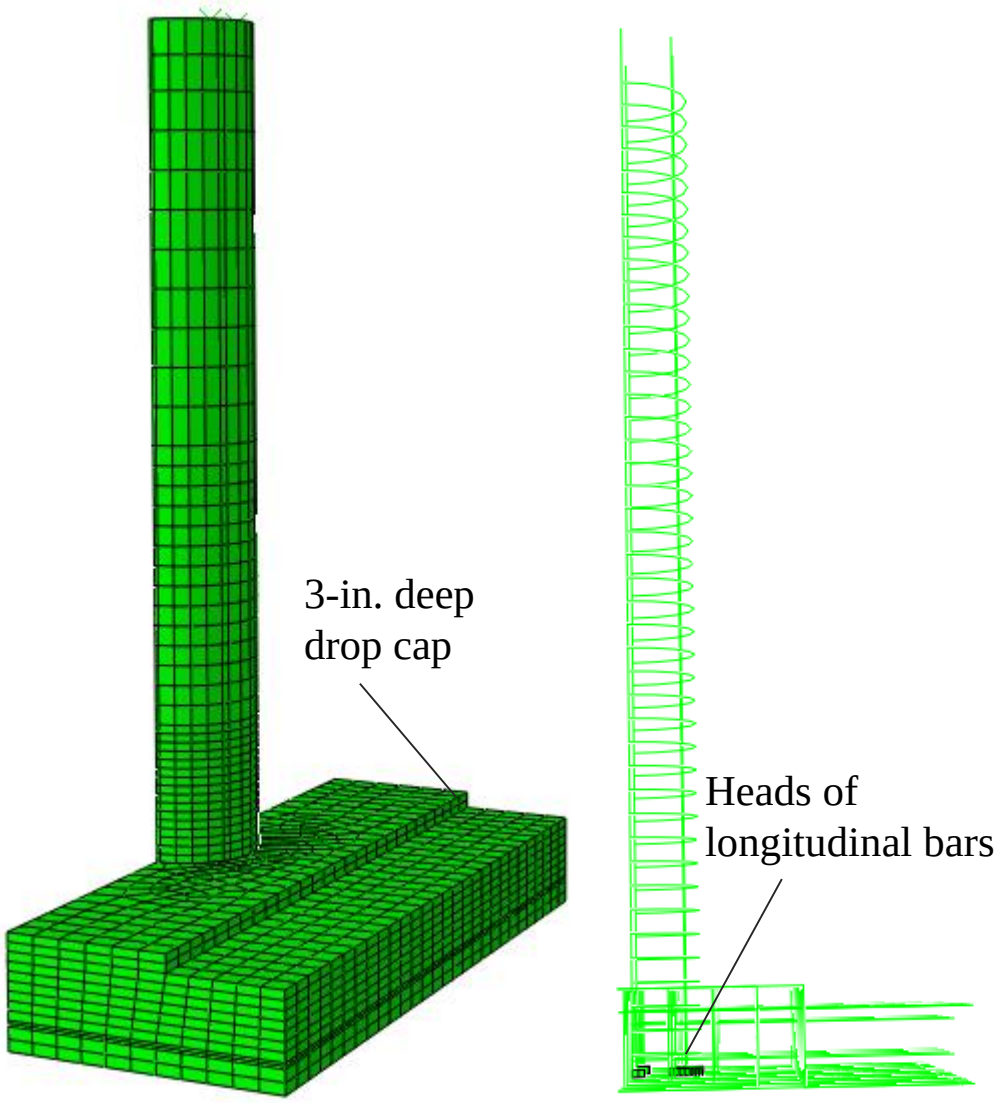

(a) Slab-column assembly (b) Reinforcement cage

Figure 6.9 – FE model of Specimen #3

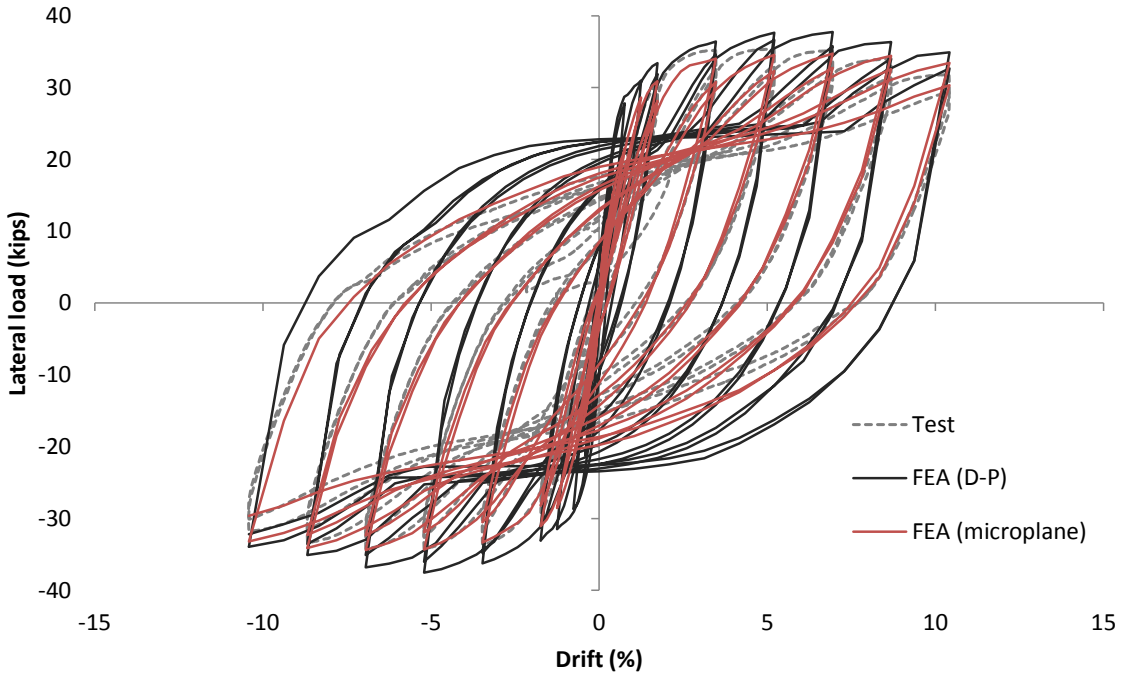

Figure 6.10 – Lateral load-vs.-top drift curves from test and FEA of Specimen #1

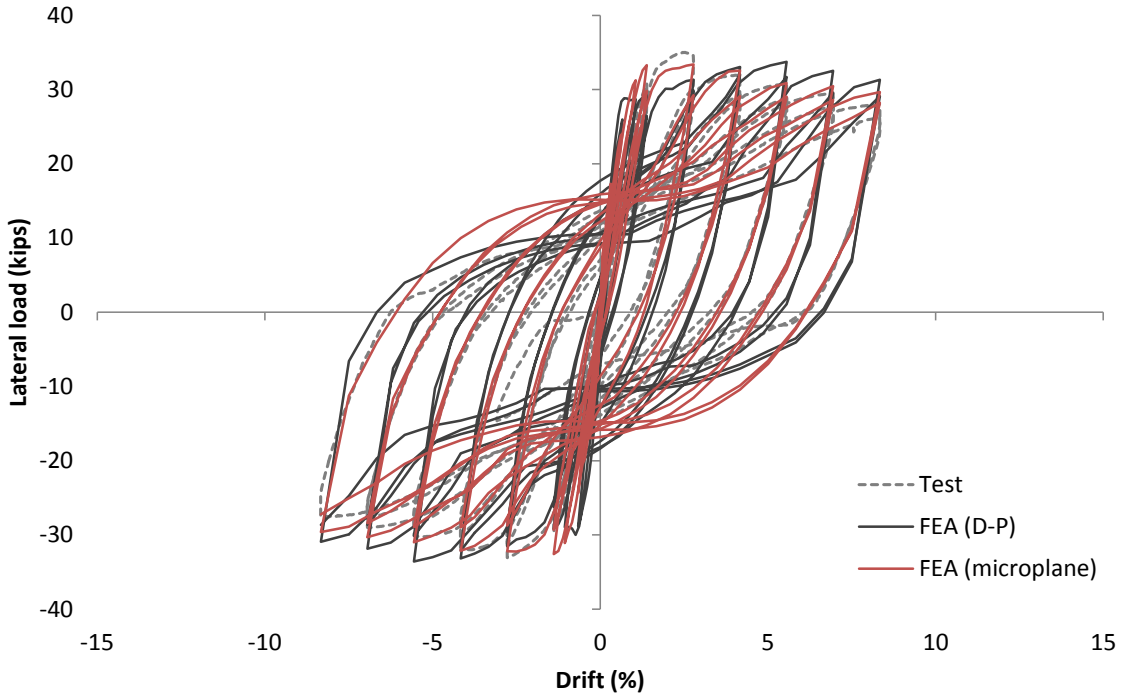

Figure 6.11 – Lateral load-vs.-top drift curves from test and FEA of Specimen #2

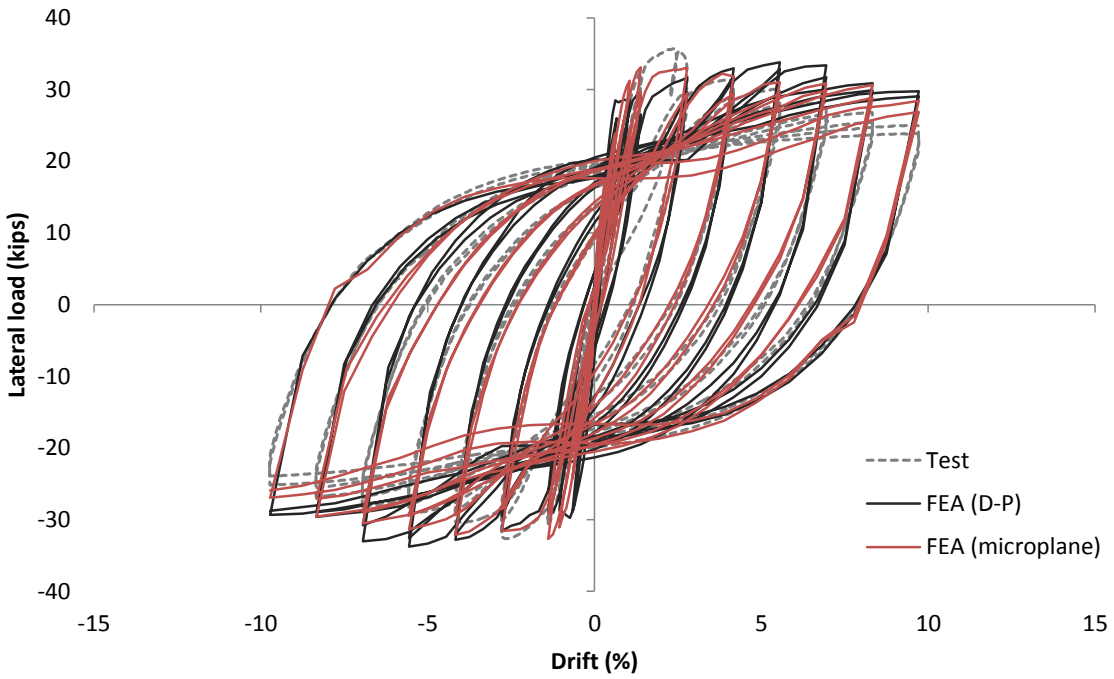

Figure 6.12 – Lateral load-vs.-top drift curves from test and FEA of Specimen #3

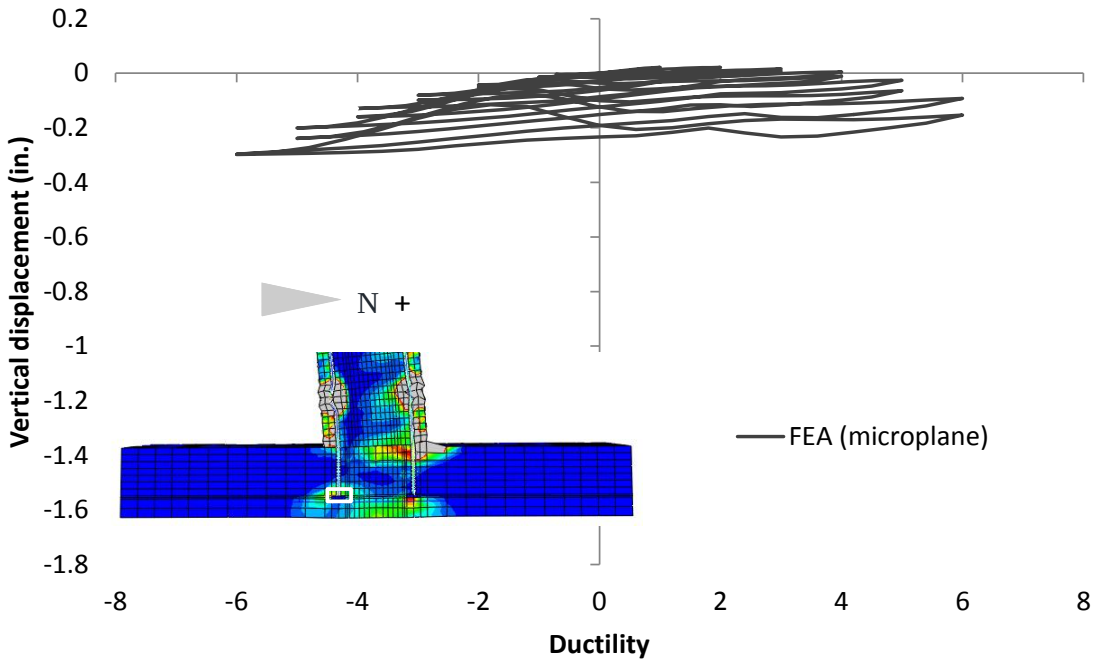

Figure 6.13 – Vertical displacement of the top face of the slab (bottom face in the specimen) at the position of the headed bar on the south side of Specimen #1 $\left(l_e = 9.8d_b\right)$

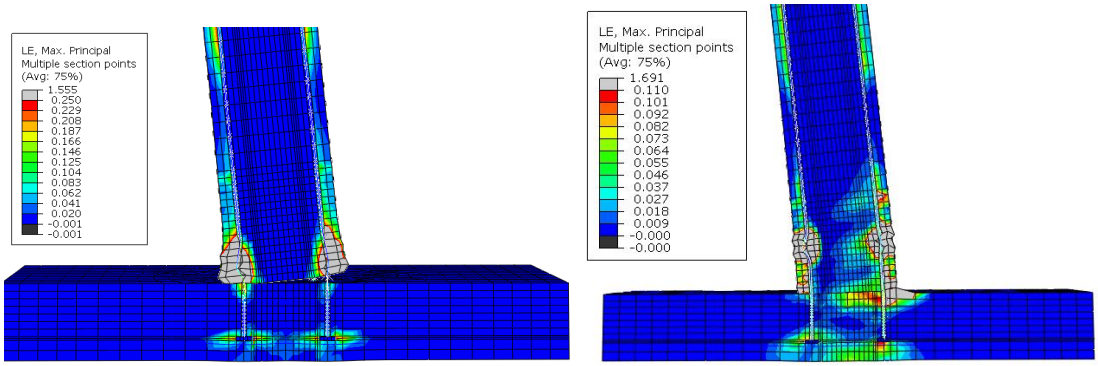

(a) FEA with D-P model (b) FEA with microplane model

Figure 6.14 – Deformed FE mesh for Specimen #1 $\left(l_e = 9.8d_b\right)$

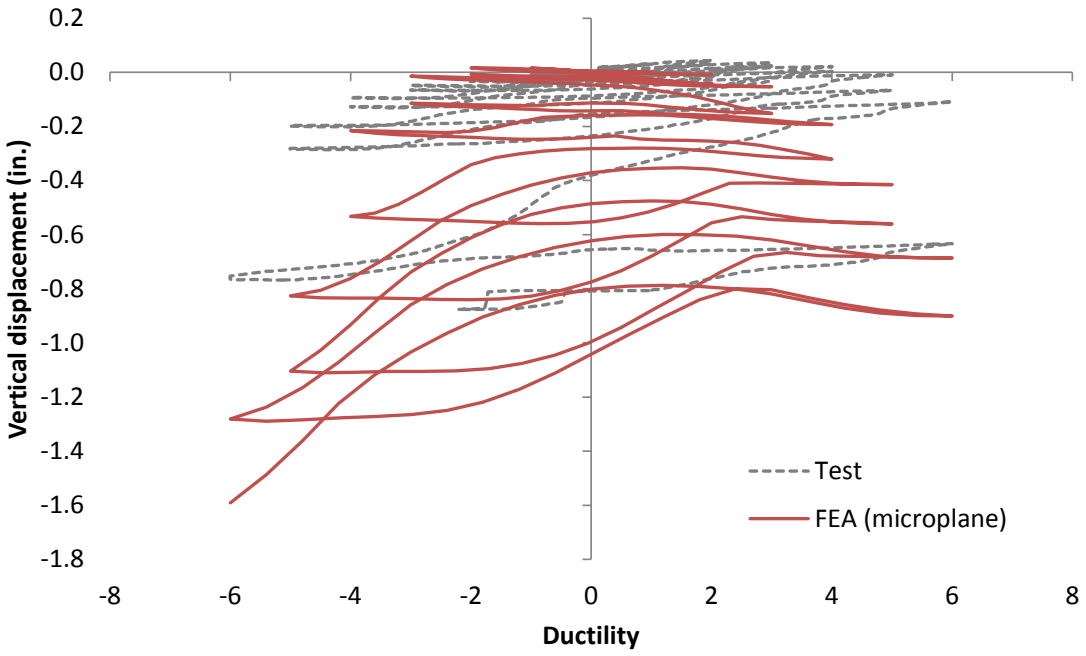

Figure 6.15 – Vertical displacement of the top face of the slab (bottom face in the specimen) at the position of the headed bar on the south side of Specimen #2 $\left(l_e = 8.7d_b\right)$

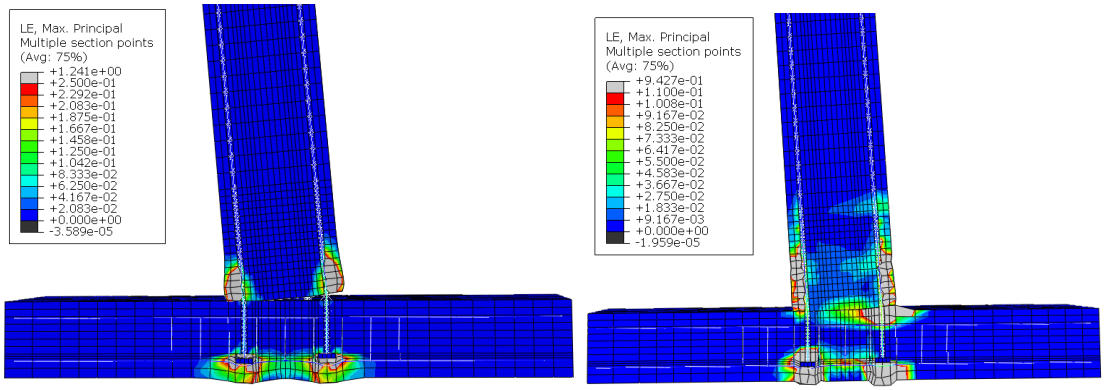

(a) FEA with D-P model (b) FEA with microplane model

Figure 6.16 – Deformed FE mesh for Specimen #2 $\left(l_e = 8.7 d_b\right)$

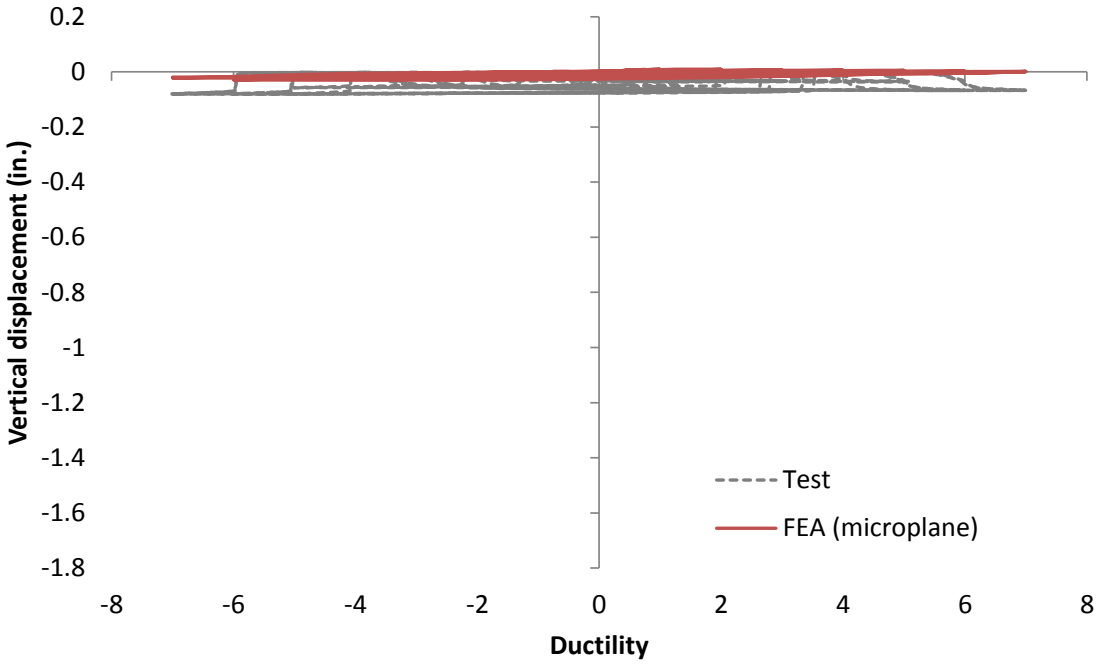

Figure 6.17 – Vertical displacement of the top face of the slab (bottom face in the specimen) at the position of the headed bar on the south side of Specimen #3 $\left(l_e = 11 d_b\right)$

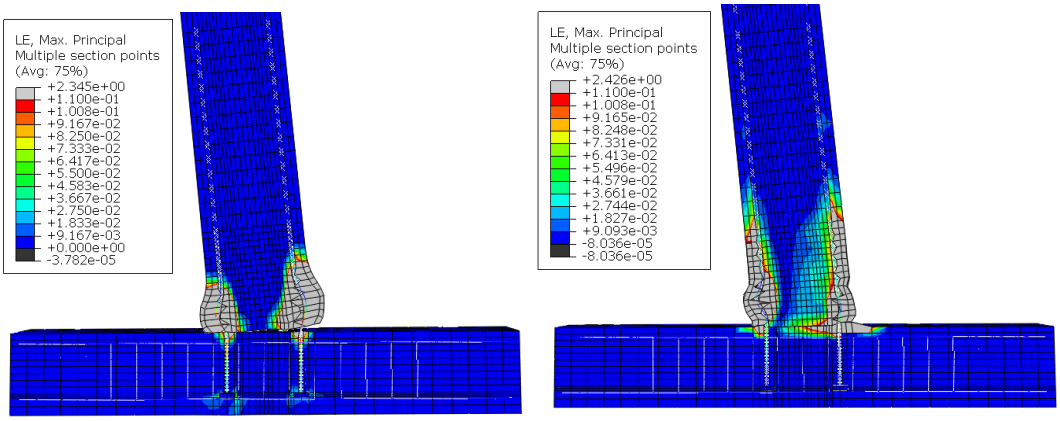

(b) FEA with D-P model (a) FEA with microplane model

Figure 6.18 – Deformed FE mesh for Specimen #3 $\left(l_e = 11 d_b\right)$

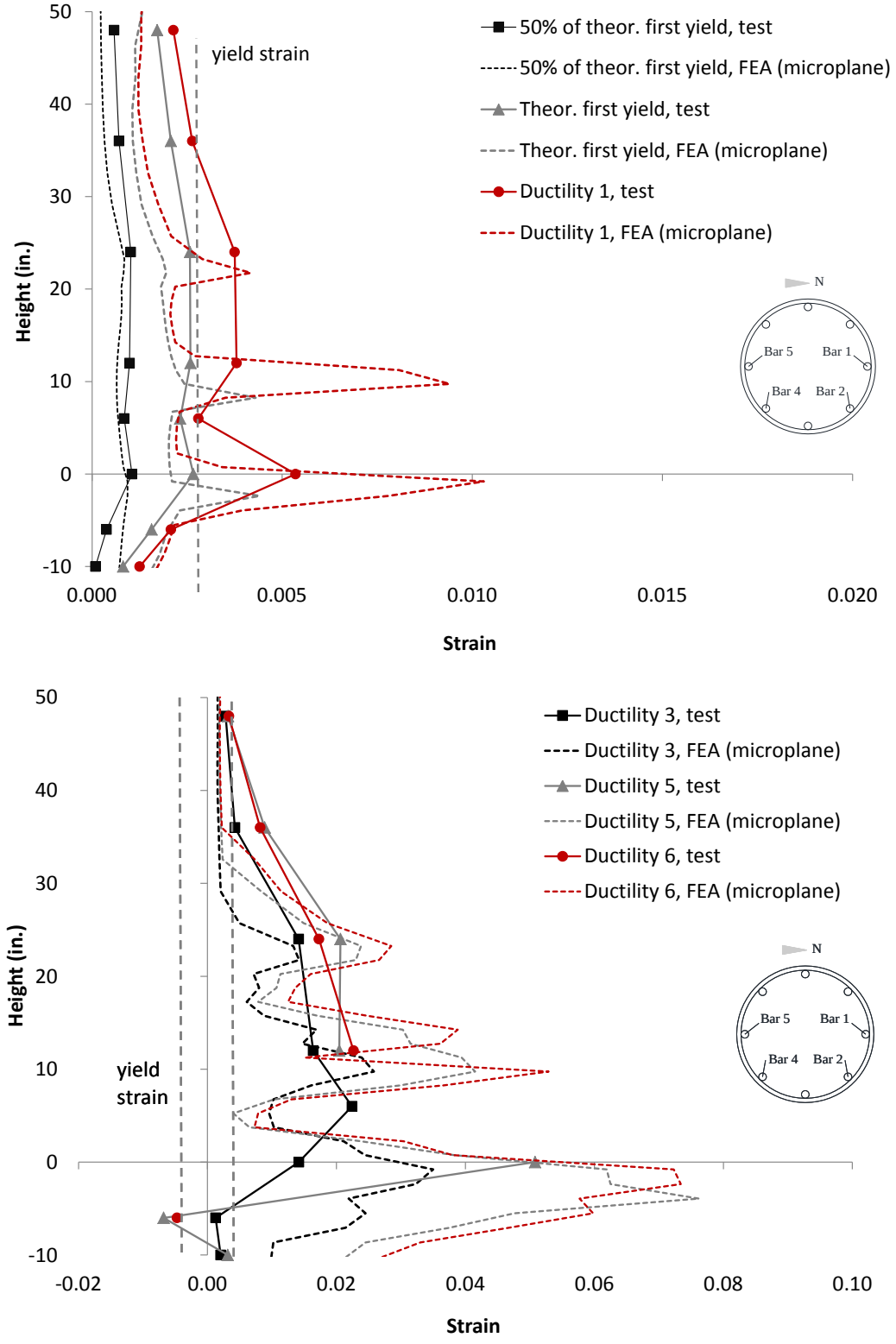

Figure 6.19 – Strains in longitudinal Bar 1 from FEA (microplane) of Specimen #1

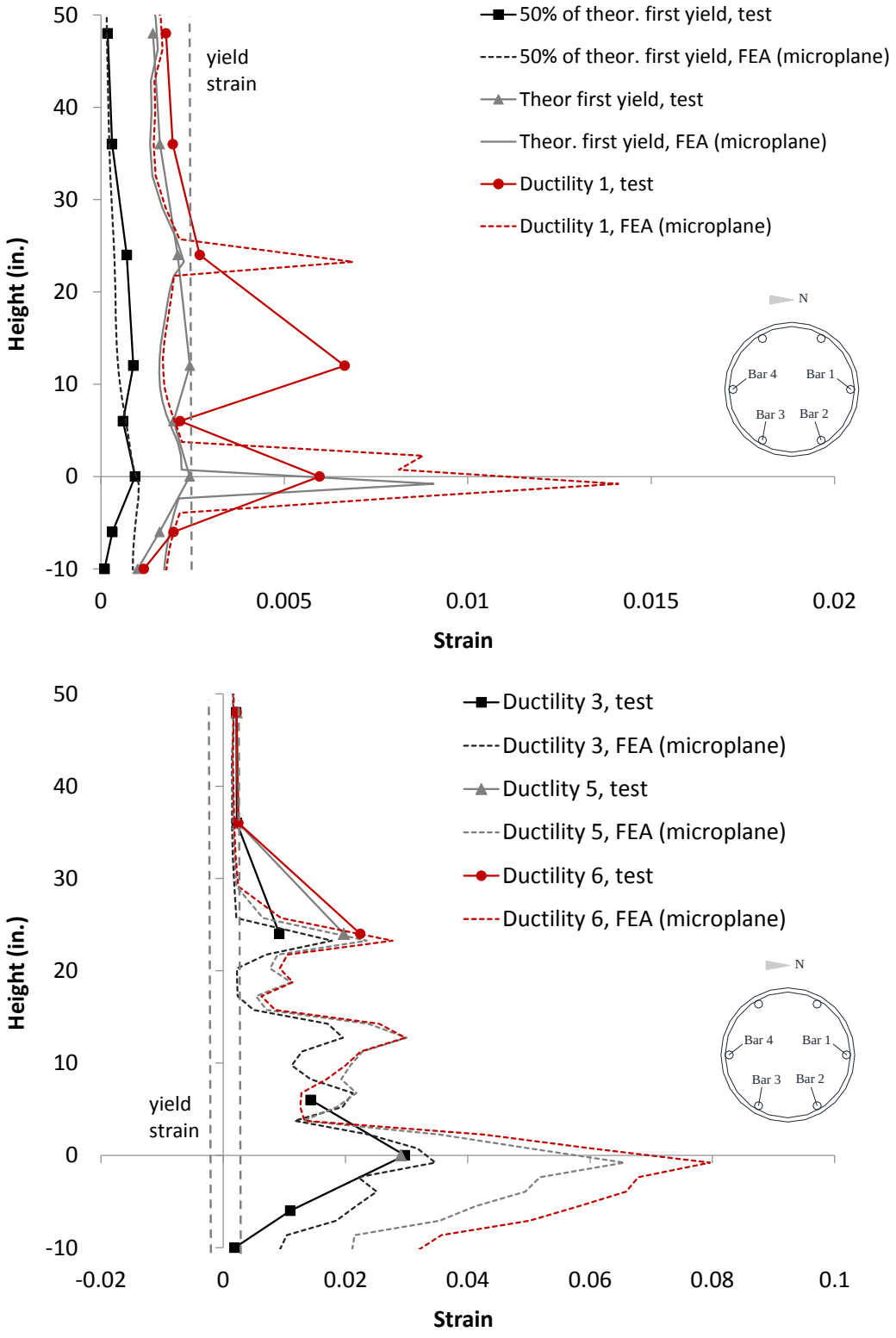

Figure 6.20 – Strains in longitudinal Bar 1 from FEA (microplane) of Specimen #2

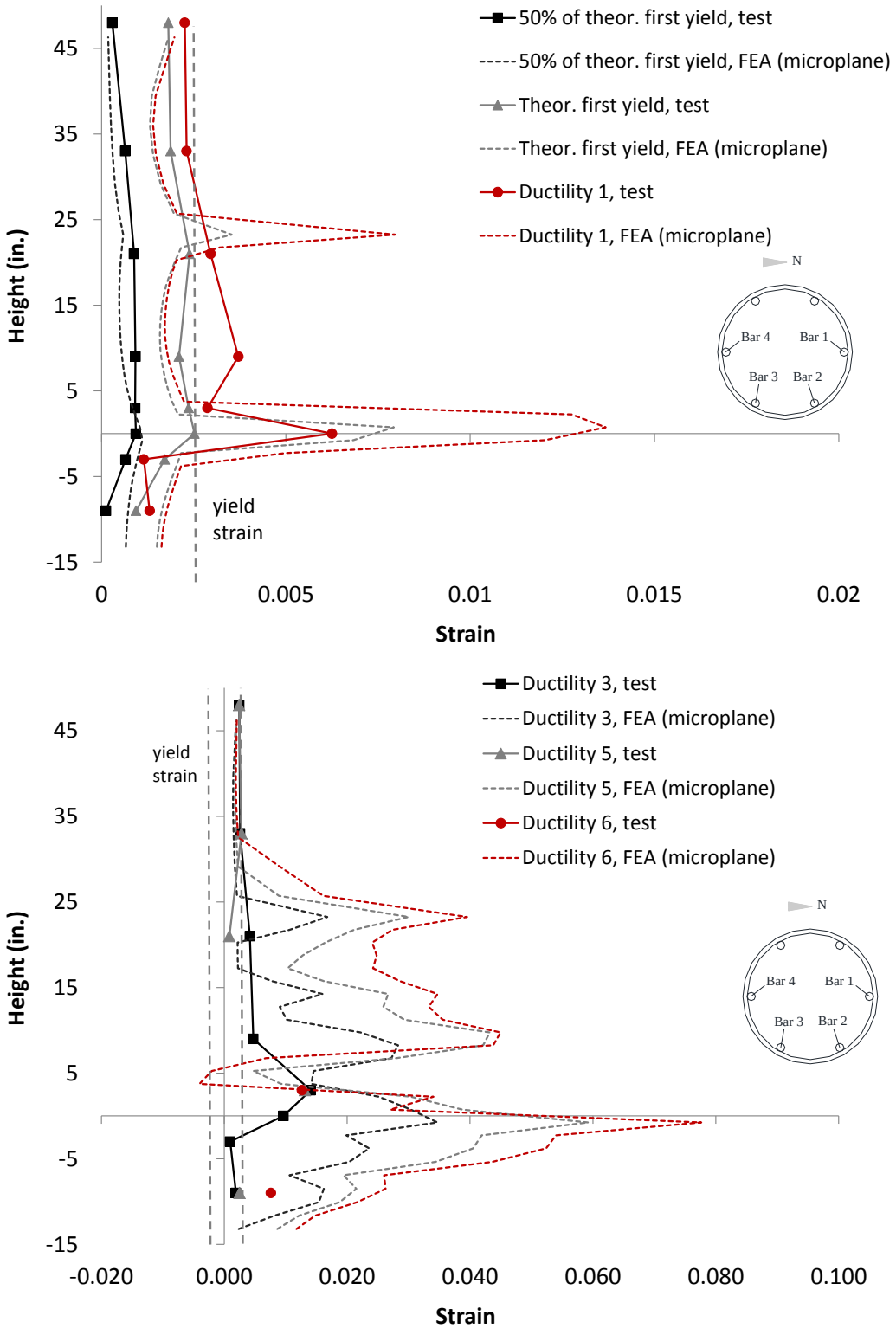

Figure 6.21 – Strains in longitudinal Bar 1 from FEA (microplane) of Specimen #3

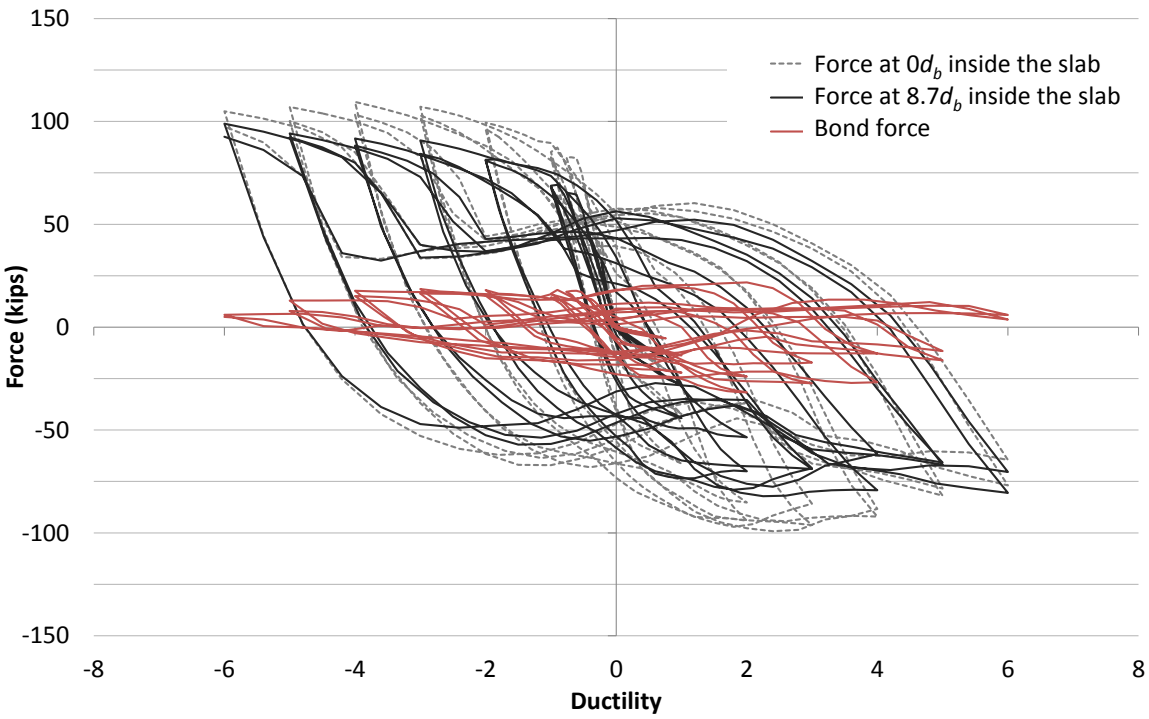

Figure 6.22 – Forces in longitudinal Bar 1 from FEA (microplane) of Specimen #2

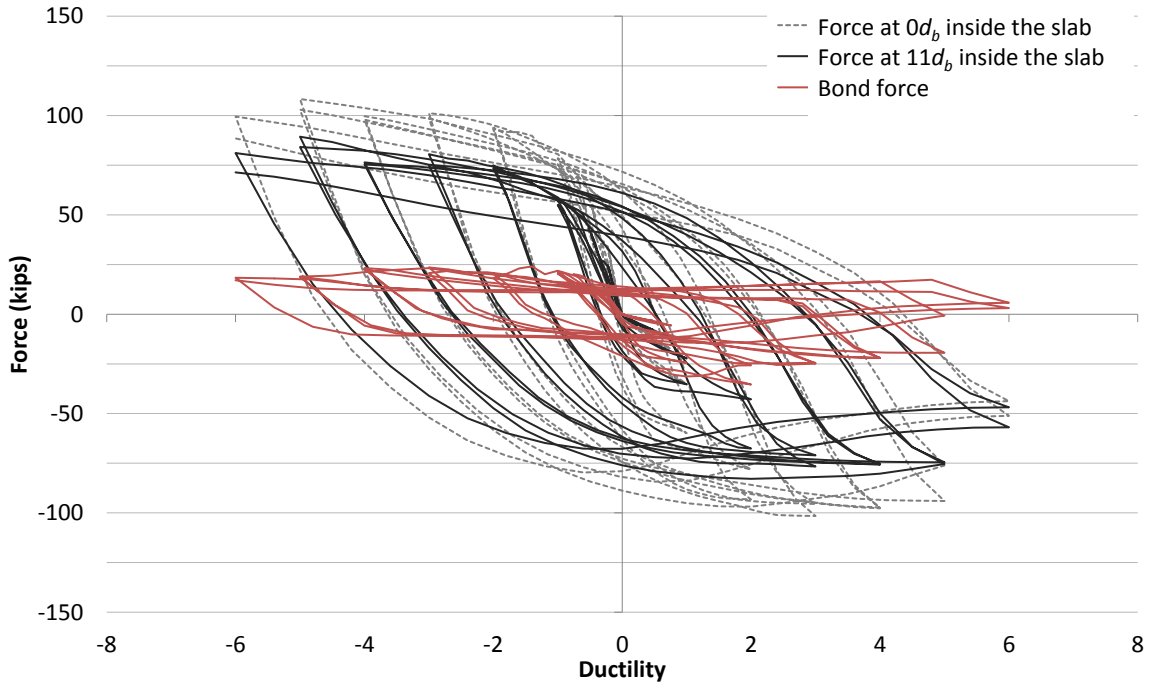

Figure 6.23 – Forces in longitudinal Bar 1 from FEA (microplane) of Specimen #3

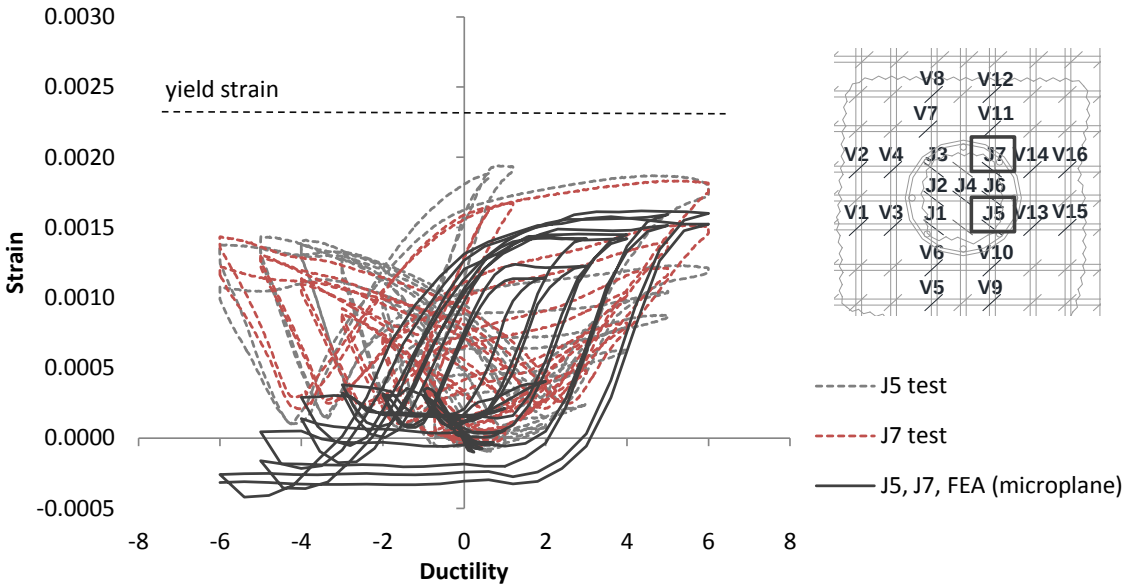

Figure 6.24 – Strains in J-bars of Specimen #1

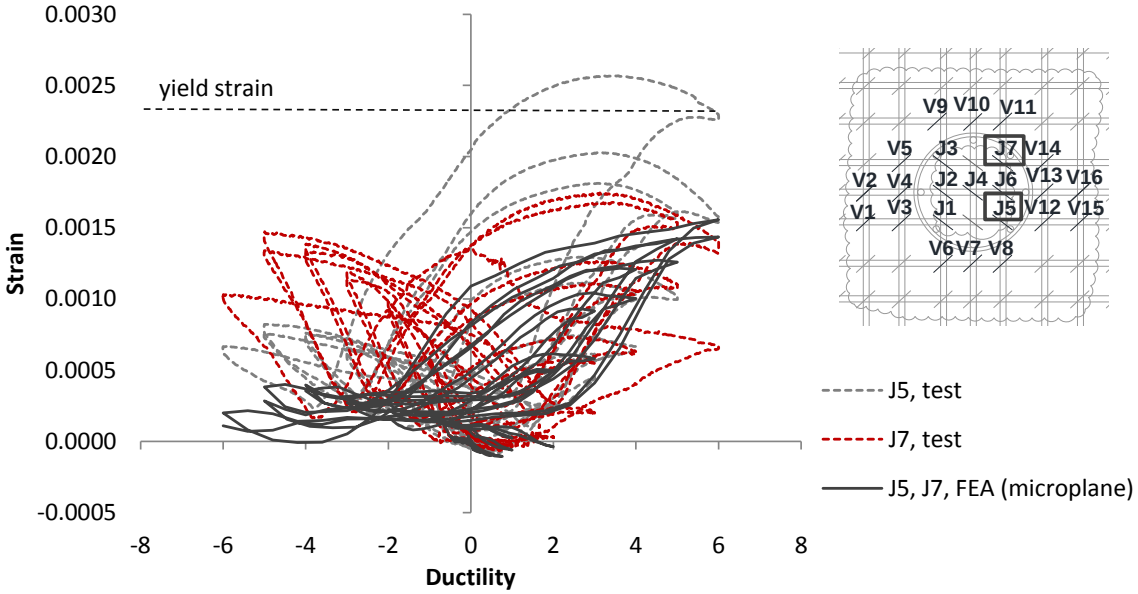

Figure 6.25 – Strains in J-bars of Specimen #2

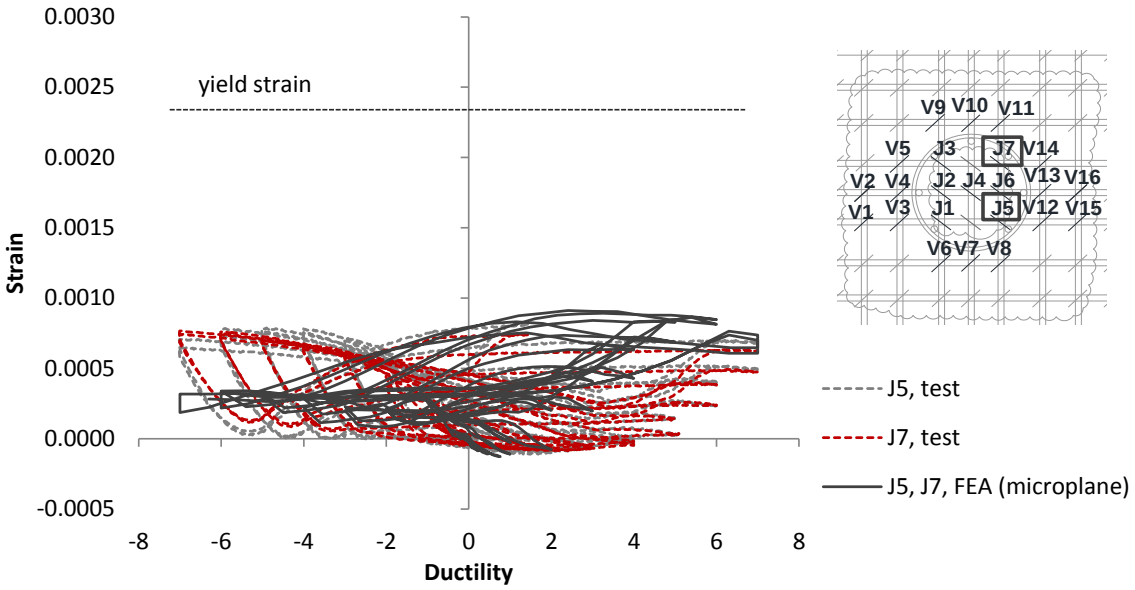

Figure 6.26 – Strains in J-bars of Specimen #3

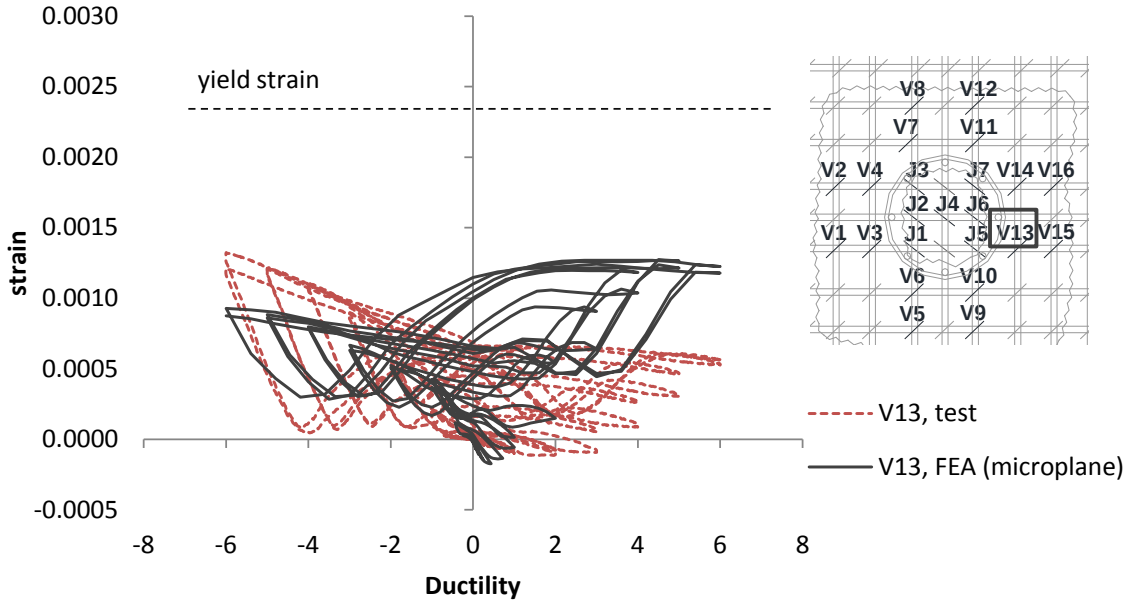

Figure 6.27 – Strains in a vertical stirrup in the 1st row in the slab of Specimen #1

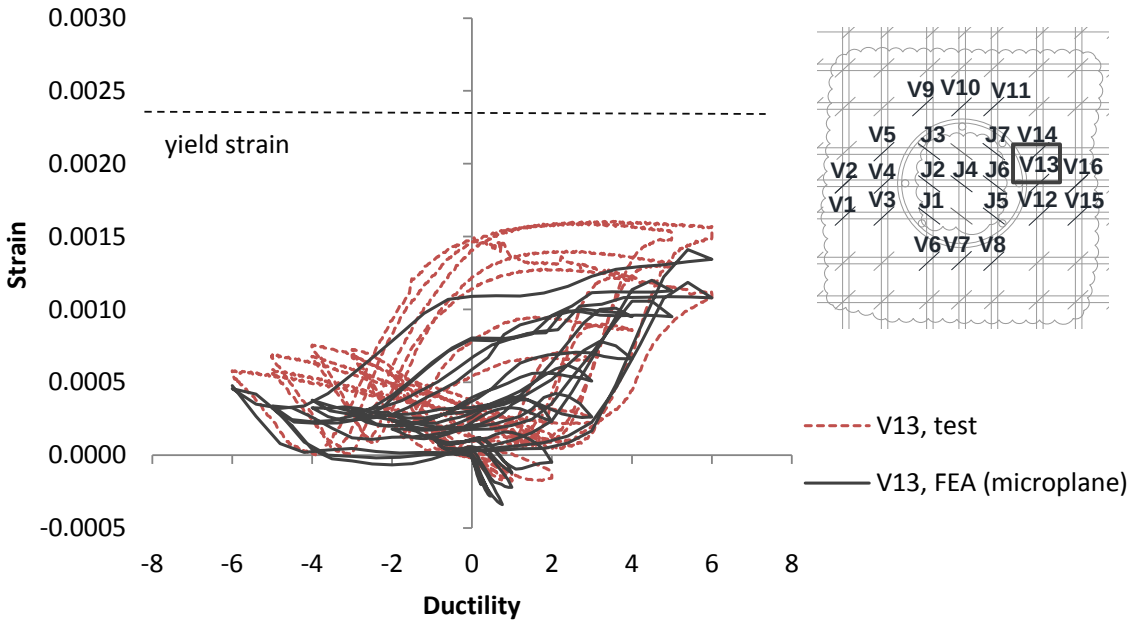

Figure 6.28 – Strains in a vertical stirrup in the 1st row in the slab of Specimen #2

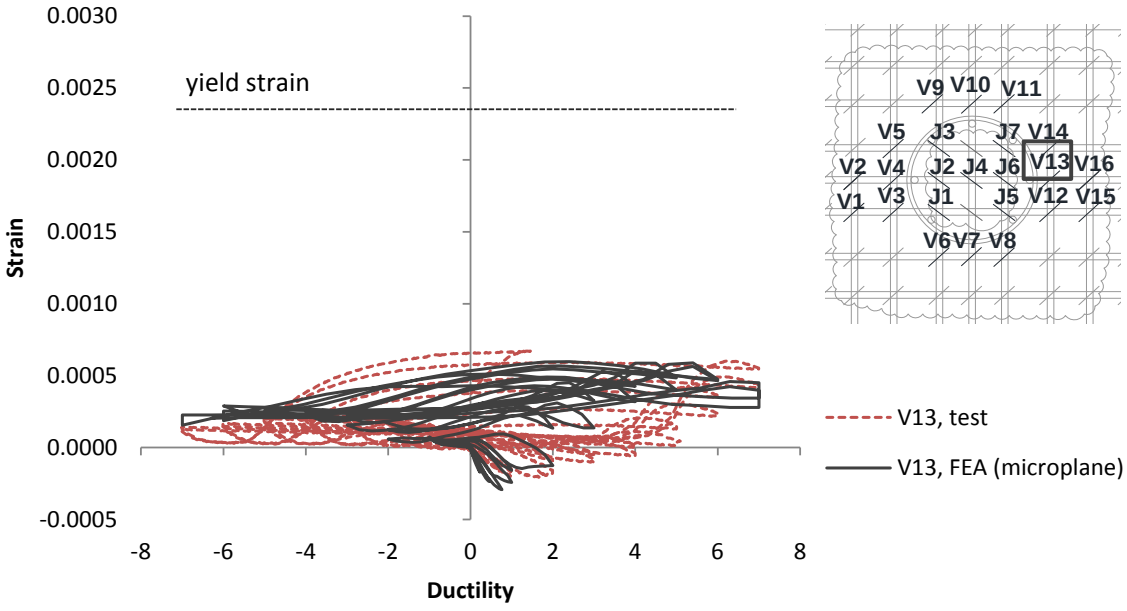

Figure 6.29 – Strains in a vertical stirrup in the 1st row in the slab of Specimen #3

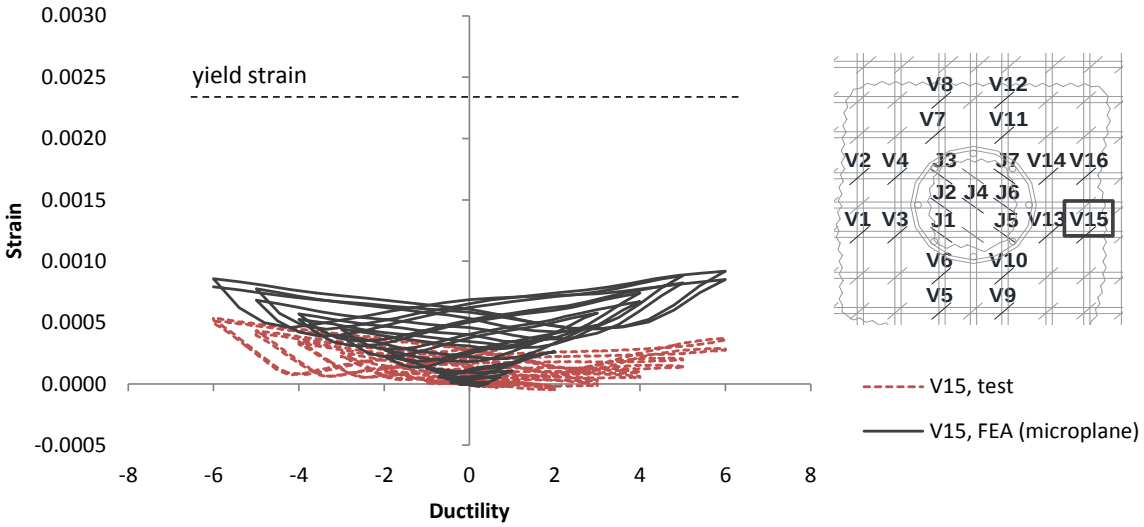

Figure 6.30 – Strains in a vertical stirrup in the 2nd row in the slab of Specimen #1

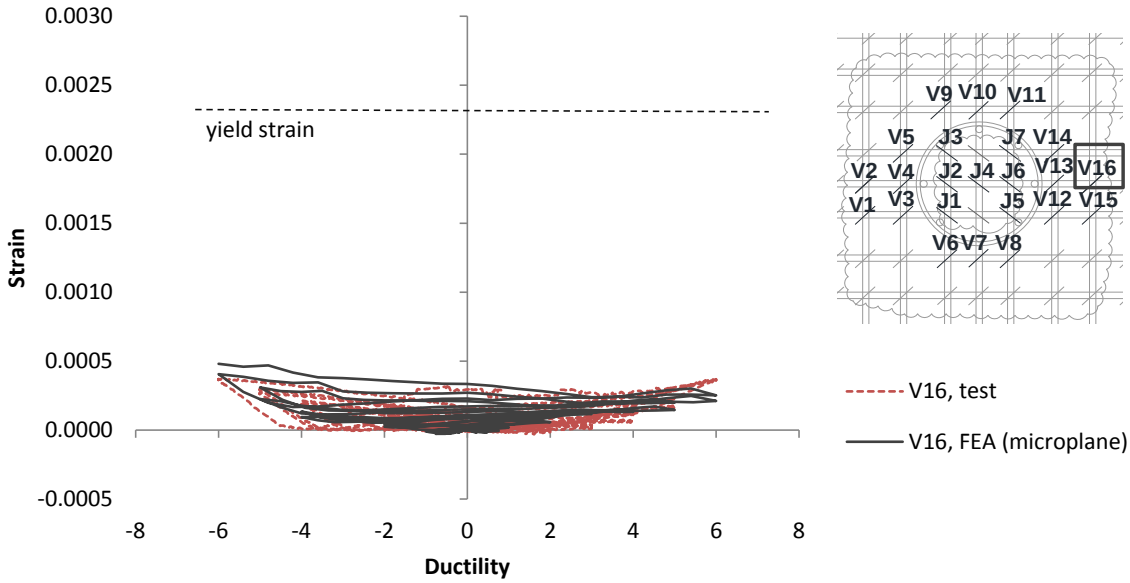

Figure 6.31 – Strains in a vertical stirrup in the 2nd row in the slab of Specimen #2

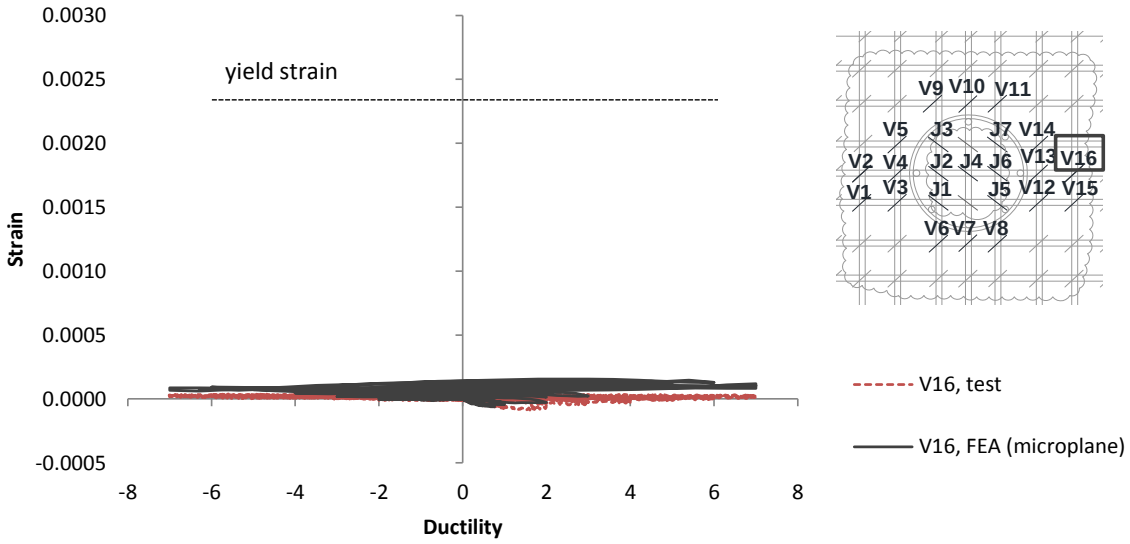

Figure 6.32 – Strains in a vertical stirrup in the 2nd row in the slab of Specimen #3

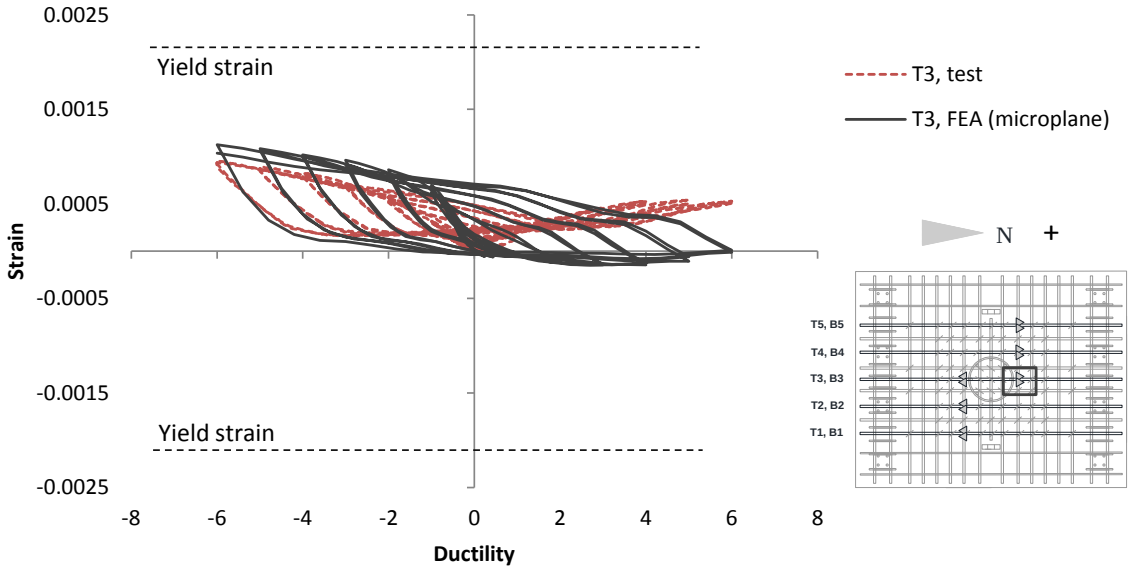

Figure 6.33 – Strains in the top longitudinal bar T3 in the slab of Specimen #1

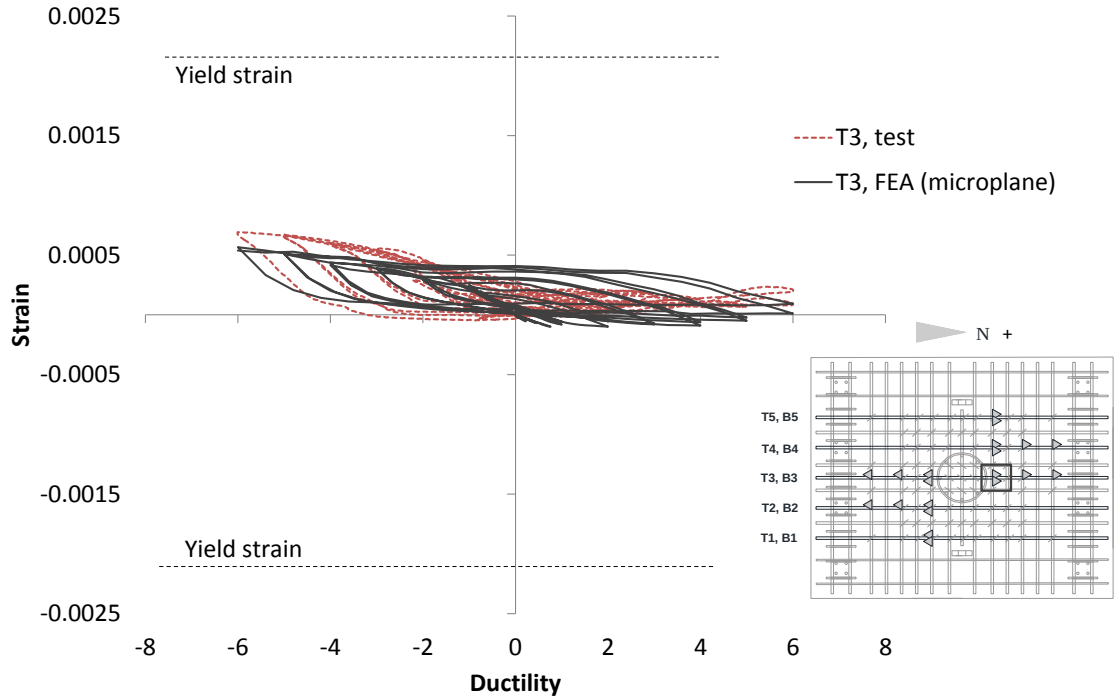

Figure 6.34 – Strains in the top longitudinal bar T3 in the slab of Specimen #2

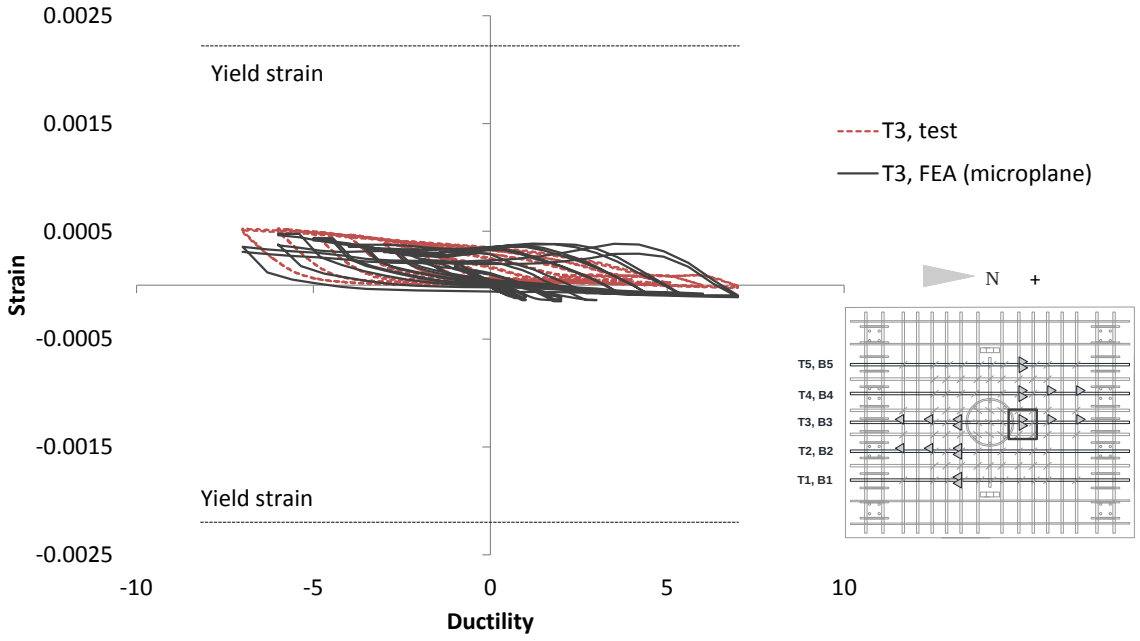

Figure 6.35 – Strains in the top longitudinal bar T3 in the slab of Specimen #3

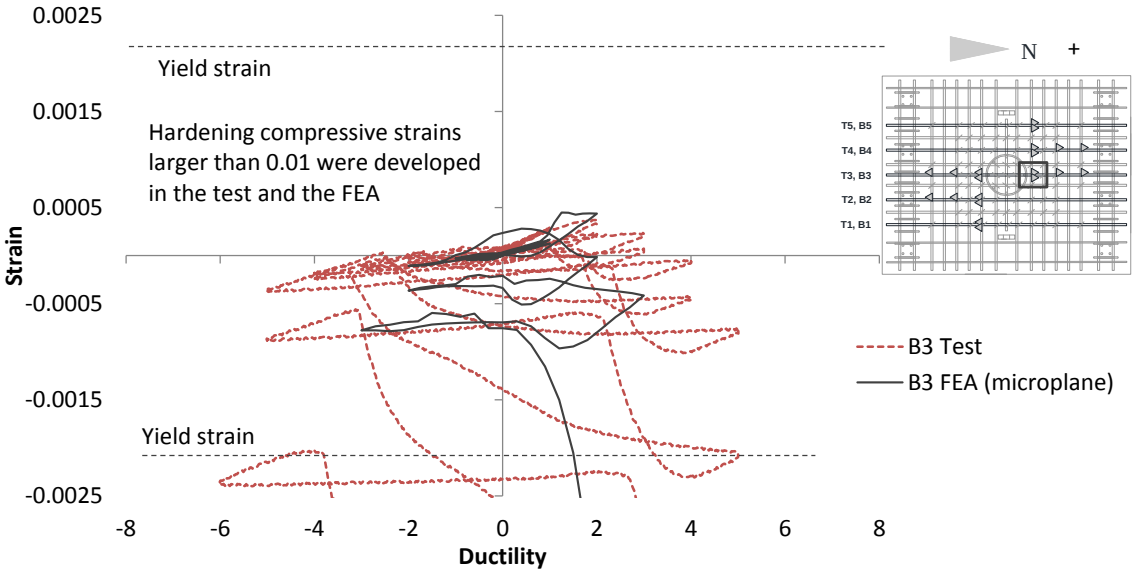

Figure 6.36 – Strains in the bottom longitudinal bar B3 in the slab of Specimen #2

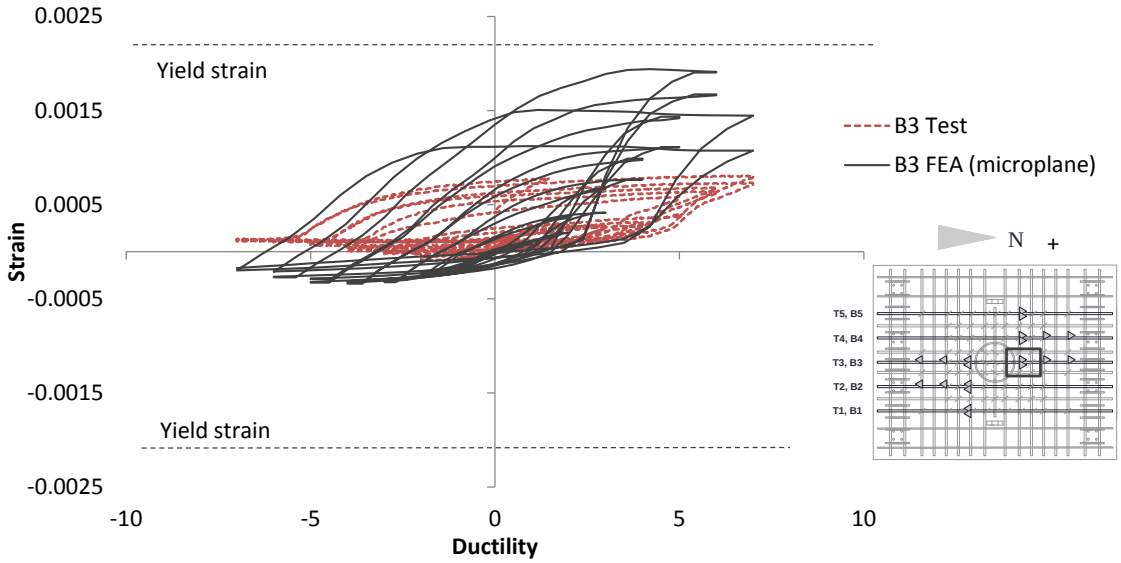

Figure 6.37 – Strains in the bottom longitudinal bar B3 in the slab of Specimen #3

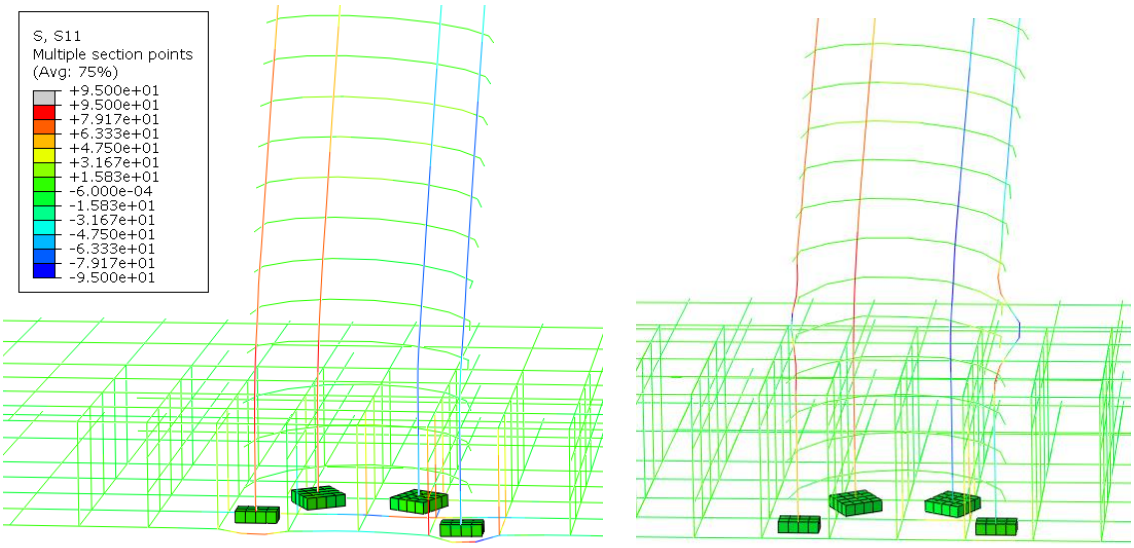

(b) Specimen #2 (a) Specimen #3

Figure 6.38 – Deformed column and slab reinforcement from the FEA with the microplane model

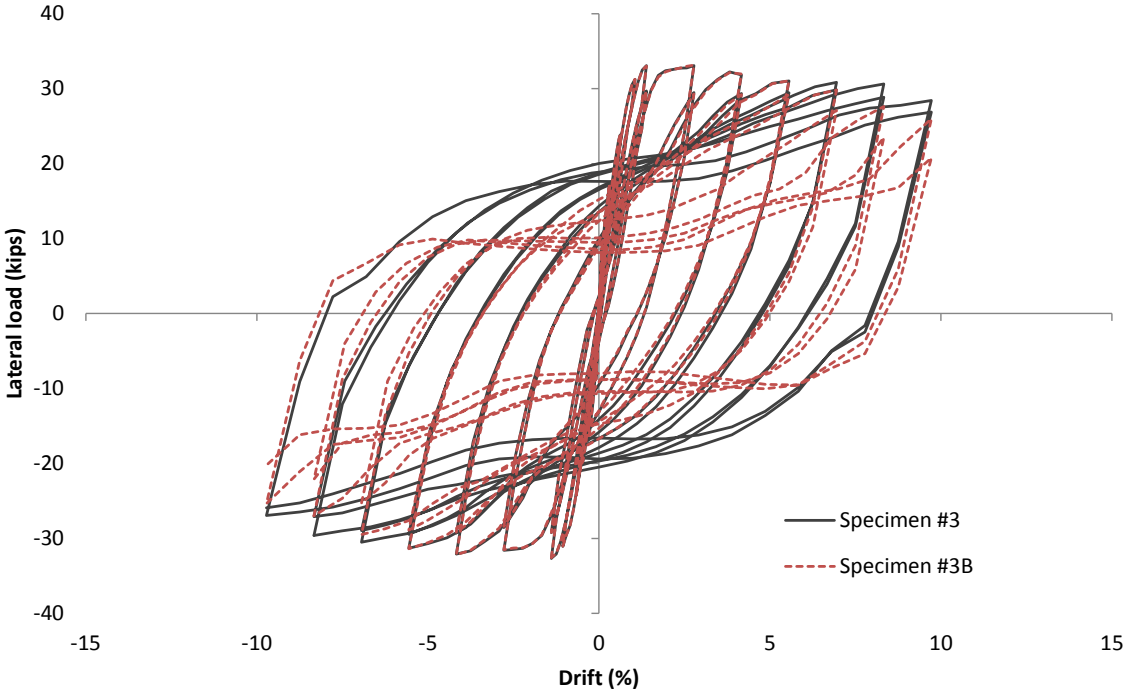

Figure 6.39 – Lateral load-vs.-top drift curve from the FEA of Specimen #3B

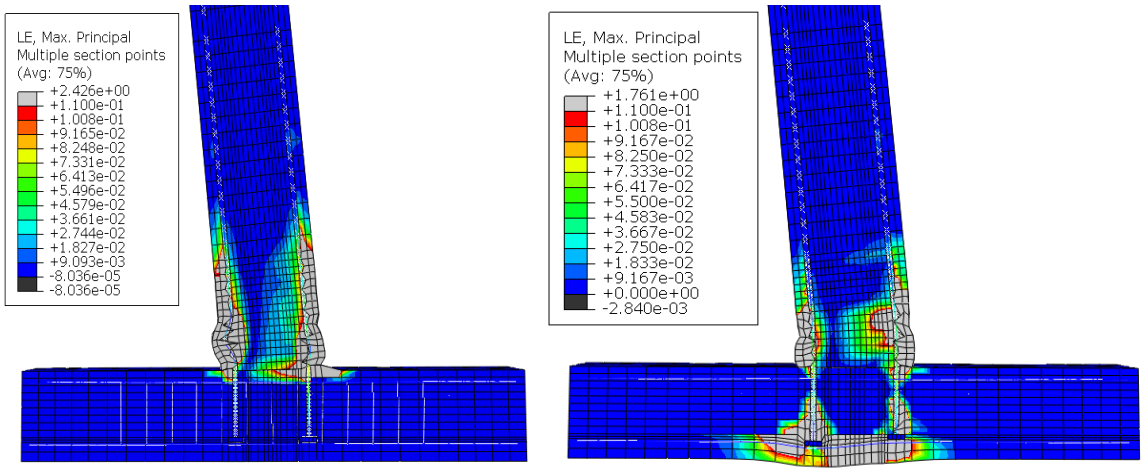

(a) Specimen #3

(b) Specimen #3B
(no J-bars and vertical stirrups)

Figure 6.40 – Deformed FE mesh for Specimens #3 and #3B $\left(l_e = 11 d_b\right)$

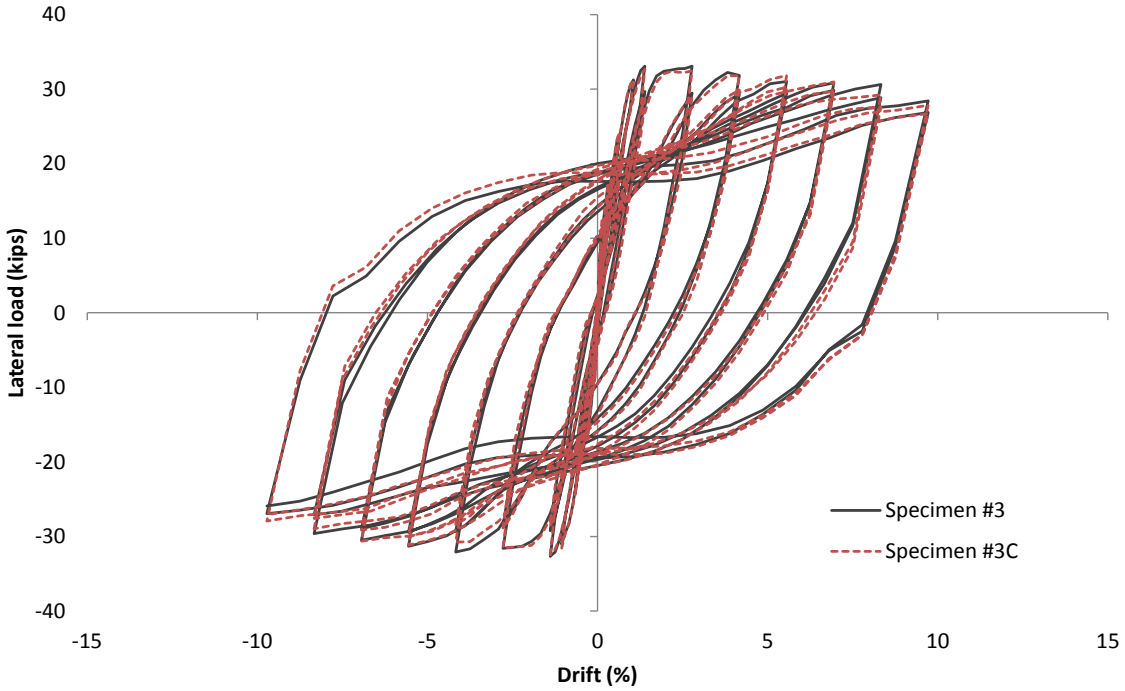

Figure 6.41 – Lateral load-vs.-top drift curve from the FEA of Specimen #3C

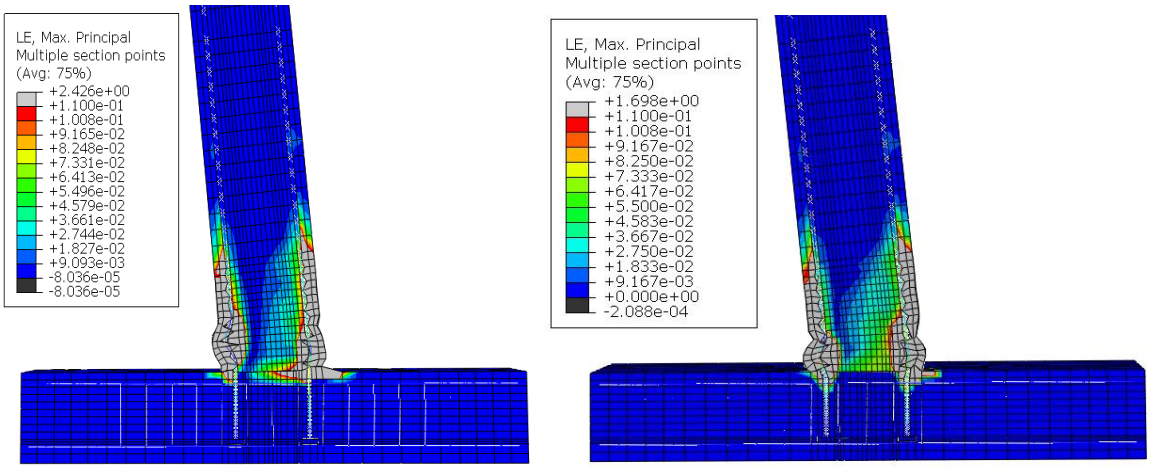

(a) Specimen #3

(b) Specimen #3C
(with J-bars and one row of vertical stirrups)

Figure 6.42 – Deformed FE mesh for Specimens #3 and #3C $\left(l_e = 11 d_b\right)$

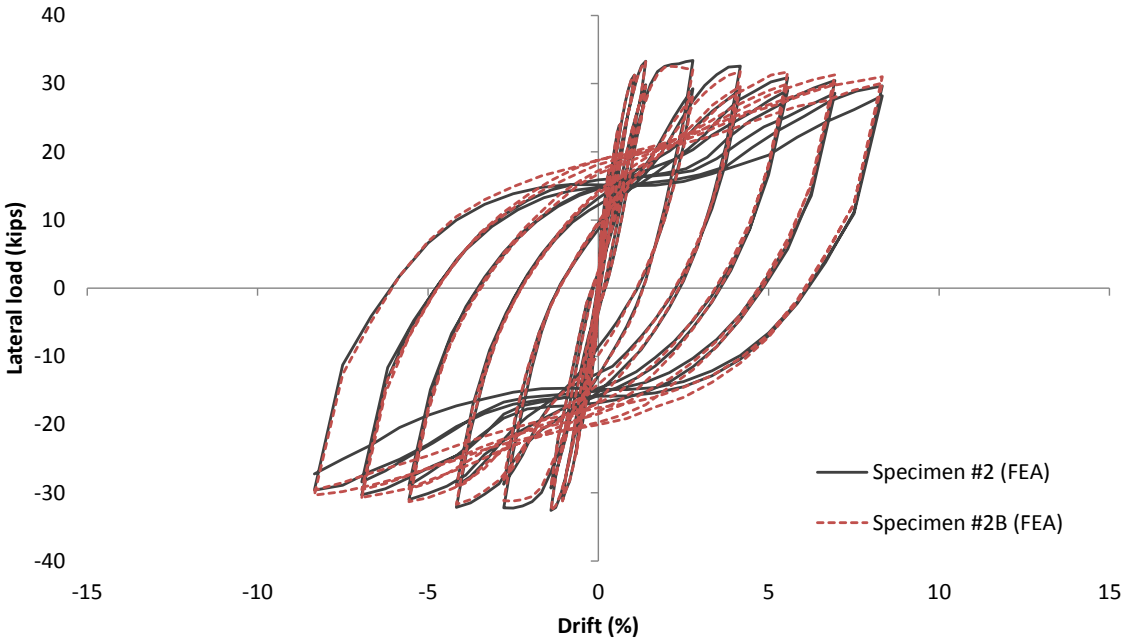

Figure 6.43 – Lateral load-vs.-top drift curve from the FEA of Specimen #2B

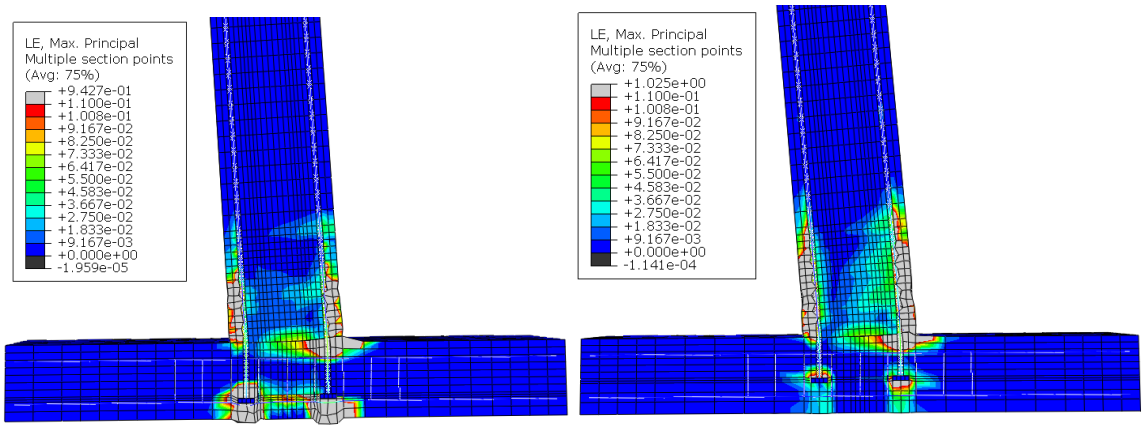

(a) Specimen #2

(b) Specimen #2B
(headed bars moved $2d_b$ upward)

Figure 6.44 – Deformed FE meshes for Specimens #2 and #2B

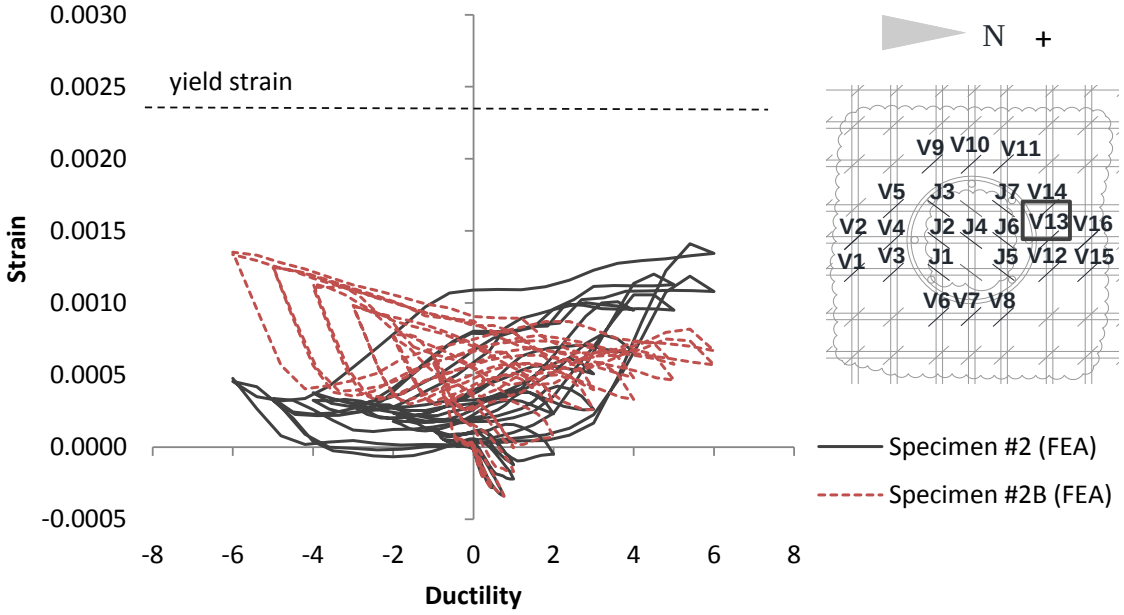

Figure 6.45 – Strains in vertical stirrup, V13, in the slab of Specimens #2 and #2B

CHAPTER 7

SUMMARY AND CONCLUSIONS

The work presented here was to investigate the seismic performance of reinforced concrete (RC) bridge components and assemblies, and advance nonlinear finite element modeling techniques to predict the behavior of RC structures. For these purposes, a constitutive model that accounts for the low-cycle fatigue behavior of steel has been developed and implemented in a finite element analysis program, and suitable constitutive models to represent the 3-diminesional behavior of concrete and the bond-slip behavior of reinforcing bars have been identified, calibrated, and validated with experimental data.

The constitutive models have been employed in two studies investigating the nonlinear behavior of RC bridge components and assemblies. The studies also consisted of large-scale experimental testing. The first study investigated the effect of the lineal spacing of longitudinal bars on the performance of circular RC piles under lateral loading. The experimental investigation consisted of the testing of two full-scale pile specimens. The second study was aimed to determine the minimum development length required for headed bars in RC slab-column joints. Three full-scale slab-column specimens with different embedment lengths were tested.

7.1 Finite Element Modeling of RC Bridge Members

A phenomenological stress-strain law has been developed to simulate the behavior of steel reinforcement under cyclic loading, incorporating the low-cycle fatigue induced by bar buckling. For modeling the nonlinear behavior of concrete, a damaged-plasticity model implemented in Abaqus has been calibrated and validated. Its limitations have been identified and remedies have been developed to circumvent them. The first limitation is that the model cannot

capture the increase in the ductility of concrete in compression due to an increase in the confining pressure. The second limitation is that the model is not able to represent large stiffness degradation during unloading and reloading in tension, resulting in a large residual tensile strain upon unloading when a large crack opening has occurred. This prevents the finite element models from accurately capturing the pinching effect in the load-displacement curve for a pile.

In addition, a microplane model for concrete, developed by Caner and Bazant (2013) has been successfully implemented and validated. The microplane model does not have the limitations of the damaged-plasticity model, and it can simulate the nonlinear behavior of concrete in tension and compression more accurately. Finally, a phenomenological bond-slip model, developed by Murcia-Delso and Shing (2015), has been used to simulate the bond behavior between the steel reinforcement and concrete

The competency of the constitutive models in simulating the different failure mechanisms in RC bridge members is demonstrated through the finite element (FE) analyses of full-scale pile and slab-column specimens tested in the course of this study. A good correlation of the experimental and numerical findings has been obtained, with the failure mechanisms adequately reproduced. The FE models are used in parametric investigations of additional design parameters.

7.2 Studies of Nonlinear Behavior of Bridge Components and Assemblies

7.2.1 Effect of Spacing of Longitudinal Bars on the Structural Performance of Bridge RC piles

7.2.1.1 Summary

An experimental and numerical investigation on the effect of the lineal spacing of longitudinal bars on the performance of circular RC piles under lateral loading was conducted. Two 28-in.-diameter piles were tested. Except for the spacing of the longitudinal reinforcement in

Specimen #1, the design details of both specimens satisfied the Caltrans Bridge Design Specifications (Caltrans 2004) and the AASHTO LRFD Bridge Design Specifications (AASHTO 2014). The specimens had the same quantity and spacing of transverse reinforcement and similar quantities of longitudinal reinforcement. Specimen #1 had 6 No. 11 bars spaced at 11 in. on center, resulting in a longitudinal steel ratio of 1.52%. The bar spacing exceeded the 8-in. maximum permitted by the Caltrans and AASHTO specifications. Specimen #2 had 10 No. 9 bars spaced at 6.75 in. on center, resulting in a longitudinal steel ratio of 1.62%.

Nonlinear FE models were developed for the RC pile specimens, where the constitutive models presented in this study were further validated. The FEA were used for pre-test analyses and a numerical parametric study to confirm and generalize the experimental observations. The parametric study considered piles of different diameters, with different lineal and angular spacings of the longitudinal bars, and with different levels of the axial load.

7.2.1.2 Observations and Recommendations

The study showed that the lineal spacing of the longitudinal bars in circular RC members does not have any impact on their ductility. The spacing can be larger than the 8-in. maximum permitted by the Caltrans and AASHTO specifications without compromising the structural performance of the RC member. However, the size of the longitudinal bars can affect the ductility of a pile. The load degradation in a pile is often associated with the spalling of the cover concrete, and the buckling and the fracture of the longitudinal bars in the plastic-hinge region of the pile. Larger-diameter bars are more resistant to buckling for the same spacing of the lateral reinforcement and therefore result in a more ductile behavior. A smaller lineal spacing with smaller-size longitudinal bars can lead to more closely spaced flexural cracks with smaller widths. These observations are true for piles of different diameters and subjected to different levels of axial loads.

7.2.2 Embedment Length of Headed Bars in Slab-Column Joints

7.2.2.1 Summary

The minimum required embedment length for headed bars anchored in slab-columns joints of RC slab bridges has been determined through an experimental and analytical investigation. Three full-scale slab-column specimens were tested under lateral quasi-static loading. The specimens were designed to comply with the AASHTO LRFD Bridge Design Specifications (AASHTO 2014), SDC (Caltrans 2013), and BDA 4-10 (Caltrans 2009). The reinforcement in the slab-column joints of the specimens also complied with the specifications in MTD 20-7 (Caltrans, October 2014). Each specimen had a 24-in.-diameter column and a 16-in.-thick slab. The column had a height of 12 ft., measured from the bottom face of the slab (top face in the specimen) to the elevation at which the lateral load was applied. Specimen #1 had an embedment length of $9.8d_b$ for the headed bars, Specimen #2 had $8.7d_b$, and Specimen #3 had $11d_b$. A 3-in deep drop cap was added to the slab in Specimen #3 in order to provide an increased embedment length in the slab-column joint. The reinforcing steel was Grade 60 and the concrete had a target compressive strength of 5,000 psi.

Along with the experimental study, three-dimensional nonlinear finite element (FE) models have been developed to analyze the performance of the slab-column assemblies before and after the tests. They have also been used in a parametric study to evaluate additional design variables that were not considered in the tests.

7.2.2.2 Observations

For Specimen #2, which had an embedment length of $8.7d_b$, the tensile yield strength of the headed bars and the plastic moment capacity of the column were developed in the test. However, the anchorage of the headed bars deteriorated significantly, leading to more pinched hysteretic load-displacement curves, as compared to the other two specimens with higher

embedment lengths. Moreover, the top face of the slab (bottom face in the specimen) was severely damaged by the punching action of the headed bars. Specimen #1, which had an embedment length of $10d_b$, had moderate punching cracks and a better hysteretic load-displacement behavior than Specimen #2. Specimen #3, which had an embedment length of $11d_b$, exhibited satisfactory performance with very minor punching cracks.

The J-bars in the slab-column joints, and the vertical stirrups in the slabs right outside the column cage were effectively engaged to restrain breakout cracks and punching cracks when the headed bars were subjected to tension and compression. However, the demand on the J-bars and stirrups was smaller for Specimen #3, which had the highest embedment length. The vertical stirrups in the 2nd row and farther away from the column cage did not develop any significant strains during the tests.

The FEA accurately reproduce the response of the slab-column assemblies under lateral loading. The analyses support the experimental observation that the vertical stirrups in the 2nd row and farther away from the column cage have little contribution to the resistance of the punching and bearing action of the headed bars. Moreover, the analyses indicate that the performance of Specimen #2 can be improved by reducing the embedment length of the headed bars to $6.7d_b$ and increasing the distance of the bar heads from the top face of the slab (bottom face in the specimen) by the same amount. The reduced embedment length can still allow the plastic moment capacity of the column to develop, while the increased concrete cover can reduce the damage induced by the punching action of the bars.

7.2.2.3 Conclusions and Recommendations

For 5,000-psi concrete and Grade-60 steel, an embedment length of $11d_b$ is adequate for headed bars in slab-column joints designed according to MTD 20-7 (Caltrans, October 2014). Nevertheless, it is recommended that MTD 20-7 be modified to include four additional stirrups

adjacent to the column cage, as it was done for Specimens #2 and #3. Furthermore, the amount of vertical stirrups in the 2nd row and farther away from the column cage can be reduced. Their quantity can be determined according to the shear strength required for the slab. The bar heads should be below the top mat of reinforcement in the deck slab.

Both the experimental and numerical investigations have indicated that the performance of the slab-column assemblies was mainly compromised by the punching cracks rather than the breakout failure caused by bar tension. Embedment lengths of $8.7d_b$ and $9.8d_b$ were able to develop the moment capacity of the columns but resulted in moderate to severe punching cracks in the cover concrete of the slabs. They also resulted in severe deterioration of the anchorage of the headed bars and more pinched lateral column force-vs.-column displacement hysteresis curves. This alludes to the possibility that an embedment length less than $11d_b$ can be sufficient to develop the tensile strength of headed bars if punching damage can be controlled. Indeed, it has been shown by FEA that if there is not enough room to provide an adequate embedment length of $11d_b$, it may be advantageous to reduce the embedment length and increase the distance of the bar head from the slab surface to reduce or avoid punching damage. Additional experimental study is recommended to verify this numerical observation.

APPENDIX A

DESIGN DRAWINGS OF SLAB COLUMN ASSEMBLIES

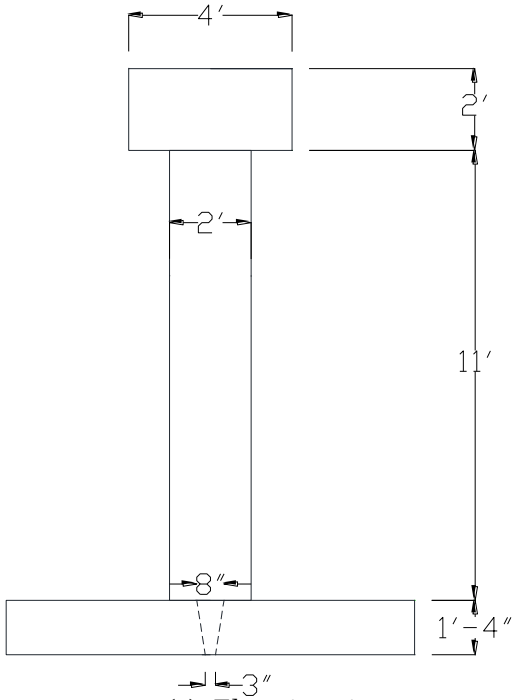

(a) Elevation view

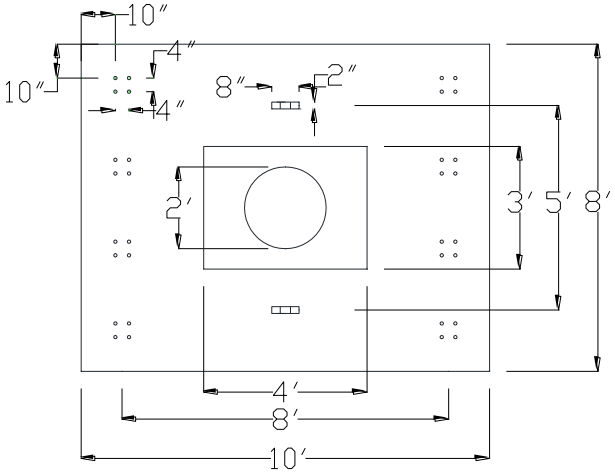

(b) Plan view

Figure A.1 – Plan and elevation views for Specimen #1

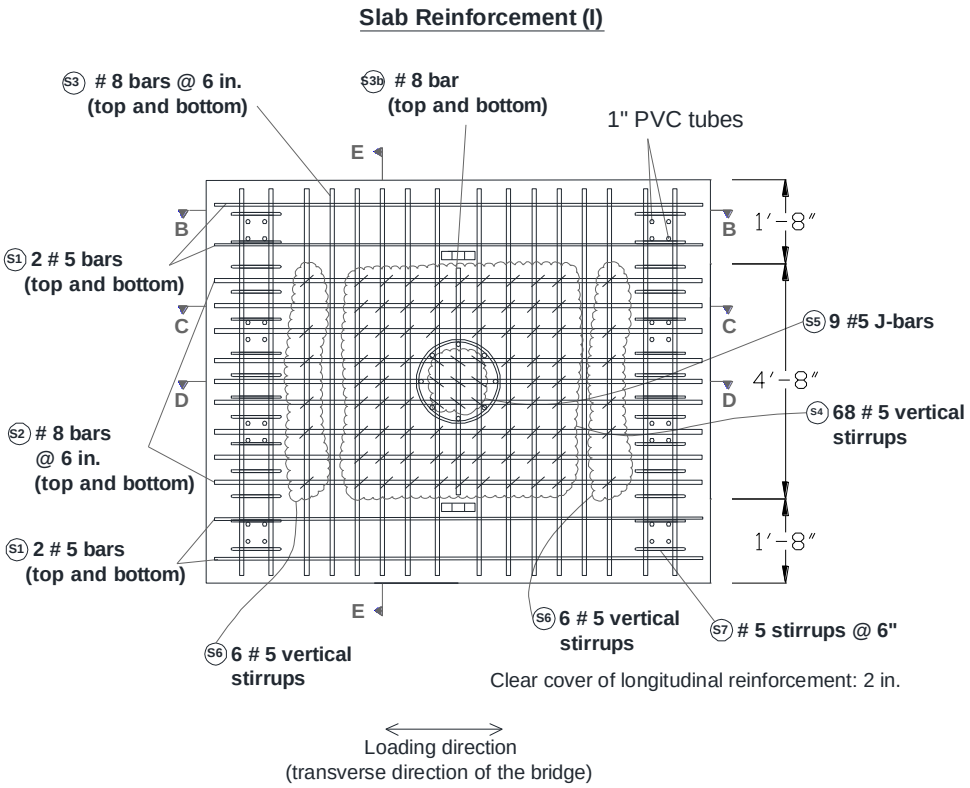

Figure A.2 – Plan view of slab reinforcement for Specimen #1

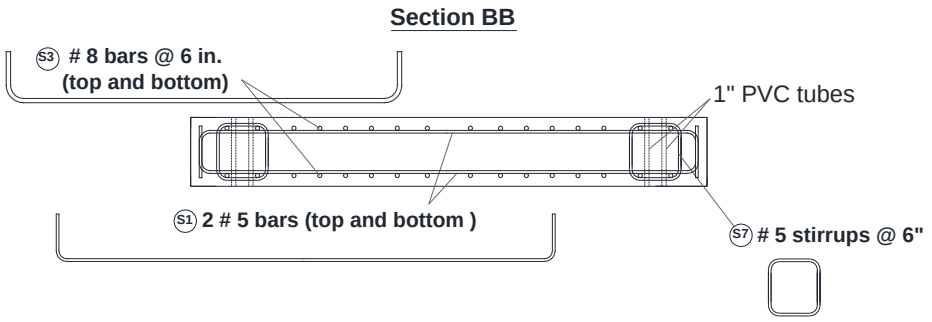

Figure A.3 – Elevation view of slab reinforcement at Section BB for Specimen #1

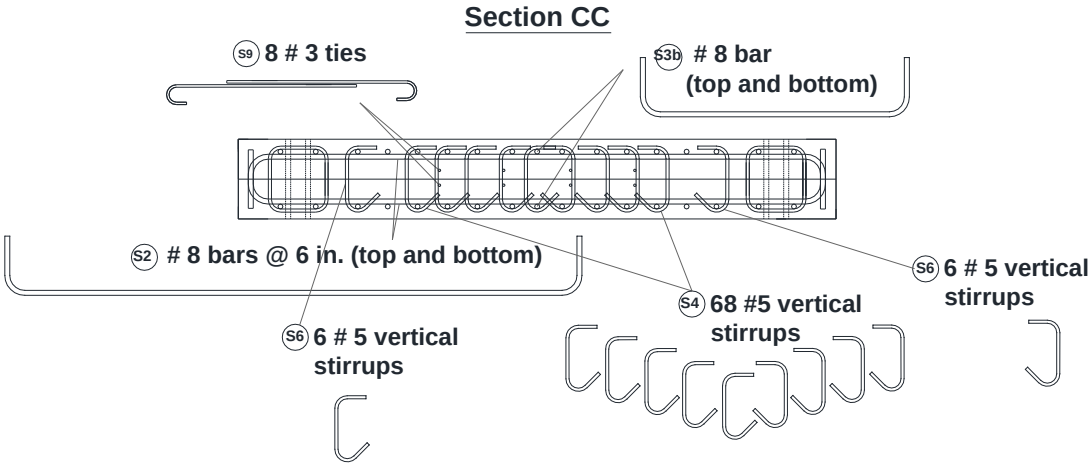

Figure A.4 – Elevation view of slab reinforcement at Section CC for Specimen #1

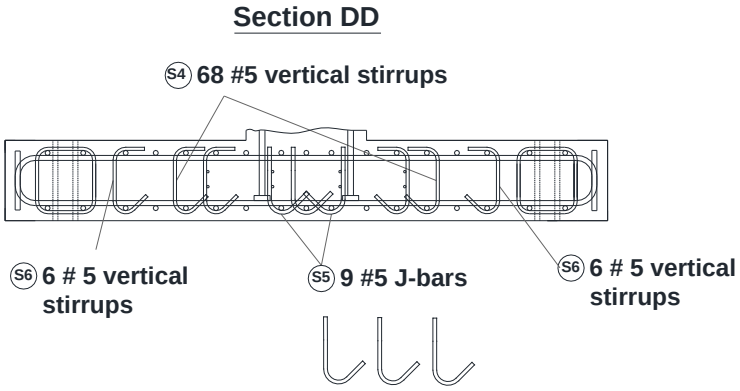

Figure A.5 – Elevation view of slab reinforcement at Section DD for Specimen #1

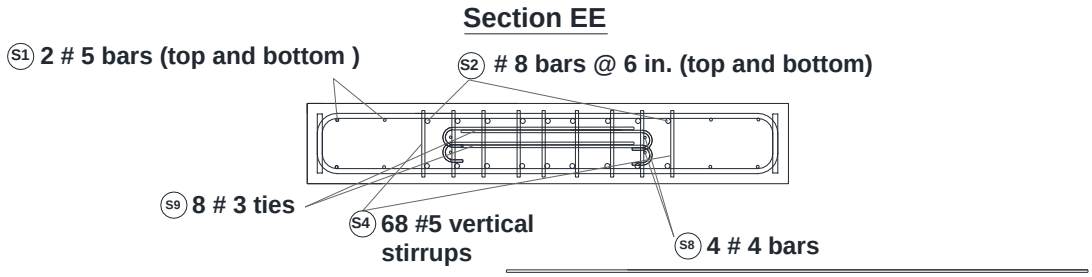

Figure A.6 – Elevation view of slab reinforcement at Section EE for Specimen #1

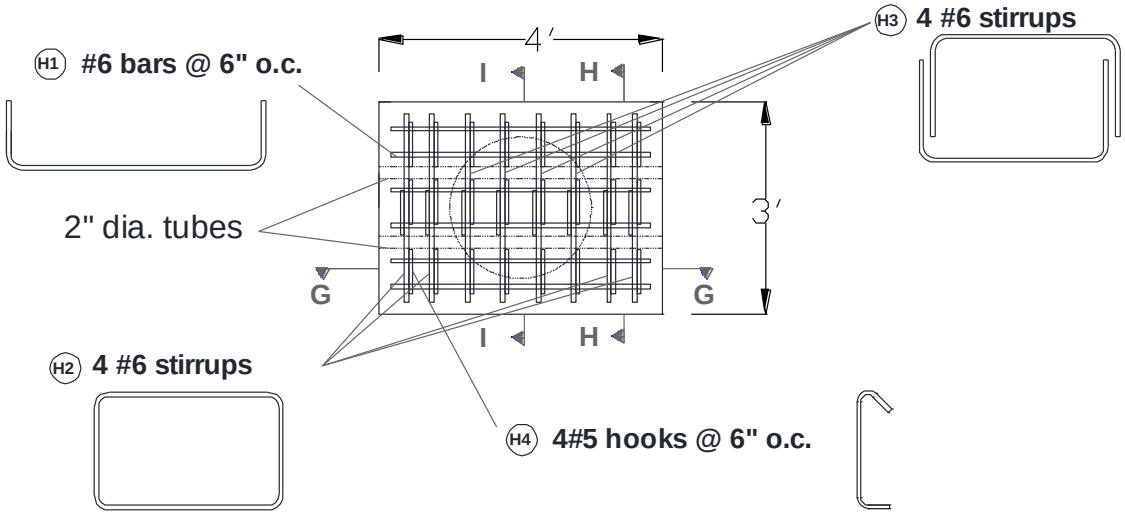

Figure A.7 – Plan view of head reinforcement for Specimen #1 (same for Specimens #2 and #3)

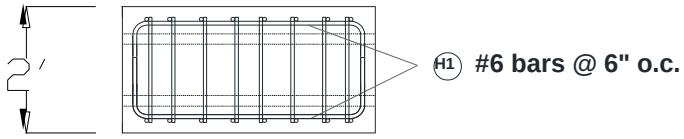

(a) Section GG

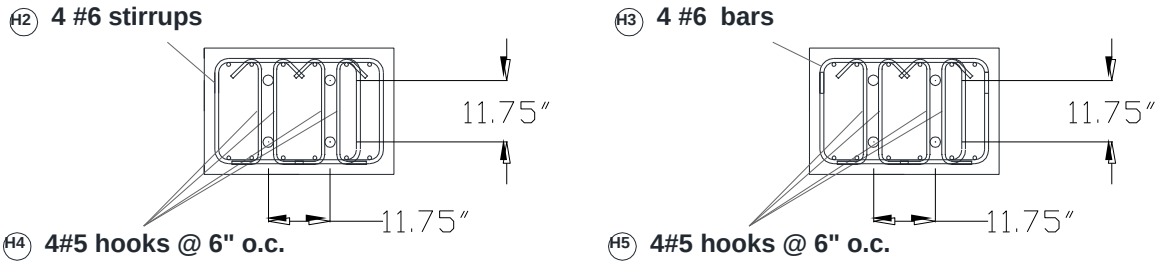

(b) Section HH (c) Section II

Figure A.8 – Elevation views of head reinforcement at different sections for Specimen #1 (same for Specimens #2 and #3)

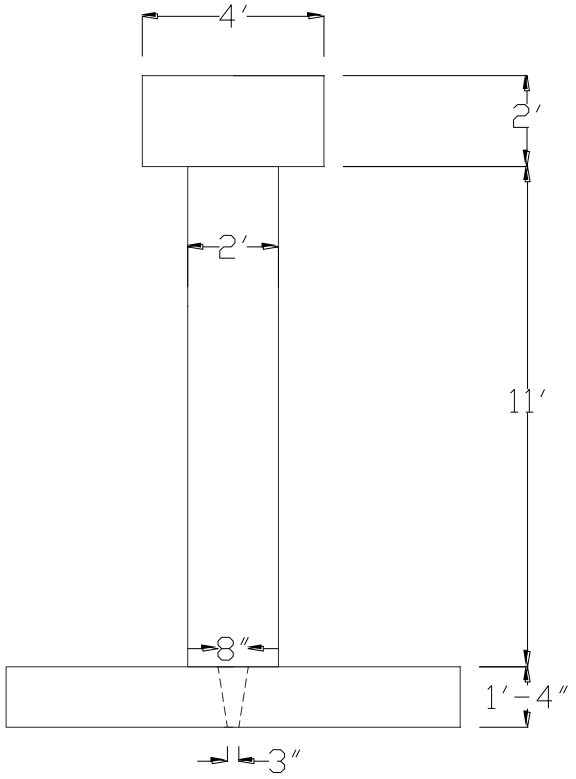

(a) Elevation view

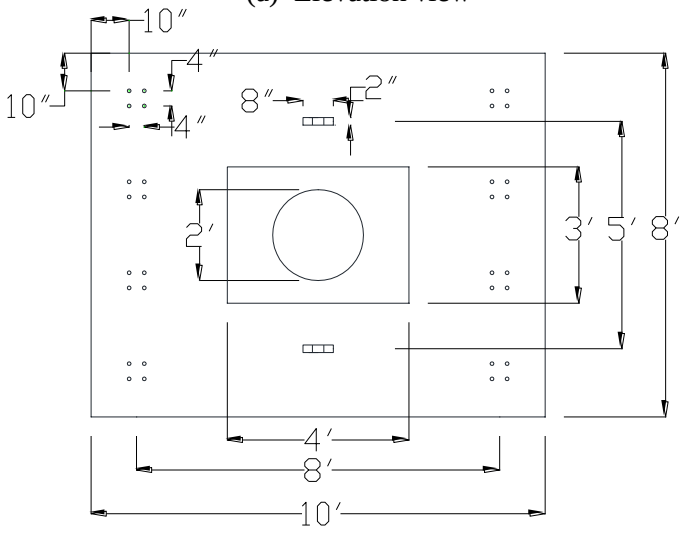

(b) Plan view

Figure A.9 – Plan and elevation views for Specimen #2

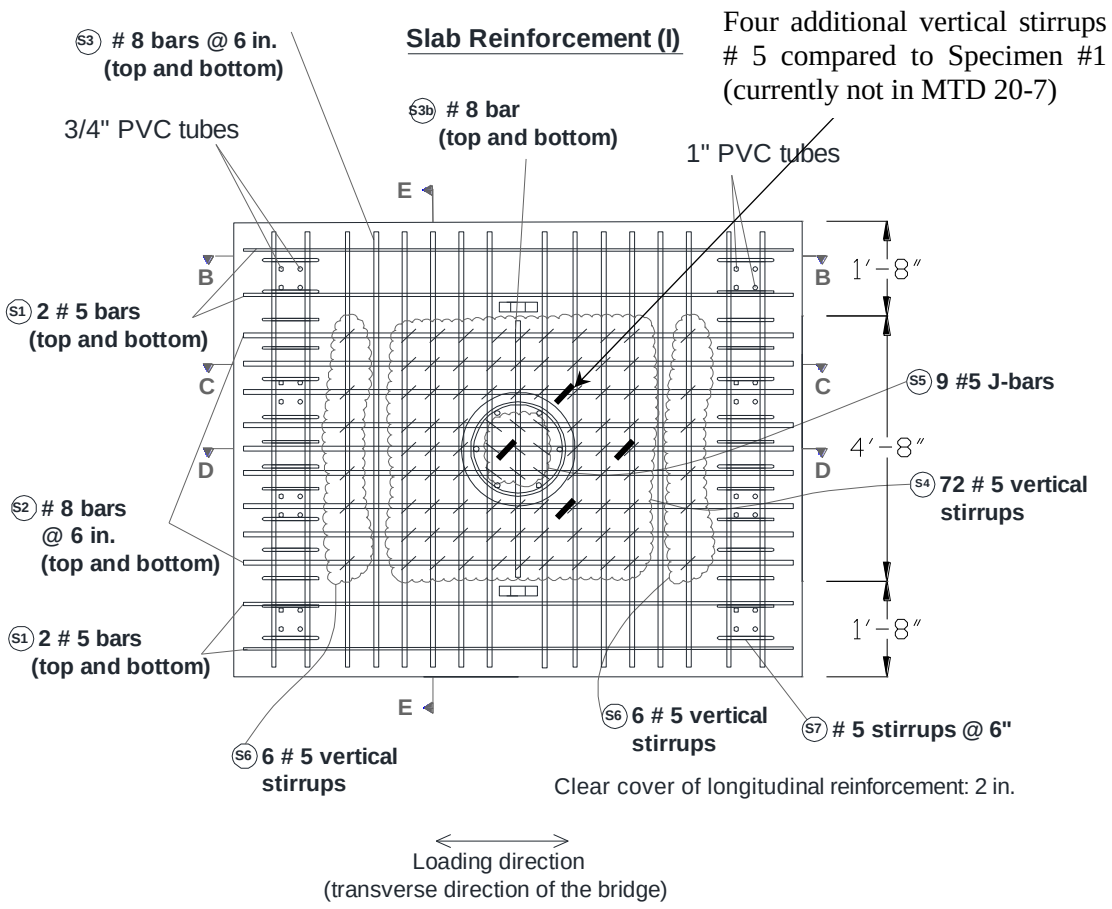

Figure A.10 – Plan view of slab reinforcement for Specimen #2

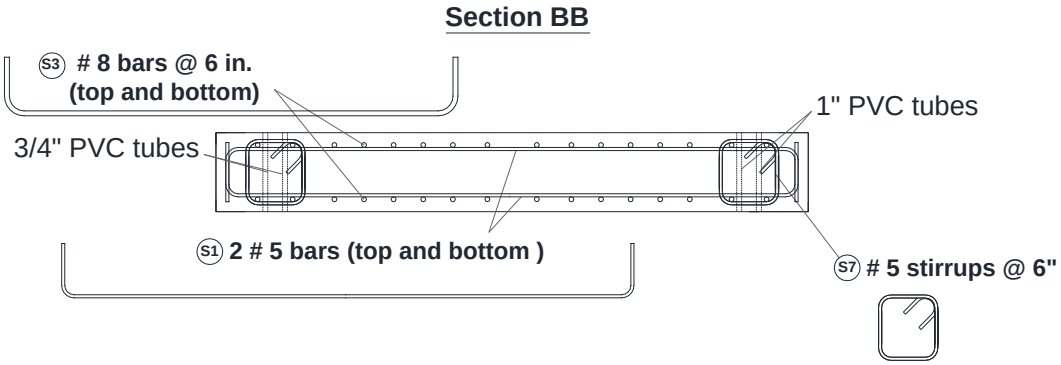

Figure A.11 – Elevation view of slab reinforcement at Section BB for Specimen #2

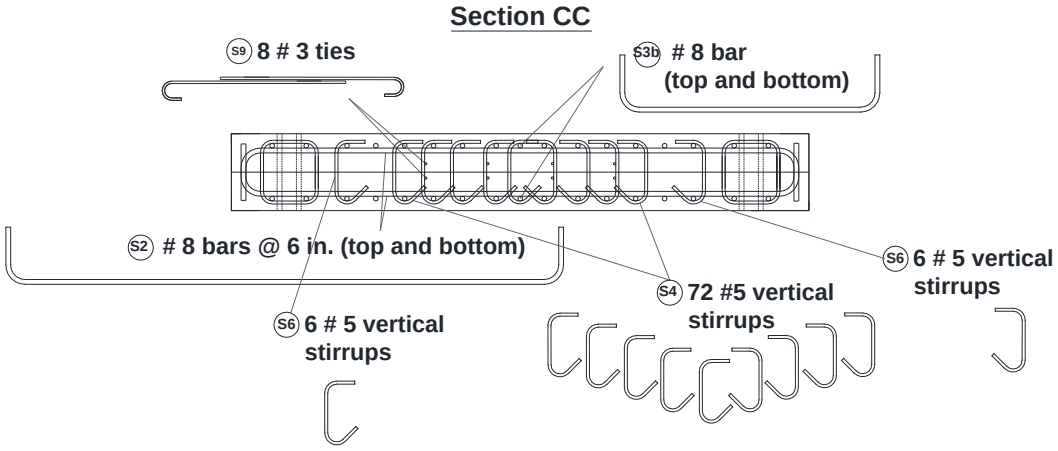

Figure A.12 – Elevation view of slab reinforcement at Section CC for Specimen #2

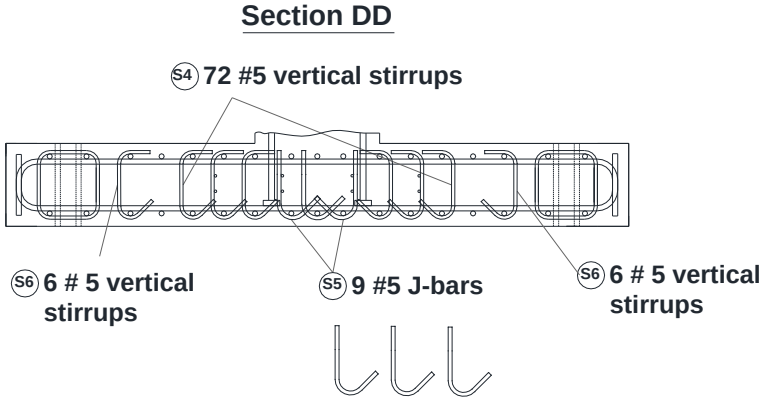

Figure A.13 – Elevation view of slab reinforcement at Section DD for Specimen #2

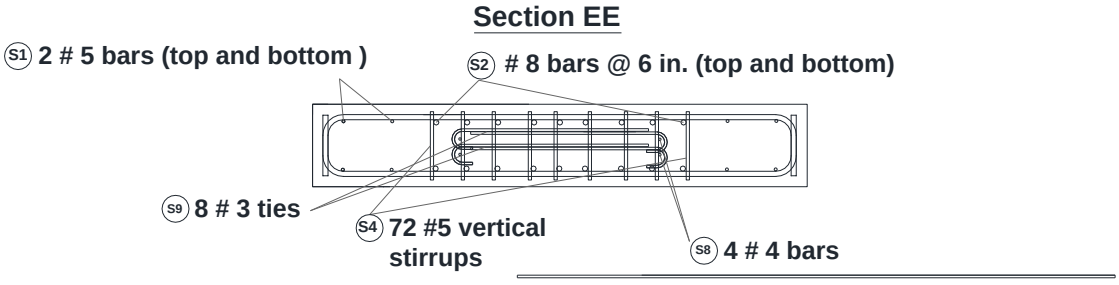

Figure A.14 – Elevation view of slab reinforcement at Section EE for Specimen #2

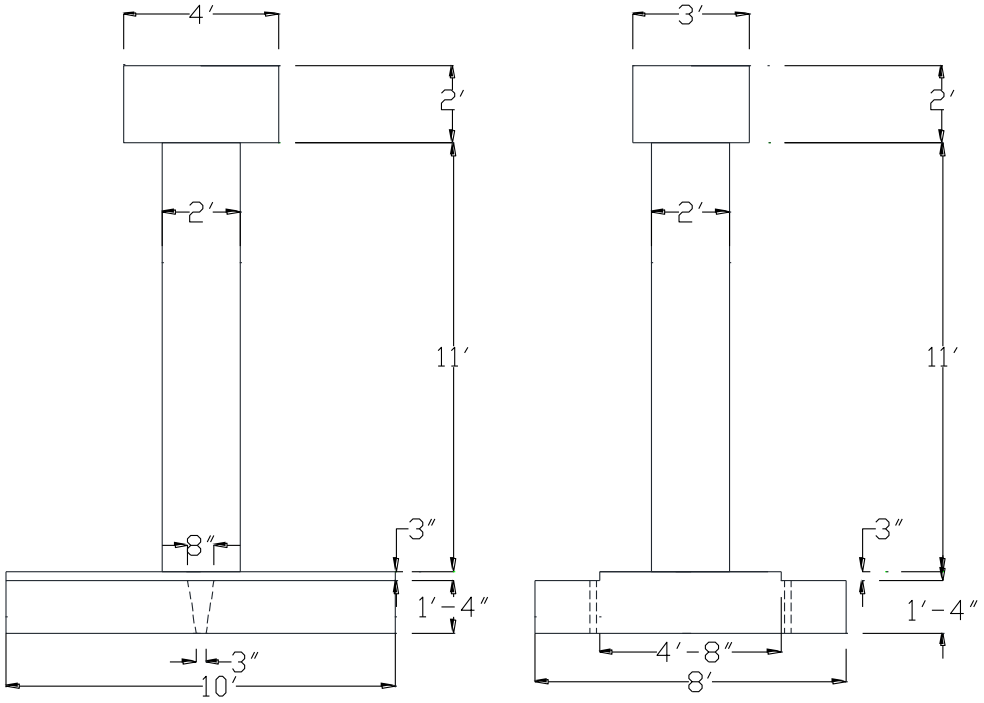

(a) Elevation view AA (east) (b) Elevation view BB (south)

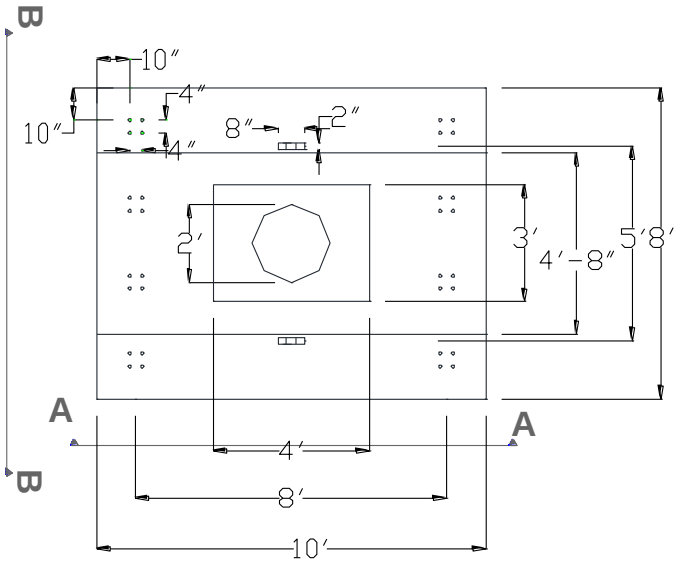

(c) plan view

Figure A.15 – Plan and elevation views for Specimen #3

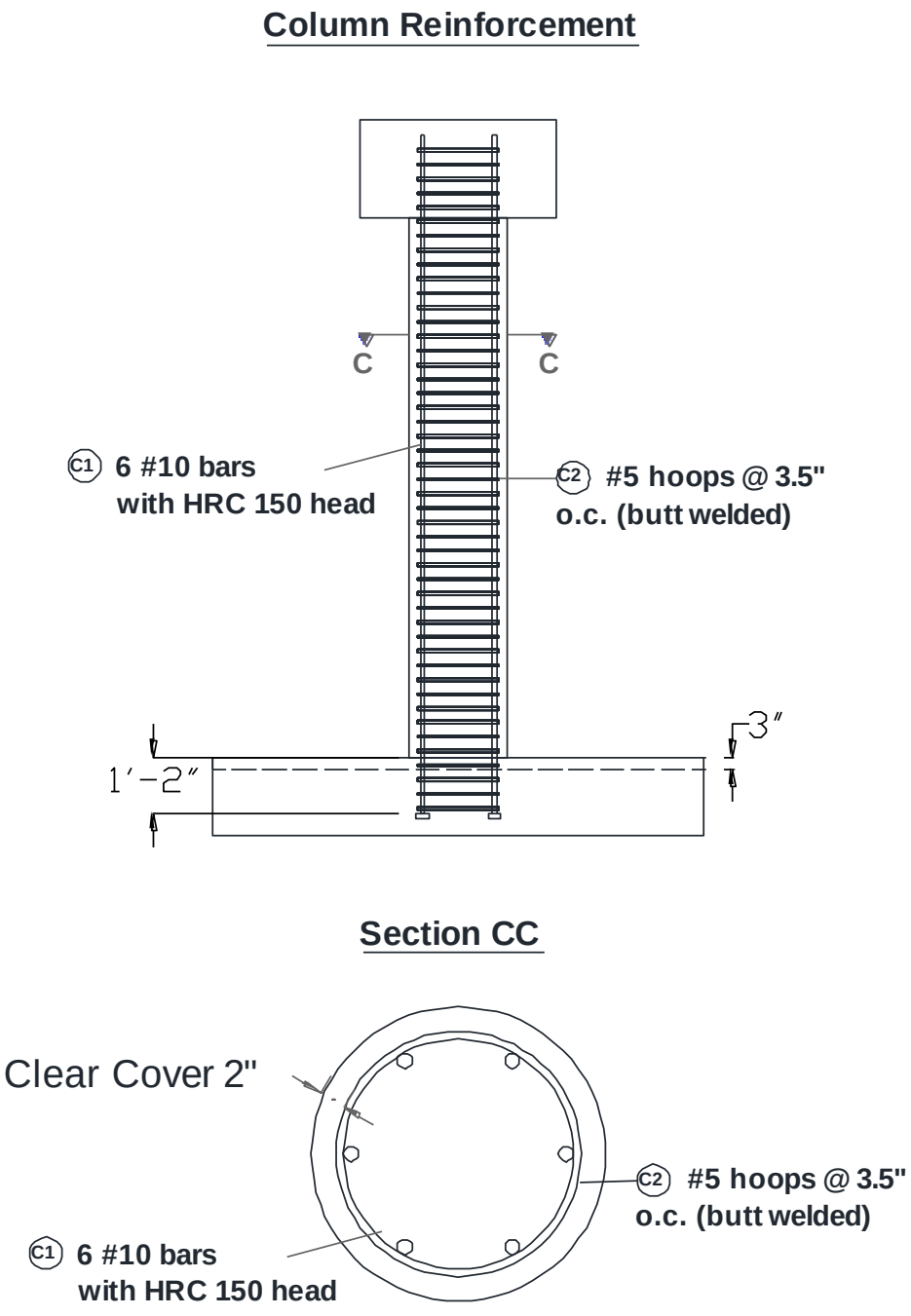

Figure A.16 – Column reinforcement for Specimen #3

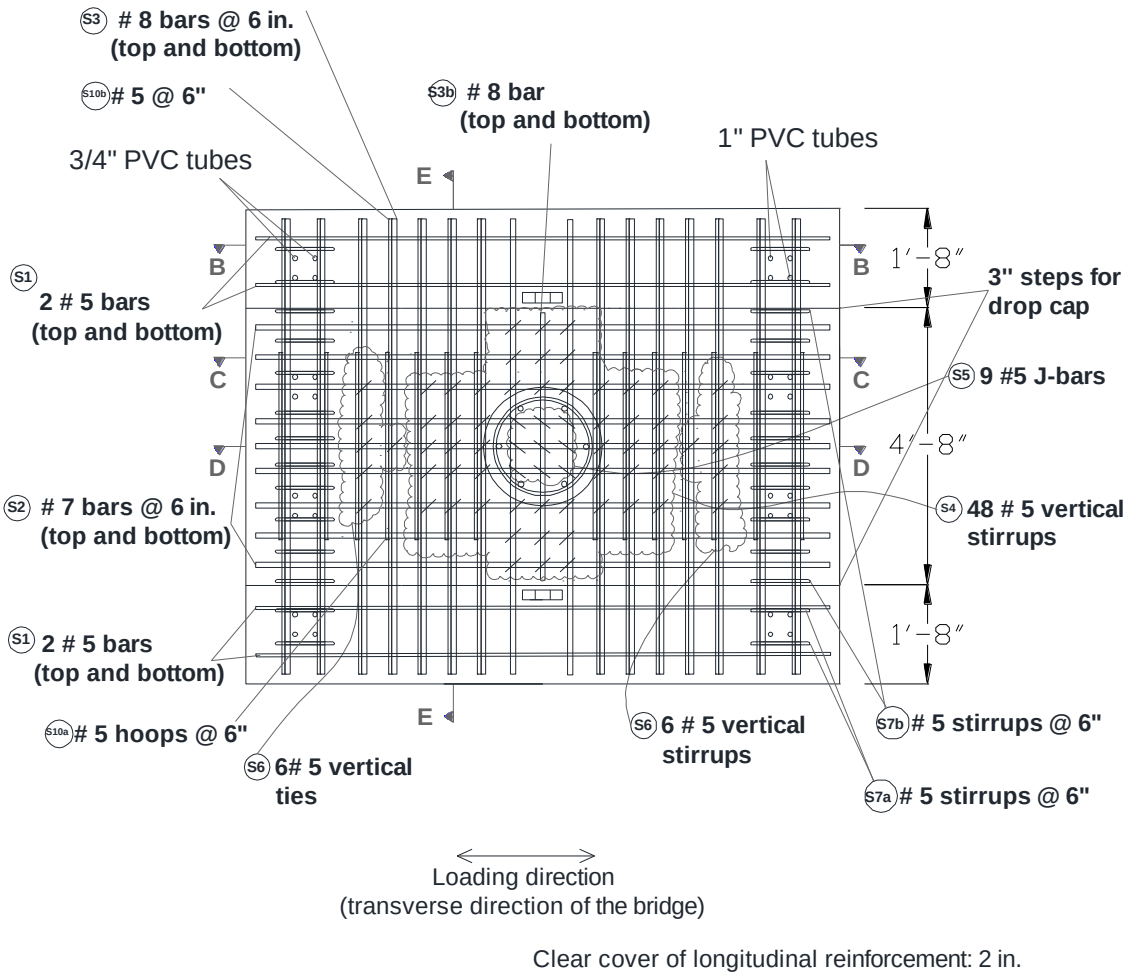

Figure A.17 – Plan view of slab reinforcement for Specimen #3

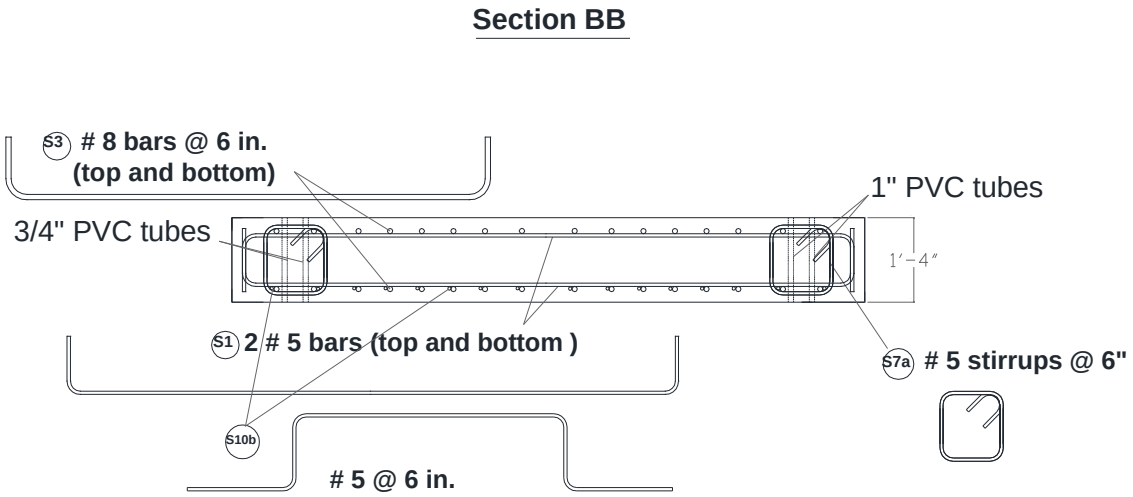

Figure A.18 – Elevation view of slab reinforcement at Section BB for Specimen #3

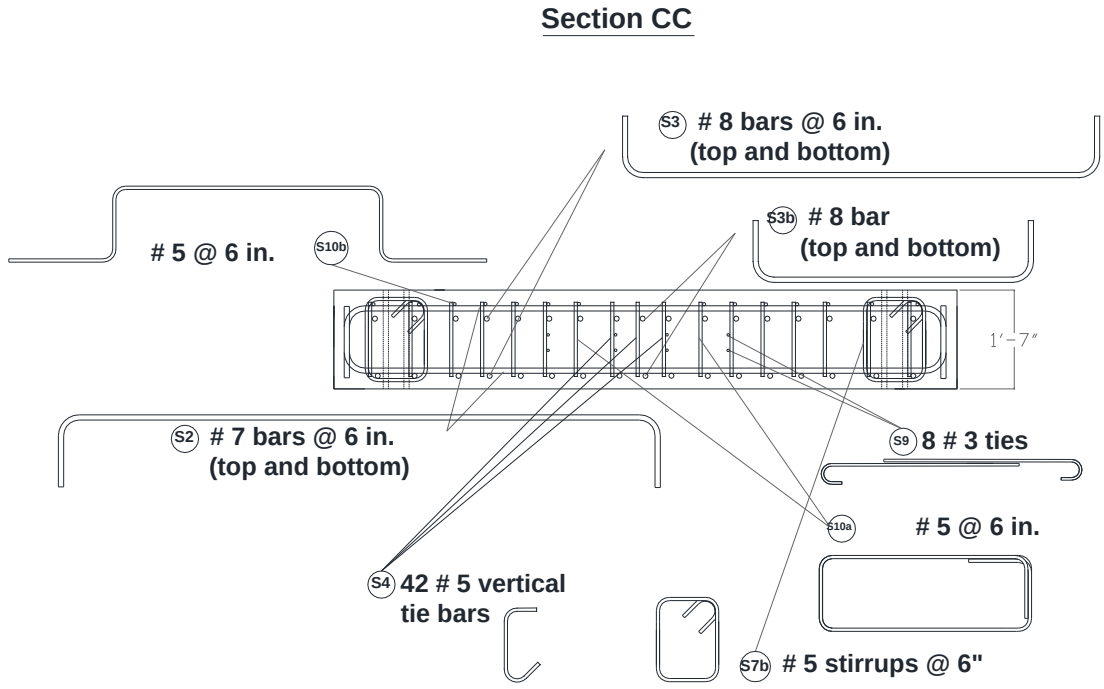

Figure A.19 – Elevation view of slab reinforcement at Section CC for Specimen #3

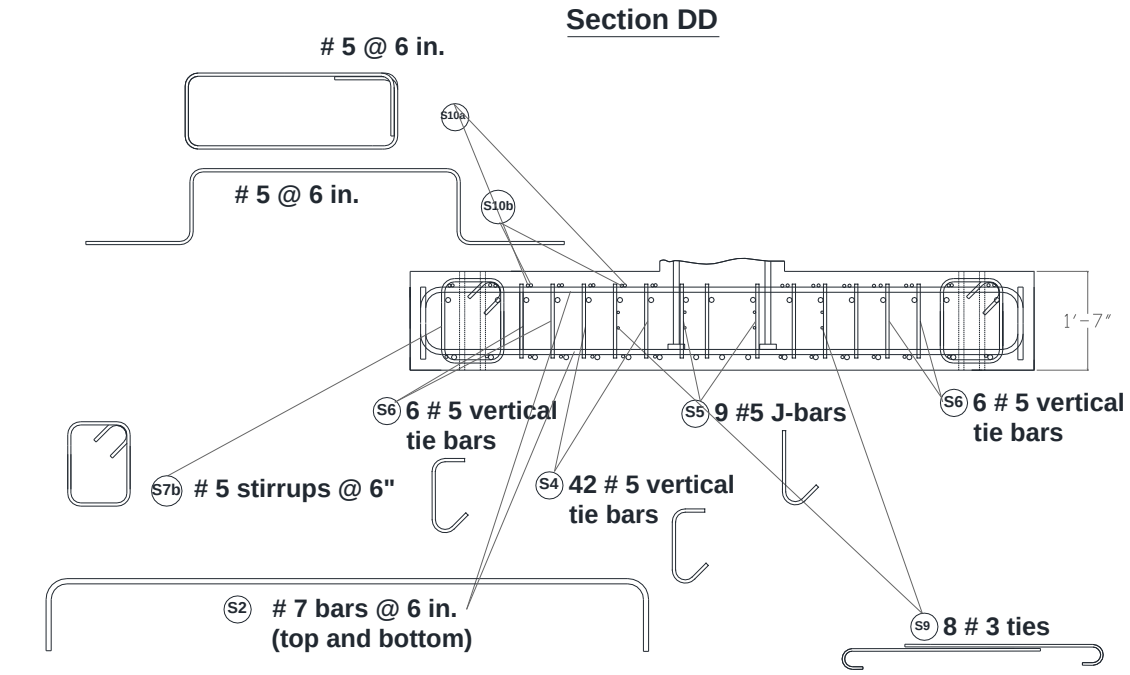

Figure A.20 – Elevation view of slab reinforcement at Section DD for Specimen #3

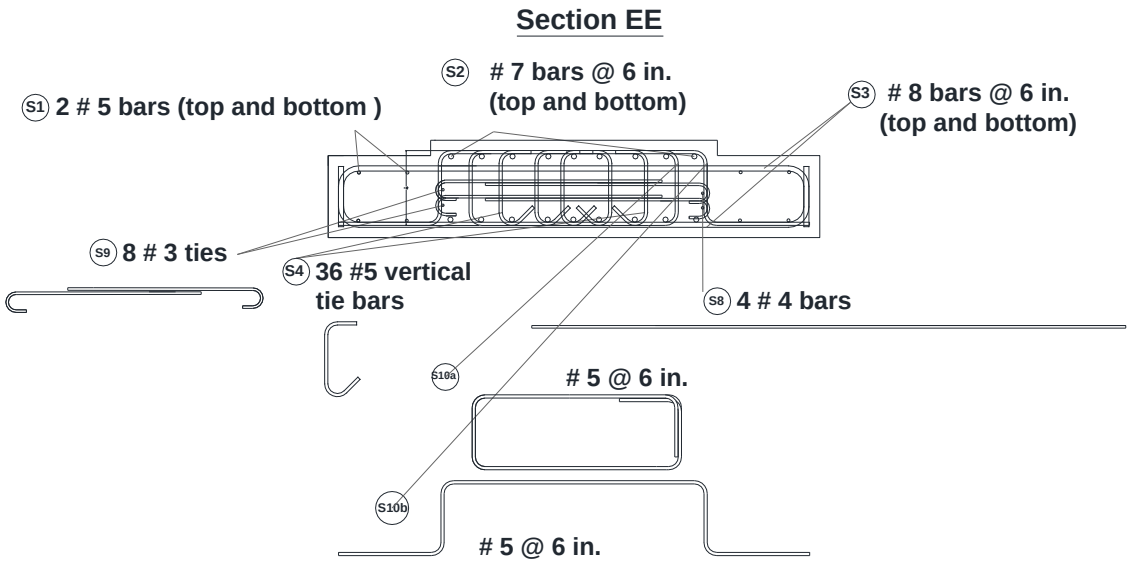

Figure A.21 – Elevation view of slab reinforcement at Section EE for Specimen #3

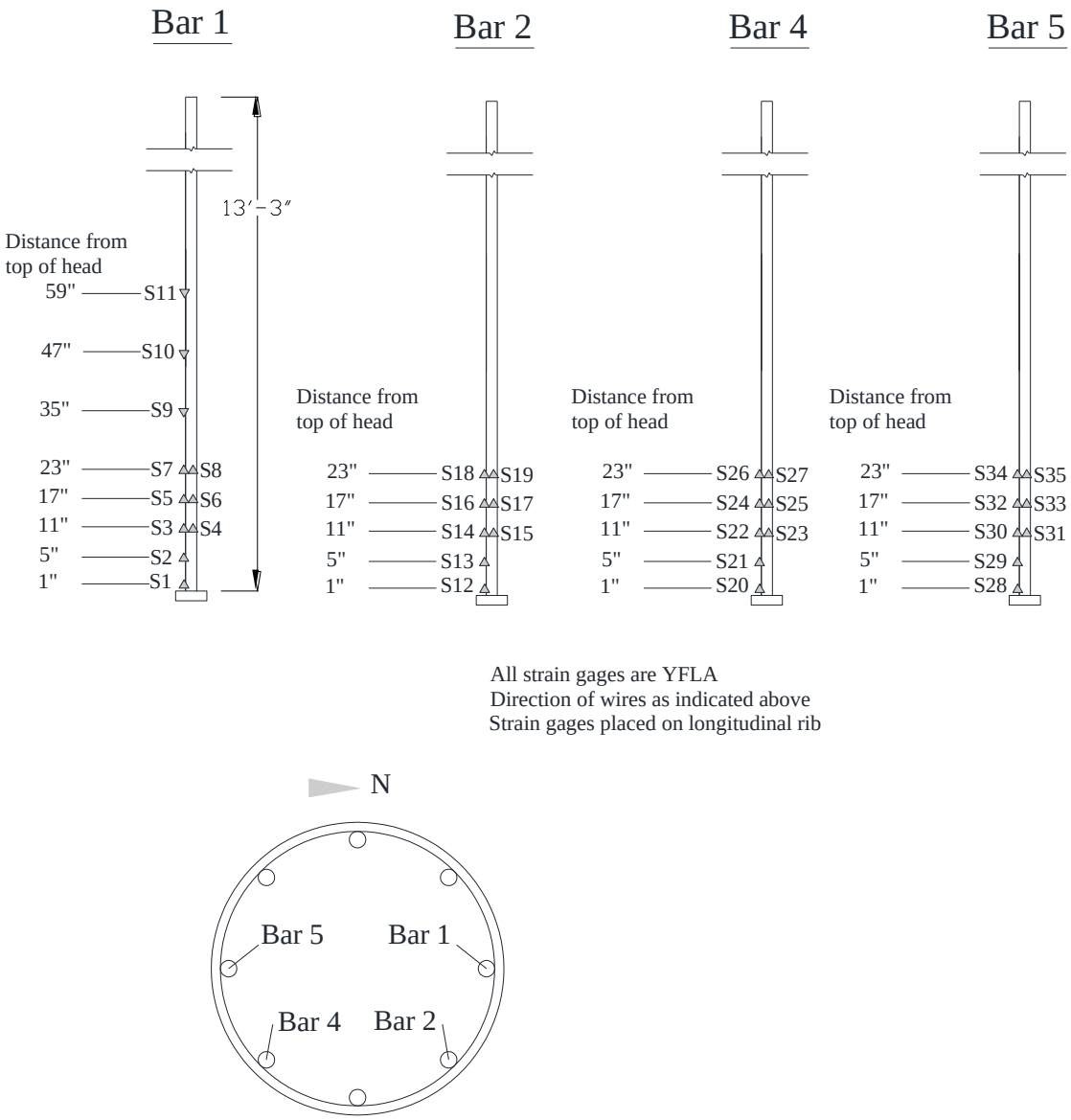

Figure A.22 – Strain gages on longitudinal bars in the column of Specimen #1

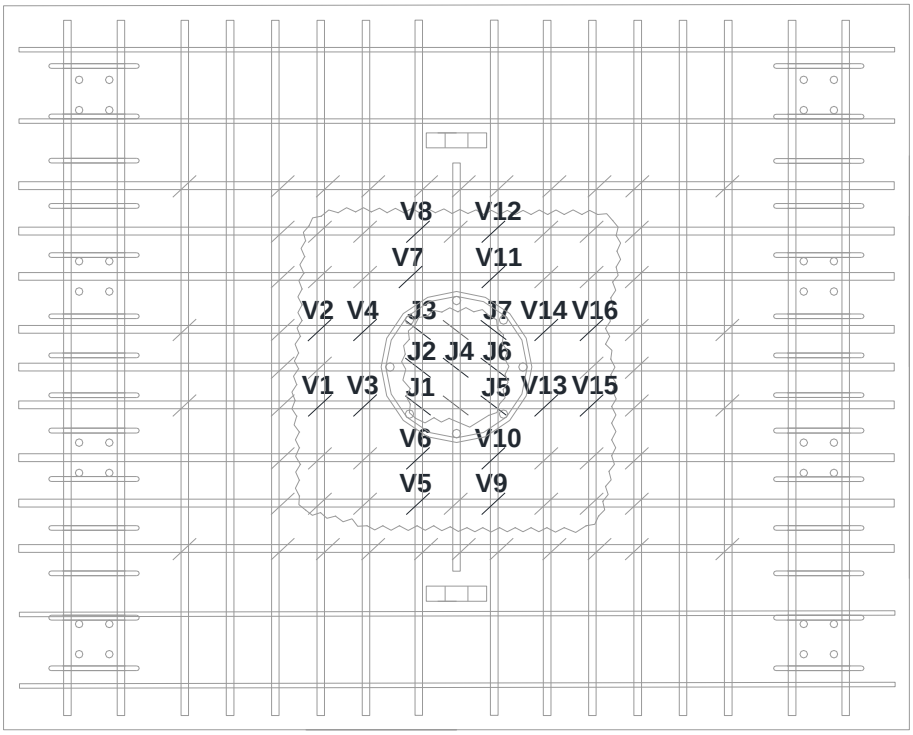

7 No. 5 J-bars instrumented

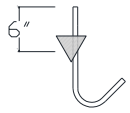

16 No. 5 vertical stirrups instrumented

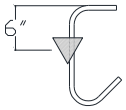

Figure A.23 – Strain gages on J-bars and vertical stirrups in the slab of Specimen #1

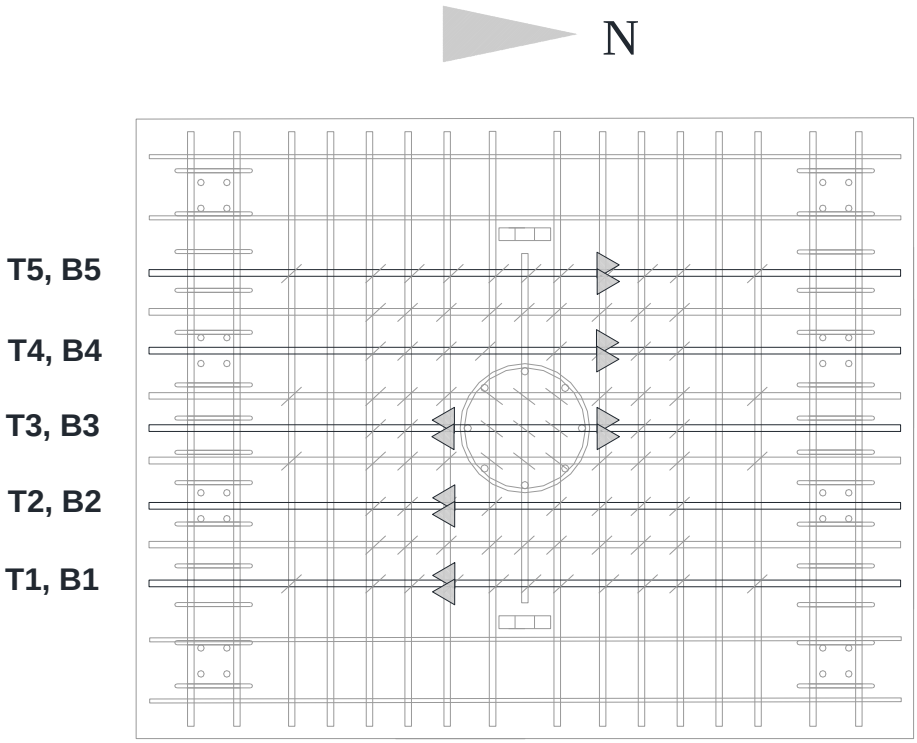

Figure A.24 – Strain gages on the longitudinal bars in the slab of Specimen #1

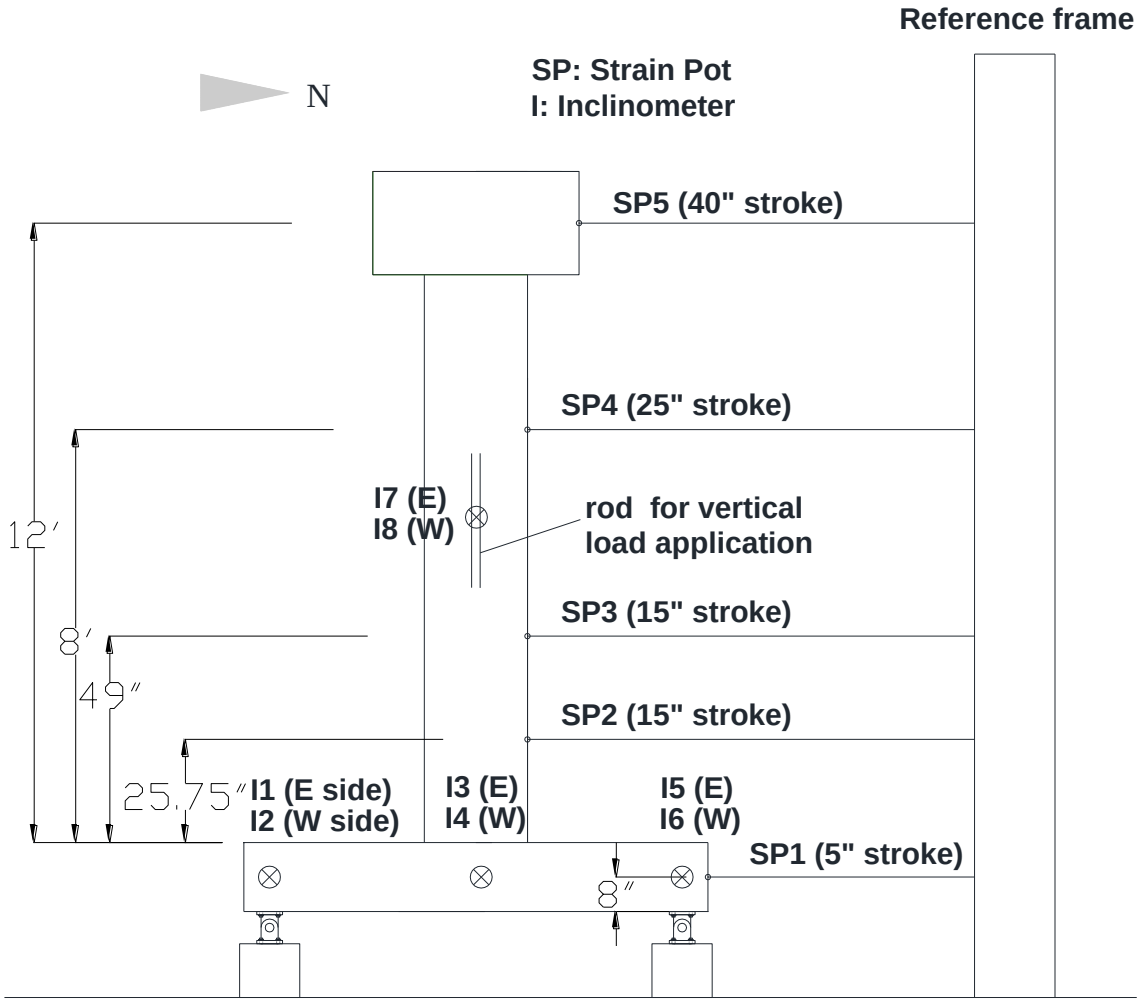

Figure A.25 – Strain pots and inclinometers mounted on Specimens #1

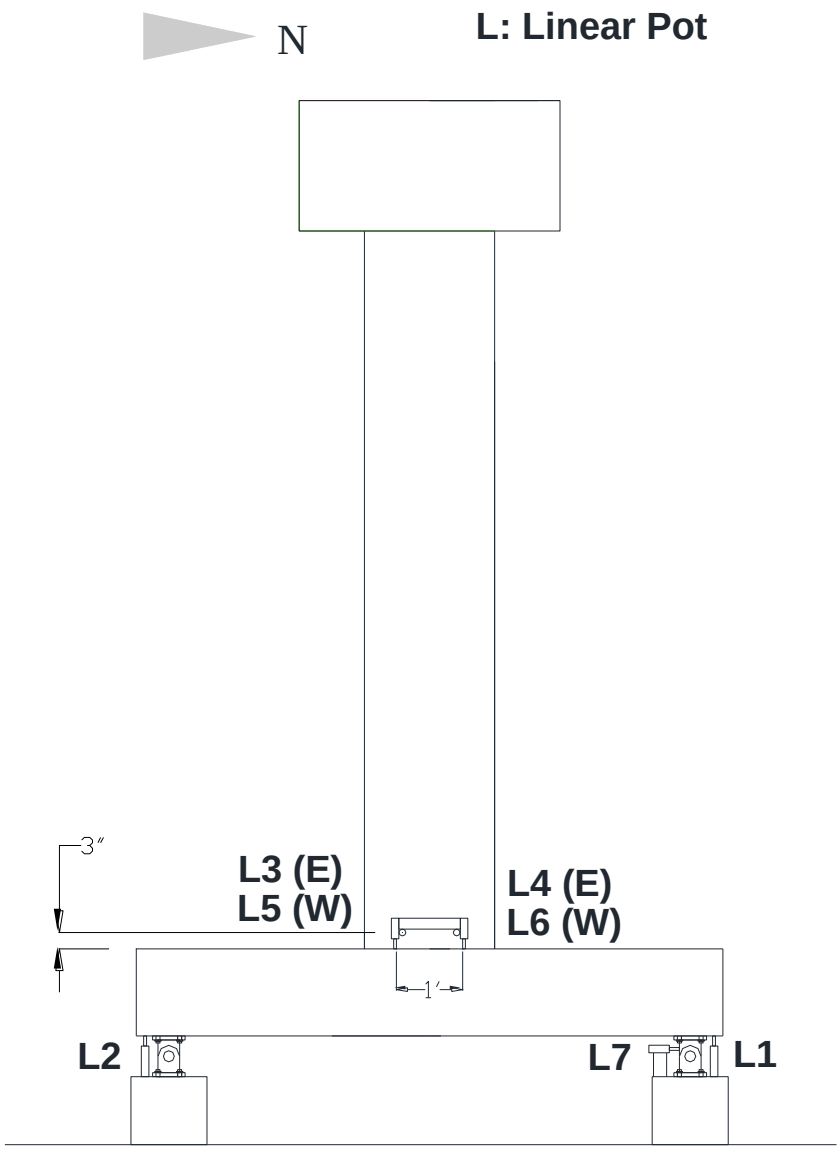

Figure A.26 – Linear pots mounted on Specimen #1

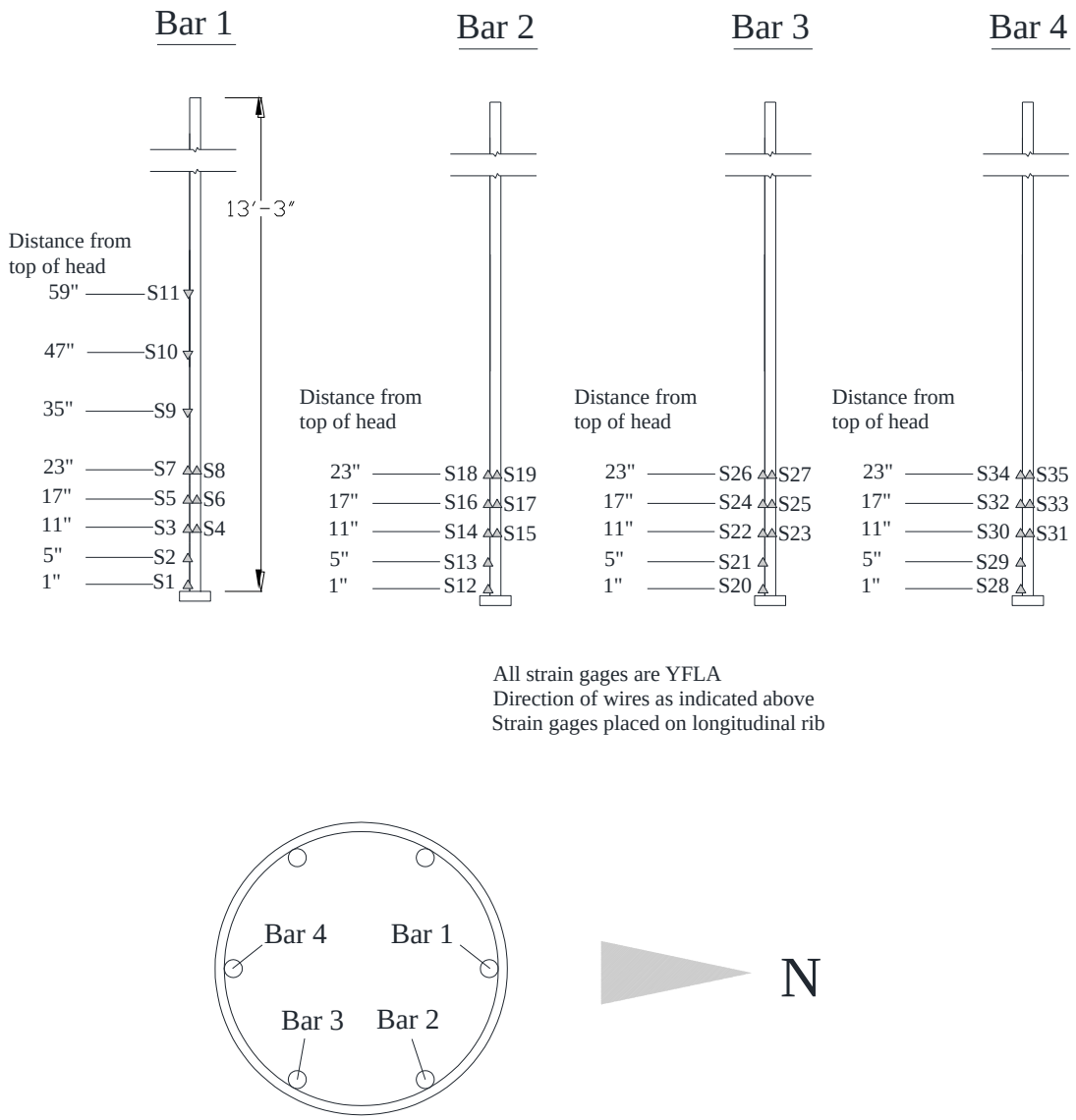

Figure A.27 – Strain gages on longitudinal bars in the column of Specimen #2

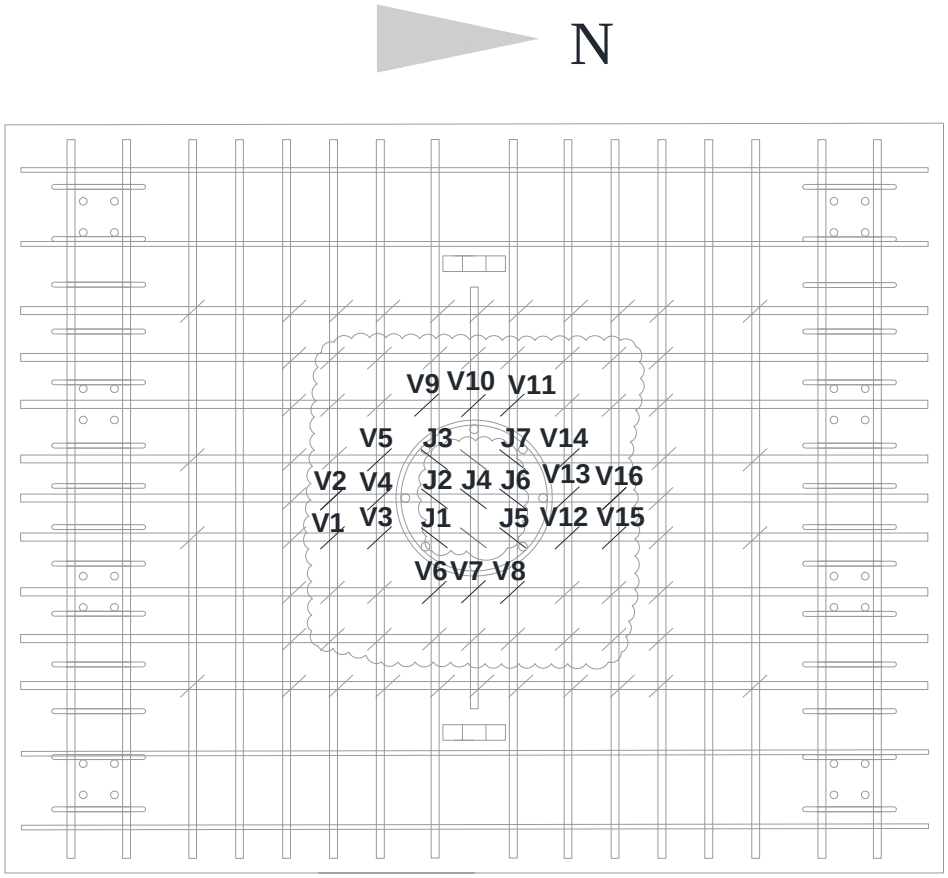

7 No. 5 J-bars instrumented

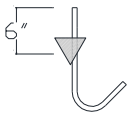

16 No. 5 vertical ties instrumented

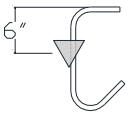

Figure A.28 – Strain gages on J-bars and vertical stirrups in the slab of Specimen #2

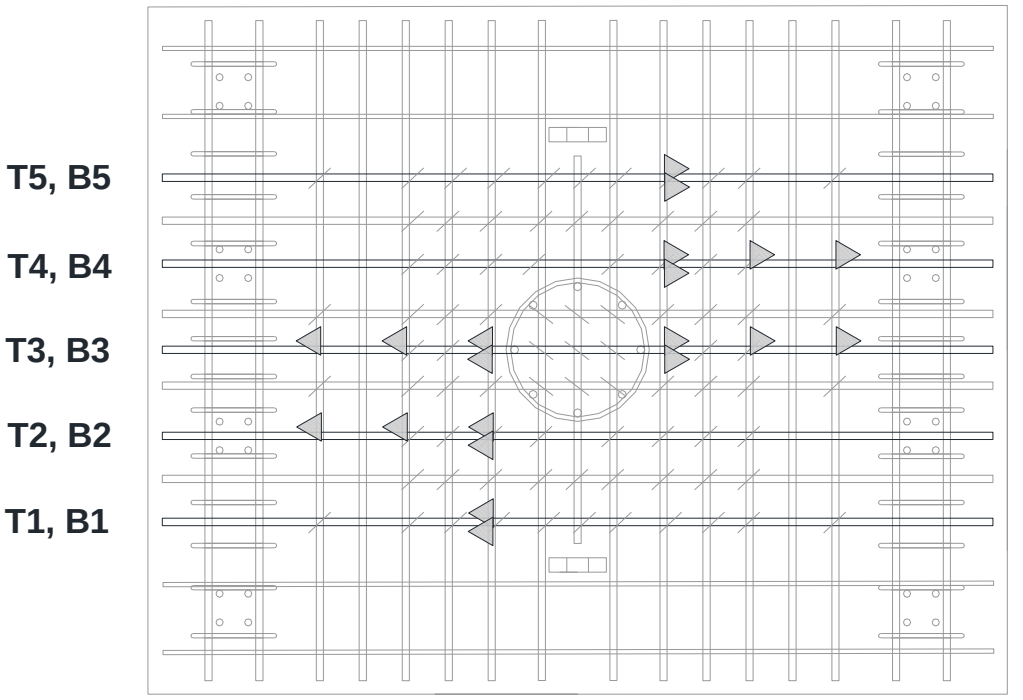

Figure A.29 – Strain gages on the longitudinal bars in the slab of Specimen #2

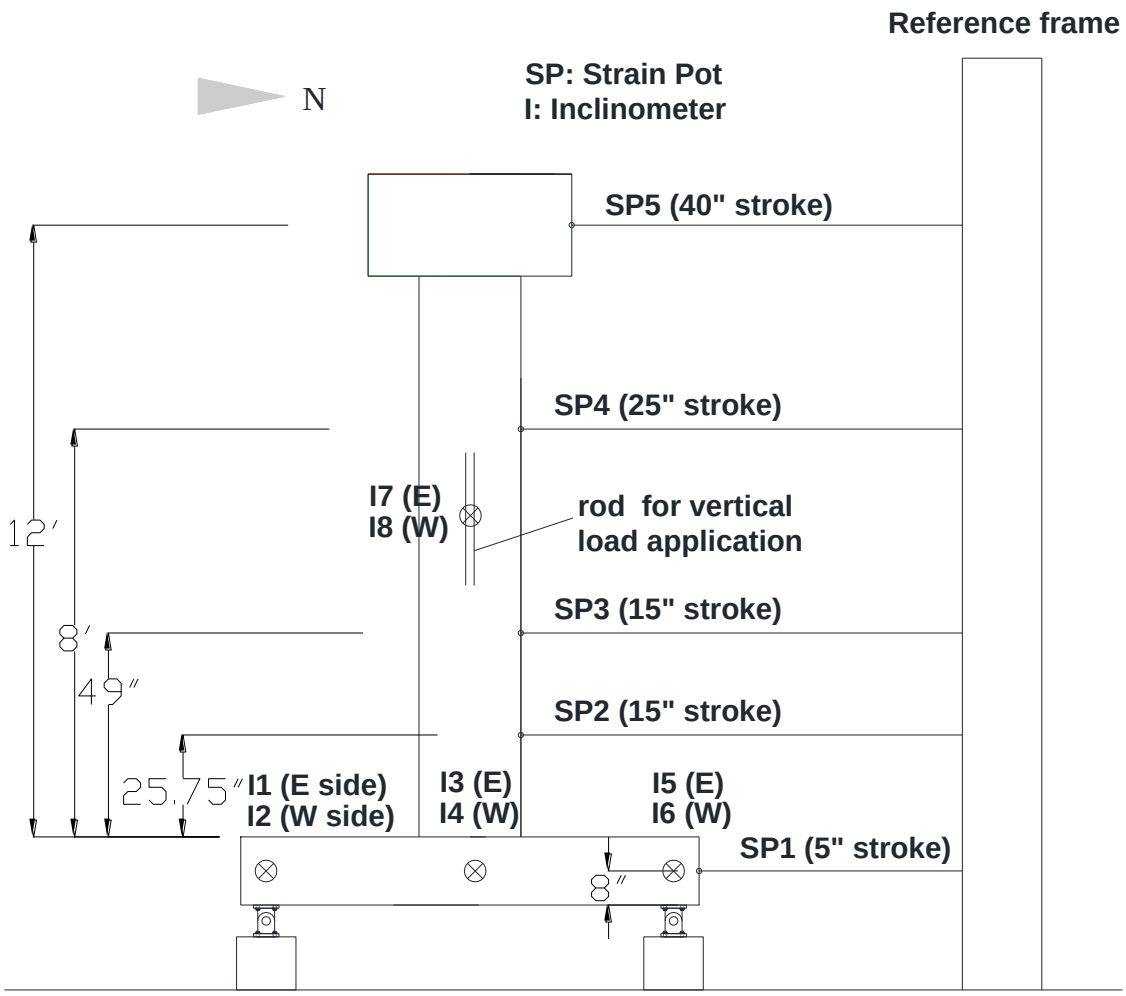

Figure A.30 – Strain pots and inclinometers mounted on Specimens #2

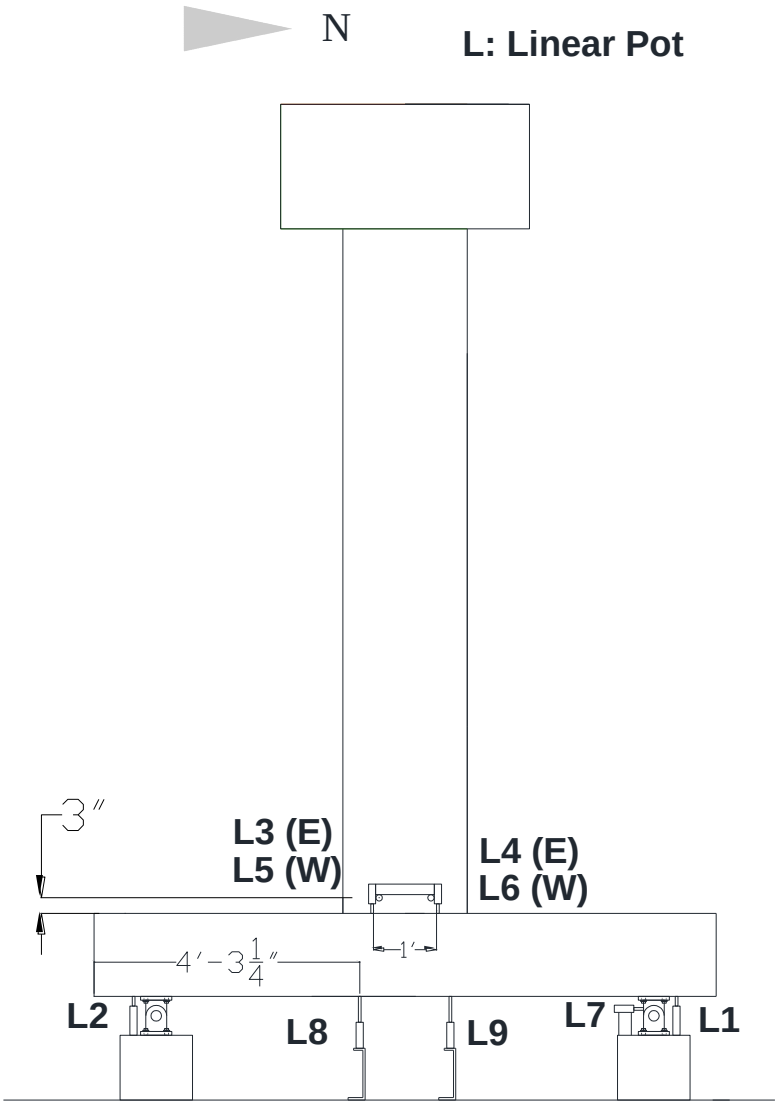

Figure A.31 – Linear pots mounted on Specimen #2

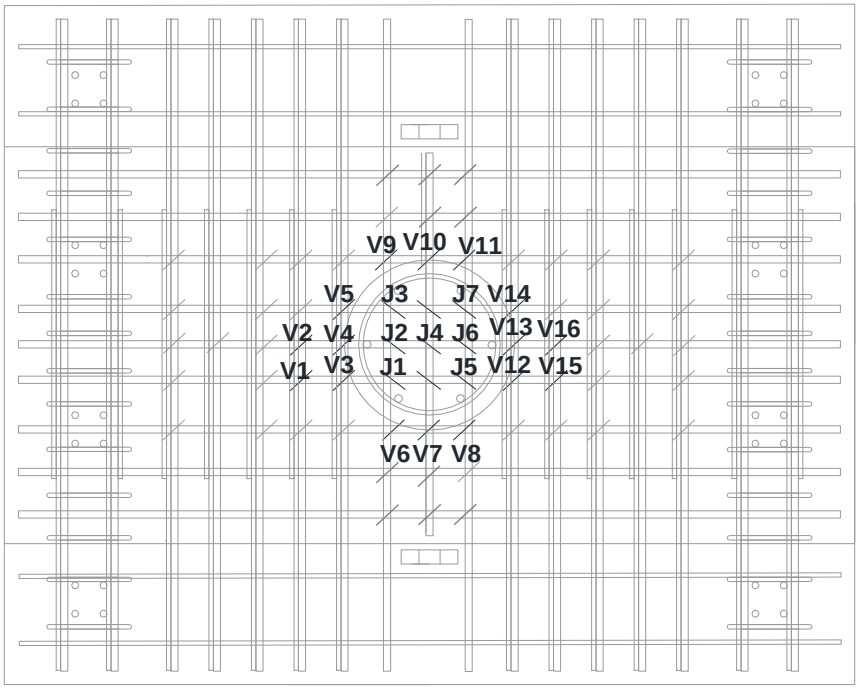

Figure A.32 – Strain gages on J-bars and vertical stirrups in the slab of Specimen #3

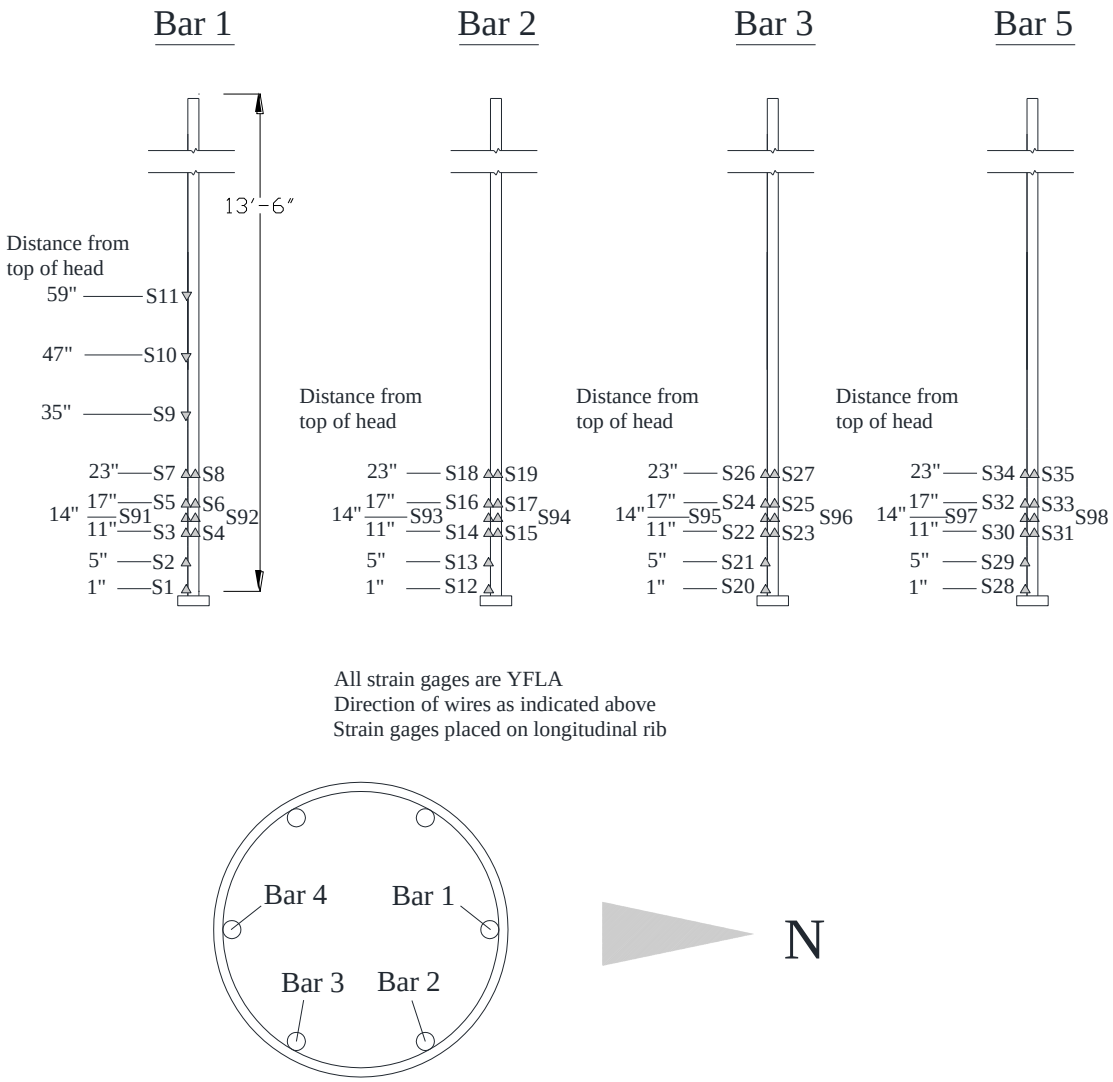

Figure A.33 – Strain gages on longitudinal bars in the column of Specimen #3

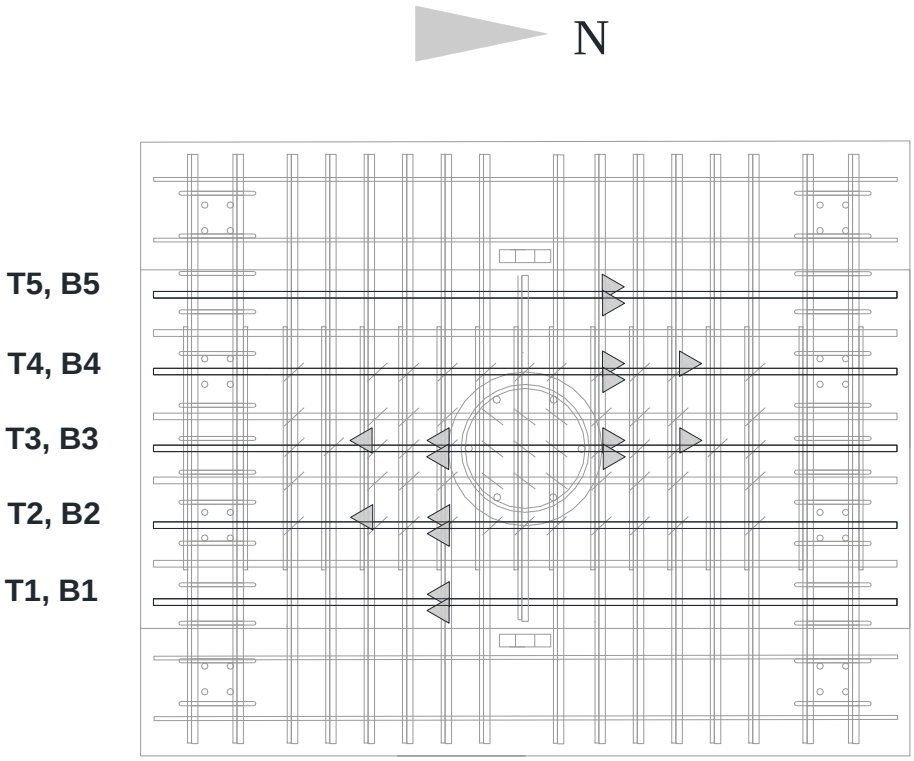

Figure A.34 – Strain gages on the longitudinal bars in the slab of Specimen #3

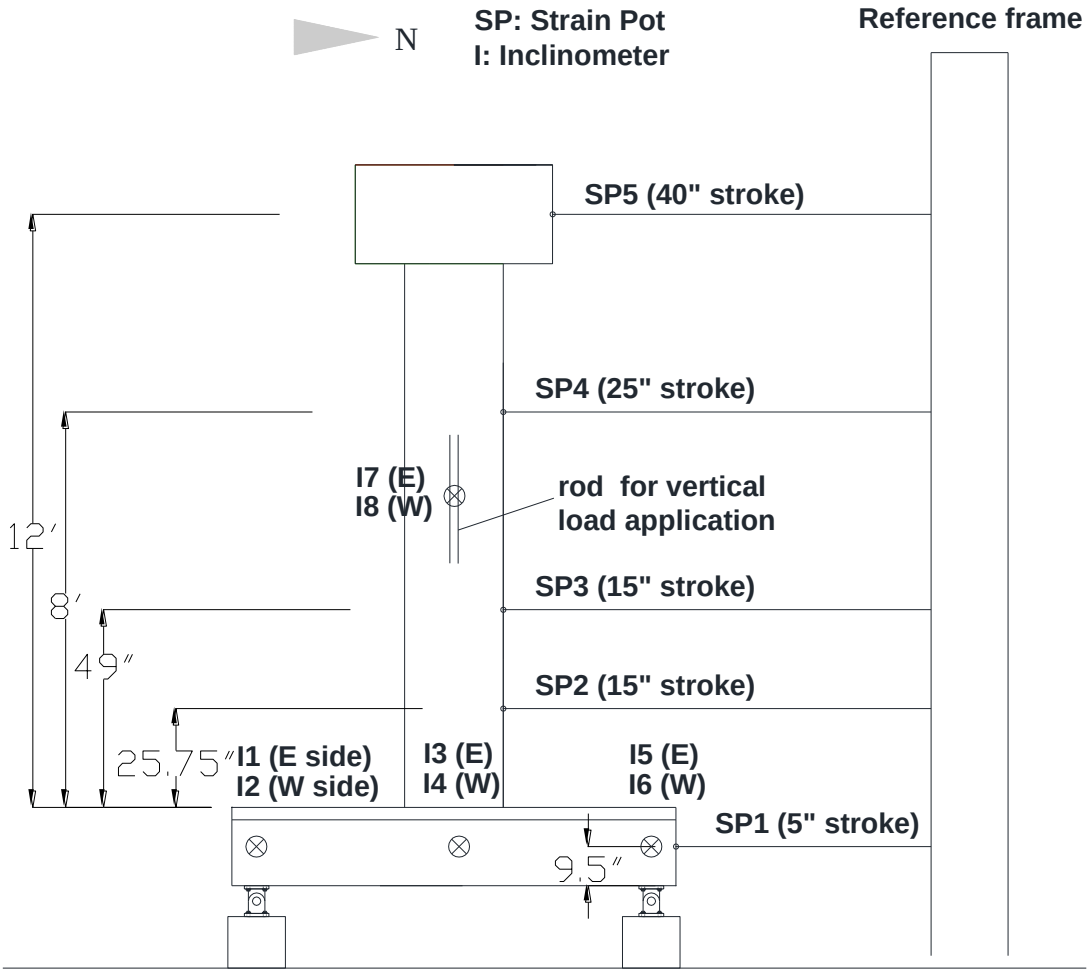

Figure A.35 – Strain pots and inclinometers mounted on Specimen #3

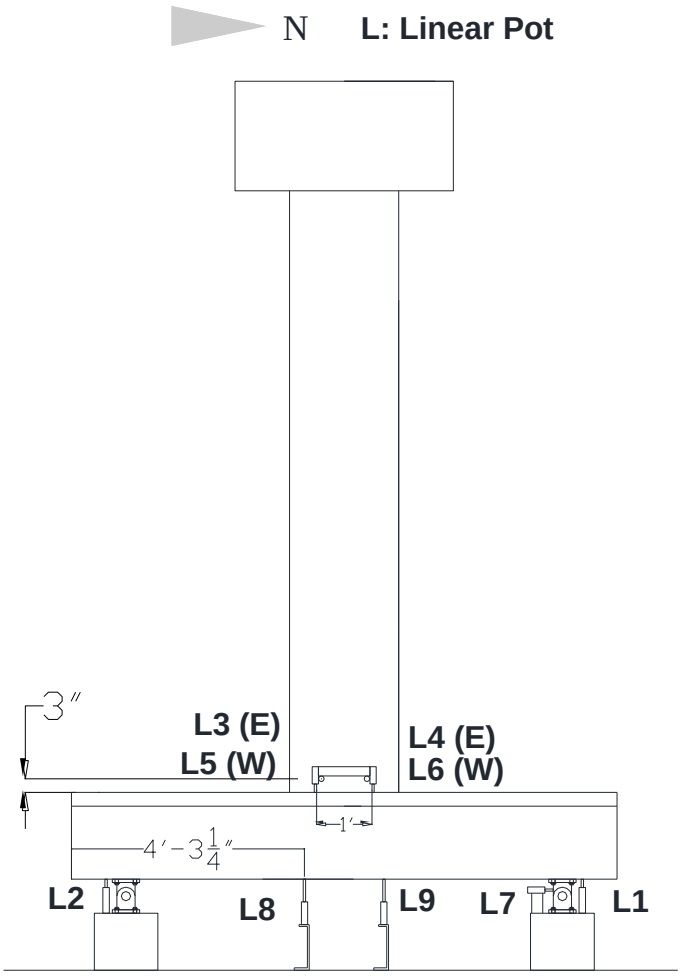

Figure A.36 – Linear pots mounted on Specimen #3

REFERENCES

ACI (2011), *Building Code Requirements for Structural Concrete (ACI 318-11)*. American Concrete Institute, Farmington Hills, MI.

Aktan, A. E., Karlsson, B. I., Sozen, M. A. (1973), " Stress-Strain Relationships of Reinforcing Bars Subjected to Large Strain Reversals", *Report UILU-ENG-73-2014*, University of Illinois at Urbana-Champaign.

AASHTO (2014), *AASHTO LRFD Bridge Design Specifications*. American Association of State Highway and Transportation Officials, Washington, DC.

Ayoub, M. and Sanders, D. (2010), "Behavior of Pile Extension Connections to Slab Bridges under Cyclic Loafing." *UNR Report No. CCER 10-06*, Center for Earthquake Engineering Research, Department of Civil and Environmental Engineering, University of Nevada, Reno, NV.

Bashandy, T.R. (1996), "Application of Headed Bars in Concrete Members." *PhD Dissertation*, University of Texas, Austin, TX.

Bazant, Z. P. (1984), "*Microplane model for strain-controlled inelastic behavior*", J. Wiley, London, Chapter 3, pp. 45-59, edited by C.S. Desai and R. H. Gallagher.

Bazant, Z. P. and Oh, B. H. (1985), "Microplane model for progressive fracture of concrete and rock", *Journal of Engineering Mechanics, ASCE*, 111, 559-582.

Brocca, F. C. and Bazant, Z. P. (2000), "Microplane constitutive model and metal plasticity", *ASME Applied Mechanics Reviews*, 53(10), pp. 265-281.

Brown, J. and Kunnath, S. K. (2004), "Low-cycle Fatigue Behavior of Reinforcing Bars", *ACI Materials Journal*, Vol. 101, No. 6, pp. 457-466.

Caltrans (2004), *Bridge Design Specifications*, California Department of Transportation, Sacramento, CA.

Caltrans (2009), "Design of Standard Slab Bridge." *Bridge Design Aids (BDA) 4-10*, California Department of Transportation, Sacramento, CA.

Caltrans (2013), *Caltrans Seismic Design Criteria*, Version 1.7, California Department of Transportation.

Caltrans (2013), "Seismic Requirements of Head Reinforcement." *Memo to Designers (MTD) 20-19 (Draft)*, California Department of Transportation, Sacramento, CA.

Caltrans (2014), "Seismic Design of Slab Bridges." *Memo to Designers (MTD) 20-7*, California Department of Transportation, Sacramento, CA.

Caner, F. C. and Bazant, Z. P. (2013a), "Microplane Model M7 for Plain Concrete. I: Formulation", *J. Eng. Mech.*, 139(12), pp. 1714-1723.

Caner, F. C. and Bazant, Z. P. (2013b), "Microplane Model M7 for Plain Concrete. II: Calibration and Verification", *J. Eng. Mech.*, 139(12), pp. 1724-1735.

Choi, D.-U., Hong, S.-G., Lee, and C.-Y. (2002), "Test of Headed Reinforcement in Pullout," *KCI Concrete Journal*, Vol. 14, No. 3, pp.102-110.

Coffin, L. F., Jr., (1954), "A Study of the Effects of Cyclic Thermal Stresses in a Ductile Metal", *ASME Transactions*, Vol. 16, pp. 931-950.

De Vries, R.A. (1996), "Anchorage of Headed Reinforcement in Concrete." *Ph.D. Dissertation*, University of Texas, Austin, TX.

De Vries, R.A., Jirsa, J.O., and Bashandy, T. (1999), "Anchorage Capacity in Concrete of Headed Reinforcement with Shallow Embedments." *ACI Structural Journal*, Vol. 96(5), 728-736.

Dhakal, R., and Maekawa, K. (2002), "Modeling for Postyield Buckling of Reinforcement", *J. Struct. Eng.*, 18, pp. 1139-1147.

Dodd, L. L., Restrepo-Posada, J. I. (1995), "Model for Predicting Cyclic Behavior of Reinforcing Steel", *Journal of Structural Engineering*, Vol. 121, No. 3, pp. 433-445.

Drucker, D. C., Prager, W. (1952), "Soil Mechanics and Plastic Analysis or Limit Design", *Quarterly of Applied Mathematics*, Vol. X, No. 2, pp. 157-165.

Eligehausen, R., Popov, E. P., Bertero, V. V. (1983), "Local Bond Stress-Slip Relationships of Deformed Bars under Generalized Excitations", *Report No. UCB/EERC-83/23*, Earthquake Engineering Research Center, University of California, Berkeley.

Fei, J., Darwin, D. (1999), "Fatigue of High Relative Rib Area Reinforcing Bars", *SM Report 54*, University of Kansas Center for Research.

Filippou, F. C., Bertero, V. V., Popov, E. P. (1983), "Effects of Bond Deterioration on Hysteretic Behavior of Reinforced Concrete Joints", *Report No. UCB/EERC-83/19*, University of California, Berkeley.

Fuchs, W., Eligehausen, R., and Breen, J.E. (1995), "Concrete Capacity Design (CCD) Approach for Fastening to Concrete." *ACI Structural Journal*, Vol. 92(1), 73-94.

Helgason, T., Hanson, J. M., Somes, N. F., Corley, G., and Hognestad, E. (1976), "Fatigue Strength of High-Yield Reinforcing Bars," *NCHRP Report* 164, Transportation Research Board, Washington D.C.

Hurblut, B. J. (1985), "Experimental and computational investigation of strain-softening in concrete", *MS Thesis*, University of Colorado, Boulder, CO.

Kang.T.H.-K., Ha, S.-S., and Choi,D.-U. (2010), "Bar Pullout Tests and Seismic Tests of Small-Headed Bars in Beam-Column Joints," ACI Structural Journal, V. 107, No. 1, pp. 32-42.

Karthik, M. M., Mander, J. B. (2011), "Stress-Block Parameters for Unconfined and Confined Concrete Based on a Unified Stress-Strain Model", *Journal of Structural Engineering*, pp. 270-273.

Kent, D. C., Park, R. (1973), "Cyclic Load Behavior of Reinforcing Steel" *Strain*, Vol. 9, No. 3, pp. 98-103.

Koh, S. K. and Stephens, R. I. (1991), "Mean Stress Effects on Low-cycle Fatigue for a High Strength Steel", *Journal of Fatigue Fracture of Engineering Materials*, Vol. 14, No. 4, pp.413-428.

Kunnath, S., Heo, Y., and Mohle, J. (2009a), "Nonlinear Uniaxial Material Model for Reinforcing Steel Bars", *J. Struct. Eng.*, 135(4), pp. 335-343.

Kunnath. S. K., Kanvinde, A., Xiao, Y., Zhang, G. (2009b), "Effects of Buckling and Low-cycle Fatigue on Seismic Performance of Reinforcing Bars and Mechanical Couples for Critical Structural Members", *Report No. UCD-SESM-08-01*, University of California at Davis.

Lee, J., Fenves, G. L. (1998), "Plastic-Damage Model for Cyclic Loading of Concrete Structures", *Journal of Engineering Mechanics*, pp. 892-900.

Lowes, L.N., Moehle, J.P., Govindjee, S. (2004), "Concrete-Steel Bond Model for Use in Finite Element Modeling of Reinforced Concrete Structures," ACI Structural Journal, Vol. 101, No. 4, pp. 501-511.

Lubliner, J., Oliver, J., Oller, S., Onate, E. (1989), "A Plastic-Damage Model for Concrete", *International Journal of Solids and Structures*, Vol. 25, No. 3, pp. 299-326.

MacGregor, J. G., Jhamb, I. C., and Nuttall, N. (1971), "Fatigue Strength of Hot-Rolled Reinforcing Bars", ACI Journal, Proceedings Vol. 68, No. 3, Mar., pp. 169-179.

Mander, J. B., Priestley, M. J. N., Park, R. (1988a), "Theoretical Stress-Strain Model for Confined Concrete" *Journal of Structural Engineering*, Vol. 114, No. 8, pp. 1804-1826.

Mander, J. B., Priestley, M. J. N., Park, R. (1988b), "Observed Stress-Strain Behavior pf Confined Concrete" *Journal of Structural Engineering*, Vol. 114, No. 8, pp. 1827-1849.

Manson, S. S. (1953), "Behavior of Materials under Conditions of Thermal Stresses", *Heat Transfer Symposium*, University of Michigan Engineering Research Institute, Ann Arbor, Michigan.

Menegotto, M., Pinto, P. E. (1973), "Method of Analysis for Cyclically Loaded Reinforced Concrete Plane Frames Including Changes in Geometry and Non-Elastic Behavior of Elements under Combined Normal Force and Bending", *IABSE*, Final Report, Lisbon.

Miner, M. A. (1945), "Cumulative Damage in Fatigue", *Journal of Applied Mechanics*, Vol. 12, No. 3, pp.159-164.

Monti, G., Nuti, C. (1992), "Nonlinear Cyclic Behavior of Reinforcing Bars Including Buckling", *Journal of Structural Engineering*, Vol.118, No. 12, pp. 3268-3284.

Murcia-Delso, J., and Shing, P. B. (2015), "Bond-Slip Model for Detailed Finite-Element Analysis of Reinforced Concrete Structures", *J. Struct. Eng.*, 141(4), 04014125.

Ottosen, N. S. (1977), "A Failure Criterion for Concrete", *Journal of the Engineering Mechanics Division*, Vol. 103, No. 4, pp 527-535.

Paulay, T., Priestley, M. J. N. (1992), *Seismic Design of Reinforced Concrete and Masonry Buildings*, John Wiley & Sons, Inc.

Pfister, J. F., and Hognestad, E. (1964), "High Strength Bars as Concrete Reinforcement, Part 6: Fatigue Tests," *Journal of PCA Research & Development Laboratories*, V. 6, No. 1, pp. 65-84.

Pochanart, S., Harmon, P. (1989), "Bond-Slip Model for Generalized Excitations Including Fatigue", *ACI Materials Journal*, Vol. 86, No. 5, pp. 465-474.

Simulia (2014), Abaqus V. 6.14, Dassault Systems Simulia Corp., Providence, RI.

Stoker, J.R., Boulware, R.L., Crozier, W.F., and Swirsky, R.A. (1974), "Anchorage Devices for Large Diameter Bars." CA-DOT-TL-6626-1-73-30, Transportation Laboratory, California Division of Highways, Sacramento, CA.

Stroud, A. H. (1971), "*Approximate Calculation of Multiple Integrals*", Prentice-Hall, Englewood Clifs, NJ.

Thompson, M.K., Jirsa, J.O., Breen, J.E., and Klingner, R.E. (2002), "Anchorage Behavior of Headed Reinforcement: Literature Review." *Research Report 1855-1*, Center for Transportation Research, University of Texas, Austin, TX.

Thompson, M.K., Ziehl, M.J., Jirsa, J.O., and Breen, J.E. (2005), "CCT Nodes Anchored by Headed Bars - Part 1: Behavior of Nodes." *ACI Structural Journal*, Vol. 102(6), 808-815.

Thompson, M.K., Jirsa, J.O., and Breen, J.E. (2006a), "CCT Nodes Anchored by Headed Bars - Part 2: Capacity of Nodes." *ACI Structural Journal*, Vol. 103(1), 65-73.

Thompson, M.K., Ledesma, A., Jirsa, J.O., and Breen, J.E. (2006b), "Lap Splices Anchored by Headed Bars." *ACI Structural Journal*, Vol. 103(2), 271-279.

Thompson, M.K., Jirsa, J.O., and Breen, J.E. (2006c), "Behavior and Capacity of Headed Reinforcement." *ACI Structural Journal*, Vol. 103(4), 522-530.

van Mier J.G.M (1986), "Multiaxial strain-softening of concrete part I: fracture", *Materials and Structures*, 111(19), pp. 179-200.

Wright, J.L. and McCabe, S.L. (1997), "The Development Length and Anchorage Behavior of Headed Reinforcing Bars." *SM Report No. 44*, University of Kansas Center for Research, Inc., Lawrence, Kansas.

Yankelevsky, D.Z., Moshe, A.A., Farhey, D.N. (1992), "Mathematical Model for Bond-Slip Behavior under Cyclic Loading", *ACI Structural Journal*, Vol. 89, No. 6, pp. 692-698.